REPORT DOCUMENTATION PAGE

AFRL-SR-BL-TR-98-

0820

1. AGENCY USE ONLY (Leave Blank)	2. REPORT DATE December, 1995	3. REPORT Final

4. TITLE AND SUBTITLE
USAF Summer Research Program - 1995 Summer Faculty Research Program
Final Reports, Volume 5A, Wright Laboratory

5. FUNDING NUMBERS

6. AUTHORS
Gary Moore

7. PERFORMING ORGANIZATION NAME(S) AND ADDRESS(ES)
Research and Development Labs, Culver City, CA

8. PERFORMING ORGANIZATION REPORT NUMBER

9. SPONSORING/MONITORING AGENCY NAME(S) AND ADDRESS(ES)
AFOSR/NI
4040 Fairfax Dr, Suite 500
Arlington, VA 22203-1613

10. SPONSORING/MONITORING AGENCY REPORT NUMBER

11. SUPPLEMENTARY NOTES
Contract Number: F49620-93-C-0063

12a. DISTRIBUTION AVAILABILITY STATEMENT
Approved for Public Release

12b. DISTRIBUTION CODE

13. ABSTRACT *(Maximum 200 words)*

The United States Air Force Summer Faculty Research Program (USAF- SFRP) is designed to introduce
university, college, and technical institute faculty members to Air Force research. This is accomplished by the
faculty members being selected on a nationally advertised competitive basis during the summer intersession
period to perform research at Air Force Research Laboratory Technical Directorates and Air Force Air Logistics
Centers. Each participant provided a report of their research, and these reports are consolidated into this annual
report.

Reproduced From
Best Available Copy

14. SUBJECT TERMS
AIR FORCE RESEARCH, AIR FORCE, ENGINEERING, LABORATORIES, REPORTS, SUMMER, UNIVERSITIES

15. NUMBER OF PAGES

16. PRICE CODE

17. SECURITY CLASSIFICATION OF REPORT	18. SECURITY CLASSIFICATION OF THIS PAGE	19. SECURITY CLASSIFICATION OF ABSTRACT	20. LIMITATION OF ABSTRACT
Unclassified	Unclassified	Unclassified	UL

DTIC QUALITY INSPECTED 8

UNITED STATES AIR FORCE

SUMMER RESEARCH PROGRAM -- 1995

SUMMER FACULTY RESEARCH PROGRAM FINAL REPORTS

VOLUME 5A

WRIGHT LABORATORY

RESEARCH & DEVELOPMENT LABORATORIES

5800 Uplander Way

Culver City, CA 90230-6608

Program Director, RDL
Gary Moore

Program Manager, AFOSR
Major David Hart

Program Manager, RDL
Scott Licoscos

Program Administrator, RDL
Gwendolyn Smith

Submitted to:

AIR FORCE OFFICE OF SCIENTIFIC RESEARCH

Bolling Air Force Base

Washington, D.C.

December 1995

PREFACE

Reports in this volume are numbered consecutively beginning with number 1. Each report is paginated with the report number followed by consecutive page numbers, e.g., 1-1, 1-2, 1-3; 2-1, 2-2, 2-3.

Due to its length, Volume 5 is bound in three parts, 5A, 5B and 5C. Volume 5A contains #1-23, Volume 5B contains reports #24-44 and 5C contains reports #45-64. The Table of Contents for Volume 5 is included in both parts.

This document is one of a set of 16 volumes describing the 1995 AFOSR Summer Research Program. The following volumes comprise the set:

VOLUME	TITLE
1	Program Management Report

Summer Faculty Research Program (SFRP) Reports

VOLUME	TITLE
2A & 2B	Armstrong Laboratory
3A & 3B	Phillips Laboratory
4	Rome Laboratory
5A, 5B & 5C	Wright Laboratory
6A & 6B	Arnold Engineering Development Center, Wilford Hall Medical Center, and Air Logistics Centers

Graduate Student Research Program (GSRP) Reports

VOLUME	TITLE
7A & 7B	Armstrong Laboratory
8	Phillips Laboratory
9	Rome Laboratory
10A & 10B	Wright Laboratory
11	Arnold Engineering Development Center, Wilford Hall Medical Center and Air Logistics Centers

High School Apprenticeship Program (HSAP) Reports

VOLUME	TITLE
12A & 12B	Armstrong Laboratory
13	Phillips Laboratory
14	Rome Laboratory
15A&15B	Wright Laboratory
16	Arnold Engineering Development Center

SFRP FINAL REPORT TABLE OF CONTENTS i-xiv

SFRP FINAL REPORTS

Invention and Evaluation of the
Barrell-Launched Adaptive Munition (BLAM)

Ron Barrett
Assistant Professor
Aerospace Engineering Department

Auburn University
Alabama

ABSTRACT

The basic properties of a newly invented class of hybrid munitions are presented. These Barrel-Launched Adaptive Munitions (BLAM) blend the characteristics of missiles and ammunition to form a new type of guided bullet or cannon shell. The chosen design is a 10° half-angle cone which is split in two with a forward spike and a truncated conical aft skirt. The two pieces are pivoted around a central ball-joint and held together by piezoelectric adaptive tendons. This allows the front portion of the cone to rotate in any direction up to ±1° with respect to the rear portion of the cone.

The first part of the study was experimental and involved the fabrication and testing of an active bench-test article and models for range firing. The adaptive tendons were fabricated using newly developed manufacturing techniques which lead to shock-resistant actuators capable of enduring hard launch loads. The prototype tendons were 0.15" (3.81mm) wide and were constructed from a pair of 2.5" (63.5mm) long 7.5 mil (190.5 μm) thick PZT-5H piezoceramic sheets which were sandwiched on either side of 4" (101.6mm) long, 5 mil (127 μm) thick aluminum foil. Test results show that at 68°F (20°C), the adaptive members were precompressed to record levels of 947μstrain (57.8 MPa or 8.37 ksi) while the aluminum substrate was pre-tensioned to 2473μstrain (173 MPa or 25.1 ksi). The low substrate-actuator strength ratio (Ψ = 0.381) lead to a 72% maintenance of active strain levels between the free-PZT sheet and combined element performance. Modified laminated plate theory was used to demonstrate that the extremely high pre-compression level was sufficient for withstanding launch loads up to 20,000 g's. At maximum ±400 μstrain levels, the elements could generate articulation angles up to ±0.28°. The BLAM bench prototype was determined to have a first natural frequency of 228 Hz (1,433 rad/s) with a full-cycle response time under 5ms.

The second section of research compares the overall performance of conventional ammunition to the projected performance of the BLAMs. Because BLAMs would be insensitive to gravity and most cross-winds (above minimum flight speeds), their effective ranges are substantially increased. A basic performance code compared the 20mm PGU-28 to an identically shaped BLAM. Considering a minimum impact velocity of 700 ft/s (213 m/s), the effective ranges were more than doubled to 2 mi (3.2km). Projections also demonstrated the potential of a 105mm BLAM fired at 2,000 ft/s (610 m/s). Domes of strike opportunity were calculated and showed that air targets traveling around Mach 1, at 10,000 ft (3.05 km) altitude could be engaged at ranges exceeding 4 mi (6.4 km). Under the same conditions, ground targets within a 7 mi (11.3 km) radius footprint could be hit. A final section examining the high altitude performance BLAMs demonstrated that from 50,000 ft (15.2 km) launch altitude, hypervelocity rounds could be used effectively against ground targets within a 30 mi (48.3 km) diameter footprint as well as satellites and ballistic missiles up to 100 mi. (161 km) in altitude.

1. INTRODUCTION

Because of page limitations, all appendices which are referenced throughout this report refer to the unabridged edition (instead of this, abbreviated version). The complete version may be obtained from the author or WL/MNAV.

For three thousand years, people have discussed and debated the concept of guided weapons. From the enchanted arrows of Artemis and Athene to Jules Verne's homing missiles, the possibility of such weapons have been widely recognized. The 20th century has seen such weapons come to fruition in the form of guided missiles which have a wide array of uses. Current developments in technology are shrinking the size of these weapons. Improvements in guidance and seeker systems have resulted in solid-state, single chip devices which are small enough to be integrated into even 2.75 in rockets. However, more breakthroughs are coming every day as evidenced by the appearance of guidance and control packages which are mounted in cannon shells. One of the earlier examples of a guided cannon shell is the Copperhead antitank round. This nearly 30 year-old, 155 mm weapon has successfully demonstrated that the critical components of guided rounds could be hardened for launch and function reliably (Ref. 1). More modern advancements have shown that video systems with live telemetry could even be packed within the 155 mm shell. Tests at Sandia National Labs with the Video Imaging Projectile (VIP) have demonstrated that these large shells could be used for battlefield reconnaissance (Ref. 2). Intercepting munitions with fast reaction times and small packages have continued to evolve and are currently being tested even as this report is being written. The Small Low-cost Interceptor Device (SLID) is among those which use impulse thrusters for flight control (Ref. 3). Because such impulsive thrusters occupy a large volume within any missile system and they provide only discreet course corrections, other approaches are being considered. Currently, the X-Rod and Smart, Target Activated Fire and Forget (STAFF) rounds are 120mm in diameter and fly with MMW sensors to attack tanks from above (Ref. 4). As with the SLID, these rounds use impulsive thrusters to discreetly steer the munitions to the target. Currently, only two different flight mechanisms are being considered: 1) aerodynamic control surfaces, and 2) steering rocket motors. Each system has strong points, but is accompanied by drawbacks. The aerodynamic control surfaces generally have relatively poor response times, heavy electromagnetic actuators, low electrical-to-mechanical efficiencies, require sizable thermal batteries and are very difficult to design to withstand launch loads. The rocket motors can easily withstand the launch loads, but, they too occupy large volumes within the round, deteriorate with time and provide only intermittent, impulsive steering which is less than optimal for terminal guidance.

To skirt these steering and guidance difficulties a new concept in flight control was conceived and developed. Using adaptive structures, numerous technologists have conceived arrangements which generate solid-state deflections of aerodynamic surfaces. Building upon earlier work which laid down the foundations of adaptive structures (Ref. 5 - 8), Crawley, Lazarus and Warkentin were the first to make and test an active flight control device (Ref. 9). They showed that bending and extension-twist coupled plates could be either actively bent or actively extended to produce small twist deflections. When exposed to air loads, the deflections grew and grew until the plate diverged at roughly 40 ft/s (12.2 m/s). Work continued in the area and more significant headway was made. One of the earlier attempts at another form of solid state control was examined, again, by Lazarus, Crawley and Warkentin (Ref. 10). They

demonstrated that flight control could achieved in a small sense through direct manipulations of wings. Immediately following these early studies, a host of other experimenters confirmed their results and showed that air loads could be called upon to further magnify deflections and that geometric parameters could be included in these active aeroservoelastic devices (11, 12).

Following much of the work in this area, Chopra and Chin showed that microscopic twist deflections could be generated on helicopter rotor blades (Ref. 13). Their investigation was a direct offshoot of preceding studies on rotor blades, missile wings and orthotropic actuator elements which were spawned by Barrett (Ref. 14 - 17). Because the deflection levels which were generated by these structures were so small as to be almost insignificant, new structural configurations needed to be developed. In 1991, a whole new type of flight control mechanism was born to provide such performance. This device used adaptive elements mounted to a plate in such a way that twist deflections would result. This torque-plate was then firmly mounted to a main spar and an aerodynamic shell was fitted to the tip of the plate. As the plate twisted, the shell moved in pitch. Numerous studies have been centered around this family of torque-plate fins which currently generate the second-highest adaptive lift coefficient changes (Ref. 18 - 23).

The most effective adaptive flight control mechanisms were recently developed for subsonic missiles and remotely piloted vehicles (RPVs). These devices use the Flexspar configuration of actuator to move an aerodynamic shell and have been tested on the bench, in the wind tunnel on 1/3 scale TOW 2B missile models, and even flown (Ref. 24 - 29). These adaptive structures have finally been proven in flight, and shown to weigh far less than conventional actuators while responding quicker with dramatically improved efficiency for less cost. Accordingly, flight control methods which were previously thought to be impossible are not only easily realized, but also highly effective.

One of the newest active munition configurations uses adaptive structures mounted within a conically shaped, hard-launched round. This round is split into two pieces: a heavy conical nose section and a light truncated conical skirt. The adaptive members pivot the forward portion independently of an aft skirt for flight control. This newly conceived Barrel-Launched Adaptive Munition (BLAM) was invented on Air Force time and funding as part of the Summer Faculty Research Program. Accordingly, this report covers the major design and modeling issues associated with the structure as well as general operational aspects of BLAM weapon systems.

2. ADAPTIVE MEMBER DESIGN

This first portion of research leads the rest of the BLAM design because of its critical importance. From the onset, it was not known if the adaptive members could actually endure hard launch loads which range up to 1,000,000 g's. Accordingly, this section lays out the extreme loading conditions which these relatively fragile materials are exposed to and the unique approach which is used to combat these loads.

2.1 STRUCTURAL ARRANGEMENTS AND MATERIAL PROPERTIES

Within the BLAM, the adaptive elements will be used to move components relative to each other. Because nearly all configurations will experience similarly applied loads, general expressions may be derived for a generic actuator configuration. Figure 2.1 shows the typical adaptive tendon arrangement which will be used for analysis.
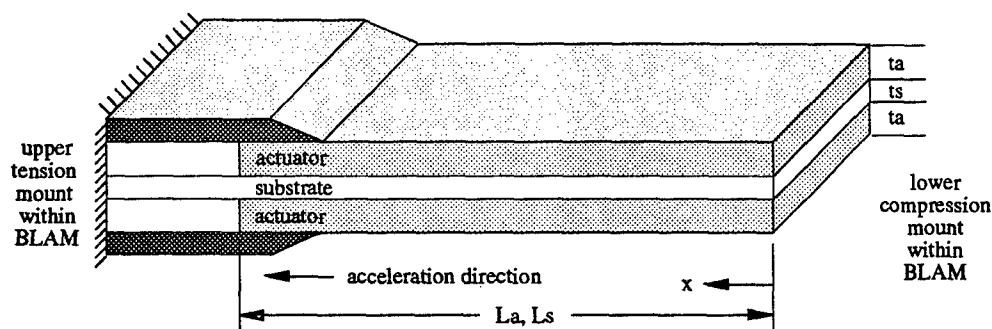

Fig. 2.1 Active Tendon Configuration

The upper portion of the tendon is bonded rigidly to an internal structural mount. During launch, the upper mount is assumed to carry all of the load. If the load were to be shared with the lower mount, then most tendons would simply buckle and accordingly transfer loads to the upper structure. The actual tendons will include a finite bond line of relatively low modulus and low density bonding agent. For this analysis, the properties of the bond will be neglected.

The properties of the actuator and substrate materials themselves, however, are of extreme importance. Because it is not clear which substrate material will provide overall superior performance, a side-by side comparison is necessary. The potential actuator materials are also numerous. From Ref. 22 it can be seen that PZT-5 is used most commonly. This type of piezoceramic material has a very high piezoelectric coefficient and this family of adaptive materials is fast becoming one of the smart structures industry standards. Because the superior properties are well understood and have been characterized by numerous years of research, PZT-5H will be used in this study as the actuator material of choice. This type of piezoceramic, like nearly all adaptive ceramics, is extremely sensitive to tensile loads and exhibits a very low fracture toughness. Accordingly, a substantial portion of this chapter is devoted to working around this problem. Other difficulties with this material is that it is fatigue sensitive. The stress-cycle curve is generally shifted one to three orders of magnitude below most structural metals. Although of great concern to helicopter and conventional airframe designers, the single-use nature of BLAMs negates this problem. Table 2.1 lays out the fundamental properties of a wide range of materials for use as substrates as well as the PZT-5H actuator element.

1 - 5

Table 2.1 Substrate and Actuator Material Properties (from Ref.'s 30 - 34)

Material	E Msi (GPa)	ρ lbm/in³ (kg/m³)	f_{ty} ksi (MPa)	ε_{ty} (μstrain)	f_{cy} ksi (MPa)
PZT-5H piezoceramic	8.84 (61)	0.271 (7500)	6.96 (48)	787	-56.6 (-390)
2024 aluminum	10.4 (72)	0.10 (2,768)	47.0 (324)	4476	39.0 (-269)
AISI 4130 steel	29.0 (200)	0.283 (7833)	75.0 (517)	2586	75.0 (-517)
Ti-8Al-1Mo-V1 titanium	17.6 (121)	0.158 (4373)	120 (827)	6838	127 (-876)
PH-15-7 Mo stainless steel	29.0 (200)	0.277 (7677)	170 (1172)	5861	179 (-1234)

	ε_{cy} (μstrain)	Λ_{max} @ 15V/mil (μstrain)	α μstrn/°F (μstrn/°C)	T_c °F (°C)	d_{31} nin/V (pm/V)
PZT-5H piezoceramic	-6393	220	~ 2.2 (4.0)	428 (220)	10.8 (-274)
2024 aluminum	-3735	~	12.83 (23.1)	~	~
AISI 4130 steel	-2586	~	6.72 (12.1)	~	~
Ti-8Al-1Mo-V1 titanium	-7237	~	4.66 (8.39)	~	~
PH-15-7 Mo stainless steel	-6171	~	13.2 (23.8)	~	~

An examination of the above properties demonstrates the wide disparity in elastic and thermo-mechanical characteristics. Through proper design, these parameters will be used to enhance the overall properties of laminated piezoelectric actuator tendons. It should be noted that the coefficients of thermal expansion listed above are nominal values for a typical cure temperature. Deviations from the above values for α are within 4% of the extremes.

2.2 LAUNCH LOADS

Two major loads will present themselves to the tendon pictured in 2.1. These are axial and perpendicular imposed body forces. Because it can easily be shown that the launch loads which are expected (up to 1,000,000 g's) will simply shear any PZT tendon with lateral forces, this loading case will not be considered. This indicates that the PZT tendons must be placed directly along the axis of acceleration. If this loading is present, and gravity forces are neglected, then an expression for load along the length of the element is obtained:

$$F(x) = ngx\left(\rho_a A_a + \rho_s A_s\right) + F_o \qquad \text{(eq. 1)}$$

Where F_o is an applied force on the end of the element from the base support.

If the laminate is assumed to be balanced and symmetric and both PZT actuators are energized in phase, then a laminate extension in two directions will occur. This active force combined with thermally induced stresses and laminate resistive forces yields an expression for overall force balance at any given point in the unloaded laminate.

$$\left(E_a A_a + E_s A_s\right)\varepsilon = \left(E_a A_a \overline{\alpha}_a + E_s A_s \overline{\alpha}_s\right)\Delta T + E_a A_a \Lambda \qquad \text{(eq. 2)}$$

Because it can easily be seen that the stress upon launch is maximized at the top of the actuator which is critical in tension (see Table 2.1), equations 1 and 2 may be combined to determine the stress level at x.

$$\left(E_a A_a + E_s A_s\right)\varepsilon = \left(E_a A_a \overline{\alpha}_a + E_s A_s \overline{\alpha}_s\right)\Delta T + E_a A_a \Lambda + ngx\left(\rho_a A_a + \rho_s A_s\right) + F_0 \qquad \text{(eq. 3)}$$

From Table 2.1 it can be seen that the materials used as substrates have significantly higher coefficients of thermal expansion than the PZT actuators. This is because an elevated temperature cure will effectively precompress the elements and make them more robust. It should be noted at this point that graphite/epoxy composites were not considered as a suitable substrate material because they would place the PZT actuators in tension after an elevated temperature cure. (Such pre-tensioning is extremely detrimental to actuator performance and has been responsible for numerous actuator element failures in many corners of the smart structures industry.) If it is assumed that the laminate is unloaded and constrained flat during the cure which is below the Curie temperature of the PZT, then the total laminate strain may be solved:

$$\varepsilon = \frac{\left(E_a A_a \overline{\alpha}_a + E_s A_s \overline{\alpha}_s\right)\Delta T}{\left(E_a A_a + E_s A_s\right)} = \frac{\left(\overline{\alpha}_a + \psi \overline{\alpha}_s\right)\Delta T}{\left(1 + \psi\right)} \qquad \text{(eq. 4)}$$

Following an elevated temperature cure, the PZT will be placed in compression while the substrate will be placed in tension. Expressions for pre-compression and pre-tensioning limitations are given as:

$$\varepsilon_{a\ \text{precompression}} = \overline{\alpha}_a \Delta T - \frac{\left(\overline{\alpha}_a + \psi \overline{\alpha}_s\right)\Delta T}{\left(1 + \psi\right)} \qquad \text{(eq. 5)}$$

$$\varepsilon_{s\ \text{pretension}} = \overline{\alpha}_s \Delta T - \frac{\left(\overline{\alpha}_a + \psi \overline{\alpha}_s\right)\Delta T}{\left(1 + \psi\right)} \qquad \text{(eq. 6)}$$

Including the effects of externally applied forces, equations 5 and 6 are modified to:

$$\varepsilon_{a\ \text{precompression}} = \frac{\left(\overline{\alpha}_a - \overline{\alpha}_s\right)\psi \Delta T + {F_0}/{E_a A_a}}{\left(1 + \psi\right)} \qquad \text{(eq. 7)}$$

$$\varepsilon_{a\ \text{precompression}} = \frac{\left(\overline{\alpha}_s - \overline{\alpha}_a\right)\Delta T + {F_0}/{E_a A_a}}{\left(1 + \psi\right)} \qquad \text{(eq. 8)}$$

Using equation 3 and assuming that the actuators will experience no shear lag at the ends of the mount, the lengths of the actuators may be solved for given a specific loading condition:

$$L_a = \frac{(E_aA_a + E_sA_s)\varepsilon_{aty} + (\overline{\alpha}_s + \overline{\alpha}_a)E_sA_s\Delta T - F_o}{ngx(\rho_aA_a + \rho_sA_s)} \qquad \text{(eq. 9)}$$

$$L_s = \frac{(E_aA_a + E_sA_s)\varepsilon_{sty} + (\overline{\alpha}_a + \overline{\alpha}_s)E_aA_a\Delta T - F_o}{ngx(\rho_aA_a + \rho_sA_s)} \qquad \text{(eq. 10)}$$

Because the area of interest is over the length of the actuator, it can be assumed that the length of the actuator and the free substrate are the same. Accordingly, equations 9 and 10 may be equated. The resulting expression assumes that the cure is high enough to bring the substrate to the tension yield strain while the actuators yield in compression.

$$\Delta T = \frac{\varepsilon_{sty} - \varepsilon_{acy}}{\overline{\alpha}_s - \overline{\alpha}_a} \qquad \text{(eq. 11)}$$

To estimate the launch loads, several fundamental estimations are used. If it is assumed that the round experiences a uniform acceleration as it travels down the length of the barrel, then it will experience a minimum peak acceleration for a given muzzle velocity. Although theorized, this has never been achieved in the real world. The closest analogy comes from the "traveling charge" concept which uses propellant which is attached to the base of the projectile. Nonetheless, this physical impossibility provides a lower limit of acceleration as a function of muzzle velocity:

$$a = V^2_{muzzle} \Big/ 2L_{barrel} \qquad \text{(eq. 12)}$$

From Ref. 35 a typical launch acceleration profile is obtained for a high speed round:
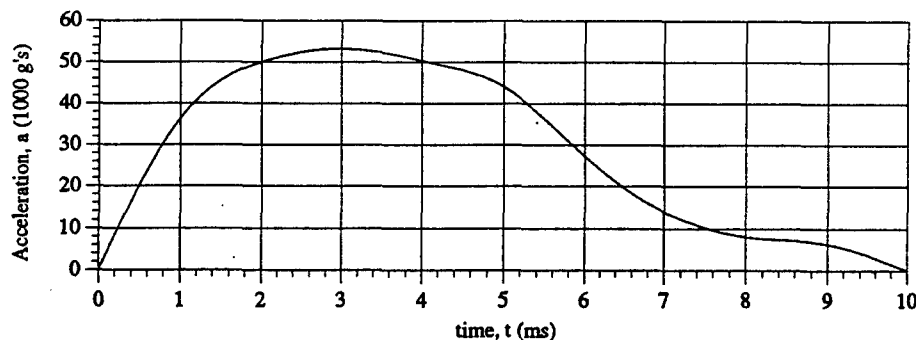

Fig. 2.2 Acceleration Profile of Hypervelocity Weapon During Launch

Using the acceleration profile of Fig. 2.2, and assuming that the general trend describes an upper bound for BLAM launch conditions, the amount of g's upon launch as a function of muzzle velocity and barrel length may be obtained as shown in Appendix A.

2.3 ACTUATOR STRENGTH ENHANCEMENT

Using the values of Table 2.1 and assuming that this ideal cure condition may be reached, then temperature differentials which will result in maximum strengthening can be calculated.

Clearly from Table 2.2, cure temperatures of 2,442°F are far in excess of typical cure temperatures. The upper bound on cure temperature will be set by the Curie temperature of the piezoceramic. The lower bound is determined by the flight condition that the round will face.

Table 2.2 Optimum Cure Conditions for Maximum Precompression and Pretensioning

Material	ε_{cy} (μstrain)	ε_{ty} (μstrain)	α μstrn/°F (μstrn/°C)	ΔT_{opt} °F (°C)	T_{cure} °F (°C)
PZT-5H piezoceramic	-6393	787	~ 2.2 (4.0)	~	~
2024 aluminum	-3735	4476	12.83 (23.1)	379 (193)	309 (154)
AISI 4130 steel	-2586	2586	6.72 (12.1)	432 (222)	362 (183)
Ti-8A1-1Mo-V1 titanium	-7237	6838	4.66 (8.39)	2512 (1378)	2442 (1339)
PH-15-7 Mo stainless steel	-6171	5861	13.2 (23.8)	493 (256)	423 (217)

This most extreme lower temperature is found above the Tropopause where temperatures dip to -70°F (-57°C). This lower bound is used to ensure that as the round is carried aloft and cold-soaked, the actuator elements will not break upon launch due to excessive precompression. From these results, it can be seen that piezoceramic actuator strength will be increased by nearly two orders of magnitude. This leads to a sizable increase in actuator length which may be used.

2.4 ACTUATOR GEOMETRY AND PERFORMANCE LEVELS

Because stress levels at the top of the element increase as a function of the length during launch, the actuator geometry becomes absolutely critical. Curiously enough, it can be seen from earlier expressions that base width and thickness play only secondary roles while the length dominates the stress levels seen by the actuator. If the maximum acceleration profiles of section 2.2 are used to determine the design loads, and the elements are precompressed to their maximum limit or the Curie temperature, then equations 9 or 10 may be used to solve for their lengths. Appendix A delivers the design charts which spell out the maximum actuator lengths which may be used with a given substrate type, muzzle velocity and barrel length.

Using equation 2 yields the maximum change in actuator element length which is possible under given launch conditions. As can be seen from the figures in Appendix B, the change in actuator length rapidly grows with area ratio, then subsides. This effect is caused by two opposing characteristics. As the cross-sectional area ratio, ψ_a, is very small, the strength of the entire actuator laminate is dominated by the piezoceramics. Accordingly, the longer the laminate, the longer the change in length at a given strain level. However, as ψ_a, moves through the 0.2 to 2.0 range the piezoceramic/substrate sandwich strength is dominated by the substrate. As the relative strength of the substrate grows, it allows for longer elements, but the retardation in active strain levels becomes too great. Accordingly, the active strain levels die at a much more rapid rate than the length grows. The result is a low change in total active member length. If the acceleration profile is used in conjunction with the design length and change in length information, then boundaries for those parameters may be established as a function of launch conditions as shown in Appendix C.

Using the information of Appendix C yields some insight into practical actuator design. For a representative barrel length of 10 ft (3.05m), at a muzzle velocity of 2,000 ft/s (610 m/s), the maximum single-length actuator may be approximately 0.35". If a single switchback actuator is used in conjunction with base support, this may be increased to an unfolded length of 1.42" (36mm). Although smaller than the 2.5" long actuators which are used in the test article, this clearly shows that reasonably sized actuators may, indeed survive hard launch conditions.

3. CONICAL BLAM TEST ARTICLE CONFIGURATION, DESIGN AND CONSTRUCTION

Two specimens were constructed for this study as basic proof-of-concept and exploratory articles. The first specimen was built to be bench tested to verify actuation ranges, frequency response and deflection characteristics. The second series of specimens were designed specifically to be launched on the outdoor Aeroballistics Research Facility range at Eglin AFB. These would demonstrate the basic aerodynamic characteristics of the conically shaped rounds. This chapter describes both families of specimens and their state of progress at time of authoring. Because the aerodynamics of conical sections is well understood and there exists a large aerodynamic data base, a 10° conical shape was chosen.

3.1 BENCH TEST SPECIMEN

The bench test specimen was designed to incorporate several major structural components. The first is the forward conical section which was machined from solid brass. This heavy component provides stability to the round as its weight moves the c.g. forward. The second conventional structure is the aft conical skirt. This portion of the round lends stability at high Mach number by shifting the center of pressure aft with minimal shift in center of gravity. The third major component is the adaptive structures. These piezoelectric tendons are used to pitch the forward portion of cone independently of the rear portion.

3.1.1 CONVENTIONAL STRUCTURE DESIGN

The bench-test article progressed through two major design iterations. Based on analysis performed on PRODAS, it was determined that a conical shape would provide the necessary stability for this type of round. Because the BLAM is to be fired from a smooth-bore gun, no gyroscopic stabilization can be called upon. Accordingly, the round must be inherently aerodynamically stable. To achieve this, a heavy nose section was designed to be mated to a much lighter tail cone section. The figures in Appendix D show the design iterations of the conventional structure. The first design, BLAM model 1, incorporated a small ball joint with a nylon bushing. This design was deemed unsuitable because the model would eventually be proposed for supersonic wind tunnel testing as well. Accordingly, a more robust ball joint with a threaded connector is needed. This manifested itself as BLAM model 2. This BLAM model is under construction as this report is being written.

3.1.2 ADAPTIVE TENDON DESIGN, FABRICATION AND INTEGRATION

The adaptive tendons were constructed from PZT-5H piezoceramic sheets and 2024-T0 aluminum substrates. Piezo Systems PSI-5H-S3 piezoelectric sheets were used for the actuators. Figure 3.1 shows the raw sheet. After the raw sheet was cut, then the 5 mil (0.127mm) thick 2024-T0 substrate was cut. A total of six elements were constructed -- four for the specimen and two reserve in case of manufacturing difficulties. Figure 3.2 shows the cut PZT and aluminum strips prior to bonding.

The bonding process was fairly involved as a range of cure temperatures were researched to discover the maximum that could safely be used. From a series of experiments, it was found that a 392°F (200°C) cure temperature with a fast ramp of 40°F/min (22.2°C/min) resulted in a suitable cure profile. After reaching the cure temperature, it was held at that level for 30 minutes,

then a slower 5°F/min (2.8°C/min) ramp was used to bring the specimens back to room temperature. The bond was formed by Scotchweld™ epoxy structural tape.

The substrates were brushed with 400 grit paper to facilitate bonding, and were cleaned with acetone and propanol. After cleaning, the substrates were stored in propanol for approximately two hours while the PZT sheets were being prepared.

After cutting, the PZT sheets were assembled in a stack and waxed together at low temperature. These stacks were then trimmed with 400 grit paper to 0.150" ±0.002" (3.81mm ± 0.05mm). After trimming, the sheets were separated and soaked in toluene to cut the wax residue. After removal of the wax film, the sheets were again cleaned with acetone and propanol and stored for approximately one hour while the substrates were being fitted with adhesive tape.

The Scotchweld™ adhesive tape was cut into 0.20" (5.0mm) wide strips and tacked to the substrates. Following this, a 0.05" (1.3mm) diameter hole was cut from the center of each adhesive strip and filled with M-Bond conducting epoxy. The PZT sheets were then laid out to dry and then assembled to within ±0.005" (0.13mm) of the edges of the substrate. The sandwiched actuator lamina were then placed on a 1 mil thick sheet of Teflon on an optically flat 0.25" (6.4mm) thick glass tool for curing. (The glass provided dimensional stability and high ramp profiles during the cure.) The actuator sandwiches were then jigged in place with 1 mil flashing tape. A layer of breather cloth was applied over the surface of the jigged elements and an upper tool was then clamped with an equivalent of 18 psi (124 kPa) of pressure. The elements were then cured in the high ramp cycle and brought back to room temperature.

Following the cure, the elements were removed from the jigs and the cure tools. The final process of PZT tendon fabrication involved trimming the flashing off of the sides of the actuator elements. The actuators were shaved with 400 grit paper to 0.15" ±0.003" (3.81mm ±0.076mm). From two-component laminate experimentation, it was determined that the PZT sheets were precompressed to 947μstrain while the substrate was pretensioned to 2473μstrain. Upon activation, it was also found that the element maintained 72% of the active strain capability with respect to the free actuator elements. Accordingly, the active tendons may generate 400 μstrain of motion during operation at the depoling limit. This corresponds to 0.001" (0.0254mm) of motion.

3.2 RANGE TEST SPECIMENS

The range test specimens were fabricated to establish a baseline of aerodynamic data and ballistic performance which could be used for code validation. These specimens, like the bench test articles were constructed from a brass nose section with an aluminum conical skirt. The major difference is that they are built so that the articulation angle is fixed. Two series of specimens were built at the Aeroballistics Research Facility machine shop. The first cones were produced with a straight 10° half-angle cone shape. The second set employed a 1° articulation angle between the front and rear portions. Appendix E contains the assembly drawing for the range test specimen. Figure 3.4 shows the "bent" and straight range test articles. Figure 3.5 more clearly shows the 1° articulation angle.

4. BLAM PERFORMANCE ESTIMATION

One of the major results of this study is an estimate of the performance of the BLAM 10° conical specimen. It should be made clear that this design has not been optimized in any way. However, this initial stab at the configuration is a method of entering the iterative, ever improving, design cycle. This section will lay out the methods which were used to model the performance of this first BLAM design.

4.1 CONICAL BLAM ACTIVE PERFORMANCE ESTIMATION

Modeling BLAM performance must include all major aspects of the design. As pointed out earlier, the launch loads are critical and will size both the actuator and the round itself. Additionally, the material chosen for the actuators has a direct bearing on the round performance.

4.1.1 AERODYNAMIC LOADS PREDICTION

The aerodynamic prediction of flow over cones is fairly straightforward. The past 30 years of analytical work has yielded some powerful methods which may easily be applied to supersonic flow over conical sections. Because this is a design-level study, a basic pressure estimation technique developed in Ref. 36 will be used to estimate the pressure over the surface as a function of: cone half angle, angle of attack, and Mach No. This code divides the cone into 72 panels (5° per step) and sums the pressure over the surface. The paneling scheme is shown in Appendix F.

Using the experimental data of Ref. 37, the code was checked for accuracy. Appendix F contains the theory and experiment correlation of data. It can be seen that the code overpredicts the lift coefficient, C_L by up to 5.4% while it underpredicts the drag coefficient, C_D, by as much as 6.6%. For an initial design-level investigation, this level of accuracy is acceptable.

A second check of the rough accuracy of the code was made with respect to the drag coefficient. From Appendix F, it can be seen that the PGU-28 C_D is 4% to 40% lower than the cone drag coefficient (Ref. 38). Normalizing the results with respect to the Prandtl-Glauert compressibility factor demonstrates that the PGU-28 experiences higher losses at increased flight speeds. Alternatively, the 10° cone starts out with a low level of base pressure with moderate losses and maintains those losses throughout the flight with only minor changes.

4.1.2 STRUCTURAL MODELING

The structural modeling of the actuators and pivot assembly was very straightforward. The linear stiffnesses of the actuator elements were calculated from the known material characteristics and geometric parameters. Following computation of the linear stiffnesses, an equivalent rotational stiffness about the pivot was determined assuming small angles. The rest of the structure is assumed to be rigid. Time limitations precluded modeling the gross structure during launch to ensure that no crushing would occur. Active deflections were determined by using classical laminated plate theory and the estimates of section 2.

4.1.3 FORCE AND MOMENT BALANCE

To determine the deflections of the forward cone with respect to the skirt, it was assumed that only the commanded articulation angle would result. In a more detailed analysis, the entire aeroservoelectroelastic model of the system must be included for accurate results. However, this basic model provides some insight into the behavior of the BLAM as a function of Mach No. and

angle of attack. Appendix F contains estimates of the forces and moments which the cone will see during flight.

The aerodynamic moments at a given angle of attack about the pivot will be the primary flight moments which the tendons must resist. Accordingly, the tendons may be spaced a given distance from the pivot. This distance, d, governs the deflection range, actuation speed and moment generation capability of the system. A chart showing the aerodynamic and structural moments as a function of this geometric parameter, Mach number and angle of attack is shown in Appendix F. Clearly, the chosen design point falls in a highly non-optimum position with respect to steady performance. However, the length of the active tendon is governed by launch considerations. The reader will note the presence of several actuator curves relating to "switchbacks." This refers to a new type of actuator design which folds around itself, effectively increasing the actuator throw within a given confined length. From the matching plot, the switchbacks have a very favorable effect on the resulting articulation angle and angle of attack.

In addition to considering the static characteristics of the actuator, the dynamic behavior deserves attention. As can be seen from the matching plot, various natural frequencies are shown next to positions on the graph. These are an indication of the speed at which the BLAM may respond. Ranging from 32.9 Hz (207 rad/s) to 342 Hz (2145 rad/s), it should be clear that this actuator system is extremely fast. It should also be noted that the actual systems are expected to suffer at least a 15% speed penalty because of finite stiffness in the rotational bearing and fixtures on the actuator ends (which were assumed rigid for analysis).

Through a simple examination of the pitching moments about the center of gravity, it can be seen that there is a direct relationship between the articulation angle and angle of attack of the various sections:

$$\alpha_n = 1.532\phi \qquad \alpha_t = 0.532\phi \qquad\qquad\qquad \text{(eq. 13)}$$

This balance roughly holds for flight speeds above Mach 1.4 and comes from a simple moment balance about the center of gravity. The large static margin is principally responsible for the low angles of attack due to cone deflection angle. From the mass balance of the specimen, the center of gravity is approximately 2.25" (57.2mm) from the base of the cone, while the center of pressure is approximately 1.76" (44.8mm) from the base of the cone. This 0.49" (12.4mm) disparity in c.g. and c.p. location leads to a static margin of approximately 27% which is phenomenal for rounds of this type. This large static margin, however, will significantly contribute to a safe test shot during actual firing.

By examining the aerodynamic prediction data of Appendix F, two approximate expressions for normal force were determined. These expressions were shown to fit the aerodynamic data to within 4% of the predicted values:

$$N_n = (-0.4746M^2 + 7.005M - 8.692)\alpha_n + (-0.4411M^3 + 3.398M^2 - 8.179M + 5.945) \quad \text{(eq. 14)}$$

$$N_t = (-0.9492M^2 + 14.01M - 17.384)\alpha_n + (-0.8822M^3 + 6.796M^2 - 16.398M + 11.89) \text{(eq. 15)}$$

By substituting equations 13 into 14 and 15, a relationship for normal force for the entire cone may be obtained as a function of Mach number and articulation angle.

$$N_c = (-1.232M^2 + 18.18M - 22.56)\phi + (-1.323M^3 + 10.19M^2 - 24.54M + 17.835) \quad \text{(eq. 16)}$$

Similarly, the axial force may be solved for by using a median angle of attack.

$$A_c = (0.0308M - 0.0198)\overline{\alpha}^2 + (-0.0173M^2 - 0.0031M + 0.0966)\overline{\alpha} + (1.72M^2 + 1.62M + 36.3)$$

$$\text{(eq. 16)}$$

4.1.4 FLIGHT PERFORMANCE

By using the estimations from equations 13 through 16, the flight performance of the BLAM cone may be estimated. These estimations were made by using the aerodynamic moment data of Appendix F to determine a trim angle. Once the trim angle was determined, the normal force on the cone was solved, as seen in Appendix G. A basic time integration code was written to step from the end of the barrel to a minimum flight speed in horizontal flight. As seen from the code, the minimum flight speed at STP which is required to maintain level flight is 1,800 ft/s (549 m/s). Below this value, the BLAM is unable to generate enough lift to sustain level flight. The results of flight performance estimations for the conical BLAM specimen show that normal accelerations up to 47g's will occur with $\phi = 1.0°$. This will result in an off-boresight capability of 5.3° at a range of 1,100 ft (335 m). Considering the nominal 0.3° articulation angle yields a more modest 1.47° off boresight capability at approximately the same range. The low range projected for the BLAM rounds is induced by the low mass in relation to the maximum cross-sectional area. The 10° cone has a mass concentration of only 0.171 lbm/in^2 (12.0 g/cm^2) while the PGU-28 weighs in at 0.459 lbm/in^2 (32.3 g/cm^2). This 2.7 times disparity in density allows the PGU-28 to have an effective range up to 4,000 ft (1,220 m) while the comparatively light 10° cone will travel only 1,100 ft (335 m).

As mentioned earlier, these flight results are dominated by the extremely large 27% static margin which provides a high degree of stability. Cutting the static margin to 2% to 5% would yield an extremely maneuverable round which would easily be capable of attaining off-boresight angles of 45° and greater. Because a type of very fast flight controller could be integrated into the munition (taking advantage of the fast actuators), then it can be foreseen that a marginally stable munition may demonstrate 180° turning capability.

4.2 COMPARISON OF CONVENTIONAL AND BLAM 20mm MUNITIONS

A comparison of the existing 20mm PGU-28 ammunition and the projected performance of the BLAM munitions is made to illustrate the capabilities of such enhanced rounds. If it is considered that the actual BLAM ammunition will be finned to provide improved lifting capability, then such a munition would be able to effectively fly at speeds as low as 700 ft/s (213 m/s). To determine the performance of such rounds, a basic performance estimation code was written and contained in Appendix H. This code uses drag data for the PGU-28 round which is found in Ref. 38. This drag data is modified to include the effects of induced drag at low Mach numbers. Accordingly, at Mach numbers above 2.0, the correlation between conventional PGU-28 and BLAM rounds is within 2%. Below Mach 2.0, the disparity grows until subsonic speeds are reached. Because the fins will become highly loaded in the subsonic range, it is assumed that the drag of the BLAM round will be approximately double that of its conventional PGU-28 counterpart. This drag data correlation is displayed in Fig. 4.1.

In addition to drag data correlation, a range track comparison was made. This range track compared the performance of a conventional BLAM to that of a PGU-28 with identical shape and mass characteristics. Because the BLAM projectile actually generates lift to maintain a level flight path, it also incurs an induced drag penalty. This is clearly shown in Figure 4.2. As the round travels downrange, the BLAM round slows more quickly because of this drag disparity. Still, there is only a 6% disparity between the two projectiles. Such projections lend a high degree of confidence to the estimation code.
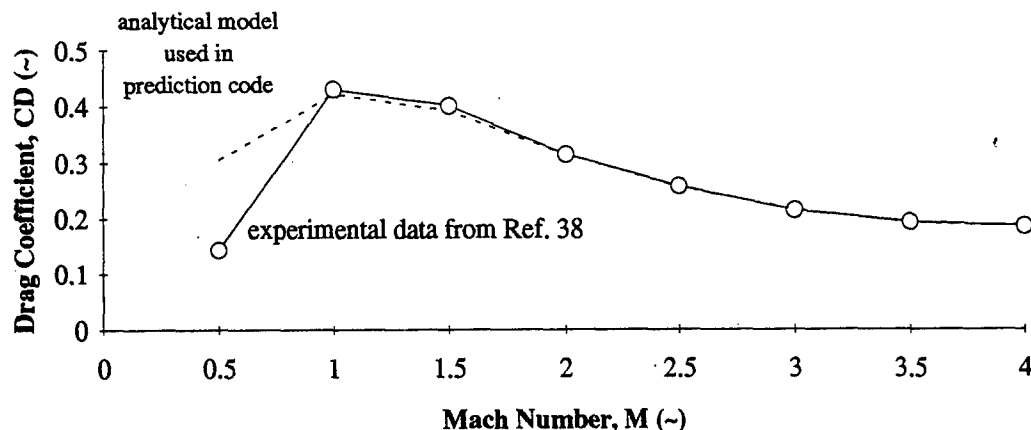
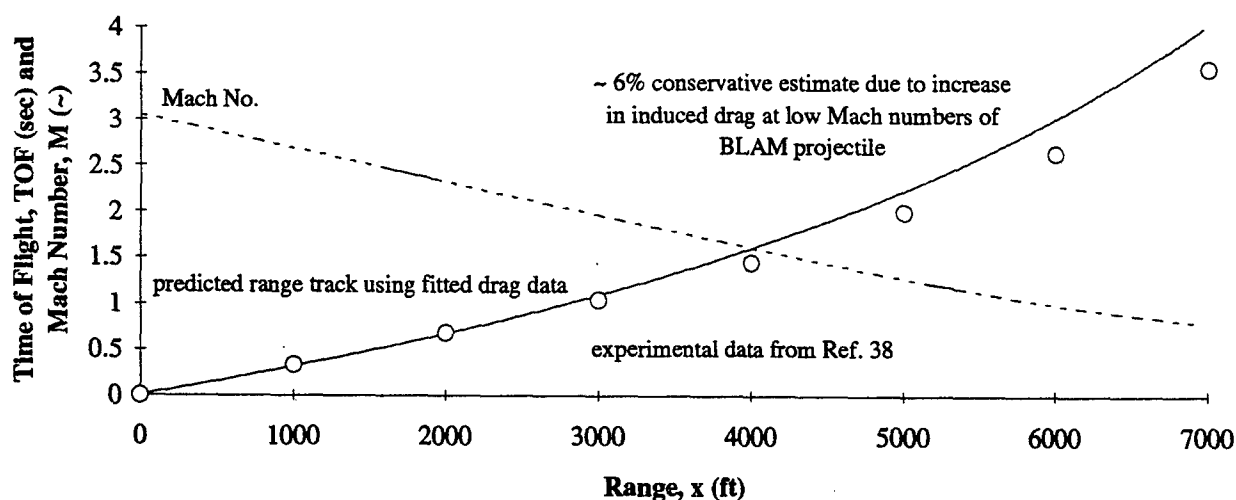**Fig. 4.1 Drag Coefficient Correlation of the PGU-28 and Comparison to BLAM Model**

Fig. 4.2 Range Data Correlation Between BLAM Code and Experimental PGU-28 Data

Following this basic verification of the kernel of the code, modifications were made. The most important involved the inclusion of different flight speeds and altitudes of the launching and target vehicles. Accompanying this modification was the addition of gravity effects, elevation and azimuth. Because this weapon system is intended for a generation of aircraft which are not yet designed, it is completely feasible that a turreted gun may be used. Such a gun would be able to fire at targets in any direction. If employed, this advantage would completely rewrite the rules of air combat. Accordingly, the code of Appendix H was used to determine the size and shape of "strike domes." These domes define boundaries, within which a target at a given flight speed may be hit. Assuming that the conventional PGU-28 rounds were also fired from a turreted gun, a series of smaller strike domes were generated. The disparity in size is attributable to the difference in impact velocities. According to Ref. 38, the PGU-28 is fired at 3410 ft/s (1040 m/s) and maintains an effective performance only out to 1,795 ft/s (547 m/s). On the other hand, the actual round requires only a 700 ft/s (213 m/s) impact to initiate detonation. This lower speed was used as the impact speed of the BLAM projectile. Analysis showed that 15° fins were sufficient for maintaining steady-level flight at these speeds. The results of the computer runs are shown in Appendix I. From these results, it is clearly seen that, through this simple decrease in impact velocity, the strike dome radii are nearly doubled.

4.3 ESTIMATION OF 105mm BLAM PERFORMANCE

Achieving a dramatic increase in effective range, beyond a simple doubling, is also of importance. If the range of a guided round could be stretched to 5 or 10 miles, then the BLAM projectiles would, indeed take on a dual-role capability. They could be effectively used against targets at close and medium ranges. To accomplish this, there are three major factors which should be considered: muzzle velocity, round size/mass and rate of fire. These parameters, lead to an effective horsepower rating of the gun which translates to steady recoil force imparted to the airframe. If it is assumed that a range increase is desired at the same horsepower, then a larger round with a lower muzzle velocity would be a prudent choice. For purposes of comparison, a 105mm size round with a muzzle velocity of 2,000 ft/s was chosen. If a constant horsepower is maintained, then the 105mm BLAM rate of fire will be only 1/50th that of the 20mm PGU-28. In practical terms, this means that the rate of fire will be cut from 4,200 to 84 rounds per minute. However, for this drop in firing rate, the accuracy will be substantially improved, the probability of a kill/given a hit will be boosted by orders of magnitude and the effective range will rise from only 4,000 ft at sea-level to more than 4.5 mi (7.2 km). At 20,000 ft, this jumps to 12 miles (19.3 km). Clearly, these types of ranges are compatible with the AIM-9 Sidewinder class of missiles which operate up to 10 mi (16 km). The inference, of course, is that eventually BLAMs could potentially augment or replace many conventional missile systems. If the muzzle velocity is increased further, to the 3,410 ft/s (1,039 m/s) (which is the speed of 20mm rounds) then the rate of fire would be decreased to 1/145th of the original rate (down from 4,200 rpm to 29 rpm), but the range would jump to 19 mi (30.6 km). This exceptionally long reach would lend AIM-7 Sparrow type range to the munitions.

The reduction in external drag and the negation of the need for internal missile bays would lead to a significantly different type of aircraft configuration. The weight reduction alone would be substantial. If conventional 105mm cartridges are compared to missiles of today, then 88 lb (40 kg) 105mm cartridges could be swapped for the 195 lb (89 kg) AIM-9 or the 500 lb (227 kg) AIM-7. Accordingly, a typical load for a fully equipped F-15 might include 23 rounds of 105mm BLAM instead of four Sparrows.

In addition to a substantial improvement in air-to-air effectiveness through the possibility of an aft or lateral firing capability, the opportunity for engaging ground targets will also increase. As seen in modern hostile areas, air operations are frequently conducted above 10,000 ft for safety. Because the altitude is so high, current 20 and 30mm weapons achieve only limited success. However, a 105mm BLAM could easily engage ground targets from this altitude as seen in the strike footprints in Appendix I. Even with the aircraft traveling near Mach 2, at 10,000 ft, the strike footprint of a 105mm BLAM is nearly 12 mi (19.3 km) in diameter.

Operationally, BLAMs would open up new tactics which are currently reserved only for missiles. Because the BLAMs can be steered after the launch, there is no longer a need for the launching aircraft to be the same as the spotting aircraft. Accordingly, a ground spotter may be used to defeat tanks while an E3 or TR-2 may be used to paint flying adversaries. If a BLAM weapon were turreted, then a ground target may be engaged during the approach, fly over and exit. If sophisticated guidance systems were built into the weapons, then BLAMs might even be used to defeat air-to-air, surface-to-air and surface-to-surface missiles. However, physical defeat of BLAMs would be challenging at best because of the robust structure.

A final possibility is easily seen if one considers a hypervelocity launch at high altitude. From Ref. 35, it was demonstrated that 105mm rounds could be launched at speeds up through 6,000 ft/s (1829 m/s) and carry instrumentation packages which survive. Accordingly, it may be possible to fly such a gun for delivery of a hypervelocity BLAM. Appendix I shows the results of these estimations considering a 50,000 ft (15.2 km) launch at 6,000 ft/s (1829 m/s). Appendix I shows that ground targets could be engaged within a 30 mi (48 km) diameter strike footprint, air targets could be engaged at ranges up to 50 mi and ballistic missiles and low-earth orbit satellites may be intercepted up to altitudes of 100 mi.

5. CONCLUSIONS

Because this is one of the first studies in the field of hard-launched adaptive munitions, several general conclusions on the actuators, configurations and responses will illuminate the entire field.

i. *Adaptive materials like piezoceramics can survive hard launches and flight loads typical of bullets and cannon shells.* The materials must be exposed principally to axial loads which indicates that they must be suspended or supported during launch. Length and substrate material guidelines for launch loads up to 1,000,000 g's have been established. The materials must also be precompressed by using a laminate composed of a precompressing substrate like aluminum or stainless steel. Experimental testing has shown that precompression levels up to 6,000 μstrain are possible.

ii. *Active materials may induce usable steady articulation angles in BLAM rounds.* On the 5.29" (134mm) long, 1.84" (47mm) diameter 10° half-angle BLAM cone demonstration article, ± 0.3° articulation angles may be generated. Deflections up to ±2° may be achieved by simply reducing the pivot-actuator distance.

iii. *Extremely fast BLAM articulation response times may be achieved.* Rates from 32.9 Hz (207 Hz) to 342 Hz (2150 rad/s) were estimated for a range of BLAM internal geometries. The maximum natural frequency of the test article would be 228 Hz (1430 rad/s).

iv. *Steady and dynamic power consumption of BLAM actuators is very low.* The adaptive tendons for the test article showed a maximum steady power consumption of 18.2 mw while the dynamic power consumption at maximum throw, maximum voltage was only 92 mw.

v. *Active tendons are capable of manipulating BLAM flight loads.* At supersonic speeds, tendon sizes and geometric guidelines were established for active tendons. The current model could manipulate flight loads up to 1° angle of attack through Mach 3.

vi. *BLAM performance estimation codes show good correlation with experiment.* The performance estimation code predicted the performance of PGU-28 shaped projectiles to within 6%. A panel-pressure estimation code predicted lift and drag characteristics with a nominal error of 4%.

vii. *Small articulation angles may generate large changes in flight path.* Because of a high round static margin (27%), the 0.3° articulation angle was predicted to generate 1.50° off boresight angles at 1,100 ft (335 m) range. However, if the static margin were reduced to the 2-5% level, then the off boresight angles would grow to more than 30°

viii. *BLAMs offer a substantial range improvement over conventional munitions of the same size and muzzle velocity*. Because the rounds actually fly, and are relatively insensitive to gravity and cross-wind effects, they fly level for a longer period of time and accrue a greater effective range. Comparisons of PGU-28 rounds to their BLAM counterparts demonstrate a two-fold increase in range.

ix. *A lower muzzle velocity, larger caliber BLAM could have effective ranges on the order of AIM-9 Sidewinder missiles.* At 2,000 ft/s (610 m/s) muzzle velocity, a 105mm BLAM would have an effective range in excess of 12 miles (19.3 km) if fired at 20,000 ft altitude.

x. *A higher muzzle velocity, larger caliber BLAM could have effective ranges on the order of AIM-7 Sparrow missiles.* At 3410 ft/s (1040 m/s), a 105mm BLAM would have an effective range in excess of 19 miles (30.6 km).

xi. *A hypervelocity, large caliber BLAM, launched from high altitude, would be able to reach air and ground targets at extended ranges as well as low-earth orbit satellites and ballistic missiles.* At 6,000 ft/s (1829 m/s) muzzle velocity, 50,000 ft (15.2 km) launch altitude, a 105mm BLAM would be able to engage ground targets within a 30 mi (48 km) diameter strike footprint, air targets up to 50 mi (80 km) away and ballistic missiles and low-earth orbit satellites up to altitudes of 100 mi (160 km).

REFERENCES

1. Riply, Tim, "Anti-Tank Weapons," *Modern US Army*, Salamander Books, Ltd., London, United Kingdom, 1992, pp. 114-115.

2. Hubbard, Judy, "Technology," *U.S. Government Video Magazine*, published by P. S. N. Publications, Inc., NY, NY 10016, pp. 37-38.

3. Hughes, David, "Tank Defense System Might Protect Patriot," *Aviation Week and Space Technology*, New York, NY, 10020, 20 June 1995.

4. Held, Bruce J., "Tomorrow's Smart Tank Munitions," *Armor*, published by the U.S. Army Armor Center, Ft. Knox, KY 40121, March - April, 1995, pp. 21 - 25.

5. Berlincourt, D. A., Curran, D. R. and Jaffe, H., "Piezoelectric and Piezoceramic Materials and Their Function in Transducers," *Physical Acoustics*, edited by Mason, W., Vol. I-A, Academic Press, New York, 1964.

6. Ogata, K., "State Space Analysis of Control Systems," Prentice Hall, Englewood Cliffs, 1967.

7. Bailey, T. and Hubbard, J. E., " Distributed Piezoelectric-Polymer Active Vibration Control of a Cantilever Beam," *Journal of Guidance, Control and Dynamics*, Vol. 8, No. 5, pp. 605-611, 1985.

8. Crawley, E. F. and De Luis, Javier, "Use of Piezoelectric Actuators as Elements of Intelligent Structures," *AIAA Journal*, Vol. 25, No. 10, Oct. 1987, pp. 987-997.

9. Crawley, E.F., Lazarus, K.B., and Warkentin, D. J., "Embedded Actuation and Processing in Intelligent Materials," *2nd Int. Workshop on Comp. Mat'ls and Struct.* Troy, NY.

10. Lazarus, K. B., Crawley, E. F., Bohlmann, J. D., "Static Aeroelastic Control Using Strain Actuated Adaptive Structures," proceedings of the First Joint U.S./Japan Conference on Adaptive Structures, Maui, Hawaii, October, 1990.

11. Song, O., Librescu, L. and Rogers, C. A., "Static Aeroelasticity Behavior of Adaptive Aircraft Wing Structures Modeled as Composite Thin-Walled Beams," presented at the International Forum on Aeroelasticity and Structural Dynamics, Aachen, Germany, June, 1991.

12. Ehlers, S. M., "Aeroelastic Behavior of an Adaptive Lifting Surface," Ph. D. Thesis, Purdue University, August, 1991.

13. Chen, P. and Chopra, I., "Feasibility Study to Build a Smart Rotor: Induced Strain Actuation of Airfoil Twist," From the *Proceedings of the 1993 North American Conference on Smart Materials and Structures*, Albuquerque, NM.

14. Barrett, R. M., "Intelligent Rotor Blade and Structures Development Using Directionally Attached Piezoelectric Crystals," M.S. Thesis, University of Maryland, College Park, MD, May, 1990.

15. Barrett, R. M., "Intelligent Rotor Blade Actuation through Directionally Attached Piezoelectric Crystals," Presented at the *AHS National Forum, Washington, D.C. , May 1990*.

16. Barrett, R. M., "Method and Apparatus for Structural Actuation and Sensing in a Desired Direction," *U. S. Patent Application 485,599/07*, 1990.

17. Barrett, R., "Active Plate and Missile Wing Development Using EDAP Elements," *Journal of Smart Materials and Structures*, Institute of Physics Publishing, Ltd., Techno House, Bristol, UK, Vol.1, No. 3, pp. 214-226, ISSN 096.

18. Barrett, R., "Active Plate and Missile Wing Development Using DAP Elements," *AIAA Journal*, March, 1994.

19. Barrett, R., "Aeroservoelastic DAP Missile Fin Development," *Journal of Smart Materials and Structures*, Institute of Physics Publishing, Ltd., Techno House, Bristol, UK, Vol. 2, No. 2, pp. 55-65, ISSN 0964-1726, June 1993.

20. Barrett, R., "Modeling Techniques and Design Principles of a Low Aspect Ratio Active Aeroservoelastic Wing," *Proceedings of the North American Conference on Smart Materials and Structures,* Albuquerque, New Mexico, pp. 107 - 118, 1993.

21. Barrett, R., "Active Composite Torque-Plate Fins for Subsonic Missiles," paper presented at the Dynamic Response of Composite Structures Conference, New Orleans, Louisiana, August 30 - September 1, 1993.

22. Barrett, R., "Advanced Low-Cost Smart Missile Fin Technology Evaluation," Final Report to Wright Laboratory, USAF Armament Directorate, contract number F08630-93-C-0039 Eglin AFB, December, 1993.

23. Barrett, R., "All-Moving Active Aerodynamic Surface Research," presented at the 31st Annual Technical Meeting of the Society of Engineering Science, College Station, TX, October 10 - 12, 1994.

24. Barrett, R., "A Solid State Apparatus for Controlling Pitch Deflections of Aerodynamic Flight Control Surfaces," Auburn Univ. invention disclosure, October, 1994 (patent pending).

25. Barrett, R., Gross, R. S., and Brozoski, F., "Missile Flight Control using Active Flexspar Actuators," proceedings of the *1995 Smart Structures and Materials Conference,* February 26 - March 3, San Diego, California.

26. Barrett, R., Gross, R. S., and Brozoski, F. T., "Design and Testing of Subsonic All-Moving Smart Flight Control Surfaces," proceedings of the *36th AIAA Structures, Structural Dynamics and Control Conference,* New Orleans, LA, April, 1995, pp. 2289 - 2296, AIAA paper no. AIAA-95-1081.

27. Barrett, R., "Aeroservoelastic Characteristics of All-Moving Adaptive Flight Control Surfaces," paper presented at the 10th VPI & SU symposium on Dynamics and Control, 8 - 10 May, 1995.

28. Cooper, Patrick, "U.S. Eyes Stealthy, Flexible Airframes," *Defense News,* published by Army Times Publishing Company, Springfield, VA, 29 May - 4 June 1995, pp. 1 & 36.

29. Svitil, Cathy, "Smart Plane," *Discover,* Published by Disney Publishing Co. New York, NY 10011, p. 29.

30. Smith, H.W., "Material Specifications for Alloy Steels," *Aerospace Materials and Processes,* published by the University of Kansas Aerospace Engineering Department, Lawrence, Kansas 1986, pp. 2.8 - 2.15.

31. Smith, H.W., "Precipitation and Transformation-Hardening Steels (Stainless)," *Aerospace Materials and Processes,* published by the University of Kansas Aerospace Engineering Department, Lawrence, Kansas 1986, pp. 2.32 - 2.41.

32. Smith, H.W., "2000 Series Wrought Alloys," *Aerospace Materials and Processes,* published by the University of Kansas Aerospace Engineering Department, Lawrence, Kansas 1986, pp. 3.12 - 3.25.

33. Smith, H.W., "Titanium," *Aerospace Materials and Processes,* published by the University of Kansas Aerospace Engineering Department, Lawrence, Kansas 1986, pp. 5.1 - 5.9.

34. Anon., "PSI-5H Piezoelectric Single Sheets," *Piezo Systems, Inc. Product Catalog,* published by Piezo Systems, Inc., Cambridge, Massachusetts, 1992, p. 26.

35. Anon., "Actual Results and Analysis," *Hypervelocity Weapon System (HVWS) Field Experiment 1 Final Report, Volume 1 Technical Report,* published by Technology Gateways, Inc., Niceville, Florida, 1993, p. IIIC-6.

36. Jones, D. J., "A Pressure Formula for an Inclined Circular Cone in Supersonic Flow," *AIAA Journal,* Vol. 10, No. 2, February, 1972, pp. 234 - 236.

37. Reggori, A., "Lift and Drag of a Wing-Cone Configuration in Hypersonic Flow," *AIAA Journal,* Vol. 9, No. 4, April 1971, pp. 744 - 745.

38. Hedd, D., "PGU Series Ammunition for the F-15," *USAF Fighter Weapons Review,* published by the USAF Fighter Weapons School, Nellis AFB, NV, Spring 1992, pp. 2 - 7.

A GENERAL METHODOLOGY FOR CLUSTERING AND SEQUENCING ALGORITHMS WITH APPLICATIONS TO INTELLIGENT KNOWLEDGE-BASED MANUFACTURING/MACHINING SYSTEMS

Georges A. Bécus, Associate Professor

and

Edward A. Thompson, Doctoral Student

Aerospace Engineering and Engineering Mechanics Department

University of Cincinnati
Cincinnati, OH 45221-0070

A GENERAL METHODOLOGY FOR CLUSTERING AND SEQUENCING ALGORITHMS WITH APPLICATIONS TO INTELLIGENT KNOWLEDGE-BASED MANUFACTURING/MACHINING SYSTEMS

Georges A. Bécus and Edward A. Thompson

ABSTRACT

Product design and process planning have been separate activities. Even with the advent of computer aided design, CAD systems have been extensively used in the automation of product design, while process design or planning has remained a separate and primarily manual effort with little or no automation. Although there have been numerous efforts (e.g. group technology involving variant and generative techniques) and research in the area of product design and process planning integration, most research has addressed only a portion of the problem, i.e., either the product design or process planning. The integration of shape, function, material and process design is a goal which offers many challenges to overcome. After reviewing Adaptive Modeling Language (AML), an approach and implementation for integrating product and process design in a virtual manufacturing environment involving competing processes, this report presents a general methodology and general purpose algorithms for clustering and sequencing under (precedence) constraints. These algorithms could easily be integrated in AML or other Intelligent Knowledge-Based-Engineering systems to perform such tasks as setup generation/sequencing and feature/operation sequencing. The algorithms employ an Annealing Genetic strategy together with special purpose operators and repair functions as the optimization engine. Our approach, flexible enough to allow user interaction, finds very quickly (near) optimal solutions of higher quality than existing methods.

KEYWORDS: Intelligent Knowledge-Based Engineering, Adaptive Modeling Language, Process Planning, Operation-Based Design, Machining, Clustering, Sequencing, Annealing Genetic Algorithm.

INTRODUCTION

Today enterprises have to compete in an ever changing global market environment which requires fast appropriate decisions. Process costs and product affordability, which form the basis for competing in the marketplace, are often adversely affected by customer demands dictating quick response and imposing continual changes to the product development cycle therby lengthening development time. Investigating new materials and processes to lower costs while enhancing product performance is a goal pursued by every manufacturer.

The standard approach to product and process design is the *specify-evaluate-revise* cycle which often involves time-consuming loops. The engineering of a product incorporates numerous stages involving design specification, manufacturing planning, finite element modeling and analysis, and inspection planning. Changes to the design (dimension, tolerance, material, process constraints, etc.) as well as rework procedures (especially costly if revisions are suggested late in the cycle) cause delays in the final production and market deployment. Often, this cycle generates new ideas or product technology. Alternative materials and processes discovered in this stage are tested in an attempt to enhance product functionality and reduce processing costs. Alternative materials and processes benefit new designs but can also affect the design of retrofit parts for maintaining/refurbishing existing systems as in the design and production of aircraft components (either the re-manufacture of parts for maintaining existing aircraft or new parts designed to replace existing ones). There is an opportunity for the inclusion of past knowledge in new designs to explore alternative materials and processes outside the lengthy *specify-evaluate-revise* cycle.

Developing a methodology to handle changes dynamically and to minimize the design cycle could lead to major savings in the product development cycle and thereby benefit product affordability. Such methodology will enable the investigation of alternative materials and processes to lower the production cost and enhance product performance. This methodology will be applied across all steps in the production process and will form the basis for the development of an Intelligent Knowledge-Based-Engineering (IKBE) system for integrating feature-based, memory-driven design, with material specification, manufacturing/inspection process planning, adaptive meshing, and finite element modeling/analysis.

Because nearly all products require some machining, the benchmark process for current efforts in integrating product and process design is machining. Machining, the most common form of material removal, is often an alternative to other processes when dealing with small quantities of parts for structural applications. In addition to functional specifications and geometric shape, process planning of machined parts requires the preparation of an outline describing all machining setups, fixtures, detailed machining operations, tooling, machining data and finally the NC part program to cut the part [1]. For small lot sizes (1-25 parts), the design and process planning steps account for a large percentage of the overall production time so that an integrated system for concurrent design and automated process planning generation will significantly improve productivity, shorten the design to fabrication cycle and lower processing costs. The system should enable the user to interactively design and plan the machining process to cut the part.

The development of an IKBE system integrating automated process plan generation in a feature-based design environment requires solving a number of problems related to setup generation, feature sequencing, fixturing, tooling, tool path logic, and machining parameter computation [2,3]. There are a number of design automation systems for cutting single features. But these systems generally are not geometry driven and often merely provide a

process plan for a limited number of prismatic shapes by generating the machining operation sequence for a single feature [1] or irrespective of feature interaction. The user input is by feature type limiting these systems to a prescribed library of features without any assistance regarding unique setup generation, fixturing, or any other process planning criteria [4]. Such systems, based on the variant approach of comparing, retrieving, and modifying similar pre-stored process plans, are limited to pre-stored patterns and do not offer a suitable solution for integrating product design and process planning.

Other attempts at automating process planning for machining are limited to simple geometry. The machining features are extracted from a computer aided design (CAD) system using a feature recognition methodology, often limited to a set of machining features with simple orientations and attachments [4-12]. Such systems do not offer an integrated solution for design and process planning, because the part design and modifications are done independently on a CAD system.

Computer Integrated Manufacturing (CIM) systems, oriented towards automating tool path generation from the part geometry created by a CAD system, produce a primitive cutting plan by mapping the tool path to follow the contour of a surface. Although they may handle complex surfaces, these systems offer little or no assistance in the selection of the tooling and machining specifications such as speed, feed and depth of cut and they rely heavily on user interactions for isolating and sequencing the surfaces to be cut. This complicates the process plan generation and tool path logic of even simple parts [13].

In contrast, the developing IKBE architecture supports a concurrent engineering system for interactive design and process planning of machined parts for rapid production. The process plan incorporates the selection of setups, their sequence, fixturing recommendations, tooling, and all the machining data for cutting the part, reflecting the part geometry, the part material characteristics, and the machine selection. In addition, the user can interactively inquire about the production plan to view the effect of the part design and characteristic modifications. The system automatically validates the changes and reconfigures the process plan reflecting the user modifications. The IKBE system supports a sophisticated feature-based design environment, enabling the user to interactively design parts with complex geometry. Form features are basically macro level descriptions of fundamental shape features (hole and profile) with position and dimensional constraints that enable the transfer of a part model without transferring the geometric instance. Most CAD systems are complemented by a Feature Based Design Environment (FBDE) providing advanced tools for interactive feature dimensioning, positioning, and orientation specifications. A free-form feature-based capability allows the user to create and customize a suitable design feature library independent of manufacturing features. Finally, the system supports a geometric reasoning algorithm to assist in feature interpretation and instantiation. Whereas previous systems [13] tend to rely heavily on user specifications to guide tool selection, machining parameters computation, and generation of the tool path, the IKBE architecture has the capability to compete alternative part geometry with optimal material selection and process design.

2-4

There are two basic approaches for automated process planning: the variant approach and the generative approach [1]. Variant process planning is based on the retrieval and modification of a stored process plan for a similar part. The parts are grouped into classes and standard plans are stored for each class. This approach is useful only when all parts being designed can be classified in a number of categories depending on certain attributes. The process plan of a particular part is generated by identifying the part class, retrieving the plan, and modifying it to fit the new part attributes. Some systems using this approach are CAPP™, MILTURN™ and MULTIPLAN™.

Generative process planning systems compose a new plan for each part. A generative process plan is synthesized based on information about the part, the machines, tooling fixturing, and certain process planning rules. There are no process plans pre-stored in a data base. The generative approach tends to be more flexible but also more complex so that these systems are not fully automated but tend to rely on human interaction to provide applicable process and material constraints. Several generative process planning systems have been developed such as APPS™, CPPP™, XPS™, AUTOPLAN™, SURFCAM™ Adlard™, GENPLAN™ and AUTAP™.

Of the various recent process planning systems for machining we mention SIPS™, a feature-by-feature process design system being integrated with the National Institute of Science and Technology's Automated Manufacturing Research Facility. CUTTECH™, another feature-by-feature system, orders machining operations and chooses tools together with cutting depths, speeds, and feeds on the basis of feature geometry and material machinability data. XCUT™, a research system similar to SIPS™, accommodates collective process plans for parts that have a one-sided geometry while decomposing features into separate cuts which use geometry and tolerance information to choose tools.

The integrated process planner reviewed in the next section focuses on more comprehensive process design, i.e., planning at a higher level of set-up organization compared to other systems which are typically limited to one set-up or non-interacting feature-by-feature process plans.

ADAPTIVE MODELING LANGUAGE (AML)

As stated earlier, process design involves several activities that are typically done manually with little or no automation, while CAD and other feature-based design systems enable the user to interactively design and edit part geometry. An integrated feature-based Adaptive Modeling Language (AML™) automating the manufacturing, inspection, and analysis of custom parts using Knowledge-Based Engineering methods has recently been developed and implemented. Critical functionalities of AML™ include a parametric FBDE, a mixed dimensional solid/surface modeler supporting non-manifold topology, and a geometrical reasoning kernel for multi-axis machining and inspection and process planning automation. The system is oriented toward enabling significant reductions in the machining cost and time to produce small quantities of structural components, i.e., automating the breadth and diversity of components typically associated with a small (fewer than 50 employees) job shop.

The AML™ process planner is a generative planner and is oriented toward addressing the above described needs of a typical job shop to enable rapid prototyping and production. AML™ not only enables automated process planning but allows the designer to change or create new parts through the evaluation of alternative process plans. AML™ is based on a single underlying object-oriented architecture incorporating two patented techniques for competing alternative design/material/process constraints. While an engineer is designing the part, AML™ generates the process plan interacting with the system to inquire about alternative materials, processes, and design specifications. Complex part designs with detailed process plans and analysis models will be concurrently developed in hours or days instead of weeks or months. The functionalities of the AML relevant to our work are summarized in the following subsections.

Part Design and Geometry, Feature Instantiation and Interpretation

The FBDE is a parametric, free-form, constraint driven, three dimensional mixed modeling design environment with an icon-based graphic window interface enabling the user to easily create, edit, and modify the part geometry. The system allows the user to create a free-form feature and parametrically associate its dimensions and orientation with other features. AML™ can reason about complex 3D geometry including multiple intersecting features such as a pocket involving edge profiles blended with a number of bosses. Unlike existing systems, AML™ is not limited to features from a library but enables the user to create and customize a feature library suitable to his/her needs. To create a feature, such as a generic 'wall-profiled' pocket, the user begins by creating a 2D profile feature which defines the pocket base, and selects a feature base-point. AML™ provides a number of alternative methods to assist in the creation of the profile and offers a number of tools to assist the user in the interactive selection of the points and vectors. When the designer uses a feature-based part model to describe part geometry, feature interactions could result in a number of different interpretations or valid aggregate feature geometries. The AML™ geometric reasoning engine enables the user to create a surface attachment constraint to limit the feature instance to only one of these interpretations or when several interpretations of the input specification exist, assists the user in the specification of the selection

Process planning

The part model (geometry) generated by the FBDE is basically a description of the part geometry in terms of the starting geometry (stock) and "design features" with their associated dimensions, tolerances and orientations. An equivalent manufacturing part model is required to account for the different (manufacturing) interpretations of the same part geometry (design). Extracting the necessary manufacturing information from the part geometric description is required to produce the process plan. Therefore a manufacturing part model, depicting the part before and after each setup in terms of the manufacturing features and the associated geometry, is generated. Each design feature is mapped into one or several manufacturing features which may be later refined and reclassified depending upon the selected setup and part orientation. A manufacturing feature is represented by a number of

machining operations satisfying the part geometric description including surface finish and tolerances. A successful automated machining process planner, integrated with a FBDE requires the solution to several fundamental problems related to features translation, intersection and sequencing, setup generation and sequencing, and 'part-stock' fixturing. The automated process planner generates a machining process plan with the following details and specifications:

1. the number of setups required to machine a part,
2. the sequence of the setups,
3. the features within each setup and their sequence,
4. the part geometry before and after each setup,
5. the intermediate part geometry after removing each feature within a setup,
6. the detailed machining operations for machining each feature (including cutting dimension, speeds, feeds, horsepower, material removal rate, etc.),
7. the tooling for each operation including alternatives,
8. the feasible sequence for the machining operations for the different features within the same setup, and
9. the recommended part orientation, and valid surfaces for contact with the fixtures.

The first problem addressed in automating the process design is to cluster the features into a number of sequenced setups and determine the appropriate fixtures to be used. A setup establishes the number of features which can be machined while the part is held within the same fixture. Grouping the features to generate the minimum number of setups while minimizing the number of operations associated with machining one setup before another requires careful visualization and analysis as the number of permutations grow exponentially with the number of features. Some features may belong to more than one setup, thus features are initially grouped into potential setups that will be later refined to minimize the overall time required to machine the part.

A manufacturing feature is comprised of a set of machining operations, related to milling and holemaking constrained by part geometry. These constraints involve conditions before and after successive machining operation and are related to the tool access, the part geometry (open-pocket vs. closed-pocket), and machining capabilities (coolant available), etc. Depending on the bounding surfaces, part-stock dimensions, and other characteristics, a feature to be machined is translated into one or more manufacturing features, each representing a number of machining operations. A number of surface and vector objects are created relative to intersections with other features and the part-stock and associated with feature type, dimensions, tolerances and orientation. These objects constrain the range of tool approach directions relative to non-interference access and orientation of tooling in addition to any required safety or preparatory operations such as drilling highly toleranced corner 'cut-in' surfaces. These additional manufacturing features must also be included in setup generation. The manufacturing part model is basically an enhanced object structure representation in terms of the machining

features. The machining operation sequence for each manufacturing feature is generated as constrained by both feature dimensions and tolerances and material machining resources.

Process Optimization - Setups

A part typically consists of several features and grouping the features into a minimum number of setups with appropriate fixtures is a difficult task. The following steps are taken to generate a minimum number of setups from the part geometry: (i) Features Translation, (ii) Potential Setups Generation, (iii) Elimination of the Redundant Setups and (iv) Setup Optimization. The setups that now remain have no common features and, as a consequence, the process plan has been globally optimized for the minimum number of setups. Further optimization can be achieved by sequencing features and operations and by eliminating intersection overlap among features.

Automated Operation Sequencing

Depending on the complexity of the feature, tolerances, material, and desired finish, up to twenty machining operations may be required to machine a feature. Features belonging to the same setup may use the same tools, but in different order. For example, feature 1 may require the use of dls-200 (a drilling tool) before the use of dls-100 (a different drilling tool), while feature 2 may require the use of dls-100 before the use of dls-200. The goal is to provide the machinist with a 'near' optimal operation sequence, taking into account the following criteria: maintaining tool dependency (for a feature), minimizing tool changes, and minimizing tool travel, thereby guaranteeing a high quality part at the lowest possible cost. AML™ uses a Genetic Algorithm to achieve this goal. The problem, a set of operations required to machine the setup, is read from an input file (see illustrative example section below for an example and typical results). The goal is to perform operation sequencing across features. The machinist is provided with a near-optimal solution. The output does not violate any of the dependency constraints and at the same time minimizes tool changes and tool travel. A globally optimal solution cannot be guaranteed.

Process Optimization - Fixturing and Features

The process plan requires the identification of fixturing surfaces, based upon the type of fixture, for holding the part while allowing machine/tool access to cut the features. The inputs to this module are: (i) the starting part-stock, (ii) the features within the setup, and (iii) the tool orientations and feed directions. Depending on the selected fixturing method, such as a vice, certain criteria are used to identify the best fixturing surfaces. AML™ uses an algorithm to analyze the part surfaces before and after the setups. The objective of the analysis is to determine a feasible, yet least time consuming fixturing method to reduce overall processing time and costs.

Within each fixtured setup a preliminary sequence of machining operations is generated for all intersecting features and subsequently adapted to include sequencing of non-intersecting features for optimization of processing

within a setup. Although not immediately apparent, the number and dimensions of the manufacturing features can be different from the associated design features. AML™ uses a patented technique to optimize the machining process by evaluating dimensions and associated machining parameters for all manufacturing features as they are recomputed based on the selected sequence for processing the design features. These machining parameters include: thin wall conditions, thin floor conditions, and tool clearance (axial and radial).

A GENERAL METHODOLOGY FOR CLUSTERING AND SEQUENCING

It should be clear from the above brief review of the salient capabilities of AML™ that clustering or grouping (e.g. of operations into features or of features into setups) and sequencing (e.g. of setups or of operations within a feature or setup) are two tasks which have to be done at different times and at different levels in an IKBE system. The development of efficient, general purpose algorithms to carry out these tasks formed the focus of our research effort for the SFRP/GSRP. The multifaceted methodology we adopted in the solution of these two problems makes, we believe, our approach and our algorithms quite novel and general. Our methodology is detailed in this section.

First, our approach is operation- based, not feature or setup based. Indeed, once geometric features to be machined have been translated into manufacturing features, each comprised of a set of machining operations related to milling and holemaking and constrained by part geometry, a part to be machined can be reduced to a list of machining operations. These are the basic (i.e. lowest level) machining elements which need to be clustered and sequenced both into setups and within setups. This operation-based approach allows for the clustering of operations accross features so that operations associated with the same feature could conceivably be done in different setups.

Second, the two tasks of clustering and sequencing in our approach are not treated separately. They are carried out simultaneously. This stems from the realization that clustering and sequencing are essentially the same problem. To see this more clearly we need to distinguish between two kinds of clustering: (1) hard or rule-based and (2) soft or metric-based. Hard clustering is based on a set of (universally) accepted rules (e.g. all operations requiring the same tool are grouped together) and can be implemented with simple logic (if-then, while loops, etc.). Soft clustering, on the other hand, is based on a metric or function which assigns a value to regrouping operations. In the first instance (hard clustering) the clustering is treated as constraints in the sequencing task, i.e. only sequences which do not violate the rule-based clustering are feasible. In the second instance (soft clustering), the clustering metric can be combined with the sequencing metric and the now combined clustering and sequencing problems are solved as one. In this case, the cluster metric is essentially a penalty (or reward) function added to the sequencing cost function. Note that this approach also allows for the simultaneous handling of hard and soft clustering with sequencing by having both clustering constraints (for hard clustering) and clustering penalty/reward (for soft clustering).

A third, unique aspect of our approach is the way in which we handle constraints. These constraints are primarily, but not restricted to, precedence constraints reflecting the order in which operations have to be machined. Here again we can distinguish between hard and soft constraints. Hard constraints, based on a set of (universally) accepted rules (for example: to machine a pocket in a hard material, a machinist has to center drill, drill, rough mill and finish mill) are handled as constraints in the sequencing problem through the introduction of a dependency matrix (see next section). Thus, only sequences which do not violate the rule-based hard constraints are feasible. Soft constraints which express preferences rather than rules can be handled via a penalty/reward approach. Here again the approach allows for the simultaneous handling of hard and soft constraints and sequencing. Note also that clustering is in effect a particular type of constraint. Note further that our treatment of hard clustering and hard constraints makes our approach resource-based. Indeed, many hard clustering rules and hard constraints are the reflection of the resources available to machine the part.

Finally, in order to ensure high quality rapid solutions, the optimization engine selected for our approach is the Annealing Genetic Algorithm as described in [14] and reviewed in the next section.

GENERAL PURPOSE ALGORITHMS FOR CLUSTERING AND SEQUENCING

The approach described in the previous section was implemented in a general purpose algorithm carrying out clustering and sequencing under constraints. Although the algorithm was only tested for operation clustering and sequencing within one setup, we believe it will work equally well for setup generation (clustering of operations into setups) and sequencing once appropriate sets of rules and fitness functions for that problem have been generated. Details of this implementation are now provided.

Annealing-Genetic Algorithm

A hybrid simulated annealing/genetic algorithm called the Annealing-Genetic (AG) algorithm is used as the optimization engine to solve the NP-hard clustering and sequencing problems. The AG algorithm was developed by Lin, Kao, and Hsu [14] to meet the following efficiency goals: (1) the algorithm should converge on a solution which is less than 3% away from the global optimum and (2) the computation time should be bounded by a polynomial function of the problem size. The authors show that the time complexity of the algorithm is empirically $O(n^2)$ for the multiconstraint zero-one knapsack, set partitioning, and traveling salesman problems. The AG algorithm is presented in Table 1 and discussed below.

The AG algorithm, as seen in the block diagram of Figure 1, may be viewed as a genetic algorithm with a Boltzman-type selection operator. An initial quasi population is randomly generated. The genetic operators are then applied to the initial quasi population producing the initial population. After computing the fitness and cost of each member in the initial population, the simulated annealing stage of the algorithm is performed.

Table 1. The Annealing-Genetic Algorithm.

```
1.    Initialize the parameters, i.e., population_size, T₀, and α (0 < α < 1);
2.    Randomly generate population P₀';
3.    Apply genetic operators to P₀' to create P₀;
4.    Calculate the fitness and the cost for each point in P₀ (a point is a member of the population);
5.    Calculate the average_cost of P₀;
6.    solution_vector := current_point := the lowest cost point in P₀;
7.    k := 0;
8.    while system is not frozen do
9.    no_of_point := 0;
10.   while no_of_point <= population_size do
11.           Generate next_point from current_point by the move generation strategy;
12.           ΔC := cost of next_point - cost of current_point;
13.           Pr := min[1,exp(-ΔC/Tₖ)];
14.           if Pr > random[0,1) then put next_point into P'ₖ₊₁;
15.                   current_point := next_point;
16.                   no_of_point := no_of_point + 1;
17.           else    pick another point from Pₖ as current_point;
18.   endwhile
19.   Apply the genetic operators to P'ₖ₊₁ to create Pₖ₊₁;
20.   Calculate the fitness and the cost for each point in Pₖ₊₁;
21.   Calculate the average_cost of Pₖ₊₁;
22.   if the lowest cost point in Pₖ₊₁ < solution_vector then update solution_vector;
23.   if it is the initial stage then determine the initial temperature T₁;
24.           T₁ := (the highest cost - the lowest cost) / (population_size/2);
25.   else    Tₖ₊₁ := Tₖ × α;
26.   current_point := the lowest cost point in Pₖ₊₁;
27.   k := k + 1;
28.   if frozen condition is signaled then set system is frozen;
29.   endwhile
30.   Print out the solution-vector as the final solution;
```

Starting with the best fit member in the initial population, a new member is generated by the move generation strategy. This new member is either placed in a new quasi population or discarded according to some probability,. If kept, the move generation strategy is applied to it to obtain another new member. If the new member is discarded, another member is selected from the initial population based on its fitness. This procedure is repeated until the quasi population is filled. The annealing temperature is then decremented and the genetic operators are applied to the quasi population producing the next generation. The process continues until one of several stopping criteria is met.
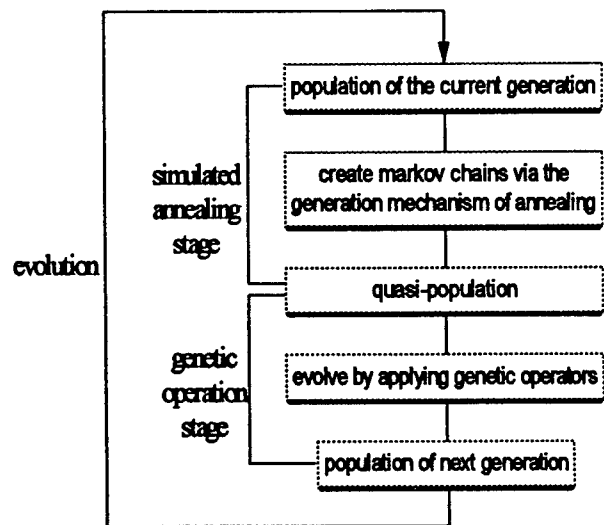

Figure 1. Block Diagram of AG Algorithm

Stopping Criteria/Frozen Condition

There are three separate stopping criterion which signal the frozen condition and stop the algorithm. These are as follows: (1) the maximum number of evolutions has been reached, (2) 80% of the population in a given generation has the same cost as the solution vector, and (3) the temperature in the simulated annealing stage has reached a minimum value. Each of these stopping criteria may be adjusted to yield the desired performance of the AG algorithm. The predetermined values for each of the stopping criterion may also be altered to produce the desired quality of the solution vector.

Genetic Operation Stage

The genetic operators implemented in the AG algorithm modify the members in the quasi population to create a new population. These operators also help to ensure that the average cost of the new population is less than that of the old one (provided the goal is minimization of a cost function). Although other operators such as edge recombination [15] and a newly developed 'forward' edge recombination were implemented, there were no noticeable improvements over the original crossover, inversion, and mutation operators. These three genetic operators are performed in the following steps.

Step 1. Two parents are selected from the quasi population based on their fitness. The crossover operator is applied to these parents producing two offspring. If the offspring have costs less than the average cost of the old generation, they are placed in the new generation. Otherwise, the parents continue the following steps.

Step 2. The inversion operator is applied to the two parents reordering their own sequence to produce two offspring. If the offspring have costs less than the average cost of the old generation, they are placed in the new generation. Otherwise, the parents continue to the next step.

Step 3. The mutation operator is applied to the parents based on a predetermined probability. Finally, the parents are copied to the new generation.

Step 4. Steps 1-3 are repeated until the new generation is filled.

Crossover Operator

Because the solution representation of the problem is not a simple binary string, a special crossover operator is needed to ensure that the bits in a genetic code are not repeated. In the operations sequencing problem, the machinist does not want to perform the same operation twice. In the traveling salesman problem, the salesperson does not want to visit the same city more than once. The crossover algorithm given in [14] is reproduced below as well as an example of its implementation. The example is a solution tour of a 10-city traveling salesman problem.

Step 1. Select two parents, Parent1 [1:n] and Parent2 [1:n], from the population based on their fitness values. Initially, Child1 [1:n] := Child2 [1:n] := 0.

Step 2. Randomly draw two indices p1 and p2 to serve as the crossover points. Then, Child1 [p1:p2] := Parent1 [p1:p2] and Child2 [p1:p2] := Parent2 [p1:p2].

Step 3. Initialize two matching vectors and then set their corresponding indices. That is, Mating1 [1:n] := Mating2 [1:n] := 0. Let Mating1 [Parent1 [p1:p2]] := Parent2 [p1:p2] and Mating2 [Parent2 [p1:p2]] := Parent1 [p1:p2].

Step 4. For each Child1 [i] = 0, 1<= i <= n, perform the following steps:

```
k := Parent2 [i];
while (Mating1 [k] != 0)
        k := Mating1 [k];
        Child1 [i] := k;
endwhile
```

Step 5. For each Child2 [i] = 0, 1<= i <= n, perform the following steps:

```
k := Parent1 [i];
while (Mating2 [k] != 0)
        k := Mating2 [k];
        Child2 [i] := k;
endwhile
```

Figure 2 below shows an example of the crossover operation.

```
Step 1  Parent1  = [9 4 1 3 10 6 8 5 7 2]    Parent2 = [8 2 10 6 7 4 3 1 5 9]
        Child1   = [0 0 0 0 0 0 0 0 0 0]      Child2  = [0 0 0 0 0 0 0 0 0 0]


Step 2  p1 = 3, p2 = 8
        Parent1  = [9 4 | 1 3 10 6 8 5 | 7 2]  Parent2 = [8 2 | 10 6 7 4 3 1 | 5 9]
        Child1   = [# # | 1 3 10 6 8 5 | 7 2]  Child2  = [# # | 10 6 7 4 3 1 | # #]


Step 3  Mating1  = [10 0 6 0 1 4 0 3 0 7]     Mating2 = [5 0 8 6 0 3 10 0 0 1]


Step 4  Child1   = [4 2 | 1 3 10 6 8 5 | 7 9]  Child2  = [9 8 | 10 6 7 4 3 1 | 5 2]
```

Figure 2. An example of a 10-city traveling salesman tour crossover operation.

Inversion Operator/Move Generation Strategy

The inversion operator and the move generation strategy are identical in the AG algorithm. The inversion operator used in the AG algorithm is a swapping move strategy called the random 2-exchange. Two points in the parent solution vector are randomly selected and the order of the elements between them is inverted. For example,

Parent = [1 2 3 4 5 6 7 8 9 10]   p1 = 4, p2 = 9   (chosen randomly)
Child = [1 2 3 | 9 8 7 6 5 4 | 10].

Instead of implementing the random 2-exchange inversion illustrated above for the move generation strategy in the simulated annealing stage of the AG algorithm, other operators such as crossover, edge recombination, and 'forward' edge recombination were attempted. We believed that a 'forward' edge recombination operator (in which forward edges have a higher probability of being selected) would help preserve the satisfaction of precedence constraints. Unfortunately, this operator was not destructive enough to prevent premature convergence of the algorithm. Since no great advantages were observed, the original inversion operator of [14] (the random 2-exchange shown above) was retained for this problem.

Mutation Operator

The mutation operator is only applied according to some very small predetermined probability, usually set close to one percent. When mutation is invoked, two points in a parent solution vector are selected at random and exchanged. The result is a mutated child. For example,

$$\text{Parent} = [1\ 2\ 3\ 4\ 5\ 6\ 7\ 8\ 9\ 10]\quad p1 = 2, p2 = 8\quad \text{(chosen randomly)}$$
$$\text{Child} = [1\ 8\ 3\ 4\ 5\ 6\ 7\ 2\ 9\ 10].$$

Dependency Constraints

Depending on the material and the feature type (shape), certain operations have to be performed in order. For example, to machine a pocket in a hard material, a machinist has to center drill, drill, rough mill, and finish mill. These operations have to be performed in this order. If a machinist tries to plunge with the mill before drilling, the mill might slip and break. The dependency list provided in the data file captures the order in which the operations have to be performed for a single feature.

However, the dependency list is not limited to single feature considerations. Common sense machining may require that certain features be machined before others to ensure the machinist's safety (hard constraints). Also, individual machinists may have their own machining preferences (soft constraints). All of these precedence constraints (i.e. which operations should be performed before others) may be captured by both user interaction/input and intelligent hard-coded rules governing common sense machining and safety considerations. In our algorithm the hard constraint are represented by a (precedence) constraint matrix in which a value of 1 in position [i,j] denotes that operation i must precede operations j.

Repairing Infeasible Solutions

The genetic operators and the move generation strategy do not guarantee that the precedence constraints are satisfied. Thus, infeasible solutions may infect the population. A common approach to avoid violating precedence constraints is to penalize invalid tours with a low fitness value. This is a valid approach but it often requires careful selection of penalizing constants, which can itself be a difficult task. Even with appropriate penalization, the penalty function approach does not guarantee that the final solution will be feasible. The ideal solution to maintaining precedence constraints is to have genetic operators which do not violate them. Until such operators are developed, infeasible solutions in the population must be repaired. In order to preserve the robustness of the genetic algorithm, the repair mechanism must both maintain some of the feasible structure of the infeasible solution and be stochastic in nature. Given such a repair mechanism, the AG algorithm can search only the feasible realm of solutions producing high quality solutions fast. The following discussion explains an inventive repair mechanism which appears to work well for the operations sequencing problem.

Precedence constraints can be handled nicely within the framework of a precedence matrix. Consider the list of operations and dependencies found in Tables 2 and 3. The corresponding precedence matrix in which a value of 1 in position [i,j] denotes a dependency on the order of operations i and j. The precedence matrix may be read as operation in row i should come before operation in column j. For example, operation 3 is performed before operation 4. The precedence matrix may also be read as an antecedent matrix in which operation in column j should come after operation in row i. An example is operation 6 should be performed after operation 5 is performed.

By transforming a simple string of operations into its corresponding precedence matrix, dependency violations can easily be recognized and repaired. Consider the solution sequence of operations {3,1,5,0,4,2,6}. The precedence matrix for this sequence is shown in Table 4. Dependency constraint violations are easily recognized by comparing the precedence constraint matrix to the precedence matrix of the solution vector. If position [i,j] of the constraint matrix contains a 1, position [i,j] of the solution vector's precedence matrix must also contain a 1. Examining row 4 of the constraint matrix in Table 3 reveals that operation 4 is not required to precede any other operation. However, column 4 requires operation 4 to follow operation 3. To determine if this constraint is satisfied by the proposed solution vector above, the precedence matrix of the solution vector must have a 1 in position [3,4]. As seen, there is a 1 located in position [3,4]. Thus, this particular dependency constraint is satisfied. If there had been a 0 in position [3,4] of the precedence matrix, the constraint would have been violated and the solution vector would need to be repaired in order to be feasible.

The repair process may be understood through a simple demonstration. Inspecting the possible solution vector of above,

| 3 | 1 | 5 | 0 | 4 | 2 | 6 |

several precedence constraint violations are revealed. The constraint matrix requires that operation 0 come before operation 1. This is denoted by a closing bracket.

| 3 |]1 | 5 | 0 | 4 | 2 | 6 |

Violation repair is accomplished by simply placing operation 0 randomly before operation 1.

| 0 | 3 | 1 | 5 | 4 | 2 | 6 |

The constraint matrix requires operation 1 to precede operation 3 and to follow operatin 0.

| 0[|]3 | 1 | 5 | 4 | 2 | 6 |

The violation is eliminated by randomly placing operation 1 within the brackets. In this case there is only one choice.

| 0[| 1 |]3 | 5 | 4 | 2 | 6 |

Continuing, the constraint matrix reveals that operation 2 must be executed before operation 3.

| 0 | 1 |]3 | 5 | 4 | 2 | 6 |

Again, the violation is eliminated by randomly placing operation 2 before the closing bracket.

| 0 | 2 | 1 | 3 | 5 | 4 | 6 |

2-15

Next, operation 3 is required by the constraint matrix to precede operation 4 and to follow operations 1,2 and 6. Since operation 6 is furthest to the right, the opening bracket may be placed there without violating the antecedent constraints on operation 3.

<div align="center">0   2   1   3   5   4]   [6</div>

When this situation occurs, the brackets must be repositioned without violating any additional constraints to form a closed set. In this example, the constraint matrix dictates that operation 6 must be performed after operation 5. Therefore, it is exceptable to rewrite the solution vector placing operation 6 appropriately after operation 5 such that the brackets are closed.

<div align="center">0   2   1   3   5   6[   ]4</div>

Operation 3 may now be placed safely within the closed brackets.

<div align="center">0   2   1   5   6[3   ]4</div>

The above sequence of operations now represents a feasible solution vector.

Table 2. Operation dependencies.

Op-ID	Dep-L
0	none
1	1
2	none
3	1,2,6
4	3
5	none
6	3

Table 3. Dependency constraint matrix.

i\j	0	1	2	3	4	5	6
0	0	1	0	0	0	0	0
1	0	0	0	1	0	0	0
2	0	0	0	1	0	0	0
3	0	0	0	0	1	0	0
4	0	0	0	0	0	0	0
5	0	0	0	0	0	0	1
6	0	0	0	1	0	0	0

Table 4. Solution vector precedence matrix.

i\j	0	1	2	3	4	5	6
0	0	0	1	0	1	0	1
1	1	0	1	0	1	1	1
2	0	0	0	0	0	0	1
3	1	1	1	0	1	1	1
4	0	0	1	0	0	0	1
5	1	0	1	0	1	0	1
6	0	0	0	0	0	0	0

Cluster-Preserving Repair

Constraint violations may involve operations belonging to the same cluster (intra-cluster violation) or operations belonging to to different clusters (inter-cluster violation). In carrying out the repair algorithm of the previous subsection it is imperative not to destroy the clustering. To this end, in case of an intra-cluster violation, the repair algorithm is carried out on the subset of operations constituting the cluster (intra-cluster repair), while in case of an inter-cluster violation, the repair algorithm is carried out on a string representing the sequence of clusters (inter-cluster repair). Clever methods for tagging operations by cluster id, for collapsing an operation string into a cluster string and for expanding back a cluster string into an operation string greatly facilitate the implementation of this cluster-preserving repair algorithm. In addition, in order to carry out inter-cluster repair, one needs to build the constraint matrix corresponding to cluster strings. This is done by collapsing rows and clumns of the operation

constraint matrix corresponding to operations belonging to the same cluster (identified by the cluster id tag).

ILLUSTRATIVE EXAMPLE

The data file (reproduced in Table 5 below) is part of a process plan for a real part (anchor plate for the F-16). It contains the following information for each operation in the setup: Feature name (id), Operation number, Operation Name, Tool id, Coordinates of the clearing starting point, Coordinates of the clearing ending point, and Dependency list. For each operation in the setup the data file contains the following information: Feature name (id), Operation number, Operation Name, Tool id, Coordinates of the clearing starting point, Coordinates of the clearing ending point, and Dependency list. An Operation-Id has been added for easy referencing.

Table 5. Sample input data file.

OP Id	Ft-n	OP#	OP-TYPE	TOOL-Id	C-S-Pt	C-E-Pt	DepL
0	PROFILE-1	11	CENTER-DRILL-NON	DLS-007	(-1.76 0.00 1.35)	(-1.76 0.00 1.35)	(0)
1	PROFILE-1	12	CENTER-DRILL-NON	DLS-007	(-0.92 1.50 1.35)	(-0.92 1.50 1.35)	(0)
2	PROFILE-1	13	CENTER-DRILL-NON	DLS-007	(0.92 1.50 1.35)	(0.92 1.50 1.35)	(0)
3	PROFILE-1	14	CENTER-DRILL-NON	DLS-007	(1.76 0.00 1.35)	(1.76 0.00 1.35)	(0)
4	PROFILE-1	15	CENTER-DRILL-NON	DLS-007	(0.92 -1.50 1.35)	(0.92 -1.50 1.35)	(0)
5	PROFILE-1	16	CENTER-DRILL-NON	DLS-007	(-0.92 -1.50 1.35)	(-0.92 -1.50 1.35)	(0)
6	PROFILE-1	17	DRILL-NON	DLS-123	(-1.76 0.00 1.35)	(-1.76 0.00 1.35)	(11)
7	PROFILE-1	18	DRILL-NON	DLS-123	(-0.92 1.50 1.35)	(-0.92 1.50 1.35)	(12)
8	PROFILE-1	19	DRILL-NON	DLS-123	(0.92 1.50 1.35)	(0.92 1.50 1.35)	(13)
9	PROFILE-1	110	DRILL-NON	DLS-123	(1.76 0.00 1.35)	(1.76 0.00 1.35)	(14)
10	PROFILE-1	111	DRILL-NON	DLS-123	(0.92 -1.50 1.35)	(0.92 -1.50 1.35)	(15)
11	PROFILE-1	112	DRILL-NON	DLS-123	(-0.92 -1.50 1.35)	(-0.92 -1.50 1.35)	(16)
12	PROFILE-1	113	DRILL-IN	DLB-005	(-0.35 0.00 1.35)	(-1.67 0.00 1.35)	(0)
13	PROFILE-1	114	R-E-MILL-NON-F&W	MLS-0996	(-0.35 0.00 1.35)	(-1.67 0.00 1.35)	(113 112 111 110 19 18 17)
14	PROFILE-1	115	FIN-END-MILL-WALL	MLS-0198	(-1.67 0.00 1.35)	(-1.67 0.00 1.35)	(114)
15	PROFILE-2	21	CENTER-DRILL-NON	DLS-009	(3.10 0.49 1.35)	(2.95 0.46 1.35)	(0)
16	PROFILE-2	22	DRILL-NON	DLS-152	(3.10 0.49 1.35)	(2.95 0.46 1.35)	(21)
17	PROFILE-2	23	R-END-MILL-F&W	MLS-0996	(3.10 0.49 1.35)	(2.95 0.46 1.35)	(22)
18	PROFILE-2	24	F-END-MILL-WALL	MLS-0198	(2.95 0.46 1.35)	(2.95 0.46 1.35)	(23)
19	PROFILE-3	31	CENTER-DRILL-NON	DLS-009	(-3.10 -0.49 1.35)	(-2.95 -0.46 1.35)	(0)
20	PROFILE-3	32	DRILL-NON	DLS-152	(-3.10 -0.49 1.35)	(-2.95 -0.46 1.35)	(31)
21	PROFILE-3	33	R-END-MILL-F&W	MLS-0996	(-3.10 -0.49 1.35)	(-2.95 -0.46 1.35)	(32)
22	PROFILE-3	34	F-END-MILL-WALL	MLS-0198	(-2.95 -0.46 1.35)	(-2.95 -0.46 1.35)	(33)
23	HOLE-1	41	DRILL-IN	DLB-005	(4.80 0.00 1.35)	(4.80 0.00 1.35)	(0)
24	HOLE-2	51	DRILL-IN	DLB-005	(-4.80 0.00 1.35)	(-4.80 0.00 1.35)	(0)

The coordinates are needed to calculate the distance the tool has to travel,. If a tool change is needed, then the machine has to go back to the tool starting point and perform a tool change. From there, it must go to the clear starting point of the next operation. If a tool change is not needed, then the tool has to travel from the end clear point of an operation to the start clear point of the next operation. Depending on the material and the feature type

(shape), certain operations have to be performed in order. For example, to machine a pocket in a hard material, a machinist has to center drill, drill, rough mill and finish mill. These operations have to be performed in this order. If a machinist tries to plunge with the mill before drilling, the mill might slip and break. The dependency list captures the order in which operations have to be machined.

If this process plan was used as is, then twelve tool changes would be required. But by running this process plan through the algorithm currently implemented in AML™, a process plan that requires less tool changes is produced. This process plan will help greatly in reducing the time it takes to machine the part, and thus reducing the cost of machining it. The following are the two best sequences (listed by Operation Id's although the actual format of the output is Feature name, Tool-id, and Operation number) found by the Genetic Algorithm employing a penalty function approach:

(19, 15, 1, 2, 0, 5, 3, 4, 20, 16, 7, 8, 11, 9, 10, 6, 12, 24, 23, 21, 17, 13, 18, 14, 22), tool_travel=112.797974, tool_changes=6

(0, 5, 4, 1, 15, 19, 2, 3, 20, 16, 7, 8, 11, 9, 10, 6, 12, 24, 23, 21, 17, 13, 18, 22, 14), tool_travel=114.963272, tool_changes=7

Note that the second of these does not have the minimum number (6) of tool changes which is guaranteed by our simultaneous clustering/sequencing approach.

In contrast, the best solution (which we believe to be the globally optimal solution) found by our algorithm is:

(12, 24, 23, 15, 19, 20, 16, 5, 0, 1, 2, 3, 4, 8, 9, 10, 11, 6, 7, 17, 13, 21, 22, 14, 18), tool_travel=100.939133, tool_changes=6

The solution most commonly found by our algorithm is:

(19, 15, 23, 12, 24, 1, 0, 5, 4, 3, 2, 16, 20, 8, 9, 10, 11, 6, 7, 17, 13, 21, 22, 14, 18), tool_travel=101.247757, tool_changes=6

which is only 0.31% away from the believed global optimum). Our approach not only guarantees the minimum number of clusters, but it optimally sequences the clusters both externally and internally producing an operations sequence which minimizes tool travel. The previous GA/penalty approach appears to get trapped in a feasible solution and is not able to optimize further. As shown above, our approach is able to reduce the tool travel an additional 13.9%.

CONCLUSIONS

A review of the issues related to the integration of product design with material and process planning has been presented in the intoduction to this report. The research issues have been discussed and a demonstrated solution presented. Previous systems have been designed to take input either from a GT code or from a descriptive file created by a user. In some instances, these previous systems have involved a descriptive language implemented via shape features (holes, pockets, etc.) to interpret the part geometry and convert it into a special format to generate prescribed process planning information.

We have seen a technological leap in the development of CAD systems, leading to a growing gap between design and process planning automation. AML™ is intended to close that gap and provide a process design capability which is completely automated. The process planner generates process specifications based on the part geometry, material, and process constraints. As exemplified by machining, the plan specifications are then passed to the tool path planner that generates and simulates the cutting path. The NC part program is automatically generated accounting for tool geometry, tool changes, machining data, and obstacle avoidance (fixtures). No user interactions are needed, all parameters are automatically extracted or computed. AML™ is capable of validating the recommended vise fixturing surfaces.

The methodology used fo developping our general purpose clustering/sequencing algorithm is novel in that (1) it is operation based, (2) it combines the two tasks of clustering and sequencing into a single one, (3) it ensures that hard constraints are satisfied directly (not through a penalty/reward approach which, as illustrated in the example may lead to solutions of a lesser quality), (4) it allows for competing soft clustering and/or soft constraints (often resulting from user 'what-if' scenarios) between themselves or with other objectives, and (5) it is general enough to be applied at every level in the product design and process.

The implementation makes use of clever mechanisms to handle constraints, repair, etc. The illustrative example suggest its superiority over existing algorithms in solving the NP-hard clustering/sequencing problem.

The algorithm can easily be integrated into a KBDE system such as AML™. Future work will concentrate on complementing the algorithm with heuristic , experience based rules. This will allow the system to present the user with suggestions regarding alternative materials and processes and ultimately, .

REFERENCES

1. T. C. Chang, "Expert System Planning for Manufacturing," Addison-Wesley, NY., 1990.

2. Chen, C.L.P., LeClair, S.R., An Integration of Design and Manufacturing: Solving Setup Generation and Feature Sequencing Using Unsupervised Learning Approach, J. of Computer Aided Design, 26, No. 1, pp. 59-75, Butterworth-Heinemann Ltd London, UK, 1993.

3. S. R. LeClair, H. N. Kamhawi, and C. L. P. Chen, "Feature Sequencing in the Rapid Design System Using a Genetic Algorithm, " North America Manufacturing Research Conf., NAMRC, XXII, pp. 95-100, May, 1994.

4. M. Kanumury and T. C. Chang, "Process planning in an automated manufacturing environment", J. of Manufacturing Systems, 10, No. 1, pp. 67-78, 1992.

5. Caroline Hayes and Paul Wright, "Automating process planning: using feature interactions to guide search", J. of Manufacturing Systems, 8, No. 1, pp. 1-15, 1990.

6. K. F. Zhang, A. J. Wright and B. J. Davies, "A feature-recognition knowledge base for process planning of rotational mechanical components", The Intl J. of Advanced Manufacturing Technology, 4, pp. 13-25, 1989.

7. P. Prabhu and H. P. Wang, "Algorithms for Computer-Aided Generative Process Planning," ibid., 6, No. 1, 1991.

8. Jonathan F. Bard and Thomas A. Feo, "The cutting path and tool selection problem in computer aided process planning", J. of Manufacturing Systems, 8, No. 1, pp. 17-26.

9. Y. H. Pao, F. L. Merat, & G. M. Radack, "Memory-Driven, Feature-Based Design," WL-TR-93-4021 , Materials Directorate, Wright-Patterson AFB, OH, January 1993, Case Western Reserve University, Air Force Contract Number F33615-87-C-5250, Distributed January 1993.

10. Y. H. Pao, K. Komeyli, D. Shei, S. R. LeClair, & A Winn, "The Episodal Associative Memory: Managing Manufacturing Information on the Basis of Simularity and Associativity," J. of Intelligent Manufacturing, 4, No. 1, pp23-32, February 1993,

11. T. E. Westhoven, C. L. P. Chen, S. R. LeClair, & Pao, Y.H., Episodal Associative Memory Approach for Sequencing Interactive Features in Process Planning, Artificial Intelligence for Engineering Design, Analysis and Manufacturing, 6, No. 4, pp 177-197, December, 1992.

12. Pao, Y., Komeyli, K., Goraya, T. & LeClair, S.R., A Computer-Based Adaptive Associative Memory in Support of the Design and Planning, Intl J. of Applied Artificial Intelligence, Hemisphere Publishing Company, Corp., New York, NY.

13. Parametric Technology, Inc., "Pro-Manufacturing", User's Manual, Waltham, MA, 1993.

14. F.T. Lin, C-Y Kao and C-C Hsu,"Applying the Genetic Approach to Simulated Annealing in Solving Some NP-Hard Problems," IEEE Trans. on Sys., Man, and Cyb., 23.,No. 6, pp.1752-1767, Nov/Dec 1993.

15. Michalewicz, Z., "Genetic Algorithms + Data Structures = Evolution Programs," Springer-Verlag, Berlin Heidelberg, 1992.

Virtual Dislocations

Victor L. Berdichevsky
Professor
Mechanical Engineering Department

Wayne State University
Detroit, MI

Virtual Dislocations

Victor Berdichevsky
Professor
Wayne State University

Abstract

Some phenomena is solid mechanics, like brittle-ductile transition can be explained by spontaneous generation of dislocations when temperature exceeds some critical value. To develop theory of such phenomena, one has to know energy of dislocations in inhomogeneous stress field. This expression is derived and discussed in this paper from various perspectives. This paper is the first one in the series of papers on spontaneous nucleation of dislocations caused by change of temperature and/or external stresses.

Virtual Dislocations

Victor Berdichevsky

1. Introduction

A motivation for this work came from the recent idea by Khantha, Pope and Vitek [1-3] that brittle-ductile transition is a Kosterlitz-Thouless type phase transition [4]. Kosterlitz and Thouless proposed that "sleeping" dislocational dipoles are always presented in a crystalline body: dipoles are permanently born due to thermal fluctuations and disappeared because dipole energy is high. However, if temperature exceeds some critical value, dislocations forming the dipoles move away due to dipole instability and become "independent" dislocations. Kosterlitz and Thouless assumed that this is the basic mechanism of crystal melting. They found from this assumption the melting temperature. Khantha, Pope and Vitek suggested that the same mecahnism is the leading one in brittle-ductile transition when brittle materials become ductile if temperature exceeds some critical value T_c: one needs only to incorporate the external stresses acting on dipoles in the vicinity of crack tip in order to find T_c. Putting aside the discussion of feasibility of such approach (it will be given elsewhere) I focus herein on a derivation of energy expression of a system of dislocations, a starting point in any theoretical estimations of T_c. The necessity to address this issue can be seen from the fact that in the literature on theory of dislocations it is considered usually a dislocation in constant stress field, while for a dipole a change of the external stress field on the distances of order of the dipole size can be important (This is one of the reasons why the calculation of critical temperature given in [1] is, I think, not correct).

Another motivation for this work came from the recent advancements in development of statistical mechanics of vortex gas [5]. It will be shown in Section 5, that energy of point vortex gas is similar to energy of system of dislocations. Therefore, the method of complex probabilities developed in [5] can be applied to prediction of brittle-ductile transition. The present work is the first one in the series of papers on brittle-ductile transition and concerns only with calculation of energy. Three different approaches to calculation of dislocation energy will be considered. The first one is based on Ericksen's idea [6] on the form of energy of a crystalline body. It is "the most fundamental" in the sense that dislocations are treated as localized solutions of a field theory. The second one inroduces plastic deformations associated with dislocations in an explicite way. It allows one to desingularize the usual approach and "spell out" all singularities. The third way of calculation of energy is the standard one (see, for example, [8]). It is derived from the second approach. The general consideration is followed by derivation of dislocation energy in the case of antiplane deformation.

2. Dislocations as Localized Solutions of a Field Theory.

It is natural to treat dislocations within a continuum theory because stresses and strains caused by dislocations are changed slow except the very vicinity of dislocation cores. The "most fundamental" level of continuum discription would be a continuum in which the lattice spacing h is considered as a finite distance.

A key to constructing a model of such continua was proposed by Ericksen [6] and discussed in more details by M. Pitteri [8] and G. Parry [9] (see also the

monograph by M. Pitteri and G. Zanzotto [10]). Ericksen made the following observation. Let $\underline{e}_i$ (i=1, 2, 3) be the basic vectors of a crystal lattice. Then the transformation

$$\underline{e}_i{}' = m_i^j \, \underline{e}_j \qquad (2.1)$$

gives another set of basic vectors $\underline{e}_i{}'$ if m_i^j are some digits and $\det \left\| m_i^j \right\| = 1$ (summation over repeated indices is implied).

Denote by U energy density of the crystal. If the crystal is deformed homogeneously U is a function of the basic vectors $\underline{e}_i$ in the deformed state:

$$U = U(\underline{e}_i) \qquad (2.2)$$

Ericksen's theorem means that energy density should be invariant under action of the group (2.1). Let ξ^a (a=1, 2, 3) are Lagrangian coordinates in an unstressed perfect lattice, and x^i are coodinates of an observer's frame. The motion of continuum particles are given by functions $x^i(\xi^a)$. If deformation is homogeneous, $\dfrac{\partial x^i}{\partial \xi^a}$ are the components of the basic vectors in the deformed state. Therefore,

$$U = U\left(\frac{\partial x^i}{\partial \xi^a} \right) \qquad (2.2)$$

The energy of the whole crystal is

$$E = \int_V U\left(\frac{\partial x^i}{\partial \xi^a} \right) d^3\xi \qquad (2.3)$$

3-5

We accept that the expression (2.3) is valid for inhomogeneous deformations as well.

Function (2.2) is invariant under transformations (2.1). This makes energy functional highly nonconvex. Therefore one might expect a lot of equilibrium states with localized solutions (see the review [11]).

Invariance (2.1) allows one to introduce plastic deformation at each point in a very natural way: for a given total deformation $x_a^i \equiv \dfrac{\partial x^i}{\partial \xi^a}$ one has to find a closest minimum of energy density $U(x_a^i)$. The value of deformation at the minimum point is, by definition, plastic deformation.

Unfortunately, it turned out to be difficult to present U in an explicite form [8-10] in general case. Herein, we do it for antiplane deformations. In this case the function $x^3(\xi^a)$ has the form

$$x^3 = \xi^3 + w(\xi^\alpha)$$

$$x^\alpha = \xi^\alpha \qquad (2.4)$$

Greek indices run values 1, 2.

The lattice transformations corresponding to (2.4) leaves the vector $\underline{e}_3$ invariant

$$\underline{e}_3{}' = \underline{e}_3 \qquad (2.5)$$

while vectors $\underline{e}_\alpha$ get transformed:

$$\underline{e}_\alpha{}' = \underline{e}_\alpha + n_\alpha \underline{e}_3 \qquad (2.6)$$

where n_α are digits.

Energy density U depends on x_a^i through the metric tensor

$$g_{ab} = x_a^i x_b^i \qquad (2.7)$$

due to invariance of energy with respect to rotations of the crystal as a rigid body. Let for simplicity,the lattice is cubic. Therefore in the undeformed state

$$g_{\alpha\beta} = \delta_{\alpha\beta}, \ g_{33} = 1, \ g_{3\alpha} = 0.$$

Deformation (2.5), (2.6) corresponds to the following transformation of the components of metric tensor

$$g'_{\alpha\beta} = \underline{e}_\alpha' \cdot \underline{e}_\beta' = \left(\underline{e}_\alpha + n_\alpha \underline{e}_3\right) \cdot \left(\underline{e}_\beta + n_\beta \underline{e}_3\right) = \delta_{\alpha\beta} + n_\alpha n_\beta$$

$$g'_{\alpha 3} = \underline{e}_\alpha' \cdot \underline{e}_3' = \left(\underline{e}_\alpha + n_\alpha \underline{e}_3\right) \cdot \underline{e}_\beta = n_\alpha$$

$$g'_{33} = 1 \qquad (2.8)$$

Energy density should be invariant with respect to transformations (2.8). Without loss of generality, energy density can be written as a function of the arguments $g_{\alpha\beta} - g_{\alpha 3} g_{\beta 3}$, $g_{\alpha 3}$ and g_{33}. Since $g_{\alpha\beta} - g_{\alpha 3} g_{\beta 3}$, $g_{\alpha 3}$ are invariant with respect to the transformations (2.8), we conclude that U is a periodic function of g_{13} and g_{23} with the period 1 which depends arbitrarily on $g_{\alpha\beta} - g_{\alpha 3} g_{\beta 3}$ and g_{33}.

$$U\left(g_{\alpha\beta} - g_{\alpha 3} g_{\beta 3}, g_{33}, g_{13}, g_{23}\right) = U\left(g_{\alpha\beta} - g_{\alpha 3} g_{\beta 3}, g_{33}, g_{13} + n_1, g_{23} + n_2\right)$$

Here n_1 and n_2 are any digits. Note that tensor $g_{\alpha\beta} - g_{\alpha 3} g_{\beta 3}$ does not depend on $w(\xi^\alpha)$ for antiplane deformations (2.4):

$$g_{\alpha\beta} - g_{\alpha 3} g_{\beta 3} = \frac{\partial x^i}{\partial \xi^\alpha} \frac{\partial x^i}{\partial \xi^\alpha} - \frac{\partial x^i}{\partial \xi^\alpha} \frac{\partial x^i}{\partial \xi^3} \frac{\partial x^j}{\partial \xi^\beta} \frac{\partial x^i}{\partial \xi^3} = \delta_{\alpha\beta} + \frac{\partial w}{\partial \xi^\alpha} \frac{\partial w}{\partial \xi^\beta} - \frac{\partial w}{\partial \xi^\alpha} \frac{\partial w}{\partial \xi^\beta} = \delta_{\alpha\beta}.$$

Therefore, energy density is a periodic function of $\frac{\partial w}{\partial \xi^1}$, and $\frac{\partial w}{\partial \xi^2}$. Dropping all other arguments one can write

$$U = U\left(w_{,1}, w_{,2}\right)$$

$$U\left(w_{,1} + n_1, w_{,2} + n_2\right) = U\left(w_{,1}, w_{,2}\right)$$

where n_1, n_2 are arbitrary digits.

The simplest form of U is

$$U = \frac{\mu}{(2\pi)^2}\left(-\cos 2\pi w_{,1} - \cos 2\pi w_{,2} + 2\right) \qquad (2.9)$$

The corresponding stresses are

$$\sigma_1 = \frac{\mu}{2\pi}\sin 2\pi w_{,1} \ , \ \ \sigma_2 = \frac{\mu}{2\pi}\sin 2\pi w_{,2} \qquad (2.10)$$

and the equilibrium equation is

$$w_{,11}\cos 2\pi w_{,1} + w_{,22}\cos 2\pi w_{,2} = 0 \qquad (2.11)$$

The search of exact localized solutions of equation (2.11) which correspond to screw dislocations is in progress now.

3. The Case of Prescribed Plastic Deformations.

The approach outlined in the previous section can be certainly useful in numerical simulations of crystal lattices because the ad hoc numerical schemes used often do not have a clear theoretical background. On the other hand a direct derivation of properties of dislocations from this approach is not simple due to high nonlinearity. A significant simplification can be made, however, by means of the following observation. Let $x_a^i(\xi)$ be some equilibrium distortion. One can calculate

the plastic distortion $\overset{(p)i}{x}_a$ using the definition given in the previous section. Then elastic distortion $\overset{(e)i}{x}_j$ is determined, by definition, by the equality

$$x^i_a = \overset{(e)i}{x}_j \overset{(p)j}{x}_a \tag{3.1}$$

Note that the total distortion x^i_a is always compatible, i.e.

$$\frac{\partial x^i_a}{\partial \xi^b} = \frac{\partial x^i_b}{\partial \xi^a} \tag{3.2}$$

while $\overset{(e)i}{x}_j$ and $\overset{(p)j}{x}_a$ are not, in general. Elastic distortion should deviate small from the unit matrix. Therefore, for given plastic distortion, elastic energy may be considered as a quadratic function of $\overset{(e)i}{x}_j - \delta^i_j$. This yields that energy density is a function of the tensor

$$\varepsilon^{(e)}_{ab} = \tfrac{1}{2}\left(g_{ab} - \overset{(p)}{g}_{ab} \right)$$

where

$$\overset{(p)}{g}_{ab} = \overset{(p)i}{x}_a \overset{(p)j}{x}_b$$

As an approximation, one can use for the total deformation a linear expression

$$\varepsilon_{ab} = \frac{1}{2}\left(\frac{\partial w_a}{\partial \xi^b} + \frac{\partial w_b}{\partial \xi^a} \right) \equiv w_{(a,b)}$$

Then energy functional takes the form

$$E = \int_V U\left(w_{(a,b)} - \varepsilon^{(p)}_{ab} \right) d^3\xi \tag{3.3}$$

where $\varepsilon^{(p)}_{ab} = \frac{1}{2}\left(g^{(p)}_{ab} - \delta_{ab} \right)$ are the components of the tensor of plastic deformation.

Tensor of plastic deformation in (3.3) is supposed to be given. Then the true displacement field is determined by minimization of energy functional with respect to the displacement field $w_a(\xi)$.

Note that the field $\varepsilon_{ab}^{(p)}$ is always smooth because in the continuum considered the interactomic spacing corresponds to some finite distance h. For a dislocation loop γ plastic deformations $\varepsilon_{ab}^{(p)}$ are given by the formula

$$\varepsilon_{ab}^{(p)} = b_{(a}n_{b)}\delta_{smooth}(\Omega) \tag{3.4}$$

where $\delta_{smooth}(\Omega)$ is a smoothed δ–function with the support in the vicinity of sliding surface Ω having the boundary γ, b_a and n_a are the components of Burger's vector and the unit normal vector to Ω. The size of the support in the normal direction to Ω is h. One of the advantages of the considered approach is a transparent calculation of the expression for the force acting on the dislocation (if dislocations are considereed as singularities, the corresponding calculations are far from being obvious). To obtain this expression let us find variation of energy due to change of the position of the loop γ, i.e. the corresponding change of the field ε_{ab}^{p}. Since the field w_a is the minimizer of the energy functional,

$$\delta E = -\int_V \frac{\partial U}{\partial \varepsilon_{ab}^{(e)}} \delta\varepsilon_{ab}^{(p)} d^3\xi$$

Derivatives $\dfrac{\partial U}{\partial \varepsilon_{ab}^{(e)}}$ are the components of the stress tensor σ^{ab}:

$$\delta E = -\int_V \sigma^{ab} \delta\varepsilon_{ab}^{(p)} d^3\xi \tag{3.5}$$

From (3.4), change δn of the position of the contour γ in the direction of vector v^a which is normal vector to γ lieing in the tangent plane, yields a variation of plastic deformations:

$$\delta\varepsilon_{ab}^{(p)} = b_{(a}n_{b)mc}\tau^m v^c \, \delta_{smooth}(\delta\Omega) \qquad (3.6)$$

Here $\delta\Omega$ is a strip with the long side γ and the short size δn, e_{bme} and τ^m are the components of Levi-Civita tensor and the unit tangent vector to γ correspondingly. From (3.5) and (3.6), tending h to zero, we obtain

$$(3.7)$$

The force f_i acting on unit length of dislocation one can introduce by the relation

$$\delta E = \int_\gamma f_i v^i ds\delta n \qquad (3.8)$$

Comparing (3.7) and (3.8) we find the Peach-Kohler formula

$$f_i = -\sigma^{ab}b_a e_{bmi}\tau^m \qquad (3.9)$$

In the derivation we did not take into account that $\delta\varepsilon_{ab}^{(p)}$ should be incompressible, i.e. $\delta\varepsilon_{ab}^{(p)}=0$. Therefore, we have to correct (3.6) putting

$$\delta\varepsilon_{ab}^{(p)} = \left[b_{(a}e_{b)mc}\tau^m v^c - \frac{1}{3}\delta_{ab}b_n e_{nme}\tau^m v^c \right]\delta_{smooth}(\delta\Omega)$$

This yields the Weertman correction of Peach-Kohler's formula

$$f_i = -\left(\sigma^{ab} - \frac{1}{3}\delta^{ab}\sigma_{kk} \right)b_a e_{bmi}\tau^m$$

4. Dual Variational Principle.

To find the stress field for a given set of dislocations one has to solve the variational problem

$$I = \min_{w(\xi)} \left[\int_V U\left(w_{(a,b)} - \varepsilon_{ab}^{(p)}\right) d^3\xi - \int_{\partial V} f_a w^a d^{2\xi} \right] \tag{4.1}$$

Here   are some given functions of ξ determining the positions of dislocations and   are the compnents of the external fractions.

Following the general scheme of constructing dual variational principles [12] we have

$$I = \min_{w(\xi)} \sup_{\sigma^{ab}} \left[\int_V \left[\sigma^{ab}\left(w_{a,b} - \varepsilon_{ab}^{(p)}\right) - U*\left(\sigma^{ab}\right) \right] d^3\xi - \int_{\partial V} f_a w^q d^{2\xi} \right]$$
$$= \sup_{\sigma^{ab}} \left[-\int \left[U*\left(\sigma^{ab}\right) + \sigma^{ab}\varepsilon_{ab}^{(p)} \right] d^3\xi \right] \tag{4.2}$$

where sup is sought on the set of all stress fields obeying the constraints

$$\frac{\partial \sigma^{ab}}{\partial \xi^b} = 0, \ \sigma^{ab} n_b = f_a \ \text{at} \partial V$$

It is seen that dislocations (i.e. $\varepsilon_{ab}^{(p)}$) are the sources of internal stresses.

5. Dislocations as Singularities.

The traditional way to describe dislocations is to determine them as the surfaces of discontinuity of displacement field. The jump b_i of displacemnt field is considered as given. If the surface of discontinuity Ω is identified with the sliding surface then b_i should be tangent to Ω. Usually b_i are considered as constants which are equal to the atomic spacing. This leads to nonintegrable singularities at the dislocation lines. Since these singularities do not have physical meaning and came

from a too rough approximation, we make the model more feasible assuming that b_i are constants everywhere on Ω except a small vicinity of $\gamma(\equiv\partial\Omega)$ where b_i smoothly change from the constant values inside Ω to zeros on γ. Eliminating in (4.1) the strip of material of atomic size h on the sliding surface, one arrives

at the variational problem

$$I = \min_{\substack{w_i: \\ [w_i]|_\Omega = b_i}} \left[\int_V U\big(w_{(i,j)}\big)d^3\xi - \int_{\partial V} f_i w^i d^2\xi \right] \tag{5.1}$$

The dual variational problem has the form

$$I = \sup_{\sigma^{ij}} \left[\int_\Omega \sigma^{ij} n_j b_i d^2 x - \int_{d^3} U*\big(\sigma^{ij}\big)d^3 x \right] \tag{5.2}$$

where *sup* is sought on the set of all stress field obeying the constraints

$$\frac{\partial \sigma^{ij}}{\partial \xi^i} = 0, \quad \sigma^{ij} n_j\big|_{\partial V} = f^i$$

The desingularization described allows one to put a clear sense in the classical relations of theory of dislocations.

6. Screw Dislocations.

There is a close relation between vortex lines in theory of ideal fluid and dislocations in solids. Roughly speaking, the vector potential of velocity vector in ideal fulid corresponds to stress function in solids. This correspondence became especially transparent in the case of antiplane deformation which is considered in this section.

In this case only one component of displacement vector $w_3 \equiv w(x_\alpha)$, $(\alpha = 1,2,)$ is not zero. Assuming for simplicity, that elastic body is isotropic and linear, from (3.3) we arrive at the variational problem

$$I = \min_w \left[\int_V \frac{\mu}{2} \left[\left(w_{,1} - \varepsilon_{13}^{(p)} \right)^2 + \left(w_{,2} - \varepsilon_{23}^{(p)} \right)^2 \right] d^2x - \int_{\partial V} fw\,ds \right] \qquad (6.1)$$

The dual problem has the form

$$I = \min_w \sup_{\sigma_\alpha} \left[\int_V \left[\sigma_\alpha \left(w_{,\alpha} - \varepsilon_{3\alpha}^{(p)} \right) - \frac{1}{2\mu} \sigma_\alpha \sigma_\alpha \right] d^2x - \int_{\partial V} fw\,ds \right]$$

$$= \sup_{\sigma_\alpha} \left[-\int_V \left(\frac{1}{2\mu} \sigma_\alpha \sigma_\alpha + \sigma_\alpha \varepsilon_{3\alpha}^{(p)} \right) d^2x \right] \qquad (6.2)$$

where sup is sought out the set of all σ_α such that

$$\sigma_{\alpha,\alpha} = 0, \qquad \sigma_\alpha v_\alpha = f \text{ on } \partial V. \qquad (6.3)$$

The general solution of (6.3) has the form

$$\sigma_\alpha = e_{\alpha\beta} \, \psi_{,\beta}, \qquad \psi = \overset{\circ}{\psi}_b(s) \text{ on } \partial V. \qquad (6.4)$$

Here $e_{\alpha\beta}$ are the Levi-Civita symbols, ψ is the stress function, and $\overset{\circ}{\psi}(s)$ is found from the relation

$$\frac{d\overset{\circ}{\psi}_b}{ds} = f(s)$$

Plugging (6.4) in (6.2) we obtain

$$I = -\inf_\psi \int_V \left[\frac{1}{2\mu} \psi_{,\alpha} \psi_{,\alpha} + e_{\alpha\beta} \, \psi_{,\beta} \varepsilon_{3\alpha}^{(p)} \right] d^2x$$

$$= -\inf_\psi \left[\int_V \left[\frac{1}{2\mu} \psi_{,\alpha} \psi_{,\alpha} - \rho\psi \right] d^2x \right] - \int_{\partial V} e_{\alpha\beta} \, v_\beta \varepsilon_{3\alpha}^{(p)} \overset{\circ}{\psi}_b\,ds \qquad (6.5)$$

3-14

where ρ is the dislocation density

$$\rho = e_{\alpha\beta}\varepsilon^{(p)}_{3\alpha,\beta} \qquad (6.6)$$

and *inf* is taken on the set of all functions ψ having the presecribed values $\overset{\circ}{\psi}_b$ at the boundary.

Comparing this problem with the problem of calculation of velocity field for given vorticity ω, we see that ψ corresponds to the stream function of vortex flow while ρ corresponds to vorticity.

If the solution is sought in the form of the sum

$$\psi = \overset{\circ}{\psi} + \tilde{\psi}$$

where $\overset{\circ}{\psi}$ is the stress function in the region V free from dislocations, $\overset{\circ}{\psi} = \overset{\circ}{\psi}_b$ at ∂V, then

$$I = -\int \frac{1}{2\mu}\overset{\circ}{\psi}_{,\alpha}\overset{\circ}{\psi}_{,\alpha}d^2x - \int_{\partial V} e_{\alpha\beta} v_\alpha \varepsilon^{(p)}_{3\alpha} \overset{\circ}{\psi}_b ds - \inf_{\tilde{\psi}}\left[\int_V \left(\frac{1}{2\mu}\tilde{\psi}_{,\alpha}\tilde{\psi}_{,\alpha} - \rho\tilde{\psi}\right)d^2x\right] + \int_V \rho\overset{\circ}{\psi}d^2x \qquad (6.7)$$

Here $\tilde{\psi}$ is subject to the constraint

$$\tilde{\psi} = 0 \text{ at } \partial V.$$

The last term in (6.7) describes the interaction of dislocations with the external field. In the case of a dislocational dipole

$$\rho = b\delta(x - r_1) - b\delta(x - r_2)$$

and the interaction energy is

$$\int \rho\overset{\circ}{\psi}d^2x = b\left(\overset{\circ}{\psi}(r_1) - \overset{\circ}{\psi}(r_2)\right) \qquad (6.8)$$

3-15

If the external field is constant, $\overset{\circ}{\psi} = \sigma^{\alpha} e_{\alpha\beta} x^{\beta}$, and one gets for interaction energy the expression used in [1-3]

$$\text{interaction energy} = \sigma^{\alpha} e_{\alpha\beta} \left(r_1^{\alpha} - r_2^{\alpha} \right) \qquad (6.9)$$

However, if the stress field is inhomogeneous, then (6.9) is a poor approximation of the true energy (6.8), expecially in the vicinity of a crack tip.

Concluding Remarks.

Two results of this paper seem to be important. The first one is the expression for energy (2.9) in a continuum theory of crystals. It is simple enough to expect to have an exact solutions which should yield the formulas for Schmid forces. The second result is an analogy between dislocations and vortices which allows one to use the recent advancements in vortex gas theory [5] to calculate the critical temperatures of brittle-ductile transition.

References

1. M. Khantha, D.P. Pope, V. Vitek, Dislocation Screening and the Brittle-to-Ductile Transition: A Kosterlitz-Thouless Type Instability, Physical Review Letters, vol. 73, N5, 684, 1994.

2. M. Khantha, D.P. Pope, V. Vitek, The Brittle-to-Ductile Transition-I: A Cooperative Dislocation Generation Instability, Scripta Metallurgica et Materialia, vol. 31, no. 10, 1349-1354, 1994.

3. M. Khantha, The Brittle-to-Ductile Transition-II: Dislocation Dynamics and the Strain-Rate Dependence of the Transition Temperature, Scripta Metallurgica et Materialia, vol. 31, No. 10, 1355-1360, 1994.

4. J.M. Kosterlitz, D.J. Thouless, Ordering, Metastability and Phase Transitions in Two-Dimensional Systems, J. Phys., vol. 6, 1181-1203, 1973.

5. V. Berdichevsky, Statistical Mechanics of Point Vortices, Physical Review E., vol. 51, 4432-4452, 1995.

6. J.L. Ericksen, On the Symmetry of Deformable Crrystals, Archive of Rational Mechanics and Analysis, vol. 72, 1-13, 1979.

7. L. Laudau, E. Lifshitz, Theory of Elasticity

8. M. Pitteri, Reconciliation of Local and Global Symmetries of Crystals, J. of Elasticity, vol. 14, 175-190, 1984.

9. G. Parry, On the Elasticity of Monoatomic Crystals, Math. Proc. Comb. Phil. Soc., vol. 80, 189-211, 1976.

10. M. Pitteri, G. Zanzotto, Continuum Models for Twinning and Phase Transitions in Crystalline Solids, Chapman & Hall, 1996 (to appear).

11. V. Berdichevsky, L. Truskinovsky, Energy Structure of Localization, Proc. of Euromech Col. "The Inclusion of Local Effects in Analysis of Structures," Cachan, 1984, Local Effects in Analysis of Structures, Ed. P. Ladevere, Amstordam, 127-158, 1985.

12. V. Berdichevsky, Variational Principles of Continuum Mechanics, Moscow, Nauka, 1983.

Evaluation of:
Defense Technology Industrial Base
Forecasting Model (DTIB-FM)

H. Marshall Booker
Professor
Economics and Finance Department

Christopher Newport University
Newport News, VA

Final Report for:
Summer Research Program
Wright Laboratory

4-1

EVALUATION OF:
I. DEFENSE TECHNOLOGY INDUSTRIAL BASE FORECASTING MODEL
II. S&T IPPD AFFORDABILITY GUIDE
III. ROADMAP REVIEW SEMINAR
IV. AFFORDABILITY WORKSHOP
V. METRIC FOR AGILE VIRTUAL ENTERPRISES
VI. AGILE LABOR UNIONS FOR VIRTUAL ENTERPRISES
VII. DECISION SUPPORT SYSTEM FOR THE MANAGEMENT OF AGILE SUPPLY CHAINS -
PHILIPS LAB

H. Marshall Booker
Professor
Economics and Finance
Christopher Newport University

Abstract

This report provides an overview and evaluation of several select and different projects reviewed while on assignment at Wright-Patterson Air Force Base Manufacturing Technology Directorate. (MT). All seven programs under study are related in some way or another, but more specifically through affordability issues, Integrated Product and Process Design, Agile Enterprise, and/or best business practices associated activities. An effort is made in the following pages to describe each activity and to then evaluate the activity from the perspective of an educator with thirty years experience in the field, and then to render recommendations with regard to programs and processes where appropriate.

Learning is a continuous process where informational gain is measured in output performance characteristics and is critical as a survival guide in the new change oriented environment of the modern competitive world. Frederich Hegel, the philosopher, argued that the only constant in this world is "change" itself. To understand and deal with change is to realize the full advantages of affordability and economic justification among competing resources. New technologies, new products, and new processes will propel us to a new era of survival.

EVALUATION OF:
I. DEFENSE TECHNOLOGY INDUSTRIAL BASE FORECASTING MODEL
II. S&T IPPD AFFORDABILITY GUIDE
III. ROADMAP REVIEW SEMINAR
IV. AFFORDABILITY WORKSHOP
V. METRIC FOR AGILE VIRTUAL ENTERPRISES
VI. AGILE LABOR UNIONS FOR VIRTUAL ENTERPRISES
VII. DECISION SUPPORT SYSTEM FOR THE MANAGEMENT OF AGILE SUPPLY CHAINS -
PHILIPS LAB

H. Marshall Booker

Introduction

As a Summer Research Fellow sponsored by the Air Force Office of Scientific Research assigned

to Manufacturing Technology Directorate, Wright Lab, Wright Patterson Air Force Base I was given the

unique opportunity to combine the experience and perspective of the highly professional personnel of MT

with my own knowledge and expertise. Few people have had an opportunity for either broader or deeper

involvement in such a short span of time. Research, scientific and technical components played a pivotal

role in the welter of programs I was able to evaluate, help design, and/or become a participant.

The educational windows afforded me at WL/MT through the summer fellowship program have

contributed enormously to my opportunities for the formulation and potential implementation of new

research, information systems, and technologies. What follows is a synopsis of the major issues of

involvement while at WL/MT, but in no means is an exhaustive analysis of the magnitude of executive

privilege extended to me at Wl/MT. Each component of the **Summary Statement Section** below is a

separate but somewhat interrelated activity.

Summary Statement Section (I-VII)

I. Defense Technology Industrial Base Forecasting Model

Budget reductions, budget restructurings, base and other facility realignments and closings,

increasing costs of evermore sophisticated ultra-high-technology military systems, reengineered

businesses, the development of virtual enterprises, risk aversion, risk uncertainties, Bottom-Up Review

recommendations, are all having an increasing impact on the United States Defense Technology and

Industrial Base (DTIB). Its stability, sustainability, and direction are in question. It is therefore becoming

more and more essential to accurately forecast the viability and agility of the DTIB in light of the repositioning of resources within the defense system and the overall federal budget as the information portrayed in the diagrams below would indicate.

A methodology is necessary to quantify changes that have occurred over the past and that will accurately predict the future course of events in this arena within a narrow range of probabilities. The Manufacturing Technology Industrial Base Forecasting Model program is an effort to accomplish this goal. This is a difficult task as outdated rules and fundamental assumptions regarding the "new" (old) defense industrial technology base are redefined and/or abandoned. As companies have changed the way they worked over the last few years, increasing dramatically their performance levels, so too will the DTIB product and design process be dramatically engaged in change. This will require new methodologies and understanding as that set of complex activities generically known as the DTIB undergoes radical changes in shape, structure and character. The direction of the defense technology industrial base over the next few years is especially important to discover.

To model this DTIB is a critical endeavor. There are numerous functions, structures, and types of models, yet it must be recognized that basically models are used to represent phenomena through the use of analogy. A model is a representation of a system, designed for the ultimate purpose of studying some aspect of that system or for that matter, the system as a whole.

The model under construction was chosen to use non-survey secondary data rather than primary data. Primary data is drawn from original sources and are collected especially for the project at hand. In this particular case the use of secondary data has especial merits since it is used primarily to fill a need for a specific reference, exploring the past as a contribution to the present and future of the industrial base. This type of retrospective research is a classical example of the use of the historical method to develop models of activity and discover relationships to determine the relevant forecast scenarios of the future.

One of the most important limitations of the use of this type of historical secondary data is that it often does not satisfy the researcher's specific needs in building the model. Differences in definitions, variations in the units of measurement, gaps in the data, different time dimensions and difficulties in

assessing the accuracy of the data as presented all contribute this dilemma. Research and model building relying heavily on secondary data as does this model, are seen as a special case of information retrieval.

Vast inventories of information stored in various forms must be searched using a multitude of indexing systems of information and presentation media to find that which is needed and useful for the model. Information requirements must be carefully matched to available indexes. The development of the DTIB-FM (Defense Technology Industrial Base-Forecasting Model) is therefore faced with significant challenges. Yet the program can also be ensured a high measure of success since it has already begun to identify critical paths to determining improved metrics of technology, integrated product and process designs, quality, and reengineered management theories and operations.

In this regard the DTIB-FM has decided to measure seven critical characteristics of the data base under study:

1)   Management/Organization

2)   Viability

3)   Capacity

4)   Factory Operations

5)   Supplier Relations

6)   Technology Development

7)   Development Processes

It is critically true as the model builders realize, the development of a reliable forecast hinges on the careful consistent use of relevant measurement criteria for each of these seven characteristics. Let us consider for example, the development of the identities of the critical components of one of these characteristics, viz., **Technology Development.** A listing of the initial variables and measures of the intensity of this characteristic is below.

Technology Development

1.   The percent of sales spent for product research
2.   The percent of sales spent for manufacturing or process research
3.   The percent of sales spent on basic research
4.   Ratio of research expenditures to that of companies or countries leading in the sector or technology
5.   Number of patents

6.   Articles or presentations produced
7.   Relevant education and experience of staff to conduct R&D
8.   List of critical technologies in the sector, subsector, or company
9.   Technology ownership; DoD, Civilian, Foreign
10.   Number of years of manufacturing experience on the research team
11.   Facilities and tools necessary to develop manufacturing technology;
               *Simulation, digital and mockup
               *Prototyping capability
12.   Associated manufacturing facilities to act as a test ground and validation of
               technology development
13.   The percent of research aimed at transitioning new technology to applications,
               products, and production
14.   The percent of research aimed at maintenance and overhaul applications

This list is carefully developed and fully representative of the elements that must be considered in constructing this characteristic. It further shows the central focus of possible data collection difficulties in this area unless each of these in turn is carefully and consistently defined in measureable metric terms.

Summary observations and comments are as follows. The Defense Technology Industrial Base Forecasting Model is an ambitious project. One of the most difficult elements of this type of model construction is in the initial testing of various components within established characteristics to determine proper fit and degree of predictability within established confidence levels. Considerable effort must be spent in developing and testing different data bases to establish consistently useable time series of data. At times this requires more effort and time applied to those which end up being rejected than for those being accepted into the model for analysis. This program has efficiently and effectively tackled some of these more difficult tasks and has now readied the model for the development of the remaining characteristics beyond those three already evaluated.

The model and demo development appear to represent a systematic and consistent approach to problem solving and forecasting and the use of the demo will be a highly useful pedagogical and informational device that will generate immediate feedback for future iterations and refinements. Overall program management would probably benefit at this juncture by the development of a system of Gantt Charts and/or other matrices of scheduled activities and processes as the model and demo mature so that all involved have the same expectations with regard to specific future courses of development and action items. Composite and diffusion indexes using time series analysis are difficult to construct and unfortunately are not easily verifiable regarding preciseness of predictability until time itself develops

allowing the model to be self-validating and to accommodate corrections and adjustments where necessary.

Those constructing the model and running its applications must continue to monitor its progress and must pay especial attention to the relevance of establishing weights for each component within each characteristic and then for each characteristic within the holistic model. Careful attention and analysis must also be used to discover the impact and outward effect of the construction of composite indexes even though the confidence levels for each component within the composite are within the same levels of degrees of confidence. Nonetheless, all considered, the time series model is extremely useful in terms of generating useable and useful forecasts and/or evaluating policy and other options. Even with its weaknesses time series models can be easily remedied to correct for potentially damaging consequences of substantive inferences. On the basis of evidence and rigorous analysis, the use of time series models for forecasting is a legitimate goal oriented process which accurately captures the basic elements of utilizable forecasts.

This is an exciting model into which a considerable amount of expertise has been invested to date and whose output is especially promising. Eventually, it might even be possible to adapt the model to some of the new uncertainty techniques being developed in the fields of fuzzy logic and artificial neural networks perhaps making use of SAS Software/Neural Net add-ons with feedforward nets with back and counterpropagation, self-organizing mapping, and various unsupervised architectures. This however goes beyond the scope of the current program.

II. S&T IPPD AFFORDABILITY GUIDE

It is evident that the structure, the management, and the performance of all aspects of the American economy are undergoing rapid change. Lean manufacturing, the agile corporation, the virtual enterprise, integrated product and process development, affordability, etc are all part of a larger concern about competitiveness and survival at all levels and the new structure of economic justification especially as these concerns translate into scientific and technological issues. It is especially critical in the areas of research and development and science and technology that these new principles of management be translated and transferred into useable and effective performance generation techniques in this new age of affordability. Strategic processes and advancement stages must be developed in the S&T arena to take full

advantage of critical paths emerging on the affordability mapping surface as potential change becomes reality.

The development of an S&T IPPD AFFORDABILITY GUIDE (AG) is an exhaustive effort to design a highly useful sourcebook to be used to instruct personnel in the basics of affordability issues as especially applicable to Science and Technology. The organizational architecture of the AG is straightforward and orchestrated around activities that explicitly and lucidly provide pedagogical awareness of the major issues involved in affordability. Each Activity Section in the AG has the same basic organization of a) Overview, b) Checklist, and c) Stem-and-leaf Steps to accomplish competent understanding of each activity level. The AG is an excellent example of some to the best practices in instructional design. It is written to and for an explicitly defined consumer, i.e., (a) Air Force project managers and engineers who are responsible for S&T 6.3 development projects and (2) contractors performing S&T projects. Knowing the audience assists in the development character of the AG and promotes consistency of design throughout each section. The use of extensive appendices, a glossary and acronym section, SOW concepts section, bibliography, and a practical case study make the AG a unique approach to the systematic study of S&T IPPD Affordability concepts and applications.

As the principles of affordability become more accepted and identified and the techniques more widely practiced by professionals, this Affordability Guide will be recognized as the Benchmark upon which other editions will be judged. Affordability is a concept term which has no concise standard definition and when used in some contexts, may imply a meaning that is difficult to relate to general attitudes towards economic justification and awareness. Many dynamical processes including S&T IPPD Affordability, have to be controlled, yet are highly complex, large-scale, nonlinear, non-stationary and infiltrated by a high degree of randomly generated events. The optimal management of these complicated and complex science and technology systems requires an integrated manner of design which considers all quantitative and qualitative aspects concurrently. The Affordability Guide is a conscientious and successful effort to develop and produce an intelligent and coherent framework for modeling and control of the S&T IPPD Affordability process using current state-of-the-art rigorous model-based control theory and application relationships.

One advantage of being the first to develop such a guide in so new an area as affordability is that a minimum amount of *a priori* information is assumed about the structure of the new process (affordability) allowing the guide to extract relevant knowledge and an identification schema rich and sufficient enough to distinguish it as a highly capable learning model. In this regard the AG model is based on references over a wide spectrum of work and is consonant with accepted best practice adaptives and experiences. The initial design of the AG is such that through training, evaluation, and test data, the model will improve in value with each refinement cycle "There exists no real alternative to learning" and the AG is a milestone in the continuation of this process making a significant contribution to knowledge optimization and acceleration of understanding in this new and ever-changing affordability functional reality process.

Summary observations and recommendations follow. The S&T IPPD Affordability Guide is an exemplary effort to explicate the many techniques currently available in the new and exciting inferential field of affordability and economic justification. Finding the *best* model and design vehicle to be used as a guide is the most difficult problem of all given the parameters involved. The product being developed it appears, is the most tractable derivative that makes sense and can be substantively useful and interpreted for goal accomplishment on a widespread basis. It is considerably worthwhile in design and content and is presented in a matrix form that is highly amenable to transformation by relatively simple techniques as the concept of affordability becomes more closely understood and structurally cohesive.

III. ROADMAP REVIEW SEMINAR

The **1995 Combined Roadmap Review** sponsored by Materials Directorate and Manufacturing Technology Directorate of Wright Laboratory was held 18-20 July at the Dayton Convention Center. This program was begun several years ago and has a highly successful track record of attendance and accomplishment. Through the years it has been able to maintain its focus on providing information regarding the Materials Directorate's and Manufacturing Technology Directorate's status of existing programs and planned next fiscal year activities, especially in the area of new starts. The program focuses its attention on its primary audience, that being contractors and government officials in order to generate

informational dialogue regarding existing programs and activities as well as technical and programmatic

needs to be assessed for future planning processes.

The three day seminar series was effective in design and completion and was organized roughly along the following schematic.

TUESDAY, 18 JULY 1995

1. Metallic Materials
2. Ceramics & Very High Temperature Metallics for Propulsion & Hypersonic Systems
3. Nondestructive Evaluation
4. Manufacturing Research
5. Defense Reinvestment/Technology Transfer
6. Breakout Workshops on Various Focal Areas

WEDNESDAY, 19 JULY 1995

1. Nonmetallic Structural Materials
2. Carbon-Carbon & Thermal Protection Materials
3. Systems Support
4. Nonstructural Materials
5. Electronic & Electromagnetic Materials
6. Industry/Lab Partnerships
7. Breakout Workshops on Various Focal Areas

THURSDAY, 20 JULY 1995

1. Status, Strategy and Future Directions
2. Department of Defense Research and Engineering Overview
3. The Manufacturing Technology Directorate Planning Process
4. MS&T for Aircraft
5. MS&T Missiles & Munitions
6. MS&T Spacecraft & C^3I
7. MS&T for Aerospace Sustainment

The Roadmap Review is a three day event-filled well structured informational seminar. All

presentations were done in a professional, pedagogically skilled fashion with easy to follow graphics,

handouts and other materials. Even in an era when there are less and less new starts the Roadmap Review

Seminar should be continued on an annual basis. Discussions with a variety of attendees including, but

not limited to representatives from industry, education, and government (military and civilian) were very

positive indicating the seminar was very worthwhile for its informational sourcing and especially for

"organized" opportunities for networking within and among various groups. The skill, patience,

knowledge and fortitude to present such a successful program year after year should be applauded and

recognized. It represents a standard of excellence that should be maintained.

IV. SCIENCE & TECHNOLOGY-INTEGRATED PRODUCT & PROCESS DEVELOPMENT STRATEGY FOR AFFORDABILITY WL WORKSHOP
JULY, 1995

The S&T IPPD Affordability Workshop was a well-conceived, conscientious endeavor to provide current state-of-the-art information on the status of the development and applicability of the design for Integrated Product and Process Development and Affordability at Wright Laboratory. A series of comments follow both from a pedagogical and informational point of view from someone who has been in education for twenty-five years.

The organization of the workshop was straight -forward combining the highest degree of time and talent efficiency available. After a general networking system, participants were told by a facilitator exactly what to expect out of the workshop, and were informed of the time-frame for precisely scheduled activities through the day. After an enthusiastic welcome and overview from Col R. Davis, WL/CC and group was informed by General R. Paul AFMC/ST of his commitment to the process of IPPD and Affordability. What followed then was a series of valuable discussions by industry leaders direction involved in their company's efforts to adapt to new technologies and change. Excellent and informative presentations were made by people of the highest quality of knowledge in their respective firms regarding IPPD and Affordability issues, viz.,

> Mr. R. Karm, Texas Instruments
> Mr. G. Robson, General Electric
> Mr. B. Birchfield, McDonnell Douglas

Each individual was outspoken and highly skilled in involving the audience in their presentations, each using approximately thirty minutes to brief the workshop on the salient features of IPPD-Affordability concepts in their firm and industry. It is recommended that if time allows when the workshop is conducted in the future, that there be time at the end of the industrial perspective presentations before lunch to allow all industry presenters to be on a panel, led by a moderator, with written questions edited by the moderator, similar in style to the National Press Club of Washington, D.C. format which is very effective in style.

The luncheon speaker was Dr. G. Denman, former ARPA director, who is currently the Vice President for Strategic Planning, GRC International who gave an enthusiastic well-informed presentation

regarding the current budget attitudes and posturing at the federal level, with special emphasis on research and development issues.

The afternoon consisted of four separate concurrent group activities from which an individual had to choose. They are listed below for reference.

Working Groups:

1. S&T IPPD Project Selection Criteria
2. IPPD Implementation in the S&T Environment
3. Technology Maturation & Measurement
4. Enhancing Industry Involvement

Each working group had a well-trained logistically oriented facilitator who kept the participants on target both topic and time-wise. Additionally, each participant in each workshop was given a Working Group Information Packet consisting of the following contents:

1. Agenda for the Session
2. Background Paper
3. Work Group White Paper
4. Work Group Charts
5. OSD Letter and Attachments

The workshop concluded with a one-hour set of outbriefings given by each of the Working Group Facilitators, summarizing the activities, conclusions and recommendations of the four groups.

In summary, it is obvious that a considerable amount of time, effort and talent when into the development, preparation, and presentation of this highly effective workshop. The overall design, educational content, logistical support, preparation of workbook guides, agenda items, support documents, choice of presenters and facilitators , et al was well thought-out and efficiently executed. In evaluating a workshop one tends to evaluate the end product only, but in this case it is obvious that a considerable degree of fore-thought and effort regarding consistency of mission and goals must have occurred with considerable lead-time before the actual workshop presentation. Presenters and facilitators must have been well-selected using specific leadership and educational guidelines for selectivity. Additionally, they must have been given explicit definitional instruction as to expectations regarding their efforts on behalf of the workshop.

Finally, it is recommended that it should be considered that this workshop be expanded to a two-day workshop in combination with sessions involving the concept of Teaming. IPPD is a team-oriented design system. IPPD is defined as

> a management technique that simultaneously integrates all essential acquisition activities through the use of multidisciplinary teams to optimize the design, manufacturing and supportability processes. ...Integrated Product Teams (IPT) are the key to making IPPD work...Wm. J. Perry

The record of team efficiency and performance is well known and documented in industry, education, government, military and other areas of activity. They invariably contribute significant achievements in productivity. However, concepts of Teaming must be clearly understood especially in the IPPD arena of activity. Teams by design and nature have dynamic in nature, constantly changing. Without losing this dynamic on the IPT, another attribute must be captured, that of cohesiveness so that all members of the IPT always see retain their vision as a member of a larger effort, the IPT itself. All elements of creating the concreteness of this type of IPT effort must be fully understood not only by the IPT members individually, but by those program managers establishing the teams in the first place, if IPT's are to surpass individuals as the primary performance unit in the organization at that level. It must be recognized that personnel are scarce resources and IPT's lay heavy claims on these resources. This does not imply that individual effort and individual accountability become either unimportant or less important, but rather that a concentrated management effort must be undertaken to avoid any misallocation of individual resources and team effort.

Additionally all members of the organization must be involved in designing and/or restructuring the institutional reward system as IPT's are developed to motivate individual team members to associate their efforts as a team. Individuals must be committed to working together to accomplish the IPT's purpose using their complementary skills and talents in a committed manner to develop a common purpose. Teams and those who form teams must recognize that teams are performance driven. This will be especially true of IPT's and Team Building Principles and Skills must be taught and cultivated in order to design a quality IPT that can connect specific achievable performance goals with the concentrated collaborative effort of the individual members of the IPT. IPT's are a critical component of the IPPD strategy and require not only a reengineering in program management but a development of a new culture

4-13

and architecture to accommodate this change. The S&T IPPD Strategy for Affordability Workshop is a superior effort in initiating this vital process endeavor.

V. METRIC FOR AGILE VIRTUAL ENTERPRISES
BEST AGILE PRACTICE REFERENCE BASE

This is an intriguing project in the domain of Best Practices which examines four types of "Agile Virtual Enterprises" (AVE's), while agility is defined in terms of ability of the enterprise to respond to *unexpected* change and the virtual enterprise is identified as "an opportunistic aggregation of business units which operates in important ways as if it were a single company." The four types are as follows:

Type 1: A partnership (perhaps with a lead) formed in response to an identified market or opportunity.

Type 2: A tentative aggregation of core competencies which collectively identifies and addresses a market or opportunity and which fully integrates some processes in response to that opportunity.

Type 3: An agile supply chain shifting in response to new or changing markets.

Type 4: An aggregation of core competencies, as in Type 2, but which do not integrate processes or adapt internally in response to the opportunity.

The case framework is extensive and well defined for the Agile Virtual Enterprise and is essential in understanding the foundation of the structure and the five main process categories as appropriate. An extensive roster of cases is well documented and referenced in the discussion .

Summary statements and recommendations follow. This program could possibly benefit from a follow-on endeavor that would further examine through the use of a matrix type of system, the match between various Agile Virtual Enterprise structures and the Best Practices discovered through this program. Further examination could be valuable in another area as well. For example, where the survey "found that each example of an advanced Agile Virtual Enterprise was empowered by focusing on a best practice in only one subcategory" an examination of the process through which this particular best practice was determined to be "the best of the best" begs for analysis.

Additionally another matrix could be devised to identify the overlap among sub--categories since "many AVEs will use some sub-categories more than others." The most beneficial questions might be to

somehow determine why this is true and how this determination of sub-categories is driven within the agile virtual enterprise. This would go a long way in making a significant contribution in the continued effort to use decisional analysis as a stratagem to determine aforehand the beneficial impact of best practices decisions. A minor consideration is in definitional use of 'benchmarking' in this program that appears to run somewhat contrary to traditional definitions of benchmarking as being forward looking rather than backward or bottom-down. This difference needs resolution.

It is interesting to note at this juncture that Capt. Paul Phillips (MT) has made a conscientious and promising effort at mapping this program as well as numerous others in MT as to their basic design characteristics, metrics, and interrelatedness. This is a bold, robust effort that should be continued. There are numerous interlocking ideas and concepts in these programs, especially the ARPA ones that indeed might be shared among participants at a later date through networking towards the growth of the virtual enterprise development theory and reality.

VI. AGILE LABOR UNIONS FOR VIRTUAL ENTERPRISES
AGILE MANUFACTURING PILOT PROGRAM

This is a unique conjuncted team project involving business development and promotion organizations, industry, labor union organizations (Pennsylvania AFL-CIO), the labor force, the Ben Franklin Technology Centers, The Pennsylvania Chamber of Business and Industry, and the Pennsylvania MILRITE Council (PMC), various university groups, other educational institutions, institutes, centers and councils and numerous labor management committees. This is an ambitious shared venture in the new manufacturing paradigm framework utilizing the Agile principles developed and described by the **Agile Manufacturing Enterprise Forum (AMEF).** The program requires considerable networking and interlooping processes examining the relationship between labor and management and other mutual interest groups in the new hierarchy of agility and the Virtual Enterprise as the world of work is reengineered and restructured. As industry continues to respond to generalized change (both anticipated and non-anticipated) by downsizing , reengineering, and the development of the agile enterprise, the labor-management archetype must also become agile oriented to fully integrate technology, organizational activity and the workforce management. The characteristics of the agile enterprise are many, but are persistently those of cooperation, innovative collaborations, knowledgeable, skilled and empowered work

4-15

forces to support the new generation of agile enterprises whose goals are benchmarked by dynamic flexibility .

The metrics of this program are clearly defined, both quantitative and qualitative, focusing on costs, time, robustness and scope. The program will generate a designed experiment with appropriately defined metrics, an assessment of results, and the development and documentation of a case study. One major value of this program is its concentration on measuring the newly organized agile model in terms of contribution value of labor and management and other constituencies to achieve the basic goals of the agile enterprise.

This program has considerable merit especially in the concern of developing long-run outlooks and possibilities of sustained commitment to joint efforts as the new age of unionism seeks its role in the agile and virtual enterprise environment as affordability and economic justification become more dominant realities.

It is difficult in this program to distinguish clearly at times between those components under study that are agile oriented as opposed to those that relate to the development of the virtual enterprise. Perhaps this is good in that there are no clear and consistent definitional lines of demarcation for agile and virtual that apply at all times and in all circumstances. The strategic partnerships being developed and explored through this particular program implies that often agile and virtual overlap and indeed in this soft area of labor-management relationships the virtual enterprise is a natural outgrowth and evolution of the agile system.

Summary comments and recommendations follow. This program has a great deal to offer in the are of enhanced interorganization learning and non-interrupted mutual trust development among the many constituencies housed within the architectural framework of this program design. The scope of this program can and should readily be expanded and developed to include other constituents in its deployment of mutual interdependence as other stakeholders such as the government, investors, and communities of individuals see the collaborative advantages offered through the flexibility agile and virtual enterprises generate.

VII. DECISION SUPPORT SYSTEM FOR THE MANAGEMENT OF AGILE SUPPLY CHAINS - PHILIPS LAB

This program proposes the development of a prototype "decision support system for tactical planning in the management of supply chains in the discrete manufacturing industry." This necessitates the design of an approach that "creates a supply-chain wide decision support-system and complementary planning processes which bring together different functional departments and enterprises in a supply chain." This program which uses Philips Laboratories as the prime contractor with participation from Philips Consumer Electronics Company, Best Products Co., Inc., and Philips Plastics Corporation. If the program was to be extended beyond the realm of those currently involved, so that others are woven into the fabric of the chain, then it would provide insightful information regarding the formation and operation of potential virtual enterprises. The program is large in scope involving a wide chain of relationships including but not limited to the following:

Market Data Analysis
Sales Forecasting and Planning
Finished Goods Inventory Management
Finished Goods Distribution Network Design
Vendor-Managed Replenishment
Aggregate Production Planning
Component Procurement Policy Development

Summary comments and recommendations follow. This program has great promise for future applicability to a variety of supply chains over a large span of typical businesses, especially in the area of discrete manufacturing. As the characteristics of an Agile Supply Chain are developed and expanded through this program, a considerable quantity of highly productive information should be available as to what makes an agile supply chain (a) rapidly reconfigurable, (b) flexible, (c) speedily adaptable to change, and (d) collaborative within the chain. This program has the potential of being expanded to explore the specific functional areas within the supply chain that develop that vital element of trust necessary in agile and virtual enterprises as derivative responsibility flows back and forth through the supply chain. There is "significant technical challenge for this project" however, it is accomplishable and with significant payoff to those involved. It represents an excellent marriage of concurrent engineering principles with those of the agile and virtual enterprise.

Acknowledgments

Although it is impossible to name all those individuals that contributed so vitally to my effort at WL/MT I would like to give special thanks to Gerald Shumaker and Richard (Dick) Thomas for selecting me for this honor and for their tireless efforts on my behalf. I am also grateful to Dr. W. C. Kessler and Mr. J. R. Fenter for their support. I have been rewarded in countless measure by being associated with the Manufacturing Directorate at Wright Laboratory. It has been an exciting educational endeavor to be associated with such a necessary, vibrant and robust organization (MT) with such a vital mission to perform. Listed below are some of those who contributed so unselfishly toward my Summer Faculty Program at WL/MT in addition to those named above.

Al Taylor	John Cantrell	Shirley Henderson
Mary Lewis	Bill Brown	Bob Reifenberg
Mickey Hitchcock	Capt. Paul Hendley	George Orzel
Dan Lewallen	Art Temmesfeld	Virginia McMillan
William Wolfe	Richard Gerth	Joe Cunningham
Noah Barr	Heather Cantrell	Mark Fraley
Stephanie Jackson	Ed Malloy	Marlon Minor
Michelle Kubal	Karla Strong	Tom Davis
Gregory Peisert	Lonnie Burnett	Timothy Miller
Dan Danishek	Lara Steinbrunner	Joel Adkins
Mark Fredrick	Skip Pullen	Talluri Madhavi
et al		

Bibliography

Adam, Everett E., Jr. and Ronald J. Ebert. **Production and Operations Management. Concepts, Models and Behavior.** Fifth Edition. Prentice Hall Publishers. Englewood Cliffs. 1992.

Bossert, James L. **Quality Function Deployment: A Practitioner's Approach. Quality and Reliability/21.** ASQC Quality Press, Milwaukee. 1991.

Department of Defense. **Defense Manufacturing Conference '93. Proceedings of Technical Presentations .** Vols I & II. "Integrating the Manufacturing Base" San Francisco. 1993.

Department of Defense. **Defense Manufacturing Conference '94. Proceedings. Defense Manufacturing Technology: Challenges for the 21st Century.** Phoenix. 1994.

Emory, C. William and Donald R. Cooper. **Business Research Methods.** Fourth Edition. Irwin Publishers. Burr Ridge. 1991.

Heizer, Jay and Barry Render. **Production and Operations Management. Strategies and Tactics.** Third Edition. Allyn and Bacon. Boston. 1993.

Hammer, Michael and James Champy. Reengineering the Corporation: A Manifesto For Business **Revolution.** Harper Business, Harper Collins Publishers. New York. 1993.

Harris, C. J., Ed. **Advances in Intelligent Control.** Taylor and Francis Ltd. London. 1994

Harrison, Bennett. **Lean and Mean. The Changing Landscape of Corporate Power in the Age of Flexibility.** Basic Books. Harper Collins Publishers. New York. 1994.

Holmes, Susan and Judy Ballance Editors. **Process Improvement Guide,** Second Edition. Air Force Quality Institute. Air University Publishing. Maxwell Air Force Base. 1994.

Humphreys, Kenneth K. and Lloyd M. English, Editors. **Project and Cost Engineers' Handbook.** Third Edition. 1993

Hutchins, Greg. **ISO 9000. A Comprehensive Guide to Registration, Audit Guidelines, and Successful Certification.** Oliver Wight Publications, Inc. Essex Junction. 1993.

Ishikawa, Kaoru. (Translation by David J. Lu) **What is Total Quality Control? The Japanese Way. TQC towa Nanika-Nipponteki Hinshitsu Kanri.** Prentice Hall, Inc. Englewood Cliffs. 1985.

Katzenbach, Jon R. and Douglas K. Smith. **The Wisdom of Teams: Creating the High-Performance Organization.** Harvard Business School Press. Boston. 1993.

Maher, Michael W. and Edward B. Deakin. **Cost Accounting.** Fourth Edition. Irwin Publishers. Burr Ridge. 1994.

McNair, C. J. and Kathleen H. J. Leibfried. **Benchmarking. A Tool for Continuous Improvement.** The Coopers and Lybrand Performance Solutions Series. Harper Business. Harper Collins Publishers. New York. 1992.

Ostrom, Charles W., Jr. **Time Series Analysis: Regression Techniques** Second Edition. SAGE Publications, Newbury Park. 1990

Ostwald, Phillip F. **Engineering Cost Estimating.** Third Edition. Prentice Hall, Englewood Cliffs. 1992.

Perry, William J. Secretary of Defense. **Memorandum (and Attachments) for Secretaries of the Military Departments.** 10 May 1995. Subject: Use of Integrated Product and Process Development and Integrated Product Teams in DoD Acquisition.

Rumelhart, D. E. and J. L. McClelland. **Parallel Distributed Processing: Explorations** in the **Microstructure of Cognition.** The MIT Press. Cambridge. 1986.

Sayrs, Lois W. **Pooled Time Series Analysis.** SAGE Publications, Newbury Park. 1989

Schonberger, Richard J. and Edward M. Knod, Jr. **Operations Management. Continuous Improvement.** Irwin Publishers. Burr Ridge. 1994.

Swezey, Robert W. and Eduardo Salas Editors. **Teams: Their Training and Performance.** Ablex Publishing Corporation. Norwood. 1992.

Tang, Victor and Roy Bauer. **Competitive Dominance. Beyond Strategic Advantage and Total Quality Management.** Van Nostrand Reinhold Publishing. New York. 1995

Teich, Albert H., Stephen D. Nelson and Celia McEnaney, Editors. **Science and Technology Policy Yearbook.** American Association for the Advancement of Science. Washington, D.C. 1994.

Theoretical Investigation of Two New types of
Cold Cathode Emitters

M. Cahay
Associate Professor
Electrical Engineering Department

University of Cincinnati
Cincinnati, OH

Theoretical Investigation of Two New Types of Cold Cathode Emitters

M.Cahay
Associate Professor
Department of Electrical Engineeering
University of Cincinnati

ABSTRACT

Ensemble Monte Carlo simulations of electron transport through a new Aluminum Gallium Nitride/Gallium Nitride ($AlGaN/GaN$) cold cathode emitter are reported. We analyze the energy spectrum of carriers prior to being injected in a low workfunction slab of Lanthanum hexaboride (LaB_6) as a function of the ramp energy of the carriers at the $AlGaN/GaN$ heterojunction. Plasmon scattering is found to be the major scattering mechanism in the structure leading to substantial shift towards the low kinetic energy end of the energy spectrum of the carriers injected into the low workfunction Lanthanum hexaboride thin film. Intervalley scattering is found to dominate in the depletion layer at the GaN/LaB_6 interface. Design improvements to increase the efficiency of the cold cathode are suggested.

Simultaneously, we have analyzed a new cold cathode emitter which consists of a thin wide bandgap semiconductor material sandwiched between a metallic material and a low workfunction semimetallic thin film. We show that under forward bias operation the electrons captured in the low workfunction material are responsible for an effective reduction of the semimetallic film workfunction together with a substantial increase of the cathode emitted current. The dynamic workfunction shift is shown to increase with the amount of injected current. Potential material candidates are suggested to achieve low-voltage (< 20 V), room-temperature cold cathode operation with emission currents approaching 100 A/ cm^2 and large efficiencies.

Theoretical Investigation of Two New Types of Cold Cathode Emitters

M.Cahay

I. INTRODUCTION

Over the past few years, following the development of vacuum microelectronics, there has been an increased interest into cold cathode emission for applications in various devices such as pressure sensors, cathodoluminescent flat panel displays, and microwave vacuum transistors, among others [1]. The design of efficient cold cathodes has been the focuss of various research efforts aiming at the development of vacuum state electronics. In that respect, new electron sources that circumvent the use of thermionic electron generation are needed. The later generation process must be avoided because of the power and temperature requirements of microelectronics. An ideal cold cathode should meet the following requirements:(1) high current density (5 A/cm^2), (2) room temperature operation, (3) and reliable and durable operation.

Recently Akinwande and coworkers [2] have reviewed the recent proposals for cold cathode technologies and discussed their limitations. The results of their analysis with regards to the three requirements listed above are summarized in Table I.

Table I: Characterization of Cold Cathode Approaches.

Cathode	Voltage of Operation	Stability	Reliability	Comments
GaN/LaB_6	10V	Stable	Reliable	
Field Emitter	50-200 V	Noisy	Reliable	
Diamond	10-30 V	Stable	Reliable	Current Limited
NEA Semiconductor	5V	Drifts	Short Lifetime	Cs required
Planar Doped Barrier	10-20 V	Drifts	Short Lifetime	CS required
Optoelectronic	5V	Drifts	Short Lifetime	CS required
MOS Tunneling	10-20 V	Decays with time	Short Lifetime	Oxide Trapping
Cermet	5-30 V			Oxide Trapping

Akinwande et al. proposed a new class of semiconductor based non thermionic cathodes based on bandgap engineering of Gallium Nitride (GaN) to achieve low-voltage, room temperature and durable emission from a flat surface. The new structure they proposed as a cold cathode emitter is shown schematically in Fig. 1. It is based on a n-p forward biased GaN diode used to inject electrons into a low-workfunction metal (LaB_6). The interface between the p-type GaN and the metal is characterized by a negative electron affinity. It is formed of a n-type GaN layer typically doped with Si, a heavily doped p-type layer doped with Mg, and a thin layer (typically around 100 Å) of LaB_6 on the surface. After injection from a forward biased p-n junction, electrons traverse the p-GaN layer under high field while approaching the GaN-LaB_6 interface. While drifting across the depleted region, electron can be scattered by lattice phonons (one of

the dominant scattering mechanisms in GaN). This scattering must be minimize by providing a very narrow layer,i.e, using a highly doped p-GaN layer ($10^{19} cm^{-3}$) that can produce steep band bending and high electric field across the p-type GaN layer [3, 4, 5]. Electrons with enough energy can then cross the thin LaB_6 layer and surmount the LaB_6-air potential barrier. The energy diagram of the device is shown in Fig.2 indicating that the conduction band in the p-GaN layer is above the vacuum level of the LaB_6 layer. To study the efficiency of GaN cold cathodes, we must calculate the fraction of emitted electrons and design the structure to maximize the emission efficiency. In that regard, we must remember that electrons drifting across the depletion layer are suffering a lot of phonon scattering, and could become eventually trapped by surface states and eventually recombine with holes in the bulk. This scattering can be minimized by using narrow layers of heavily doped p-GaN, which will lead to steep band bending and large electric field in the proximity of the p-GaN and LaB_6 interface.

During this Summer, we have used Ensemble Monte Carlo simulations of electron transport through a new Aluminum Gallium Nitride/Gallium Nitride ($AlGaN/GaN$) cold cathode emitter are reported. We analyze the energy spectrum of carriers prior to being injected in a low workfunction slab of Lanthanum hexaboride (LaB_6) as a function of the ramp energy of the carriers at the $AlGaN/GaN$ heterojunction. Plasmon scattering is shown to be the major scattering mechanism in the structure leading to substantial shift towards the low kinetic energy end of the energy spectrum of the carriers injected into the low workfunction Lanthanum hexaboride thin film. Intervalley scattering is found to play dominate in the depletion layer at the GaN/LaB_6 interface. Design improvements to increase the efficiency of the cold cathode are suggested.

Simultaneously, we have analyzed a new cold cathode emitter which consists of a thin wide bandgap semiconductor material sandwiched between a metallic material and a low workfunction semimetallic thin film. We show that under forward bias operation the electrons captured in the low workfunction material are responsible for an effective reduction of the semimetallic film workfunction together with a substantial increase of the cathode emitted current. The dynamic workfunction shift is shown to increase with the amount of injected current. Potential material candidates are suggested to achieve low-voltage (< 20 V), room-temperature cold cathode operation with emission currents around 100 A/ cm^2 and large efficiencies.

II. Monte Carlo Simulation of GaN Cold Cathodes

To date, few theoretical investigations have been made of the electronic properties of GaN. The steady-state electron drift velocity has been calculated by several authors using the EMC method [6, 7, 8]. The latest study by Kolnik et al. [8] includes the details of the first four conduction bands within the full Brillouin zone for both zincblende and wurtzite crystal phases of bulk GaN. Hereafter, we assume that the structure proposed by Akinwande et al. [2] is made of the zincblende phases of $Al_xGa_{1-x}N$ and GaN.

The Monte Carlo program used for this study is based on a three-valley (Γ, X, L) model with position dependent scattering mechanims which include non polar acoustic phonon (through deformation potential coupling), screened polar optical phonons, screened ionized impurity scattering, intervalley, and plasmon scattering. Parameters to characterize the various scattering mechanisms for GaN were the same as those of Kolnik et al. [8]. We neglected the coupling between plasmons and polar optical phonons. Such coupling is important when the plasmon and longitudinal phonon frequencies are comparable. Since the longitudinal

optical phonon energy is equal to 92 meV which is more than three times smaller than the 290 meV plasmon energy (using a hole effective mass of 0.87 m_0 , m_0 being the free electron mass) in the heavily doped GaN layer, coupling of polar optical phonons and plasmons was neglected. Scattering of electrons by plasmons was taken into account following Das and Lundstrom [9]. For the effective masses in the Γ and X valleys, we used 0.15 and 0.41 m_0, respectively [10]. The electron effective-mass in the upper L-valley is not very well known and was set equal to the free-electron mass. Only the non-parabolicity of the Γ-valley was taken into account and set equal to 0.187 eV^{-1} in agreement with ref. [6].

Introduction

Figure 1 shows that, after injection across the forward biased p-n junction, electrons first diffuse through the neutral p-GaN layer before approaching the GaN-LaB_6 interface. While diffusing across the p-type GaN region, electrons can be scattered by phonons, impurities, but also by plasmons. The latter scattering mechanism is known to play a major role on electron transport through heavily doped base regions in $Al_xGa_{1-x}As/GaAs$ heterojunction bipolar transistors [11]. As will be shown in this paper, plasmon scattering plays a dominant role in the operation of the cold cathode proposed by Akinwande et al. [2]. Another important scattering process is intervalley scattering which plays a dominant role in the very narrow depletion layer formed at the p-GaN/LaB_6 interface.

To contribute to the cold cathode emitted current, electrons reaching the p-GaN/LaB_6 interface must have enough energy to cross the thin LaB_6 layer and surmount the LaB_6-air potential barrier. This emission process is supposedly quite efficient since the interface between the p-type GaN and the metal is characterized by a negative electron affinity [12]. To study the efficiency of the electron injection process into vacuum, we use an Ensemble Monte Carlo (EMC) technique to calculate the energy distribution of electrons reaching the GaN/LaB_6 interface and design the structure to maximize the high energy tail of the energy spectrum of the collected carriers.

The energy band parameters for both materials (effective masses, valley separations) were determined using the pseudopotential method in the local density approximation [10].

The energy band diagram of the cold cathode is shown schematically in Fig 2. The structure parameters listed in Fig.2 are those corresponding to zincblende GaN. In that case, the effective electron affinity for electrons is χ_{eff} = -0.7 eV [2]. Recent experimental reports have confirmed a type-I band alignment for the wurtzite AlN/GaN heterojunction with an extraordinary high conduction band offset, ΔE_c = 2.3 eV [13]. Hereafter, we assume that a similar conduction band-offset exists for zinc-blende structures. We therefore expect the energy ramp of electrons injected from a forward biased zinc-blende $Al_xGa_{1-x}N/GaN$ interface to vary between zero and 2.3 eV while varying the Aluminum fraction from 0 to 1.

Furthermore, under the assumption that effective-mass filtering across heterojunctions is as effective in $Al_xGa_{1-x}N/GaN$ as in $Al_xGa_{1-x}As/GaAs$ [14], most of the electrons injected in p-type GaN will reside in the Γ-valley. For zinc-blende GaN, this requires the ramp energy to be below 1.5 eV, the $\Gamma - X$ separation in zinc-blende GaN [10]. Furthermore, most of the electrons in zinc-blende $Al_xGa_{1-x}N/GaN$ will reside in the Γ -valley as long as $x < 0.6$ [10]. The GaN/LaB_6 interface is modeled as a Schottky barrier with an amount of band bending equal to 2eV as shown in Fig. 2 [2].

Approach

In the EMC simulations, the areas that bound the p-GaN region are treated as follows: each carrier injected in the p-GaN region is selected using a rejection technique applied to a semi-Maxwellian distribution of carriers injected with an additional ramp energy to simulate the effect of the band discontinuity at the Al_xGa_{1-x}/GaN interface. The left boundary ($Al_xGa_{1-x}N/GaN$ interface) is assumed to reflect completely electrons impinging from the p-GaN region. Electron histories are terminated when the carriers have been absorbed at the right boundary (GaN/LaB_6 interface). This assumes that the probability for electrons to tunnel from GaN to the LaB_6 layer is unity. This assumption is better known as the *one-chance* model in the modeling of the quantum efficiency of photocathodes [15]. The electric field profile through the p-GaN layer is calculated using the simple Schottky barrier model of the GaN/LaB_6 interface [16]. In the neutral p-GaN region, the electric field is assumed to be constant and equal to -100 V/cm, a common practice in EMC simulations of carriers in quasi-neutral regions. In all EMC simulations, 5,000 carriers are injected across the from $Al_xGa_{1-x}N/GaN$ interface. The energy spectrum of the carriers collected at the GaN/LaB_6 interface are computed as a function of the ramp energy (See Fig.2).

Results

Figure 3 is a histogram of the energy spectrum of the electrons collected at the GaN/LaB_6 interface for a cathode in which the neutral GaN region was assumed equal to 2650Å as in the design of Akinwande et al. [2]. The length of the depleted region was calculated to be 150Å [2]. Energies are measured with respect to the bottom of the conduction band in GaN at the GaN/LaB_6 interface. The ramp energy of the electrons injected across the $Al_xGa_{1-x}N/GaN$ interface was assumed equal to 0.5 eV. Neglecting the bowing parameters for $Al_xGa_{1-x}N$ and making use of the recent report of 2.3 eV [13] as the conduction band discontinuity of AlN/GaN interface, a ramp energy of 0.5 eV corresponds roughly to an Aluminum fraction $x = 0.2$ for the n-$Al_xGa_{1-x}N$ emitter. In Fig. 3, the lower graph shows the energy populations of the three different valleys. It was found that most the electrons reach GaN/LaB_6 surface while residing in the Γ-valley (96.3%). The histogram maximum is located slightly above 2 eV, the amount of band bending at the GaN/LaB_6 interface (ballistic transport would lead to a hemi-Maxwellian energy histogram with a peak at 2.5 eV). The downward shift in energy compared to the injected electron beam results from the importance of plasmon scattering which quickly thermalizes the injected electron beam prior to entering the depleted layer at the GaN/LaB_6 interface. Figure 3 also shows that a large fraction of electrons have an energy above the 1.3 eV threshold needed to be emitted into vacuum (See Fig.2). One should keep in mind that an accurate estimate of the cold cathode emission efficiency must await modeling of carrier transport through the low workfunction LaB_6 thin film. A large fraction of electrons will be removed from the emitted beam as a result of scattering mechanisms such as electron-electron and electron-phonon scattering in the LaB_6 material. To reduce these *trapping* mechanisms, we can try to improve the design (i.e, efficiency) of the cold cathode by increasing the high energy tail ($> 2.2eV$) of the collected energy spectrum. We investigated this possibility first by increasing the ramp energy to 1.3 eV (this would correspond to an Aluminum fraction closer to 0.5 for the $Al_xGa_{1-x}N$ emitter). Figure 4 shows that there is a minor increase in the high energy tail of the collected carriers with most of them (96.4%) still in the Γ-valley. Next, the length of the neutral GaN region was reduced to 1250Å while keeping the doping the same. Figure 5 indicates that the high

energy tail of the spectrum has substantially increased compared to the cases discussed above. For a ramp energy of 1.3 eV, 52% of the collected electrons have an energy in excess to 2.2 eV when the neutral GaN region is $1250\mathring{A}$ wide compared to 12% only when the GaN neutral region is $2650\mathring{A}$ wide.

Tables II and III summarize the percentage of electrons collected in each valley at the GaN/LaB_6 interface as a function of the ramp energy and the width of the neutral GaN region. Clearly, most electrons reach the surface in the Γ-valley. However, the importance of intervalley scattering is found to be more pronounced while increasing the ramp energy and/or decreasing the length of the neutral GaN region. The transfer of electrons to upper valleys could have a detrimental effect on their transmission to the LaB_6 layer since tunneling across heterostructure interfaces is known to be either forbidden or substantially smaller for electrons in upper valleys [12].

In Fig. 2, the top of the first conduction band is shown to be 3.8, 2.3, and 2.1 eV above the bottom of the Γ, X and L valley minima, respectively [10]. Accurate EMC simulations must take into account the reduction in the density of states upon approaching the top of the conduction band in that case. For L and X valley electrons, this reduction in the density of states can be neglected here. For the Γ-valley electrons, most of the electrons collected at the GaN/LaB_6 interface have an energy below 3.3 eV, the maximum energy at which electrons would hit the surface if they were moving ballistically across the structure while injected at a ramp energy of 1.3 eV at the $AlGaN/GaN$ interface. Since the high energy tail of the collected electrons is substantially below the top of the conduction band, modeling the Γ-valley electrons using a non-parabolicity factor is a fairly good approximation. Detailed results of the collection efficiency of $Al_xGa_{1-x}N/GaN$ cold cathodes taking into account the full Brillouin zone description of the GaN conduction band [8] will be published elsewhere.

Table II: Valley population of electrons collected at the GaN/LaB_6 interface as a function of ramp energy. The neutral base region is $2650\mathring{A}$ wide.

Ramp Energy (eV)	Γ -valley	X-valley	L-valley
0.5	96.3 %	2.4 %	1.3 %
0.9	96.4 %	2.7 %	0.9 %
1.3	94.7 %	3.8 %	1.5 %

Table III: Valley population of electrons collected at the GaN/LaB_6 interface as a function of ramp energy. The neutral base region is $1250\mathring{A}$ wide.

Ramp Energy (eV)	Γ -valley	X-valley	L-valley
0.5	95.4 %	3.3 %	1.3 %
0.9	92.7 %	5.3 %	2.0 %
1.3	86.0 %	10.5 %	3.5 %
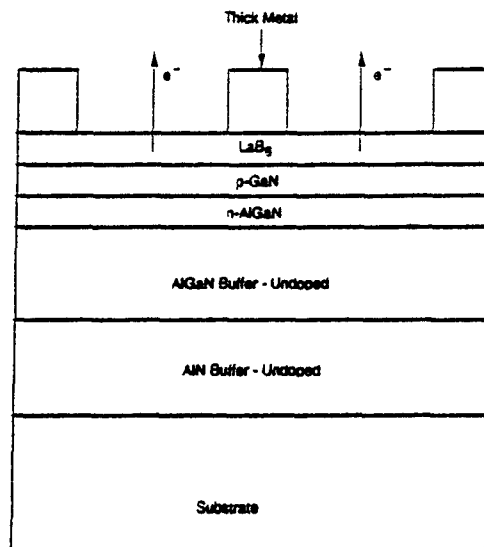
Figure 1: Cross-section of the $Al_xGa_{1-x}N/GaN$ cold cathode proposed by Akinwande et al. [2].
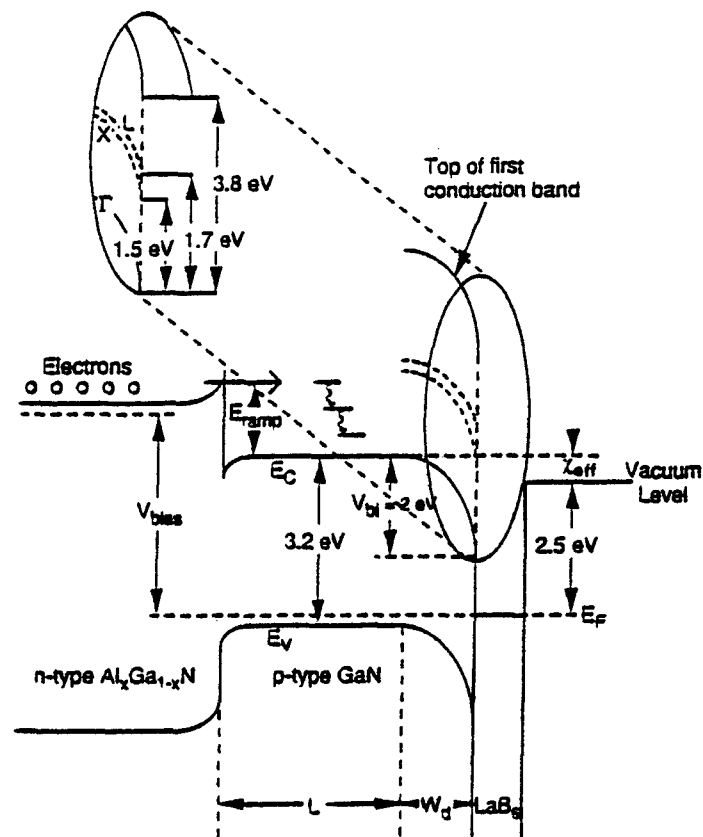
Figure 2: Schematic representation of the conduction band profile throughout the cold cathode shown in Fig. 1.
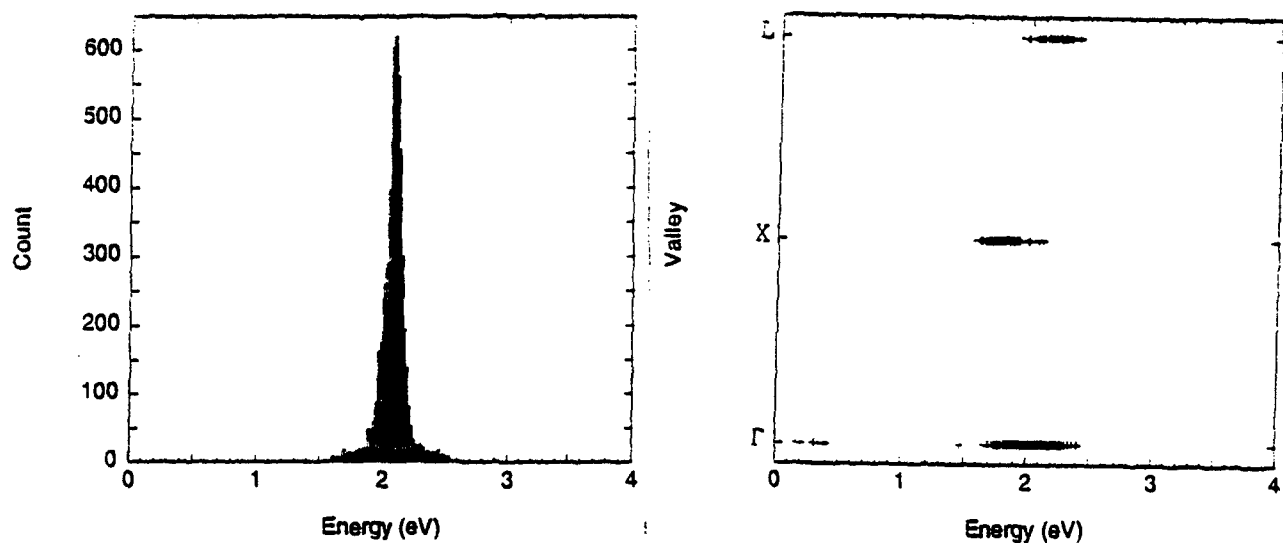
Figure 3: Energy distribution of electrons collected at the GaN/LaB_6 interface prior to injection in the low workfunction material (see Fig. 2). The zero of energy is the minimum of the conduction band in GaN at the GaN/LaB_6 interface. The injected electrons at the $AlGaN/GaN$ interface was assumed to be a hemi-Maxwellian distribution of carriers. The ramp energy was assumed to be 0.5 eV. The length of the neutral GaN region and depleted GaN region were set equal to 2650Å and 150Å, respectively. The bottom graph shows the energy spread in the first three valleys (Γ, X, L) of the first conduction band.
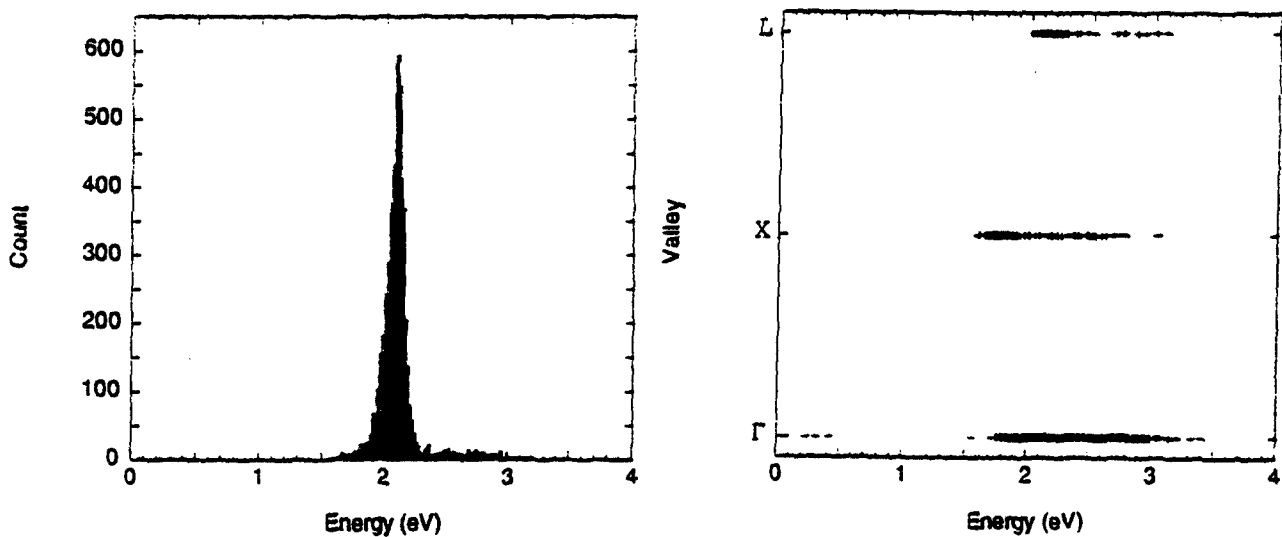
Figure 4: Same as Fig. 3 for a ramp energy of 1.3 eV.

5-9
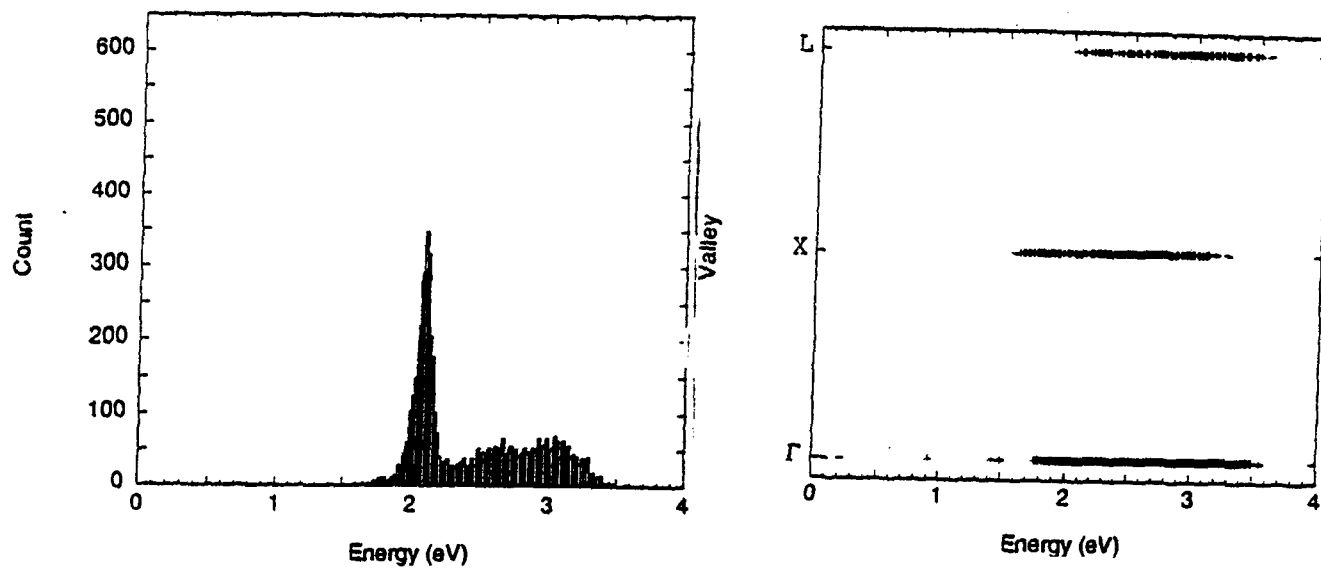
Figure 5: Same as Fig. 3 for a ramp energy of 1.3 eV after reducing the length of the neutral GaN region to 1250$\mathring{A}$.

IV. Dynamic Workfunction Shift in Cold Cathode Emitters Using Current Carrying Thin Films

Recently, there has been renewed interest into cold cathode emitters for applications to a variety of electronic devices, including microwave vacuum transistors and tubes, pressure sensors, thin panel displays, high temperature and radiation tolerant sensors, among others [1, 17, 18]. Introduction of such emitters would permit an unprecedented compactness and weight reduction in device and equipment design. Low temperature operation in nonthermionic electron emitters is very desirable for keeping the statistical energy distribution of emitted electrons as narrow as possible, to minimize thermal drift of solid state device characteristics, and to avoid accelerated thermal aging or destruction by internal mechanical stress and fatigue. To keep the emitter temperature rise small appears easy if the emitters are built thin epitaxial films using vertical layering technology due to the extremely short heatpaths and excellent heatsinking possibilities offered with this architecture.

For an electron emitter to be useful in microwave tube applications it should be capable of delivering current densities in excess of 10 A/cm^2 and to sustain emission during operational lifetimes over periods of 10^5 hrs. To satisfy this requirement, the structural and chemical composition must be stable. This rules out the historically practiced use of alkali metal films on emitter surfaces for the lowering of electronic workfunctions. These films sublimate, evaporate or surface migrate over time and end up on various surfaces inside the vacuum envelop.

Several cold cathode emitters have been proposed since their first successful demonstration by Williams and Simon [19] using a cesiated p-type GaP structure. A review and criticism of the different cold cathode approaches was given recently by Akinwande et al. [2]. In this work, we propose a new cold cathode emitter concept and use a simple model to show that the new emitter is capable of achieving low voltage (< 20 V) room temperature operation with emission current around 100 A/cm^2 and large efficiencies.

A schematic energy band diagram throughout the proposed structure is shown in Fig. 6. The architecture of the structure is shown in Fig. 7. The main elements in the design and functioning of such an emitter are : (1) a wide bandgap semiconductor slab equipped on one side with a metallic contact [20] that supplies electrons at a sufficient rate into the conduction band and (2) on the opposite side, a thin semimetallic film that facilitates the coherent transport (tunneling) of electrons from the semiconductor conduction band into vacuum. Of importance is the mutual alignment of the crystalline energy levels at the semiconductor-semimetal film junction. This requires the use of new materials and development of their epitaxial growth technologies.

If the applied voltage is equal or larger than the semiconductor bandgap energy and the quotient of the applied voltage divided by the semiconductor thickness approaches 0.1$eV/\mathring{A}$, then electrons are tunnel injected into the conduction and ascend during their travel across the semiconductor film to levels of increasing energy. Referring to Fig. 6, the conduction band of the wide bandgap semiconductor provides the launching site for electrons where they are - through a thin film - injected into vacuum. This injection of electrons into vacuum becomes possible and is effective as long as the semimetallic film is very thin and has a workfunction small enough so that its vacuum edge is located energetically below the conduction band edge of the semiconductor. This situation is referred to as negative electron affinity (NEA) for the semiconductor

material [12]. Depending on the particular materials choices, this implies that the semimetal workfunction ϕ_M in relation to the semiconductor energy bandgap E_G must obey one of the inequalities $\phi_M < 0.5 E_G$ or $\phi_M < E_G$ if an intrinsic or p-type doped wide bandgap semiconductor is used, respectively.

THE MODEL

For a cathode operated at room temperature, we model this internal field emission at the injection junction using a Fowler-Nordheim (FN) type expression for the injected current (in A/cm^2) [16]

$$J_0 = C_1(E^2/\Delta)e^{C_2\Delta^{3/2}/E} \tag{1}$$

where C_1 and C_2 are constants which depend on the wide bandgap semiconductor. In our numerical simulations, we chose $C_1 = 1.5 X 10^6$ A/V and $C_2 = 6.9 X 10^7 (V^{1/2}cm)^{-1}$ which are of the same order of magnitude as the constants appearing in the FN expression [16]. In Eq.(1), Δ is the barrier height (in eV) at the metal-semiconductor junction and E is the electric field (in V/cm) in the wide bandgap semiconductor [21]. We assume that the semiconductor layer thickness is such that the transport of injected electrons is close to being ballistic up to the interface between the semiconductor and the thin semimetallic film. In so doing, we also neglect carrier ionization processes in the semiconductor slab which could be the main antagonist to ballistic transport in that region.

Because of the finite probabilities for the injected current to be transmitted at the semiconductor/semimetal (probability T_1) and semimetal/vacuum interfaces (probability T_2), the contributions to the total emitted current can be calculated as the sum of the contributions resulting from the mutiple reflections of electrons in the semimetallic layer (See Fig. 6). The magnitudes of the emitted current components decreases with the number of multiple reflections in the semimetallic layer. Rather than trying to calculate these contributions exactly, we assume that the current amplitude is decreased by a factor $\alpha = exp(-L_2/\lambda)$ for each traversal of the semimetallic layer, where λ is the collisional mean free path in the semimetallic layer (Typically, $10^2 \AA < \lambda < 10^4 \AA$) and L_2 is the length of the semimetallic layer. Adding the contributions resulting from multiple crossings of the semimetallic layers, the total emitted current is found to be

$$J_0{}^{em} = \alpha T_1 T_2 J_0 (1 + x + x^2 + ...) \tag{2}$$

where $x = \alpha^2(1 - T_1)(1 - T_2)$. In calculating $J_0{}^{em}$ we limited the number of traversals of the semimetallic slab to five to include the fact that electrons loose energy in each crossing and eventually do not have enough energy to surmount the barrier at the semimetal-vacuum interface. According to Eq.(2), the contributions from the multiple reflections decrease rapidly since, in general, the quantity x will be much smaller than unity [22]. Once the emitted current is found, the total current contributing to the increase in the sheet carrier concentration in the thin semimetallic film can easily be written as $J_0{}^{capt} = J_0 - J_0{}^{em}$. The total trapped current is then given by $i_T = W^2 J_0{}^{capt}$, where W^2 is the area of the semimetallic thin film (See Fig. 7). The semimetallic thin film can be modeled as a quantum well (Q.W) which will loose the trapped electrons essentially at its lateral boundaries. In reality, Figure 7 indicates that not all electrons will move to the three-dimensional contact regions surrounding the thin semimetallic layer but many of them will get reflected at the lateral thin film layer with an average probability r (calculated for electrons with the Fermi velocity in the thin film). The exiting number of electrons will depend on the thickness of the semimetallic layer and

could be adjusted by intentional passivation so that reflection at the boundaries of the thin semimetallic film could be tuned from almost zero to nearly unity. Taking into account the finite reflection amplitude at the thin film boundaries, the leakage current of the Q.W can be rewritten

$$\frac{dQ_T}{dt} = eWN_{2D}v_F(1-r) \tag{3}$$

where Q_T is the total charge captured by the well, e is the magnitude of the electronic charge, N_{2D} is the *excess* sheet carrier concentration in the thin film due to the captured electrons, and $< v_e >$ is the average electron velocity which is approximated hereafter as the Fermi electron velocity v_F in the semimetallic thin film. Under steady state operation of the cold cathode, the excess charge in the two-dimensional semimetallic film is found using Eq.(3) and imposing the current balance requirement $\frac{dQ_T}{dt} = i_T = W^2 J_0{}^{capt}$. This leads to

$$N_{2D} = WJ_0{}^{capt}/e(1-r)v_F. \tag{4}$$

Simultaneously, the change N_{2D} in the sheet carrier concentration in the Q.W due to trapped electrons leads to the occupation of the boundstate energy levels according to the energy density of states up to an energy level which will establish the dynamic Fermi level $E_F{}^1$ (See Fig. 6). The Fermi velocity v_F entering Eq.(4) must be calculated self-consistently because of the dynamic workfunction shift $|\Delta\chi|$ illustrated on Fig. 6. This dynamical shift $|\Delta\chi|$ is equal to $|E_F{}^1 - E_F{}^0|$, where $E_F{}^0$ is the Fermi level in the thin semimetallic layer under zero bias. For simplicity, we assume that the electrons in the conduction band of the semimetallic films can be described using the Sommerfeld theory of metals while assuming s-band conduction in the semimetallic thin film and while modeling the thin film using the particle in a box model for the quantum well [23]. The set of equations (1-4) is then solved self-consistently to calculate the workfunction shift $|\Delta\chi|$ as a junction of the externally applied bias. Once the dynamic shift has been determined self-consistently, Eq.(2) can then be used to determine the emitted current.

RESULTS

We consider a specific structure with the material parameters listed in Table IV. Both Au and Ag are known to form contacts to thin films of semiconducting (n-type) CdS. In that case, the barrier height Δ shown in Fig. 6 is quite small and is equal to 0.78 eV and 0.56 eV for the case of Au and Ag contacts, respectively [16]. The lattice constant of CdS (5.83Å) is very close to the lattice constant of the thin semimetallic surface layer LaS (5.85 Å) which in its cubic crystalline structure will therefore be lattice matched to the semiconducting material. Additionally, LaS has a quite low room temperature workfunction (1.14 eV), a feature when combined with the large energy gap (2.5 eV) of CdS leads to NEA of the semiconductor material. In our numerical simulations, the thicknesses of the CdS (L_1) and LaS (L_2) layers are set equal to 500 Å and 24.6 Å (4 monolayers), respectively. The area of emission of the cathode W^2 is set equal to 1 cm^2.

Figure 8 is a plot of the dynamic workfunction shift as a function of applied bias for the cold cathode emitter with both Au and Ag injecting contacts. The following parameters were used: $\lambda = 300\text{Å}$, $T_1 = T_2 = 0.5$, and $v_F = 1.36 X 10^8 cm/s$. Figure 8 indicates that the dynamic shift of the LaS workfunction is sensitive to the quality of the interface between the two-dimensional semimetallic layer and the three-dimensional contacts which we model by varying the reflection coefficient r between the two-dimensional

semimetallic thin film and the three-dimensional contact regions (See Fig. 7). It should be noticed that the LaS workfunction shift can approach the LaS workfunction even for the case of a *leaky* interface between the thin semimetallic layer and the 3D contact regions. The dynamic shift $|\Delta\chi|$ is comparable to the workfunction of LaS for a smaller value of the applied bias in the case of Ag contact because of the lower barrier at the Ag/CdS interface.

Figure 9 compares the emitted current densities J_0^{em} for the structure with Au and Ag contacts calculated while including or neglecting the effects of the dynamic shift of the LaS workfunction. In Fig. 9, the following parameters were used: $\lambda = 300\overset{\circ}{A}$, $T_1 = T_2 = 0.5$, r = 0.75, and $v_F = 1.36 \times 10^8 cm/s$. The current density versus bias plots are stopped at the values of V_{bias} at which $|\Delta\chi| = \phi_M(LaS) = 1.14eV$. Beyond that point, the theory exposed here is no longer valid since we would need to include the spill over of the excess trapped carriers into vacuum. As can be seen in Fig. 9, the emitted current densities can be more than a factor two larger when the effects of the dynamic shift of the workfunction of the semimetal are included. The effects could be made more drastic if a set of materials and device parameters could be found for which the dynamic shift of the workfunction could be made comparable to the workfunction itself at fairly low value of the applied bias $(< 5V)$. Finally, for the choice of parameters listed in the inset and caption of Fig. 9, the $Al/CdS/LaS$ cold cathode has an efficiency $\eta = J_0^{em}/J_0$ around 0.29 at $V_{bias} = 20V$.

Table IV: Material Parameters of the Cold Cathode

Material	Au (Ag)	i-CdS	LaS
Lattice Type	fcc (fcc)	Zincblende.c	fcc Rocksalt
Lattice Constant ($\overset{\circ}{A}$)	4.04 (4.09)	5.83	5.85
Workfunction (eV)	4.3 (4.3)	4.2	1.14
Bandgap (eV)		2.5	
# of free electrons ($10^{22}cm^{-3}$)	5.9 (5.86)	—	1.99
Electron Mass (m_0)	1.	0.14	1.
Electron Mobility ($cm^2V^{-1}s^{-1}$)		400.	
Electrical resistivity (273K) ($\mu\Omega cm$)	1.51 (2.04)		92.
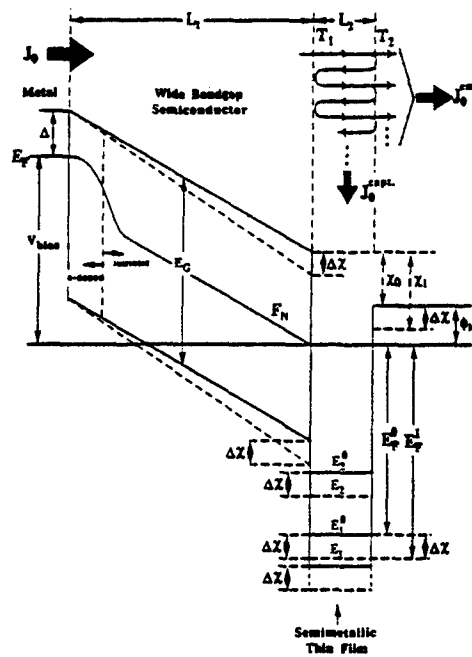
Figure 6: Schematic representation of the conduction band profile throughout the cold cathode emitter described in the text. Under forward bias, a fraction of the emitted current is captured in the semimetallic slab. The subsequent excess sheet carrier concentration in the quantum well formed by the semimetallic slab lead to a shift of the fermi level in the thin film which is similar to a lowering of the workfunction of the thin film. For a given forward bias, this leads to an increase in the electric field in the wide bandgap semiconductor (dashed line versus full line) and in an increase in the injection and emitted currents. Also shown in the quasi Fermi level spatial dependence across the wide bandgap semiconductor.
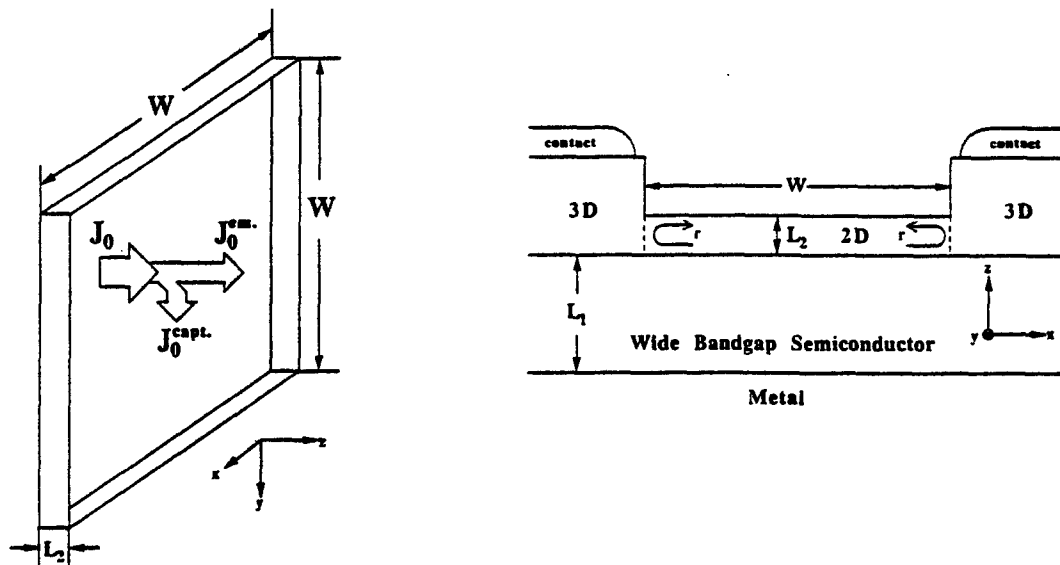
Figure 7: Illustration of the capture of the injection current by the thin film (quantum well) formed by the semimetallic thin film grown on top of the wide bandgap semiconductor. The diagram on the right illustrates the partial reflection of the two-dimensional electron gas in the thin semimetallic film upon entering the three-dimensional contact regions where the external bias is applied.
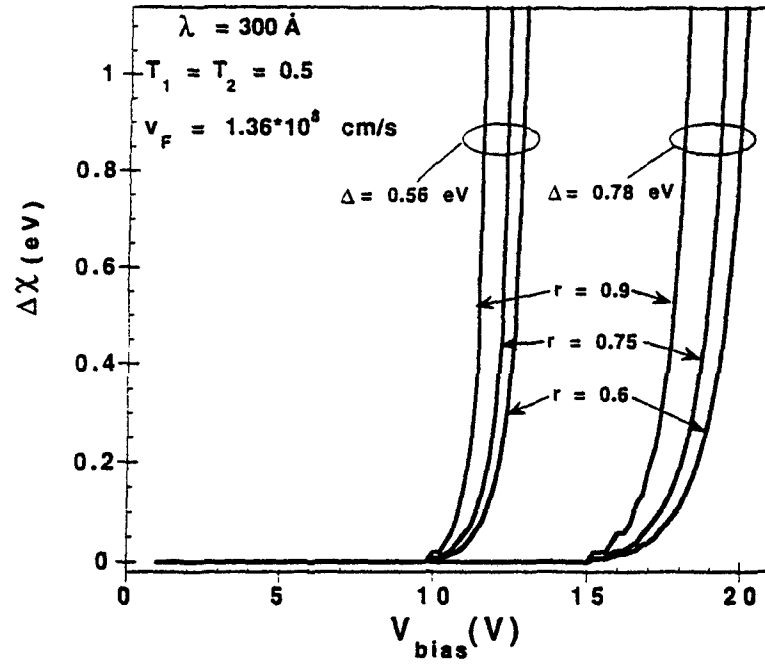
Figure 8: Dynamical shift of the workfunction as a function of the external applied bias for a cold cathode emitter with the parameters listed in Table IV. For each group of curves, r = 0.9, 0.75, and 0.6, from left to right.
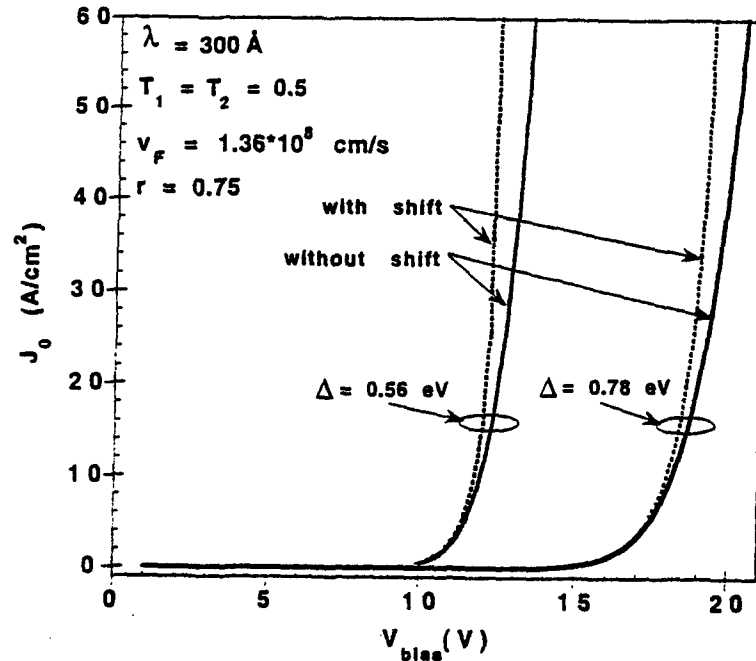
Figure 9: Comparison between the emitted current as a function of the applied bias while including (dashed line) and neglecting (full line) the dynamical shift of the workfunction of the semimetallic slab described in the text. The parameters of the device are listed in Table IV. The coefficient C_1 and C_2 in Eq.(1) were chosen equal to 1.5×10^6 A/V and 6.9×10^7 $(V^{1/2}cm)^{-1}$, respectively. Other choices for the parameters C_1 and C_2 with similar magnitudes lead to similar dynamical shift of the workfunction. The reflection coefficient r shown in Fig. 7 was set equal to 0.75.

V. Conclusions

The design of efficient cold cathodes has been the focuss of various research efforts aiming at the development of vacuum state electronics. In that respect, new electron sources that circumvent the use of thermionic electron generation are needed. The later generation process must be avoided because of the power and temperature requirements of microelectronics. An ideal cold cathode should meet the following requirements:(1) high current density (5 A/cm^2), (2) room temperature operation, (3) and reliable and durable operation.

During this Summer research effort, two new types of Cold Cathodes Emitters were analyzed. First, We have used Ensemble Monte Carlo simulations of carrier transport through p-type (zincblende) GaN to investigate the energy distribution of carriers injected across a GaN/LaB_6 interface in a new cold cathode design [2]. We have shown that the transfer of electrons from the Γ to X and L-valleys occurs predominantly in the depletion region due to the Schottky barrier at the GaN/LaB_6 interface. For the range of ramp energy and neutral GaN region width considered here, it was found that a large fraction ($> 85\%$) of electrons reach the surface in the Γ-valley. The energy distribution of carriers was found to be predominatly affected by plasmon scattering in the neutral region of GaN prior to injection in the depletion region. To increase the high energy tail in the spectrum of collected carriers and increase the emission efficiency of the cathode, it was suggested to use a $Al_xGa_{1-x}N$ emitter with an Aluminum fraction close to 0.5 and a p-type heavily doped ($10^{19}cm^{-3}$) GaN layer with a length around $1,000\text{\AA}$.

While proposing another cold cathode emitter, we have shown that the capture of electrons by thin semimetallic layers grown on the escape surface of wide bandgap semiconductors can lead to a dynamical shift of the workfunction of the semimetallic layers together with an increase of the cathode emission current. Potential material candidates were proposed for cold cathode operation with applied bias under 20 V, with current densities around 100 A/cm^2, and with large efficiencies (η approaching 30 %). Improvements to the theory exposed here should include a more realistic model for the energy density of states (to account for the possible d-band character of the conduction band in semimetallic samples [23]), the finite probability for electron wavefunctions in the thin semimetallic films to extend in the semiconductor material [24], a more accurate description of the energy loss mechanisms [25] and screening effects (including lateral ohmic voltage drop) in thin metallic layers [26]. However, once all these effects are taken into account, we believe the quantitative operation of the cold cathode exposed here will stay essentially correct predicting a dynamical shift of the workfunction of the thin semimetallic film of the same order of magnitude than the one reported here.

References

[1] S. Ianazzo, Solid State Electronics, Vol. 36(3), 301 (1993).

[2] A. I. Akinwande, P. P. Ruden, B. L. Goldenberg, D. K. Arch, and John King, Proceedings of 1994 Tri-Service (NASA) Cathode Workshop, Cleveland, Ohio, March 1994, p. 105.

[3] Towards that goal, Akinwande and coworkers are trying to grow highly-doped p-type layers to reach levels around $10^{19} cm^{-3}$ as successfully reported by Nakamura et al. [?, 4, 5]

[4] S. Nakamura, T. Mutai, M. Senoh, and N. Isawa, Japenese Journal of Applied Physics, Vol. 31, L139 (1992).

[5] S. Nakamura, M. Isawa, M. Senoh, M. Masayuki, and T. Mukai, Japenese Journal of Applied Physics, Vol. 31, 1258 (1992).

[6] M. A. Littlejohn, J. R. Hauser, and T. H. Glisson, "Monte Carlo Calculation on the Velocity-filed relationship for Gallium Nitride", Applied Physics Letters, Vol. 26, No.11, 625 (1975).

[7] B. Gelmont, K. Kim, and M. Shur, "Monte-Carlo Simulation of Electron Transport in Gallium Nitride", J. Appl. Phys., Vol. 74(3), 1818 (1993).

[8] J. Kolnik, I. H. Oguzman, K. F. Brennan, R. Wang, P. P. Ruden, Y. Wang, Journal of Applied Physics, Vol. 78(2), 1033 (1995).

[9] A. Das and M.S. Lundstrom, Journal of Applied Physics, 66(5), 2168 (1989).

[10] D. Talwar, private communication.

[11] T. Kumar, M. Cahay, S. Shi, K. Roenker, and W. E. Stanchina, Journal of Applied Physics, Vol.77(11), 5786 (1995).

[12] P. R. Bell, Negative Electron Affinity Devices, Oxford: Claredon Press, 1973

[13] J. Baur, K. Maier, M. Kunzer, U. Kaufmann, and J. Schneider, Applied Physics Letters, Vol. 65(17), 2211 (1994).

[14] L. P. Ramberg and T. Ishibashi, Journal of Applied Physics, 63(3), 809 (1988).

[15] T. J. Maloney, M. G. Burt, J. S. Escher, P. E. Gregory, S. B. Hyder, and G. A. Antypas, Journal of Applied Physics, 51(5), 2879 (1980).

[16] Sze, Physics of Semiconductor Devices, 2nd Edition, Wiley, p. 291 (1981).

[17] I. Brodie and C. A. Spindt, Advances in Electronics and Electron Physics, Vol. 83, p.2 (1992).

[18] The work presented here follows suggestions which are documented in two in-house reports by W. Friz, Final Technical Report, Task ELM-9, June 1992, and Technical Note, Task ELM-6, January 1995 (Wright-Patterson Air Force Base).

[19] B. K. Williams and R. E. Simon, Physical Review Letters, Vol. 18(13), 485 (1967).

[20] The most desirable form of electron injection is accomplished by an ohmic contact because it puts minimal electrical stress on the material and, at the same time, provides the highest current densities.

[21] Assuming that the most part of the wide bandgap semiconductor is an intrinsic material (See Fig. 1), accumulation and depletion effects can be ignored. Referring to Fig. 1, the resulting uniform electric field across the wide bandgap semiconductor is then given by

$$E = \frac{1}{L_1}[V_{bias} + \Delta - (\frac{E_G}{2} - |\Delta\chi|)]. \tag{5}$$

[22] Both T_1 and T_2 should actually be function of the number of reflections in the semimetallic slab since the electrons loose energy during each traversal. This is however just a refinement to the general theory exposed in this paper.

[23] N. W. Aschcroft and N. D. Mermin, Solid State Physics, Saunders College, Philadelphia, 1976.

[24] M. L. Huberman and J. Maserjian, Physical Review B, Vol. 37(15), 9065 (1988).

[25] R. C. Jaklevic and J. Lambe, Phys. Rev. B, Vol. 12, 4146 (1975).

[26] Y. Silberberg and T. Sands, IEEE Journal of Quantum Electronics, Vol. 28 (7), 1663 (1992).

JAMES CARROLL

NO REPORT

The Ballistic Range as a Tool for Validation of Unsteady Computational Fluid Dynamic Codes

Gary T. Chapman
Adjunct Professor
Mechanical Engineering Department

The University of California, Berkeley
Berkeley, CA

THE BALLISTIC RANGE AS A TOOL FOR VALIDATION OF UNSTEADY COMPUTATIONAL FLUID DYNAMIC CODES

Gary T. Chapman
Adjunct Professor
Department of Mechanical Engineering
The University of California, Berkeley

Abstract

Unsteady computational fluid dynamics (CFD) codes are beginning to be used to analyze unsteady aerodynamics problems like store separation, and have the potential for many other applications. Some potential applications are: Control system design and evaluation, and the study of the effects of atmospheric winds on vehicle aerodynamics and flight dynamics and control. To be a viable tool in these roles CFD codes need to be validated with experimental data. Wind tunnel and flight testing to obtain data suitable for validation of unsteady CFD codes is very expensive and time consuming. Ballistic range testing is inherently unsteady and relatively inexpensive. The ballistic range as a tool for CFD code validation is evaluated. The capabilities and costs of the ballistic range testing and some existing data are examined in light of CFD validation.

The Aeroballistic Research Facility at the Wright Laboratory, Armament Directorate at Eglin Air Force Base has the capability to provide high quality trajectory and aerodynamic data and high quality shadowgraphs for precise flow field measurements (e.g., shock shapes) and density fields from interferograms. A set of data is available to provide some preliminary CFD validation. The limitations of this data set are evaluated and suggestions for additional tests and facility capability enhancements are put forward.

THE BALLISTIC RANGE AS A TOOL FOR VALIDÁTION OF UNSTEADY COMPUTATIONAL FLUID DYNAMIC CODES

Gary T. Chapman

Introduction

Computational fluid dynamics (CFD) is being used extensively in the design and analysis of aerodynamic systems under steady state conditions. It is also beginning to be used for unsteady flight conditions like store separation. In addition CFD has the capability to be used in several new and different ways. Some examples are: (1) In the design and evaluation of flight control systems. (2) As a source of unsteady aerodynamic data for piloted, ground-based flight simulators. (3) As a tool in the study of the effects of atmospheric winds on vehicle flight dynamics and control. To be a viable tool in any of these areas requires that the CFD codes be extensively validated against experimental data. CFD code validation has received considerable attention for steady state conditions although much work remains to be done. In the case of unsteady codes relatively little validation has been done. This is principally because the unsteady wind tunnel and flight testing required for validation are complicated and expensive. In general there is also a lack of priority within the CFD community and management for code validation.

Ballistic range testing, by its very nature, is unsteady, and hence, could provide a source of data for the validation of unsteady CFD codes. Well designed and executed ballistic range tests could provide data for CFD code validation at a reasonable cost.

This paper will evaluate the ballistic range as tool for CFD validation. First, we will examine the capabilities and testing costs of the ballistic range in light of code validation. Second, some of the existing ballistic range data base will be examined for cases suitable for code validation. Third, suggestions will be made for additional tests that could provide data with characteristics better suited for CFD validation. And forth, suggestions for relatively inexpensive augmentations to the ballistic range test capability, that will significantly enhance its code validation capabilities, will be suggested. Finally, a few issues related to the unsteady CFD codes themselves, that are important for validation using ballistic range data, will be noted.

Ballistic Range Capabilities and Testing Costs

There are two modes of data acquisition in a ballistic range. They are, onboard telemetry and remote instrumentation. The onboard telemetry mode is not well developed at the present time and full development could be expensive and time consuming. Remote measurements are the major sources of ballistic range data. The principal remotetechnique in use over the last 4 decades is the shadowgraph optical technique. The more common arrangement is many orthogonal pairs of spark shadowgraph stations located along the flight path of the ballistic range. An example is the 50 orthogonal pairs of spark shadowgraph stations distributed along the 200 meters of the Aeroballistic Research Facility (ARF) of the Wright Laboratory, Armament Directorate located at Eglin Air Force Base (Ref. 1).

Shadowgraph information can be used in two ways: (1) To determine coordinates of the flight trajectory. (2) To measure flow field features like shock waves. In the trajectory mode, each pair of shadowgraph stations are used to determine the 6 coordinates (3 spatial and 3 angular) of the vehicle trajectory. In addition the time is recorded when each pair of shadowgraphs is taken. With these stations the 6 coordinates are obtained as a function of time along the flight path of the vehicle. This trajectory information can be used directly in CFD code validation by comparison to trajectories generated using the aerodynamic data predicted with a CFD code and a 6-degree of freedom program (6-DOF). This is illustrated in figure 1.
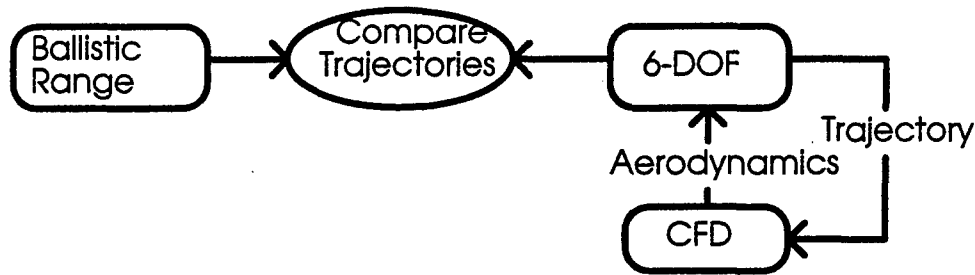
Figure 1. Validation Using Trajectory Data

It is possible to use this approach to validate CFD codes even if some of the aerodynamics from the CFD code are not very good or is lacking, such as drag, in the case of an Euler Code. In these cases aerodynamics from another source can be substituted for the poor or lacking CFD aerodynamics, for example the drag determined from the ballistic range data itself. This will be described below. This does not render the validation process for the other aerodynamic parameters invalid nor does it degrade the validation process.

Another mode of validation is to use ballistic range trajectory data along with an aerodynamic parameter identification program (Ref. 2) to determine the aerodynamics of the flight vehicle and compare these to the aerodynamics computed with the CFD code of an aerodynamic vehicle flying the same trajectory as the ballistic range test. This mode of validation is illustrated schematically in figure 2.
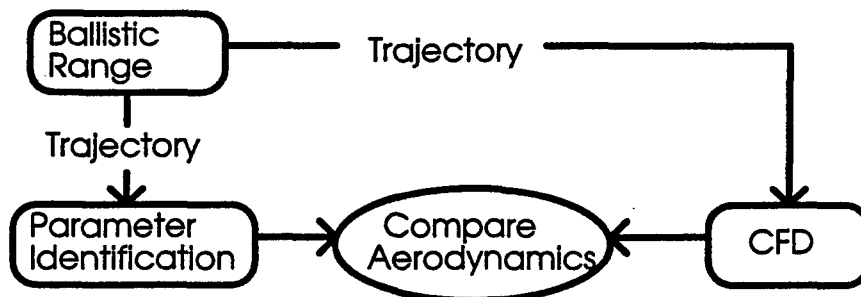
Figure 2. Validation Using Aerodynamic Data

Note, here the ballistic range trajectory data is used to drive the CFD code. 'This may require some smoothing and interpolation of the trajectory data. This can be accomplished using the aerodynamics obtained from the parameter identification program.

For these two modes of validation to be successful the trajectory data and the aerodynamics derived from this information must be of very high quality. To arrive at a high level of confidence in the validation process using the ballistic range aerodynamic information it would be valuable to provide some validation of the parameter identification process itself and the aerodynamic modeling used therein. This ballistic range validation mode is illustrated in figure 3.
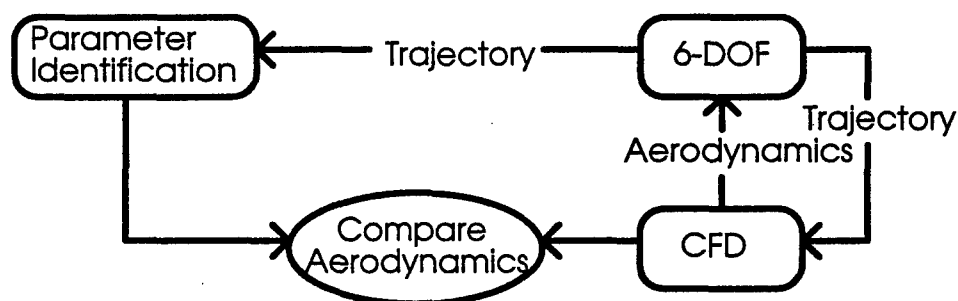
Figure 3. Validation of the Parameter Identification Process

Here we take the trajectories, developed with the 6-DOF program and CFD generated aerodynamics, run it through the parameter identification program and compare the aerodynamic coefficients with those determined directly from the CFD code. For details of the parameter identification program used on ARF data see Ref. 3. It should be noted that the ballistic range validation process is not dependent on an accurate CFD code. All that is required is that the CFD aerodynamics are representative of actual vehicle aerodynamics.

The second use of the shadowgraphs is to make measurements directly from the shadowgraphs of flow field features like shock wave shapes, locations of separation, and slip lines, to mention a few. These experimental measurements can then be compared to corresponding values determined with the CFD code. This process can be augmented using the optical reconstruction techniques developed by Leslie Yates (Ref. 4). In that technique the CFD density fields are used to construct shadowgraphs which can be compared directly to the experimental shadowgraphs. This step has to be quantitative to be useful in CFD code validation. This will require high quality shadowgraphs. Many ballistic range shadowgraphs are taken on a beaded screen resulting in some lose in resolution of flow field features. The direct shadowgraph technique projects the shadowgraph image directly on to the film providing a much higher quality shadowgraph. A typical direct shadowgraph taken in the ARF at Eglin Air Force Base is shown in figure 4.
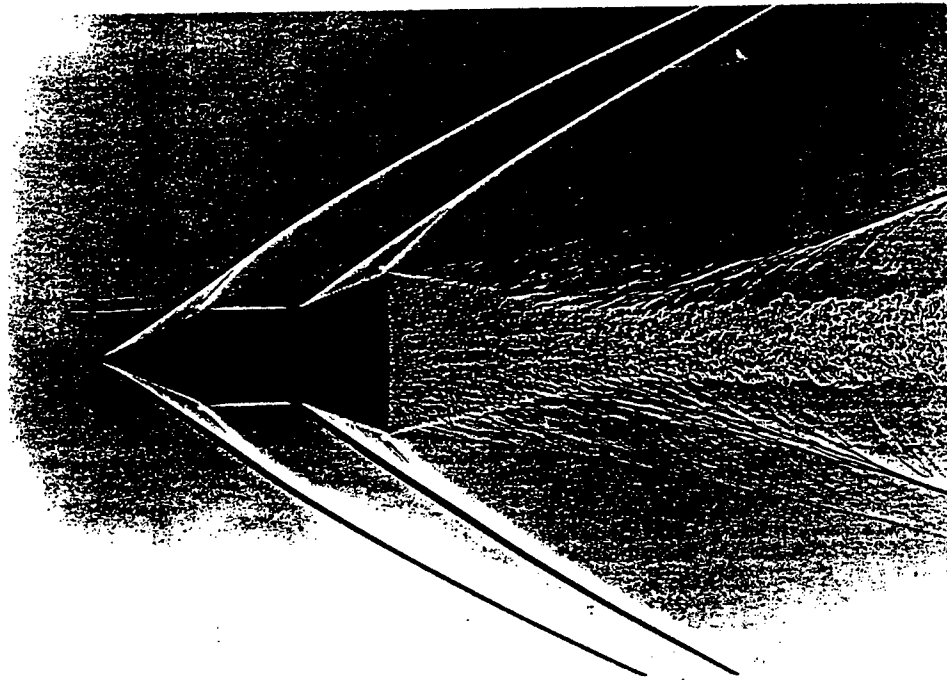
Figure 4. A Direct Shadowgraph

Over the years other specialized optical techniques have been used in the ballistic range that can be useful in code validation. The most common of these is the method of interferometry. An example of an interferogram taken in the ARF at Eglin Air Force Base is shown in figure 5. In some cases only a single interferogram is taken. If the flow field is axisymmetric we can determine a density field using an Abel integral inversion technique. If the flow field is not axisymmetric we can construct an interferogram from the CFD density field, again using the techniques developed by Leslie Yates (Ref. 4), and compare it with the experimental interferogram. If we get good agreement everything is probabley correct. However, if the agreement is not good it is difficult to determine where the difficulty lies in the CFD solution. It is preferable to be able to determine the density field directly from the experiment. To do this requires an interferometric station that can take multiple interferograms simultaneously at different viewing angles. Such a station exists in the ARF at Eglin Air Force Base. There 6 simultaneous double plate holograms are taken of the flow field at normanaly 30 degree increments in viewing angle (Ref. 5). With these 6 holograms it is possible to construct 6 or more interferograms. With the use of tomography these interferograms can be reduced to a density field in three dimensions.

To use the ballistic range for CFD code validation will require use of both the trajectory data and the flow field measurements. The trajectory data by itself provides good validation of the overall aerodynamics, which is what is needed in the final analysis, but, if the validation at that level is not adequate more detailed information is required. In that case the flow field measurements from shadowgraphs and the density fields

from the interferometry are essential. Hence, it is important when conducting ballistic range tests for CFD validation that both sets of data be obtained during the same test. Even in this case there will be insufficient data for validation of some details, for example the structure of turbulent boundary layer flows.
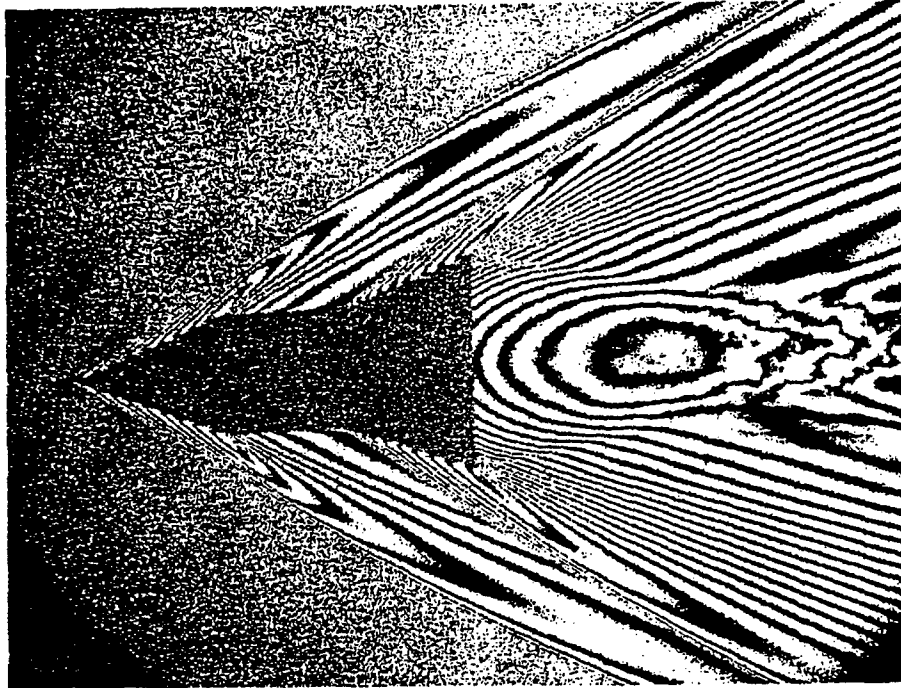
Figure 5. A Typical Interferogram

Before we proceed on to a discussion of the existing data base a few words need to said about costs of ballistic range testing. The cost are composed of two major components; model and sabot construction, and test operation, which includes the data analysis. Construction costs for a typical model and sabot combination is less than $1,000 per model sabot combination. The cost of test operations at the ARF at Eglin Air Force Base runs less than $2,000 a shot. Hence, for a 10 shot test program the cost is less than $30,000.

Existing Ballistic Range Data Base

Over the years thousands of ballistic range tests have been conducted on hundreds of configurations. For a variety of reasons most of this data is not suitable for CFD code validation The configurations may be too complex for easy geometry definition (e.g., rotating bands on spinning projectiles), the test conditions do not yield data with sufficient trajectory definition for good code validation (e.g., too few data points per cycle of motion, this normally happens for rapidly spinning projectiles), or the vehicle aerodynamics do not have sufficient unsteady characteristics to be useful for validation of unsteady codes (e.g., a very lightly damped vehicle will not exhibit sufficiently complex dynamics to be of use in the validation of all aspects of the CFD code) etc.

7-7

Recently a series of tests have been conducted at the ARF at Eglin Air Force Base with the primary objective of obtaining density flow fields on simple projectiles for validation of CFD codes. These tests used the 6 simultaneous double plate hologram station. Tests have been conducted on the three configurations shown in figure 6. Configuration 2 was tested in both an open and closed base configuration. Models are normally hollowed out in the base region to place the center of gravity at a position that will ensure stability of the model. However, for the closed base models tested the base closure was accomplished with a thin disk. The physical characteristics of these configurations are tabulated in Table I.
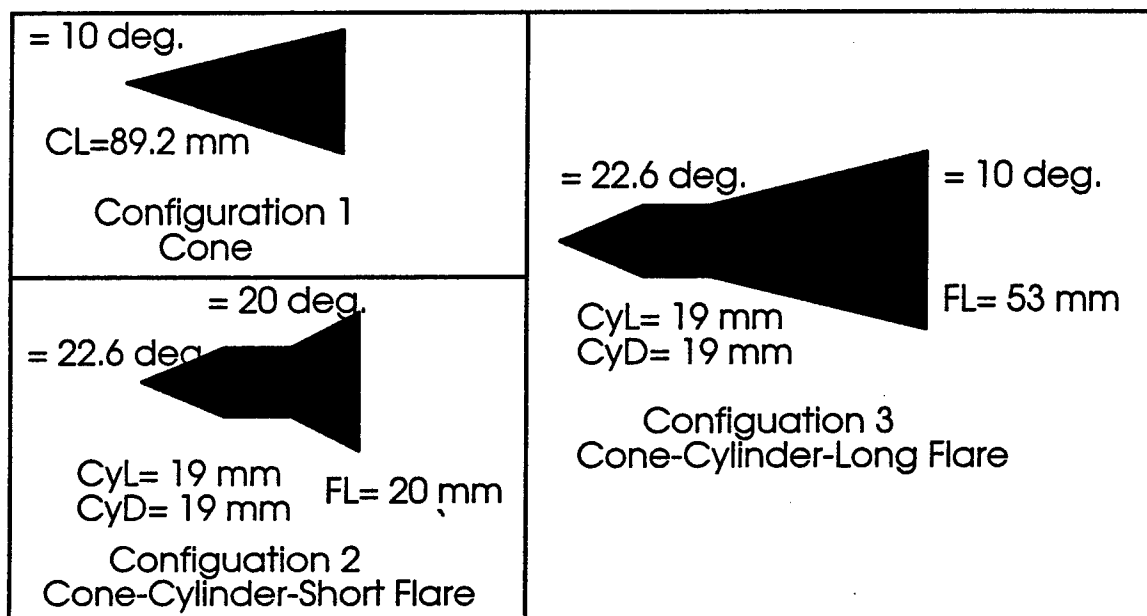
Figure 6. Configurations Tested

TABLE I				
Nominal Physical Properties of Test Models				
Configuration	Mass (Kg)	X-Moment of Inertia (gr-cm²)	Y-Moment of Inertia (gr-cm²)	Center of Gravity (mm)
1-Open	0.0416	31.13	206.222	49.619
2-Open	0.06423	36.816	142.79	30.585
2-Closed	0.08167	50.495	206.597	35.85
3-Open	0.1009	91.17	593.688	43.525

The tests were all conducted at a nominal Mach number of 2.5 and atmospheric conditions. Examples of the pitch (theta) and yaw (phi) angles, and the y and z components of swerve are shown in figure 7a, and 7b respectively for a cone-cylinder-short flare model (configuration 2). Also shown in these figures are computed trajectories based on aerodynamics determined from the trajectory data using the parameter identification program.
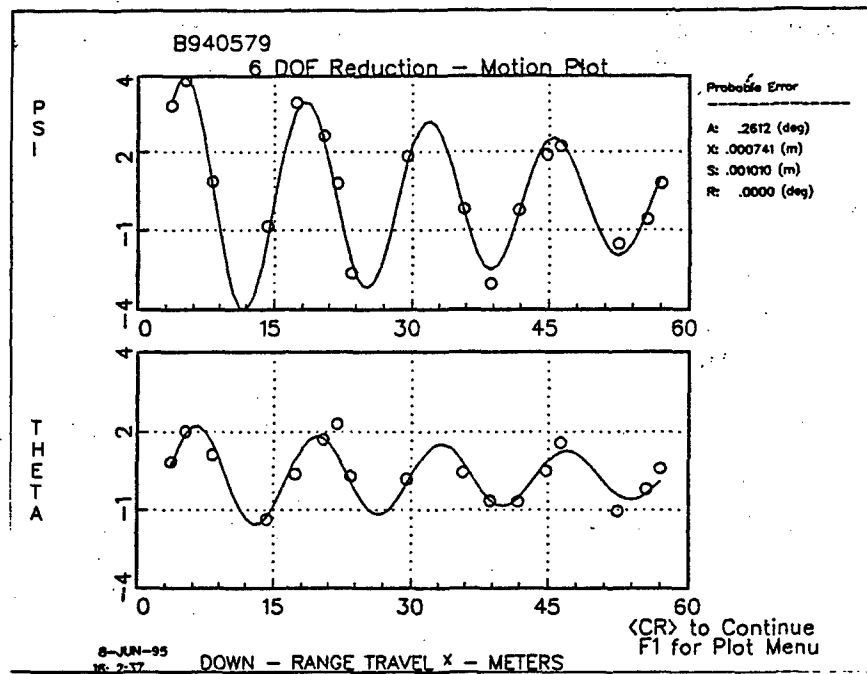
Figure 7a. Yaw and Pitch Versus Down Range Distance
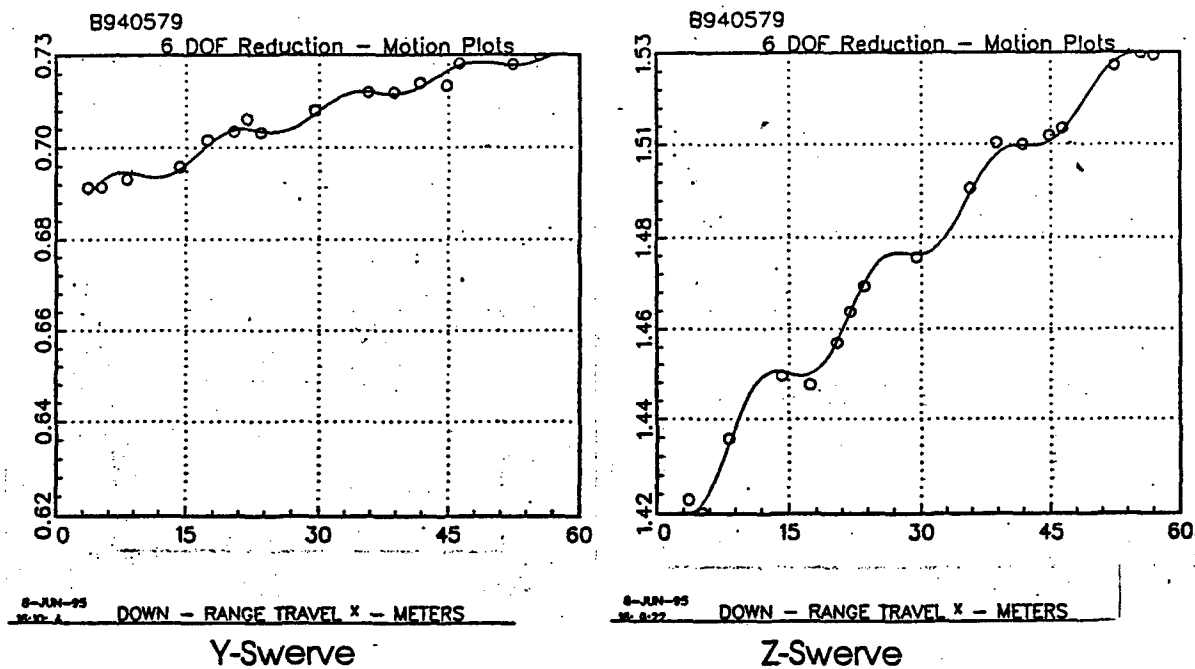
Y-Swerve

Z-Swerve

Figure 7b. Y and Z Swerve Versus Distance Down Range

Because this test was designed to obtain interferograms for use in developing the tomography proceedure to determine density profiles for CFD validation the trajectory characteristics were not tailored for optimum CFD validation. An examination of Figure 7 illustrates trajectory characteristics that are sub optimal, from a CFD validation stand point, on two counts. First, only a third of the ballistic range was used (60 of 200 meters and hence only 17 of 50 shadowgraph stations). Second, the wave length of the pitching motion is on the order of 15 meters and hence there are, on the average, only 4 data point per cycle of motion. In addition it would not be practical to use the present models, as designed, in tests over the full length of the range because the mass and drag characteristics result in significant velocity loss over the length of the range. This can be seen in Figure 8 were the derived velocity curve is shown as a function of the down range distance.
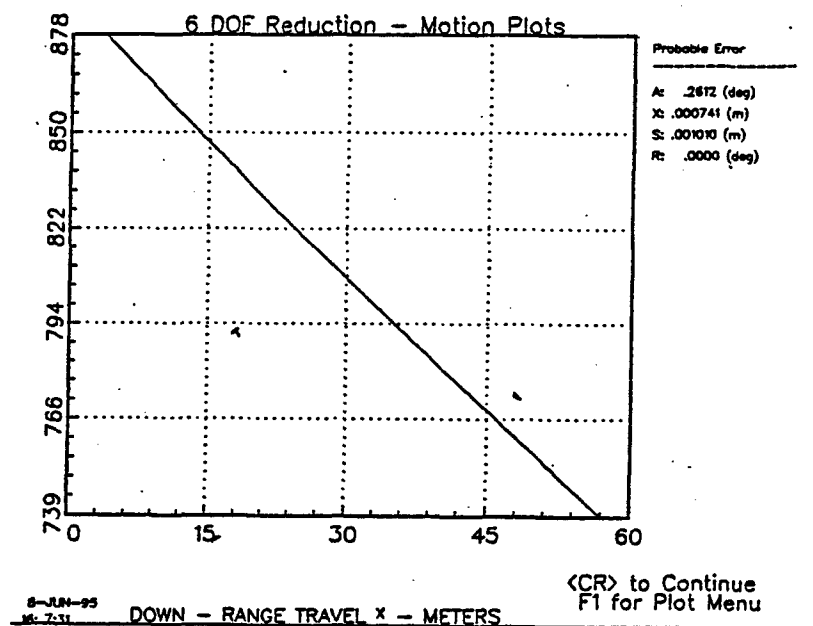
Figure 8. Velocity (m/s) Vs Down Range Distance (m)

Here we see that this configuration loses nearly 150 m/s in 60 meters of flight. Hence, over 200 meters of flight it would have a velocity loss of over 450 m/s. This is not acceptable. The only way to reduce the velocity loss and retain the configuration would be to increase the mass and/or size. The wave length of the pitching also needs to be extended to obtain more data points per cycle of motion. This would improve the definition of the trajectory and hence provide better trajectory data for direct CFD validation and better data for the determination of the aerodynamic characteristics using the ballistic range parameter identification program. An optimum trajectory over 200 meters of flight for CFD code validation would be to have 4 to 5 cycles of motion resulting in 10 to 12 points per cycle of motion with a velocity loss of around 50 m/s or less.

Although this test exhibited trajectory characteristics that were sub optimal from two stand points, there were some good characteristics demonstrated. First, there was sufficient pitch damping for good CFD validation, a decrease in the pitch amplitude by over 50 per cent in 4 cycles of motion. Second, there was sufficient swerve to allow validation of the normal force characteristics. The lift, drag and pitching moment coefficients determined with the parameter identification program and experimental trajectory data shown in figure 7 are tabulated in Table II Also tabulated in Table II are the probable errors of each coefficient.

TABLE II Aerodynamic Coefficients and Probable Errors (Configuration 2)					
Shot No.	Alpha Max	C_{d0} (PE)	$C_{m\alpha}$ (PE)	C_{mq} (PE)	$C_{n\alpha}$ (PE)
B940579	4.4 deg.	1.51(0.002)	-1.27(0.07)	-11.62(2.8)	11.32(.78)

The probable errors on all of these coefficients suggest extremely good aerodynamic data. However, preliminary analysis of 2 additional tests on this cone-cylinder-short flared model (configuration 2) with differing amplitudes of motion show considerable variations in the aerodynamic characteristics, particularly the drag coefficients. Values of the aerodynamics coefficients for these two additional tests are tabulated in Table III along with the parable errors (where available). The shot to shot variation is well beyond that expected from angle of attack variation or experimental accuracy. This suggests that there may be dynamic effects on flow separation on the flare. It should be noted that configuration 2 was designed to have a region of flow separation at the junction of the cylinder and flare. It is suspected that the separtion is behaving in a vary non consistant manner that depends on the specific dynamics of the body. To test out this hypothesis additional analysis needs to be done on the cone (configuration 1) and the cone-cylinder-long flared (configuration 3) models. If the shot to shot consistantancy for these configuration is well with in the acceptable limits the prelimeary hypothesis of dynamics dependent separation would appear to be true. This would require further testing to verify. If dynamics dependent separation is the principal reason for the shot to shot variation it could be that configuration 2 is a very good candadate for validation of unsteady viscous CFD codes under extreme conditions. Preliminary evaluation of results on cones (configuration 1) suggest that this is the case. The testing of the separation hypothesis is continuing.

TABLE III Aerodynamics for two Additional Shots (Configuration 2)					
Shot No.	Alpha Max	C_{d0} (PE)	$C_{m\alpha}$ (PE)	C_{mq} (PE)	$C_{n\alpha}$ (PE)
B950461	1.1 deg.	1.84()	-1.22(0.06)	-6.15(0.14)	7.85()
B950460	0.6 deg.	1.17(0.001)	-1.34(0.02)	-8.3(3.0)	11.4(0.24)

From a code validation stand point the present set of data has at least one other deficiency. That is it does not cover the transonic speed range where the shock wave dynamics would be expected to be much more extreme, particularly around Mach number 1. At these conditions for a decelerating, pitching and plunging model the shock dynamics will be extremely complex and time dependent.

In spite of the various deficiencies given above this current set of data can be useful in CFD code validation.

Additional Tests

Although the tests described above can be used for code validation they do not represent the best that can be achieved nor do they cover a sufficient Mach number range. In the following, two sets of tests that could provide better data and cover a wider Mach number range are described briefly.

1. The first set is to modify the existing configurations to move the center of gravity slightly rearward to increase the wave length of the pitching oscillation and to increase the mass and/ or decrease the base area to reduce the velocity loss. These configurations should be designed to fly the entire length of the 200 meter long range. A reduction of the flare length for both configurations could go a long way to meeting these objectives with out significant change to the configurations. All though these models do not tend to roll it would also prove beneficial to install at least one roll pin in the base of the model to asses the amount of roll

2. A second set of test in the transonic speed range is essential to validate codes that must operate in that speed range. The configuration here could be the cone-cylinder-long flare. The use of an aerodynamic design program called PRODAS shows that this configuration as designed would have a much longer wave length in pitch than it did at M=2.5.

Another potential transonic configuration is illustrated in Figure 9. This configuration was tested in 1958 in the 1 foot transonic wind tunnel at AEDC, see Ref. 6. These tests showed positive static and dynamic stability about the center of gravity position (the pivot location for the wind tunnel test). The aerodynamic coefficients are; $C_{M_\alpha}=-0.08$, $C_{M_q}=-1.7$, and $C_{D_o}=0.63$. All coefficients are based on base area and diameter. The pitching moment coefficient depended on the base configuration. The data above is for the flat base as illustrated in Fig. 9. AEDC is already performing CFD calculations for the case of a free oscillation, and with a mechanical spring. Both oscillations are about the listed center of gravity. These cases are compared to the wind tunnel data in Ref. 6. The comparison looks good but the spring used in the wind tunnel test was strong and hence the aerodynamic moment contribution is small. A CFD computation for comparison with a free flight test would provide a much better validation of the CFD. To get a body that is sufficiently stable for a good ballistic range test may require moving the center of gravity slightly forward.

=13.3 deg.

D

R=.1925D

1.469D

CG=0.762D from Nose
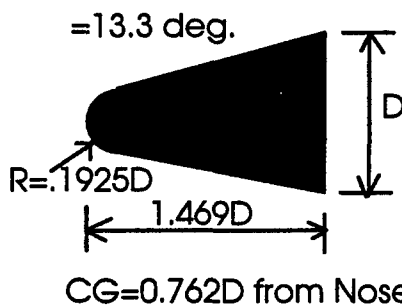
Figure 9. Potential Transonic Configuration

Another potential configuration is the Mark 82 bomb. This configuration is presently being computed in a pure roll mode to determine spin damping. This work is being done at AEDC. Here again a ballistic range test could go a long way to providing validation data for spinning configurations.

Capability Enhancements

There are several enhancements to the facility capability that could improve the over all data quality or add some capability that could prove beneficial for code validation. Some of these capabilities already exist but may not be in use at present. Some of these facility capability enhancements will now be considered.

1. One way to increase the data per cycle and hence to improve the overall data quality, particularly for partial range tests is to make use of multiple exposure shadowgraph stations. Here multiple spark shadowgraphs are taken at the same station with a multiple spark arrangement. This capability has been developed and installed in the ARF at Eglin but rarely used. Each of these stations takes 4 shadowgraphs with the images of the model about 0.25 meters apart. This capability exists at 5 station along the ARF. If the multiple exposure stations were applied to the conditions of the data in Figure 7 it would provide up to 5 clusters of data points and improve the definition of the trajectory.

2. As noted earlier the shadowgraphs used in determination of trajectories does not have good properties for flow field visualization. However, direct shadowgraphs, an example was shown in Figure 4, provide much better quality picture for flow field measurements. More of these shadowgraph stations need to be included in tests that are meant to be used for CFD code validation. Here again the ARF has capabilities for this that are normally not used.

3. The present automated film reading technique developed by Leslie Yates of AeroSpaceComputing (Ref. 7) appears to have good film reading accuracy for long bodies but for shorter bodies and particularly short bodies with asymmetric separation there may be a degradation of the accuracy. This could be improve by using a silhouette matching procedure. This capability needs to be added to the capabilities for the film reading.

4. The classical double plate holography technique use in the multiple simultaneous holographic technique described above may prove to be too sensitive and time consuming to obtain density fields for a large number of test cases. A much simpler technique may be the cylindrical holographic technique presently being developed by the University of Florida under contract to Armament Directorate at Eglin Air Force Base. The limitations of the cylindrical holographic technique need to evaluated before a switch to this technique is made, particularly distortion effects that may be present in the cylindrical technique need to be quantified.

5. Another capability that could provide very useful information is an air flow system normal to the ballistic range flight path. This could be useful in studying the effects of atmospheric winds on vehicle dynamics and assessing unsteady effects normally not modeled in flight simulations. This could be

accomplished in the ARF by inserting a simple closed return wind tunnel normal to the flight path. The tunnel shown have a test section that is at least 0.4 meters high and 2 meters across (distance along the flight path) and provide velocities of about 12 m/s. A quick analysis shows that it would be possible to place such a wind tunnel in the 3.6 meter square portion of the ARF. This wind tunnel would require a drive system with about 10 horse power. A sketch of a potential configuration is illustrated in Figure 10.

With a distance of 2 meters of travel a projectile 10 cm in length would experience a flight path of 20 body lengths in a cross flow velocity of 12 m/s. If the projectile has a velocity of 300 m/s it would experience a perturbation in angle of attack of about 2.5 degrees.
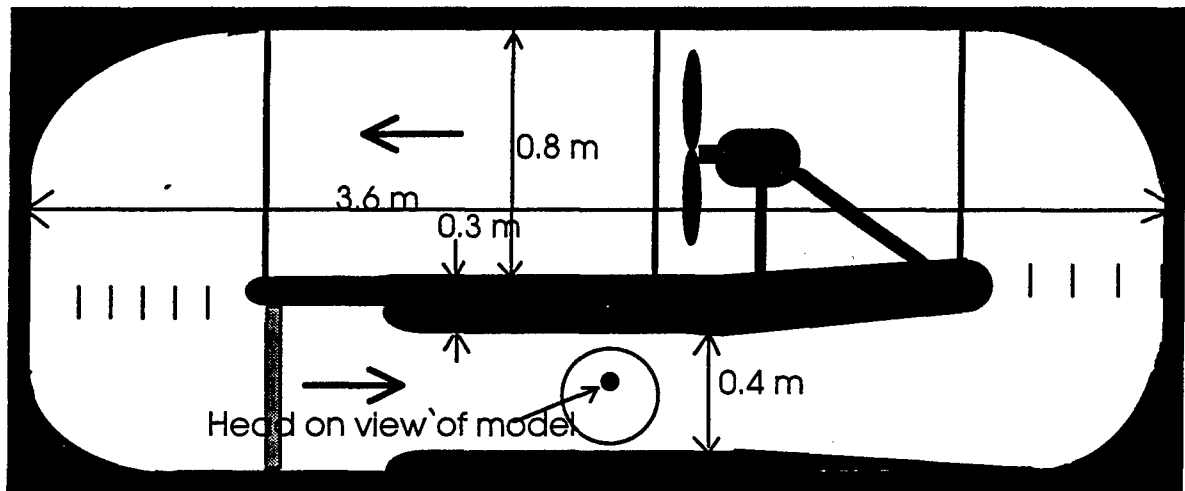
Figure 10a. Side View of Wind Tunnel
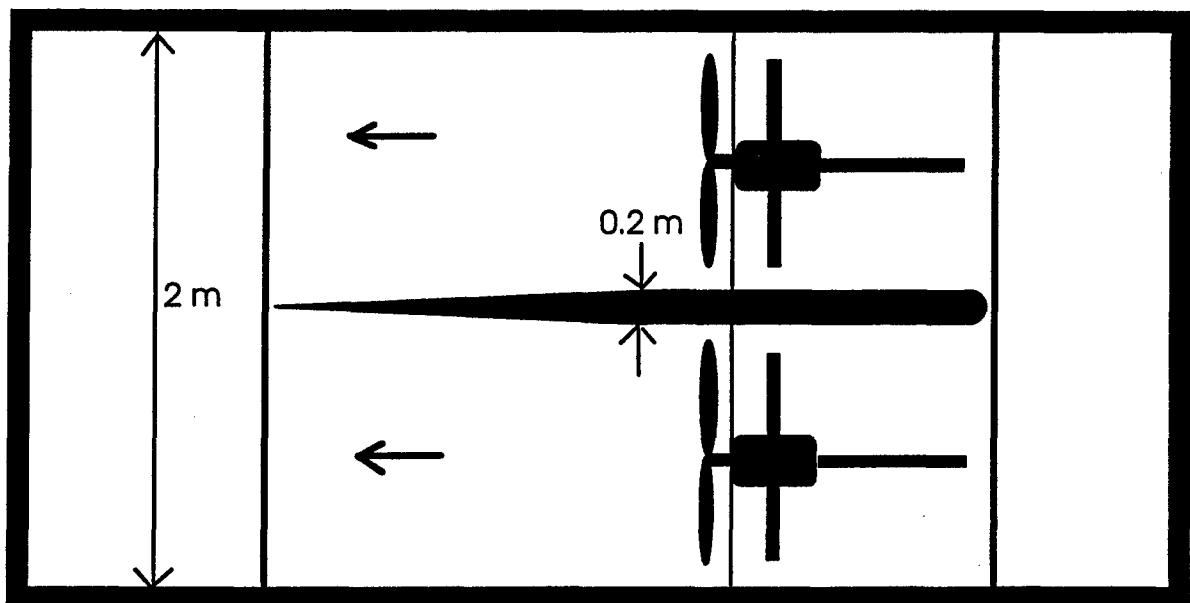
Figure 10b. Top View of Wind Tunnel

To use this wind tunnel for CFD code validation may require that the holes in the side of the wind tunnel (shown as round circles in figure 10a), through which the model enters and leaves wind tunnel, be covered with mylar or some similar very light material through which the model must fly. This will keep the turbulence generated by an open window from causing turbulence in the ballistic range as well as producing additional turbulence inside of the wind tunnel. In addition the flow field in the wind tunnel test section where the model will fly must be surveyed in detail to provide the known wind field information.
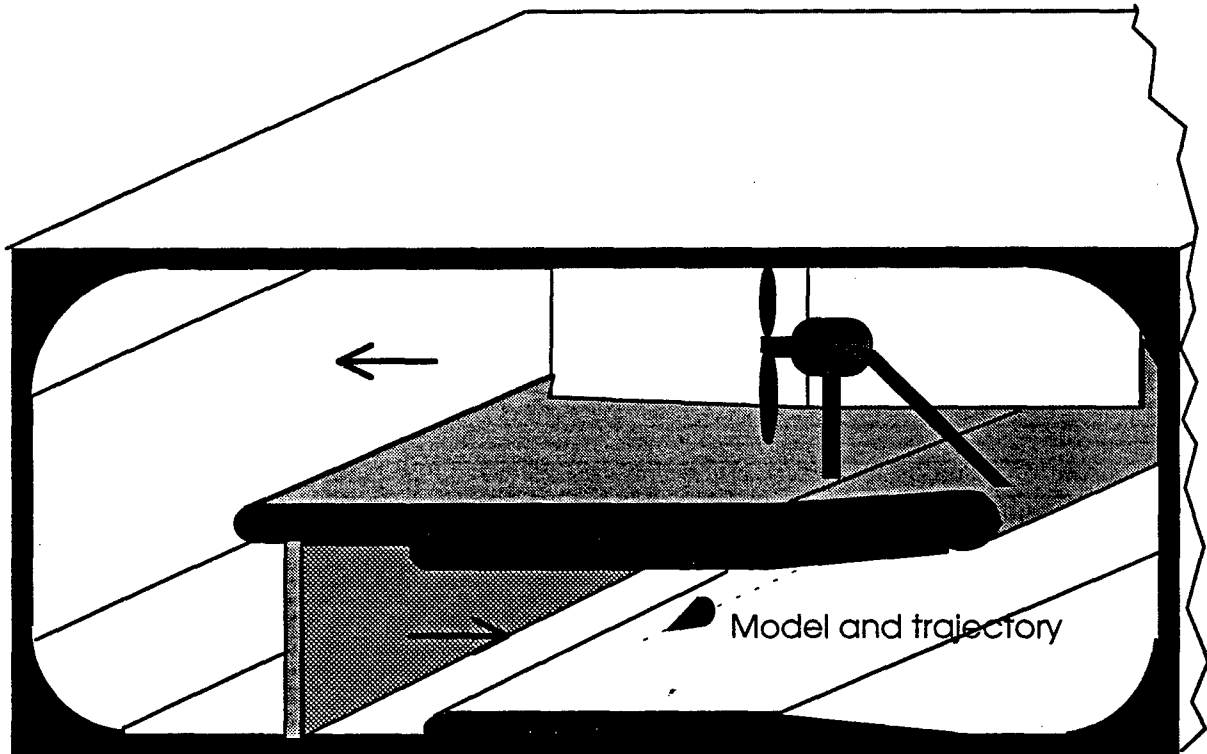
Figure 10c. Isometric View of Wind Tunnel

Some CFD Issues

Although the principal purpose of this paper was to assess the capability of the ballistic range for CFD code validation a few issues need to be pointed out concerning the computational aspects of validating CFD codes with ballistic range data.

1. If Chimera grid schemes are to be used care must be taken to account for the deceleration of the test vehicle and hence the inner grid may move significantly with respect to the outer grid.

2. For validation of unsteady tests the issue of initialization of the CFD procedure needs serious consideration. For example one might use the solution for a forced periodic motion with an amplitude and wave length similar to the test case. Here we would be starting at the same angle of attack with a solution history that is nearly that which the vehicle had experienced. The best achievable initialization of the CFD program would be as follows: (1) Obtain the best curve fit to the ballistic range trajectory with the aerodynamics identified with the ballistic range parameter identification program. (2) Using the initial

conditions and these aerodynamic coefficients, calculate the trajectory backwards in time for some prescribed period of time, t`, for example about one cycle of motion. (3) Perform a CFD computation for the steady state conditions at t=-t` (4) Now continue the CFD solution using the trajectory from t= -t` to t=0. (5)At t=0 activate the 6-DOF program and continue the computation using the trajectory from the 6-DOF program. In this way the flow field predicted with the CFD program will have a very good representation of the motion history for the initial conditions at t=0.

3. If external winds are to be considered the CFD code must account for the winds. This will require a modification to the outer boundary conditions. A graduate student is presently working on this at AEDC as part of the AFOSR Summer Faculty and Graduate Student Research Program.

Concluding Remarks

This brief analysis reported here shows that the ballistic range posses many characteristics that make it a promising cost effect tool for the validation of unsteady CFD codes. To illustrate this more completely CFD computations need to be performed for some of the data sets that presently exist for supersonic conditions, or better yet for transonic data should it become available. Effort also needs to be expended to obtain density flow fields from the inteferograms for some of the existing tests.

References

1. Kittyle, R. L., Parkard, J. D., and Winchenbach, G. L., "Description and Capabilities of the Aeroballistic Research Facility," AFATL -TR-87-08, May 1987.

2. Chapman G, T., and Kirk, D, B, "A Method for Extracting Aerodynamic Coefficients From Free-Flight Data," AIAA J, Vol. 8, No. 4, April 1970, pp. 753-758.

3. Hathaway, W., Whyte, R. and Burnett, J., " Aeroballistic Range Facility Data Analysis System (ARFDAS) User Manual," Armament and Electrical Systems Department, General Electric Company, Feb. 1982.

4. Yates, L. A., "Images Constructed from Computed Flowfields", AIAA J, Vol. 31, No. 10, October, 1993.

5. Valentino, M., Winchenbach, G. L. and Weissert, D., "A Multiview Holographic Interferometry System for Flow Field Studies", Presented at the 45th Meeting of the Aeroballistic Range Association, Huntsville, AL, Oct. 1994.

6. Bauer, R. C., and Riddle, C. D., "Transonic Dynamic Stability Tests of a Small Scale Model of the ABMA "Jupiter" W_{14} Nose Cone Forebody in Combination with Three After Bodies," AEDC-TN-58-42, July 1958.

7. Yates, L. A., "Automated Film Reading for Ballistic Ranges," J. Spacecraft and Rockets., Vol. 30, No. 2, March-April, 1993.

GENETIC ALGORITHMS AND THE SENSOR MANAGER SCHEDULER

Milton L. Cone
Associate Professor
Department of Computer Science/Electrical Engineering

Embry-Riddle Aeronautical University
3200 Willow Creek Road
Prescott, AZ 86301-3720

GENETIC ALGORITHMS AND THE SENSOR MANAGER SCHEDULER

Milton L. Cone
Assistant Professor
Department of Computer Science/Electrical Engineering
Embry-Riddle Aeronautical University

Abstract

A genetic algorithm scheduler is developed that solves a simple sequencing problem. The effect of various crossover and mutation rates on the best ten solutions found and on the average solution of the last generation is presented as a study of 25 experiments. The most important result is that the closer the average solution for the last generation gets to the optimal result, the farther the average of the best solutions is from that optimal result. This suggests using the average of the best solutions and the generation average solution as measures to adjust the crossover and mutation rates to produce a better solution in a fixed amount of time or to arrive at the same solution sooner. These are important considerations if the scheduler is to be used in a real-time system.

GENETIC ALGORITHMS AND THE SENSOR MANAGER SCHEDULER

Milton L Cone

Introduction

The sensor manager scheduler is an example of a real-time problem solver. Real-time means that the value of the solution depends not only on the correctness (how close to the optimal schedule a result is) but also on how long it takes to produce the results. A real-time scheduler has to be able to trade time for correctness and correctness for time. This paper proposes an approach to scheduling using genetic algorithms. The basic idea is to use a deterministic scheduling rule to produce an initial schedule, then let the genetic algorithm improve on that schedule. Then, if necessary and time and resources permitting, a heuristic search can be used to traverse the remaining space to the optimal solution (Bagchi, et al. - 1991).

Genetic algorithms have many features that make them attractive schedulers. First, they always have an answer ready. This allows them to easily integrate into a real-time system. Second, they are a naturally parallel algorithm. The most time consuming calculation, evaluating the fitness of all of the proposed schedules, can proceed at the same time for each of the proposed schedules. Next, scheduling is hard. The sensor manager scheduler is faced with a task that is very similar to the job-shop scheduling problem which has been shown (Gary & Johnson - 1979) to be among the worst of the NP-complete problems. This almost guarantees that some type of search algorithm will be required to find workable schedules for a real-life problem. Finally, a genetic algorithm is a very efficient way to search large spaces. Genetic algorithms are especially effective in optimizations involving discontinuous, noisy, high dimensional and multimodal objective functions (Grefenstette et al. 1991). These features make them a good candidate as a sensor manager scheduler.

This article is organized as follows: First, some introductory material on scheduling is provided. This is followed by an introduction to genetic algorithms and to the computer program GENESIS (Grefenstette, et al - 1991). Next, a simple scheduling problem is stated and changes necessary to GENESIS are outlined. The next section describes a performance study of the modified GENESIS program and makes some observations about the operation of a genetic algorithm. The final section proposes future work.

Classical Scheduling Results

There are many good articles on classical scheduling. (Graves - 1981) and (Stankovic, et al - 1995) are two examples. Graves highlights the status of current research on classical production scheduling versus current practice at the time of the article. His review article is drawn mostly from operations research, industrial engineering and management disciplines. Stankovic is concerned with scheduling real-time

tasks on computer systems. Most of the summary that follows comes from the Stankovic article. References for the results not cited in this section can be found in Stankovic.

Scheduling can be broken into four areas. They are static, dynamic, off-line and on-line. Most of the classical scheduling theory reviewed by Graves is static. A static scheduler knows all of the pertinent information about the jobs it has to schedule. This information might include execution times, start times, deadlines, priority, sensor preference, alternate sensors capable of collecting the required data, and any other information necessary to generate a schedule. Once a static schedule is determined, it is fixed for all time. There is no new information generated during the schedule execution that will change the schedule. Most scheduling systems develop a static schedule over a finite horizon.

The dynamic scheduler differs from the static scheduler in that it only knows complete information about the tasks that are currently executing. New jobs may arrive that require the schedule to evolve. The sensor manager scheduler operates in a dynamic environment, hence it needs to be a dynamic scheduler. Most schedulers are static schedulers that plan a schedule to the next planning horizon then go into hibernation while new jobs come in. The scheduler is then activated for the next scheduling cycle that includes all of the new jobs plus all of the old jobs that did not start execution.

Off-line scheduling refers to any activities that are performed that do not affect the schedule while it is being executed. Many times static and off-line are used interchangeably but that is not strictly correct. It is true that a static schedule is developed off-line with some worst case assumptions and then applied on-line assuming that all of the assumptions remain true. But off-line scheduling also refers to any off-line analysis that might be performed. This can be before, during or after schedule execution. For example, setting job priorities for the next scheduling cycle might be an off-line scheduling function that would operate at the same time as the current schedule is executing.

On-line scheduling means that the schedule is developed while the schedule is executing. While an off-line schedule is usually developed before the schedule is executed, it can be developed during or after execution. The difference is that the off-line schedule does not affect the execution of the current schedule.

Metrics are very important to scheduling algorithms as they determine the adequacy of the final result irrespective of the algorithm used. Generally metrics are applied to the schedule as a whole not to individual jobs within the schedule. Typical metrics from classical scheduling theory are schedules that minimize the sum of completion times; minimize the weighted sum of completion times; minimize schedule length (also known as makespan); minimize number of sensors, processors or machines used; or

minimize the maximum lateness of any task. Constraints, such as all tasks must meet specified deadlines, can be added to these metrics. Frequently the weight added to the metric is based on some outside evaluation of a job's priority.

The metrics that are of most interest to the sensor manager scheduler are ones that combine a job's priority with its deadline. These are the metrics that include a weighted sum. For example, a schedule that minimizes the weighted sum of completion times captures the notion that an efficient system is one that completes all jobs as soon as possible but that it is more important to complete some jobs than others. Adding the constraint that all jobs that have deadlines must meet them completes the idea that a good schedule is one that processes jobs through the system as fast as possible, that some jobs are more important than others and that all jobs should meet their deadlines.

While all of these metrics are important, Stankovic, et al suggest that the optimal scheduling algorithm is one that fails to meet a deadline only if no other scheduling algorithm can meet it. This metric is a good goal but hard to implement in a real-time system.

There are several simple scheduling algorithms that are optimal for some set of system objectives, task model and metric. For example the earliest-due-date (EDD) algorithm in which the jobs are taken in order of nondecreasing due dates, is optimal for a single sensor trying to minimize the maximum lateness. Lateness is difference between when a job completes and when it is due. This is known as Jackson's rule. If all the jobs to be scheduled have release times when they can start, then making a schedule is NP-hard. NP-hard means that any algorithm which computes an exact solution requires an exponential time in the size of the problem. If the sensor allows the jobs to be preempted (interrupt driven processor) then the EDD is optimal with respect to minimizing maximum lateness if the EDD algorithm is taken to mean that all the jobs, with release times earlier than or equal to the present time, are scheduled by earliest-due-date. This example illustrates a general theme in scheduling: A simple task can become a very hard task with a small change to the system model yet become simple when the model is changed again. The EDD algorithm is typical of the simple deterministic algorithms that can be used to seed the genetic algorithm's search for a workable schedule.

Multitasking is another application that is common in sensors. Here several tasks share common resources such as memory or a processor. Since several tasks are executing over the same time interval this means that some tasks are repetitive. Generally this scheduling problem exists at a lower level, closer to the sensor handler (Musick & Malhotra - 1994). (Mok - 1983) showed that the problem of deciding if it is possible to schedule a set of periodic tasks by using semaphores (for example semaphores or flags

might be set to keep other tasks from accessing a common hard drive) to enforce mutual exclusion is NP-hard.

When the scheduler is overloaded (too many jobs), the performance of many deterministic scheduling algorithms degrades. (Baruah, et al. - 1991) showed that any on-line (preemptive) algorithm working in overload conditions could not perform any better than 25% of a clairvoyant (perfect) scheduler.

If there are multiprocessors running in the sensor manager system then most of the results reported in Stankovic's review article deal with how hard the problem is. Quoting Stankovic,

> "Most multiprocessor scheduling problems are NP, but for deterministic scheduling this is not a major problem. We can use a polynomial algorithm and develop an optimal schedule if the specific problem is not NP-complete, or we can use off-line search techniques based on classical theory implications. These off-line techniques usually need to find only feasible schedules, not optimal ones."

This is where the genetic algorithm enters as a search technique that seamlessly integrates classical scheduling results.

Genetic Algorithms

While many deterministic scheduling algorithms exist that produce a valid schedule under specific assumptions, many, if not most, real-world problems do not exactly match the assumptions. The scheduling task then falls to a nondeterministic scheduler to try to develop a workable schedule. Nondeterministic schedulers are based on searching through the space of all schedules for a schedule that meets the sensor manager's requirements and constraints. The more efficient the search technique, the more likely it is that a good schedule will be found. The genetic algorithm provides such a technique.

Since the sensor manager operates in a real-time system, the scheduler must also operate real-time. This requires the scheduler to produce a schedule in a guaranteed amount of time or to always have an answer ready. The genetic algorithm is capable of always retaining the best solution found so far thus being able to provide a schedule. While this schedule may not meet all of the requirements or constraints imposed by the sensor manager, it will be the best schedule that the genetic algorithm can find in the time allotted.

Many search techniques have special requirements on the search space in order for them to work. For example, derivative techniques require the search space to be continuous, low dimension, and unimodal. A genetic algorithm generally has no special requirements on the search space. While some search techniques have difficulty getting trapped by a local peak and fail to find a higher peak located in a

different area, the genetic algorithm has a natural protection from this problem. There is a finite probability that every point in the search space will be searched. The genetic algorithm is very robust, generally outperforming both gradient techniques and other search techniques on discontinuous, noisy, high dimension and multimodal search spaces (Grefenstette, et al. - 1991).

How does a genetic algorithm work? Genetic algorithms maintain a population of candidate solutions to a fitness or evaluation function which evolve over time to produce better candidate solutions. The algorithm is inspired by the genetic model of nature and many of the terms are drawn from that analogy. Each member of the population is composed of one or more chromosomes. The chromosomes are made up of genes. For the simple sensor manager scheduler considered in the next section, each job is a gene and a chromosome is a sequence of jobs. The sequence reflects the order in which the jobs (jobs and tasks are used interchangeably) are to be processed by the sensor. Thus the sequence is a schedule. Each gene is a particular task to be submitted to the sensor. If the tasks are identified by the numbers 0 - 9, an example of a chromosome is the sequence (0 1 2 3 4 5 6 7 8 9).

The genetic algorithm repeatedly executes the following steps until the termination condition is met.
1. Selection
2. Mutation
3. Crossover
4. Evaluation
5. Data collection, if necessary

Generally, the termination condition is some maximum number of trials, where a trial is the processing of one chromosome through the five steps of the genetic algorithm. Termination can be based on other criteria such as determining the length of time the algorithm will run or finding a satisfactory schedule.

To start itself, a genetic algorithm creates an initial population of schedules. These generally number from 50 to 100 and are created randomly using a random number generator to select genes to build a chromosome. An initial population of 50 schedules for the 10 jobs above was created by shuffling the numbers 50 times. Each shuffle produced a new schedule. The initial population can be seeded with nonrandom schedules. Usually only a few schedules are used since too many nonrandom schedules in the initial population can lead to premature convergence of the algorithm.

The initial population is the zeroth generation of the genetic algorithm. Just as a species develops by selecting the fittest of the population to survive, the genetic algorithm selects the best of the current generation of schedules. Survival is a stochastic process. The better a chromosome is, the more likely it is to have more offspring in the next generation. The selection process determines how many copies of

each chromosome (schedule) make it to the next generation. The total number of chromosomes is controlled to the same number as the initial population. This means that some of the chromosomes do not survive while others may have multiple copies in the following generation.

There are two popular ways to determine how many offspring a chromosome is likely to get. The first is to base the selection on an evaluation of the chromosome's fitness. The fitter chromosomes are more likely to get more offspring (it's still a random process) than the weaker chromosomes. This process has the advantage that it converges to a good solution faster than the second method but that is also its drawback. If the initial population has a super chromosome in it then that chromosome can dominate all future generations limiting the search. The second method uses an evaluation function to rank the chromosomes. The number of offspring is based on the rank that a chromosome has, not its absolute evaluation. While this keeps an unusually strong chromosome from dominating the population, it slows the rate of convergence to a good solution.

The next two steps, mutation and crossover, are the genetic operators. They are responsible for creating new chromosomes which cause the population to evolve. After selection, each gene is given a chance to mutate. If selected, one bit in the representation of the gene will be replaced by a random selection from the set {0, 1}. This causes the gene's value to change to a new value that has nothing to do with the value its parent had. This is the source of new genes into the population. The mutation rate is generally very small, typically one in a thousand.

The second genetic operator is crossover. This operator is comparable to mating. Two chromosomes are chosen to mate. Two points are selected at random in the chromosome. This divides the chromosome into three parts. The middle parts of the two chromosomes are then swapped and the new chromosomes replace their parents in the current generation. While all members of the current population have a chance to mutate, only a fraction of the population crossover. The number of chromosomes that crossover is selected at the beginning of a run. Typically about 60% of the population undergo crossover.

The last step in creating a new generation is evaluation. An evaluation function (frequently called a fitness function since it determines the fitness of the chromosomes) has to be developed. It represents the environment in which the chromosomes are to develop. For a scheduler this determines the metrics and constraints by which a schedule is judged. A good evaluation function should return a range of values so as to grade a chromosome's fitness. If the evaluation function returns only a 0 or 1, then there is no pressure driving the solution towards a better result. An evaluation function should also be based on the fitness of the chromosome as a whole not just on its individual genes. For example, an evaluation

function that is based on adding up the priorities of the scheduled jobs is not as good as one that multiplies the order of the job times its priority.

Data collection is the final activity in each pass through the genetic algorithm. While this step might be skipped in a real-time scheduler, it seems likely that at least some statistics would be retained in order to monitor the progress of the algorithm.

The genetic program used for this study is called GENESIS. It was developed by Grefenstette (Grefenstette, et al. - 1991) and is probably the most popular of the genetic algorithm incarnations. The next section covers the GENESIS program and the modifications made to it for this study.

GENESIS

GENESIS is a simple genetic algorithm. It supports the usual genetic operators of mutation and crossover. In addition, it has several routines to collect data on the performance of the algorithm. The example problem in (Grefenstette, et al. - 1991) tries to find the minimum of a paraboloid, $f = x^2 + y^2 + z^2$, assuming the variables can range between -5.12and 5.11. Figure 8.1 shows a sample

Experiments	= 1
Total Trials	= 1000
Population Size	= 50
Structure Length	= 30
Crossover Rate	= 0.600
Mutation Rate	= 0.001
Generation Gap	= 1.000
Scaling Window	= 5
Report Interval	= 200
Structures Saved	= 5
Max Gens w/o Eval	= 2
Dump Interval	= 0
Dumps Saved	= 0
Options	= acefgL
Random Seed	= 123456789
Rank Min	= 0.750

MEAN

Gens	Trials	Lost	Conv	Bias	Online	Offline	Best	Average
1	50	0	0	0.569	2.622e+01	5.271e+00	2.795e+00	2.622e+01
3	200	0	0	0.617	1.951e+01	2.859e+00	7.049e-01	1.518e+01
7	400	0	0	0.690	1.467e+01	1.633e+00	3.097e-01	7.546e+00
11	600	1	2	0.723	1.146e+01	1.185e+00	2.485e-01	3.514e+00
15	800	2	5	0.742	9.329e+00	9.362e-01	1.861e-01	2.665e+00
19	1000	3	5	0.753	7.860e+00	7.837e-01	1.202e-01	1.791e+00

Figure 8.1 Sample output from GENESIS

output. The top of the listing is the setup information that governs how the simulation will execute. The number of experiments is the number of independent optimizations of the same function. Total trials is the number of (x, y, z) sets (solutions) that will be generated and evaluated for fitness.

The population size is the number of trials in one generation. In this case 50 (x, y, z) triplets between -5.12 and 5.11 will be generated by a random number generator. This will be the zeroth generation. These 50 trials will be mutated where an x, y, or z value will randomly change thus producing a new offspring. Looking down Figure 8.1, a mutation rate of 0.001 means that on average every 1000th bit will be randomly changed. If each gene is 10 bits long, then every 100th gene on average will be changed. For this process all of the chromosomes in a population are viewed as one long string of bits.

The second genetic operator is crossover. Crossover means combining (x_1, y_1, z_1) with (x_2, y_2, z_2) to produce two new offspring that are some combination of these. As an example the crossover operator might produce an offspring of (x_1, y_2, z_1) or it might come up with (x_2, y_2, z_1). The number of chromosomes subject to crossover is determined by the product of crossover rate, population size and gap size. These are parameters set by the user at the beginning of a GENESIS run. Values for crossover rate, population size and gap size from Figure 8.1 are 0.6, 50, and 1.0. This means that 30 chromosomes will be paired together and mated. The offspring then replace their parents in the current population. The current generation now consists of the offspring generated through selection, mutation and crossover.

The structure length is the number of bits in one trial. In the usual genetic lingo this is the number of bits in one chromosome. A structure of thirty in this example means that there are three genes (the genes are the x's, y's and z's) each ten bits long. This allows each of the 10 bit patterns to represent one of the 1024 numbers from -5.12 to 5.11 where the numbers are taken in steps of 0.01.

The scaling window is the number of generations that pass before the scaling of the evaluation function is adjusted. In this case, the evaluation function is adjusted every five generations. The reason for the adjustment is that the fitness values determined by substituting in a particular set of (x, y, z) put pressure on the evolution of good values of x, y and z. If the optimal value of the evaluation function is 0, as it is in this example, and all the (x, y, z)'s are evaluating from 25 to 27 it is hard to distinguish better chromosomes. If we subtract 24 from all values then the range of values is from 1 to 3, a factor of three times from minimum to maximum. This rescaling puts pressure on the chromosomes since the number of offspring selected is based on the value of the evaluation function (when ranking is not selected). A three times better evaluation leads to more offspring for the better parent than a 1.04 times improvement.

The report interval is the number of trials between data collections. In the trials column at the bottom of Figure 8.1, there are 200 trials between times when statistics are printed. The results are always printed after the initial population which in this case is 50 trials.

Structures saved is the number of solutions (trials) to be saved. For this run GENESIS saves the five best solutions. Each unique solution is saved only once. If the best solution is found ten times only the first instance would be recorded. The next four best solutions fill out this table and are stored in a file.

The max generations without an evaluation specifies how many consecutive generations can occur before an evaluation is forced. A dump is a complete listing of all the chromosomes in a population. This allows the simulation to start from that point by using those chromosomes as the initial population in a new run. The dump interval is the number of generations between dumps. A 0 indicates that no dumps occur. Dumps saved are the total number of dumps to be saved.

There are several options available to the GENESIS user that tailor the algorithm for a particular application. The most important for this study are "i" and "R". The i option seeds the initial population with nonrandom chromosomes. For example, to see how (0, 0, 0) was handled select the i option and specify that the initial population contains the triplet (0, 0, 0).

The R option changes how the number of offspring from the parent generation are determined. When the R option is set the evaluation is used to rank the members of the current generation. The number of offspring that a parent produces is determined by its rank not the numeric value of its fitness evaluation. This prevents super strong solutions from dominating future generations and causing premature convergence of the algorithm to a local peak. It also slows the convergence of the algorithm.

The random seed sets the starting point for the random number generator.

The rank min is the minimum expected number of offspring assigned to the solution with the lowest rank. It is only used when the R option is set. The algorithm used in GENESIS is a linear mapping where the worst parent is assigned rank min offspring and the best is assigned (2 - rank min) offspring.

Next are the results of the genetic algorithm run. For this example each generation is made up of 50 trials. Bias is the average percentage of the most prominent value in each position. It is an indication of the overall convergence of the algorithm. The minimum bias is 0.50. In the example a 0.569 bias means that on average each bit position in a gene has converged to 56.9% ones or zeros.

Frequently two other measures of performance, Lost and Conv, are reported. Lost indicates the number of positions in which 100% of the population has the same value. Conv is the number of positions in which at least 95% of the population has the same value.

Online performance is the mean of all evaluations. Offline performance is the mean of the current best evaluations. The Best is the best solution found so far. Average is the average performance of the current population (generation). In the example in Figure 8.1, the average performance of the current population approaches zero with each successive generation. The best solution also gets closer to zero (a major problem if it doesn't). Average performance of each generation is better than the average performance of all trials (Online).

The best solutions are stored in a file called min. Figure 8.2 shows the min file for this example. There is no order to the solutions; the best may occupy any position in the list. The first three columns are the x, y

-0.29	0.19	0.00	0.1202	19	972
0.36	0.14	0.17	0.1781	18	921
-0.30	-0.31	0.00	0.1861	12	617
0.32	0.29	0.00	0.1865	18	902
-0.29	0.30	0.00	0.1741	18	923

and z values that led to the evaluation in the next column. The last two columns are the generation and trial in which this solution was first found.

Figure 8.2 Min file from GENESIS

This section has described how GENESIS is set up. Unfortunately in its present form it does not work for the scheduling problem. The next section describes the modifications that were made to GENESIS.

Modifications to GENESIS

GENESIS works at the bit level. This means that mutation and crossover can occur at any bit within any byte that is in any chromosome. This gives the scheduler a problem if the ground rule is that jobs are only scheduled once. Both operators can easily lead to illegal schedules where one job appears multiple times. In order to perform a genetic search, new crossover and mutation operators need to be found and all of the bit operation routines in GENESIS need to be modified to work at the gene level .

Fortunately, some new crossover operators have been developed. Five crossover operators suitable for scheduling are summarized by (Cleveland & Smith - 1989). They are:

(1) Goldberg's PMX
(2) Grefenstette's Subtour-swap

(3) Grefenstette's Subtour-chunk

(4) Subtour-replace - no reference given so it might be Cleveland & Smith's

(5) Weighted Chunking - again no reference so credit Cleveland & Smith

In Cleveland and Smith's study PMX, Weighted Chunking and Subtour-chunk performed similarly and were effective. Subtour-replace consistently performed poorly. Subtour-swap sometimes did well and sometimes not. The PMX operator was chosen for this study because it is well documented and easy to program.

The following example, showing how PMX works, is taken from (Cleveland & Smith - 1989). Assume there are two parent trials given by:

$$A = 9\ 8\ 4\ 5\ 6\ 7\ 1\ 3\ 2\ 10$$
$$B = 8\ 7\ 1\ 2\ 3\ 10\ 9\ 5\ 4\ 6$$

The PMX operator produces the following offspring:

$$A' = 9\ 8\ 4\ 2\ 3\ 10\ 1\ 6\ 5\ 7$$
$$B' = 8\ 10\ 1\ 5\ 6\ 7\ 9\ 2\ 4\ 3$$

by the following operations.

1. Choose an interval to be swapped. In this example it includes positions four through six.

2. Create a map from the selected interval. In this example, the 5 in solution A maps to the 2 in solution B, the 6 to 3, and the 7 to the 10.

3. Exchange the two intervals.

4. Use the map to alter the new solutions so that they are once again legal. In this example, the 2 in solution A' is replaced by a 5, the 3 by a 6, and the 10 by a 7. Similarly for solution B'.

Cleveland and Smith had some concern that the intervals that were swapped might get modified by the mapping process. They modified the PMX algorithm so that all the positions are changed in parallel. It wasn't exactly clear how they did this. The algorithm used here is:

1. Choose interval to be swapped.

2. Store chromosome A in temporary location.

3. Find position of the gene in chromosome A that matches the gene in chromosome B. For the example, position 9's gene in A matches the gene in position 4 of chromosome B.

4. Swap the two genes in A. 5 and 2 exchange positions.

5. Increment to next gene in segment and repeat steps 3 through 5 until all of the segment in chromosome B is mapped into A.

6. Repeat steps 3 through 5 using chromosome B and the copy of A.

8-13

Following these steps keeps all of the disturbances outside the swapped segments. This algorithm has the appearance of being much simpler than that reported by (Goldberg & Lingle - 1985).

The mutation code in GENESIS was also altered. The standard mutation operator modifies a random bit chosen from a random gene in a random chromosome. This leads to jobs occurring more than once in a schedule (same as a trial or chromosome). The modification to the mutation operator is to swap randomly chosen genes within a randomly chosen chromosome. This keeps each schedule valid while introducing new search spaces to the genetic algorithm.

Crossover and mutation operators take advantage of the fact that the manipulation functions they call return integers that represent genes. GENESIS, though, represents genes as a character string of 1's and 0's that is the binary pattern of a chromosome. That is how GENESIS is able to manipulate chromosomes at the bit level. Two routines were added to GENESIS that the new crossover and mutation routines call that convert the character string for each gene into an integer. These routines are called pack_genes and unpack_genes and are in the convert.c file.

With these changes GENESIS was ready to start building schedules. The nest section describes a simple, if not the simplest, scheduling problem and presents the results of the genetic search for the optimal schedule.

Results of the Genetic Search

First, a simple problem was chosen so that a simple evaluation function could be developed. The problem selected was to sequence a prioritized list of jobs so that the highest priority job is always scheduled next. The evaluation function consists of multiplying a job's priority by its position in the schedule. Ten jobs, whose job number and priority were the same and ranged from 0 to 9, were created. Each job number is considered a gene. A schedule is made up of 10 genes, no job number appearing more than once. A schedule may sometimes be called a chromosome or a trial, depending on the context. A sample schedule is (8 7 1 2 3 0 9 5 4 6); job 8 is first, 7 is second etc. The evaluation function returns the value:

$$f = 0*8 + 1*7 + 2*1 + 3*2 + 4*3 + 5*0 + 6*9 + 7*5 + 8*4 + 9*6$$
$$= 202$$

The best schedule is (0 1 2 3 4 5 6 7 8 9) which evaluates to 285. That is the value the genetic algorithm is trying to reach. The average evaluation for a randomly chosen schedule is 202.5.

8-14

The performance of the genetic algorithm was studied with the R option turned on and off, with the optimal schedule as part of the initial population, with crossover only, with mutation only and with both mutation and crossover. Table 8.1 summarizes the results of those runs. The detailed information on each study is contained in (Cone - 1995).

Study	Online	Offline	Best	Average
Crossover				
R option				
with opt	228.5	285	285	247.0
w/o opt	224.7	270.5	278.3	238.1
w/o R option				
with opt	244.3	285	285	272.6
w/o opt	236.8	271.9	280.4	260.9
Mutation				
R option				
with opt	240.1	285	285	268.6
w/o opt	232.6	259.5	261.4	252.9
w/o R option				
with opt	252.2	285	285	284.3
w/o opt	237.9	260.2	262.9	258.4
Crssvr + Mut				
R option				
with opt	228.7	285	285	246.2
w/o opt	224.7	271.5	278.4	238.9
w/o R option				
with opt	243.1	285	285	270.3
w/o opt	236.9	272.9	281.7	261.6

Table 8.1 Comparison of Genetic Operator Performance

Each run consists of 20 generations of 50 trials each for a total of 1000 trials. A study is the average from repeating each run 25 times with a new randomly drawn initial population. Crossover rate equaled 0.6, mutation rate equaled 0.001, and the generation gap was 1.0 for all runs except where noted.

The Study column is interpreted as follows. The first row of numbers contains the results for the crossover operator as the only operator used, the R option set which slows the convergence of the genetic

algorithm in order to prevent premature convergence to a local maximum, and the initial population containing the optimal schedule. As another example, the third row of numbers from the bottom is the study where both crossover and mutation operators were used, the ranking option was set, and the initial population is determined by a random number generator (no optimal schedule intentionally placed in initial population).

The next four columns report average results of 25 experiments. Online is the average evaluation of Online taken from the 25 runs. Offline, Best, and Average are similarly averaged over the 25 run that constitute a study.

As expected when the optimal schedule is included in the initial population the genetic algorithm finds it and retains it for the search (see cells Best with opt). While this is not impressive by itself it shows that deterministic schedules can be integrated into the initial population and the genetic algorithm search for better solutions.

The Best runs without the optimal schedule included in the initial population show the ability of the genetic algorithm to find the best schedule from a blind start. There are 10! possible schedules. Crossover and crossover + mutation found a solution that was over 97% of the optimal evaluation by searching less than 0.03% of the possible solutions. Mutation came within 91.7% of the optimal evaluation.

The R option does not make much difference in the ability of the algorithm to find the best solutions. Generally the best evaluations come within 1% of each other. Comparing similar runs that only differ by whether the R option is used or not, the Online averages are lower when the R option is chosen. This is expected since the R option slows convergence of the algorithm.

Mutation means exchanging jobs within one schedule. The higher the mutation rate, the more stirring of schedules thus increasing the likelihood of finding a good schedule. On the other hand, too much stirring breaks up good schedules preventing convergence of the population as a whole to good solutions. Table 8.2 shows the effect of changing the mutation rate on the genetic algorithm when crossover is disabled, R option is selected, and the optimal solution is not in the initial population.

Mutation Rate	Online	Offline	Best	Average
0.001	232.6	259.5	261.4	252.9
0.01	231.1	264.8	271.5	249.8
0.1	218.0	271.7	277.1	222.6
0.9	203.9	270.5	274.9	204.1
1.0	204.2	270.6	274.6	203.6

Table 8.2 Effect of Changing Mutation Rates

Since the Best value is lower for the 0.001 rate compared to the other rates, the 0.001 mutation rate doesn't create enough mixing in the schedules to search a very large solution space. The other rates do a better job of finding a good schedule. If the average evaluation for all schedules (Online) and last generation (Average) are considered, 0.001 and 0.01 are better rates. For this problem finding the best schedule is the goal. The scheduler does not care about the population averages, thus a mutation rate of 0.1 would seem to be a good choice. A mutation rate of 0.1 means that on average every 10th gene (job) gets swapped. Since there are 10 genes in a chromosome (10 jobs in a schedule), the 0.1 mutation rate makes one change, on average, in each chromosome (schedule) in a population. As the mutation rate approaches 1.0 every gene is swapped. This amounts to a random shuffle of each schedule in a generation. This is equivalent to drawing a new random population in each generation. The Online and Average values for a 1.0 mutation rate are approximately the value of a random draw, 202.5.

There is an inverse relationship between the Best and Average values. Higher Average values yield lower Best values. The Average is as a measure of the randomizing of the schedules. The closer an average value is to 202.5, the more random is the schedule. What is interesting is that the better Best values come with more mixing. At first thought it seems contrary that the better Best values come from a lower population average but the fact is more mixing produces more opportunity for the exceptional values to be discovered.

Finally, can any of the statistics be used as measures of performance of the genetic algorithm? For low mutation rates the Best value shows a rapid increase but for higher rates it loses its sensitivity. On the other hand, when the Best values start to saturate the Average value sees big changes. This suggests that an adaptive genetic algorithm could be developed that watches the Best and Average values. When the Best is rapidly improving and the Average is changing little then more randomizing of the population is called for. When the Best saturates and Average is falling then there is too much mixing and the rates should be reduced. This technique should speed convergence of the algorithm.

Does these trends hold true for Crossover? A higher crossover rate means that more chromosomes are

Crossover rate	Online	Offline	Best	Average
0.2	231.1	268.5	276.0	252.1
0.4	227.9	272.0	278.4	245.8
0.6	224.7	270.5	278.3	238.1
0.8	223.2	272.1	279.3	234.9
1.0	222.0	272.3	279.6	232.2

Table 8.3 Effect of Changing Crossover Rates

experiencing crossover thus the lower Average value and the higher Best values. Table 8.3 lists the results for a range of crossover rates. The pattern is the same as for mutation.

Next consider graphs of the convergence of the algorithm. Graph 8.1 shows the

Graph 8.1 Best Schedule for Each Generation, R Option, No Optimal Schedule
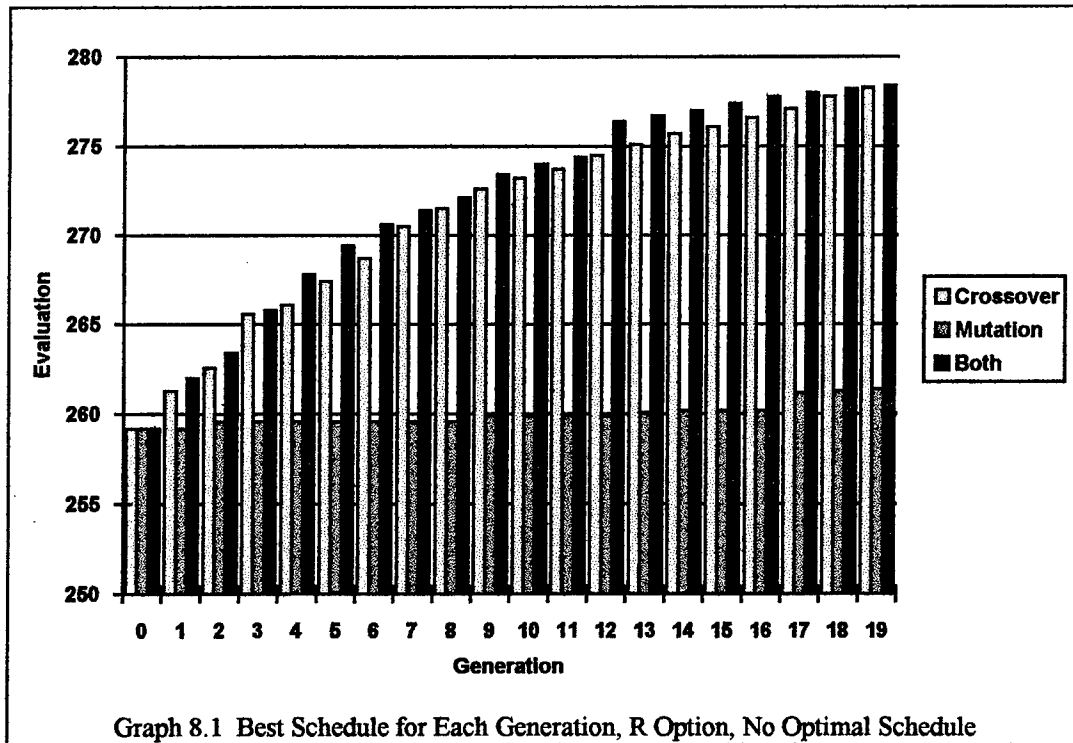
evolution of the best schedule each operator was able to find for the R option set without the optimal schedule in the initial population. Notice that the mutation operator was unable to improve on the original choice. Crossover and Both operators performed similarly but Both improved slightly sooner than crossover.

8-18

Graph 8.2 shows the same information as Graph 8.1 except that the Average evaluation for each generation is plotted instead of the Best evaluation. Mutation dominates Crossover and Both. While Crossover and Both do a better job of finding the best solutions, Mutation does a better job of raising the performance of the average schedule. Another way to explain this phenomena is that the slow rate of mixing with mutation only lets a few members of a generation dominate. They may not be super

Graph 8.2 Average Schedule for Each Generation, R Set, No Optimal Schedule
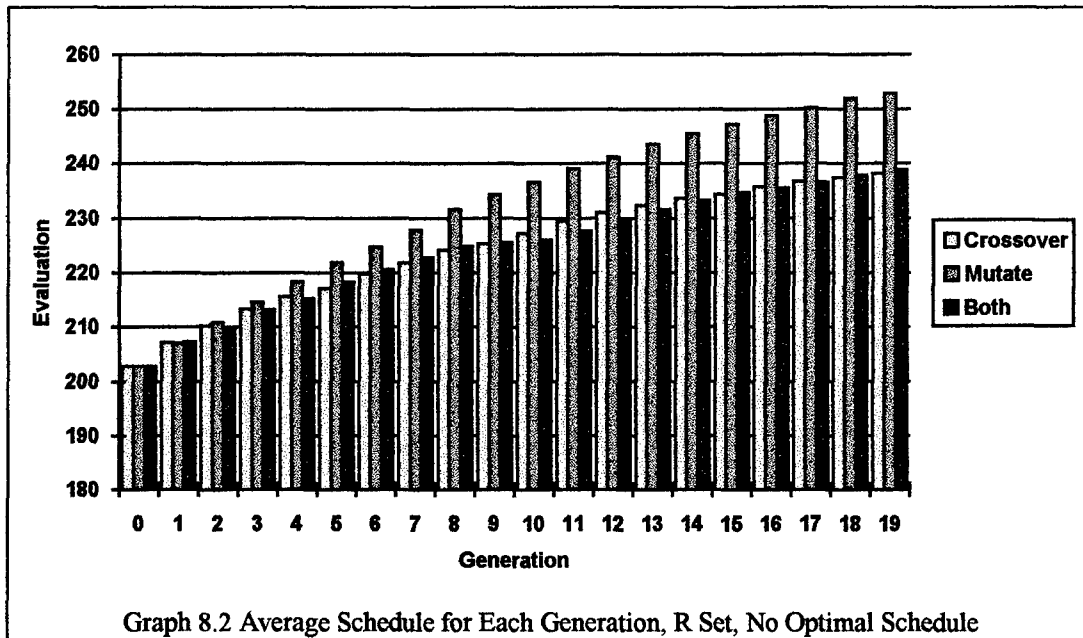
schedules but there is so little mixing the genetic algorithm is left searching in the area around those less than sterling schedules.

Mutation is like a fine tuning operator. It causes less disruption in the better schedules thus letting a larger number of schedules improve while not destroying the best schedules. Crossover on the other hand can cause large disruptions in a schedule. This is good early in the scheduling process, when the genetic algorithm needs to search in many widely separated areas, but towards the end this operator holds back the average performance of a generation. Graph 8.2 shows the effect. Average performance of the Crossover operator does not get to the level of Mutation. Still, the best performing schedules are more likely to come from Crossover or Both.

Future Work

With the foundations laid for an understanding of how genetic algorithms work, the next step is to make the problem more realistic. There are several examples from the job-shop scheduling literature (Cleveland & Smith - 1989) that are very similar to the scheduling problem faced by the sensor manager.

8-19

The next task is getting a working program that can solve these problems and studying the genetic algorithm's performance. This will include seeding the initial population with schedules derived by deterministic algorithms to find out if the genetic algorithm can integrate those schedules into its population and whether that improves the genetic algorithm's ability to build good schedules.

References

S. Bagchi, S. Uckum, Y. Miyabe, & K. Kawamura (1991). Exploring problem-specific recombination operators for job shop scheduling. In L. Booker (ed) *Proceedings of the Fourth International Conference on Genetic Algorithms*, pages 10-17. San Mateo: Morgan Kaufman, 1991.

S. Baruah, G. Koren, D. Mao, B. Mishra, A Raghunathan, L. Rosier, D. Shasha, & F. Wang (1991). On competitiveness of on-line real-time task scheduling. *Proceedings Twelfth Real-Time Systems Symposium*, pages 106-114. Los Alamitos, CA: IEEE Computer Society Press, 1991.

G. A. Cleveland & S. F. Smith (1989). Using genetic algorithms to schedule flow shop releases. In J. Shaffer (ed) *Proceedings of the Third International Conference on Genetic Algorithms*, pages 160-169. San Mateo: Morgan Kaufman, 1989.

M. L. Cone (1995). RDL week 8 report. Internal report available from author, 1995.

M. R. Gary & D. S. Johnson (1979). *Computers and Intractability: a Guide to the Theory of NP-Completeness.* Freeman, 1979.

D. E. Goldberg & R. Lingle Jr. (1985). Alleles, loci, and the traveling salesman problem. In J. Grefenstette (ed) *Proceedings of the First International Conference on Genetic Algorithms and their Applications*, pages 154-159. Hillsdale, NJ: Lawrence Erlbaum Associates, Publishers, 1985.

S. C. Graves (1981). A review of production scheduling. *Operations Research*, vol. 29, no. 4, Jul-Aug 1981.

J. J. Grefenstette, L. Davis, & D. Cerys (1991). *GENESIS and OOGA: Two Genetic Algorithm Systems.* TSP, Melrose MA, 1991.

A. K. Mok (1983). Fundamental design problems of distributed systems for a hard real-time system. PhD dissertation, Dept. of Electrical Engineering and Computer Science, MIT, Cambridge, MA, May 1983.

S. Musick & R. Malhotra (1994). Chasing the elusive sensor manager. *Proceedings of the NAECON, May 1994.* Dayton, Ohio, 1994.

J. A. Stankovic, M. Spuri, M. Di Natale, & G. C. Buttazzo (1995). Implications of classical scheduling results for real-time systems. *Computer*, Jun 1995.

Associate did not participate in program.

NON-CONVERGENCE OF STREAMLINE CURVATURE
FLOW ANALYSIS PROCEDURES

Stephen F. Davis

Associate Professor

Department of Mathematics and Statistics

P.O. Drawer MA

Mississippi State University

Mississippi State, MS 39762

NON-CONVERGENCE OF STREAMLINE CURVATURE
FLOW ANALYSIS PROCEDURES

Stephen F. Davis

Associate Professor

Department of Mathematics and Statistics

Mississippi State University

Abstract

The axial compressor aerodynamics computer program UD0300 sometimes fails to compute the performance of high throughflow, transonic compressor stages. This report describes efforts to determine the cause of this failure. These efforts primarily consist of numerical studies of special cases because the algorithm is too complex to study analytically. These studies indicate that, if an unconverged iterate cannot satisfy the continuity constraint, the iteration algorithm used in the code may not be able to find a solution that satisfies this constraint. Preliminary attempts to modify the algorithm are described and suggestions for additional work proposed.

NON-CONVERGENCE OF STREAMLINE CURVATURE
FLOW ANALYSIS PROCEDURES

Stephen F. Davis

Introduction

Streamline curvature throughflow computer programs have been used for more than twenty years to study axial flow compressors. Despite the advances made in computational fluid mechanics since that time, these programs are still heavily used because of their versatility and efficiency. Such programs usually have options which permit them to design compressors, analyze the performance of compressors or process experimental data. Since these programs take only minutes of computer time on modern workstations, engineers can easily vary parameters for design optimization or compute a compressor map in a very short time. The computer program UD0300, which is considered here, allows computing stations to be placed within blade rows. This provides the information needed to use sophisticated shock loss models with supersonic stages.

The axial compressor design program UD0300 operates in two modes. In both cases, the user specifies the desired mass flow, the annular geometry, the wheel speed and the locations of the blades. For the design mode, the user also specifies the work distribution through the machine. The computer program calculates the velocity distribution and uses it to compute blade angles. For the analysis mode, the inverse problem is solved. Blade angles are specified, the velocity distribution is calculated and the results are used to determine the performance of the machine.

For high throughflow, transonic fan stages, the design mode has no difficulty producing a set of blades for a machine that meets the specified work distribution. However, when these blades are entered into the analysis mode of the program, the program is unable to compute a converged solution. This means that the program is unable to analyze its own design. The purpose of this project is to determine why this is happening and what can be done about it.

The first step is to look for an error in the program. A careful check of the equations, how

they are approximated and how they are coded turns up no errors. This is expected because the computer program has been used for design and analysis of turbomachines for many years. The difficulty indicates that the new problems are too difficult for the old algorithms. The next step is to study these algorithms.

Overall Algorithm

The way that the computer code operates is as follows. In the beginning, the intersection of each streamline with each computing station is estimated along with the velocity vector at each of these points. At each pass, the intersections are held fixed and velocity vectors which satisfy conservation of momentum and mass are computed. Based on this velocity distribution, the intersections are changed so that a specified percentage of the mass flows between each pair of streamlines. For a successful calculation, this process is continued until both velocity changes and streamline location changes become smaller than some specified tolerance. A converged set of streamline coordinate values and velocity vectors is a solution to the problem.

To describe the velocity update in more detail, we note that the momentum equation is formulated as a differential equation for the distribution of meridional velocity along a computing station. The mass flow corresponding to any velocity distribution is computed by evaluating an integral along the computing station. Thus, to update the velocities at a station, the momentum equation is integrated from an estimated initial value and this velocity distribution is used to compute the mass flow at the station. If the mass flow does not match the specified mass flow, the initial velocity value is changed and a new velocity distribution is computed. Any scalar root finding method can be used to determine the next estimate for the initial velocity. This process is repeated until the mass flow matches the specified value to within some specified tolerance.

Once a converged solution is obtained at a station, the streamline intersection points are updated so that a specified fraction of the mass flows between each pair of streamlines. This is accomplished by interpolating a plot of cumulative mass flow fraction (the fraction of mass flow between the hub and the radius) vs. radius. Since this process is unstable, the changes in the streamline locations are underrelaxed. This process is analyzed in detail in the classic paper by Wilkinson [4]. Note, for later reference, that this analysis derives the relaxation factor for the streamline intersections under the assumption that the velocity distribution satisfies the

continuity constraint.

The process described above is repeated at each station to complete a pass. Convergence means that the changes in streamline locations and velocities are within a specified tolerance between successive passes. More details can be found in the UD0300 users manual [2] and the paper by Novak [3]. Below, each part of this algorithm is studied in turn to determine whether or not it contributes to the failure of the method.

Momentum Equation

In the current code, different forms of the momentum equation are used in design and analysis modes. Furthermore, each of these equations is integrated using different numerical integration methods.

To determine whether or not the two forms of the momentum equation are consistent with each other, both equations are integrated using the same numerical method. The initial velocity and the other data required to evaluate the terms in each momentum equation are taken from a converged design mode solution. Both solutions are virtually identical when plotted on the same graph.

To determine how much the different integration schemes change the solution, each momentum equation is integrated using the numerical method from the current code. The initial velocity and other data are the same as from the previous paragraph. Since all of the numerical methods considered are second order accurate, the differences between solutions are very small, as expected. However, some differences could be seen when the solutions are plotted on the same graph. To simplify the programming slightly, we replace both integration schemes by a single different scheme. The new scheme is a modified Newton predictor-corrector method. This change did not significantly change the performance of the code. We do not replace both forms of the equation by a single form, although this is not difficult to do and it has been done in other programs. We may do this in the future.

Momentum/Continuity Iteration

The present code uses a hybrid Newton-bisection method to carry out the mass flow iteration. The way this works is that Newton's method is used if the slope of the mass flow vs. initial

10 - 5

velocity curve matches the desired solution type (i.e. positive slope for a subsonic solution and negative slope for a supersonic solution). If the slope does not match, the initial velocity is moved in a direction that would put it onto the desired branch of the curve. The bisection part of the algorithm enters in that the program checks if any new iterate which does not satisfy the continuity constraint is larger than the maximum previous iterate that gave a subsonic solution or is less than the minimum previous iterate that gave a supersonic solution. If one of these conditions is satisfied, the appropriate bound is changed. On the other hand, if a Newton step makes the new initial velocity less than the saved maximum velocity for a subsonic solution or greater than the saved minimum velocity for a supersonic solution, the new initial velocity is taken to be half the distance between the previous iterate and the bound that was exceeded. If a solution exists, this algorithm converges to it. If the solution doesn't exist, this algorithm converges to a velocity that is very close to the velocity that corresponds to the maximum mass flow.

To simplify the programming and to better visualize the behavior of the solution near the point of maximum mass flow, we replace the present mass flow iteration with Muller's method. The idea of Muller's method is to fit a quadratic to three unconverged initial velocity vs. mass flow points. The next estimate for the initial velocity is one of the values where the quadratic is equal to the desired mass flow, if such a point exists. Which value is chosen depends on whether a subsonic or supersonic solution is desired. If no such point exists, the point of maximum flow is chosen. The mass flow corresponding to the new initial velocity value is computed and a new iteration is started by fitting a new quadratic to the new mass flow and two previous mass flow values. The process is continued until the new mass flow value matches the specified mass flow to within some tolerance or some specified number of iterations is performed. If the solution doesn't exist, the final velocity is very close to the velocity corresponding to maximum mass flow. Since two velocity values correspond to a given mass flow near the point of maximum mass flow, a quadratic is a better approximation to the behavior of the solution in this region than the linear approximation generated by Newton's method. Details of Muller's method can be found in many Numerical Analysis texts e.g. [1].

The program computes a converged solution in all test cases where the mass flow condition can be satisfied at all passes and all stations. If, at some pass, the mass flow condition is not satisfied at a station, the program may recover and eventually compute a converged solution but more

often the calculation eventually fails. This seems to be particularly true when the failed station is within a rotor. In this case, the velocity distribution corresponding to a reduced flow is used in the next pass to move the intersection points and to generate the coefficients in the momentum equation. Under these circumstances, it is observed that the maximum mass flow decreases in each subsequent pass and eventually the calculation fails when negative static enthalpy is generated.

At this time, we are unable to explain this phenomenon or propose a remedy. Some conjectures and possible approaches are discussed at the end of this report.

Continuity Equation

To further compare design and analysis computations, the results from the momentum calculations are used to compute the mass flow. The initial velocity and other data required to solve the momentum equations are taken from a converged design mode solution. These calculations are repeated twice more, once with the initial velocity increased by ten percent and once with the initial velocity decreased by the same amount. All other data is unchanged.

Figures 1,2 and 3 show the results of the design calculation. Note that the general shape of the meridional velocity profile and the meridional momentum profile remain the same as the initial velocity is changed. Note also that the mass flow distribution changes very little. This implies that the streamline locations remain essentially converged for velocity distributions near the exact velocity distribution. A momentum/continuity iteration from a perturbed initial velocity converged in one or two steps.

By contrast, figures 4,5 and 6 show that each distribution changes significantly when the initial velocity is changed. In particular, the meridional momentum increases at the hub and decreases at the tip when the initial velocity is increased and decreases at the hub and increases at the tip when the initial velocity is decreased. As a result, the mass flow distribution changes significantly. This could lead to large changes in the streamline positions. This was not examined in this case but should be examined in the future. Instead a momentum/continuity iteration was carried out from each of the perturbed initial velocities with fixed streamline positions. These iterations converged in seven to ten steps.

Figure 7 is the most revealing. It shows the computed mass flow plotted against initial velocity for both the design and analysis computations. Note that, in the design case, the mass

flow increases monotonically with initial velocity. By contrast, in the analysis case, the mass flow varies very little with initial velocity and appears to have a local maximum near the design point. This behavior is explained by the following analysis.

In both the design and analysis modes, the mass flow is computed by evaluating the integral

$$W = \int_{l_{hub}}^{l_{tip}} dW$$

(1)

$$= \int_{l_{hub}}^{l_{tip}} \rho V_m \cos(\phi + \delta) 2\pi r (\lambda - B) dl$$

where λ and B are blockage factors and $\delta = dl/dr$. Where the two cases differ is in how they determine V_m and ρ. The different equations used to evaluate V_m were discussed above. Here we examine the different density calculations and how they affect the mass flow.

For a perfect gas, if losses are neglected, the density in the design case and in regions without blades is given by

$$\rho = \rho_0 \left(1 - \frac{\gamma - 1}{2} \frac{(V_m^2 + V_\theta^2)}{\gamma R T_0}\right)^{\frac{1}{\gamma - 1}}$$

(2)

where the total density ρ_0 and total temperature T_0 are constant and the absolute tangential velocity V_θ is specified. If this is substituted into equation (1) and the resulting equation differentiated with respect to V_m, the result is

$$\frac{dW}{dV_m} = \int_{l_{hub}}^{l_{tip}} \frac{1 - M_m^2}{V_m} dW$$

(3)

This equation shows that as long as the meridional velocity profile at a station is entirely subsonic or entirely supersonic at the desired mass flow, the velocity profile can be adjusted to match this flow. Since most compressors are designed with subsonic meridional velocities, the design calculations should proceed without difficulty. This is what happened in the test cases considered here.

Within a blade row, for a perfect gas, if losses are neglected, the density is

$$\rho = \rho_{0r} \left(1 - \frac{\gamma - 1}{2} \frac{(V_m^2(1 + \tan^2 \beta))}{\gamma R T_{0r}}\right)^{\frac{1}{\gamma - 1}}$$

(4)

where the relative total density ρ_{0r} and relative total temperature T_{0r} are constant and the relative flow angle β is specified. Substitute this into equation (1) and differentiate with respect to V_m to get

$$\frac{dW}{dV_m} = \int_{l_{hub}}^{l_{tip}} \frac{1 - M_r^2}{V_m} dW$$

(5)

10 - 8

This equation shows that, if the mass flow has a maximum in analysis mode, it occurs at a station with both subsonic and supersonic relative velocities. The test cases considered here had two such stations within the rotor. The design calculation showed that, at convergence, neither of these stations was choked but, in analysis mode, an unconverged solution would choke at one of these stations and the code would not converge.

Attempts

Although the problem has been identified, more information is needed before a robust solution can be found. Since there was not enough time in the summer to carry out these systematic studies, we tried various random ideas that were easy to implement and hoped to get lucky. Unfortunately, this did not happen. We record some of these attempts here for future reference.

1. Since it is possible to obtain a converged solution with a reduced mass flow, attempts were made to approach a solution by incrementing the mass flow. At each step, the converged streamlines from the previous calculation were used to start a new calculation with an increased mass flow. This approach allowed converged solutions at higher mass flows than what could be computed using the design streamlines but it could not compute a converged solution at the design mass flow. Even very small mass flow increments eventually failed.

2. Since the program failed when solutions to the momentum equation failed to satisfy the mass flow constraint, attempts were made to adjust parameters in the momentum equation so that the solution would produce an increased mass flow. Among the parameters that were adjusted were the wheel speed and the flow angle. Unfortunately, there is no theory that determines how much adjustment is needed and it is not possible to obtain sufficiently predictable control by trial and error. If some analysis can be found to guide the control process, this approach may eventually succeed.

3. Wilkinson's [4] analysis shows that convergence is slowed when computing stations are close together. Because of this, it was possible to obtain a converged solution in analysis mode at the design mass flow when two computing stations were removed from inside the rotor. Although the stations that were removed were those at which previous calculations failed, it was still necessary to increment the mass flow to obtain a converged solution. This suggests

that it might be possible to obtain a solution to a desired problem by adding stations to converged coarse grid problems. This would require a major restructuring of the input data in the present code and is probably not practical.

Conclusions and Suggestions

This study shows that the streamline curvature code UD0300 fails in analysis mode within transonic blade rows when an unconverged solution chokes. The present algorithm is not able to recover from this choking condition and compute a converged solution. Follow-on efforts should determine, in detail, how the unconverged solution behaves at failure and determine how the algorithm can be modified to either avoid the choking situation or recover from it. Below is an outline of a proposal for such a study.

1. The streamline curvature code UD0300 is a production code. This means that it contains options that permit it to solve very complex problems. As a result, the input data and output results are both long and involved. It is not easy to modify this code because a modification may inadvertently destroy a desired capability. It is also difficult to query intermediate results without generating huge output files. The normal results printed out by the code relate to the performance of the compressor rather than the performance of the algorithm. They do not provide sufficient diagnostics to determine what the algorithm is doing. Overall, this is too much code for an algorithm study.

   In the present study, parts of the code were run independently using dummy drivers and dummy data. This proved to be a useful way to compare the two momentum/continuity iterations but it was not possible to simulate the behavior of the entire algorithm.

   For the follow-on study, the streamline curvature algorithm should be implemented on a simple problem such as a converging-diverging duct. This problem should cause the method to fail and should give a clear picture of the failure mechanism. Because of its limited applicability, such a computer program should be easy to write, easy to change and require very little input data. Detailed algorithm diagnostics and intermediate results could be generated without creating huge files.

2. The momentum equation simplifies considerably for the duct flow problem. With some guidance from numerical results, the iteration might be simplified to the point where an analysis of the choked case might be possible.

3. Modifications to the present algorithm need to be studied both experimentally and theoretically. Two approaches that might show promise are the following.

    (a) Modify the velocity profile when choking occurs. Work is needed to show how much modification is required to satisfy continuity and what kind of modification moves the streamlines closer to convergence.

    (b) Modify the streamline shift algorithm when the flow is choked. The current algorithm does not work. It is necessary to determine what the current algorithm does and how to change it.

References

[1] N.S. Asaithambi, *Numerical Analysis, Theory and Practice*, Saunders College Publishing, (1995).

[2] C.H. Law and S.L. Puterbaugh, *A Computer Program for Axial Compressor Design (UD0300M)*, AFWAL-TR-82-2074, (1982).

[3] R.A. Novak, Flow field and performance map computation for axial-flow compressors and turbines, in *Modern Prediction Methods for Turbomachine Performance*, AGARD-LS-83, (1976).

[4] D.M. Wilkinson, Stability, convergence and accuracy of two dimensional streamline curvature methods using quasi-orthogonals, *Proc. I. Mech. Engrs.* , **184**, Part 3G(I), 108-119, (1969-1970).
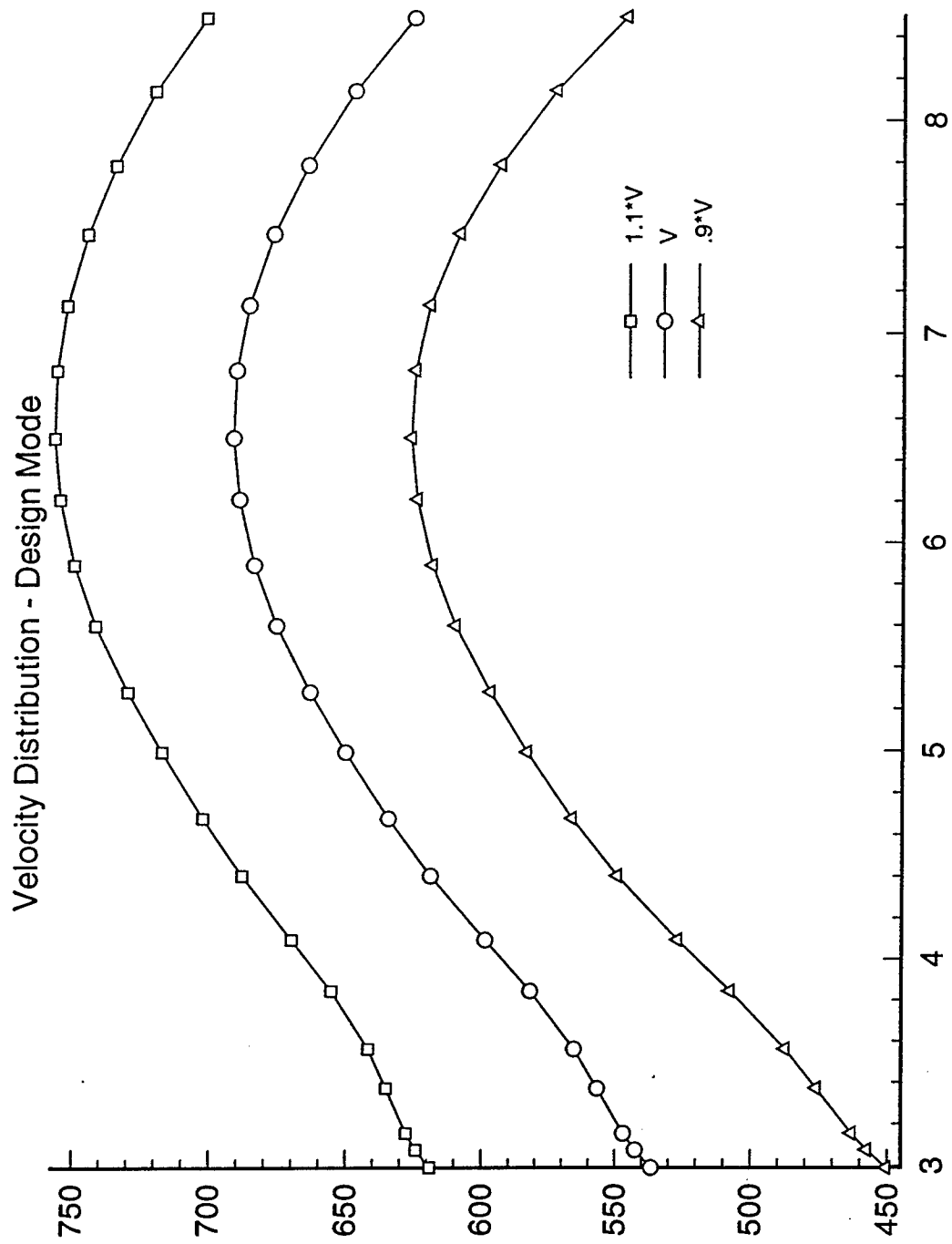
Figure 1. Velocity distribution *vs.* radius using design mode momentum equation
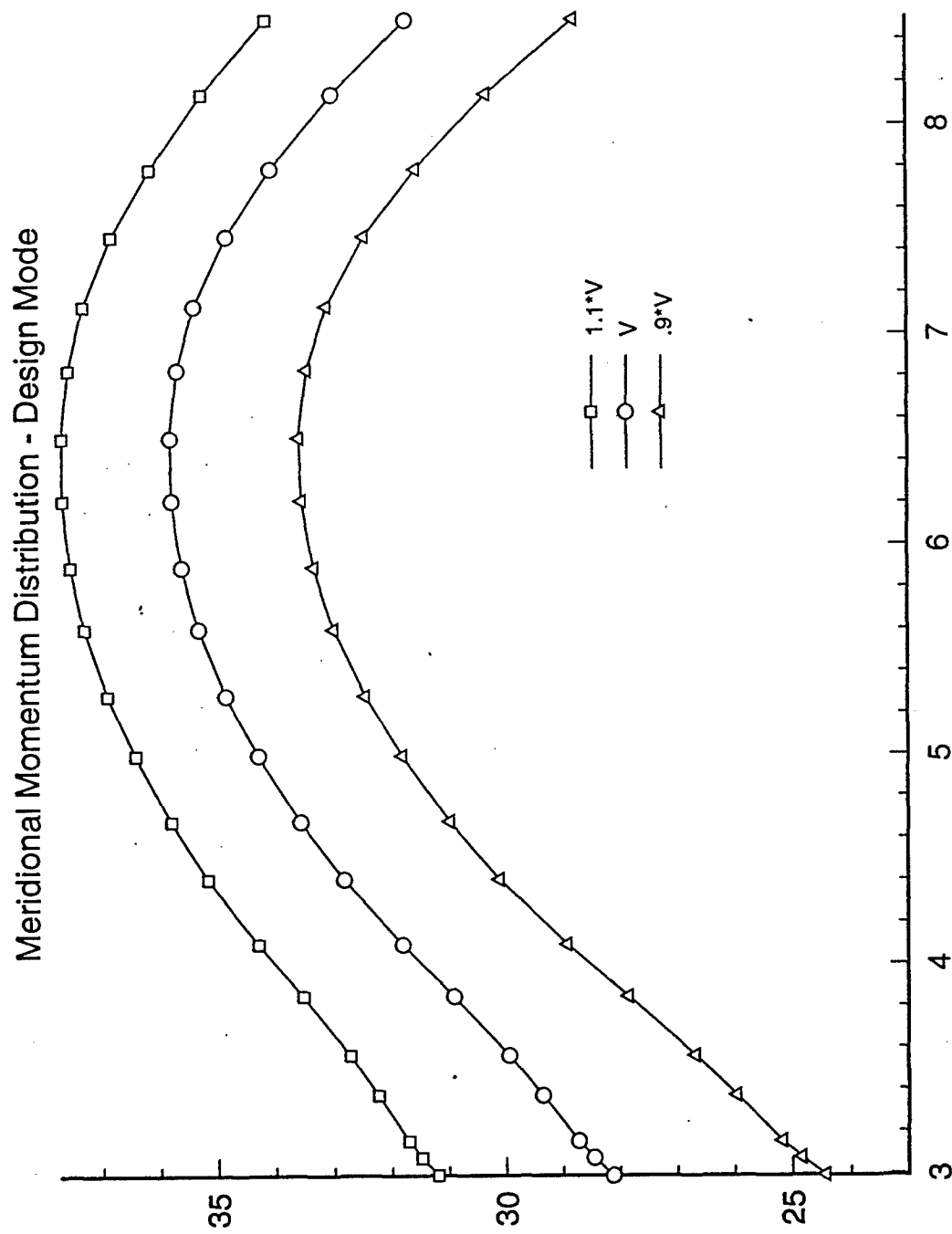
Figure 2. Momentum distribution vs. radius using design mode momentum equation, and specified tangential velocity and total enthalpy.
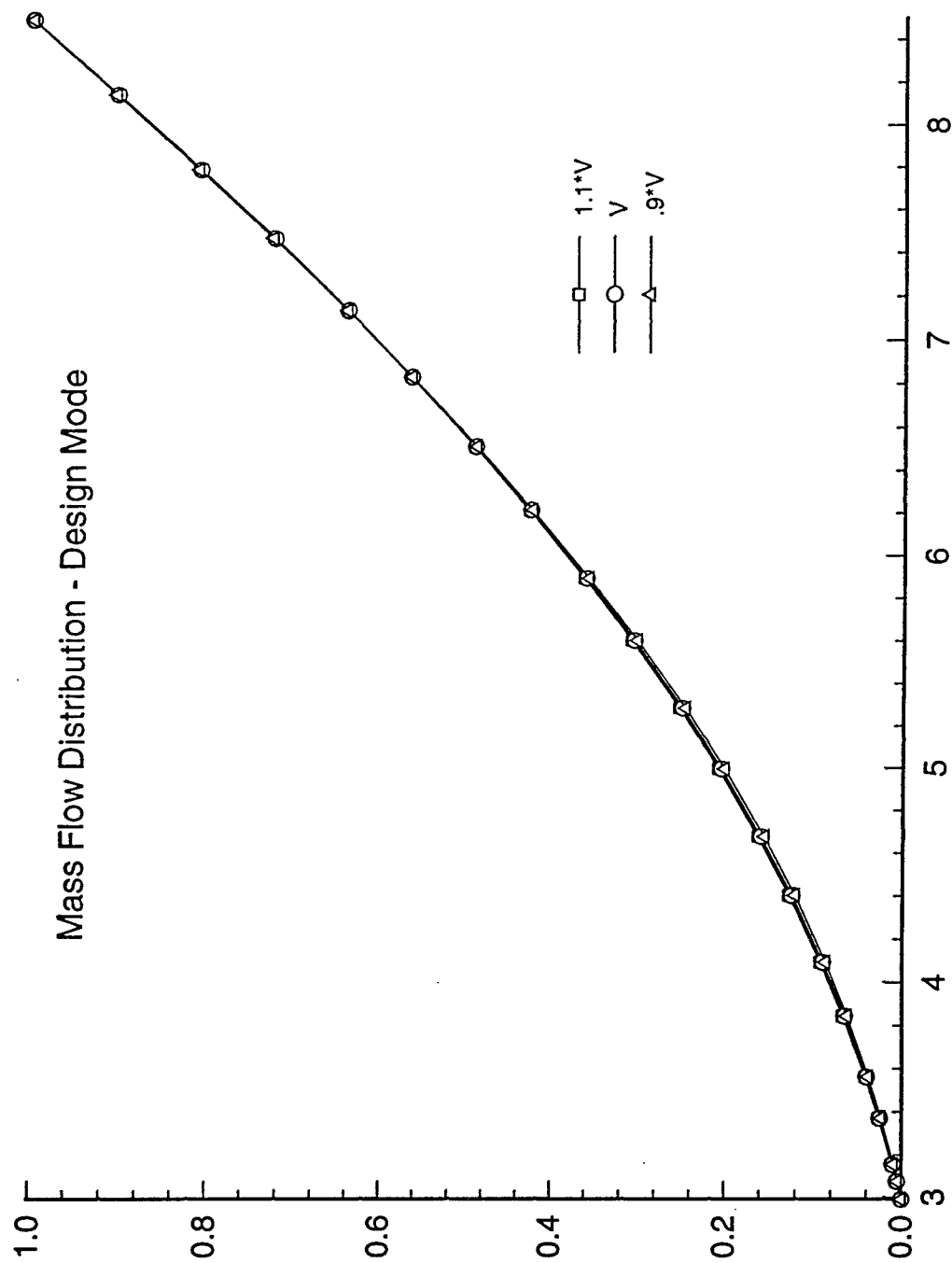
Figure 3. Mass flow distribution *vs.* radius using design mode momentum and continuity equations

Velocity Distribution - Analysis Mode
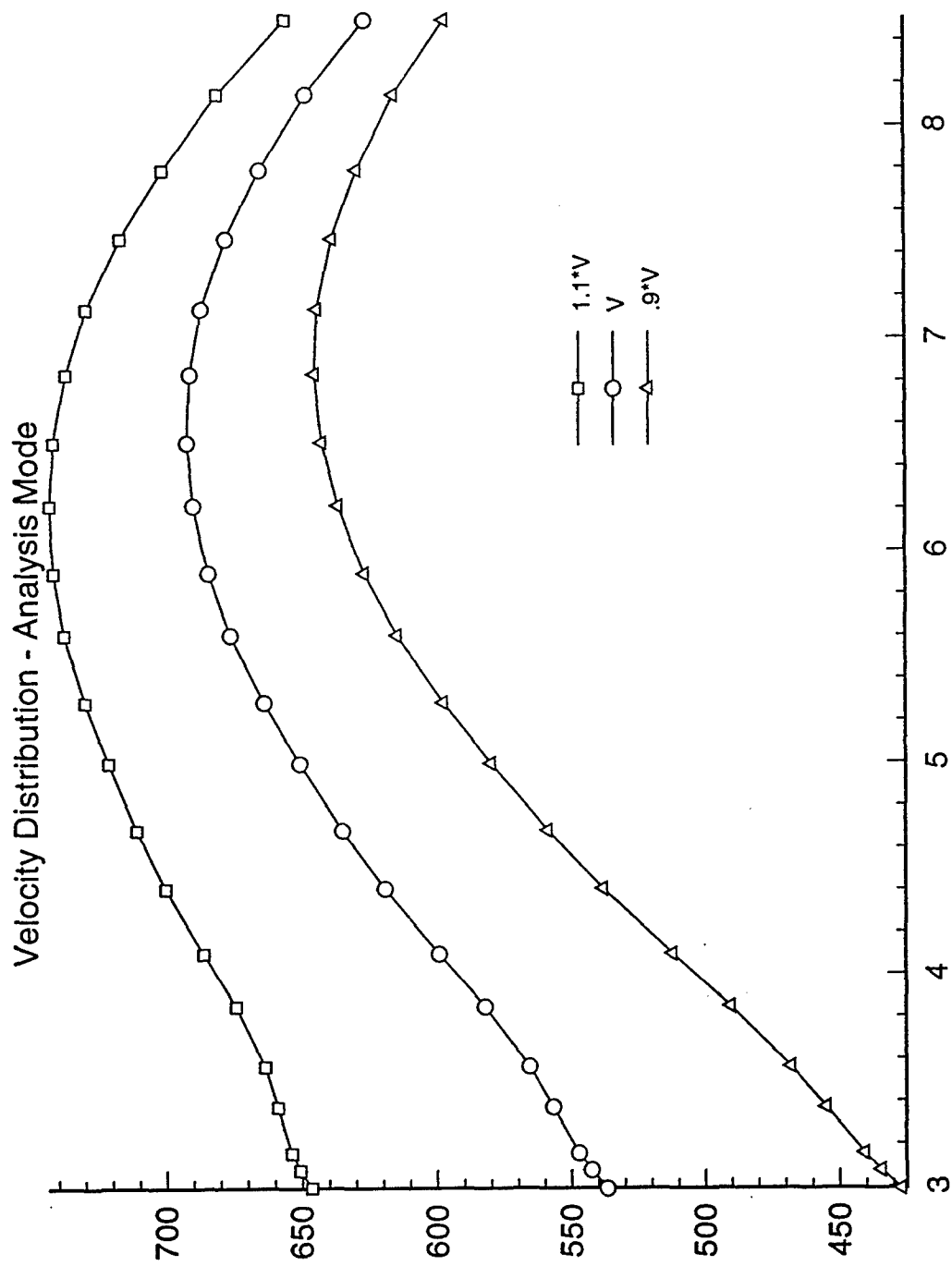
Figure 4. Velocity distribution *vs.* radius using analysis mode momentum equation
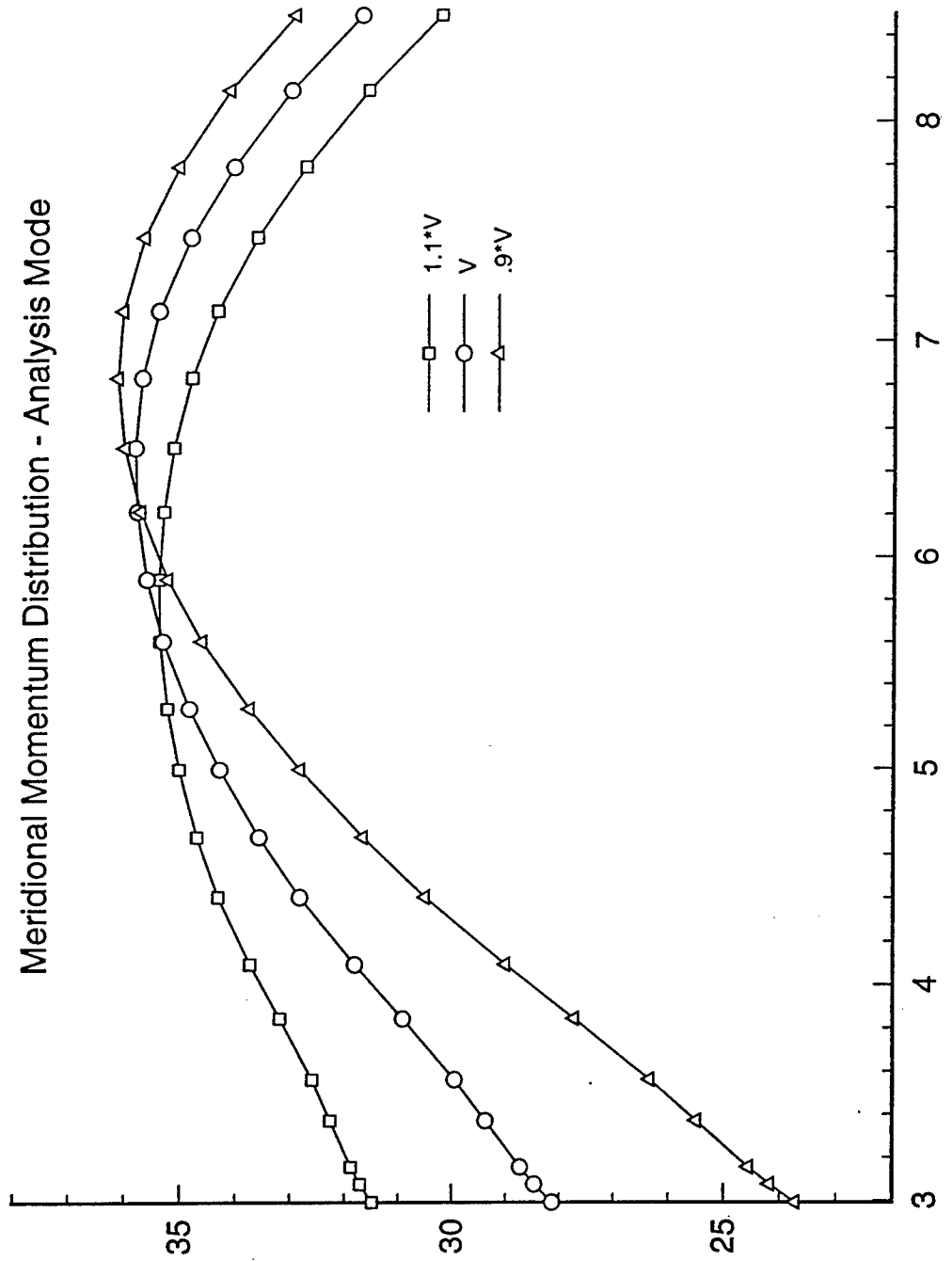
Figure 5. Momentum distribution vs. radius using analysis mode momentum equation, specified flow angle and constant rothalpy
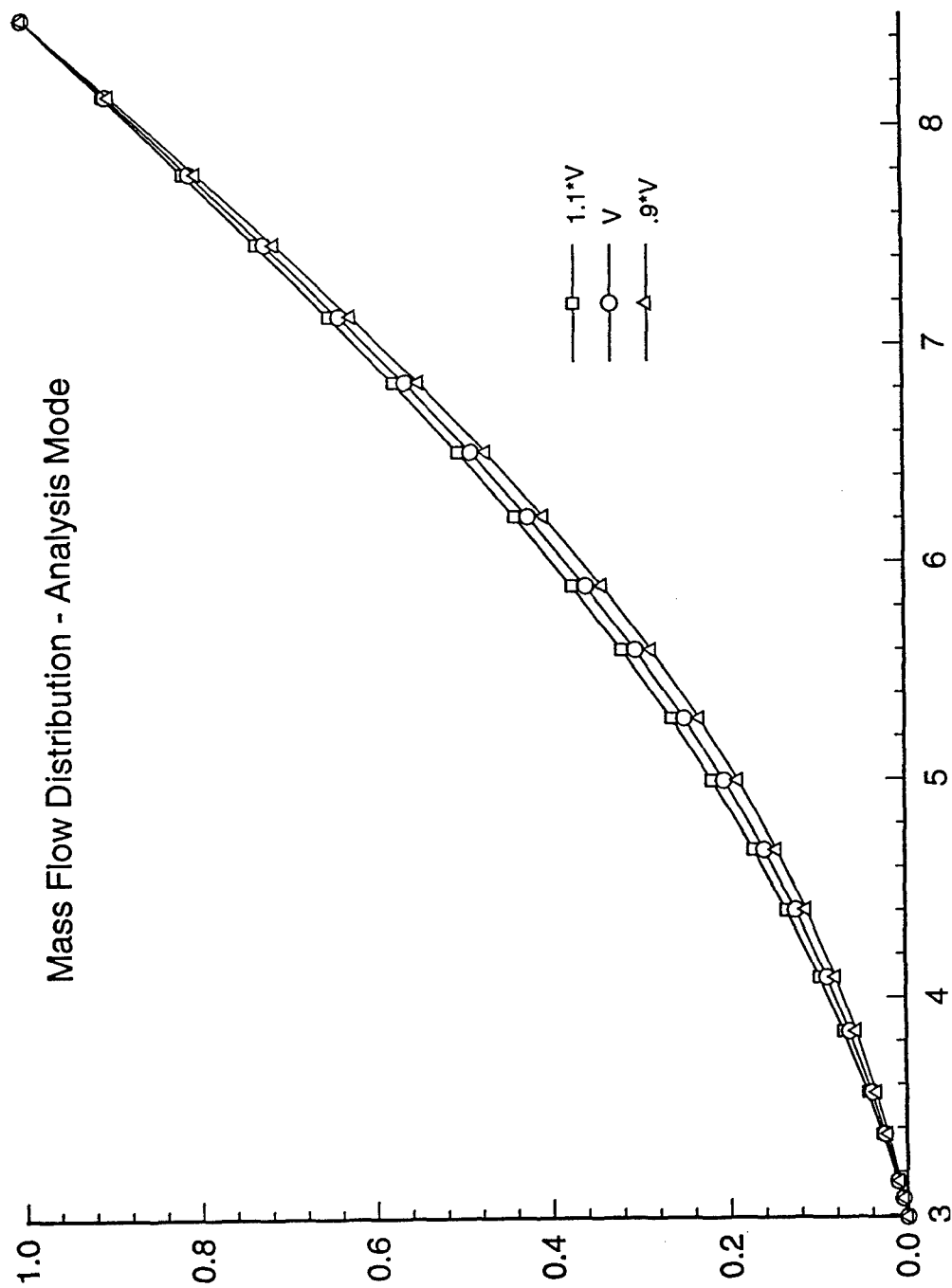
Figure 6. Mass flow distribution vs. radius using analysis mode momentum and continuity equations
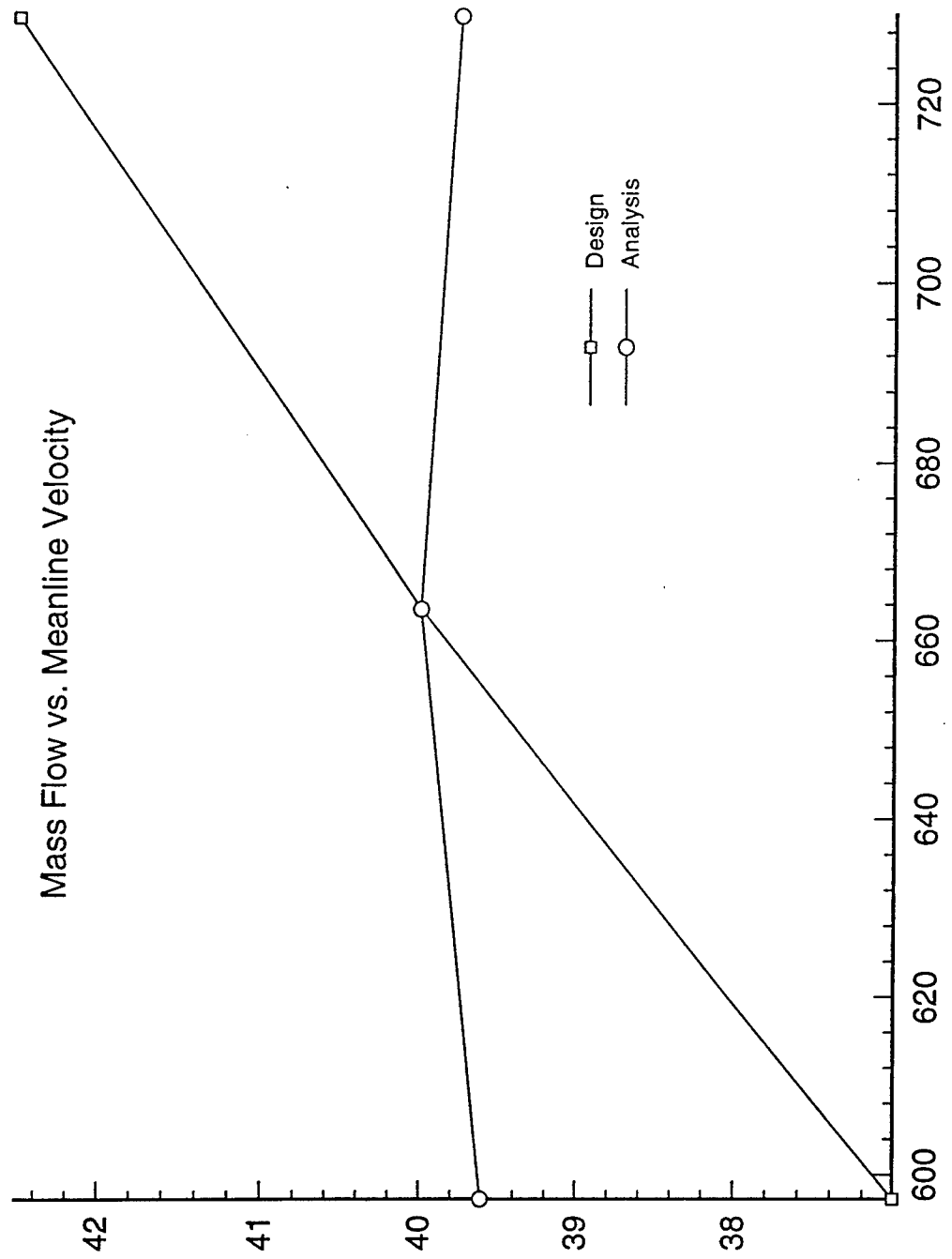
Figure 7. Mass flow vs. meanline velocity, design and analysis modes.

THE SIMULATION OF X-RAY POLE FIGURES
AND
ORIENTATION DISTRIBUTION FUNCTIONS

Robert J. De Angelis
Professor
Department of Mechanical Engineering

University of Nebraska-Lincoln
255 Walter Scott Engineering Center
Lincoln, Nebraska 68588-0656

THE SIMULATION OF X-RAY POLE FIGURES
AND
ORIENTATION DISTRIBUTION FUNCTIONS

by:
Robert J. De Angelis
Department of Mechanical Engineering
University of Nebraska-Lincoln
Lincoln, Nebraska 68588-0656

Abstract

The production of metallic materials with controlled degrees of anisotropy is important because the controlled texture provides significant assurance that subsequent plastic deformation can be performed successfully and reproducibly. To proceed to this condition, the degree of anisotropy must be quantified by the experimental determination of x-ray pole figures and the orientation distribution functions (ODF) calculated from the pole figure data. Orientation distribution functions are plotted in three dimensional Eulerian space which makes it difficult for the casual observer to extract even the simplest texture information from ODF plots. The main objective of this research was to develop a method to simulate x-ray pole figures and orientation distribution functions from materials of any combination of crystallographic textures. Through the use of straight forward overlay techniques the results obtained from the simulations can easily determine the types and strengths of textures that exist in processed materials.

THE SIMULATION OF X-RAY POLE FIGURES
AND
ORIENTATION DISTRIBUTION FUNCTIONS

Robert J. De Angelis

Introduction

Since the 1980's the description of material textures or crystal orientations in polycrystalline wires and sheets stated to move beyond the x-ray determined pole figures which was the norm since the 1930's. The orientation distribution function (ODF) has become the method of choice for presenting the description of material textures. This change was driven by the need for a more complete method of describing and quantifying textures in the tailor making of materials and was made possible by the advances in computer speed and capacity. Essentially the ODF is computed from pole density data usually represented on pole figure plots which give the density of poles (normals to a crystallographic plane) of a specific {hkl} plane in units of multiples of the random pole density for that particular {hkl} pole. Pole figures are usually represented on two dimensional polar coordinate plots where the center of the pole figure is the normal to the sheet surface and the direction to the right is parallel to the rolling direction. Therefore it is clear that the pole figure gives the position of the orientation of the specified {hkl} poles relative to and axial system based on the sample; e.g. rolling plane and rolling

direction in the case of sheet textures or wire axis direction in the case of wire textures. The ODF gives the statistical distribution of crystallites in a small range of orientations plotted on an angular axial system related to the crystallographic axis. A great advantage of this method of texture representation is that the coefficients of the harmonic equations employed to describe the function provide weighing factors for the determination of the anisotropic elastic and plastic properties of the material. These coefficients also are sensitive to orientation changes that occur during certain solid state processes, such as; phase transformations, plastic deformation and recrystallization. The major difficulty in the ODF description of texture is the inability of investigators who are primarily interested in the application of the collected data to interpret pole densities plotted in three dimensional angular ODF space. One of the objectives of this work is to furnish the application oriented engineer a method to unravel ODF space and be in a position to quantify the details of the textures in a processed part. The method employed to arrive at this was by simulation and ODF analysis of ideal pole figures.

Methodology

The method of simulation of x-ray diffraction ideal texture data and the ODF representation of single or combination textures was accomplished by employing the Siemens software on the D5000 diffractometer system at Eglin Air Force Base AWEF. To accomplish

the simulations the software packages PRINTTX and MAKERAW were utilized in addition to the standard pole figure and ODF analysis and plotting software. The total collection of software purchased with the diffraction system is extremely useful and versatile. The PRINTTX program takes x-ray intensity data that describe a pole figure stored in machine format and forms a file containing the same data in ASCII format. This file was edited using the DOS editor to describe a single or a combination of textures. The edited file containing intensity description of a particular ideal texture is written into machine format by employing the program MAKERAW. Once this is accomplished it was a straightforward step to make the complete pole figures and to represent the selected ideal textures in ODF space. The ODF representation is a series of two angular dimensional cuts at a constant angular interval (e.g. every ten degrees) of the third angular dimension. These angular sections are easily copied onto transparencies and overlaid onto experimentally determined data obtained from processed materials to determined the types of textures present and their relative magnitudes.

The overall usefulness of this approach is optimum if the ideal textures consist of combinations of wire, sheet and random texture components expressed in sums of corrected intensity data. The major correction to the intensity data is due to variations in the absorption characteristics of the incident and diffracted beams as a function of the diffractometer measurement angles Khi and Psi. It the work presented here the absorption effects were not included

in the intensity formulation of the ideal texture data sets. The
data employed in this investigation described the desired textures
well enough to obtain excellent qualitative and rough quantitative
comparisons between ODFs.

Results

The following ideal textures were generated and analyzed employing
the software PRINTTX and MAKERAW described above:

TEXTURE TYPE	TEXTURE COMPONENTS AND FRACTIONS
Wire	[220]-1.0
Wire	[220]-0.25 [200]-0.75
Wire	[220]-0.33 [200]-0.67
Wire	[220]-0.50 [200]-0.50
Wire	[220]-0.75 [200]-0.25
Sheet	(100)[001]-1.0
Sheet	(100)[011]-1.0

A very small portion of the intensity data set which describes the
[220] wire texture is given in TABLE I. Notice the data is zero at
all Phi (5 degree increments) angular positions except at the Khi
angle of 35 degrees (the angle between [111] and [110]) for the
(111) pole figure. The complete data set contains intensity values
at seventy two Phi angular positions at every five degree increment
in Khi from zero to 80 degrees for each of the (111), (200) and
(220) pole figures. Wire textures contain non-zero data at all
values of Phi for a specific value of Khi that satisfies the
crystallography of the pole figure and the wire texture component.
An ideal sheet texture contains a few intensity values which fix
the (hkl) in the rolling plane and the [uvw] in the rolling
direction of the sheet.

TABLE I. Sample of Data Set for the (111) Pole Figure of The [220]

Wire Texture

*Reflexion ranges * Phi range   0.00 - 360.00 Step   5.00
*Pole figure: 111
*Khi =   0.00
Rescaled, averaged background at 2 theta 41.000 :   000.00
Rescaled, averaged background at 2 theta 46.000 :   000.00
```
    00.00    00.00    00.00    00.00    00.00    00.00    00.00    00.00
    00.00    00.00    00.00    00.00    00.00    00.00    00.00    00.00
    00.00    00.00    00.00    00.00    00.00    00.00    00.00    00.00
    00.00    00.00    00.00    00.00    00.00    00.00    00.00    00.00
    00.00    00.00    00.00    00.00    00.00    00.00    00.00    00.00
    00.00    00.00    00.00    00.00    00.00    00.00    00.00    00.00
    00.00    00.00    00.00    00.00    00.00    00.00    00.00    00.00
    00.00    00.00    00.00    00.00    00.00    00.00    00.00    00.00
    00.00    00.00    00.00    00.00    00.00    00.00    00.00    00.00
```
*Khi =   5.00
```
    00.00    00.00    00.00    00.00    00.00    00.00    00.00    00.00
    00.00    00.00    00.00    00.00    00.00    00.00    00.00    00.00
    00.00    00.00    00.00    00.00    00.00    00.00    00.00    00.00
    00.00    00.00    00.00    00.00    00.00    00.00    00.00    00.00
    00.00    00.00    00.00    00.00    00.00    00.00    00.00    00.00
    00.00    00.00    00.00    00.00    00.00    00.00    00.00    00.00
    00.00    00.00    00.00    00.00    00.00    00.00    00.00    00.00
    00.00    00.00    00.00    00.00    00.00    00.00    00.00    00.00
    00.00    00.00    00.00    00.00    00.00    00.00    00.00    00.00
```
*Khi =   10.00
```
    00.00    00.00    00.00    00.00    00.00    00.00    00.00    00.00
    00.00    00.00    00.00    00.00    00.00    00.00    00.00    00.00
    00.00    00.00    00.00    00.00    00.00    00.00    00.00    00.00
    00.00    00.00    00.00    00.00    00.00    00.00    00.00    00.00
    00.00    00.00    00.00    00.00    00.00    00.00    00.00    00.00
    00.00    00.00    00.00    00.00    00.00    00.00    00.00    00.00
    00.00    00.00    00.00    00.00    00.00    00.00    00.00    00.00
    00.00    00.00    00.00    00.00    00.00    00.00    00.00    00.00
    00.00    00.00    00.00    00.00    00.00    00.00    00.00    00.00
    00.00    00.00    00.00    00.00    00.00    00.00    00.00    00.00
```
(Intermediate Khi angle data is skipped)
*Khi =   35.00
```
 2000.00 2000.00 2000.00 2000.00 2000.00 2000.00 2000.00 2000.00
 2000.00 2000.00 2000.00 2000.00 2000.00 2000.00 2000.00 2000.00
 2000.00 2000.00 2000.00 2000.00 2000.00 2000.00 2000.00 2000.00
 2000.00 2000.00 2000.00 2000.00 2000.00 2000.00 2000.00 2000.00
 2000.00 2000.00 2000.00 2000.00 2000.00 2000.00 2000.00 2000.00
 2000.00 2000.00 2000.00 2000.00 2000.00 2000.00 2000.00 2000.00
 2000.00 2000.00 2000.00 2000.00 2000.00 2000.00 2000.00 2000.00
 2000.00 2000.00 2000.00 2000.00 2000.00 2000.00 2000.00 2000.00
 2000.00 2000.00 2000.00 2000.00 2000.00 2000.00 2000.00 2000.00
```

The (111), (200) and (220) pole figures generated from the intensity data describing an ideal [220] wire texture are shown in Fig.1. The ODF calculated from these is shown in Fig. 2. Notice that all of the constant psi-2 sections are exactly alike due to the cylindrical symmetry of the wire texture. A single psi-2 section of the ODFs calculated from the wire texture simulated in this investigation are show in Fig, 3. Sections, at constant psi-2, of the ODF calculated from the pole figure intensity describing an ideal diagonal cube orientation sheet texture, (100)[011], is shown in Fig. 4. Here, of course, the ODF maximizes at a particular point in Eulerian space.

The (111), (200) and (220) pole figures experimentally determined from a copper specimen of copper processed from slab thickness to 0.375 inch thickness by cold upsetting and cold rolling are shown in Fig. 5. The ODF calculated from these pole figures is shown in Fig.6. The unequivocal resemblance between an ODF section from the ideal [220] wire texture and the ODF of the processed copper can be recognized by comparing the two ODFs shown in Fig. 7.

Conclusions

A method was developed to simulate any single or combination of crystallographic textures with a random component. ODFs calculated a simulated texture provides a fast and informative method to determine the types and magnitudes of textures present in processed materials.

REFERENCES:

H. J. Bunge, Texture Analysis in Materials Science, Butterworth, London 1982

Siemens Analytical X-ray Insturments, Inc., 6300 Enterprise Lane, Madison, WI 83719

IDEAL [220] WIRE TEXTURE POLE FIGURE
(equal-area proj.)

max. = 9.32

9.32
3.51
1.32
.50
.19
.07
.03
.01
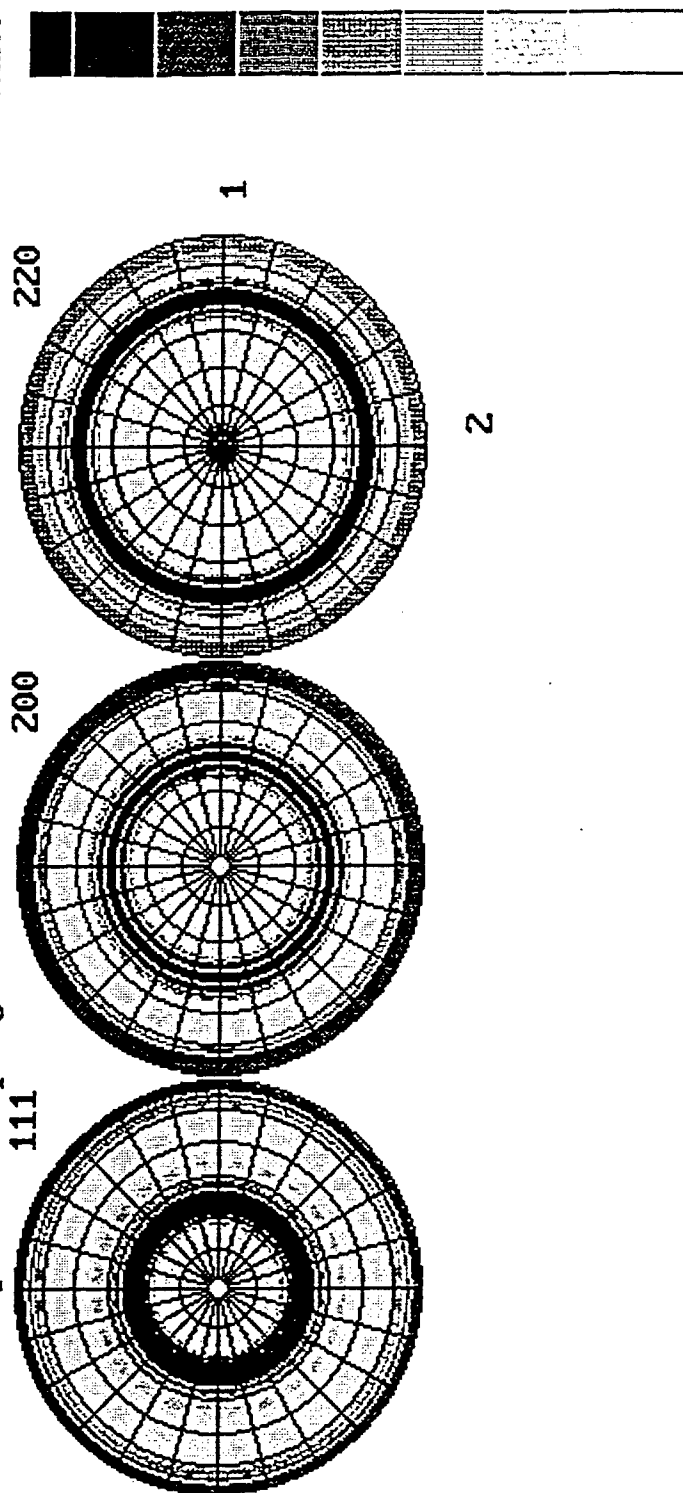
log. scale

6-SEP-95

Fig. 1. The (111), (200) and (220) Pole Figures that Describe an
Ideal [220] Wire Texture.

ODF OF IDEAL [220] WIRE TEXTURE
SHDBphi1=   (Read phi2 from 010 toward 100)

max.=18.26

18.68
6.37
2.17
.74
.25
.09
.03
.01
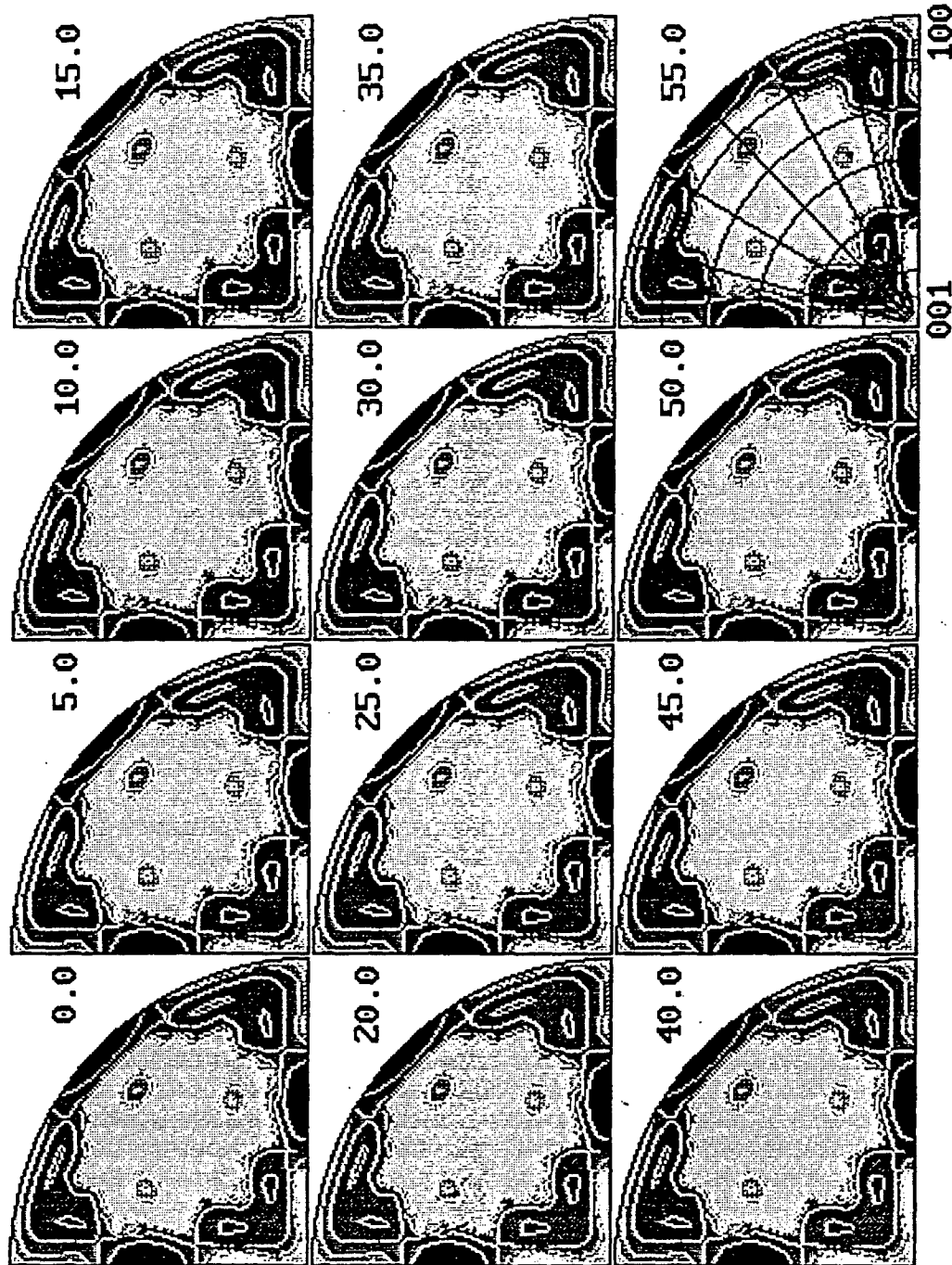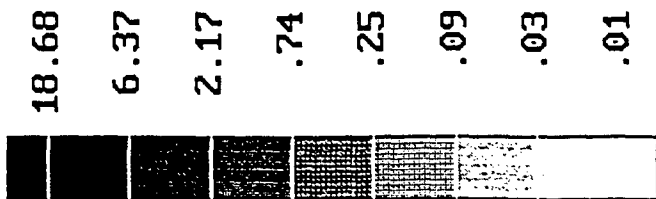
log. scale

6-SEP-95

Fig. 2. The Orientation Distribution Function that Describes an
Ideal [220] Wire Texture.
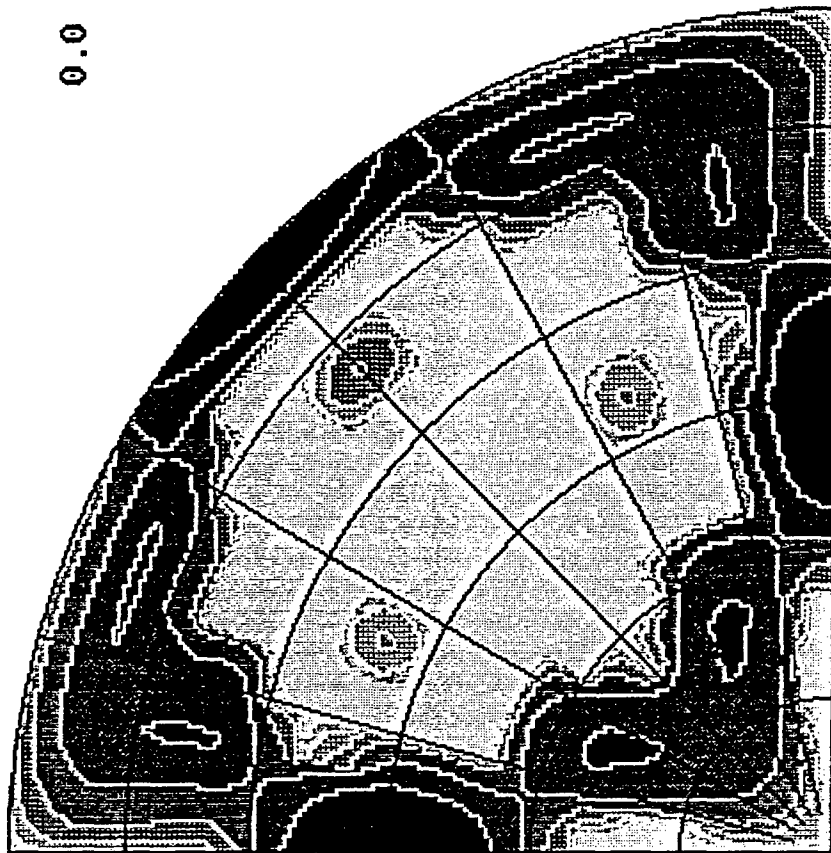
ODF OF IDEAL [220] WIRE TEXTURE
SHDBphi1=   (Read phi2 from 010 toward 100)

Fig. 3. The Phi-1 of Zero Section of the [220] Wire Texture
Orientation Distribution Function.

ODF OF IDEAL (100)[011] SHEET TEXTURE
SHDBphi1= (Read phi2 from 010 toward 100)

max. =******
99.99
30.92
9.56
2.96
.91
.28
.09
.03
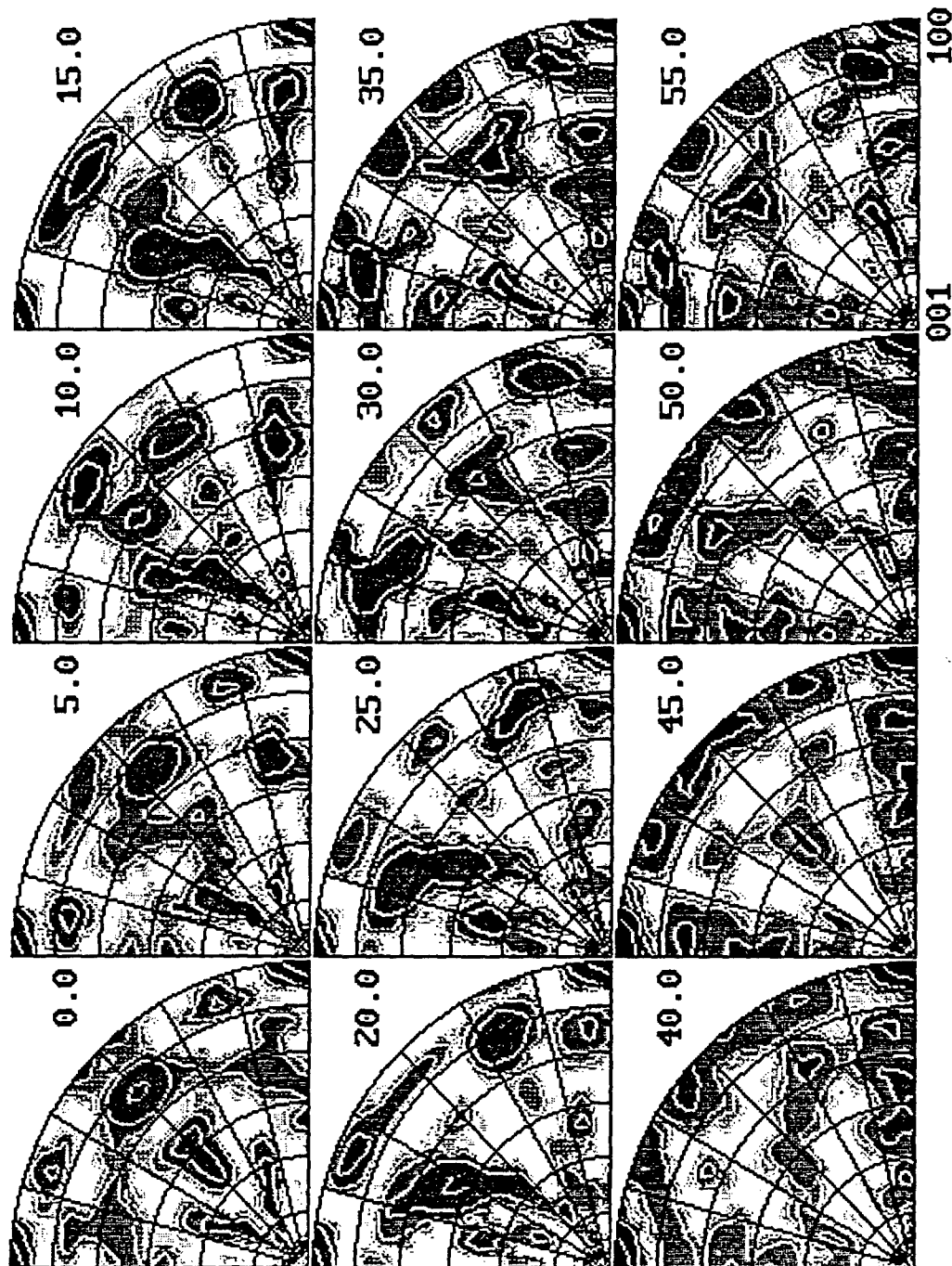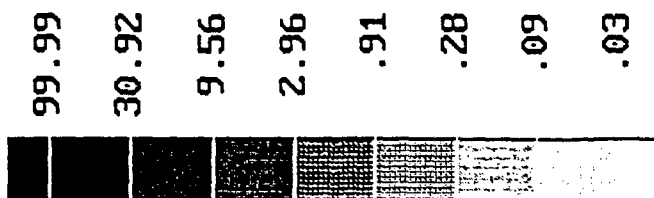
log. scale
6-SEP-95

Fig. 4. The Orientation Distribution Function that Describes an Ideal (100)[011] Sheet Texture.

POLE FIGURE OF AS ROLLED COPPER HRCU7
(equal-area proj.)

max.=12.81

12.99	
4.66	
1.67	
.60	
.22	
.08	
.03	
.01	
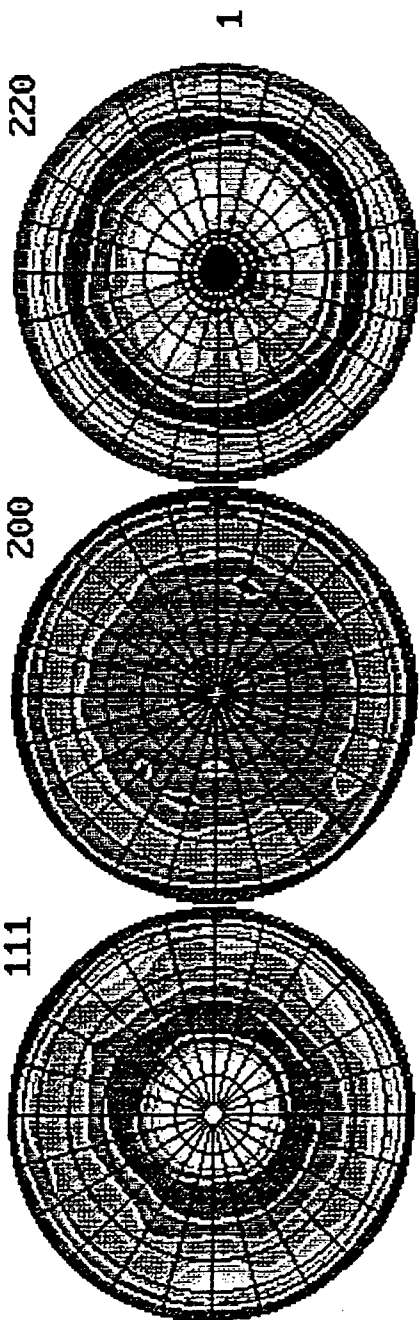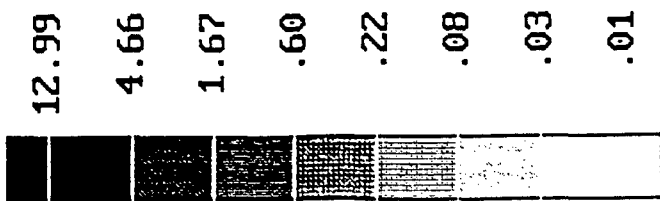
log. scale

7-SEP-95

Fig. 5. The (111), (200) and (220) Pole Figures that Describe the Texture in the Rolled Plate HRCU7AR.

ODF OF AS ROLLED COPPER PLATE HRCU7
SHDBphi1=   (Read phi2 from 010 toward 100)

max.=12.05

12.19
4.42
1.60
.58
.21
.08
.03
.01

log. scale

7-SEP-95

0.0

100

001
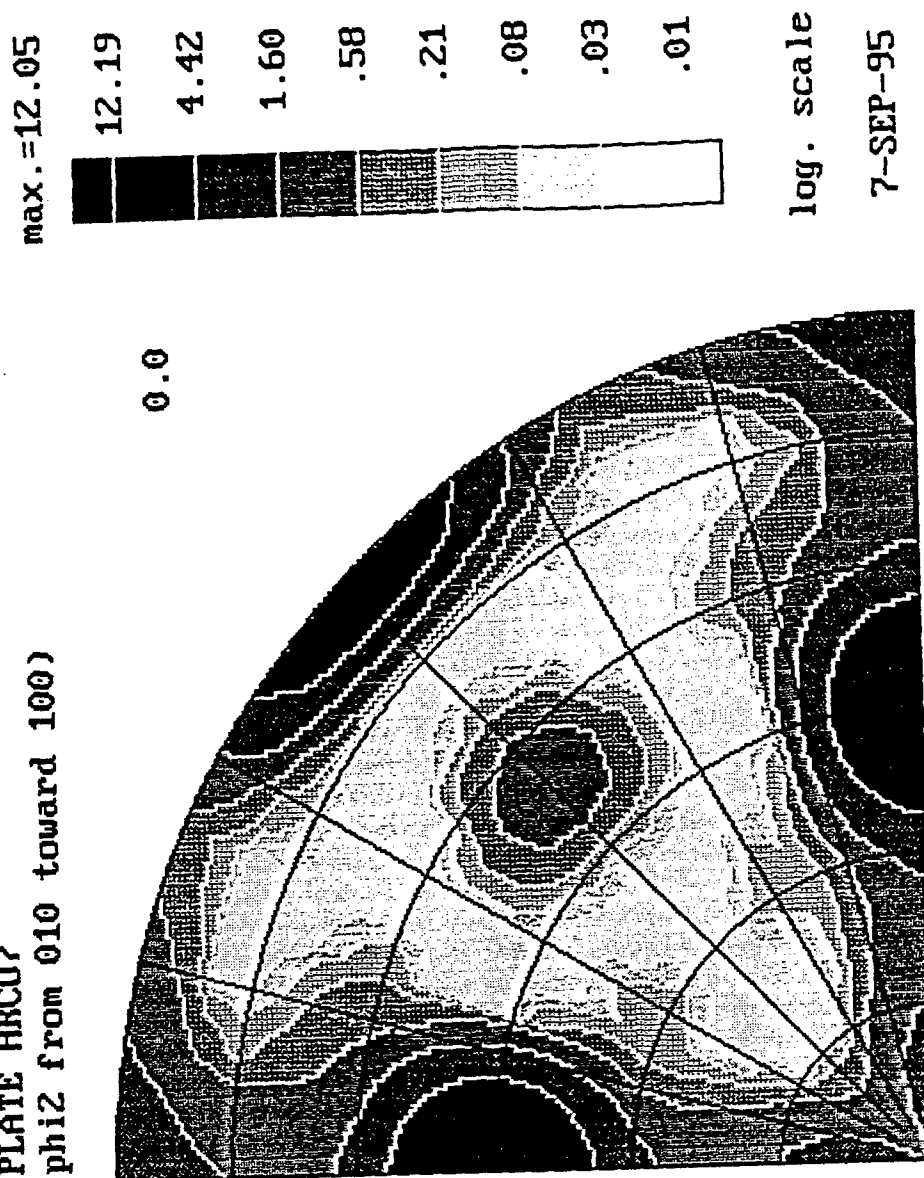
Fig. 6. The Phi-1 of Zero Section of the Orientation Distribution
Function that Describes the Texture in the Rolled Plate
HRCU7AR.

ODFs OF IDEAL [220] WIRE TEXTURE AND AS ROLLED COPPER HRCU7
18.09 SHDBphi1=
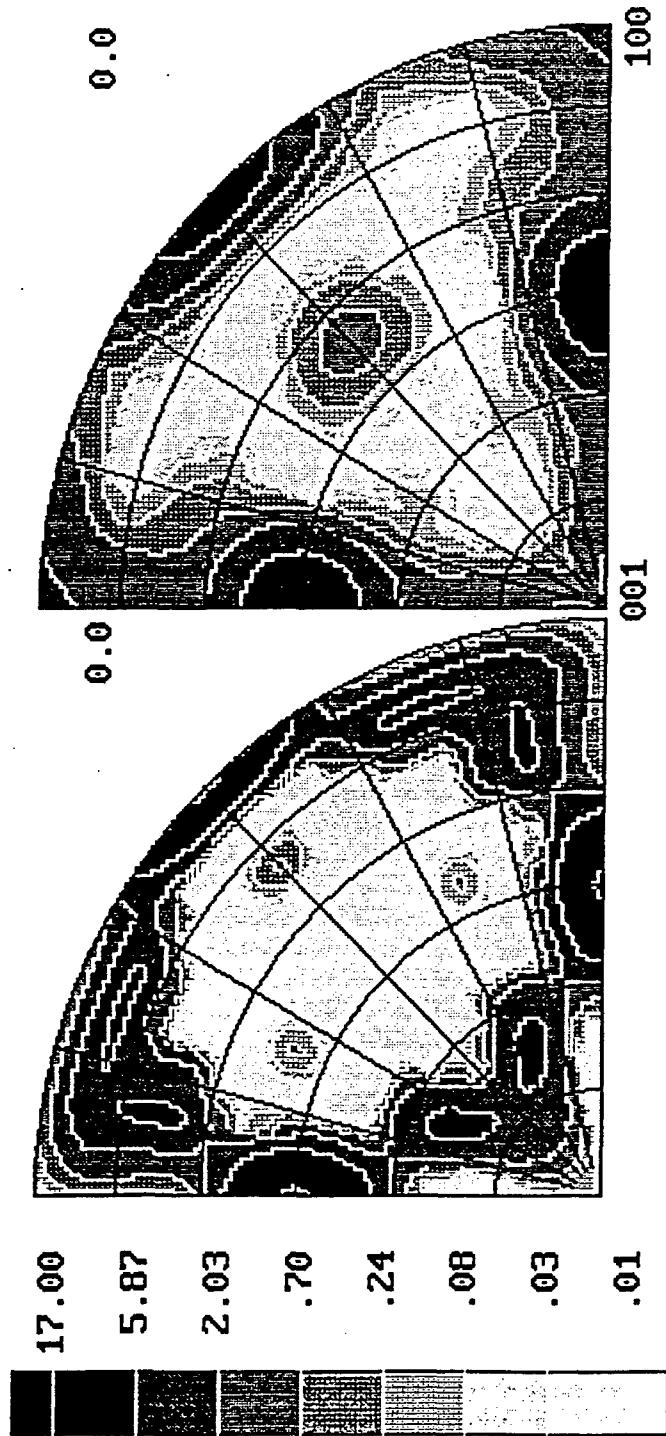
log. scale

7-SEP-95

Fig. 7. The Phi-1 of Zero Section of the Orientation Distribution
Functions of: (on right) [220] Wire Texture and (on left)
Rolled Copper Plate HRCU7AR.

INVESTIGATION OF
FRANZ-KELDYSH OSCILLATION, PHOTOLUMINESCENCE DECAY AND SPECTRUM, AND SECOND-ORDER NONLINEAR OPTICAL DEVICES IN SEMICONDUCTOR STRUCTURES

Yujie J. Ding
Assistant Professor
Department of Physics and Astronomy

Bowling Green State University
104 Overman Hall/Ridge Street
Bowling Green, OH 43403

INVESTIGATION OF
FRANZ-KELDYSH OSCILLATION,
PHOTOLUMINESCENCE DECAY AND SPECTRUM,
AND SECOND-ORDER NONLINEAR OPTICAL DEVICES
IN SEMICONDUCTOR STRUCTURES

Yujie J. Ding

Assistant Professor

Department of Physics and Astronomy

Bowling Green State University

Abstract

We present a new technique that accurately extracts the bandgap from Franz-Keldysh oscillations (FKOs) by perturbing the internal electric field of a SIN structure or a laser PIN diode with a second, unmodulated laser pump. FKOs observed when the sample is illuminated by this perturbing pump shows small shifts in the peak energies relative to those in the unperturbed FKOs. These shifts are analyzed, using only linear least-square fitting, to provide both the phase and the critical point energy in the asymptotic expression for the FKOs. The technique works even when the near-bandgap spectrum is distorted. We have applied the perturbed photoreflectance technique to GaAs surface-intrinsic-n-doped (SIN) structures and to laser PIN diodes. In the SIN sample, we extract bandgaps within several meV of the expected values of the band-gaps. We have particularly tested our technique on the laser PIN diode. We extract the bandgap of the AlGaAs confinement barriers corresponding to an Al composition of 18% in good agreement with the nominal value.

We have measured the photoluminescence decay of various coupling structures of quantum wells. We have determined the carrier densities for band-filling effects.

We have measured photoluminescence spectrum of an asymmetric-coupled quantum-well structure. We have observed that the ratio of the first two heavy-hole transition strengths increases as the pump intensity increases due to nonlinear coupling of the wells.

We have designed a structure for demonstrating transversely-pumped counter-propagating (mirrorless) optical parametric oscillation and amplification, and achieving surface-emitting second-harmonic generation in a vertical cavity.

INVESTIGATION OF
FRANZ-KELDYSH OSCILLATION,
PHOTOLUMINESCENCE DECAY AND SPECTRUM,
AND SECOND-ORDER NONLINEAR OPTICAL DEVICES
IN SEMICONDUCTOR STRUCTURES

Yujie J. Ding

1. Introduction

Photo-reflection (PR) modulation spectroscopy becomes essential to characterize semiconductor microstructures. Sharp oscillating features due to Franz-Keldysh oscillation (FKO) can be used to study the variation of the material properties on pressure, temperature, electric fields, etc. The basic principle of the PR modulation spectroscopy, rigorously formulated in Ref. [1], is based on evaluating the derivative with respect to some parameter, such as electric field. The derivative nature of the modulation spectra suppresses uninteresting background effects and emphasizes structure localized in the energy region of interband transitions at critical points in the mini-Brillouin zone. In addition, weak features that may not be have been seen in the absolute reflectance spectra are enhanced. Because of this derivative-like nature a large number of sharp spectral features can be observed even at room temperature. Furthermore, the spectrum also contains the information on the other modulation variables such as phase [2], modulation frequency [3], modulation amplitude, wavelength of the modulating pump beam [4], broadening, etc.

Recently, it has been shown that by interrupting sample growth at every interface, one can obtain multiple photoluminescence (PL) peaks with separate emission energies that correspond to the excitonic emissions at interface islands of different sizes [5-8]. Because of the formation of these interface islands, the well widths at these islands generally differ by one monolayer with respect to the designed width in high quality samples [9]. However, the area ratios among all these islands of different well widths are random, which cannot be controlled in growth process. Without the growth interruption, the recombination of the carriers in the wells with different widths results in the inhomogeneous broadening in the PL spectrum. At low temperatures, all the carriers generated by the pump will be eventually relaxed down to the lowest energy levels and localized in the islands, resulting in very large carrier densities. If the total area of the islands is small, it would be possible to completely fill exciton states in these islands at relatively low intensities that may manifest as the saturation of the PL peaks. By the same token, the carrier density can be sufficiently high to strongly renormalize the band-gap (BGR), which manifests as change of the PL linewidth of the

exciton peak. It is worth noting that in growth-interrupted samples, BGR and band-filling effects are spatially-localized effects, due to additional confinement along the interface, similar to situation in quantum dots (i.e. all the islands are spatially isolated).

Previously [10], we have demonstrated that the ratio of the first two heavy-hole transition strengths in the asymmetric-coupled quantum-well structure increases as the temperature increases at the beginning. It deceases as the temperature increases further. We believe this behavior is due to the intersubband transitions between two quantum wells via acoustic phonons.

Recently, surface-emitting green light was obtained [11] by frequency-doubling infrared laser beam (1.06 μm) in the waveguide based on periodically modulated second-order susceptibility in alternating $Al_xGa_{1-x}As$ and $Al_yGa_{1-y}As$ ($x \neq y$) layers. When the multilayers are sandwiched between two quarter-wave stacks, large increase in the conversion efficiency was observed [12] though quasi phase-matching was not established. Following Ref. [13], second-order susceptibility of asymmetric-coupled quantum-well (QW) domain structures have been measured in the surface-emitting geometry [14]. The maximum conversion efficiency so far is still less than 1%/W. Recently, we proposed a novel practical scheme for implementation of the cascaded nonlinearity using surface-emitting second-harmonic generation (SHG) in the Fabry-Perot cavity. We have shown that such scheme can be efficiently used for optical power limiting and optical phase conjugation at low input power [15]. Most recently [16] for the first time to the best of knowledge, we propose to achieve nearly 100% conversion efficiency of SHG for the low input power, by combining quasi phase-matching and cavity enhancements in semiconductor multilayers or asymmetric QW domain structures. Thus, our investigation leads to the implementation of *practical* frequency doublers which can cover the range from blue to infrared. More importantly, we have proposed to implement tunable optical parametric oscillators (OPOs) and amplifiers [17] based on a novel configuration. Frequency doublers, optical parametric oscillators and amplifiers, and the nonlinear optical devices based on the cascaded second-order nonlinearities have potential applications in generation of blue light, generation and amplification of tunable mid-IR light, optical communication, ultrafast detection, sensor protection, real-time holography, or optical lithography.

2. Discussion of Problem

a. Franz-Keldysh oscillation

Previously, the ability to fit the lineshape [18] gives PR modulation spectroscopy an important advantage over other optical methods such as photoluminescence,

photoluminescence excitation spectroscopy, photoconductivity, resonance Raman scattering, etc. It is possible to evaluate energy positions of spectral features to within several meV even at room temperature, to extract small and important features, to obtain accurate broadening parameters, etc. However, in some cases, the lineshape fitting is not accurate to determine parameters of the materials such as the band-gap. For example, near the band-edge, there are some features due to presence of trap sites that may distort the FKOs. Therefore, we have developed a modified PR modulation technique to extract the band-structure parameters based on all the oscillating cycles observable, rather than a few cycles near the band-edge.

b. Photoluminescence decay

The sample was grown by MBE on a semi-insulating GaAs substrate in collaboration with Naval Research Labs. The epitaxial layers consist of 10 periods, each of which is composed of three narrow asymmetric coupled GaAs quantum wells with the designed thicknesses of $45\,\text{Å}$, $30\,\text{Å}$ and $50\,\text{Å}$, coupled by $40\,\text{Å}$-$Al_{0.3}Ga_{0.7}As$ barriers, see Fig. 1. The thicknesses of the barriers between the adjacent periods are $40\,\text{Å}$. One sample is undoped while the other one is doped with silicon ($10^{17}\,\text{cm}^{-3}$) in the barrier layer between the 30-Å and 50-Å wells. During the sample growth there is an interruption for 60 seconds at every interface. Because of this growth interruption, interface islands with sizes larger than the average exciton radius are formed, allowing excitons being spatially-localized within these islands with separate optical transition energies from that of free-excitons [5]. As a result, in each designed well the absorption and/or emission peaks are separated from each other corresponding to one monolayer thickness ($2.8\,\text{Å}$) difference. In our low temperature photoluminescence excitation (PLE) spectra, we have clearly observed both the primary excitonic emission peaks (I) for the designed quantum well widths and the secondary excitonic emission peaks (II) that correspond to interface islands with the well widths one monolayer thicker than the designed ones. The emission peaks corresponding to interface islands are much narrower than those without growth-interruption. At 0.54 W/cm^2 for the e_1hh_1 (II) emission, the half width at the half maximum determined from the low energy side is $\sim 4.5\,\text{Å}$ (0.95 meV). This is the narrowest linewidth obtained so far. When we change the intensity from 0.54 W/cm^2 to 1.9 kW/cm^2 at 4 K, we can see that the linewidth of the PL peak increases dramatically. Indeed, it increases from 0.95 meV to 4.4 meV. However, the energy of the emission peak stays the same for all the intensities. Following the argument in Ref. [19], We attribute the large increase of the PL linewidth to the band-gap renormalization.

As mentioned above, a single PL peak breaks into two because of the formation of interface islands with the size larger than the exciton radius. At low temperatures, all the

carriers generated by the pump laser will be eventually relaxed down to the lowest energy levels and localized in the islands, resulting in large carrier densities. If the total area of the islands is small, it would be possible to completely fill exciton states in these islands at relatively low intensities, which manifests as the saturation of the PL peaks. This type of the band-filling effect only occurs at the spatially-localized islands.

It is expected that the carrier density required to observe these effects should be subsequently lower than that outside the islands. We intend to measure the photoluminescence decay time to determine the carrier densities.

c. Photoluminescence spectrum

In our previous work on asymmetric-coupled quantum wells [10], within a large range of the pump intensities, we did not observe any nonlinear coupling between two wells because of our unique design of the structure. We designed and grew a new structure to study dependence of the degree of the coupling between two wells on the pump intensity.

d. Design of a multilayer structure for OPOs and frequency doublers

Following the quasi-phase matching scheme by spatially modulating second-order susceptibility [20,13], we have systematically investigated the SHG under relatively higher pump power [16]. Because of the large enhancement due to the presence of the vertical cavity, the saturation power density is greatly reduced. Therefore, the saturation of the conversion efficiency can occur at relatively low input power density. For realistic dimensions based on ZnSe/ZnS or GaAs/AlGaAs materials, the saturation power density is 0.11 W/μm-4.9 W/μm for the wavelength range of the fundamental beam: 0.98-1.8 μm. If a horizontal cavity formed by two mirrors (with the reflectivities of R_3 and R_4) is included, the saturation power density is 0.2 mW/μm-8.7 mW/μm.

The backward parametric oscillations in the parallel propagation configuration [21] have not been observed due to the lack of appropriate materials for achieving quasi-phase matching. Recently, following Ref. [19], quasi-phase matching was achieved based on GaAs/AlGaAs multilayers [11] or asymmetric quantum-well domain structures [14]. For the first time to the best of our knowledge, we have proposed [17] to use second-order optical nonlinearities of these structures in a vertical cavity to achieve tunable and efficient transversely-pumped counterpropagating optical parametric oscillations (TPCOPOs) and amplifications (TPCOPAs). Similar to Refs. [13,11], the quasi-phase matching can be achieved in these structures by spatially modulating the second-order susceptibility along the growth direction. Without mirror feedback for the signal and idler, optical parametric oscillations can occur, similar to the backward OPOs [21], but fundamentally different from the

conventional OPOs [22] where oscillations cannot occur without the mirror feedback. If the pump power is sufficiently large, the efficient sum-frequency generation saturates TPCOPOs. The output wavelengths from the signal and idler can be tuned in a large range by changing the incident angle of the pump wave, see Fig. 8.1. The maximum tuning range is limited by the phase matching condition along the propagation direction of the signal or idler. Consider GaAs/Al$_{0.8}$Ga$_{0.2}$As multilayers with the optimized structure dimensions: if $\lambda_3 \approx 0.9\,\mu$m, tuning range: 1.4–2.6 μm.

3. Methodology

a. Franz-Keldysh oscillation

In this new scheme for the PR modulation spectroscopy, we have used two laser beams as pump beams with their frequencies above the frequency of the band-gap of the GaAs or AlGaAs layer (forming the Surface-Intrinsic-N-doped, SIN, structure or a laser PIN diode). A chopped He-Ne laser beam is used to modulate the bias, and therefore, the reflectance of a probe beam. A second, unmodulated, Argon laser beam is used to change the total bias across the GaAs or AlGaAs layer or the internal electric field. We can measure the modulated, relative reflectivity of a probe beam obtained by sending the lamp light through a monochromator. One should observe strong dependence of the Frank-Keldysh oscillation (FKO) on the intensity of the Argon pump: the extrema in the spectrum should shift when the Argon beam intensity increases. In the PR modulation spectrum, we can determine the photon energies of the extrema for the FKO. Based on the changes of the energies between two different intensities of the Argon pump beam and the linear least-square fitting, we can obtain the phase for the FKO. We can determine the band-gaps of GaAs or AlGaAs layer by least-square-fitting the energies vs. the 2/3 power of the phase-shifted FKO index. Fig. 2(a) shows our schematic set-up.

b. Photoluminescence decay

For the measurement of the PL decay, we used a mode-locked Ar$^+$ laser as our excitation pulse with the pulse duration of 150 ps and output wavelength of 5145 Å. The temporal traces of the PL signal were taken via a streak camera with a time resolution of 20 ps. Fig. 2(b) shows our schematic set-up.

c. Photoluminescence spectrum

Our asymmetric-coupled quantum-well structure is pumped by a CW Argon laser at the wavelength of 5145 Å. The photoluminescence was collected by a monochromator via a

lens.

d. Design of a multilayer structure for OPOs and frequency doublers

Our optimized design of the multilayer structure is based on our vigorous consideration of surface-emitting frequency doublers [Fig. 3(a)] and TPCOPOs and TPCOPAs [Fig. 3(b)], see Refs. [16,17].

4. Results

a. Franz-Keldysh oscillation

We studied two pieces of SINs cut from two different wafers. The intrinsic layer of each SIN consists of a thin GaAs layer. Fig. 4(a) shows the PR modulation spectra for one of the samples at two different intensities of the Argon pump: zero and high intensity. We can clearly see the FKOs in the spectra. Furthermore, there are obvious shifts between the corresponding extrema of two spectra. The photon energies of the extrema can be determined from Fig. 4(a) for both spectra; we call them $E_m^{(0,h)}$ where m = 1 corresponds to the first clearly resolved extremum and 0,h - zero and high pump intensity. We have plotted $[E_m^{(0)} - E_m^{(h)}]^{3/2}$ vs. the FKO index, m, in Fig. 4(b). From the least-square fit, we have determined the phases for the FKO for these two samples: $\phi_1 \approx -1.648\,\pi$ and $\phi_2 \approx 0.8343\,\pi$. Following Ref. [1], we obtain

$$E_m - E_g = [(3/2)(m\pi - \phi)]^{2/3}\hbar\Omega \tag{1}$$

where E_g is the band-gap, ϕ is the phase for the FKO, and $\hbar\Omega$ is the electro-optic energy, which is related to the electric field F through

$$(\hbar\Omega)^3 = e^2\hbar^2F^2/2\mu \tag{2}$$

where μ is the reduced interband mass of the electron-hole pair along $\vec{F}$. In Eq. (1) we can replace E_m by $E_m^{(0)}$ and ϕ by two different phases determined from our experiments. We have plotted $E_m^{(0)}$ vs. $[(3/2)(m\pi - \phi_1)]^{2/3}$ for one sample in Fig. 4(c). By least-square fitting the data in Fig. 4(c), we can determine the band-gap to be $E_{g,1} \approx 1.425\,eV$. Similarly, for the second sample, $E_{g,2} \approx 1.447\,eV$. The value of the band-gap for the second sample is larger than the accepted value for bulk GaAs (1.424 eV). We believe this is probably due to the presence of some intentionally incorporated AlAs layer during growth.

Our third sample is a laser pin diode structure. It consists of an InGaAs layer sandwiched by two GaAs layers. Next to each of the GaAs layers, there is an AlGaAs

confinement barrier with the nominal value of the aluminum concentration of 20%. Next to each of these AlGaAs layers, there is a AlGaAs layer with much higher aluminum concentration. Fig. 5(a) shows the PR modulation spectra for two different pump intensities. We can clearly see the shifts of the corresponding extrema between two spectra. We can follow exactly the same procedure for determining the band-gap of GaAs as shown above. (It is difficult for us to use the lineshape fit for determining the band-gap of the AlGaAs layer because of the presence of an additional set of the FKOs in the GaAs layers.) The phase of the FKO is 0.8191 π from Fig. 5(b). We can then determine the band-gap of AlGaAs to be 1.687 eV from Fig. 5(c). This translates into 18.1% of aluminum in the AlGaAs layers in good agreement with the nominal value (20%).

b. Photoluminescence decay

We have made the time-resolved PL measurements in both types of our samples. Fig. 6 shows the typical temporal PL traces detected at the center wavelengths of e_1hh_1 (II) emission peaks (the excitonic emission peaks) as a result of the carrier recombination at the interface islands in the 18 ML well. After the excitation, the PL signals at the e_1hh_1 (II) emission peak maximize at about 700 ps and 650 ps in the undoped [Fig. 6(a)] and the modulation doped [Fig. 6(b)] samples, respectively. This is due to the competition between the carrier intersubband relaxation and the carrier recombination. As indicated in Fig. 6, by fitting the decay portions of these traces to the exponential functions, we have obtained the PL decay time constants of 357 ps and 438 ps for the undoped [Fig. 6(a)] and the modulation doped [Fig. 6(b)] sample, respectively.

The life time of the excitons is determined by [23]

$$\tau = \frac{2\pi\varepsilon_0 m_0 c^3}{n_b e^2 \omega^2 f} \tag{3}$$

where ε_0 is the dielectric constant, m_0 is the electron free mass, c is the speed of light, n_b is the background refractive index, ω is the frequency of the radiative optical transition, and f is the corresponding transition strength. We therefore obtain the oscillator strengths for the e_1hh_1 (II) excitons to be 6.13 for the undoped sample and 5 for the doped sample. This explains why the islands related emission peaks in our PLE spectra is weaker in the modulation doped sample than that in the undoped sample.

In the quasi-CW regime, the density of excitons can be determined as

$$N_{ex} = \tau \frac{I_{laser} \alpha}{\hbar\omega_{laser}} \tag{4}$$

where I_{laser} is the laser intensity, α is the absorption coefficient, and $\hbar\omega_{laser}$ is the energy of a single photon. The saturation intensity to completely fill the e_1hh_1 (II) excitons states in the modulation doped sample is about $1.2\,kW/cm^2$. Assuming $\alpha \approx 10000\,cm^{-1}$ at the pumping wavelength in our experiments, the exciton density is then estimated to be $2.03 \times 10^{16}\,cm^{-3}$. The corresponding area density is $1.04 \times 10^{10}\,cm^{-2}$. Assuming that for $I_{laser} \sim 1.2\,kW/cm^2$, all the quantum states have been almost occupied, we can estimate the exciton density at the interface islands using the two dimensional density of states and the estimates of the island area ratio above. The carrier density in the first electron energy level with the energy position ε_1 and the linewidth $\Delta\varepsilon$ can be determined by

$$N(e_1) = \int_{\varepsilon_1 + \Delta\varepsilon/2}^{\varepsilon_1 - \Delta\varepsilon/2} \rho_{2D}(\varepsilon)f(\varepsilon)d\varepsilon \qquad (5)$$

where the two dimensional density of states, $\rho_{2D} = m^*/\pi\hbar^2$, is a constant, with m^* the effective mass, $f(\varepsilon) = 1/[1 + \exp(\varepsilon - \varepsilon_F)/kT]$ is the Fermi-Dirac distribution function, with ε_F the Fermi energy and k the Boltzmann constant. In the case of almost complete band filling at low temperatures, we may treat the electrons at the energy level ε_1 as degenerate electron gas. In this case, $f(\varepsilon) \approx 1$. Eq. (5) then reduces to

$$N(e_1) = \rho_{2D}\Delta\varepsilon(e_1) \qquad (6)$$

From the PLE spectrum, we estimated that the linewidth $\Delta\varepsilon(e_1)$ is about 5 meV in our samples. Based on the area ratio determined above, the carrier density to completely fill the interface islands regarding e_1hh_1 (II) transition is estimated to be $\sim 1.12 \times 10^{10}\,cm^{-2}$. This is in good agreement with the estimate obtained based on Eq. (4) above. This carrier density is an order of magnitude smaller than that outside the islands.

We have also measured PL decay of several other coupling structures with and without the presence of a dc magnetic field. We are in the process of analyzing our results.

c. Photoluminescence spectrum

The structure of the asymmetric-coupled quantum-well is shown in Fig. 7(a). Fig. 7(b) shows our results of photoluminescence spectra under different pump intensities at 4 K. We have determined the peak wavelengths to be 7890 Å and 7946 Å that correspond to the two lowest heavy-hole transitions, see Fig. 7(a). The ratio of the total photoluminescence of the the second peak (7890 Å) with respect to that for the first peak (7946 Å) is plotted vs. the pump intensity in Fig. 7(c). One can see that the ratio is always increasing when the pump intensity increases. This corresponds to nonlinear coupling between two wells. We are currently working on the origin of this nonlinear coupling.

d. Design of a multilayer structure for OPOs and frequency doublers

Based on Refs. [16,17], we have already designed an optimized structure [see Fig. 3(c)]. We will grow this structure in collaboration with Drs. R. Sherriff and K. Evans at Wright Patterson AFB. We will test the performance of this structure as an efficient frequency doubler and optical parametric oscillator and amplifier at Bowling Green State University.

5. Conclusion

We have developed a modified photo-reflectance modulation technique that can be used to characterize semiconductor structures, especially to determine the bandgaps and aluminum concentration. We have measured time-resolved photoluminescence decay in growth-interrupted multiple asymmetric three narrow quantum wells. We have subsequently determined decay times and characteristic carrier densities for observing pronounced band-filling effects. The spatially-localized band-filling effect in our sample is more pronounced than the conventional one for the same irradiance. We have observed evidence of the nonlinear coupling in asymmetric-coupled quantum-well structure. We have also designed a multilayer structure that can be used to implement an optical parametric oscillator and amplifier and frequency doubler in a novel configuration.

Some of our results have already been submitted for publication [24,25].

6. Acknowledgement

We are indebted to Dr. R. Sherriff, Mr. J. Hoelscher, and Dr. D. C. Reynolds for their expertise in the areas above, that had made it possible for us to complete four different projects during twelve-week period.

7. References

[1] D. E. Aspnes and A. A. Studna, Phys. Rev. B7, 4605 (1973).

[2] H. Shen, S. H. Pan, F. H. Pollak, M. Dutta, and T. R. AuCoin, Phys. Rev. B 36, 9384 (1987).

[3] H. Shen, Z. Hang, S. H. Pan, F. H. Pollak, and J. M. Woodall, Appl. Phys. Lett. 52, 2058 (1988).

[4] H. Shen, X. C. Shen, F. H. Pollak, and R. N. Sacks, Phys. Rev. B36, 3487 (1987).

[5] D. Bimberg, D. Mars, J. N. Miller, R. Bauer, O. Oertel, and J. Christen, Supperlatt. Microstruc. 3, 79 (1987).

[6] M. Kohl, D. Heitmann, S. Tarucha, K. Leo, and K. Ploog, Phys. Rev. B39, 7736 (1989).

[7] D. C. Reynolds, K. K. Bajaj, C. W. Litton, P. W. Yu, J. Singh, W. T. Masselink, R. Fischer, and H. Morkoc, Appl. Phys. Lett. 46, 51 (1985).

[8] K. Fujiwara, K. Kanamoto, and N. Tsukada, Phys. Rev. B40, 9698 (1989).

[9] B. Devcaud, A. Chomctte, N. Roy, B. Scrmagc, and D. S. Katzer, Sur. Sci. 267, 199 (1992); D. Gammon, B. V. Shanabrook, and D. S. Katzer, Appl. Phys. Lett. 57, 2710 (1990).

[10] A. G. Cui, Y. J. Ding, O. Gorbounova, J. V. D. Veliadis, S. J. Lee, J. B. Khurgin, and K. L. Wang, 1995 OSA Ann. Meet., Paper MYY4.

[11] R. Normandin, R. L. Williams, and F. Chatenoud, Electr. Lett. 26, 2088 (1990); R. Normandin, H. Dai, S. Janz, A. Delage, J. Brown, and F. Chatenoud, Appl. Phys. Lett. 62, 118 (1993); D. Vakhshoori, R. J. Fischer, M. Hong, D. L. Sivco, G. J. Zydzik, G. N. S. Chu, and A. Y. Cho, Appl. Phys. Lett. 59, 896 (1991).

[12] R. Lodenkamper, M. L. Bortz, M. M. Fejer, K. Bacher, and J. S. Harris, Jr., Opt. lett. 18, 1798 (1993).

[13] J. Khurgin, Appl. Phys. Lett. 21, 2100 (1987); Phys. Rev. B38, 4056 (1988); J. Appl. Phys. 64, 5026 (1988); J. Opt. Soc. Amer. B 6, 1673 (1989).

[14] S. Janz, F. Chatenoud, and R. Normandin, Opt. Lett. 19, 622 (1994).

[15] J. B. Khurgin and Y. J. Ding, Opt. Lett. 19, 1066 (1994).

[16] Y. J. Ding, S. J. Lee, and J. B. Khurgin, J. Opt. Soc. Am. B 12, 1586 (1995).

[17] Y. J. Ding, S. J. Lee, and J. B. Khurgin, Phys. Rev. Lett. 75, 429 (1995); Y. J. Ding, S. J. Lee, and J. B. Khurgin, IEEE J. Quant. Electr. 31, 1648 (1995).

[18] C. Van Hoof, K. Deneffe, J. De Boeck, D. J. Arent, and G. Borghs, Appl. Phys. Lett. 54, 608 (1989).

[19] S. Schmitt-Rink, D. S. Chemla, and D. A. B. Miller, Adv. Phys. 38, 89 (1989).

[20] N. Bloembergen, U.S. Patent No. 3 384 433 (1968).

[21] S. E. Harris, Appl. Phys. Lett. 9, 114 (1966).

[22] S. E. Harris, Proc. IEEE 57, 2096 (1969).

[23] J. Feldmann, G. Peter, E. O. Göbel, P. Dawson, K. Moore, C. Foxon, and R. J. Elliott, Phys. Rev. Lett. 59, 2337 (1987).

[24] A. G. Cui, Y. J. Ding, S. J. Lee, J. V. D. Veliadis, J. B. Khurgin, S. Li, D. S. Katzer, D. C. Reynolds, J. Grata, and R. E. Sherriff, submitted to J. Opt. Soc. Am. B.

[25] Y. J. Ding, J. Grata, J. Hoelscher, and R. E. Sherriff, submitted to 1995 Amer. Phys. Soc. Ohio Section Meeting.

Figure 1

Figure 2

(a)

(b)
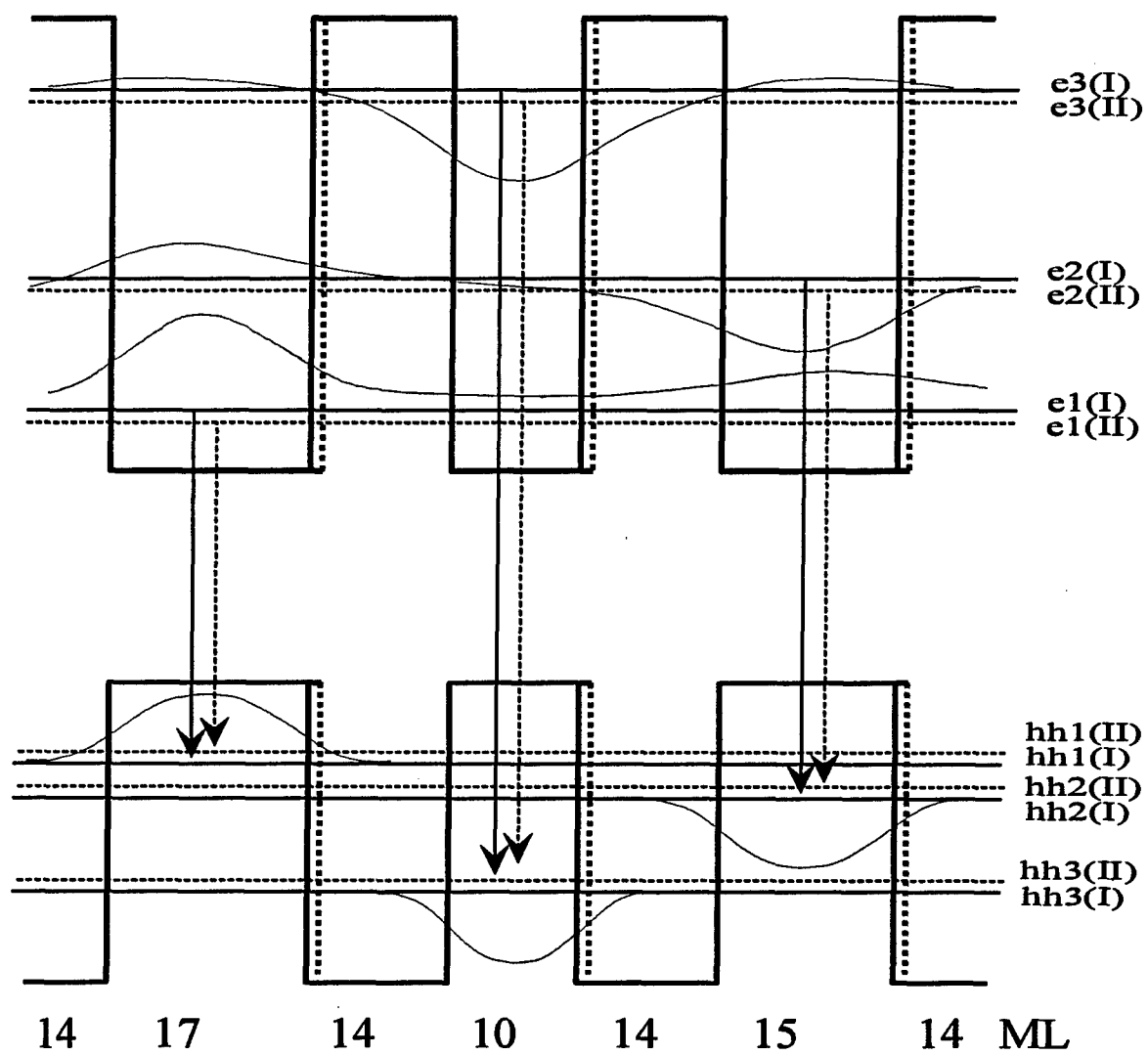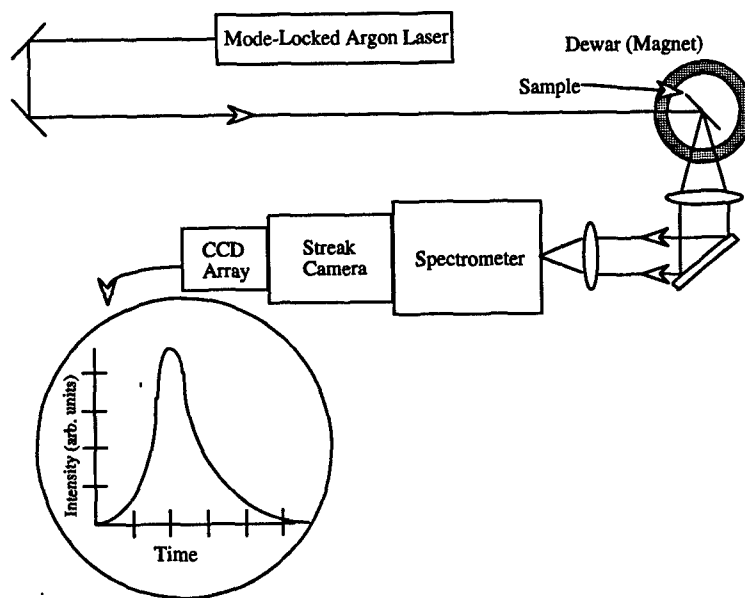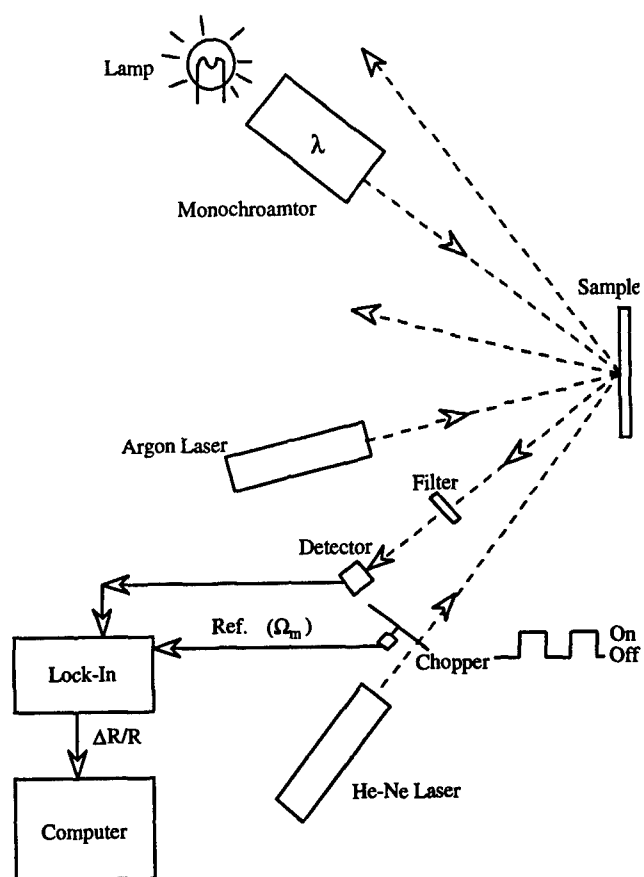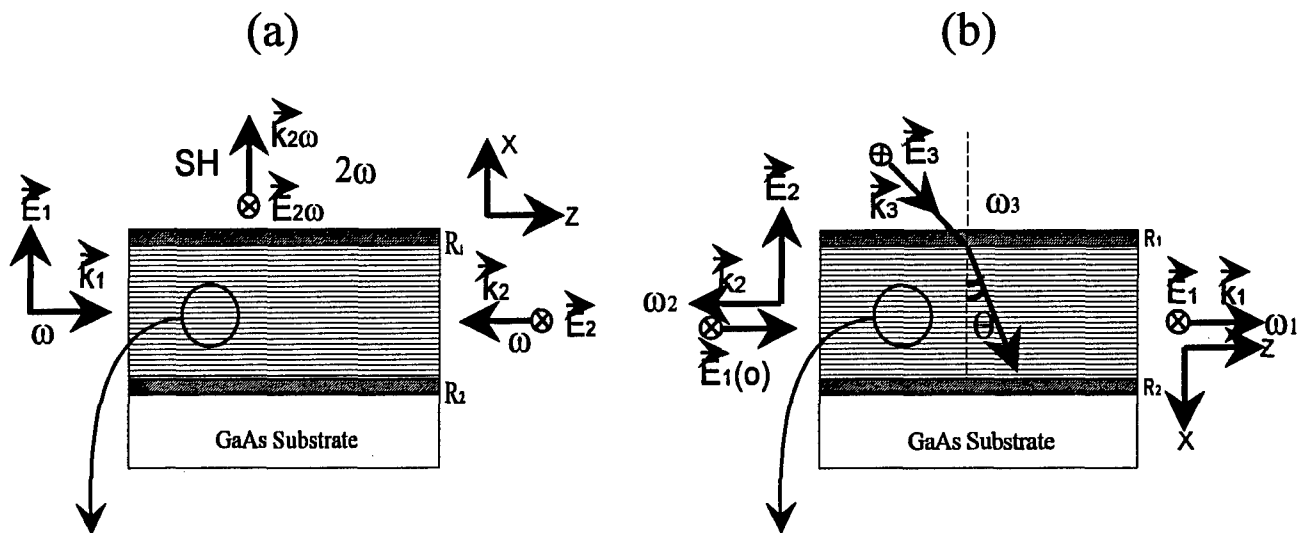
500 Å	GaAs	
550 Å	$Al_{0.5}Ga_{0.5}As$	} x 15
620 Å	AlAs	
1080Å	$Al_{0.4}Ga_{0.6}As$	} x 4
1240Å	AlAs	
550 Å	$Al_{0.5}Ga_{0.5}As$	} x 15
620 Å	AlAs	

(100) GaAs Substrate

(c)

Figure 3

12-16

Figure 4

Figure 5

12–18

Figure 6

e2

e1

hh1
hh2

$Al_{0.35}Ga_{0.65}As$

150
$Al_{0.35}Ga_{0.65}As$

65
GaAs

35

50
GaAs

150   Å
$Al_{0.35}Ga_{0.65}As$

a)

I = 186.7 W/cm²
I = 101.9 W/cm²
I = 76.4 W/cm²
I = 50.4 W/cm²
I = 25.5 W/cm²

T = 4 K

b)

c)

Figure 7

12–20
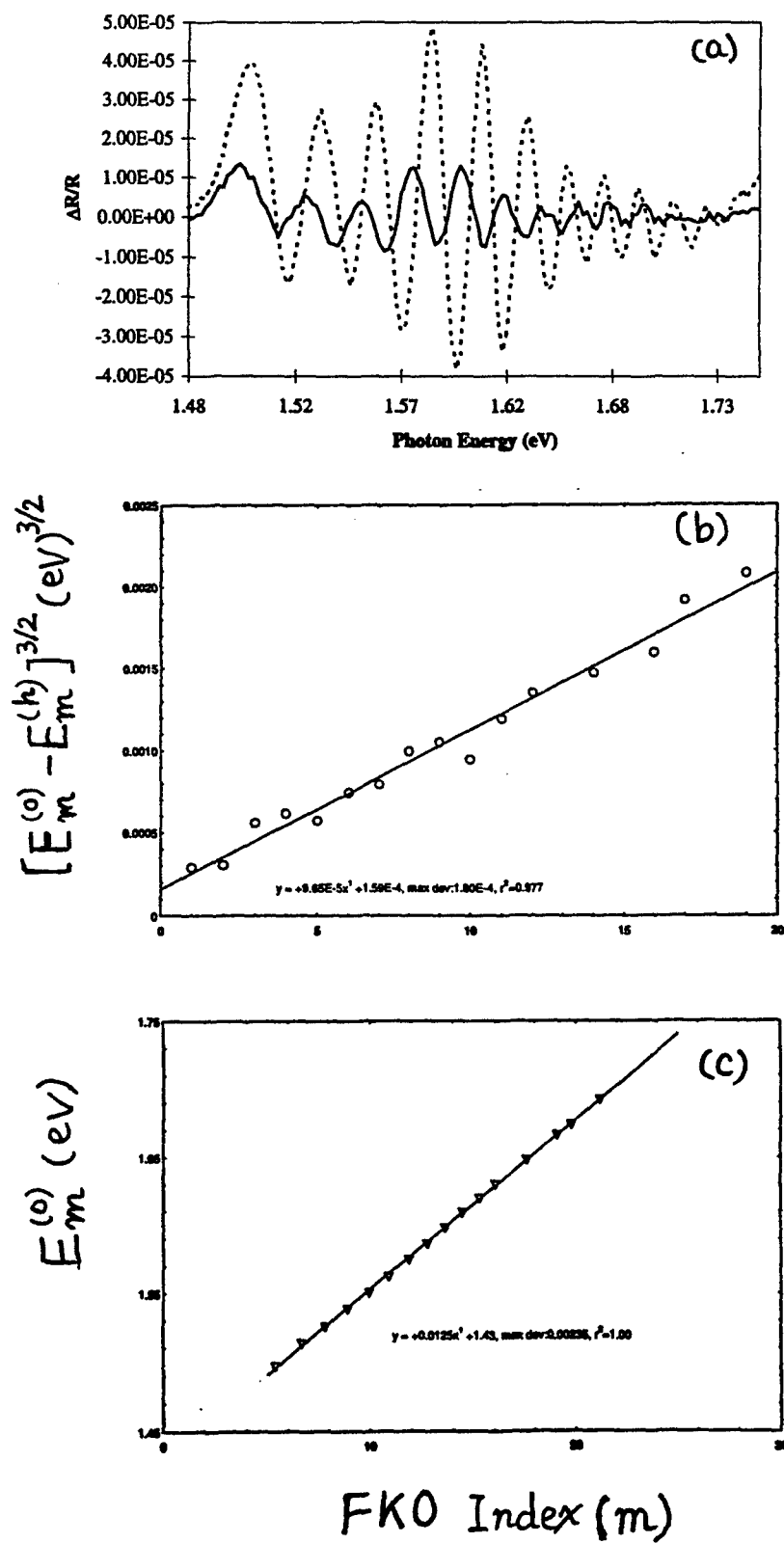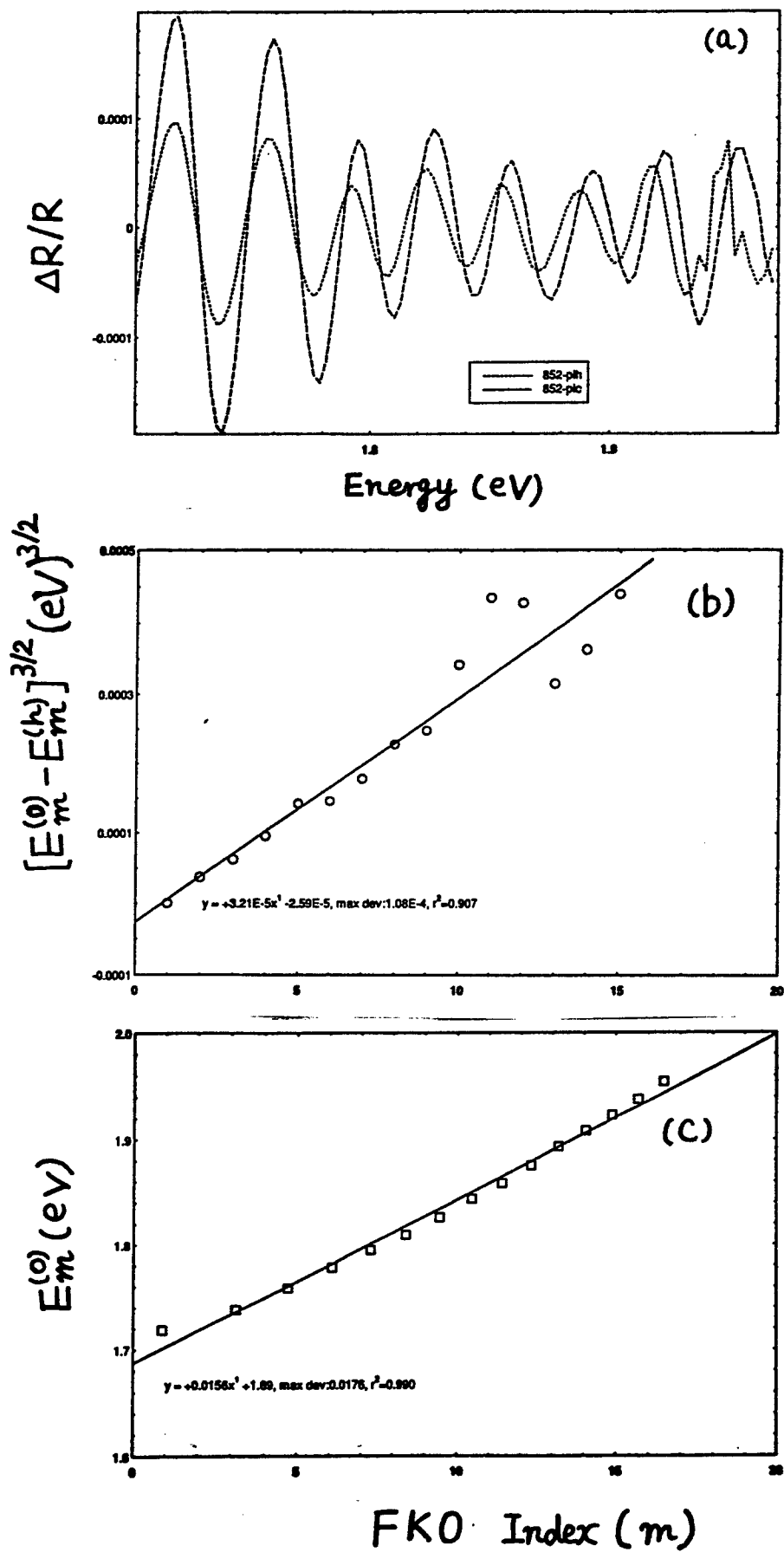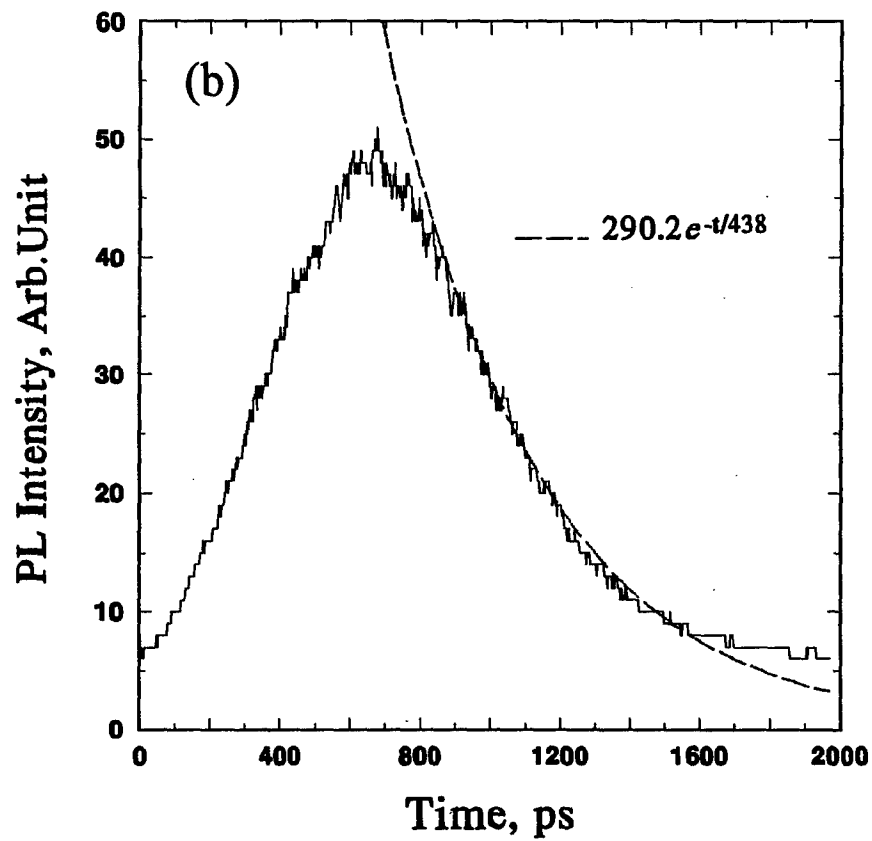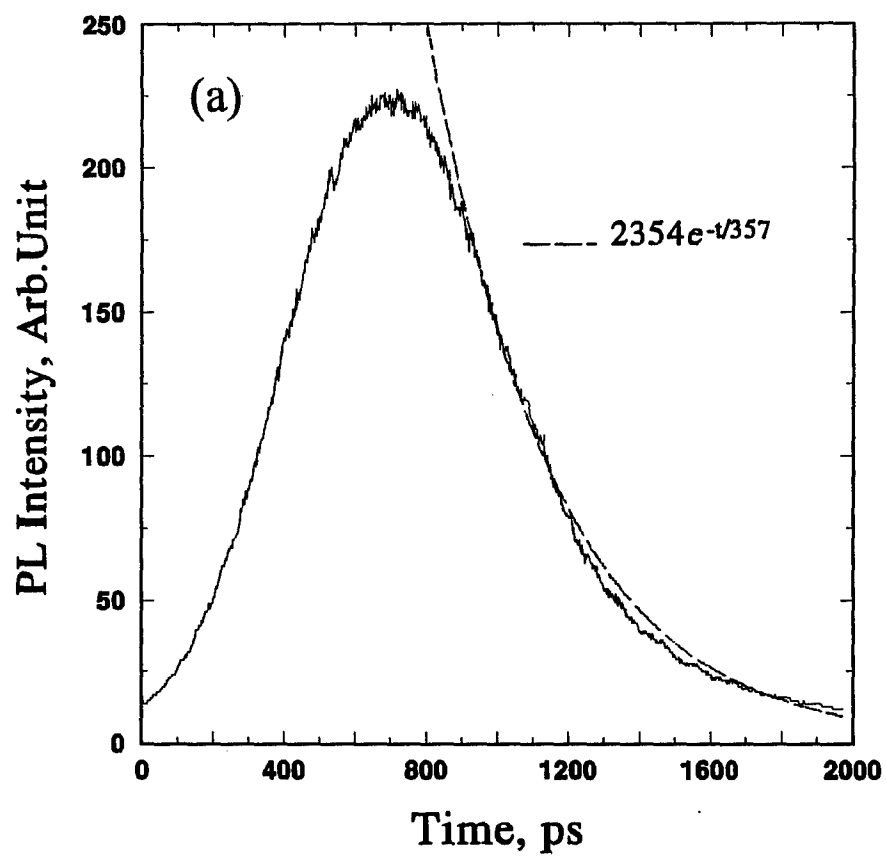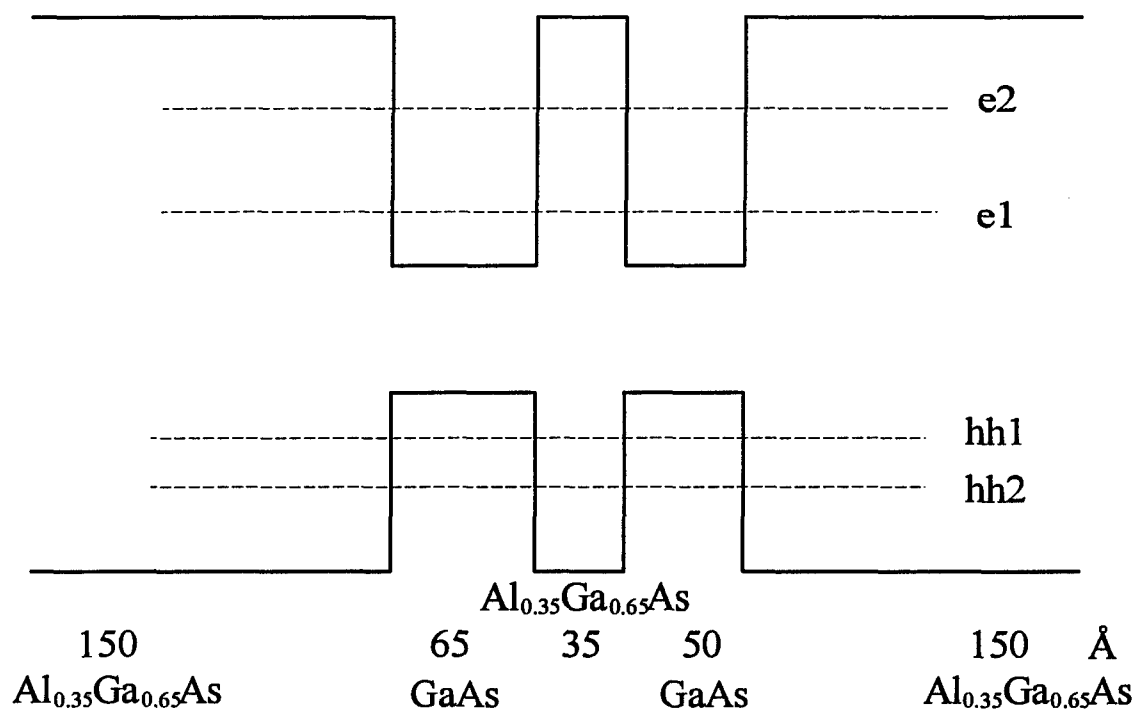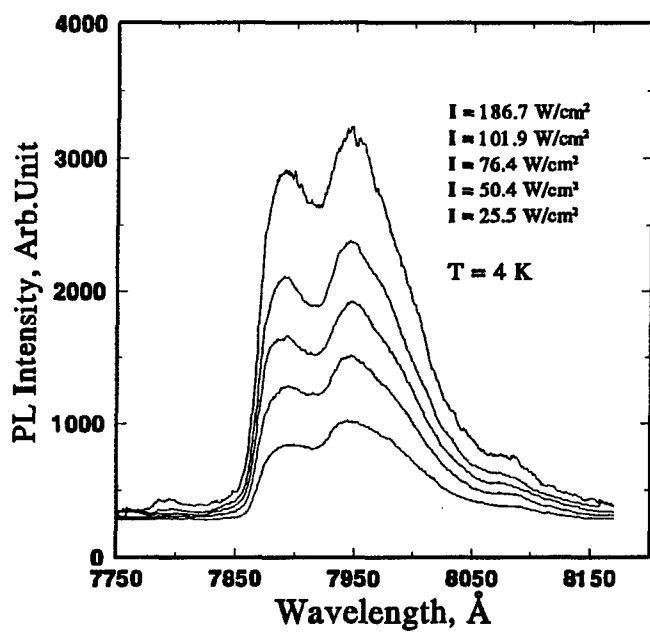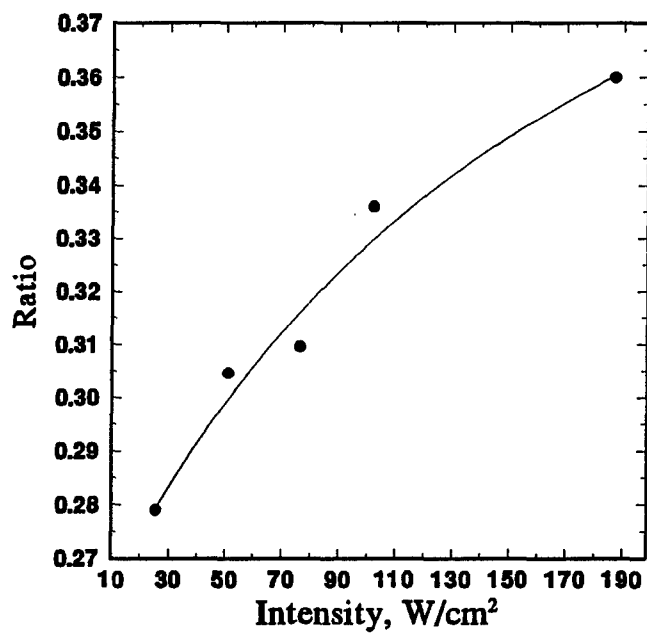
DAVID DOLSON

NO REPORT

ELECTRO-REFRACTION AND ELECTRO-ABSORPTION
IN POLED POLYMER FILMS

Vincent G. Dominic
Assistant Professor
Electro-Optics Program

Center for Electro-Optics
University of Dayton
300 College Park
Dayton, OH 45469-0245

ELECTRO-REFRACTION AND ELECTRO-ABSORPTION IN POLED POLYMER FILMS

Vincent G. Dominic
Assistant Professor
Electro-Optics Program
University of Dayton

Abstract

We developed and analyzed a new technique to simultaneously measure electro-refraction and electro-absorption in poled-polymer Fabry-Perot cavities. Both effects generally contribute to the measured signal from such material systems and we distinguish them by rotating the étalon and observing asymmetric peaks in our signal. We found the expected increase in both electro-refraction and electro-absorption as the probe wavelength approaches the absorption band of the chromophore. We also observed an oscillation in the electro-absorptive signal that we identified as multiple-étalon interference. This multiple-étalon interference artifact will pollute most of the standard electro-optic characterization techniques for poled-polymer films.

ELECTRO-REFRACTION AND ELECTRO-ABSORPTION
IN POLED POLYMER FILMS

Vincent G. Dominic

Introduction

Organic polymers for thin film optical devices are a very promising recent development in the field of nonlinear optics. Once the polymer sample has been poled to align the chromophores and remove the centrosymmetry then the system obtains an approximately permanent electro-optic nonlinearity. The low dielectric constant of polymer films and the fast response time of the nonlinearity are quite useful for opto-electronic applications requiring high-speed electro-optic switching or modulation. In addition to their speed, poled-polymer systems are much less expensive than lithium niobate ($LiNbO_3$) - the current electro-optic material-of-choice. Poled-polymers are also compatible with integrated circuit processing and manufacturing technology. The great promise of this technology has spurred tremendous interest in the recent past and many poled-polymer material systems and devices have been fabricated and tested. Current research focuses on just how permanent the induced nonlinearity is, especially at elevated temperatures (room temperature stability is generally not a problem). A second area of active research lies in developing chromophore/polymer systems with larger nonlinearities. In either case, a standard, reliable optical characterization technique is required to study the systems of interest.

Many standard measurement techniques determine the electro-optic activity of poled polymers including: Michelson and Mach-Zehnder interferometric techniques,[1,2] attenuated total reflection,[3,4] ellipsometric/reflection techniques,[5-10] and Fabry-Perot étalon modulation schemes.[11-13] All these methods have advantages and disadvantages in terms of optical stability constraints, difficulty in sample preparation, and required instrumentation. Our method is an extension of previous Fabry-Perot measurement methods: we fabricate much thicker étalons (millimeters instead of microns) by including the glass substrate within the cavity. This allows us to easily measure not only the usual electro-optic (electro-refractive) contribution to the signal but also the electro-absorptive contribution as well. The experimental setup is conspicuously simple and interpretation of the results is straightforward. The sample preparation is also simple because we use the air/glass interface as one of the mirrors in our cavity. Thus we can switch the sample into a Mach-Zehnder or ellipsometric/reflection setup to verify our measurements.

In the past, poled-polymer investigations generally concentrated on the electro-refractive effect since most proposed devices are phase controlled. Relatively few papers discuss the concurrent electro-

absorption effect.[7-9,13-18] We distinguish in this paper between the field-induced change in the refractive index Δn which we call electro-refraction (ER) and the field-induced change in the absorption $\Delta \alpha$ which we call electro-absorption (EA). The total change in the material's optical properties is referred to as the electro-optic (EO) effect. One method to increase the electro-optic coefficient is to utilize the well-known resonant enhancement of electro-refraction near the chromophore absorption band.[9,19] Unfortunately this enhancement is accompanied by increased electro-absorption which must then be considered in the electro-optic characterization technique. One might significantly over- or under-estimate the electro-optic coefficient if electro-absorption is ignored. We also found that unwanted surface reflections gave signal asymmetries that might be incorrectly interpreted as electro-absorption. We develop a simple model to show how multiple étalons produce pure electro-refractive signals that interfere to give the appearance of electro-absorption. By measuring the dispersion of both the electro-refractive and electro-absorptive signal components we can readily separate the spurious effect (which oscillates with wavelength) from the real underlying wavelength dependence of the material behavior.

Experimental Arrangement

This paper describes a wonderfully simple experimental technique that measures the field-induced change in both the refractive index and the absorption. References 7-9 and 17-18 describe techniques that make the same determination, but not with the simplicity of our method. When a new polymer/chromophore system is developed, it is prudent to fabricate simple samples to determine the usefulness (size of the EO coefficient) of the new system. One of the simplest ways to make new samples is to spin-coat a solution of the desired polymer onto a microscope slide. We start with a glass slide that is coated on one side with ITO that forms a transparent conducting electrode. The ITO is masked and etched to give a narrow stripe that extends the length of the slide. The polymer/chromophore layer is then spin-coated onto the slide to a thickness of ≈ 2 μm. After allowing the film to dry in air overnight (to remove most of the solvent), the slide is placed inside a vacuum oven at slightly elevated temperature ($\approx 70°C$). After this drying, a thin film of gold is coated on top of the polymer with the gold stripe perpendicular to the ITO stripe. The gold will serve as both an electrical connection and an optical mirror. The structure of a typical substrate/ITO/polymer/gold sandwich sample is shown in Fig. 1. The polymer is contact poled by raising the temperature to near the glass transition and applying a dc field of ≈ 100 V/μm. Upon cooling the sample in the presence of the field the polar alignment of the chromophore molecules is retained and the sample is electro-optically active. The ITO and gold electrodes overlap in a small 25 mm^2 rectangular region and the polymer is only poled in this region. All of the data below was gathered using a golden yellow colored sample supplied by the Dow Chemical Company and labeled TP86.
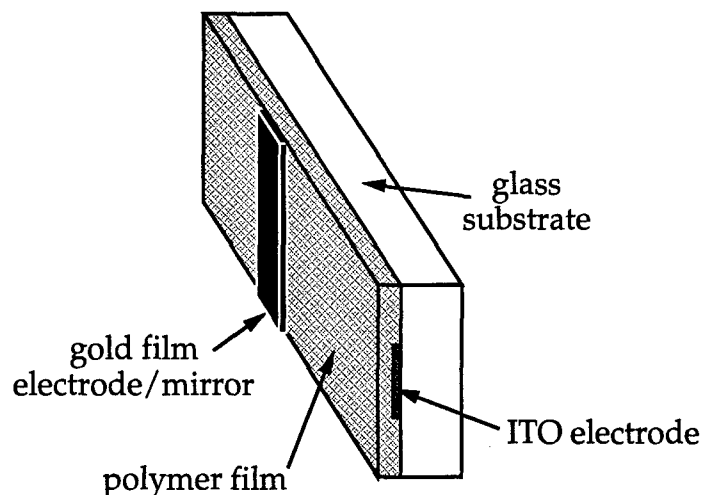
Figure 1)   Schematic view of the generic poled-polymer bulk sample geometry. The dimensions are inaccurate in the figure since the substrate is typically ~1 mm thick, the ITO ~60 nm thick, the polymer ~2 μm thick, and the gold ~35 - 50 nm thick. Note that the ITO electrode runs the entire length of the glass slide so that the poled region lies in the region where the ITO and gold electrodes cross.

Figure 2 shows the simple geometry for our experiment. We pass a laser beam through the poled region of the sample and loosely focus the transmitted light onto a photodiode. The gold and ITO serve as modulation voltage contacts whereas the gold and air/glass interface provide the mirrors for our Fabry-Perot cavity. A sinusoidal voltage (±16 V, 5kHz) applied across the ≈2 μm thick polymer layer induces refractive index and absorption changes in the sample. A Stanford Research SR530 lockin amplifier measures both the average and time-varying (*1f*) components of the transmitted light signal while a controlled actuator slowly rotates the sample through ±2.5° (0° = normal incidence). We are careful to insure that the rotational axis is centered on the incidence spot so that the beam does not translate across the poled region as the sample rotates. This is important because the spin-coating process results in a polymer layer with varying thickness and sub-wavelength thickness variations strongly affect a Fabry-Perot's throughput. The input beam is vertically polarized so that we measure the $\tilde{r}_{13} = r_{13} + i\,s_{13}$ component of the complex electro-optic coefficient. (using the notation of ref. 7). The incidence angle is small enough so that we may safely ignore the contribution of the $\tilde{r}_{33}$ component even if we choose to utilize horizontally polarized light.
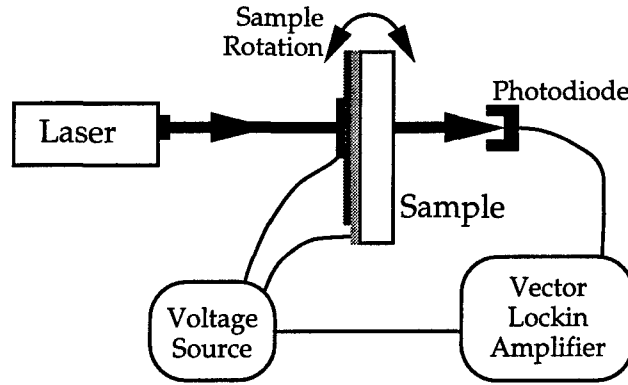
Figure 2) Schematic drawing of the experimental setup. The sample is mounted on a motorized rotation stage and the rotation axis is centered on the incidence spot within the poled region. A photodiode monitors the laser transmission through our poled-polymer Fabry-Perot structure. The sample consists of the following layers: gold electrode/mirror, polymer layer, ITO contact, and the glass substrate. A computer (not shown) controls the sample rotation and acquires the data.

Simple Model

Let us, for the moment, ignore some of the reflecting surfaces in our sample and model the sandwich structure as being composed of only two reflecting surfaces: the gold film and the air/substrate interface. The étalon thickness includes the electro-optically active polymer layer, the ITO and the glass substrate. We label the surface reflectivities and transmisivities r_i, t_i ($i = 1,2$) and we denote the refractive indices of the glass and polymer as n_g and n_p, respectively. Because of our chosen polarization we use the ordinary refractive index of the polymer $n_p = n_o$. The layer thicknesses are L_g and L_p and we assume that the glass substrate has no absorption at any of the wavelengths of interest. The ITO is very thin compared to either the polymer or the glass layer and is therefore ignored in this simple model. We can show that the intensity transmission of this simplified Fabry-Perot étalon is:

$$I_{trans} = \frac{I_{inc} \, e^{-\alpha_p \, L_p} \, (t_1 \, t_2)^2}{\text{denom}}$$
(1a)

where:

$$\text{denom} = \left(1 - r_1 \, r_2 \, e^{-\alpha_p \, L_p}\right)^2 + 4 e^{-\alpha_p \, L_p} \, r_1 \, r_2 \sin^2(\delta/2),$$
(1b)

α_p is the absorption in the polymer and:

$$\frac{\delta}{2} = \frac{2\pi}{\lambda}\left\{L_g \sqrt{n_g^2 - \sin^2\theta_i} + L_p \sqrt{n_p^2 - \sin^2\theta_i}\right\}$$
(2)

with the wavelength λ and the external angle of incidence θ_i

The applied modulation voltage induces a change in both n_p (the electro-refractive effect) and α_p (the electro-absorptive effect). In the case were the absorption is reasonably small such that $\alpha_p \lambda \ll 1$, we can use the results of Clays and Schildkraut[7] to show that the field-induced perturbations Δn_p and $\Delta \alpha_p$ may be written in terms of the real and imaginary parts of the complex electro-optic coefficient $\tilde{r}_{13}$:

$$\Delta n_p = -\frac{1}{2} n_p^3 r_{13} E_\Omega \tag{3a}$$

and:

$$\Delta \alpha_p = -\frac{2\pi}{\lambda} n_p^3 s_{13} E_\Omega \tag{3b}$$

where E_Ω is the applied modulation field.

The differential change in the transmitted intensity caused by the field-induced modulation Δn_p and $\Delta \alpha_p$ is:

$$\Delta I_{trans} = -\frac{I_{trans}}{\text{denom}} \left\{ \begin{array}{l} \left(\Delta \alpha_p L_p\right)\left(1 - r_1 r_2 e^{-\alpha_p L_p}\right)\left(1 + r_1 r_2 e^{-\alpha_p L_p}\right) \\ + 4 r_1 r_2 e^{-\alpha_p L_p} \sin\delta \, \frac{2\pi}{\lambda} \frac{\Delta n_p \, n_p \, L_p}{\sqrt{n_p^2 - \sin^2 \theta_{inc}}} \end{array} \right\}. \tag{4}$$

Equations 1 and 4 provide a theoretical model to fit the measured data. Notice that once we utilize Eqn. 1 to fit the dc signal measured by the photodiode, all the parameters except Δn_p and $\Delta \alpha_p$ are determined. Both Δn_p and $\Delta \alpha_p$ contribute to the $1f$ lockin signal because they vary linearly with the applied sinusoidal voltage (Eqn. 3):

$$E_\Omega = \frac{V_\Omega}{L_p} \cos\Omega t = \frac{V_\Omega}{L_p} \cos 2\pi f t. \tag{5}$$

We verified the linear dependence of the electro-refractive and electro-absorptive perturbations with applied modulation voltage. We ignore the electro-strictive, electro-mechanical, and the Kerr effects because they would appear as $2f$ signals on the lockin (they vary as $|E_\Omega|^2$). The piezoelectric effect (ΔL_p) sometimes pollutes electro-optic measurements and the equations above give no account of it. However, inspection of the equations will show that the functional form of the piezoelectric effect is precisely the same as Eqn. 4 but with the Δ shifted to the L_p in both the terms in braces. Because of the large numerical factor $2\pi/\lambda$ in the second term in braces, the piezoelectric effect will have essentially the same angular dependence as the electro-refractive term Δn_p. Thus the asymmetry demonstrated below cannot be caused by the piezoelectric effect and any piezoelectric pollution of our signal will only affect the electro-

refraction results and not the electro-absorption results. Moreover, we used a Michelson interferometer with the gold film as one of the retroreflecting mirrors (the light did not pass through the polymer layer). In this orientation field induced perturbations in the refractive index and absorption cannot contribute to the signal but a voltage dependent thickness variation will produce a signal. We observed no evidence of piezoelectricity in our sample.

Notice that the angular dependence of the electro-absorptive term is determined by the variation of I_{trans} whereas the electro-refractive term varies according to $I_{trans} \sin \delta$. This gives a strong asymmetry to the magnitude of the lockin signal peaks as the incidence angle changes such that δ shifts by $\approx \pi$. If we re-write Eqn. 1b as:

$$\text{denom} = 1 + \left(r_1 r_2 e^{-\alpha_p L_p} \right)^2 - 2 e^{-\alpha_p L_p} r_1 r_2 \cos \delta \tag{6}$$

then because of the $\cos \delta$ term, the transmitted intensity is at the mid-visibility point of the Fabry-Perot resonance when δ is approximately $\pi/2$ or $3\pi/2$. At both these points, labeled A and B in Fig. 3 below, the electro-absorptive (EA) contribution to the lockin signal is the same (magnitude and sign) whereas the electro-refractive (ER) signal is of equal magnitude but opposite sign. We illustrate this behavior in Fig. 3. At point A we have constructive interference (the ER & EA signal components add) while at point B we have destructive interference (the ER & EA signal components subtract).
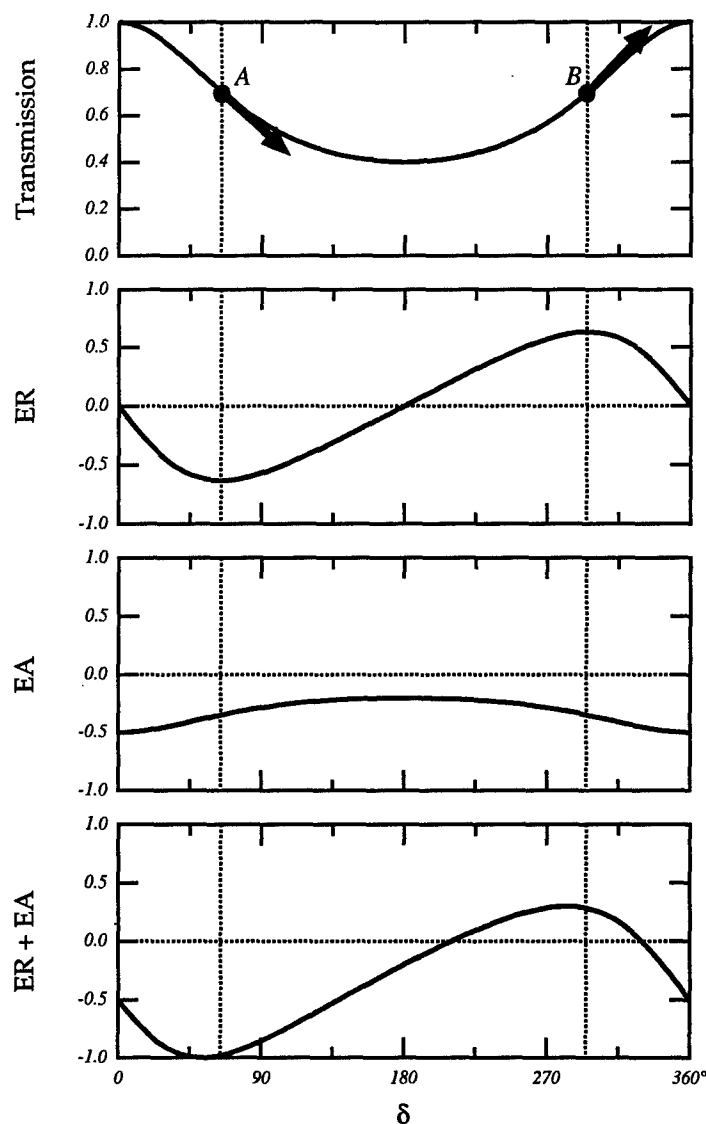
Figure 3) This figure shows how the electro-refractive (*ER*) signal and the electro-absorptive signal (*EA*) interfere to give an asymmetric response as the Fabry-Perot structure is rotated. Part (a) shows the low finesse ($\mathcal{F} = 1.5$) transmittance variation with δ and indicates two points where the *ER* signal magnitude is maximized. The arrows indicate how a positive Δn affects the transmittance. Part (b) shows the expected *ER* response (positive Δn) while part (c) shows the *EA* response (positive $\Delta \alpha$). The total signal, *ER+EA*, in part (d) displays a strong asymmetry.

Experimental Results

Figure 4 displays the angular variation of the average photodiode signal along with the magnitude of the *1f* lockin signal as we rotate the poled-polymer Fabry-Perot. The data are represented by dots and the theoretical curve fits using Eqns. 1 and 4 are displayed as solid lines. The average signal shows the expected low-finesse Airy function behavior. According to the simple model discussed above, there is no

14-9

electro-absorptive contribution to the modulation signal because the positive and negative peaks of the lockin signal are of equal magnitude. The signal variation with incidence angle is shaped as one would expect for the purely electro-refractive electro-optic effect. The advantage of our thick étalon (mm) versus the thin (μm) étalons studied previously[11,12] is the appearance of many resonances even while tuning over small angles (±2.5°). This gives ample data to precisely determine the Δn variation here. We analyze our data sets by first using Eqn. 1 to fit the average signal variation as the étalon is rotated. This is a three parameter fit where the incident power, the gold reflectivity, and the thickness of the polymer are allowed to vary. We only vary the polymer thickness by $\pm\lambda$. After fitting the average photodiode signal, we hold all parameters fixed except Δn and $\Delta\alpha$ to fit the lockin signal variation. Since one of our mirrors has low reflectivity, the finesse of our cavity is only ≈1.37.
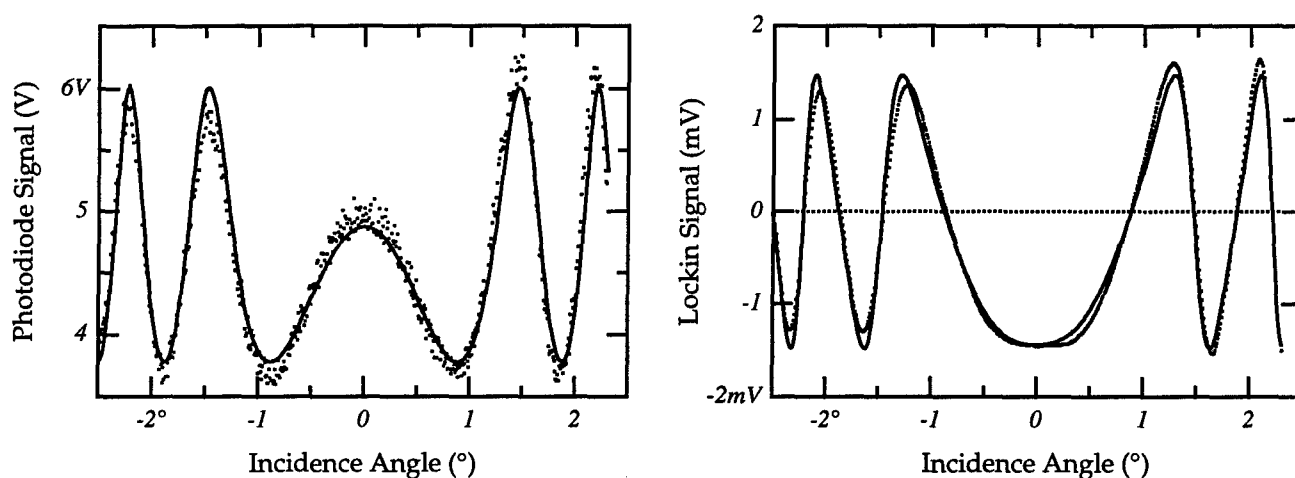
Figure 4)   (a) Average photodiode signal and theoretical fit (dots=data, line=fit) as the étalon is rotated with λ = 604.8 nm. (b) Lockin signal dependence on the incidence angle with the raw data (dots) and the theoretical fit (solid line). The average signal shows the expected low-finesse étalon behavior and the lockin signal displays symmetric peaks that reach their maximum where the slope of the average signal is highest.

If we now tune the probe laser to λ = 594.1 nm then the appearance of the lockin signal variation is dramatically altered. According to the simple model, the asymmetry of the modulation signal apparent in Fig. 5a is the signature of the electro-absorptive effect interfering with the electro-refractive effect. Such asymmetric peaks in the modulation signal on either side of an étalon resonance are also apparent in the data of C. H. Wang et al.[13] These authors utilized a Fabry-Perot at normal incidence and scanned the wavelength (rather than the incidence angle) to study the étalon resonance behavior. Also, note that asymmetric electro-optic signals were reported by Norwood et al.[2] in Mach-Zehnder interferometric measurements and attributed to rf pickup or intensity modulation in the film. We have shown that electro-absorption can also be responsible for such asymmetries, as has been observed by others.[17,18]

If we tune the laser even closer to the absorption edge of the chromophore then the lockin signal never flips sign and the electro-absorption completely dominates the measurement.[13] We illustrate this in Fig. 5b below where we utilized a probe laser wavelength of $\lambda = 543.5$ nm on our golden yellow sample whose absorption edge lies at approximately $\lambda = 520$ nm. Notice that the lockin signal never decreases to zero (compare to Fig. 4b, 5a).
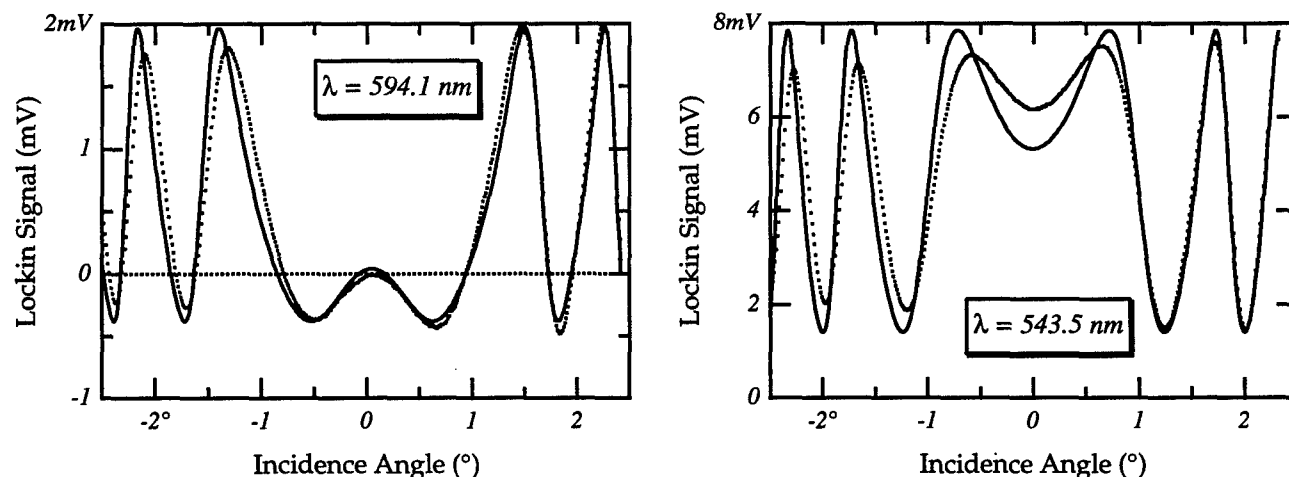
Figure 5) (a) Lockin signal variation as the étalon is rotated in a $\lambda = 594.1$ nm probe beam. The peaks of the lockin signal are quite asymmetric with the positive excursion about four times larger than the negative excursion. (b) Lockin signal dependence on the incidence angle at $\lambda = 543.5$ nm. In this case the signal never crosses zero and electro-absorption completely dominates the measurement. In both (a) and (b) the dots are raw data and the solid curve is the theoretical fit. The average signals incident on the photodiode are not shown here, but they once again displayed low-finesse étalon behavior much like Fig. 4a.

If we continue to use our tunable HeNe laser to measure the dispersion of the complex electro-optic coefficient, then we find the dependence illustrated in Fig. 6. Notice that both the electro-refractive (ER) and electro-absorptive (EA) contributions to the signal increase dramatically as the probe wavelength approaches the edge of the chromophore absorption band. This behavior is generally expected in terms of two-level models, such as those developed in refs. 9 and 19. Curiously, the measured EA coefficient switches sign at a probe wavelength of $\lambda = 612$ nm which is difficult to explain since the chromophore absorption monotonically decreases for wavelengths longer than $\lambda = 520$ nm. In fact, further investigations revealed that the EA coefficient magnitude varied and switched sign as we moved the probe beam to different spots within the poled region. We know that the spin-coating process creates layers of nonuniform thickness across the substrate and we believe that the variation of the EA coefficient with position is an artifact of this thickness variation. The electro-optic coefficient represents a fundamental property of the material and should be independent of the sample thickness. The actual electro-absorption at this wavelength is very small and we show below that multiple étalons within the sample lead to asymmetric lockin signal peaks that are incorrectly interpreted as the EA effect in Fig. 6.

The erratic behavior of the *EA* coefficient at this wavelength occurs because the multiple étalon interference is very sensitive to small thickness variations.
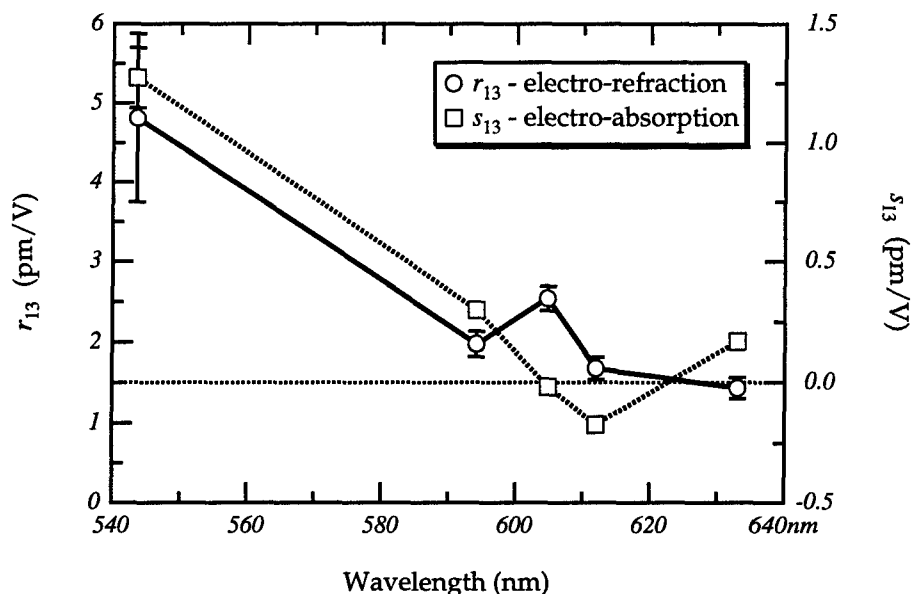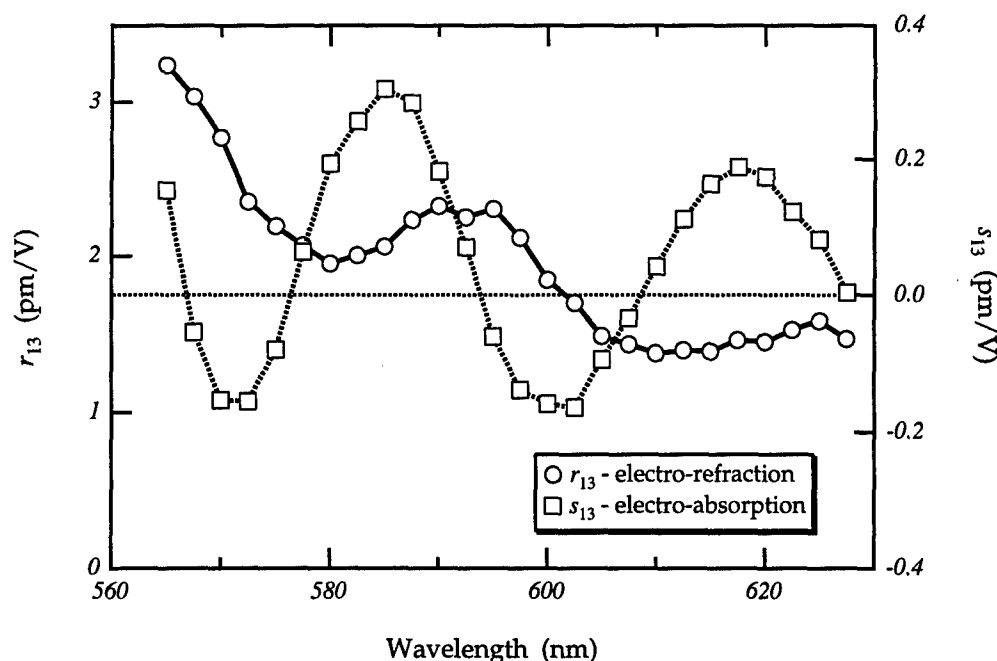

Figure 6)   Dispersion of the electro-refractive r_{13} and electro-absorptive s_{13} effects measured with a tunable HeNe laser. Notice that the electro-absorption changes sign near 612 nm. The sample (labeled TP86) was supplied by the Dow Chemical Company. The error bars represent confidence intervals derived from the fitting algorithm and are, in some cases, smaller than the graphic symbol. Both effects increase rapidly as the probe wavelength approaches the chromophore absorption band. The longer wavelength data is polluted by multiple reflections that give the appearance of electro-absorption.

To better understand the multiple étalon problem, we re-measured the electro-optic dispersion of the TP86 sample with a tunable dye laser. We pumped a rhodamine-6G dye with an argon laser to achieve tunability of the probe wavelength over the range λ = 565 nm - 627.5 nm. Figure 7 shows the wavelength dependence of the real and imaginary parts of the complex electro-optic coefficient $\tilde{r}_{13}$, determined at 2.5 nm intervals. Notice that the imaginary part (*EA*-component) shows a clear periodic variation with a period of $\approx$42 nm. This variation is unphysical based on the monotonic decrease of the absorption over this wavelength band and will be shown to be due to the spurious interference effects. Note that the sinusoidal variation of the *EA* component is superimposed on a curve that decreases at longer wavelengths. The absorbance spectra (measured with a Perkin-Elmer spectrophotometer) of this sample shows a monotonically decreasing absorbance for wavelengths λ < 520 nm. The oscillation period in the imaginary part of the electro-optic coefficient corresponds to an étalon with the thickness and refractive index of the TP86 polymer:

$$\Delta\lambda = \lambda^2/(2 n_p L_p) = 43 \text{ nm} \tag{7}$$

where the measured parameters are L_g = 2.55 μm and n_p = 1.7.

Figure 7) Dispersion of the electro-refractive r_{13} and electro-absorptive s_{13} effects of TP86 measured with a tunable dye laser. Notice that both the electro-absorption and the electro-refraction periodically oscillate. Both components of the total electro-optic coefficient seem to be superimposed on curves that increase at shorter wavelengths. The oscillation behavior is an artifact caused by unwanted surface reflections. The true behavior of the *ER* and *EA* coefficients is believed to be contained in the underlying monotonic increase at shorter λ.

The various Fabry-Perot cavities contained in our sample are shown in Fig. 8. The unwanted reflectivity of the polymer/ITO/substrate interface is ignored in most analyses and gives rise to the unphysical, oscillatory contribution to the fitted *EA* coefficient s_{13}. Étalon 3 is the primary étalon discussed in the "Simple Model" section above. The thickness of étalon #1 is approximately equal to the polymer thickness and the transmissivity of this étalon will remain essentially constant over the narrow angular range probed in our experiments because the étalon is so thin. Therefore, the electro-refractive signal from this étalon by itself remains constant as the sample rotates by ±2.5°. By contrast, the electro-refractive signal from étalon #3 contains several resonant peaks as the incidence angle varies. The electro-refractive signal (#3) switches sign on either side of a resonance and therefore the signal from étalons #1 and #3 will add constructively/destructively on either side of a resonance. Notice that étalon #2 will contribute nothing to the modulated signal since the spacer layer (glass) is inactive. The interference of the two electro-refractive signal components (étalon #1 and #3) will again give asymmetric peaks to the lockin signal.

Thus, the interference of all the different surface reflections can give a signal that appears to be electro-absorption but in fact is not. This point has been carefully explored and explained by the authors

of refs. 8 & 9 in the context of the ellipsometry/reflection geometry frequently used to measure the electro-optic properties of poled polymers. This effect might also be the source of the asymmetric signals observed in the Mach-Zehnder experiment of ref. 2. The importance of this multiple reflection effect must be emphasized: most of the common electro-optic characterization techniques (Fabry-Perot, ellipsometry/reflection, Mach-Zehnder) for polymer thin films are susceptible to pollution when multiple reflections are present. The popular method of Teng & Man[5] is certainly affected (ref. 7-9) and one should be careful in interpreting the coefficients reported without accounting for this spurious effect. With respect to the dispersion measurements shown in our Fig. 6, near the absorption band ($\lambda = 543.5$ nm) the signal is definitely dominated by electro-absorption. The unwanted surface reflection seems to give a periodic oscillation in s_{13} with a magnitude of ≈ 0.2 pm/V. The EA coefficient is considered unpolluted when $s_{13} \gg 0.2$ pm/V. We conclude that the data shown in Fig. 7 contains both the artificial oscillation from multiple-étalon interference **as well as** a real electro-absorptive effect that increases at the shorter wavelengths.
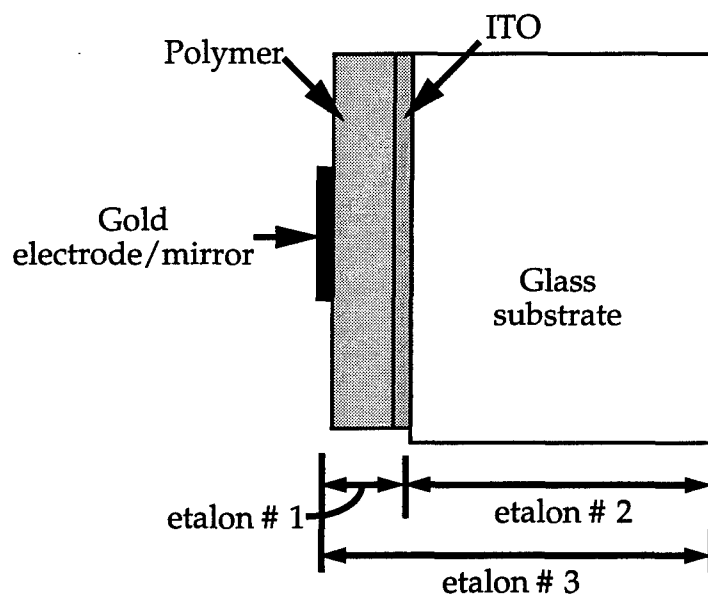
Figure 8) Schematic diagram showing the three different Fabry-Perots included in the model. Notice that we are not completely treating the ITO layer since we simply treat it as a partially reflecting interface with not thickness. We make this approximation because the layer is so thin.

More Complicated Model

Multiple étalon interference is best handled using the method described in chapter 4 of Heavens book.[20] First we find the transmission and reflection coefficients for the last two layers of the sample as if they were the only layers present. The reflectivity of the jth layer is:

$$r_{j,j+1} = \frac{r_j + r_{j+1}\, e^{i\delta_j}}{1 + r_j\, r_{j+1}\, e^{i\delta_j}} \tag{8}$$

where:

$$\delta_j = \frac{4\pi}{\lambda}\, n_j\, L_j \cos\phi_j \tag{9}$$

and n_j, L_j, & ϕ_j are the refractive index, thickness, and propagation angle in the jth layers The transmissivity is:

$$r_{j,j+1} = \frac{t_j\, t_{j+1}\, e^{i\delta_j/2}}{1 + r_j\, r_{j+1}\, e^{i\delta_j}} \tag{10}$$

where the t's are the Fresnel transmissivities of the surfaces. Once we find the field reflectivity and transmissivity of the jth layer we replace this layer by an effective surface having the properties dictated by Eqns. 8 and 10. We iterate this process until all layers are included.

In our model we again ignore the thickness of the ITO layer. We do, however, include its reflectivity and this gives us a three reflecting surfaces as illustrated in Fig. 8. Only the polymer layer is electro-optically active. We developed a numerical model to predict the wavelength dependence of the electro-optic signal from the coupled Fabry-Perot cavities. In this model there is no electro-absorptive contribution to the signal. We predict the angular dependence of the lockin signal with this multiple étalon model and then fit the data with the equations governing the interference of electro-refraction and electro-absorption (Eqns. 1 and 4). The functional fits to the model data are quite good. The coupled Fabry-Perot curve prediction (with **no electro-absorptive contribution** $\Delta\alpha = 0$) look almost identical to the curve fits using Eqns. 1 and 4. We then vary the wavelength of the probe beam and re-run the simulation. A summary of the results of our simulations is shown in Fig. 9. The fitted electro-absorptive coefficient oscillates with a period of ≈ 42 nm. This shows that the apparent oscillation of the *EA* coefficient in Fig. 7 above is indeed caused by multiple étalon effects and not by real variations of the coefficient.
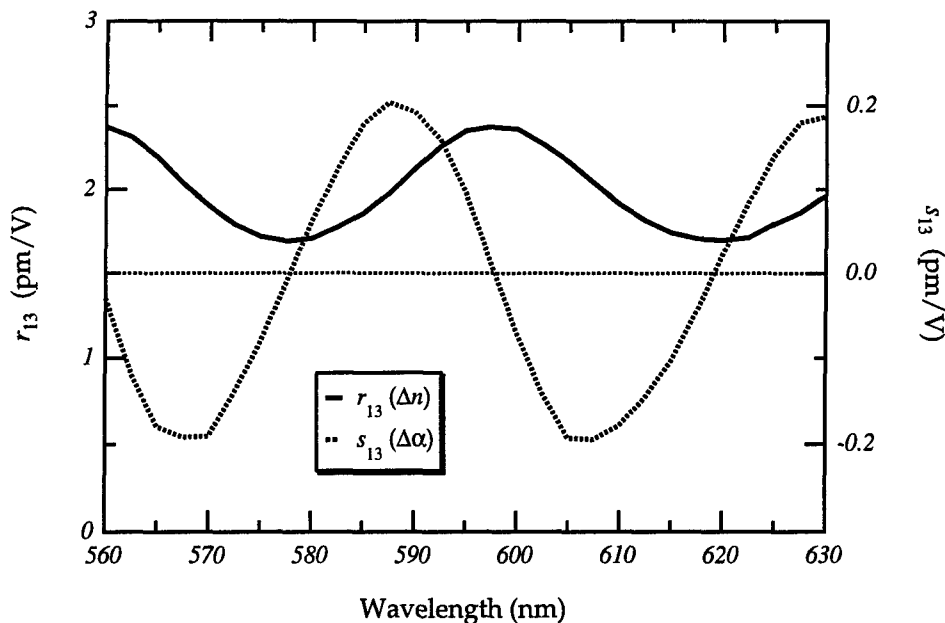
Figure 9) We generate sample data with a model that includes three reflecting surfaces in a sandwich structure and pure electro-refraction (**no** electro-absorption) in the polymer layer. We then fit the predicted variation vs. incidence angle with the function that assumes that we have a single étalon that exhibits both *ER* and *EA* effects. Both the real and imaginary parts of the complex electro-optic coefficient oscillate with a period of ≈ 42 nm. The imaginary part s_{13} changes sign and has an average value of zero. The average value of r_{13} is 2 pm/V which was the assumed *ER* coefficient of the polymer in the model. The field reflectivities are 0.2, 0.08, & 0.7 for the air/glass interface, the glass/ITO/polymer interface, and the gold layer, respectively. Notice that a reflectance as low as 0.6% from the ITO layer gives the appearance of electro-absorption that can be as large as 0.2 pm/V.

If we probe the TP86 sample with a wavelength of $\lambda = 612$ nm we expect very little contribution from electro-absorption since this wavelength is so far from the chromophore absorption edge. However, we did in fact observe asymmetric peaks in the lockin signal as shown in Fig. 10. We can fit this dependence with either the model that uses one étalon and both electro-absorption and electro-refraction within the polymer or the model that includes multiple étalons but only electro-refraction in the polymer layer. The functional fits are equally satisfactory as shown by parts (a) and (b) of Fig. 10. Because both models yield extremely nice predictions of the signal dependence on incidence angle it will be difficult to combine all effects into a single comprehensive model since the two concepts will compete to fit the asymmetry. We believe that a better approach is to increase the finesse of our primary cavity and so decrease the importance of the unwanted surface reflection. We are currently pursuing this idea. An alternative approach is to ignore oscillations in the imaginary part of the electro-optic coefficient on the order of 0.2 pm/V. Certainly, when s_{13} is much greater than 0.2 pm/V one can safely conclude that the asymmetry in the lockin signal arises from electro-absorption and is not an artifact of the spurious étalons present in the sample.

14-16
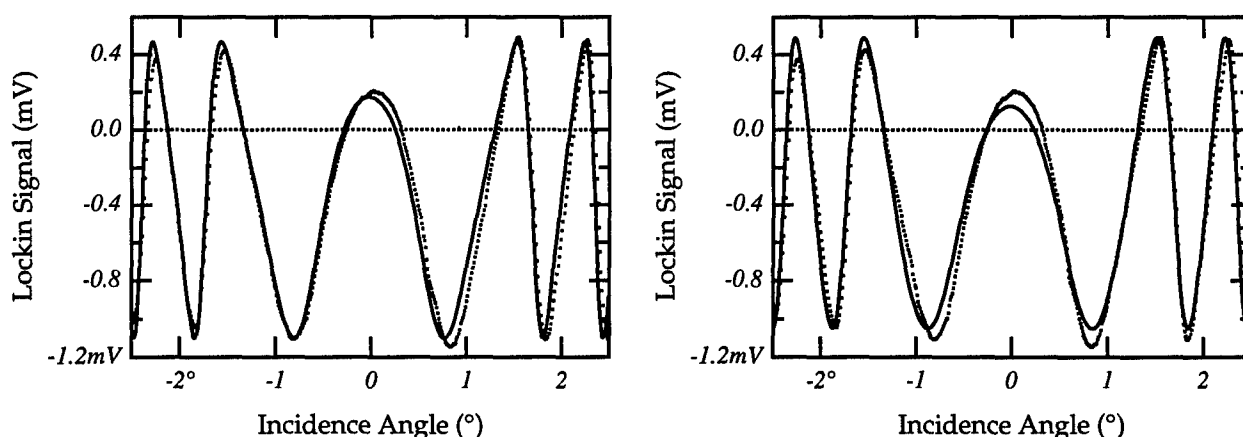
Figure 10) (a) At a probe wavelength of $\lambda = 612$ nm (tunable HeNe) we find an asymmetric lockin signal that is well fit by the functions based on the interference of the *ER* & *EA* effect. (b) Here the same data is also well fit by considering three reflecting surfaces (the field reflectivities are as given in Fig. 9 caption) and only electro-refraction in the polymer layer (**no** electro-absorption).

Conclusions

We use Fabry-Perot étalons with electro-optically active spacer layers to modulate the transmitted signal via both electro-refraction Δn and electro-absorption $\Delta\alpha$. As we rotate the étalon with a controlled stage the dependence of the modulated light signal determines the complex electro-optic coefficient $\tilde{r}_{13}$. The beauty of this method is its simplicity and the fact that strong electro-absorption ($s_{13} \gg 0.2$ pm/V) is immediately recognized by asymmetric modulation signals with unequal peaks on either side of a Fabry-Perot resonance. Unfortunately, multiple (>2) surface reflections cause spurious effects in our experiments that masquerade as electro-absorption. This multiple étalon effect is rather difficult to avoid since reflectances as low as 0.6% can produce it. The unwanted étalon problem can appear not only in Fabry-Perot experiments but also ellipsometry/reflection and Mach-Zehnder experiments. We regard with caution results that don't properly account for this spurious effect. We are currently working to overcome the spurious effects by coating the air/glass interface to increase its reflectivity. In this manner we can increase the finesse of the thick étalon cavity and decrease the interference from the thin étalon.

Acknowledgments

14-17

and fellowship over the course of the summer. Finally, we thank Pat Hemenger for making this summer research possible.

References

1. K. D. Singer, M. G. Kuzyk, W. R. Holland, J. E. Sohn, S. J. Lalama, R. B. Comizzoli, H. E. Katz, and M. L. Schilling, "Electro-optic phase modulation and optical second-harmonic generation in corona-poled polymer films," Appl. Phys. Lett. **53**, 1800-1802 (1988).

2. R. A. Norwood, M. G. Kuzyk, and R. A. Keosian, "Electro-optic tensor ratio determination of side-chain copolymers with electro-optic interferometry," J. Appl. Phys. **75** (4), 1869-1874 (1994).

3. V. Dentan, Y. Levy, M. Dumont, P. Robin, and E. Chastaing, "Electro-optical properties of ferroelectric polymers studied by attenuated total reflectance," Opt. Commun. **69**, 379-383 (1989).

4. S. Herminghaus, B. A. Smith, and J. D. Swalen, "Electro-optic coefficient in electric-field-poled polymer waveguides," J. Opt. Soc. Am. B **8**, 2311 (1991).

5. C. C. Teng and H. I. Man, "Simple Reflection Technique for Measuring the Electro-Optic Coefficient of Poled Polymers," Appl. Phys. Lett. **56** (18), 1734-1736 (1990).

6. J. Schildkraut, "Determination of the electro-optic coefficient of a poled polymer film," Appl. Opt. **29** (19), 2839-2841 (1990).

7. K. Clays and J. S. Schildkraut, "Dispersion of the complex electro-optic coeficient and electrochromic effects in poled polymer films," J. Opt. Soc. Am. B **9** (12), 2274-2282 (1992).

8. Y. Levy, M. Dumont, E. Chastaing, P. Robin, P. A. Chollet, G. Gadret, and F. Kajzar, "Reflection method for electro-optical coefficient determination in stratified thin film structures," Mol. Cryst. Liq. Cryst. Sci. Technol. - Sec. B: Nonlinear Optics **4** (4), 1-19 (1993).

9. P.-A. Chollet, G. Gadret, F. Kajzar, and P. Raimond, "Electro-optic coefficient determination in stratified organized molecular thin films: application to poled polymers," Thin Solid Films **242**, 132-138 (1994).

10. Y. Shuto and M. Amano, "Reflection measurement technique of electro-optic coefficients in lithium niobate crystals and poled polymer films," J. Appl. Phys. **77** (9), 4632-4638 (1995).

11. H. Uchiki and T. Kobayashi, "New determination of electro-optic constants and relevant nonlinear susceptibilities and its application to doped polymer," J. Appl. Phys. **64** (5), 2625-2629 (1988).

12. C. A. Eldering, A. Knoesen, and S. T. Kowel, "Use of Fabry-Perot devices for the characterization of polymeric electro-optic films," J. Appl. Phys. **69**, 3676-3686 (1991).

13. C. H. Wang, B. S. Wherrett, J. P. Cresswell, M. C. Petty, T. Ryan, S. Allen, I. Ferguson, M. G. Hutchings, and D. P. Devonald, "Observation of electro-optic and electroabsorption modulation in a Langmuir-Blodgett film Fabry-Perot étalon," Opt. Lett. **20** (14), 1533-1535 (1995).

14. J. L. Stevenson, S. Ayers, and M. M. Faktor, "The linear electrochromic effect in meta-nitroaniline," J. Phys. Chem. Solids **34**, 235-239 (1973).

15. R. H. Page, M. C. Jurich, B. Reck, A. Sen, R. J. Twieg, J. D. Swalen, G. C. Bjorklund, and C. G. Willson, "Electrochromic and optical waveguide studies of corona-poled electro-optic polymer films," J. Opt. Soc. Am. B **7** (7), 1239-1250 (1990).

16. A. Horvath, H. Bassler, and G. Weiser, "Electroabsorption in conjugated polymers," Phys. Stat. Sol. B **173**, 755-764 (1992).

17. F. Qiu, K. Misawa, X. Cheng, A. Ueki, and T. Kobayashi, "Determination of complex tensor components of electro-optic constants of dye-doped polymer films with a Mach-Zehnder interferometer," Appl. Phys. Lett. **65** (13), 1605-1607 (1994).

18. H. Ono, K. Misawa, K. Minoshima, A. Ueki, and T. Kobayashi, "Complex electro-optic constants of dye-doped polymer films determined with a Mach-Zehnder interferometer," J. Appl. Phys. **77** (10), 4935-4940 (1995).

19. K. D. Singer, M. G. Kuzyk, and J. E. Sohn, "Second-order nonlinear-optical processes in orientationally ordered materials: relationship between molecular and macroscopic properties," J. Opt. Soc. Am. B **4** (6), 968-976 (1987).

20. O. S. Heavens, *Optical Properties of Thin Solid Films*, (Dover Publications, New York, 1965).

An Investigation of the Effect of Post-Fabrication Processing on the
Microstructure and Properties of a SiCp - 6092 Al Composite

Indranath Dutta
Associate Professor
Mechanical Engineering Department

Naval Postgraduate School
Monterey, CA

Final Report for:
Summer Research Program
Wright Laboratory

August 1995

AN INVESTIGATION OF THE EFFECT OF POST-FABRICATION PROCESSING ON THE MICROSTRUCTURE AND PROPERTIES OF A SiCp - 6092 Al COMPOSITE

Indranath Dutta
Associate professor
Department of Mechanical Engineering
Naval Postgraduate School

Abstract

The evolution of microstructure and mechanical properties of a 17.5 vol.% SiCp reinforced 6092 Al - matrix composite during post-fabrication deformation processing was studied. The effects of process temperature and strain rate were investigated. The objective was to determine whether appropriate process conditions can yield matrix grain refinement via particle stimulated nucleation (PSN) of recrystallization in addition to achieving particle redistribution during extrusion, and whether such grain refinement has a positive impact on the resultant properties. It was found that following processing, the tensile properties of the composite were significantly improved. Some grain refinement was also achieved, and the material with the highest likelihood of PSN of recrystallization appeared to have better fracture properties than a control material where no PSN was expected. Further, it was found that the fracture behavior of the composite can be substantially altered by appropriate heat treatment following processing, with properties ranging from brittle to tough behavior being obtainable.

AN INVESTIGATION OF THE EFFECT OF POST-FABRICATION PROCESSING ON THE MICROSTRUCTURE AND PROPERTIES OF A SiCp - 6092 Al COMPOSITE

Indranath Dutta

Introduction

Discontinuously reinforced aluminum (DRA) composites are promising candidates for a number of aerospace and automotive applications where the stiffness-to-weight and strength-to-weight ratios of currently used materials are not adequate. Substitution of aluminum aircraft parts, which are generally susceptible to failure after short periods of service, by DRA parts has been explored with considerable success under the Title III program of the U.S. Air Force. In addition to strength and stiffness limited applications, DRA also offers advantages in terms of wear resitance and can withstand higher temperatures than conventional aluminum alloys. Yet, despite these advantages, DRA composites have not found widespread commercial or military application because of two reasons. One is that it is costlier than monolithic aluminum, and the other is that the fracture toughness of DRA is typically substantially lower than that of unreinforced aluminum. While the extra cost may be outweighed by the design benefits (such as extra payload capacity due to stronger and stiffer material) and longer component life that can be obtained with DRA, an essential pre-requisite to its acceptance as a reliable structural material is improved fracture resistance. The present study was aimed at addressing this issue.

Background

Although DRA is inherently brittle in the as-fabricated state, it has been demonstrated that with appropriate post-fabrication processing, particulate reinforced aluminum composites with tensile ductilities close to those of unreinforced matrices can be produced [1,2]. The primary role of such processes is to homogenize the particulate distribution in the matrix, and thereby improve properties [3-5]. While some matrix microstructural refinement may also occur during processing, the role of such refinement on composite properties has not been explicitly studied to date, although it is well known that microstructural refinement can enhance fracture toughness as well as strength in metallic alloys [6]. The effect of microstructures resulting from conventional aging processes on fracture behavior have been studied previously [e.g., 7], but as will be demonstrated in this report, unconventional heat treatments may need to be utilized to maximize crack growth resistance in these materials. Therefore, in order to design processes to optimize the fracture resistance and strength of DRA, the precise relationship

between microstructural features and mechanical properties needs to be established, based on a thorough understanding of the effects of the process-dependence of microstructural parameters such as particulate size and spatial distribution, matrix grain and sub-structure, and matrix precipitate structure.

Methodology

This study was aimed at investigating the influence of matrix grain, sub-structure and precipitation state, as influenced by post-fabrication extrusion, on the tensile and fracture properties. An attempt was made to exploit the phenomenon of particle stimulated nucleation (PSN) of recrystallization to refine the matrix grain structure. The basis of PSN constitutes deforming the material to large total strains at as low a temperature and as high a strain rate as practicable, so as to minimize recovery processes and force substantial matrix lattice rotations to occur adjacent to the undeformable reinforcement particles [8,9]. Because of these lattice rotations, the matrix is likely to undergo recrystallization via nucleation of new grains at the particle-matrix interface, either dynamically during processing or statically after a heat treatment subsequent to processing, producing a fine grain size which is of the order of the inter-particle spacing. Several parameters, such as particle size and volume fraction, of course influence this process, and it is generally observed that higher volume fractions and larger particle sizes promote PSN. However, larger particle sizes also give larger final grain sizes, and therefore, appropriate optimization of microstructural and process conditions are necessary to yield the desired properties.

Three extrusion conditions were investigated : (1) one corresponding to the condition where PSN is expected (400°C, strain rate = 5.6/s; *sample designation : 13185*); (2) one where PSN is not expected (400°C, strain rate = 0.56/s; *sample designation : 13186*); and (3) one where PSN may or may not have occured (450°C, strain rate = 5.6/s; *sample designation 13184*). In addition to grain size control, the precipitate structure of the material was controlled by three different heat treatments : (1) natural aging for 3 weeks; (2) artificial aging at 170°C for 8 hours (-T6); and (3) a static annealing process (450°C, 20 minutes) which is likely to have produced a precipitate structure similar to that in the severely overaged state.

Experimental

The material used for the above experiments comprised a 3 inch diameter billet of 17.5% vol.% SiCp reinforced 6092 Al composite, which was supplied by DWA composites, Chatsworth, CA, after being extruded to a true strain of 3.38 between 450 and 560°C from the

as-compacted P/M billet. All further extrusions (*13184, 13185 and 13186*) were conducted at the Wright Laboratory, producing an additional true strain of 2.3. The total strain was kept constant to minimize the variability of particle distribution, so that the primary variable parameter would be the matrix microstructure. Following extrusion, the samples were variously heat treated as indicated above (naturally aged, artificially aged, or static annealed). Sub-size tensile and compact tension specimens were then fabricated from the extruded and heat treated billets using electic discharge machining, and the samples were tested at ambient temperature using a servo-hydraulic mechanical test system. In addition, the particle distribution resulting from each of the three extrusion conditions was investigated by optical microscopy, and the matrix microstructure was examined by transmission electron microscopy (TEM).

Results

1. Microstructure :

Figures 1a-c show the particulate distributions in the as extruded samples of extrusions 13184, 13185 and 13186, respectively. In general, the particulate spatial distributions are observed to be similar, suggesting that the distribution is influenced primarily by the total strain, and not as much by the details of the extrusion process. However, subtle differences are noticeable. The more rapid extrusions (13184, 13185 : strain rate 5.6/s) seem to cause more alignment of the longer axes of the SiC particles along the extrusion direction relative to the slow extrusion (13186 : strain rate = 0.56/s). This is likely to cause more anisotropy in the rapid extrusions, and result in improved tensile and fracture properties when the loading axis is along the extrusion direction, while possibly deteriorating transverse properties somewhat. The mechanism of this alignment is not clear yet, and needs further investigation.

Figures 2 through 4 show TEM micrographs of the three extruded materials following solution treatment (at 560°C) and natural aging for 3 weeks. Under these conditions, the materials are expected to be fully recrystallized. It is observed that the grain/sub-grain sizes resulting from the two rapid extrusions [13184 (Figure 2) and 13185 (Figure 3)] are similar (~2-4 μm), whereas the grain size in the slow extrusion (13186, Figure 4) is larger (~ 6-8 μm). Further, it is observed that while dislocations are easily resolvable in many of the grain/sub-grain boundaries in the higher temperature extrusion (13184, Figure 2b), suggesting that at least some of the boundaries are low-angle, dislocations are not resolvable in the boundaries of the lower temperature extrusion with the same strain rate (13185).

However, not all the boundaries are traditional high angle boundaries in 13185, as indicated by the selected area diffraction patterns in Figures 3b and 3c, which represent two grains across a boundary. Both grains are observed to be near the {122} pole, with the misorientation between them being only about 5-7°, although no dislocations are resolvable on the boundary.

The above difference in grain sizes resulting from high and low strain rate extrusions suggests that PSN is probably operative at the higher rates, resulting in the observed smaller grain sizes. However, it is also clear that the grain boundaries developing after PSN are not all high angle boundaries, which are the preferred type to yield the maximum benefit in terms of strength, ductility and toughness. Although initial results indicate that the higher temperature extrusion (13184) results in lower angle boundaries, at present it is not clear why this is so. Further, as observed in Figure 3, the lower temperature extrusion (13185) has significantly more residual dislocations following recrystallization than the higher temperature extrusion (Figure 2). While more dislocation generation and less strain relief are expected at the lower temperature, it is not clear why the dislocations would not get absorbed into the sweeping boundaries during recrystallization. These features are likely to be of importance to mechanical properties, and require investigation in the future.

Another feature of importance in the microstructures of all the extrusions is that the grains nucleating at the interfaces of the matrix with larger SiC particles seem to be stabilized by finer SiC particles. This is clearly observed in Figure 3d. This suggests that having a bi-modal distribution of SiC particles is likely to be beneficial to the matrix grain structure. While the larger particles result in PSN of new grains, the grain size is stabilized by the smaller particles, helping keep the overall grain size fine.

2. Mechanical Properties :

Table I summarizes the mechanical properties of the three extrusions (13184, 13185, 13186) under various heat treatment conditions. Figure 5 shows a comparison of the tensile stress-strain responses of the three extrusions following solution treatment and natural aging for 3 weeks. It is apparent that the strength levels are nearly identical in all materials. This suggests that the strength levels in the aged state are controlled primarily by the precipitate structure (which consists of a very fine dispersion of β' rods, see Figure 6) with grain structure playing little role. However, the ductility of the higher temperature extrusion (13184) is significantly lower (7.4%), although the two lower temperature extrusions (13185

and 13186) display similar ductilities (~9%). This may be associated with the low angle character of the grain boundaries in 13184 (Figure 2b). Therefore, at least in the naturally aged state, the strength parameters of the composite does not seem to be significantly influenced by the presence or absence of PSN, although preliminary results suggest that the presence of high angle boundaries may be beneficial to ductility.

Figure 7 plots the stress-strain responses of the as-received composite, along with those of the high and low strain rate extrusions (13185 and 13186, respectively) following static annealing at 450°C for 20 minutes. The purpose of this treatment was to fully recrystallize the microstructure following extrusion, without going to the high solutionization temperature (560°C) so as to minimize the extent of grain growth. Obviously, at 450°C, full solutionization did not occur, and the microstructure is expected to consist of large overaged particles of β with no transition precipitates, which constitute the hardening phase. Accordingly, the strength levels following this treatment are significantly lower than those under the naturally aged (-T4) condition. Of interest is the substantial improvement in both strength and ductility in the extruded materials relative to the as-received material. Also of note is the observation that while the ductilities resulting from the high and low strain rate (13185 and 13186, respectively) extrusions are nearly identical, 13185 has a significantly higher strength level. This is attributable to the difference in grain sizes (2-4 μm in 13185 vs. 6-8 μm) in 13186. Although the grain size contribution to strength was not significant in the -T4 condition (Figure 6), a larger proportion of the overall strength arises out of grain boundary contributions when the total strength level is lower due to severe overaging as in the present case.

The grain size contribution also appears to be appreciable in terms of fracture toughness. This is apparent from a comparison of the K_Q values of the three extrusions under the -T6 condition (Table I). While 13184 and 13185 have nearly identical fracture toughnesses, the fracture toughness of 13186, which has larger grain sizes, appears to be significantly smaller (~18%). It thus appears that matrix grain refinement is a desirable goal to pursue for fracture toughness improvement in the peak aged condition, as well as for improved ductility and strength levels when the matrix is likely to be overaged.

The fracture behavior of the composite changes dramatically from that in the -T6 condition when the composite is static annealed at 450°C following extrusion. This is shown in Figure 8, which plots the load versus clip gage displacement for 13185 (extruded at 400°C at 5.6/s)

in the peak aged and static annealed conditions. It is clear that while in the peak aged condition, the composite shows unstable crack growth with K_{IC}-controlled failure, in the static annealed condition, the composite shows stable crack growth over an extended period, without ever undergoing unstable failure. Figure 9 shows the J vs. Δa behavior of the composite in the static annealed condition. It is apparent that the composite shows a steep R curve, with a very high crack propagation resistance. The crack initiation toughness, as indicated by $J_Q = J_{IC}$, and the crack propagation toughness as indicated by the tearing modulus T, are shown in Table I. The J_{IC} value of the composite under these conditions is 13.3 kJ/m^2, and compares favorably with the range 7 to 16 kJ/m^2 reported for a 15 vol.% SiCp - 7xxx Al MMC reported in Manoharan and Lewandowski [7]. The tearing modulus T of our composite is ~30, which is more than an order of magnitude larger than that reported in ref. 7. This is also apparent from a comparison of the R curves of the present material with those reported in [7]. Whereas typical R-curves of most DRA composites are shallow [7], the R curve shown in Figure 8 is steep, resulting in the very good crack propagation resistance obtained. Certainly, this clearly indicates that when subjected to appropriate thermo-mechanical processing, DRA composites can become very tough. It should also be pointed out that the J_{IC} value of 13.3 kJ/m^2 is likely to be an underestimate of the true J_{IC}, since for steep R curves, the standard procedure for J_{IC} determination yields a very conservative measurement of toughness as it may not account for the full extent of crack tip blunting that may be present in very tough materials (for a discussion, see ref. 10).

Summary

Four points emerge from the present work.

1. First, processing in the PSN regime does appear to result in some matrix grain refinement. While similar grain sizes may be obtainable by working close to the boundaries of the PSN regime, the character of the grain boundaries is likely to be different. This, as shown in Figure 5, can result in a lower tensile ductility. In general, relatively high angle grain boundaries, as obtained in the PSN regime, appear to be better for properties.

2. Secondly, although matrix grain refinement has only a minor effect on strength and ductility levels in the age hardened condition (-T4), it improves strength levels significantly when the matrix is in an overaged state due to static annealing following extrusion. Grain refinement also appears to improve the fracture toughness (K_Q) in the age hardened state (-T6) significantly, even though the tensile ductility in the age hardened condition is not impacted appreciably.

3. Thirdly, following a static recrystallization anneal which results in a microstructure containing equilibrium precipitates, the composite becomes very tough and displays extremely high crack growth resistance. While the strength level in this material is not adequate for applications, it is expected that this can be rectified via special aging processes. A short solutionization at a temperature lower than the β solvus to produce a controlled amount of equilibrium precipitates, followed by aging at a temperature below the β' solvus to produce hardness-imparting transition precipitates should yield an acceptable combination strength and fracture toughness. However, further work is necessary to determine the precise microstructural features in the annealed materials which contribute to the observed tough behavior, and to determine the process conditions necessary to produce the desired strength-toughness combinations.

4. Finally, the above work demonstrates that a number of issues need to be resolved in order to intelligently design microstructures via processing so that mechanical property improvements can be achieved. First, the relationship between grain boundary character and mechanical properties needs to be clearly established. Secondly, the fracture mechanisms in the composite under -T4, -T6 and the static annealed conditions need to be clearly established so that a combination of static annealing, sub-solvus solution treatment, and artificial aging can be utilized to optimize strength, ductility and fracture resistance. Finally, in order to maximize the beneficial effects of fine matrix grain size, and refine the grain size as much as practically feasible, innovative approaches such as having a large number of very fine SiC particles in addition to the large particles may be necessary. Studies focussing on optimum size and shape distributions, and the grain boundary pinning effects of such particles are necessary. Also necessary is a thorough evaluation of the impact of such particle size distributions on the fracture properties.

References

1. T. R. McNelley and P.N. Kalu, Scr. Metall., 25, 1991, p. 1041.
2. T. R. McNelley and P.N. Kalu, in Proc. Int'l. Conf. Advanced Synthesis of Engineered Structural Materials, J.J. Moore, E.J.Lavernia and F.H. Froes, eds, ASM, 1993, p.209.

3. J.J. Lewandowski, C. Liu and W.H. Hunt, Mater. Sci. Eng., A107, 1989, 241.

4. T.G. Nieh and R.F. Karlak, J. Mater. Sci. Lett., 2, 1983, 119.

5. A. Sato and R. Mehrabian, Metall. Trans., 8B, 1976, 443.

6. R.W. Hertzberg, "Deformation and Fracture Mechanics of Engineering Materials", John Wiley, 1983, p. 354.

7. M. Manoharan and J.J. Lewandowski, Acta Metall., 38, 1990, 489.

8. F.J.Humphreys, Acta Metall., 25, 1977, 1323.

9. F. J. Humphreys, W.S.Miller and M.R. Djazeb, Materials Sc. Tech., 6, 1990, 1157.

10. R.W. Hertzberg, "Deformation and Fracture Mechanics of Engineering Materials", John Wiley, 1983, p. 321.

Table I : Summary of Mechanical Properties : DWA 6092 Al - 17.5v/o SiCp MMC

Material	E (GPa)	YS (MPa)	UTS (MPa)	Elong. %	K_Q MPa$\sqrt{m}$	J_{IC} (kJ/m^2)	Tearing Modulus
As received HT : 450°C, 20 m.	90	145	240	8			
13184 Extr : 450°C, 5.6/s HT : 450°C, 20 m.						*	*
13185 Extr : 400°C, 5.6/s HT : 450°C, 20 m.	102	170	305	12.6		13.3	31
13186 Extr : 400°C, 0.6/s HT : 450°C, 20 m.	94	160	270	13.1		*	*
13184 Extr : 450°C, 5.6/s HT : -T4, 3 wks.	97	270	450	7.4			
13185 Extr : 400°C, 5.6/s HT : -T4, 3 wks.	103	280	448	9.7			
13186 Extr : 400°C, 0.6/s HT : -T4, 3 wks.	101	280	450	8.9			
13184 Extr : 450°C, 5.6/s HT : -T6					26		
13185 Extr : 400°C, 5.6/s HT : -T6					27		
13186 Extr : 400°C, 0.6/s HT : -T6					22		

Figure 1 (caption on next page)
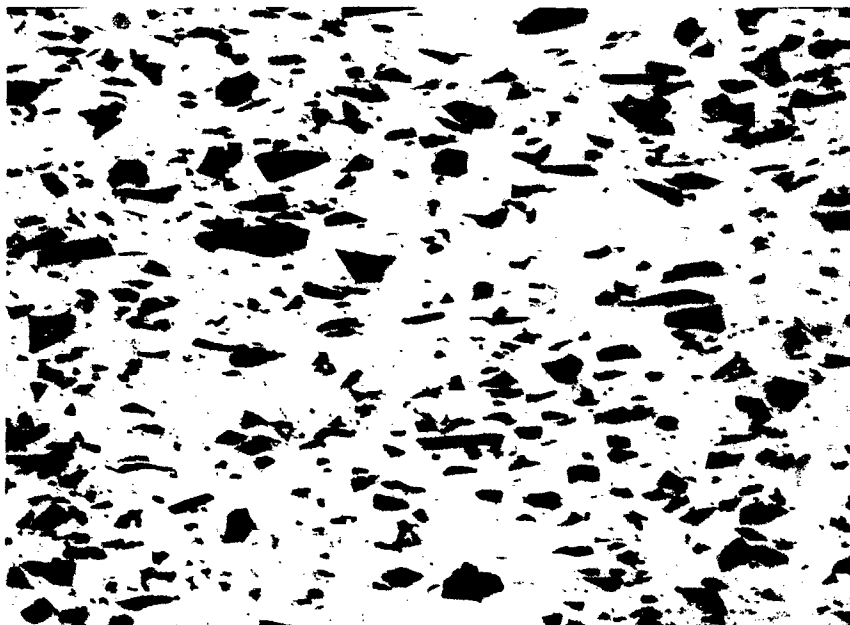
(a)
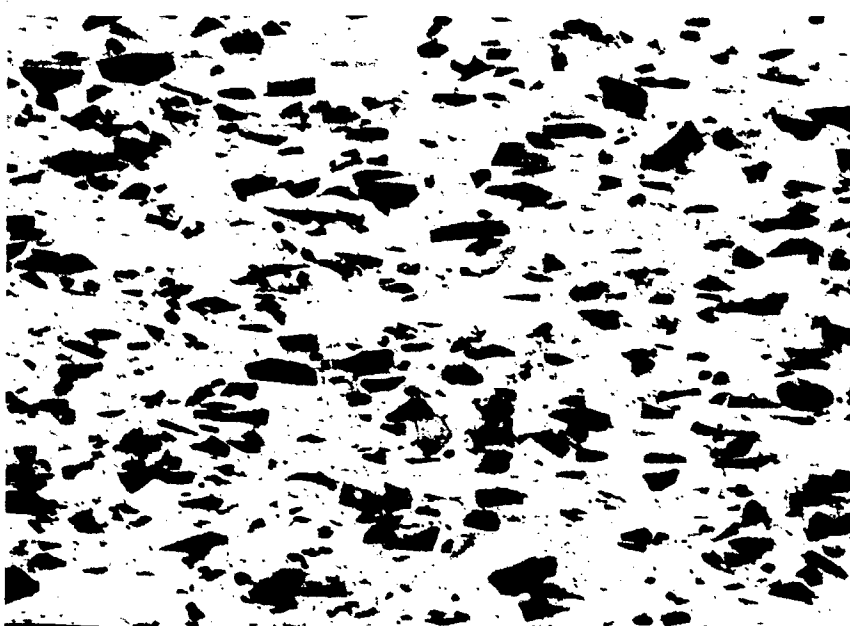
(b)
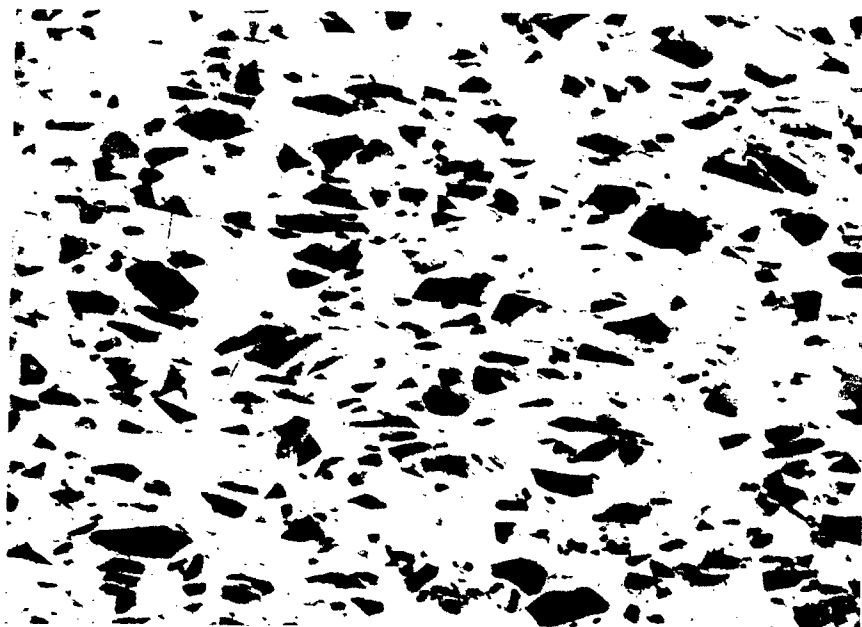
(c)

Figure 1: Optical micrographs showing the particle distributions in the three extruded samples (13184, 13185, 13186) following a solution treatment after extrusion. (Magnification : 500 X).
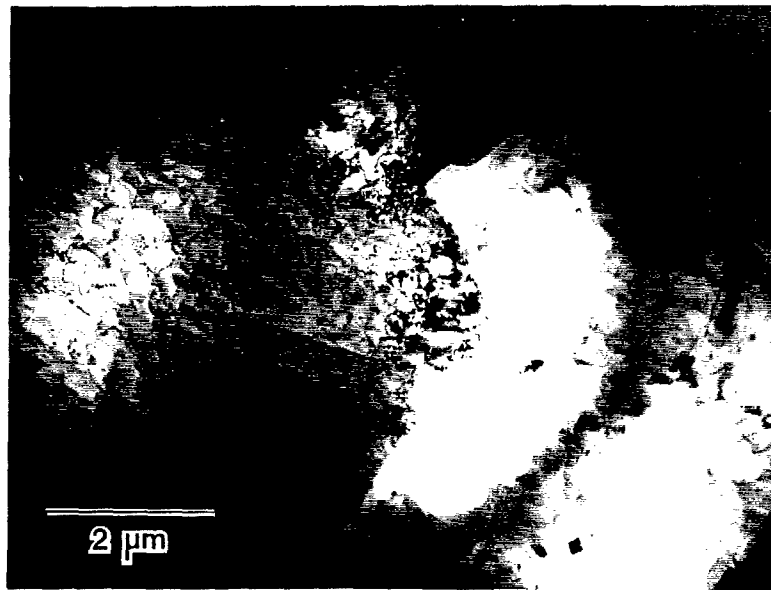
(a)
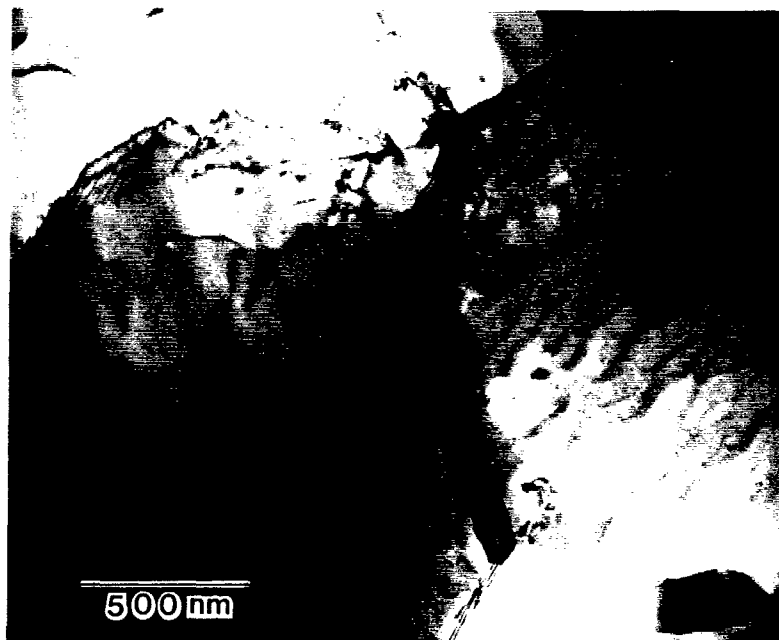
(b)

Figure 2 :   Bright field TEM micrographs of composite extruded at 450°C at a strain rate of
5.6/s, showing fine grained matrix microstructure. Figure 2b shows that some of
the boundaries are low-angle, and dislocations can be readily resolved in these
boundaries.

15 - 13

(a)

(b)

(c)

15 - 14
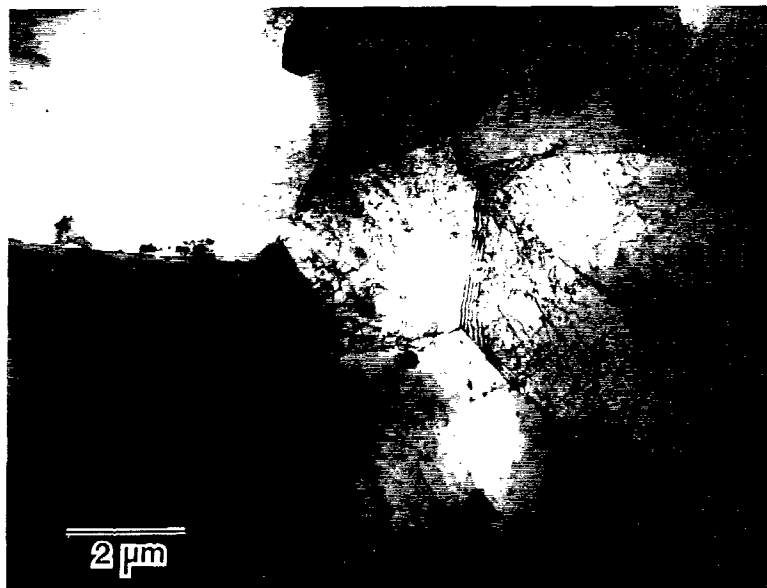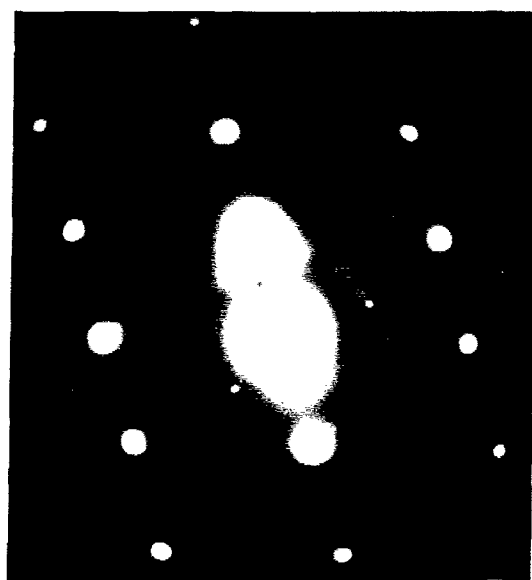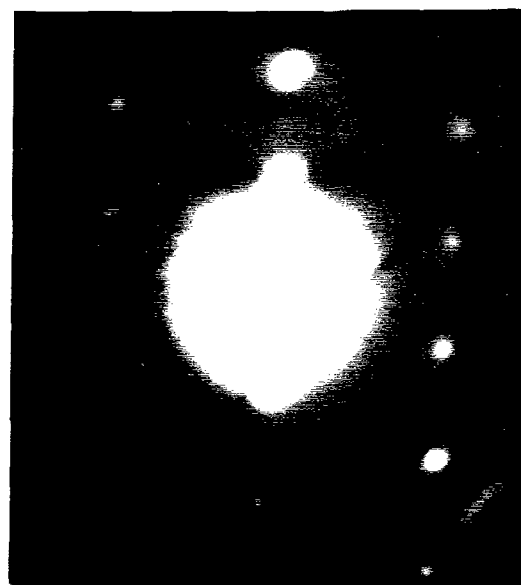
(d)

Figure 3 :   Bright field TEM micrographs and SADPs of the composite extruded at 400°C at a strain rate of 5.6/s (13185), showing fine grained matrix microstructure. The near [122] SADPs (b and c) from two adjacent grains show that the boundary misorientation is not necessarily high in all cases, although no dislocations are resolvable.   Figure 3d shows that some of the grain boundaries are pinned by small SiC particles.

Figure 4 :   Bright field TEM micrograph of composite extruded at 400°C at a strain rate of
            0.56/s (13186), showing relatively coarse grain matrix microstructure next to a
            SiC particle.
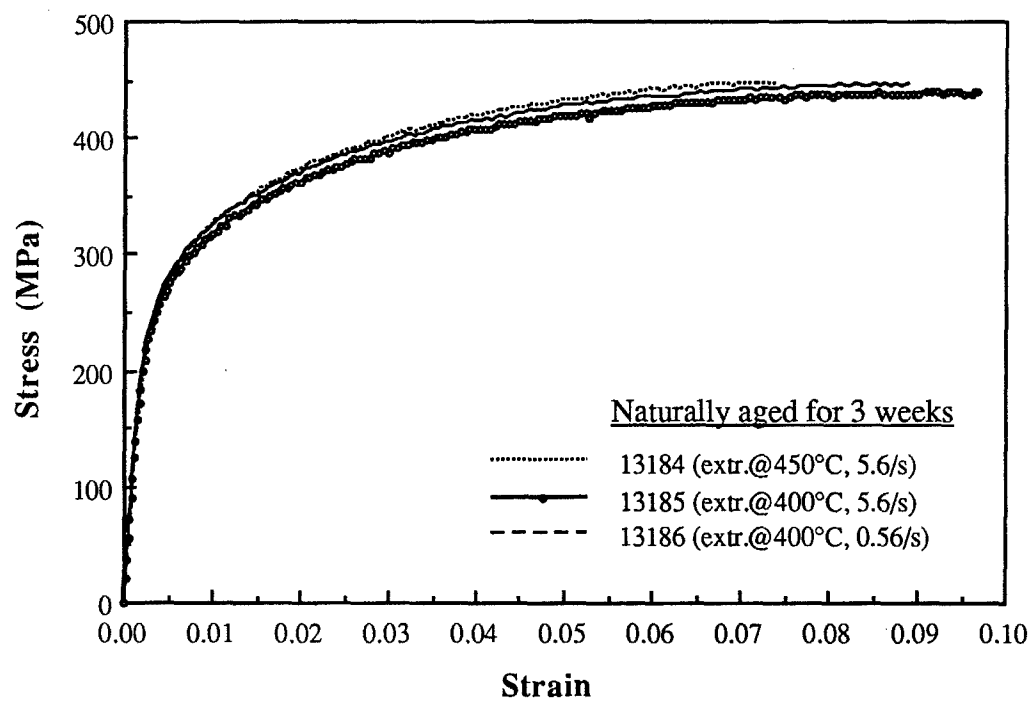
Figure 5 :   A compilation of the tensile stress-strain behaviors of the three extrusions (13184, 13185, 13186) following solution treatment and natural aging for 3 weeks.
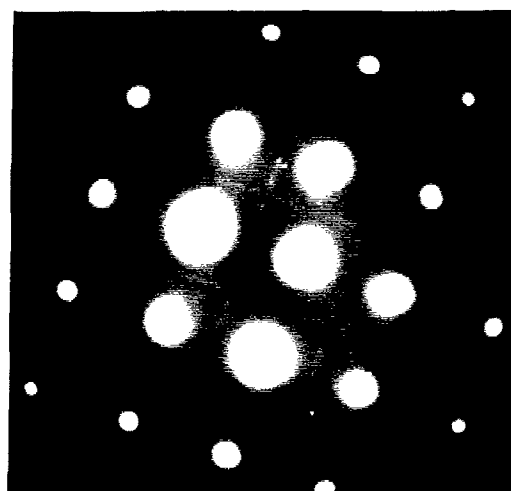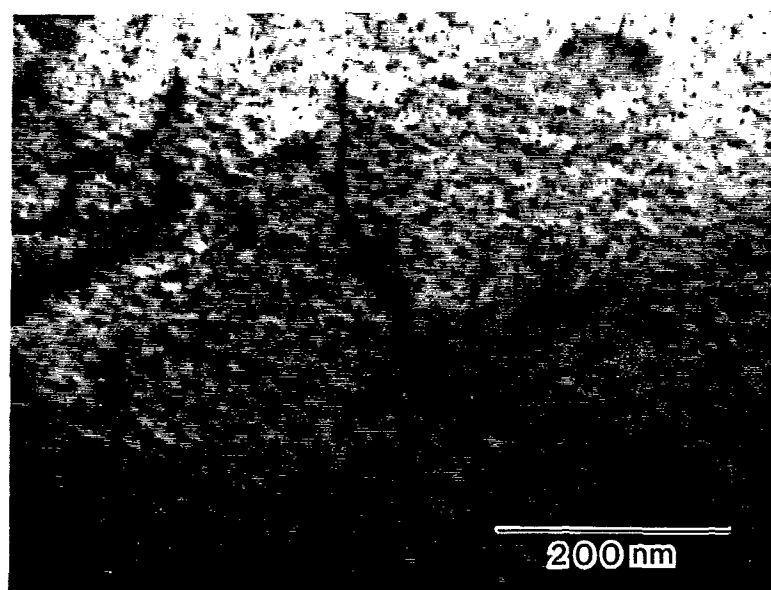
Figure 6 :   The matrix microstructure of extrusion # 13185, showing the representative microstructure of all the extrusions following three weeks of natural aging. A very fine distribution of β' rods is present on the Al {001} planes, running parallel to the <100> directions, as evident from the SADP.
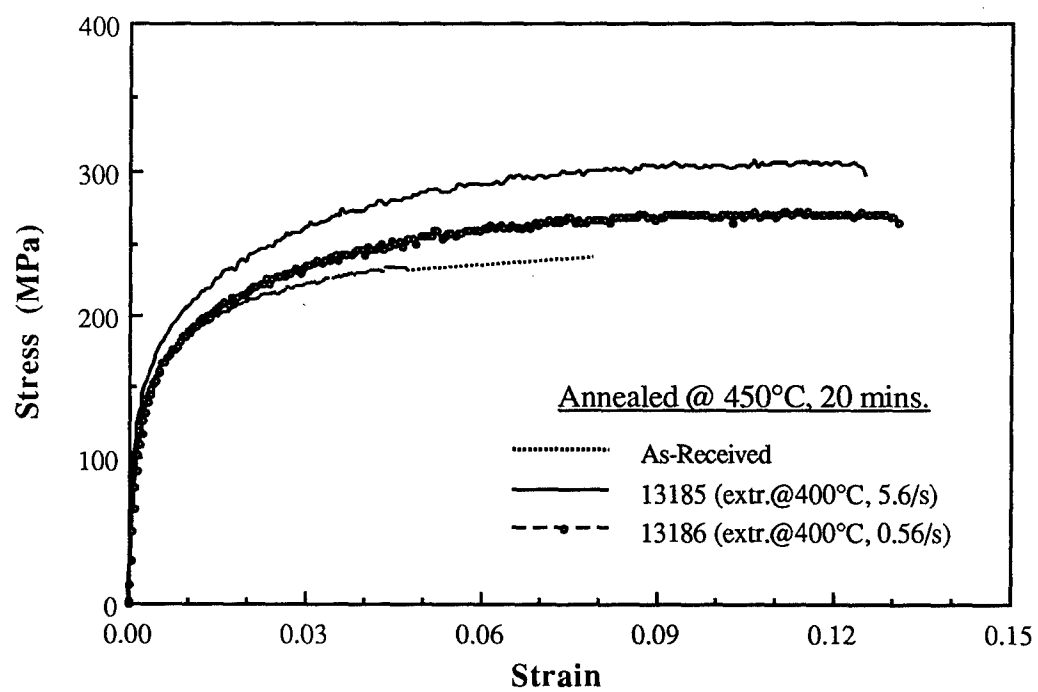
Figure 7 : A compilation of the tensile stress-strain behaviors of the three extrusions (13184, 13185, 13186) following a static anneal at 450°C for 20 minutes.
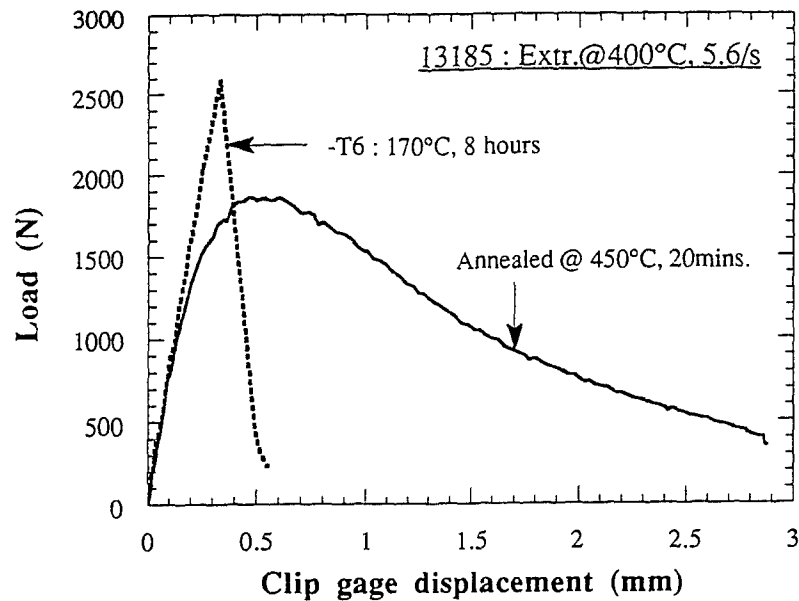
Figure 8: Load vs. clip gage displacement plots of extrusion # 13185 following a -T6 heat treatment and a static anneal at 450°C for 20 minutes. The -T6 material demonstrates unstable crack growth, whereas the annealed material displays stable crack growth.
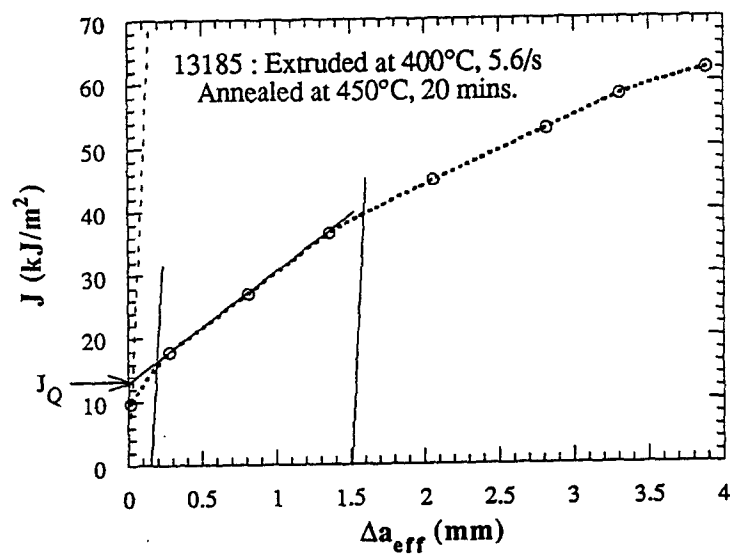
Figure 9: J vs. Δa behavior of extrusion # 13185 following a static anneal at 450°C for 20 minutes, showing a steep R curve and very high crack propagation resistance. The blunting and exclusion line constructions for J_{IC} determination are also shown.

15 - 20

TRANSITION AND SEPARATION COMPUTATIONS ON TURBINE BLADES

Elizabeth A. Ervin
Assistant Professor
Department of Mechanical and Aerospace Engineering

University of Dayton
300 College Park
Dayton, Ohio 45469

TRANSITION AND SEPARATION COMPUTATIONS ON TURBINE BLADES

Elizabeth A. Ervin
Assistant Professor
Department of Mechanical and Aerospace Engineering

Abstract

A numerical study of turbine blade flows was conducted. The primary focus of the study was to study the effect of low Reynolds number flows, typical of low pressure turbines at cruising altitudes, on transition and separation. Prior experimental investigations have shown a greater tendency for transition and separation at lower Reynolds. Numerical results confirm these findings. The influence of pitch to axial chord ratio was also considered.

TRANSITION AND SEPARATION COMPUTATIONS ON TURBINE BLADES

Elizabeth A. Ervin

Introduction

The low pressure turbine blade chord Reynolds number, based on exit conditions, in a number of engines, falls from a typical value of 10^6 at take-off to 150,000 to 50,000 at higher cruising altitudes. Low Reynolds number flows increase the likelihood of flow separation on the suction surface, resulting in a loss of engine efficiency (Sharma and Tanrikut, 1994). This type of problem has been seen on smaller engines such as the C-17 (F-117). The unsteady interaction of the vane with the blade and turbulence intensity both play a great role in the boundary layer development (Halstead et al., 1995). Transitional boundary layer development is a complex process. It is affected by the interaction of the viscous sublayer with the outer regions of the boundary layer. Previous unsteady numerical analyses have neglected the viscous terms near the surface (Dorney, et al., 1995). A fundamental study using a computational model of the full transient Navier-Stokes equations is essential to understanding the low Reynolds number flows of a low pressure turbine stage.

This report concerns the first phase of a full vane-blade interaction study. In this phase, steady calculations of the full Navier-Stokes equations were conducted. The Langston cascade geometry is well documented (see Langston et al., 1977) and is a reasonable representation of current low pressure turbine geometry. Furthermore, recent steady experimental measurements have been performed with this cascade geometry at low chord Reynolds numbers of 67,500, 110,000 and 134,000 (Baughn et al., 1995) and provide a basis for comparison. In the second phase, both experimental and numerical calculations of an unsteady Langston cascade at low Reynolds numbers will be performed here at Wright Laboratory.

Methodology

The software used for the simulation of the Navier-Stokes equations was developed by Allison Engine Company, under U. S. Air Force contract for Wright Laboratory, to study vane-blade interaction. A three-dimensional version is described by Rao, et al. (1994). The transient two-dimensional Reynolds-averaged Navier-Stokes, continuity, and energy equations are solved using a numerical finite difference technique with central differencing for second order accuracy in space, and a five-stage Runge-Kutta

algorithm for second order accurate integration in time. The method is based on that of Swanson and Turkel (1987). A variant of implicit residual smoothing is incorporated into an explicit time-accurate method for convergence acceleration (Jorgensen and Chima, 1989). A uniform time increment is selected based on the minimum time increment that satisfies the Courant-Friedrichs-Levy (CFL) stability criterion at any point in the flow field. An artificial dissipation model that blends second and forth order differences is added to damp out non-physical oscillations produced by central differencing. It utilizes pressure as a sensor to capture physical discontinuities such as shock waves and stagnation points.

The code uses a body fitted hyperbolic O-grid embedded in a rectangular H-grid as shown in Figure 1 with the Langston geometry. The outer grid resolves the free stream flow and the O-grid is used in the boundary layer region, with y+ values as low as 0.002.

Non-reflective inflow and outflow boundary conditions are calculated based on the methodology developed by Cline (1977). No-slip conditions are used on the airfoil surface(s) and periodic boundary conditions are used in the polar direction. The interface between the stator exit and the rotor inlet can be modeled with overlapping H-grids and a time-space phase-lag procedure, originally developed by Erdos (1977).

The conservative forms of the governing equations are used on a blade-to-blade stream surface of revolution:

$$\frac{\partial Q}{\partial t} + \frac{\partial E}{\partial m} + \frac{\partial F}{\partial \theta} = H = H_i - H_v + \frac{\partial E_v}{\partial m} + \frac{\partial F_v}{\partial \theta}$$

where:

$$Q = rb\begin{bmatrix} \rho \\ \rho u \\ \rho v \\ \rho e \end{bmatrix}, \ E = rb\begin{bmatrix} \rho u \\ \rho u^2 + p \\ \rho uv \\ u(\rho e + p) \end{bmatrix}, \ F = rb\begin{bmatrix} \rho v \\ \rho uv \\ \rho v^2 + p \\ v(\rho e + p) \end{bmatrix}, \ E_v = \frac{rb}{Re}\begin{bmatrix} 0 \\ \sigma_{11} \\ \sigma_{12} \\ E_4 \end{bmatrix}, \ F_v = \frac{b}{Re}\begin{bmatrix} 0 \\ \sigma_{12} \\ \sigma_{22} \\ F_4 \end{bmatrix}$$

and:

$$H_i = rb \begin{bmatrix} 0 \\ (\rho v^2 + p)\dfrac{1}{r}\dfrac{\partial r}{\partial m} + p\dfrac{1}{b}\dfrac{\partial b}{\partial m} \\ -\rho u v \dfrac{1}{2}\dfrac{\partial r}{\partial m} \\ 0 \end{bmatrix}, \quad H_v = \dfrac{rb}{Re} \begin{bmatrix} 0 \\ \sigma_{22}\dfrac{1}{r}\dfrac{\partial r}{\partial m} + \sigma_{33}\dfrac{1}{b}\dfrac{\partial b}{\partial m} \\ -\sigma_{12}\dfrac{1}{r}\dfrac{\partial r}{\partial m} \\ 0 \end{bmatrix}$$

$$E_4 = u\sigma_{11} + v\sigma_{12} + \dfrac{1}{\gamma-1}\dfrac{\mu}{Pr}\dfrac{\partial a^2}{\partial m}, \quad F_4 = u\sigma_{12} + v\sigma_{22} + \dfrac{1}{\gamma-1}\dfrac{\mu}{Pr}\dfrac{1}{r}\dfrac{\partial a^2}{\partial \theta}$$

The shear stress terms, σ_{ij}, are defined as follows:

$$\sigma_{11} = 2\mu\dfrac{1}{r}\dfrac{\partial u}{\partial m} + \lambda \vec{\nabla}\cdot\vec{V}, \quad \sigma_{12} = \mu\left(\dfrac{\partial v}{\partial m} - \dfrac{v}{r}\dfrac{\partial r}{\partial m} + \dfrac{1}{r}\dfrac{\partial u}{\partial \theta}\right)$$

$$\sigma_{22} = 2\mu\left(\dfrac{1}{r}\dfrac{\partial v}{\partial \theta} + \dfrac{u}{r}\dfrac{\partial r}{\partial m}\right) + \lambda\vec{\nabla}\cdot\vec{V}, \quad \sigma_{33} = 2\mu\dfrac{u}{b}\dfrac{\partial b}{\partial m} + \lambda\vec{\nabla}\cdot\vec{V}$$

where:

$$\vec{\nabla}\cdot\vec{V} = \dfrac{1}{rb}\left(\dfrac{1}{r}\dfrac{\partial(rbu)}{\partial m} + \dfrac{\partial(bv)}{\partial \theta}\right)$$

In these equations, m and θ are the meridonial and polar coordinates, respectively; r is the radius and b is the span, which can vary with r; u and v are the velocity components in the m and θ directions, respectively; p is the pressure, μ is the effective dynamic viscosity, ρ is the density, e is the total internal energy, γ is the ratio of specific heats, and $a = \sqrt{\gamma p / \rho}$ is the speed of sound. Pr and Re are the Prandtl and Reynolds numbers, respectively. The second viscosity coefficient, λ, is set equal to -2/3 μ and Pr is constant.

The viscosity, μ, is equal $\mu_l + \mu_t$, where μ_l is the actual material property, calculated from Sutherland's law (White, 1974) and μ_t is added to account for turbulence, obtained from the Baldwin-Lomax model (Baldwin and Lomax, 1978.) The μ/Pr terms are actually $\mu_l/Pr + \mu_t/Pr_t$, where Pr_t is a turbulent value

taken to be 0.9. The turbulent viscosity, μ_t, is set to zero if the maximum dimensionless value is less than the recommended value of 14.

In the numerical simulation, body-fitted curvilinear coordinates are utilized and the flow is mapped to uniformly spaced rectangular coordinate region with the Jacobian matrix of the transformation. Also, the variables are non-dimensionalized. Further details of the software can be found in Rao, et al. (1994).

Results and Discussion

The calculations were performed for four axial chord Reynolds numbers (Re = 50,000, 200,000, 300,000 and 10^6) at two pitch to axial chord ratios, p/c_x = 0.93 and 1.18, both used in the experimental study reported by Baughn, et al. (1995). The Reynolds numbers are based on inlet stagnation conditions and compare with the experimental values of 67,500, 110,000 and 134,000, based on inlet conditions. The experiments were conducted both with a turbulence grid to produce a turbulence intensity (Tu) of 9% or 10%, and without the grid (Tu = 0.5% or 1%). The computations were clean (Tu = 0%).

The following plots show results for the cases of Re = 300,000 (300K) and 10^6 (1M) at p/c_x = 0.93. Figures 2 through 7 are airfoil surface plots using s/s_{max} as the distance along the airfoil. The variable, s_{max}, is defined separately for the pressure ($s/s_{max} < 0$) and suction ($s/smax > 0$) surfaces so that s/s_{max} varies from zero at the leading edge to +/- 1 at the trailing edge.

Figure 2 depicts the calculated pressure ratio, p/p_o, around the airfoil surface, where p_o is the total pressure. As can be seen from the figure, there is not a significant pressure drop between the leading and trailing edge for this cascade. Skin friction and heat transfer are of primary interest and these are described in the following two figures.

In Figure 3, the skin friction coefficient, C_f, around the airfoil is described. C_f is actually the shear stress at the wall, calculated with dimensionless velocity, distance and laminar viscosity. On the pressure surface ($s/s_{max} < 0$), the negative C_f values correspond to the region between the two stagnation points, both located on this side of the airfoil. On the suction surface ($s/s_{max} > 0$), the region of negative C_f for the case of Re = 300K, corresponds to a region of separation ($0.55 \leq s/s_{max} \leq 0.78$). This was confirmed by an examination of velocity profiles in this region (not shown).

The heat transfer is characterized in Figure 4 using the Stanton number, St, defined here as:

$$St = \frac{\left(\dfrac{\partial T}{\partial n} * \mu_l * k\right)_{wall}}{T_o - T_w}$$

where T is the temperature, n is the direction normal to the surface, μ_l is the laminar viscosity, k is the thermal conductivity of the gas, T_w is the wall temperature and T_o is the total temperature. The temperatures are non-dimensionalized with T_o and the other variables are non-dimensionalized as well. The heat transfer is a maximum at the leading edge stagnation point and just before the trailing edge on the suction side. The minimum values occur at the trailing edge stagnation point and at the transition to turbulence on the suction side ($s/s_{max} \sim 0.26$). A second minimum occurs for the Re = 300K case at the onset of separation. The transition to turbulence is further described below.

The momentum thickness, θ, and boundary layer shape factor, H, are shown in Figures 5 and 6, respectively. H is the ratio of δ^*/θ, where δ^* is the displacement thickness. The displacement and momentum thickness are defined in the traditional manner for a compressible flow using dimensionless velocities (White, 1974). In both of these figures, the separation region on the suction surface, for the case of Re = 300K, is clearly seen. As s/s_{max} is increased from zero, θ reaches a maximum value and H reaches a minimum value just beyond the leading edge. The momentum thickness gradually decreases from this point until $s/s_{max} = 0.26$, where it starts to increase rapidly. The shape factor reaches a local maximum of 2.04 or 2.05 at this location, which corresponds to the onset of transition to turbulence. The turbulent viscosity, μ_t, is turned on, that is, the maximum μ_t in the O-grid $\geq$ 14, at $s/s_{max} = 0.29$. (This is intermittent for the Re = 300K case until $s/s_{max} = 0.36$.) As s/s_{max} is raised from 0.26, the shape factor generally decreases, indicating a progression of turbulence. For Re = 300K, H has a secondary peak of 1.96 at $s/s_{max} = 0.32$, perhaps related to the intermittence of using μ_t. At $s/s_{max} = 0.45$, the low Reynolds number flow begins to act distinctly different from the case of Re = 10^6. The shape factor increases to 2.12 and θ increases at a much more rapid rate up to 0.0191, both at $s/s_{max} = 0.53$. This change can be attributed to the greater influence of the adverse pressure gradient over that of the transition to turbulence. After these peaks, the separation begins ($0.55 \leq s/s_{max} \leq 0.78$). The momentum and displacement thickness have no meaning in this region. After reattachment, the θ is very small due to the

16-7

low velocity flow in a very thin boundary layer and H begins to decrease again due to turbulence from a value of 2.64.

On the pressure side of the airfoil, H increases from the leading edge to 2.83 or 2.85 at the stagnation point. The momentum thickness is very small in this region. As the flow redevelops after the stagnation point, H decreases steadily from about 1.71 and θ increases rapidly, especially in the low speed flow, and tapers off to the low values associated with the trailing edge stagnation point. The turbulent viscosity is used in the region of the leading edge stagnation point, but its use becomes intermittent after s/s_{max} = -0.24 for Re = 10^6 and after s/s_{max} = -0.39 for Re = 300K. The leading edge turbulence calculations may be related to the brief rapid growth of the momentum thickness. As the flow approaches the trailing edge, the laminar viscosity is generally used alone due to the lower freestream velocity. The shape factor increases to values more associated with laminar flow and impending separation. Turbulent calculations are used again in the trailing edge stagnation region, and the shape factor decreases again after the stagnation point.

Figure 7 depicts the maximum y+ = $yu*/\nu$ in the O-grid, where y is the normal distance from the airfoil surface and ν is the kinematic viscosity. The friction velocity, u*, is the square root of the dimensionless shear stress at the wall, C_f, divided by the dimensionless density ratio. The maximum y+ tends increase as pressure decreases and vice versa (Figure 2). The peak y+ values occur in regions of low pressure, near the trailing edge stagnation point and in the acceleration region of the suction surface. The velocity profile in these two regions is described in Figures 8 and 9. The suction surface separation region, for Re = 300K, can be clearly seen in Figure 7. The plot of u* follows the same trends as for y+ (not shown).

Figure 8 shows the velocity profile in the O-grid for a location on the accelerating portion of the suction surface, plotting u+ versus y+, where u+ = u/u*, and u is the dimensionless velocity tangential to the surface. The velocity increases sharply with y+, in a linear relationship very near the wall, as expected. The velocity gradually levels off as the velocity profile becomes more developed, and then decreases somewhat beyond the boundary layer. The velocity profiles near the trailing edge (s/smax = -0.93) are shown in Figure 9. These profiles are similar to those in Figure 9 except that the edge of the boundary layer is more sharply defined.

The experimental results showed separation on the suction surface in the case of lower chord Reynolds number of 67,500, and low turbulence intensity (Tu = .5%), with the looser blade spacing (p/c_x = 1.18). Increasing Tu to 9% eliminated the separation. At a Reynolds number of 110,000, the cascade with p/c_x = 0.93 (Tu = 1%) exhibited separation but the cascade with p/c_x = 1.18 (Tu = 0.5%) did not. The computations showed separation with the tighter blade spacing for Re up to 300,000, with Tu = 0%, but did not show separation for the cases of p/c_x = 1.18.

Conclusions

A fundamental study using a computational model of the full transient Navier-Stokes equations was used to examine low Reynolds number flows typical of a low pressure turbine stage. The calculations confirmed the phenomena of separation at low Re, low Tu and p/c_x = 0.93. Separation was not seen in the case of p/c_x = 1.18, at Re = 50,000, although the experiments did show separation for chord Reynolds number of 67,500 at this wide blade spacing (Tu = 0.5%). The computations showed the interaction of the competing influences of adverse pressure gradient and transition to turbulence on the suction surface, and their relationship to separation.

This report concerns the first phase of a full vane-blade interaction study. Future calculations will vary the inlet conditions to simulate the presence of a stator vane. Ultimately, the stator and rotor will be modeled concurrently to simulate the change in the stator wake with time. The transient results will be compared with experimental measurements an unsteady Langston cascade at low Reynolds numbers.

References

Baldwin, B. S. and Lomax, H., 1978, "Thin Layer Approximation and Algebraic Model for Separated Turbulent Flows," AIAA Paper 78-0257.

Baughn, J. W., Butler, R. J., Byerley, A. R. and Rivir, R. B., 1995, "An Experimental Investigation of Heat Transfer, Transition and Separation on Turbine Blades at Low Reynolds Number and High Turbulence Intensity," 1995 ASME International Mechanical Engineering Conference and Exhibition.

Cline, M. C., 1977, "NAP: A Computer Program for the Computation of Two-Dimensional, Time-Dependent, Inviscid Nozzle Flow," Los Alamos National Laboratory Report LA-5984.

Dorney, D. J., Davis, R. L. and Sharma, O. P., 1995, "Unsteady Multi-Stage Analysis Using a Loosely-Coupled Blade Row Approach," AIAA Paper 95-0179.

Erdos, J. I., Alzner, E. and McNally, W., 1977, "Numerical Solution of Periodic Transonic Flow through a Fan Stage," *AIAA Journal,* Vol. 15, pp. 1559-1568.

Halstead, D. E., Wisler, D. C., Okiishi, T. H., Walker, G. J., Hodson, H. P. and Shin, H.-W., 1995, "Boundary Layer Development in Axial Compressors and Turbines," Four Parts, ASME Papers 95-GT-461, 95-GT-462, 95-GT-463 and 95-GT-464, accepted for publication in the Transactions of the ASME.

Jorgensen, P. C. E. and Chima, R. V., 1989, "An Unconditionally Stable Runge-Kutta Method for Unsteady Flows," AIAA Paper 89-0205.

Langston, L. S., Nice, M. L. and Hopper, R. M., 1977, "Three Dimensional Flow within a Turbine Cascade Passage," *Journal for Engineering and Power*, Vol. 99, pp. 21-28.

Rao, K. V., Delaney, R. A., and Dunn, M. G., 1994, "Vane-Blade Interaction in a Transonic Turbine, Part 1 Aerodynamics," *Journal of Propulsion and Power*, Vol. 10, pp. 305-311.

Rao, K. V., Delaney, R. A., and Topp, D. A., 1994, "Turbine Vane-Blade Interaction, Vol. 1, 2-D Euler/Navier-Stokes Aerodynamic and Grid Generation Developments," Wright Laboratory Report WL-TR-94-2073.

Sharma, O. P. and Tanrikut, S., 1994, "Unsteady Flows in Turbines-Impact on Design Procedure," AGARD Lecture Series 195, *Turbomachinery Design Using CFD*.

Swanson, R. C. and Turkel, E., 1987, "Artificial Dissipation and Central Difference Schemes for the Euler and Navier-Stokes Equations," AIAA Paper 87-1107.

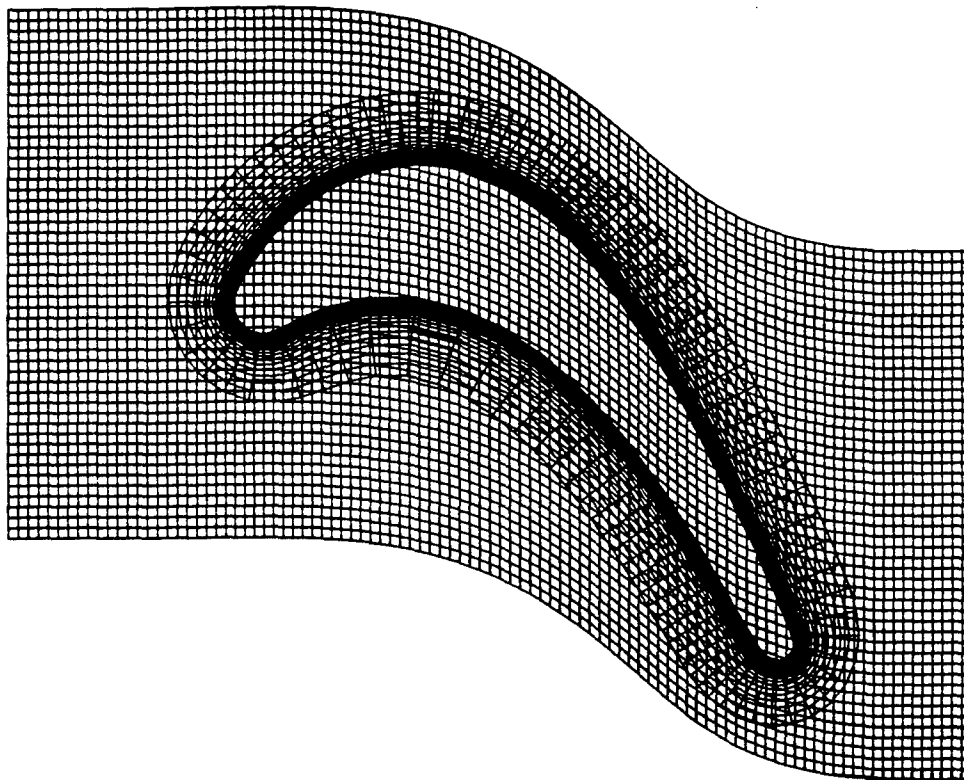White, F. M., 1974, *Viscous Fluid Flow*, McGraw Hill, Inc., New York, NY.

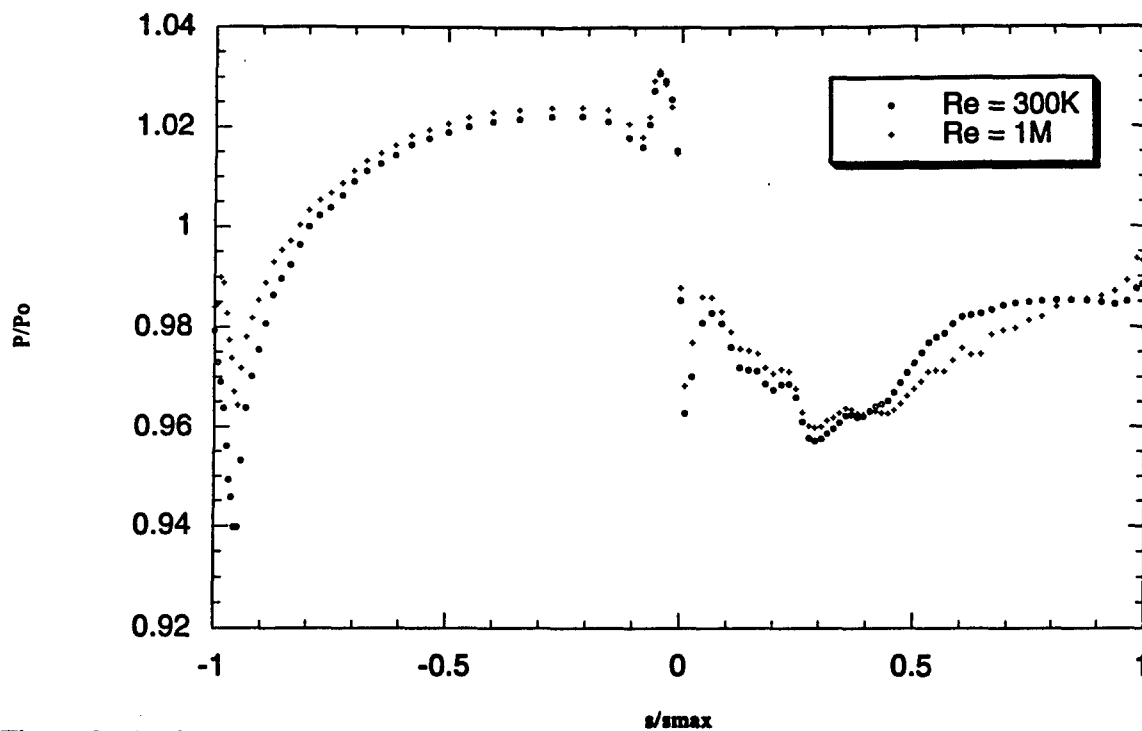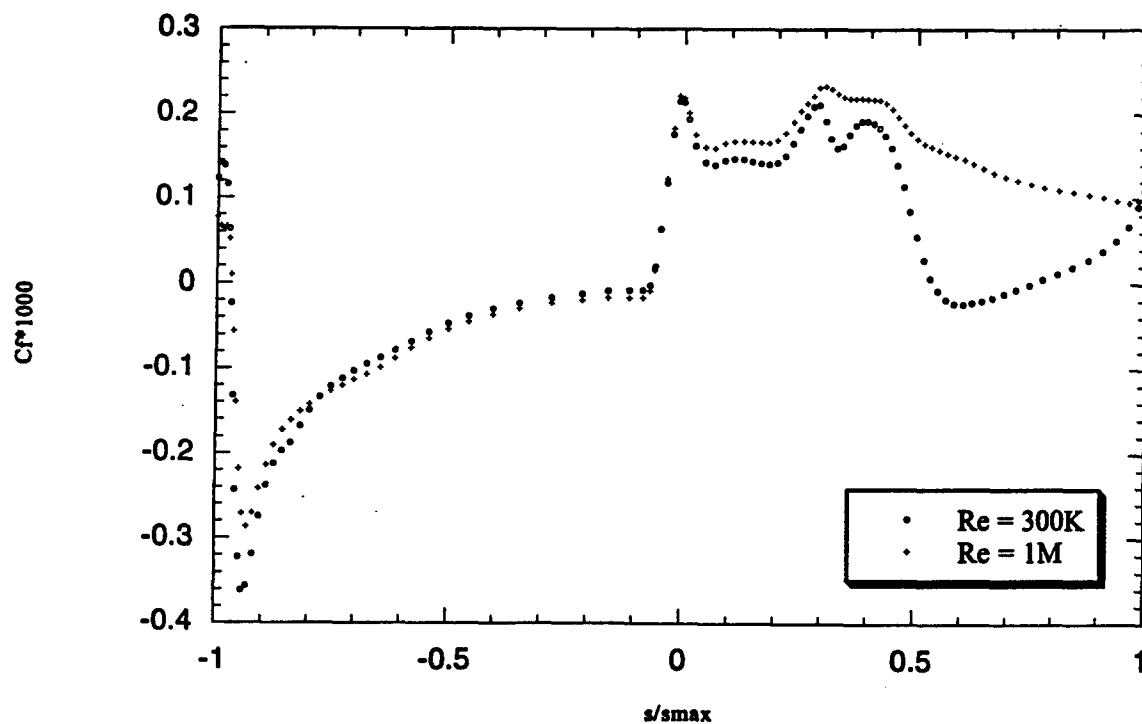Figure 1. Overlaid H- and O-Grids, 99x29 and 99x51, respectively.

Figure 2. Static pressure ratio, p/p_o, as a function of the wetted distance along the airfoil, s/s_{max}. Re = 300,000 (300K) and 10^6 (1M) at $p/c_x = 0.93$.

Figures 3. Skin friction coefficient, C_f, as a function of the wetted distance along the airfoil, s/s_{max}. Re = 300,000 (300K) and 10^6 (1M) at $p/c_x = 0.93$.
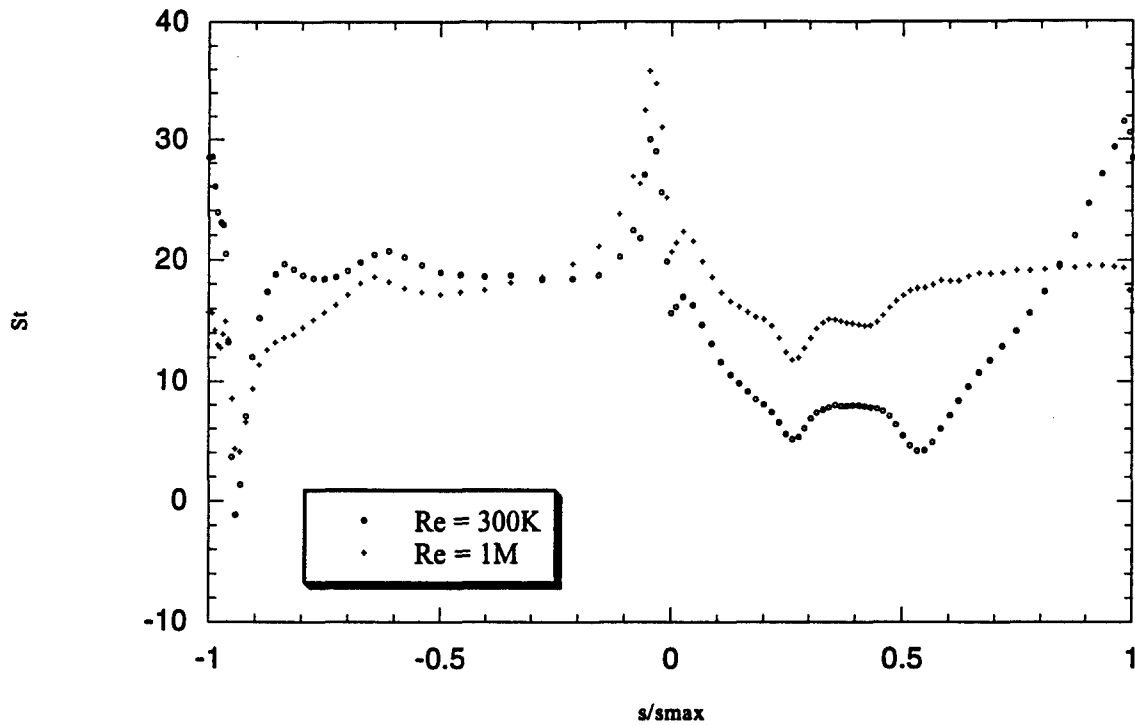
16-12

Figure 4. Stanton number, St, as a function of the wetted distance along the airfoil, s/s_{max}. Re = 300,000 (300K) and 10^6 (1M) at $p/c_x = 0.93$.
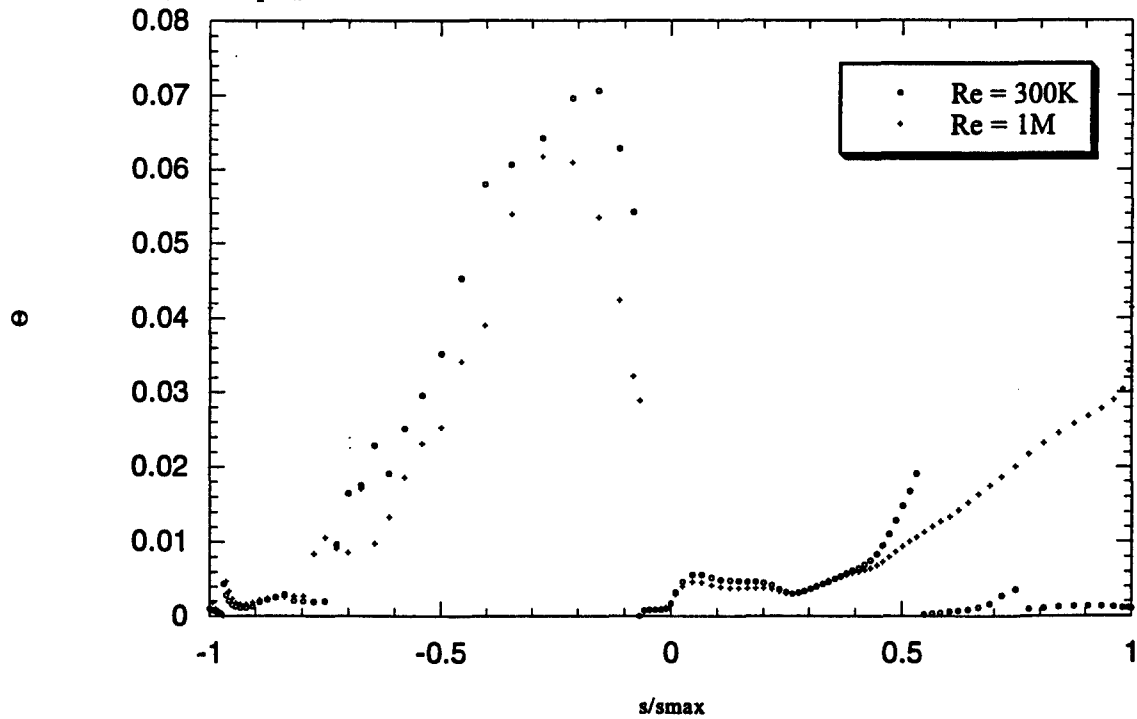

Figure 5. Momentum thickness, θ, as a function of the wetted distance along the airfoil, s/s_{max}. Re = 300,000 (300K) and 10^6 (1M) at $p/c_x = 0.93$.
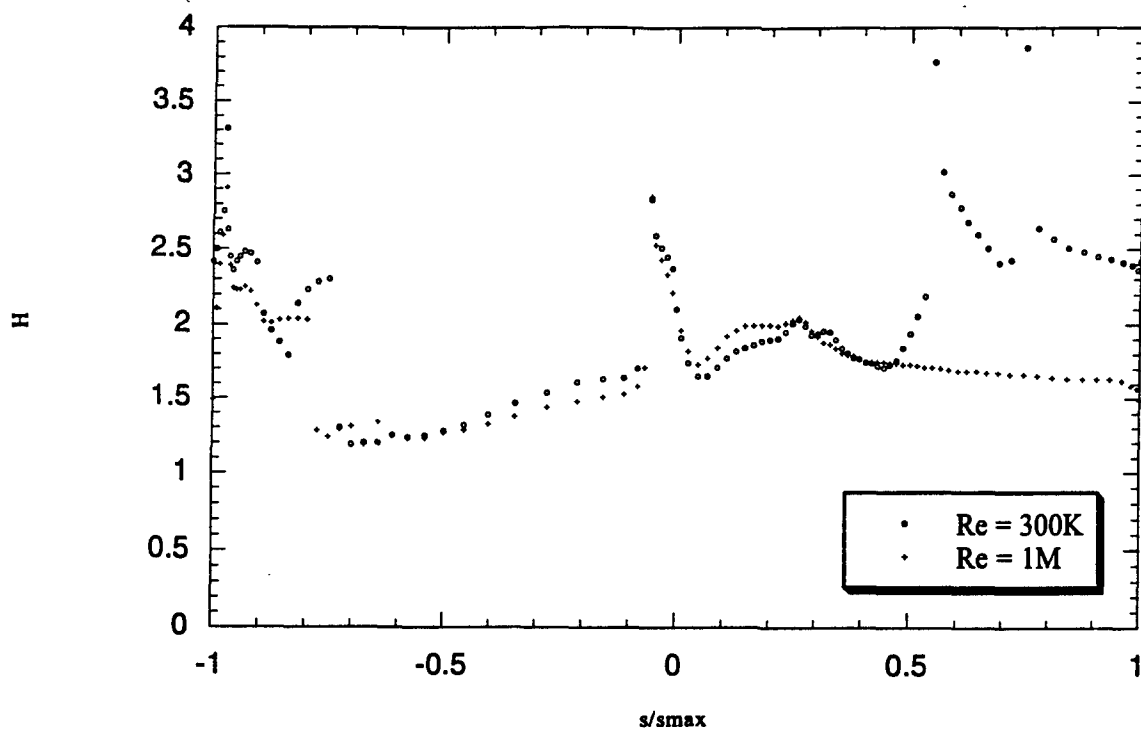
16-13

Figure 6. Shape Factor, H, as a function of the wetted distance along the airfoil, s/s_{max}. Re = 300,000 (300K) and 10^6 (1M) at $p/c_x = 0.93$.
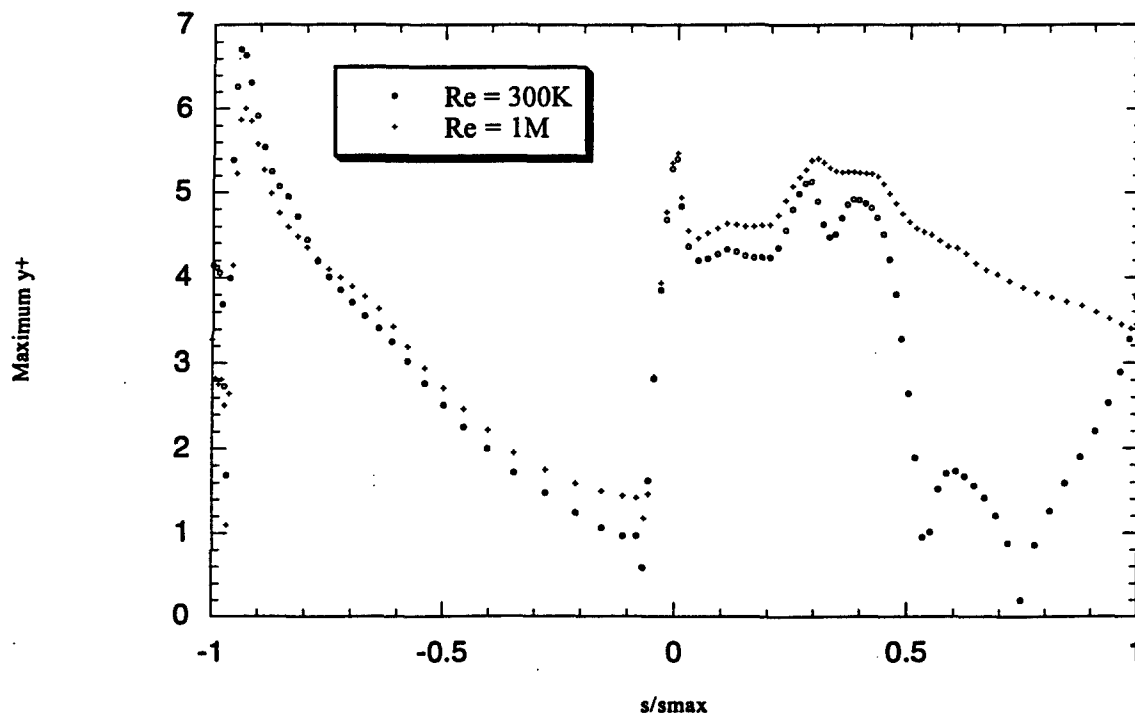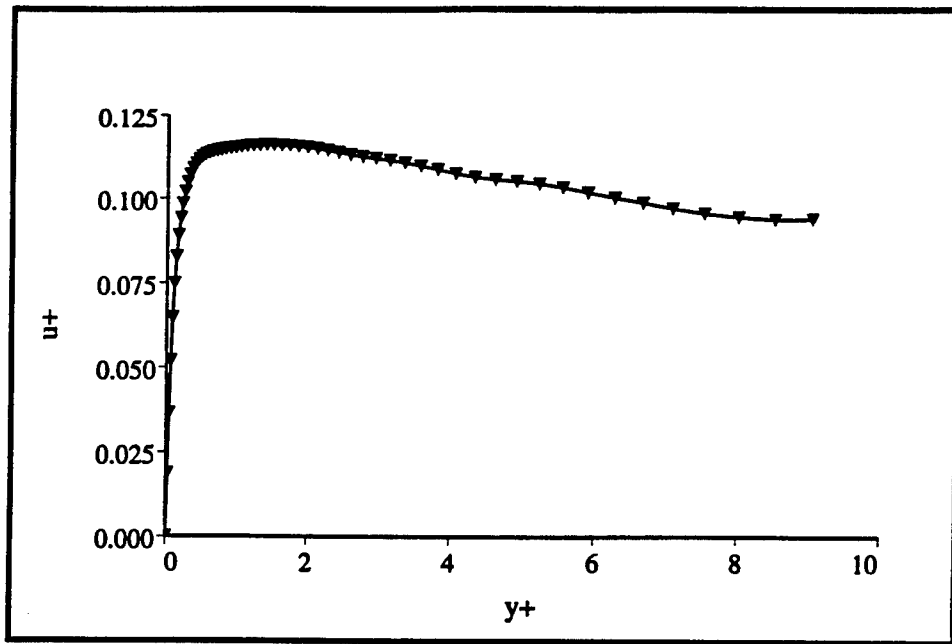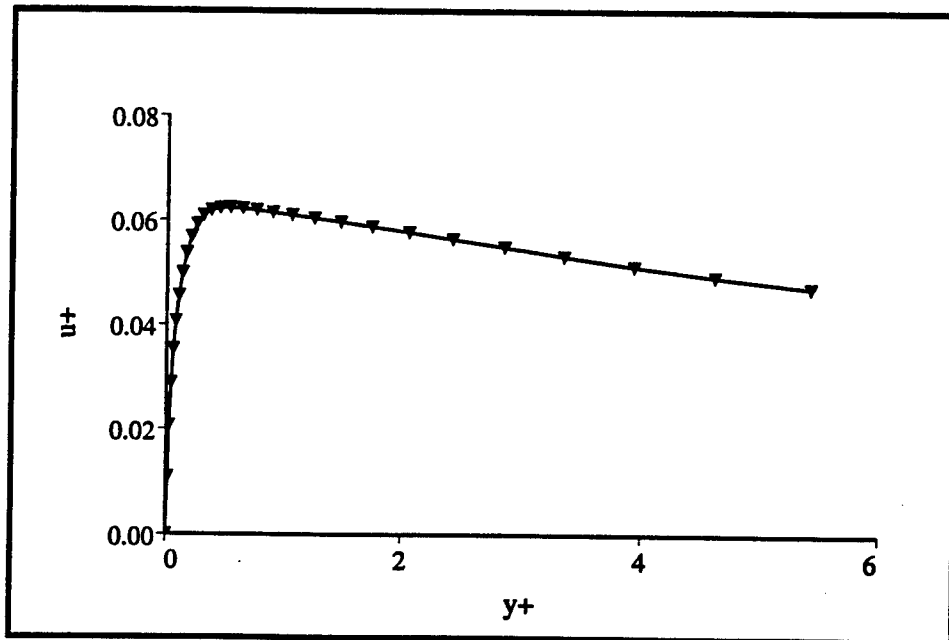

Figure 7. Maximum y+ in the O-grid, as a function of the wetted distance along the airfoil, s/s_{max}. Re = 300,000 (300K) and 10^6 (1M) at $p/c_x = 0.93$.
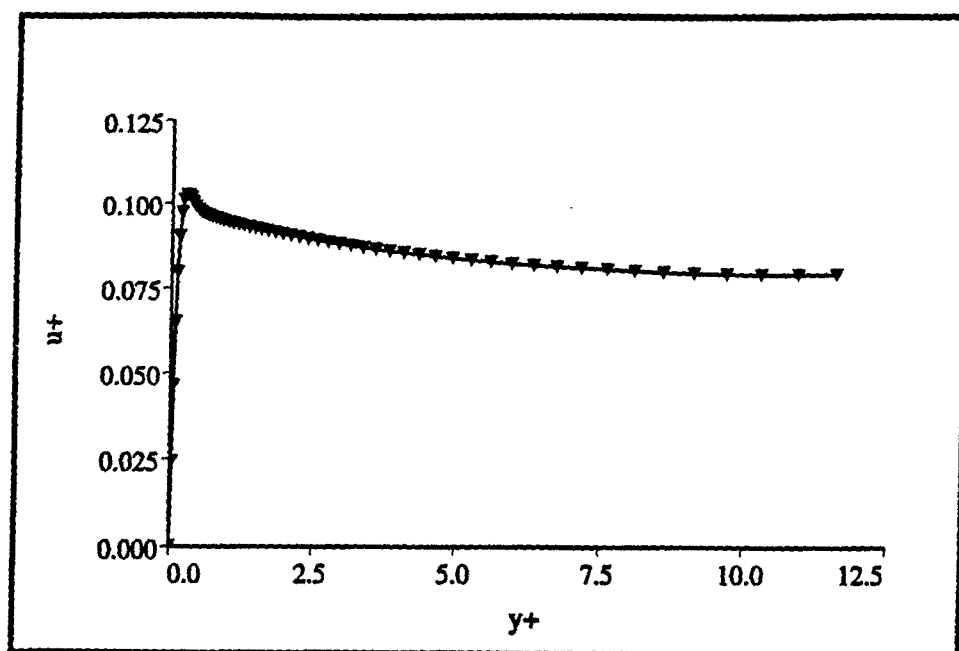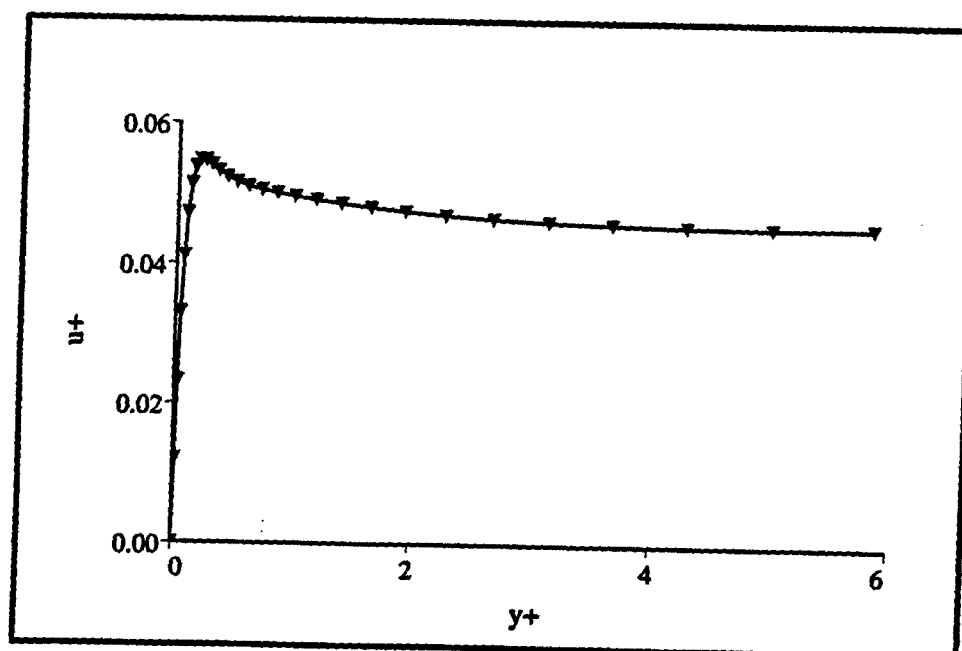
(a)

(b)

Figure 8. Velocity profile: u+ versus y+, on the suction surface ($p/c_x = 0.93$). (a) Re = 300,000, $s/s_{max} = 0.29$. (b) Re = 10^6, $s/s_{max} = 0.30$.

(a)

(b)

Figure 9. Velocity profile: u+ versus y+, on the pressure surface at $s/s_{max} = -0.93$ ($p/c_x = 0.93$). (a) Re = 300,000 (b) Re = 10^6.

INTERACTION OF MATRIX CRACKING AND INELASTIC DEFORMATION IN CERAMIC COMPOSITES

Zhanjun Gao
Department of Mechanical & Aeronautical Engineering
Clarkson University
Potsdam, NY 13699

and

Joseph R. Zuiker
Wright Laboratory Materials Directorate
WL/MLLN Bldg. 655
2230 Tenth Street, Suite 1
Wright-Patterson AFB, OH 45433-7817

Final Report for:
Summer Research Program
Wright Laboratory

August 1995

INTERACTION OF MATRIX CRACKING AND INELASTIC DEFORMATION IN CERAMIC COMPOSITES

Zhanjun Gao
Department of Mechanical & Aeronautical Engineering
Clarkson University
Potsdam, NY 13699

and

Joseph R. Zuiker
Wright Laboratory Materials Directorate
WL/MLLN Bldg. 655
2230 Tenth Street, Suite 1
Wright-Patterson AFB, OH 45433-7817

ABSTRACT

The interactions of matrix cracks and inelastic deformation of an eight-harness satin weave (8H SW) Nextel 610/Aluminosilicate ceramic matrix composite is studied. A variational approach is proposed to derive a nonlinear differential equation for the stress function which represents the stress field of the composite. The Green's function of the nonlinear differential equation is then obtained. Using the Green's function and a constitutive equation, a two-dimensional stress and creep strain states in the woven composites are evaluated. This new microcracking/inelastic deformation analysis is more accurate than previous attempts at the same problem. The predicted creep strain of the woven composite shows good correlation with experimental data at different levels of temperature and stress conditions.

Introduction

A variational approach for analyzing laminate containing matrix cracks has been provided by Hashin (1985a). One of the advantages of the variational solution is that it accurately includes transverse stresses and therefore distinguishes between $[0_m/90_n]_s$ and $[90_n/0_m]_s$ laminates. The shear-lag analyses (Highsmith and Reifsnider, 1977; Parvizi et al., 1978; Bailey et al., 1979; Flaggs, 1985) do not distinguishes between $[0_m/90_n]_s$ and $[90_n/0_m]_s$ laminates. As a matter of fact, Narin (1989) has shown that a better analytical result by variational approach cannot be obtained. However, inelastic deformation of the matrix material is not considered in the existing variational analyses.

In this research, a variational approach is proposed to analyze the response of woven oxide-oxide ceramic matrix composites which contain matrix cracks as well as inelastic deformation. The material considered here is an eight-harness satin weave (8H SW) Nextel 610/Aluminosilicate ceramic matrix composite. The material is the subject of concentrated research due to its superior performance at high temperatures. Typically, no interface coating is required to protect the fiber from environmental attack. An approximation to the eight-harness satin weave (8H SW) is made, following the mosaic model (Ishikawa and Chou, 1983) which treats woven composites as cross-ply laminates. Such a treatment provides a good representation of stresses and strains away from the region where the fibers cross.

Variation Formulation For Composites With Matrix Cracks and Inelastic Deformation

An admissible stress field for a cross-ply laminate under tension with cracks in $90°$ plies, Fig. 1, is constructed by using the approach suggested by Hashin (1985a) for a cracked cross-ply with no inelastic deformation. It is assumed that σ_{xx} is only a function of x, and $\sigma_{yz} = \sigma_{xy} = 0$. The systematic integration of the equations of equilibrium, taking into account traction continuity and boundary conditions defines an admissible stress field in terms of an unknown function, $\phi(x)$, as follows

$$\sigma_{11}^{(90°)} = \sigma^{(90°)}{}_{xx} = \sigma_{x0}^{(90°)} [1 - \phi(x)]$$

$$\sigma_{11}^{(0°)} = \sigma_{xx}^{(0°)} = \sigma_{x0}^{(0°)} + \frac{1}{\lambda} \sigma_{x0}^{(90°)} \phi(x)$$

$$\sigma_{13}^{(90°)} = \sigma_{xz}^{(90°)} = \sigma_{x0}^{(90°)} \phi'(x) z$$

$$\sigma_{13}^{(0°)} = \sigma_{xz}^{(0°)} = \frac{1}{\lambda} \sigma_{x0}^{(90°)} \phi'(x) (h - z),$$

$$\sigma_{22}^{(90°)} = \sigma_{yy}^{(90°)} = \sigma_{y0}^{(90°)}$$

$$\sigma_{22}^{(0°)} = \sigma_{yy}^{(0°)} = \sigma_{y0}^{(0°)}$$

$$\sigma_{33}^{(90°)} = \sigma_{zz}^{(90°)} = \frac{1}{2} \sigma_{x0}^{(90°)} \phi''(x) [ht_1 - z^2]$$

$$\sigma_{33}^{(0°)} = \sigma_{zz}^{(0°)} = \frac{1}{2\lambda} \sigma_{x0}^{(90°)} \phi''(x) [h - z]^2$$

$$\lambda = t_2/t_1$$

(1)

where superscripts $0°$ and $90°$ represent $0°$ and $90°$ plies; prime indicates derivative with respect to x; σ_0 and σ denote stresses in uncracked and cracked laminate, respectively; and t_1 and t_2 are the thicknesses of the $90°$ and $0°$ plies. The boundary conditions for function, $\phi(x)$, are

$$\phi(\pm a) = 1, \quad \frac{d\phi}{dx}(\pm a) = 0 \qquad\qquad\qquad (2)$$

where a is the half length of the crack spacing shown in Fig. 1. It should be emphasized that the matrix crack spacing needs not be uniform.

The complementary energy of the composite is given by

$$\Gamma = \frac{1}{2}\iiint_V S_{ijkl}\sigma_{ij}\sigma_{kl}\,dV + \iiint_V \sigma_{ij}\alpha_{ij}\Delta T\,dV + \Gamma^{in} \qquad\qquad (3)$$

where S_{ijkl}, α_{ij}, ΔT are the compliance tensor, thermal expansion coefficient tensor and the temperature difference between the current temperature and the stress free temperature, respectively; Γ^{in} represents the contribution of the inelastic strain to the complementary energy of the system, which will be discussed in some details later.

The first two terms in Γ for the region between two micro-cracks; i.e., for the region -a < x < a and -h < z < h are evaluated by substituting the stress expressions in Eqn. (1) into Eqn. (3). Therefore,

$$\Gamma = \Gamma^0 + (\sigma_{x0}^{(90°)})^2 \int_{-a}^{a} dx \int_{0}^{t_1} dz \left[-\frac{2\phi}{E_T} - \frac{\nu_T\,(ht_1 - z^2)\,\phi''}{E_T} + \right.$$

$$\frac{\phi^2}{E_T} + \frac{\nu_T\,(ht_1 - z^2)\,\phi\,\phi''}{E_T} + \frac{(ht_1 - z^2)^2\,\phi''\,\phi''}{4E_T} + \frac{z^2\,\phi'\,\phi'}{G_T}$$

$$\left. - 2\alpha_T\Delta T\,\phi + \alpha_T\Delta T\,(ht_1 - z^2)\,\phi'' \right] +$$

$$(\sigma_{x0}^{(90°)})^2 \int_{-a}^{a} dx \int_{t_1}^{h} dz \left[\frac{2\phi}{\lambda E_T} - \frac{\nu_A\,(h - z)^2\,\phi''}{\lambda E_T} + \right.$$

$$\frac{\phi^2}{\lambda^2 E_A} - \frac{\nu_A\,(h - z)^2\,\phi\,\phi''}{\lambda^2 E_A} + \frac{(h - z)^4\,\phi''\,\phi''}{4\lambda^2 E_A} + \frac{(h - z)^2\,\phi'\,\phi'}{\lambda^2 G_T}$$

$$\left. + \frac{2\alpha_A\Delta T\,\phi}{\lambda} + \frac{\alpha_T\Delta T\,(h - z)^2\,\phi''}{\lambda} \right] + \Gamma^{in}.$$

Let $\xi = x/t_1$ and we have

$$\Gamma = \Gamma^0 + (\sigma_{x0}^{(90^\circ)})^2 (t_1)^2 \int_{-\rho}^{\rho} [C_1 \phi^2 + C_2 \phi \phi'' + C_3 (\phi'')^2 + C_4 (\phi')^2$$
$$- 2(\alpha_T - \alpha_A) \Delta T \phi + C_5 \phi''] \, d\xi \qquad (4)$$

where E_A, E_T, G_A, G_T, ν_A, ν_T, α_A, α_T, are the axial and transverse Young's moduli, shear moduli, Poisson's ratios, and thermal expansion coefficients respectively; and

$$\Gamma^0 = \int_{-a}^{a} dx \int_{0}^{t_1} dz [\frac{\sigma_{x0}^{(90^\circ)}}{E_T} + 2\alpha_T \Delta T] \, \sigma_{x0}^{(90^\circ)} +$$

$$\int_{-a}^{a} dx \int_{t_1}^{h} dz [\frac{\sigma_{x0}^{(0^\circ)}}{E_A} + 2\alpha_A \Delta T] \, \sigma_{x0}^{(0^\circ)}$$

is the complementary energy of the laminate without any damage and inelastic strain, and

$$C_1 = \frac{hE_0}{t_2 \, E_A \, E_T} \qquad\qquad C_2 = \frac{\nu_T}{E_T} (\lambda + \frac{2}{3}) - \frac{\lambda}{3} \frac{\nu_A}{E_A}$$

$$C_3 = \frac{\lambda + 1}{60E_T}(3\lambda^2 + 12\lambda + 8) \qquad C_4 = \frac{1}{3} (\frac{1}{G_T} + \frac{\lambda}{G_A})$$

$$C_5 = (\alpha_T \Delta T - \frac{\nu_T}{E_0} \sigma_{applied}) (\lambda + \frac{2}{3}) + (\alpha_T \Delta T - \frac{\nu_A}{E_0} \sigma_{applied}) \frac{\lambda^2}{3}.$$

The first order variation of the functional Γ, $\delta\Gamma$ is found, using Eqn. (4)

$$\delta\Gamma = \delta\Gamma^{in} +$$

$$2C_3 \, \sigma_{x0}^{(90^\circ)})^2 (t_1)^2 \int_{-\rho}^{\rho} [\frac{d^4\phi(\xi)}{d\xi^4} + p \frac{d^2\phi(\xi)}{d\xi^2} + q \, \phi(\xi) - \frac{(\alpha_T - \alpha_A) \Delta T}{C_3}] \, \delta\phi(\xi) \, d\xi \qquad (5)$$

where $p = (C_2 - C_4)/C_3$ and $q = C_1/C_3$.

The contribution of the inelastic strain, ε_{ij}^{in}, to the variation of the total complimentary energy is given as

$$\delta\Gamma^{in} = \iiint_v \varepsilon_{ij}^{in} \delta\sigma_{kl} \, dV$$

$$= \int_{-a}^{a} dx \int_{0}^{t_1} dz \{ \varepsilon_{11}^{in}(90°) \, \delta\sigma_{11}(90°) + \varepsilon_{33}^{in}(90°) \, \delta\sigma_{33}(90°) + 2\varepsilon_{13}^{in}(90°) \, \delta\sigma_{13}(90°) \}$$

$+$

$$\int_{-a}^{a} dx \int_{t_1}^{h} dz \{ \varepsilon_{11}^{in}(0°) \, \delta\sigma_{11}(0°) + \varepsilon_{33}^{in}(0°) \, \delta\sigma_{33}(0°) + 2\varepsilon_{13}^{in}(0°) \, \delta\sigma_{13}(0°) \}$$

$$= \sigma_{x0}(90°) \int_{-a}^{a} dx \int_{0}^{t_1} dz \{ \varepsilon_{11}^{in}(90°) \, \delta[-\phi] + \varepsilon_{33}^{in}(90°) \, \delta[\frac{1}{2}\phi''(x)(ht_1 - z^2)] +$$

$$2\varepsilon_{13}^{in}(90°) \delta[\phi'(x) z] \} +$$

$$\sigma_{x0}(90°) \int_{-a}^{a} dx \int_{t_1}^{h} dz \{ \varepsilon_{11}^{in}(0°) \delta[\frac{\phi}{\lambda}] + \varepsilon_{33}^{in}(0°) \, \delta[\frac{1}{2\lambda}\phi''(x)(h - z)^2] +$$

$$2\varepsilon_{13}^{in}(0°)[\frac{1}{\lambda}\phi'(x)(h-z)] \}$$

Let $\xi = x/t_1$ and $\omega = z/t_1$, we have

$$\delta\Gamma^{in} = (t_1)^2 \sigma_{x0}(90°) \int_{-\rho}^{\rho} \{ A_1(\xi) \, \delta\phi(\xi) + A_2(\xi) \, \delta\phi''(\xi) + A_3(\xi) \, \delta\phi'(\xi) \} \, d\xi +$$

$$+ (t_1)^2 \sigma_{x0}(90°) \int_{-\rho}^{\rho} \{ B_1(\xi) \, \delta\phi(\xi) + B_2(\xi) \, \delta\phi''(\xi) + B_3(\xi) \, \delta\phi'(\xi) \} \, d\xi$$

$$= (t_1)^2 \, w \, \sigma_{x0}(90°) \int_{-\rho}^{\rho} \{ A_1(\xi) + \frac{d^2 A_2(\xi)}{d\xi^2} - \frac{d A_3(\xi)}{d\xi} \} \, \delta\phi(\xi) \, d\xi$$

$$+ (t_1)^2 \, \sigma_{x0}(90°) \int_{-\rho}^{\rho} \{ B_1(\xi) + \frac{d^2 B_2(\xi)}{d\xi^2} - \frac{d B_3(\xi)}{d\xi} \} \, \delta\phi(\xi) \, d\xi \qquad (6)$$

where

$$A_1(\xi) = - \int_{0}^{1} \varepsilon_{11}^{in}(90°) \, d\omega \qquad (7)$$

$$A_2(\xi) = \int_0^1 \frac{1}{2} \left[h/t_1 - \omega^2\right] \varepsilon_{33}^{in}(90°) \, d\omega \tag{8}$$

$$A_3(\xi) = 2 \int_0^1 \varepsilon_{13}^{in}(90°) \, \omega \, d\omega \tag{9}$$

$$B_1(\xi) = \frac{1}{\lambda} \int_1^{h/t_1} \varepsilon_{11}^{in}(0°) \, d\omega \tag{10}$$

$$B_2(\xi) = \frac{1}{2\lambda} \int_1^{h/t_1} (h/t_1 - \omega)^2 \, \varepsilon_{33}^{in}(0°) \, d\omega \tag{11}$$

$$B_3(\xi) = 2 \frac{1}{\lambda} \int_1^{h/t_1} (h/t_1 - \omega) \, \varepsilon_{13}^{in}(0°) \, d\omega \tag{12}$$

Substituting Eqn. (6) into Eqn. (5) and using the condition $\delta\Gamma = 0$, one obtains the governing equation for function $\phi(\xi)$

$$\frac{d^4\phi(\xi)}{d\xi^4} + p \frac{d^2\phi(\xi)}{d\xi^2} + q \, \phi(\xi) = F(\xi) \tag{13}$$

where

$$F(\xi) = \frac{(\alpha_T - \alpha_A)\Delta T}{C_3}$$
$$- \left\{ A_1(\xi) + \frac{d^2 A_2(\xi)}{d\xi^2} - \frac{dA_3(\xi)}{d\xi} + B_1(\xi) + \frac{d^2 B_2(\xi)}{d\xi^2} - \frac{dB_3(\xi)}{d\xi} \right\} / [2C_3 \sigma_{x0}(90°)]$$

The boundary conditions for Eqn. (13) is, from Eqn. (2)

$$\phi(\xi)|_{\xi = \pm\rho} = 1, \qquad \frac{d\phi(\xi)}{d\xi} \Big|_{\xi = \pm\rho} = 0. \tag{14}$$

Constitutive Equations

The inhomogeneous term, $F(\xi)$, in Eqn. (13) is related to the inelastic strain of the laminate. This section deals with the constitutive relationships which describe

17-7

such a strain using the response of the $0°$ and $90°$ Plies. Creep deformation is used here to demonstrate the proposed model.

A one dimensional creep response is given by Dorn's law (Mukherjee, et. al., 1969)

$$\dot{\varepsilon}^c = A\{\frac{|\sigma|}{G}\}^n \frac{G\,b}{k\,T} D_0 \, Exp\{-\frac{Q}{R\,T}\} \tag{15}$$

where $\dot{\varepsilon}^c$ and σ are the creep rate and stress of the material, A and n are constants that can be determined experimentally, G is the shear modulus, b is the Burger's vector, k is Boltzmann's constant, and D_0 and Q are pre-exponential constant and activation energy for self-diffusion.

For two-dimensional and three-dimensional problems, the Prandtl-Reuss relations can be used for computing the creep increments. Thus we assume an equivalent stress defined the same way as in plasticity theory and an equivalent creep strain increment and write

$$\dot{\varepsilon}^{c,eff} = A\{\frac{\sigma^{eff}}{G}\}^n \frac{G\,b}{k\,T} D_0 \, Exp\{-\frac{Q}{R\,T}\} \tag{16}$$

where $\dot{\varepsilon}^{c,eff}$ and σ^{eff} are the von Mises' effective strain rate and effective stress defined as

$$\sigma^{eff} = \sqrt{(\frac{3}{2}\sigma^*_{ij}\sigma^*_{ij})} \tag{17}$$

and

$$\dot{\varepsilon}^c_{ij} = \frac{3}{2}\frac{\dot{\varepsilon}^{c,eff}}{\sigma^{eff}}\sigma^*_{ij} \tag{18}$$

$$\dot{\varepsilon}^{c,eff} = \sqrt{(\frac{2}{3}\dot{\varepsilon}^c_{ij}\dot{\varepsilon}^c_{ij})} \tag{19}$$

respectively. σ^*_{ij} is the deviatoric stress.

Equations (16) and (18) are written in an incremental form

$$\Delta\varepsilon^{c,eff} = A\{\frac{\sigma^{eff}}{G}\}^n \frac{G\,b}{k\,T} D_0 \, Exp\{-\frac{Q}{R\,T}\}\Delta t \tag{21}$$

$$\Delta\varepsilon^c_{ij} = \frac{3}{2}\frac{\Delta\varepsilon^{c,eff}}{\sigma^{eff}}\sigma^*_{ij} = \frac{3}{2} A\,(\frac{1}{G})^n \frac{G\,b}{k\,T} D_0 \, Exp\{-\frac{Q}{R\,T}\}\,(\sigma^{eff})^{(n-1)}\,\sigma^*_{ij}\,\Delta t. \tag{22}$$

Therefore, the total creep strain at the instant, $t+\Delta t$, is

$$\varepsilon_{ij}^c = \varepsilon_{ij}^{co} + \Delta\varepsilon_{ij}^c = \varepsilon_{ij}^{co} + (\sigma^{eff})^{(n-1)} \sigma_{ij}^* w \Delta t \tag{23}$$

where ε_{ij}^{co} is the known creep strain at the instant, t; and w is independent of stresses and is defined as

$$w = \frac{3}{2} A \left(\frac{1}{G}\right)^n \frac{G}{k} \frac{b}{T} D_0 \, Exp\{-\frac{Q}{R\,T}\}. \tag{24}$$

The constitutive law in Eqns. (16) to (23) are for isotropic materials. To applied them to a composite laminate, different values of exponents are used

$$\varepsilon_{ij}^c(90°) = \varepsilon_{ij}^{co}(90°) + \Delta\varepsilon_{ij}^c(90°) = \varepsilon_{ij}^{co}(90°) + (\sigma^{eff})^{(n_m-1)} \sigma_{ij}^* w_m \Delta t \tag{25}$$

$$\varepsilon_{ij}^c(0°) = \varepsilon_{ij}^{co}(0°) + \Delta\varepsilon_{ij}^c(0°) = \varepsilon_{ij}^{co}(0°) + (\sigma^{eff})^{(n_f-1)} \sigma_{ij}^* w_f \Delta t \tag{26}$$

where n_m (or w_m) and n_f (or w_f) are the parameters of experiments for creep deformation with loading along transverse and fiber directions, respectively.

The expressions of stresses as functions of x and ω are obtained from Eqn. (1) and the relationships $\xi = x/t_1$ and $\omega = z/t_1$

$$\sigma_{11}(90°) = \sigma_{x0}(90°) [1 - \phi(\xi)]$$

$$\sigma_{11}(0°) = \sigma_{x0}(0°) + \frac{1}{\lambda} \sigma_{x0}(90°) \phi(\xi)$$

$$\sigma_{13}(90°) = \sigma_{x0}(90°) \omega \frac{d\phi(\xi)}{d\xi}$$

$$\sigma_{13}(0°) = \frac{1}{\lambda} \sigma_{x0}(90°) \frac{d\phi(\xi)}{d\xi} (h/t_1 - \omega),$$

$$\sigma_{22}(90°) = \sigma_{y0}(90°)$$

$$\sigma_{22}(0°) = \sigma_{y0}(0°) \tag{27}$$

$$\sigma_{33}(90°) = \frac{1}{2} \sigma_{x0}(90°) \frac{d^2\phi(\xi)}{d\xi^2} [h/t_1 - \omega^2]$$

$$\sigma_{33}(0°) = \frac{1}{2\lambda} \sigma_{x0}(90°) \frac{d^2\phi(\xi)}{d\xi^2} [h/t_1 - \omega]^2$$

Stresses used in Eqns. (17) to (26) are written below as function of ξ and ω

$$\sigma_{\alpha\alpha}(90°) = \sigma_{11}(90°) + \sigma_{22}(90°) + \sigma_{33}(90°)$$

$$\sigma^*_{11}{}^{(90°)} = \sigma^*_{11}{}^{(90°)}(\xi, \omega) = \sigma_{11}{}^{(90°)}(\xi, \omega) - \frac{1}{3}\sigma_{\alpha\alpha}{}^{(90°)}$$

$$\sigma^*_{22}{}^{(90°)} = \sigma^*_{22}{}^{(90°)}(\xi, \omega) = \sigma_{22}{}^{(90°)}(\xi, \omega) - \frac{1}{3}\sigma_{\alpha\alpha}{}^{(90°)}$$

$$\sigma^*_{33}{}^{(90°)} = \sigma^*_{33}{}^{(90°)}(\xi, \omega) = \sigma_{33}{}^{(90°)}(\xi, \omega) - \frac{1}{3}\sigma_{\alpha\alpha}{}^{(90°)}$$

$$\sigma^*_{13}{}^{(90°)} = \sigma_{13}{}^{(90°)}(\xi, \omega) = \omega\sigma_{x0}{}^{(90°)}\frac{d\phi(\xi)}{d\xi}$$

$$\sigma^{eff,90°} = \sigma^{eff,90°}(\xi, \omega)$$

$$= \{\frac{3}{2}[(\sigma^*_{11}{}^{(90°)})2 + (\sigma^*_{22}{}^{(90°)})2 + (\sigma^*_{33}{}^{(90°)})2 + (\sigma^*_{13}{}^{(90°)})2]\}^{0.5}$$

$$\sigma_{\alpha\alpha}{}^{(0°)} = \sigma_{11}{}^{(0°)} + \sigma_{22}{}^{(0°)} + \sigma_{33}{}^{(0°)} .$$

$$\sigma^*_{11}{}^{(0°)} = \sigma^*_{11}{}^{(0°)}(\xi, \omega) = \sigma_{11}{}^{(0°)}(\xi, \omega) - \frac{1}{3}\sigma_{\alpha\alpha}{}^{(0°)}$$

$$\sigma^*_{22}{}^{(0°)} = \sigma^*_{22}{}^{(0°)}(\xi, \omega) = \sigma_{22}{}^{(0°)}(\xi, \omega) - \frac{1}{3}\sigma_{\alpha\alpha}{}^{(0°)}$$

$$\sigma^*_{33}{}^{(0°)} = \sigma^*_{33}{}^{(0°)}(\xi, \omega) = \sigma_{33}{}^{(0°)}(\xi, \omega) - \frac{1}{3}\sigma_{\alpha\alpha}{}^{(0°)}$$

$$\sigma^*_{13}{}^{(0°)} = \sigma_{13}{}^{(0°)}(\xi, \omega) = \frac{1}{\lambda}\sigma_{x0}{}^{(90°)}\frac{d\phi(\xi)}{d\xi}(h/t_1 - \omega)$$

$$\sigma^{eff,0°} = \sigma^{eff,0°}(\xi, \omega)$$

$$= \{\frac{3}{2}[(\sigma^*_{11}{}^{(0°)})2 + (\sigma^*_{22}{}^{(0°)})2 + (\sigma^*_{33}{}^{(0°)})2 + (\sigma^*_{13}{}^{(0°)})2]\}^{0.5}.$$

(28)

The Green's Function

The proposed problem of analyzing a laminate with cracked 90° plies and inelastic strain is reduced to solving Eqn. (13) for the stress function, $\phi(\xi)$. Since the inhomogeneous term, $F(\xi)$, in Eqn. (13) is a function of inelastic strain which depends on time and stress history, an incremental analysis is needed to determine the stress function, $\phi(\xi)$, during the loading history. For this purpose the Green's

function for the system is constructed. We seek the solution of the following boundary value problem

$$\frac{d^4 G(\xi,\eta)}{d\xi^4} + p \frac{d^2 G(\xi,\eta)}{d\xi^2} + q\, G(\xi,\eta) = \delta(\xi-\eta) \tag{29}$$

$$G(\xi,\eta)|_{\xi=\pm\rho} = 0, \quad \frac{dG}{d\xi}(\xi,\eta)|_{\xi=\pm\rho} = 0$$

where $\delta(\xi-\eta)$ is the Dirac delta function.

The solution to Eqn. (29) can be obtained by the following heuristic procedure. Let ϕ_1 and ϕ_2 be two general solutions of the homogeneous equation

$$\frac{d^4\phi(\xi)}{d\xi^4} + p \frac{d^2\phi(\xi)}{d\xi^2} + q\, \phi(\xi) = 0 \tag{30}$$

where ϕ_1 satisfies the boundary conditions at $\xi = -\rho$ and ϕ_2 satisfies the boundary conditions at $\xi = \rho$, i.e., $\phi_1(\xi)|_{\xi=-\rho} = 0, \frac{d\phi_1(\xi)}{d\xi}|_{\xi=-\rho} = 0; \phi_2(\xi)|_{\xi=\rho} = 0, \frac{d\phi_2(\xi)}{d\xi}|_{\xi=\rho} = 0$. If ϕ_1 and ϕ_2 also satisfy the conditions at $\xi = \eta$,

$$\phi_1(\xi)|_{\xi=\eta} = \phi_2(\xi)|_{\xi=\eta}, \quad \frac{d\phi_1(\xi)}{d\xi}|_{\xi=\eta} = \frac{d\phi_2(\xi)}{d\xi}|_{\xi=\eta},$$

$$\frac{d^2\phi_1(\xi)}{d\xi^2}|_{\xi=\eta} = \frac{d^2\phi_2(\xi)}{d\xi^2}|_{\xi=\eta}, \quad \frac{d^3\phi_1(\xi)}{d\xi^3}|_{\xi=\eta} = \frac{d^3\phi_2(\xi)}{d\xi^3}|_{\xi=\eta} - 1, \tag{31}$$

then

$$G(\xi,\eta) = \begin{cases} \phi_1(\xi) & \text{for } \xi < \eta \\ \phi_2(\xi) & \text{for } \xi > \eta \end{cases}$$

The above procedure of determining the Green's function in Eqn. (29) is an extension of the approach described by Stakgold (1970) on Green's function for a second order ordinary differential equation.

It is not difficult to verify that ϕ_1 and ϕ_2 take the following form

$$\phi_1(\xi) = -b_1 u_1(\xi) - b_2 u_2(\xi)$$

$$\phi_2(\xi) = b_3 u_3(\xi) + b_4 u_4(\xi) \tag{32}$$

where

$$u_1(\xi) = \text{Sin}[\beta(\xi+\rho)] \; \text{Sinh}[\alpha(\xi+\rho)]$$

$$u_2(\xi) = \text{Sin}[\beta(\xi+\rho)] \; \text{Cosh}[\alpha(\xi+\rho)] - \frac{\beta}{\alpha} \text{Cos}[\beta(\xi+\rho)] \; \text{Sinh}[\alpha(\xi+\rho)] \tag{33}$$

are the solutions for the homogenous equation satisfying the homogenous boundary conditions at $\xi = -\rho$, and

$$u_3(\xi) = \text{Sin}[\,\beta\,(\xi-\rho)]\quad\text{Sinh}[\,\alpha\,(\xi-\rho)]$$

$$u_4(\xi) = \text{Sin}[\,\beta\,(\xi-\rho)]\quad\text{Cosh}[\,\alpha\,(\xi-\rho)]\;-\;\frac{\beta}{\alpha}\;\text{Cos}[\,\beta\,(\xi-\rho)]\quad\text{Sinh}[\,\alpha\,(\xi-\rho)] \qquad (34)$$

are the solutions for the homogenous equation satisfying the homogenous boundary conditions at $\xi = \rho$; b_1, b_2, b_3 and b_4 are constants (related to η) to be determined from the matching conditions at $\xi = \eta$, Eqn. (31). The values of α and β are given as,

when $\dfrac{4q}{p^2} - 1 > 0$:

$$\alpha = q^{\frac{1}{4}}\,\text{Cos}[\theta/2], \qquad\qquad \beta = q^{\frac{1}{4}}\,\text{Sin}[\theta/2]$$

$$\theta = \text{ArcTan}\sqrt{\frac{4q}{p^2} - 1}$$

and when $\dfrac{4q}{p^2} - 1 < 0$:

$$\alpha = \sqrt{\frac{-p}{2} + \sqrt{\frac{p^2}{4} - q}}\,, \qquad\qquad \beta = \sqrt{\frac{-p}{2} - \sqrt{\frac{p^2}{4} - q}}\,.$$

Substituting Eqns. (32), (33) and (34) into Eqn. (31), one obtains the following condition to determine constants b1, b2, b_3 and b_4

$$\begin{pmatrix} u_1(\eta) & u_2(\eta) & u_3(\eta) & u_4(\eta) \\ u_1{}'(\eta) & u_2{}'(\eta) & u_3{}'(\eta) & u_4{}'(\eta) \\ u_1{}''(\eta) & u_2{}''(\eta) & u_3{}''(\eta) & u_4{}''(\eta) \\ u_1{}'''(\eta) & u_2{}'''(\eta) & u_3{}'''(\eta) & u_4{}'''(\eta) \end{pmatrix} \begin{bmatrix} b_1 \\ b_2 \\ b_3 \\ b_4 \end{bmatrix} = \begin{Bmatrix} 0 \\ 0 \\ 0 \\ 1 \end{Bmatrix}. \qquad (35)$$

Therefore,

$$b_1 = b_1(\eta) = - \,W[u_2(\eta),u_3(\eta),u_4(\eta)]\ /\ W[u_1(\eta),u_2(\eta),u_3(\eta),u_4(\eta)]$$

$$b_2 = b_2(\eta) = \ W[u_1(\eta),u_3(\eta),u_4(\eta)]\ /\ W[u_1(\eta),u_2(\eta),u_3(\eta),u_4(\eta)]$$

$$b_3 = b_3(\eta) = - \,W[u_1(\eta),u_2(\eta),u_4(\eta)]\ /\ W[u_1(\eta),u_2(\eta),u_3(\eta),u_4(\eta)]$$

$$b_4 = b_4(\eta) = \ W[u_1(\eta),u_2(\eta),u_3(\eta)]\ /\ W[u_1(\eta),u_2(\eta),u_3(\eta),u_4(\eta)] \qquad (36)$$

where W[......] is the Wronskian of the function involved. For example,

$$W[u_1(\eta), u_2(\eta), u_3(\eta), u_4(\eta)] = \text{Det} \begin{pmatrix} u_1(\eta) & u_2(\eta) & u_3(\eta) & u_4(\eta) \\ u_1'(\eta) & u_2'(\eta) & u_3'(\eta) & u_4'(\eta) \\ u_1''(\eta) & u_2''(\eta) & u_3''(\eta) & u_4''(\eta) \\ u_1'''(\eta) & u_2'''(\eta) & u_3'''(\eta) & u_4'''(\eta) \end{pmatrix} \quad (37)$$

and

$$W[u_2(\eta), u_3(\eta), u_4(\eta)] = \text{Det} \begin{pmatrix} u_2(\eta) & u_3(\eta) & u_4(\eta) \\ u_2'(\eta) & u_3'(\eta) & u_4'(\eta) \\ u_2''(\eta) & u_3''(\eta) & u_4''(\eta) \end{pmatrix}.$$

The solution of the Eqn. (13) is then given as

$$\phi(\xi) = \phi_0(\xi) + \int_{-\rho}^{\rho} F(\eta)\, G(\xi, \eta)\, d\eta \quad (38)$$

where $\phi_0(\xi)$ is the solution of the homogenous equation (with $F(\xi)=0$ in Eqn. (13)) under the boundary condition shown in Eqn. (14), and is given as

when $\dfrac{4q}{p^2} - 1 > 0$:

$$\phi_0(\xi) = \frac{2(\beta\, \text{Sinh}[\alpha\rho]\, \text{Cos}[\beta\rho] + \alpha\, \text{Cosh}[\alpha\rho]\, \text{Sin}[\beta\rho])}{\beta\, \text{Sinh}[2\alpha\rho] + \alpha\, \text{Sin}[2\beta\rho]} \text{Cosh}[\alpha\xi]\, \text{Cos}[\beta\xi]$$

$$+ \frac{2(\beta\, \text{Cosh}[\alpha\rho]\, \text{Sin}[\beta\rho] - \alpha\, \text{Sinh}[\alpha\rho]\, \text{Cos}[\beta\rho])}{\beta\, \text{Sinh}[2\alpha\rho] + \alpha\, \text{Sin}[2\beta\rho]} \text{Sinh}[\alpha\xi]\, \text{Sin}[\beta\xi]$$

and when $\dfrac{4q}{p^2} - 1 < 0$:

$$\phi_0(\xi) = \frac{\beta\, \text{Cosh}[\alpha\xi]}{\text{Sinh}[\alpha\rho]\, (\beta\, \text{Coth}[\alpha\rho] - \alpha\, \text{Coth}[\beta\rho])}$$

$$+ \frac{\beta\, \text{Cosh}[\beta\xi]}{\text{Sinh}[\beta\rho]\, (\alpha\, \text{Coth}[\beta\rho] - \beta\, \text{Coth}[\alpha\rho])}.$$

Procedure for solution

The procedure for solving the stress function, $\phi(\xi)$, is as follows:

(1). At the start of the first time interval $t = \Delta t$, ε_{ij}^c is zero. From Eqns. (7) to (13), one finds that $F(\xi) = \dfrac{(\alpha_T - \alpha_A)\Delta T}{C_3}$. The stress function for Eqn. (13) with the above inhomogeneous term, $F(\xi)$, is constructed as

$$\phi(\xi) = (1 - \frac{(\alpha_T - \alpha_A)\Delta T}{C_1}) \, \phi_0(\xi) + \frac{(\alpha_T - \alpha_A)\Delta T}{C_1}.$$

(2). The stress components are then derived from Eqn. (27) using the stress function obtained above. The approximation of stress is then substituted into Eqn. (21) through Eqn. (23) to obtain the incremental creep strain, $\Delta\varepsilon_{ij}^c$.

(3). The incremental creep strain, $\Delta\varepsilon_{ij}^c$, is added to the creep strain accumulated during all previous steps, ε_{ij}^{co}, to obtained the total creep strain, ε_{ij}^c. For the first iteration step $\varepsilon_{ij}^c = \Delta\varepsilon_{ij}^c$ because $\varepsilon_{ij}^{co} = 0$,

(4). The above creep strain is substituted into Eqn. (7) through Eqn. (12) to obtain $A_1(\xi)$, $B_1(\xi)$, etc. and then $F(\xi)$. The stress function is then obtained as

$$\phi(\xi) = \phi_0(\xi) + \int_{-\rho}^{\rho} F(\eta) \, G(\xi,\eta) d\eta. \qquad (39)$$

(5). The creep strain at the beginning of next time interval is known and is equal to the accumulated incremental strains up to the time interval. The procedure for calculating the stress function, stresses and displacements for the other time interval is the same as in steps 2 to 4.

Results

The eight-harness satin weave (8H SW) Nextel 610/Aluminosilicate ceramic matrix composite is examined using the proposed approach. The laminate properties are given in Table 1. The creep strains, averaged in the z-direction, of the $0°$ and $90°$ plies, after 10 hours, are shown in Fig 2 as functions of distance from the crack face of two adjacent matrix cracks, one at $x/t_1 = -2$, the other at $x/t_1 = 2$. The crack spacing a is chosen to be $2t_1$, according to experimental observation (Zuiker, 1995), where t_1 is the thickness of one $90°$ ply. The applied stress an temperature on the composite are 75 MPa and $1100°$ C, respectively. As shown in Fig. 2, the creep strain of the $90°$ ply is negligibly small when compared to that of the $0°$ ply. Since the total strains of the $0°$ and $90°$ plies are equal to maintain the global deformation compatibility, the deformation caused by crack opening of the $90°$ ply are considerable. A 3-dimensional distribution of axial creep strains, ε_{11}^c or ε_{xx}^c, in the $0°$ and $90°$ plies are shown in Figs. 3 and 4 where z and x are the directions along the thickness and axial directions as shown in Fig. 1.

The normal stresses along the loading direction in $0°$ and $90°$ plies, under an applied load of 75 MPa after 10 hours at a constant temperature of $1100°$ C, are shown in Fig. 5. The stresses are normalized by $\sigma_{x0}^{(90°)}$, the stress of the $90°$ plies from the linear classic laminate analysis when no matrix cracks and nonelastic deformation are considered. As shown in Fig. 5, due to the relatively larger creep strain in the $0°$ ply, relaxation in the $0°$ ply occurs which reduces the magnitude of the stress as compared to the elastic stress also shown in Fig. 5. The elastic stress is the stress of the composite at time equal to zero when cracks exist in the $90°$ plies, but no inelastic stress has been developed. The stress in the $90°$ ply increases as creep strain develops. The stress changes in the $0°$ and $90°$ plies, and the stress transfer from between these two plies are expected to be more pronounced as time goes by.

The transverse normal and shear stresses of the 90 ply are functions along the thickness and axial directions, and are shown in Figs. 6 and 7.

Figure 8 shows the comparison of the total strain of the composite at $1100^{\circ}C$ under two load levels, 50 MPa and 75 MPa. The constants $w_f=w_m$ in the constitutive model, Eqn. (23), is determined using a data point at the load level of 75 MPa. The same w_f and w_m are used in the prediction of the curve for the load level of 50 MPa. The creep behavior of the 0° ply is dominated by fiber and the creep behavior of 90° ply is dominated by matrix. Therefore, n_f is taken as 3 after Wilson et al. (1995) for that of the fiber, and n_m is taken as 4 after Zuiker (1995) for that of the matrix.

The sensitivity of the total strain to the exponent n_m, in an equation similar to Eqn. (16) which represents the creep behavior of the matrix material, is shown in Fig. 9. The Young's modulus of the matrix material is taken as 50 GPa according to the literature for the undamaged monolithic matrix material (Zuiker, 1995). It is seen from Fig. 9 that when n_m is taken as 1.927, the predicted total strains match the experimental data well for both load levels, 75 MPa and 50 MPa.

Table 1. Material Properties of the Unidirectional Laminate

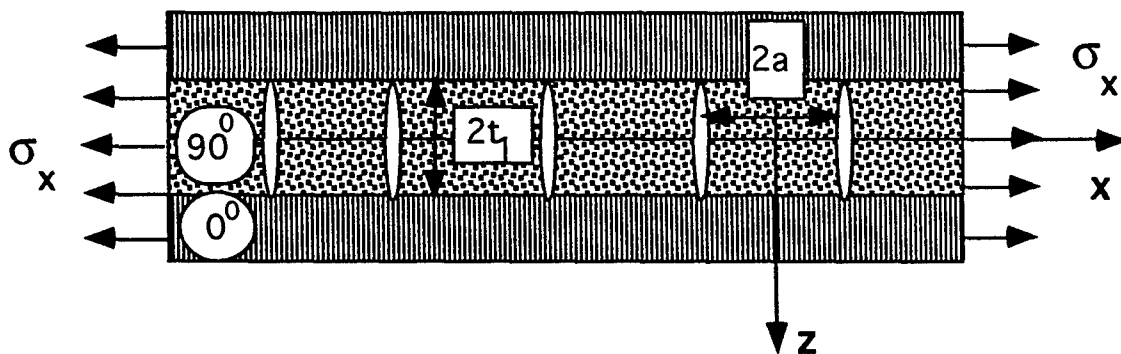| E_a	E_t	G_a	G_t	v_t	v_a
109 GPa	14.6 GPa	6.26 GPa	6.18 GPa	0.1878	0.236

Figure 1. A schematic representation of a cross-ply laminate with matrix cracks in 90° plies. Here 2a is the distance of two cracks between which the stresses and strains are to be solved. It should be noted that the crack spacing needs not to be uniform.
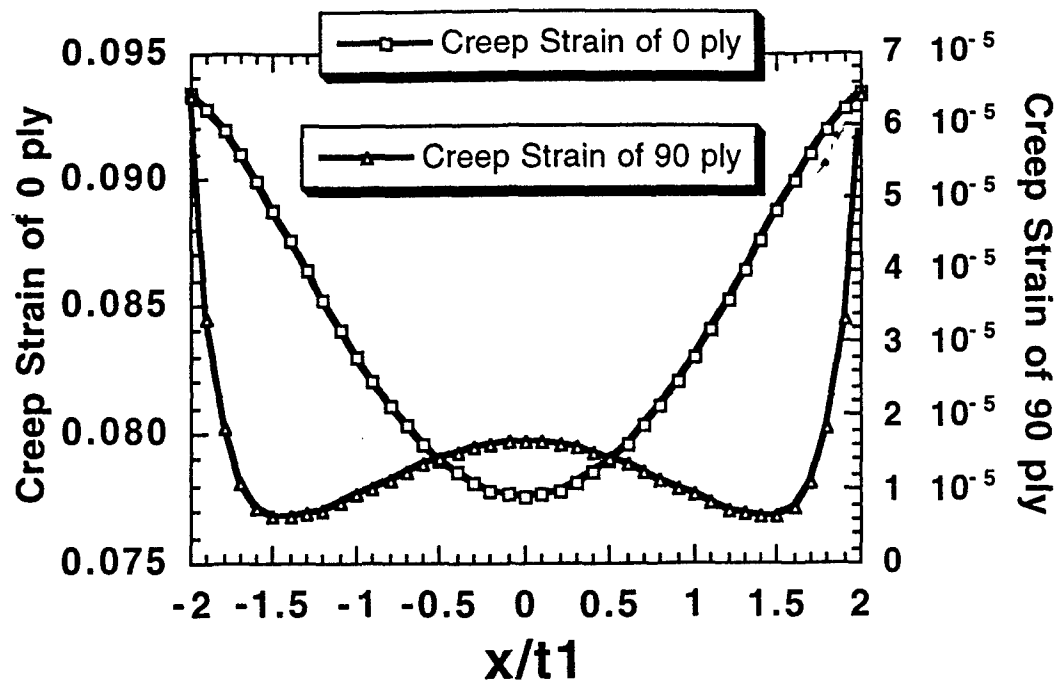
Fig. 2. Creep strain of $0°$ and $90°$ plied averaged along the thickness direction.
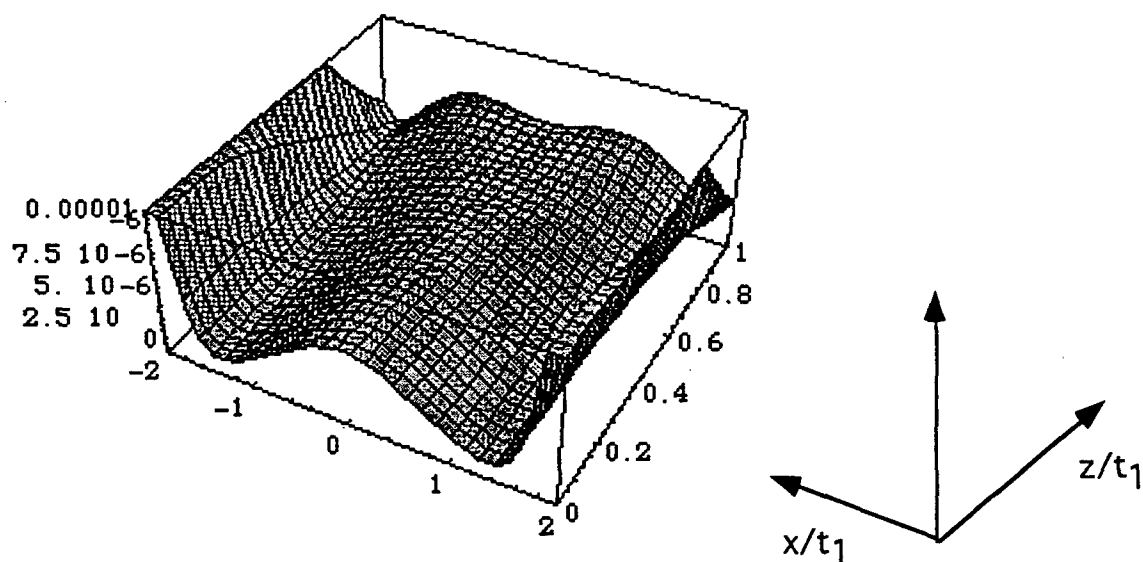
Fig. 3. Axial creep strains, ε_{11}^c or ε_{xx}^c, in the 90 plies.
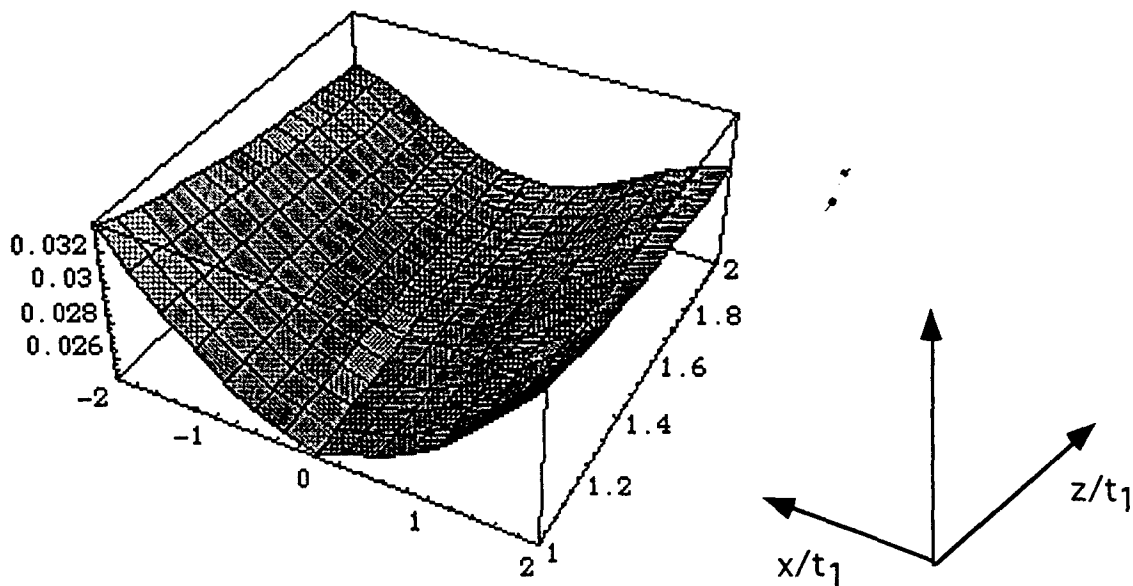
Fig. 4. Axial creep strains, ε^c_{11} or ε^c_{xx}, in the 0 plies.
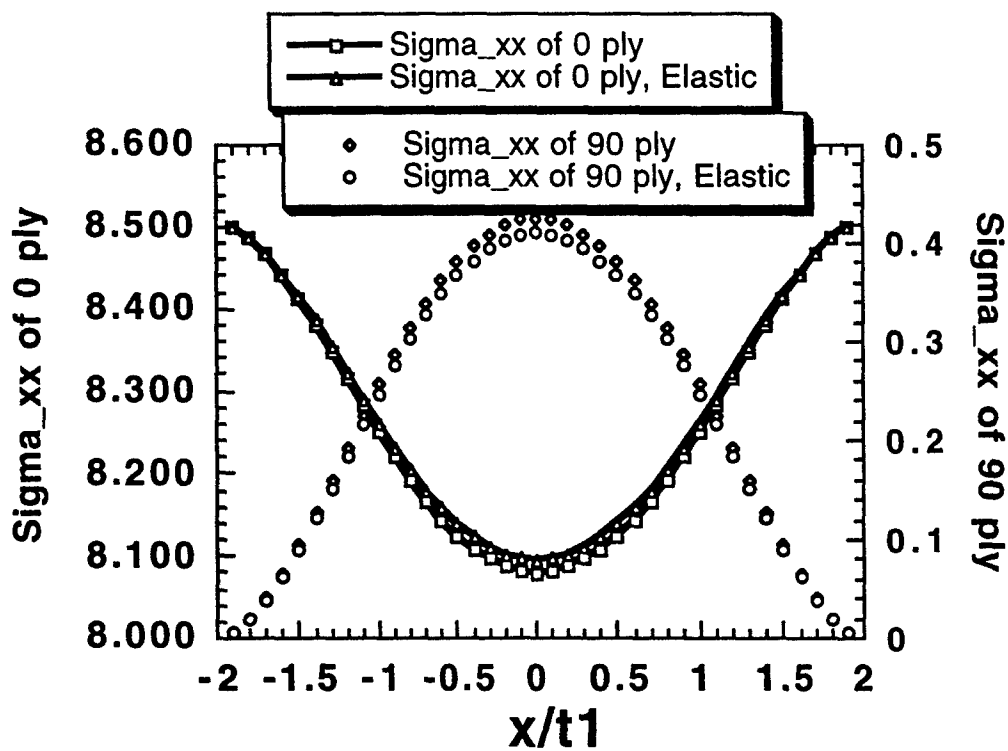

Fig. 5. Stresses in $0°$ and $90°$ plies which are normalized by the stress of the $90°$ plies (i.e., $\sigma^{(90°)}_{x0}$) when no matrix cracks and inelastic deformation exist.
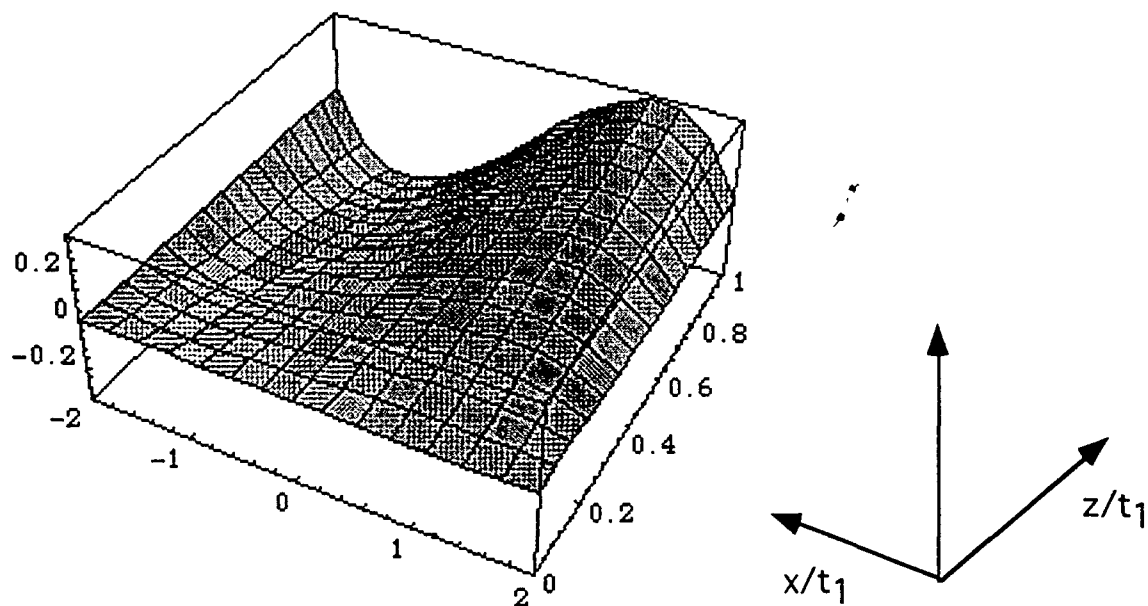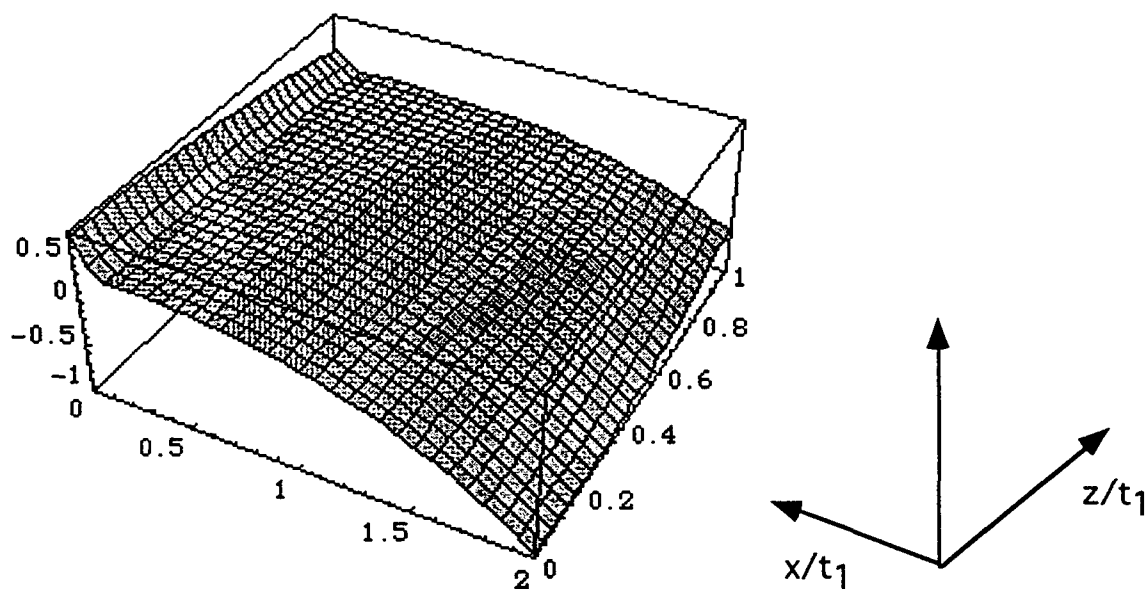
17-17

Fig. 6. S_{xz} of $90°$ ply.
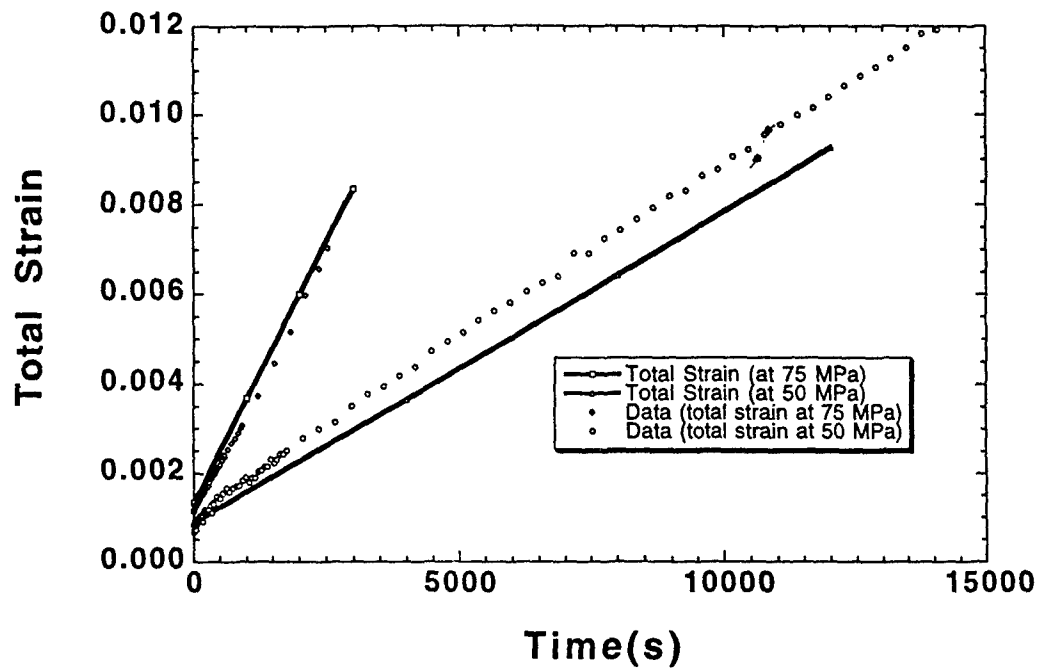

Fig. 7. S_{zz} of $90°$ ply.

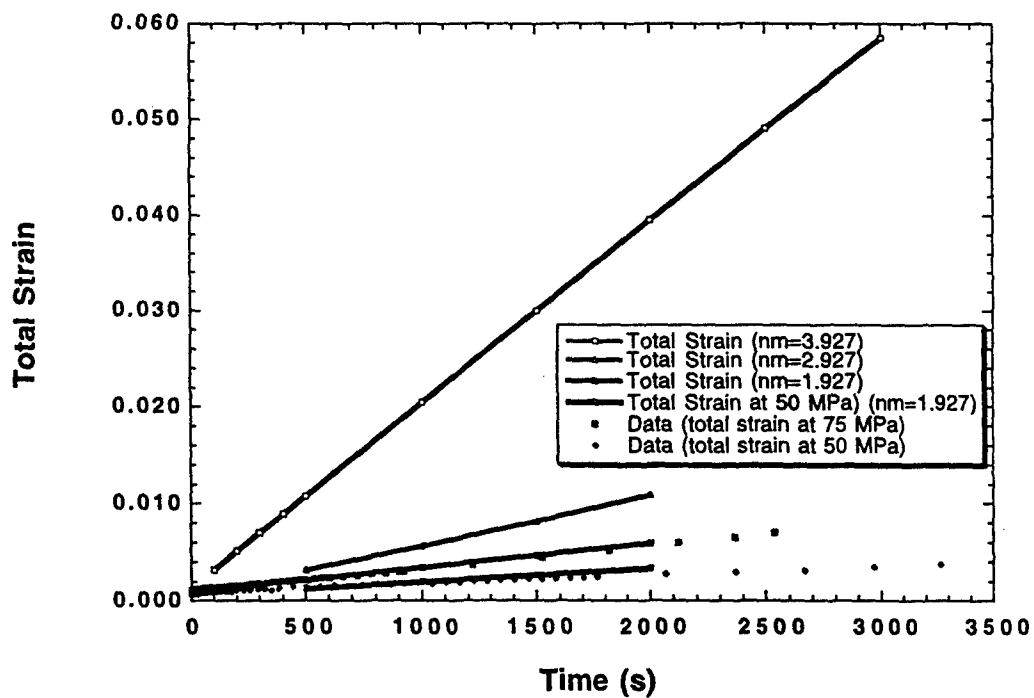Fig. 8. Comparison of predicted strains with experimental data.

Fig. 9. Sensitivity of predicted total strain to matrix creep response.

REFERENCES

Bailey, J. E., Curtis, P. T. and Parvizi, A. (1979) *Proc. Roy. Soc. London*, A366. 16, pp. 599.

Flaggs, D. L. (1985) *Journal of Composite Materials*, Vol. 19, pp. 29.

Hashin, Z. (1985a) Analysis of cracked laminates: a variational approach, *Mechanics of Materials*, Vol. 4, pp. 121-136.

Hashin, Z. (1985b) Cumulative damage theory for composite materials: residual life and residual strength method, *Composite Science and Technology*, Vol. 23, pp. 1-19.

Hashin, Z. (1990) Analysis of damage in composite materials, *Yielding, Damage, and Failure of Anisotropic Solids*, EGF5 (eds. Boehler, J. P.), Mechanical Engineering Publications, London, pp. 3-31.

Highsmith, A. L. and Reifsnider, K. L. (1977) *ASTM STP*, 775: 103.

Parvizi, A., Garrett, K. W. and Bailey, J. E. (1978) *Journal of Material Science*, Vol. 13, pp. 195.

Ishikawa, T. and Chou, T. W. (1983) One-dimensional micromechanical analysis of woven fabric composites, *AIAA Journal*, Vol. 21, pp. 1714-1721.

Mukherjee, A. K., Bird, J. E. and Dorn, J. E. (1969) *Trans. ASM*, Vol 62, pp. 155-179.

Narin, J. A. (1989) The strain energy release rate of composite microcracking: a variational approach, *Journal of Composite Materials*, Vol. 23, pp. 1106-1124.

Stakgold, Ivar (1970) Boundary Value Problems of Mathematical Physics, Vol. I. The MacMillan Company, Collier-MacMillan Limited, London, pp. 63.

Wilson, D. M., Lueneburg, and Lieder, S. L. (1993) High temperature properties of Nextel 610 and alumina-based nanocomposites fibers, *Ceramic Eng. Sci. Proc.*, Vol. 14, 7-8, pp. 609-621.

Zuiker, J. R. (1995) A model for the creep response of woven oxide-oxide ceramic matrix composites (in preparation).

ACKNOWLEDGMENT

A CASE STUDY FOR THE INTEGRATED PRODUCT AND PROCESS DESIGN GUIDELINE

Richard J. Gerth
Assistant Professor
Department of Industrial and Manufacturing Systems Engineering

Ohio University
277 Stocker Center
Athens, Ohio 45701

A CASE STUDY FOR THE INTEGRATED PRODUCT AND PROCESS DESIGN GUIDELINE

Richard J. Gerth
Assistant Professor
Department of Industrial and Manufacturing Systems Engineering
Ohio University

Abstract

The Integrated Product and Process Development (IPPD) Guide is a design guideline to help 6.3 development programs consider cost and risk issues in their technology development efforts. The guideline is based upon modern quality and concurrent engineering concepts and techniques as used by leading commercial industries, such as Motorola and Texas Instruments. My duty was to write a case study, based on an actual development program that highlights the manner in which the IPPD guide functions. The case study served 3 purposes:

1. identify missing steps
2. test the guide procedures for consistency and flaws
3. create an example from which the interrelationships of the guide steps can be understood.

In addition, appendices and descriptions of the specific tools were written.

The case study revealed many problems and issues that were addressed and resolved. The major unresolved issues are:

1. The manner in which the Air Force pays contractors, i. e., a profit margin based on a percentage of cost, encourages the contractor to increase costs to increase profits. A fixed contract fee where the contractor can increase profits by decreasing cost, similar to the commercial market, may be preferable.

2. It may be difficult to implement the concurrent engineering approach in the early stages of the design process (prior to the PR - purchase request) because contractors, who are the immediate customer of 6.3 development programs, cannot be included in the process until the PR is released. This requires that some sort of in-house manufacturing and design expertise be available during the early planning stages.

3. Cost and risk are prominent criteria within the guidelines, but are not well integrated with traditional performance measures because of a lack of a generally accepted integrating framework. It has been proposed to represent the risk by stating a range for each performance requirement, and to estimate the cost associated with each requirement separately. Unfortunately, for most requirements there are no quantitative methods to estimate the associated cost and risk.

A CASE STUDY FOR THE INTEGRATED PRODUCT AND PROCESS DESIGN GUIDELINE

Richard J. Gerth

Introduction

The Integrated Product and Process Development (IPPD) Guide is a design guideline to help 6.3 development programs consider cost and risk issues in their technology development efforts. The guideline is mostly based upon modern quality engineering and concurrent engineering concepts and techniques that are being used by leading commercial industries, such as Motorola and Texas Instruments. My duty was to write a case study, based on an actual development program that highlights the manner in which the IPPD guide functions. The case study served 3 purposes:

1. identify missing steps
2. test the guide procedures for consistency and flaws
3. create a learning example from which the interrelationships of the various guide steps can be understood.

In addition, appendices and descriptions of the specific tools were written.

IPPD Guide

The IPPD Guide is a concurrent engineering (CE) approach to technology development. The purpose of the guide is to provide 6.3 program managers and researchers a methodology to develop technology that is cost effective for industry. The process begins with the formation of a cross functional team that includes an SPO officer, manufacturing specialists, technology specialists, etc. The next step is to conduct a value analysis of the system for which the technology is to be developed. The purpose of the value analysis is two fold: first to define the cost within which the effort must remain so that the project is of value, and second to identify the high cost contributors.

Once the cost goals have been established, exit criteria and measures are established. Exit criteria are quantitative and verifiable measures used to:

1. measure the degree to which the final project results met the stated requirements.
2. judge the potential of alternative technology solutions.

An initial list of criteria and their measures were developed (see Table 1). The exit criteria should be stated as a range within which acceptable project results must lie, as well as a relative weight or priority for each criteria. The guide emphasizes the use of quality function deployment (QFD) for this activity. One of the difficulties with using the exit criteria is the concept of cost and risk, which was not satisfactorily concluded.

Table 1. List of Exit Criteria and Measures

Criteria	Metric
Quality	Product defects (yield, first pass capability, ppm, dpm, dpu, etc.) Process capability (Cp, Cpk)
Performance	Product-specific performance metrics Robustness: $R = \dfrac{(\text{average performance})^2}{\text{performance variance}}$
Producability	Yield, Cp, Cpk, ease of applying SPC, ease of control parts count ease of assembly
Reliability	MTTF, MTBF
Schedule	time
Maintainability	Ease of access skill level required $\text{Availability} = \dfrac{\text{MTBF}}{\text{MTBF} + \text{Repair Time}}$
Supportability	Impact on storage requirements Impact on training requirements Impact on transport Support equipment required Impact on shelf life Software requirements
Disposal/Disassembly	Environmental Impact (see below) Potential for recycle (disassembly)
Environmental	HAZMAT required or generated during mfg., operation, or disposal Waste generated during mfg., operation, or disposal

Cost
 (applies to all others above)
	Roll-up: Target price. Depends on:
	
	     materials
	
	     mfg. costs
	
	     tech transition costs

Risk (applies to all others above)	customers tolerance for uncertainty.

Once the exit criteria have been satisfactorily established, a list of promising technology alternatives is compiled using all available data sources including commercial and civil databases, research journals, the Defense Technical Information Center (DTIC), the Technology Transfer Office (TTO), the Information Analysis Center (IAC), and the Office of Technology Transition (OTT).

The technology alternatives are then evaluated according to the exit criteria. For each technology alternative, one must estimate their exit criteria performance and the cost associated with meeting that performance. The risk of meeting that criteria is also supposed to be estimated, although tools for doing that are lacking. A weighted average score for each technology alternative is then computed based on how well they meet the criteria and the criteria's weighting. The highest scoring technologies are recommended for development. If none of the alternatives are satisfactory, the exit criteria are either reexamined and changed, or the project is canceled.

A purchase request (PR) is then written for the alternative(s) that was selected for further development. The PR must contain specific language that relates to affordability and the exit criteria. Specifically the PR should state that the degree to which the technology meets the exit criteria must be demonstrated to a statistically satisfactory degree (if possible). A major portion of the proposal response must be a plan that shows explicitly how this will be accomplished, including statistical issues, such as sample size, destructive testing, etc.

The project may be terminated at any stage should projected cost figures exceed the cost exit criteria.

Case Study and Problems

The majority of time was spent writing various sections of the guide. I either wrote or added to the following sections of the guide:

1. Step A1.   Determine Requirements (added).
2. Step A2.   Establish Affordability Exit Criteria and Metrics (added).
3. Appendix :   statistical methods (probability, probability distributions, descriptive statistics, confidence intervals, hypothesis testing), Pareto analysis, cause and effect diagrams, quality function deployment, industrial engineering standards (wrote).
4. Case study: TR module (wrote).

Steps A1 and A2 form the Value analysis and Quality Function Deployment aspect of the guide. Within these sections the case study was the most complex and most difficult section to write because the material had to be gathered and learned.

The main purpose of applying the IPPD framework to an existing case study was to identify any major inconsistencies in the IPPD framework, and determine if the methodology is practically applicable. The case study was the TR module, a transmit-receive module used for active radar applications. It was performed in a concurrent engineering environment with Texas Instruments (TI), Westinghouse, Delco Electronics, and Hughes Aircraft. It was selected because it was one of the first CE ManTech development efforts. The two major technology advances were in the area of flip-chip manufacturing process development and low temperature co-fired ceramics (LTCC). It was, of course, necessary to modify the case study to fit the IPPD framework.

The CE environment contributed to some major breakthroughs that were unlikely to have been discovered otherwise. For example, the contractors had data to indicate that on-line product testing according to the required MIL-STD was a major cost driver. Thus, the team developed alternative testing methods that would perform equally well, without much of the unnecessary testing required by the MIL STD. It is unlikely that in a traditional 6.3 program that would be concerned with the manufacturing process and material development, product testing and statistical process control issues would have been identified and addressed. However, there were a number of problems encountered with the current IPPD process when is was applied to the TR module.

The case study did highlight a number of problems, several of which were resolved. For example, the initial guide was not sufficiently concise with regards to the exit criteria, simply stating that various "-ilities" needed to be considered. Thus, a list of exit criteria and metrics were developed (see Table 1).

A major addition was the understanding that a relationship existed between the exit criteria and the technology solution demonstration plan. Specifically, the improper selection of exit criteria could raise cost or not be realistically measured in a demonstration plan. Also, the demonstration plan would have to have sufficient detail to judge whether all criteria would be measured to the desired degree of accuracy considering statistical issues such as requisite sample size. For example, it would be nonsensical to state reliability as an exit criteria if there were no means to estimate reliability from software or hardware tests. This is especially true, if no hardware is to be destroyed, or otherwise "used" or "consumed". This underscored the importance of understanding statistical, measurement, and manufacturing issues during the exit criteria determination phase. This resulted in the demonstration plan becoming another "make or break" point in the guide, although the specific location, within the technology selection phase, or after the PR phase was still being debated.

There were, also, several other issues that were not resolved, and are worth mentioning.

The first issue is, given the manner in which Air Force procurement functions, there is little incentive for contractors to lower cost. The contractor's profit is a fixed percentage of the cost. Thus, the contractor's

profit increases as their cost increases. This is in contrast to commercial businesses, where the profit is the difference between sales price and cost. Thus, lowering the cost increases the profit. This issue is beyond the scope of this project, but it does raise the question how much benefit can be reasonably expected from concurrent engineering methods when there is incentive on the contractor's part to increase costs.

The second issue is team composition. Clearly the CE team must have practical industrial manufacturing expertise present at the earliest stages. This is because the immediate "customer" of the 6.3 program results are the contractors, who will presumably use the technology to manufacture more cost effectively advanced weapons systems for the "end customer", the SPO. Thus, the manufacturing and cost concerns of the contractors must somehow be represented. However, at the early stages contractors have not been identified nor has a PR been released. Thus, the question is raised how will their concerns be addressed and their knowledge and experience incorporated into the early phases of the design? This question was not conclusively answered. Two possible solutions might be to A) have internal manufacturing expertise, or B) have a permanent group consisting of various contractors / consultants on retainer.

The third issue is the application of QFD and the generation of the exit criteria. The main purpose of the exit criteria are to establish quantitative measures that represent the customer's requirements. Ideally this is done by listing the customer's requirements in the first column of a matrix, and stating how these customer requirements will be met in quantitative terms along the top of the matrix. There were several areas of confusion. The first confusion revolved around the definition of the customer, namely the SPO, who will benefit from the technology, and the contractor, who must implement the technology. In a sense they are both customers, and both their requirements must be met to achieve an affordable, implementable technology.

As a result of the confusion, in the case study, the first column represented the SPO requirements, and the top row reflected the contractor's requirements. Although the creation of the matrix may have brought issues to light and created consensus and team building, the matrix itself does not say much, nor provide any useful analysis. The two most important issues were shown to be cost and the validation of the technology. However, since cost and validation were related to everything on both the side and the top, this result is obvious.

The correct method would have simply been to list the SPO and contractor's requirements in a single column, with metrics along the top row. Then draw correlations between each. In the vast majority of cases there will be a one to one correlation in which case the matrix degenerates to a list or table. This is not surprising given that many of the requirements will be stated in quantifiable terms, such as minimum MTBF of 10,000 hours, or acquisition cost must be $400 or less.

Another confusion was treating cost and risk as independent exit criteria, on par with the other exit criteria, such as performance and process yield. This is clearly not true, for almost any exit criteria can increase or lower cost and risk, but not vice versa. Thus, cost and risk are really functions of the other exit criteria. They are not independent exit criteria, but rather dependent exit criteria. For example, in the case study one of the SPO's major requirements was that the project demonstrate that the TR module could be produced in quantity at low cost and still perform within stated parameters. The contractor, in turn requires that the technology achieve a high process yield at low cost and be easy to test. Both want a reliable, low cost, low risk technology. Although metrics for cost and risk exist, dollars and probability of achieving some goal X respectively, neither are actually independent of the other exit criteria, or even from each other. That is why cost and risk are usually not included in a QFD matrix, every one wants the result at the lowest possible cost with minimum risk.

A proposed method, is to keep cost and risk separate, and determine them as a function of the other criteria. For the exit criteria risk tolerance levels can be expressed by the size of the range of the other cost and performance criteria: a wide range means high risk tolerance, a narrow range means low risk tolerance. For example, the statement yield must be better than 80% could be a very large range if typical yields for similar processes are greater than 95%. Conversely, the statement detection accuracy must be 98% +/- 2% could be a very narrow range indicating a low risk tolerance. A difficulty will be encountered, however, when attempting to estimate the risk of the various technology solutions and estimating their performance. In general the best that can be hoped for is a yes/no, we can /cannot achieve a level within the specified range, or a relative measure between technologies: technology A is less risky than technology B, although it cannot be quantified.

Similarly cost should also include a range. Thus, the designers can then determine what design will potentially work within the required cost, risk, performance design space. The theory is to predict how much it will cost to achieve each performance requirement and sum the individual costs for a total cost. In practice, this will not be possible. The best one can hope for is a total cost estimate based on manufacturing considerations and overhead. If none of the proposed technology solutions meet the stated cost requirement, then the design must be changed, or the requirements must be altered. The point is that risk is not stated as its own criteria, and that cost is a function of the other requirements.

A fourth issue is that the guide emphasizes cost, performance, and risk estimation with data and statistical methods. However, in the case study, and presumably other 6.3 programs, data was not available in the early stages. Thus, technology alternatives were evaluated based on their relative merits, and not based on quantitative assessment of their performance and comparison with the exit criteria. Also, the cost estimation methods used in the TR program were proprietary to the contractors. Rapid cost estimation tools, aside from manufacturing specific tools based on machining parameters, are not available. Even if

they were available, the overhead cost for aerospace companies is often 2 to 5 times the direct cost, making it difficult to accurately predict the cost impact of technology. Indeed, overhead, which is usually a function of direct material and labor, often drives the technology development effort to lower direct labor and material content. Thus, if contractors are not included early in the design stage, non-proprietary software that quantitatively predicts the effect of differing engineering decisions on total cost, including overhead, will be necessary.

The last issue is the final steps of the guide that deal with the contractors, the technology demonstration and exit criteria validation was sparse. I was not directly involved in the writing of those sections.

Conclusions and Recommendations

Overall the guide is in good shape, albeit still under development. There are several tools and methods that will likely still need to be developed, and will not be understood until the guide is applied. To that end it is recommended that some sort of monitoring and reporting structure by put in place so that future versions of the guide can be updated and improved to reflect the experiences gained.

There is a need for a unifying foundation that reflects the relationship between cost, performance, and risk at all project levels. There are heuristics in the [1,2] that argue the use of curves to understand these three measures. But there are no methods provided on how these curves are to be generated, nor any data to support their particular choice of relationships or shape of curve. Thus, there is a need to create a integrative framework, possibly based on curves or other form of relationships, that relate cost, performance, and risk in research and development. This framework will need to be validated with data, which in turn requires a methodology for developing the models postulated by the framework.

Lastly, for a true cost prediction model in aerospace, there needs to be a better understanding of how engineering and manufacturing decisions and operations impact cost. Specifically considering the greatest contributor to cost: indirect cost and overhead. In the aerospace industry it is estimated that overhead account for 20% to 80% of the total per unit acquisition cost [3,4]. Current cost estimation methods are either proprietary, or based on direct labor and material costs. However, these methods lead to the conclusions that reducing direct labor and material costs will greatly reduce overall costs, when this is not in fact true. New accounting methods, such as ABC costing and Precision Manufacturing Costing [5] recognize this problem and are great leaps forward to creating a more accurate cost picture, but are also heuristic based accounting methods. They are not based on known engineering design and indirect cost relationships.

For example, purchasing, accounting, marketing, design engineering are departments that are usually charged to overhead. There must be an underlying rational why they are the size that they are, occupy the

space that they do, utilize the resources that they need, etc. Purchasing may be of a particular size because of the variety of parts required, number of vendors, variety of products, supplier certification procedures, size of the company, variety of other departments that are charged to overhead, etc. Thus, some engineering design decisions, such as reducing part count may have an impact not only on manufacturing cost due to the reduced assembly operations, but also on purchasing because of the fewer parts required. Similarly part standardization and single source suppliers would reduce the resources used in purchasing. Design itself has a relationship to total cost and manufacturing. For example, concurrent engineering design is likely to be more costly in overhead, but less costly in manufacturing due to fewer engineering change orders post production, fewer scrap, rework, and warranty claims, and better process selection.

Thus, there is a need for research to determine the various cost relationships within a manufacturing organization. This should then lead to better engineering costing tools for product design. This should not be considered to be competing with existing accounting systems, which exist primarily for reporting purposes, but rather augmenting current engineering design tools. The vision is to have multiple costing systems for accounting and reporting, business management, and engineering design which will provide for each the information they require to make sound decisions based on cost.

References

1. Michaels, Jack V. and Wood, William P., (1989). Design to Cost, John Wiley & Sons, New York.

2. Smith, Preston G. and Reinertsen, Donald G., (1991). Developing Products in Half the Time, Van Nostrand and Reinhold, New York.

3. Thomas, Richard D., (1994). Manufacturing Cost Estimation, Modeling, and Control, Report, Stratech, Inc., Beavercreek, Ohio.

4. Boger, Dan C., (1983). Statistical Models for Estimating Overhead Costs, Technical Report No.: NPS-54-83-014. Naval Postgraduate School, Monterey, California.

ANALYSIS OF TURBULENCE MEASUREMENTS BEHIND A BLUFF BODY FLAME HOLDER AND IN A HIGH SWIRL DUMP COMBUSTOR

Dr. Richard D. Gould
Associate Professor
Dept. of Mechanical & Aerospace Engineering

Campus Box 7910
North Carolina State University
Raleigh, NC 27695

ANALYSIS OF TURBULENCE MEASUREMENTS BEHIND A BLUFF BODY FLAME HOLDER AND IN A HIGH SWIRL DUMP COMBUSTOR

Dr. Richard D. Gould
Associate Professor
Dept. of Mechanical & Aerospace Engineering
North Carolina State University

ABSTRACT

The following two technical papers concerning laser Doppler velocimeter (LDV) measurements in the flow behind a bluff body flame holder were co-authored with WL/POPT scientists as part of this summer assignment. Since the first paper is 11 pages and the second is 7 pages, both in 9 point double column format, they will not be included here due to space limitations.

"Simultaneous 3-D LDV Measurements in the Isothermal Flow Behind a Bluff Body Flameholder," with C. N. Raffoul and A. S. Nejad, *12th International Symposium on Air Breathing Engines*, Ed. F. S. Billig, Melbourne, Australia, pp. 1045 - 1055, 1995.

"Investigation of Three-Dimensional Turbulent Transport Behind a Bluff Body," with C. N. Raffoul and A. S. Nejad, *ASME 1995 Separated and Complex Flows,* FED-Vol. 217, pp. 121-128, 1995.

In addition, further analysis of the two component LDV and single point temperature measurements made during the summer of 1992 in the highly swirling flow field of a model dump combustor was also performed during this assignment. A lean propane-air diffusion flame with an overall equivalence ratio of $\phi = 0.45$ was stabilized in the combustion chamber by the flow pattern of the Wright Laboratory/Rolls Royce (WL/RR) swirler for this study. A complete description of this flow and the measurements made are given in this report. In particular, the time averaged temperature measurements made using a type S Platinum/10% Platinum-Rhodium thermocouple probe were corrected for radiation losses. Also, a numerical mass flux balance was performed at each axial station and was found to give agreement to within $\pm 20\%$.

ANALYSIS OF TURBULENCE MEASUREMENTS BEHIND A BLUFF BODY FLAME HOLDER AND IN A HIGH SWIRL DUMP COMBUSTOR

Dr. Richard D. Gould

INTRODUCTION

The interaction between combustion and turbulence has been the subject of much research in the past few years. The effect of combustion on turbulence structure and the effect of turbulence on combustion are of great interest to the combustion engineer. Knowledge of these effects would permit the design of more compact energy efficient combustion systems with low pollutant emission while minimizing costly test programs.

The objective of most recent experimental work in turbulent flows has been to obtain data for comparison with numerical prediction codes that model turbulence, combustion, and heat transfer. Velocity, temperature, and species concentration measurements in reacting flows have been made in various geometries including: 1) co-axial jets, 2) diffusion flame jets, 3) bluff body flame holders in ducts, 4) industrial furnaces, 5) two-dimensional and axisymmetric rearward facing steps, 6) confined swirling flows. All of these geometries have a common feature in that they induce a separated flow region which acts as an anchor for the flame front. High turbulence intensities and well defined recirculation zones are characteristic of these flows. Comparisons of mean velocities, turbulence intensities, temperature distributions and recirculation zone sizes have been made in flows with and without combustion in an effort to understand the turbulence-combustion interaction process. Turbulence structure parameters (*i.e.* skewness and flatness) are also often compared to give additional insight into interaction mechanisms. Although substantial literature exists, there is still an incomplete understanding of the turbulence-combustion interaction. This is because turbulent combustion is highly inhomogeneous, involving large fluctuations in temperature, composition, density and velocity. There also can be a strong interaction between the aerodynamic and heat release mechanisms. Modeling of turbulent aerodynamics requires the use of statistical properties including the fluctuation intensity, covariance, energy spectrum and probability density functions. The development of accurate models is dependent upon reliable experimental information concerning these quantities. This study was undertaken to provide data necessary to improve the turbulent combustion modeling process in a highly swirling diffusion flame dump combustor.

EXPERIMENTAL APPARATUS

A swirling axisymmetric sudden expansion flow geometry was produced by joining a 3.5 m long entry pipe having a 101.6 mm(4 in.) inside diameter to a water cooled 152.4 mm(6 in.) inside diameter test section pipe as shown in Figure 1. A specially built swirler, through a collaborative effort between Wright Laboratory and Rolls Royce, having a 30 mm inside diameter and 61 mm outside diameter was used to produce the swirl in the combustion chamber. The swirler had 20 curved vanes and was designed to give a mean airflow turning angle of 45°. Well regulated gaseous propane was fed through a central tube to the fuel injector. The fuel injector consisted of a reservoir, a mixing chamber and a movable pintle for control of the fuel exit velocity. The fuel flow annulus area for this study was 0.000307 m^2 giving a fuel exit velocity of approximately 4.4 m/s for the flow conditions used here. The entry pipe-swirler-fuel injector assembly and sudden expansion face were mounted on a movable table and thus could be positioned at various axial locations in the rigidly fixed test section. This arrangement allowed for measurements at various downstream positions within the sudden expansion flow field without having to move the LDV probe volume location in the axial direction. It should be noted that measurements were made only on the diameter of the test section. The face of the sudden expansion is moved to place the probe volume at a new axial position. High quality optical access can be limited to a small window with this apparatus. A metal ring was used to seal the small gap between the sudden expansion face and the inside diameter of the test section.
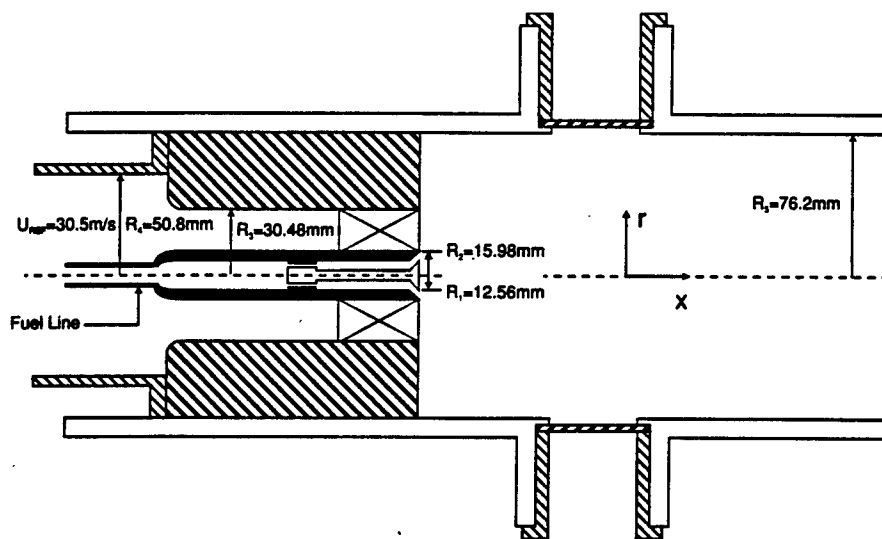

Figure 1. Model dump combustor geometry.

Air was provided by well regulated air compressors and was monitored using a calibrated orifice plate located upstream of a large settling chamber which precedes the entrance pipe. Flat quartz windows 50 mm in diameter and 3.2 mm thick (2 in. × .125 in.) where mounted in optical access ports on both sides of the 152.4 mm diameter test section such that the inner flat surfaces were nearly flush (0.060 in. inset) with the inside diameter of the test section.

A TSI two-component dual-beam LDV system, operating in forward scatter mode, was used in this study. This system was oriented to make direct measurement of the axial and tangential velocity components on the diameter of the test section. Measurements were made at 16 radial locations and at 14 axial planes. The 514.5 μm argon laser line was used to measure the axial velocity component while the 488 μm argon laser line was used to measure the tangential velocity component with this system. Bragg cells shifted the frequency of one beam in each component by 40 MHz causing the fringes to move in the downstream direction for the axial component and vertically upward for the tangential component. Fringe spacing were measured and found to be 1.825 μm ± .006 for the axial component and 1.731 μm ± .006 for the tangential component. The LDV transmitting(fiber optic head) and receiving optics were mounted on a precision xyz positioning table with resolution of ± 2.5 μm in each axis. The LDV system employed × 3.75 beam expansion optics and gave probe volumes approximately 60 μm in diameter and 450 μm in length. Beam blocks were placed in front of the collection optics when measurements were being made so that the Doppler signal could be detected. Large refractive index gradients in the combustion chamber, due to the combustion process, made it necessary to adjust the photodetector pinhole locations at every third or fourth measurement point along the radius. This procedure involved turning off the photodetectors, removing the beam blocks, adjusting the relay lens just upstream of the photodetector so that the image of the beam crossing is located on the pinhole plane, and lastly, adjusting the pinhole position so that the beams pass through. Narrow bandpass filters were placed in front of each photomultiplier tube to eliminate cross-talk between the two channels.

Two TSI Model 1990 counter processors interfaced to a custom built coincidence timing unit were used in the data collection and processing system. High and low pass filters were set to 10 MHz and 100 MHz for both channels, respectively. Both processors were set to make a single measurement per burst, count 16 fringes and use a 1% comparator. A hardware coincident window was set at 20 μs for all of the tests. Data(two velocities and the running time for each realization) were transferred through two DMA ports to a MicroVax minicomputer and later uploaded to a VAX 8650 for analysis.

The flow field was seeded using titanium dioxide (TiO_2) particles generated by reacting dry titanium tetrachloride ($TiCl_4$) with the moist shop air. Craig et al. (1984) measured the particle sizes generated by this device and found that they were fairly uniform and in the 0.2 - 1 μm diameter range. Data validation rates varied between 10000 and 200 per second on each counter processor and depended mainly on how clean the quartz windows were and on the location in the flow field. Low data validation rates occurred in the central recirculation zone and near the windows. Coincident data validation rates ranged from 3000 to 50 measurements per second. Velocity bias was corrected for using the time between data correction scheme.

Single point temperature measurements were made by manually traversing a type S Platinum/10% Platinum-Rhodium thermocouple probe across the radius of the test section at each axial plane. The thermocouple bead was unshielded and was approximately 0.020 in. in diameter. A NEFF analog signal data acquisition system with a built in electronic ice point junction and ANSI standard thermocouple tables was used to acquire the mean temperature at each point in the flow field. The mean temperature at each point was calculated by averaging 225 temperatures sampled over a 10 second period. A description of the temperature correction scheme used to account for radiation losses is given below.

TEMPERATURE CORRECTION

Energy losses from a thermocouple by thermal radiation and conduction can produce significant temperature measurement errors when the gas stream is at elevated temperatures. However, an estimate of these losses enables one to correct the measured values to obtain the true gas temperature. An energy balance (see Figure 2) was used to estimate the losses from the thermocouple. This correction was applied to all mean temperature measurements.
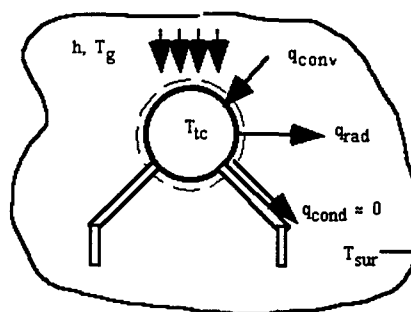

Figure 2. Energy balance on thermocouple bead.

A steady state energy balance on the thermocouple element gives $q_{conv} = q_{rad} + q_{cond}$. Substituting for convective and radiative heat fluxes while neglecting conduction heat fluxes from the spherical thermocouple bead ($D_{bead} = 0.020$ in.) to the two lead wires ($D_{wire} = 0.003$ in.) due to the small cross-sectional area of the lead wires gives,

$$hA_{tc}\left(T_g - T_{tc}\right) = A_{tc}F_{tc-sur}\varepsilon_{tc}\sigma T_{tc}^4 - A_{sur}F_{sur-tc}\varepsilon_{sur}\sigma T_{sur}^4 + q_{cond} \tag{1}$$

where q is the heat transfer rate, h is the convection heat transfer coefficient, A is the surface area, T is the absolute temperature, ε is the emissivity, σ is the Sefan-Boltzmann constant, F is the shape factor and where the subscripts g, tc and sur denote gas properties, thermocouple junction properties and surrounding combustion chamber wall properties, respectively. The last term on the right of Eq. 1 gives the radiative emission from the combustor wall and can be neglected in this work because the combustor wall were relatively cool(< 500 K) due to water cooling. Solving Eq. 1 for the gas temperature and using $F_{tc-sur} = 1$ since the combustor walls completely surround the thermocouple gives,

$$T_g = T_{tc} + \varepsilon_{tc}\sigma T_{tc}^4/h \tag{2}$$

The convection heat transfer coefficient for the thermocouple, h, has been estimated at each point in the flow field using the Whitaker convective heat transfer correlation for flow around a sphere. A computer program listed in Appendix A was developed and used to calculate the actual gas temperature at each point in the flow. The normal emissivity of oxidized platinum at 1500 K was estimated to be 0.25 (Touloukian and DeWitt(1972)).

EXPERIMENTAL PROCEDURE

All flow conditions were maintained at near constant values throughout the testing procedure. The inlet reference velocity, U_{ref}, was maintained at 30.5 m/s ± 0.9 m/s(100 ft/s ± 3.0 ft/s) giving an air mass flow rate of 0.091 kg/s ± 0.0027 kg/s (12 lbm/min ± 0.36 lbm/min). The propane fuel flow rate was maintained at 0.0026 kg/s ± 0.000078 kg/s (0.35 lbm/min ± 0.011 lbm/min) giving an overall equivalence ratio of $\phi = 0.45 ± 0.014$. Turbulent velocity statistics and histograms were formed by using 5000 individual realizations for each velocity channel at each measurement point. This data was then filtered to remove data which deviates more than 3 standard deviations from the mean. Finally, revised statistics were calculated once these additional outliers were discarded. For a properly operating LDV system very few points are removed during the first step(typically less than 10 out of 5000) and less than 1% of the data

should be discarded. Mean temperature measurements were formed by using 225 individual measurements taken over a 10 second period. No data were discarded from the temperature samples.

EXPERIMENTAL RESULTS

Two-component velocity measurements were made at 16 radial positions and at 14 axial planes in the swirling, axisymmetric reacting flow field of a model dump combustor. An overall lean diffusion flame was stabilized by the swirling shear layer. Figures 3 through 5 show the measured profiles of the mean axial and tangential velocities, and the corrected mean temperature in this combustor at 14 axial locations. Confidence in these measurements was gained by numerically integrating the mass flux at each axial station. Theses mass fluxes agreed with the mass flow rate measured by the flow meter to within ±20%. Measurements of the rms axial and tangential velocities and the $\overline{u'v'}$ turbulent shear stresses were also made and are shown in Figures 6 through 8. All measurements were non-dimensionalized with U_{ref} = 30.5 m/s and R_{ref} = 76.2 mm. The first axial position, x = 25.4 mm (1 in.), was located as close to the sudden expansion face as possible with the beam angles and beam orientation (*i.e.* 0° and 90°) used in this study. Measurements were made at axial stations every 12.8 mm (0.5 in.) from this first position up to x = 152.4 mm (6 in.) in order to capture the detailed velocity and temperature field in the highly swirling region of the flow field. Measurements were made at three additional downstream axial locations, x = 203.2 mm (8 in.), 254 mm (10 in.) and 304.8 mm (12 in.), to complete the description of the flow field. Also included in these figures, for comparative purposes, are the velocity measurements made by Ahmed et al. (1992) for the isothermal swirling flow case using the same geometry, swirler, and inlet reference flow velocity as used in this reacting flow study.

The mean velocity profiles show that higher velocities are present in the reacting flow case when compared to the isothermal flow case. This is to be expected due to volumetric expansion caused by heat release associated with the combustion process. The higher mean velocities near the combustor wall produce a well defined central recirculation bubble. This central recirculation bubble was found to be approximately 140 mm (5.5 in.) long in the reacting flow case which is much shorter than in the isothermal flow case. This strong, short central recirculation zone is probably why this combustor is stable at low overall equivalence ratios. In fact, flow visualization studies indicated that lean blowout occurred at ϕ = 0.21. It would be interesting to calculate the swirl number for the reacting flow case to determine the combined effects of

reduced density and increased mean velocity on the axial momentum flux. The maximum values of turbulent normal stresses were found to be larger in the reacting flow case than in the isothermal flow case. These larger fluctuations in velocity may be due to fluctuating heat release which is known to be highly non-linear. Further data analysis is required to determine if this increase in fluctuations is due to acoustic phenomena (*i.e.* unsteady flow). The axial and tangential turbulent normal stresses were found to be nearly equal to one another suggesting that isotropic turbulence models may be sufficient. It should be mentioned however, that the radial velocity fluctuation was not measured in this study, but that it may show larger anisotropy than the two components measured here, thereby negating the above comment. The maximum $\overline{u'v'}$ turbulent shear stress value was found to be much lower in the reacting flow case when compared to the isothermal flow case. This may be due to the larger value of kinematic viscosity(*i.e.* a factor of 10 - 15 larger due to increased temperature) in the reacting flow case causing increased turbulence dissipation. Temperature measurements indicate that the peak occurs at the boundary of the central recirculation bubble and the high speed wall flow. This temperature peak location also corresponds to the location where turbulent stresses peak and suggests that gradient transport modeling may be appropriate to predict this flow field.

CONCLUSIONS

Successful two component laser Doppler velocimetry (LDV) and single point temperature measurements were made in the highly swirling flow field of a model dump combustor. The velocity measurements were possible only because forward scatter signal collection was used. The reacting flow case was found to have higher axial and tangential mean velocities throughout most of the flow field than the isothermal flow case due to heat release. A shorter, stronger central recirculation bubble was found in the reacting flow case due to the pressure gradients produced by these higher mean velocities. Turbulent normal stresses were found to be larger while the maximum value of the $\overline{u'v'}$ turbulent shear stress was found to be less in the reacting flow case when compared to the isothermal flow case. Maximum mean temperatures occurred were maximum turbulent stresses occurred thus suggesting that gradient transport modeling may be successful in predicting this flow field.

ACKNOWLEDGMENTS

REFERENCES

Ahmed, S. A., Rose, A., and Nejad, A. S., (1992) "Three Component LDV Velocity Measurements in a Can Type Research Combustor for CFD Validation Part 1 Isothermal," Presented at the Int'l Gas Turbine and Aeroengine Congress and Exposition, Cologne, Germany, June 1-4.

Craig, R. R., Nejad, A. S., Hahn, E. Y. and Schwartzkopf, K. G., (1984) "A General Approach for Obtaining Unbiased LDV Data in Highly Turbulent Non-Reacting and Reacting Flows," AIAA Paper. No. 84-0366.

Touloukian, Y. S. and DeWitt, D. P. , editors, (1972) *Thermophysical Properties of Matter, The TPRC Data Series, Vol. 7, Thermal Radiative Properties of Metallic Elements and Alloys*, IFC/Plenum, p. 21.
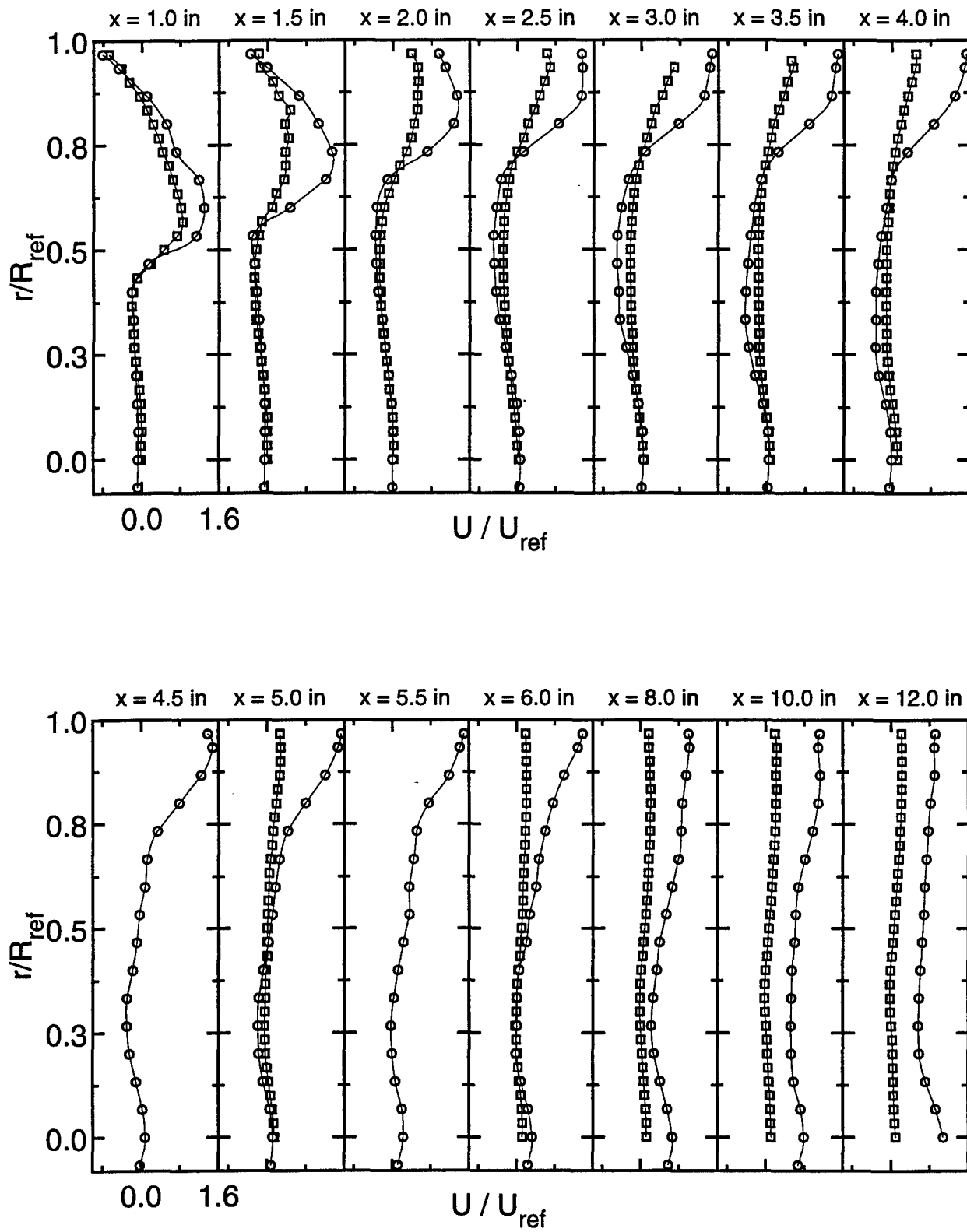
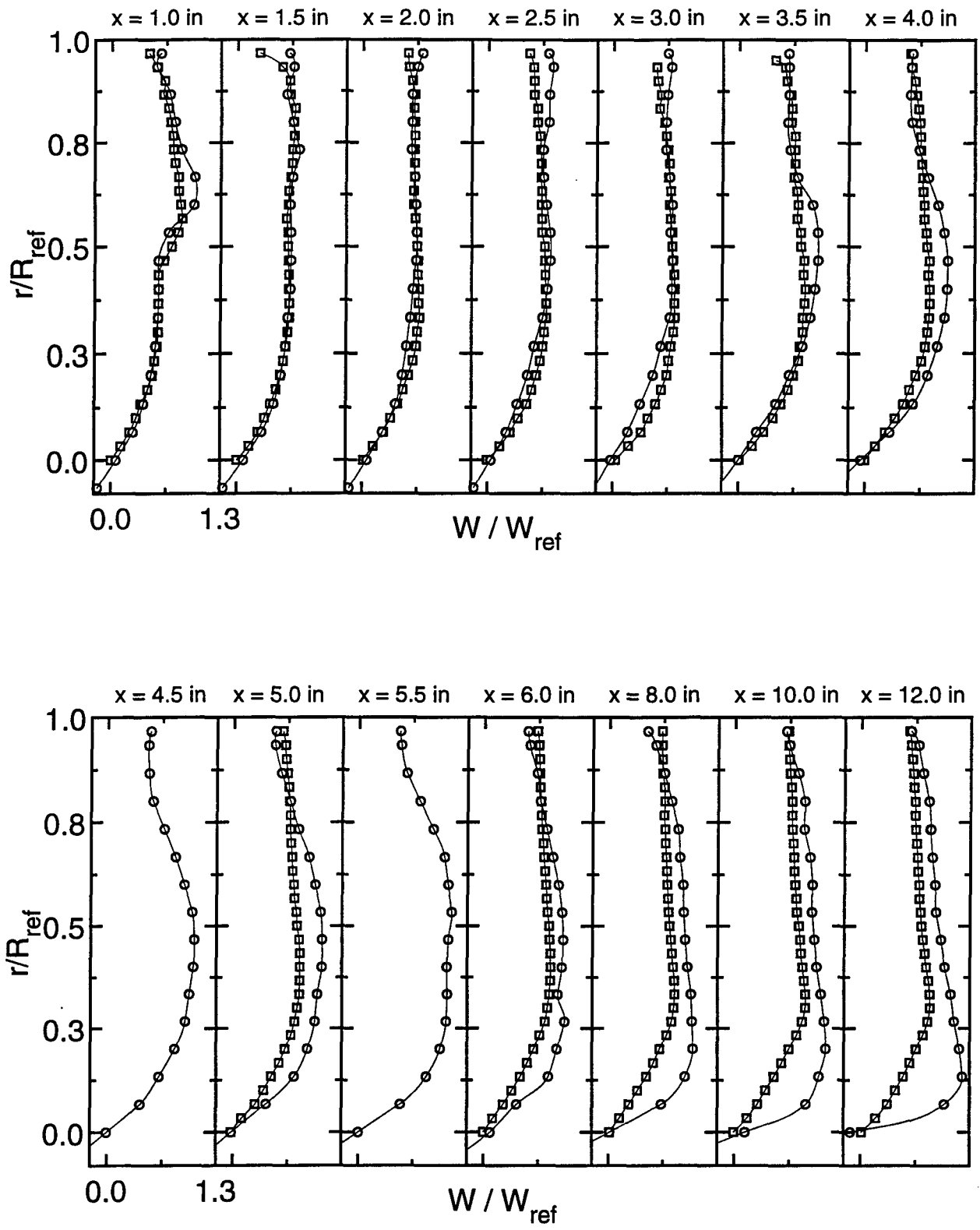Figure 3. Normalized mean axial velocity profiles.

Figure 4. Normalized mean tangential velocity profiles.
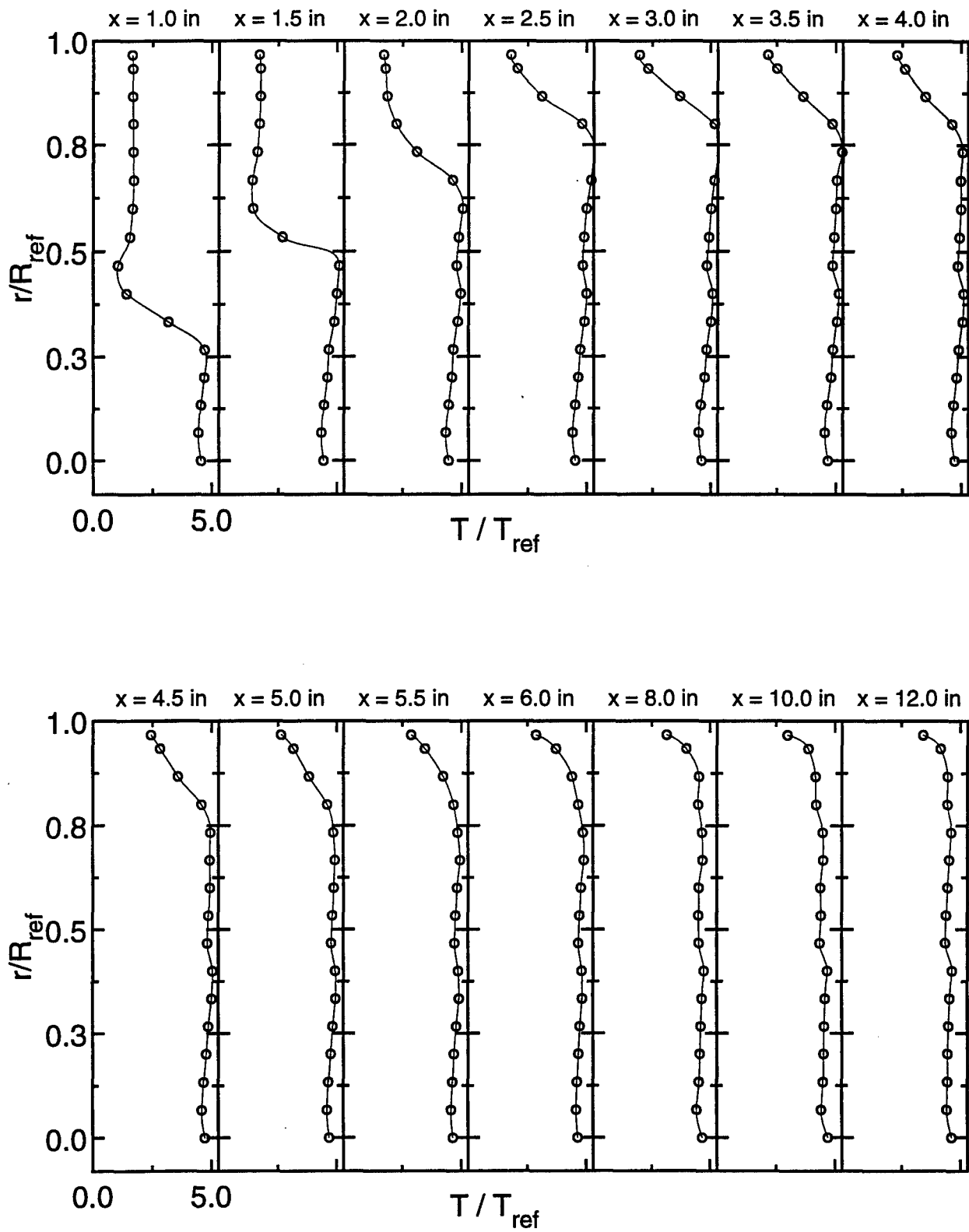
Figure 5. Normalized mean temperature profiles.
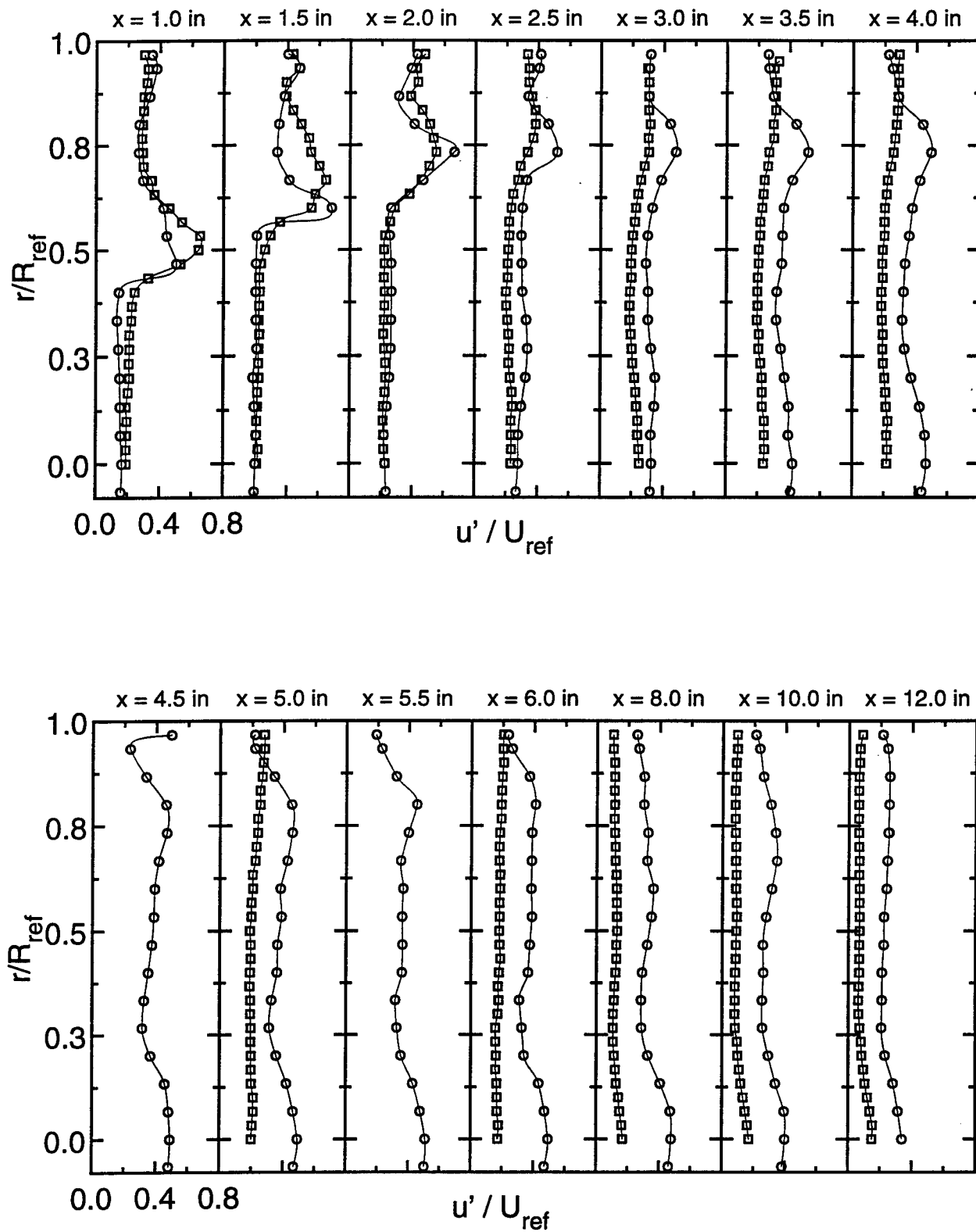
Figure 6. Normalized axial standard deviation profiles.
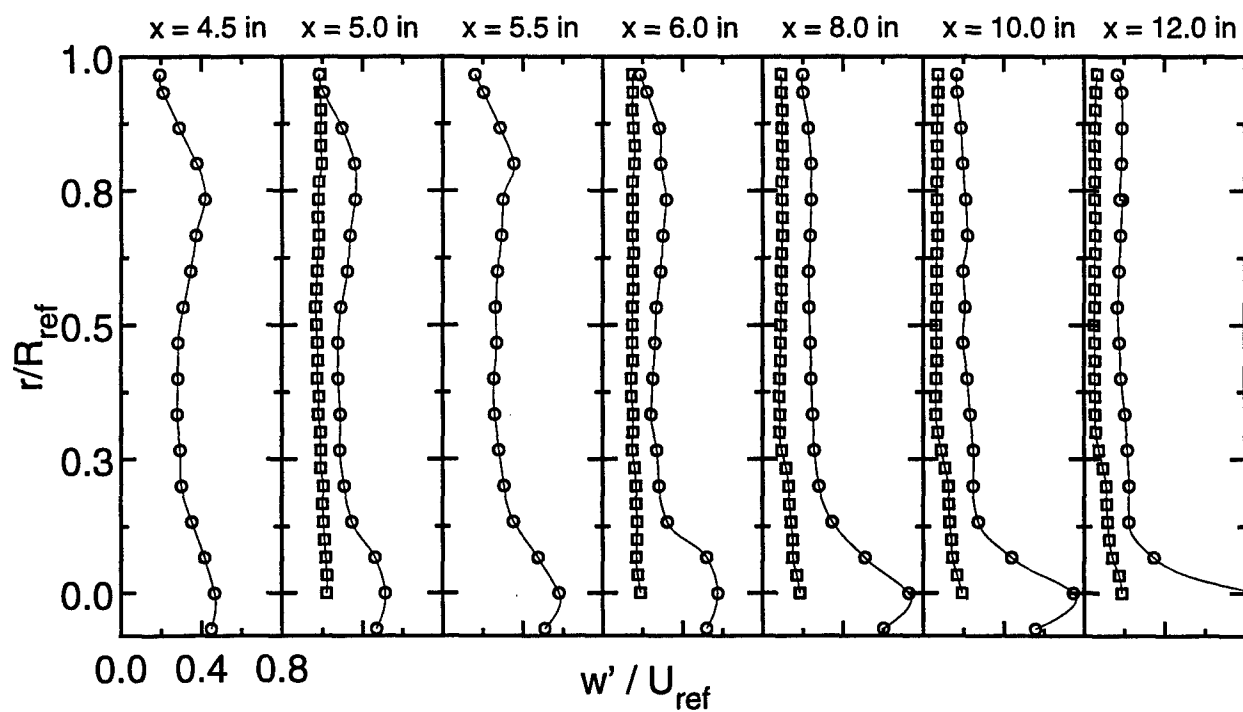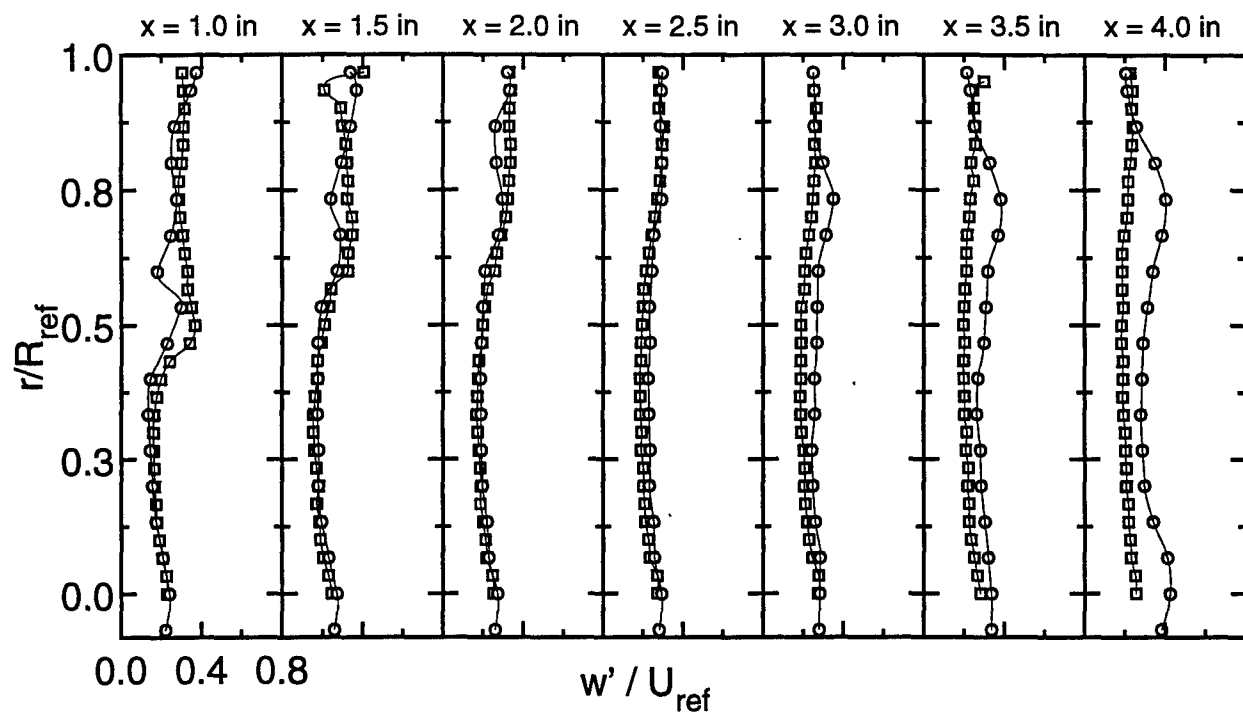
Figure 7. Normalized tangential standard deviation profiles.
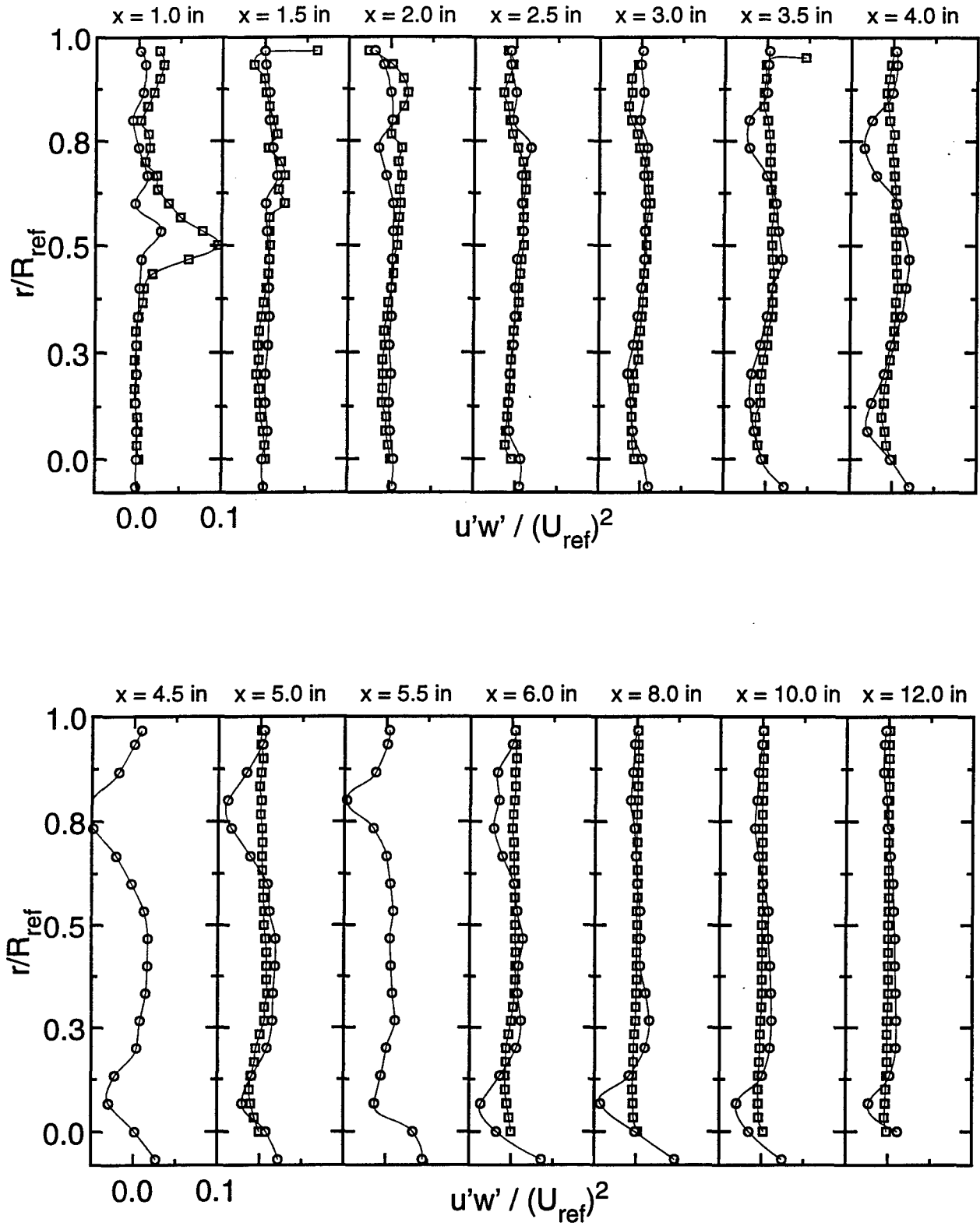
Figure 8. Normalized u'v' Reynolds stress profiles.

APPENDIX A

```
program tcradcor
c
c       Corrects thermocouple measurements made in Rolls Royce
c       swirl combustor during summer of 1992 for radiation heat
c       loss.
c
        dimension property(7)
        character*11 staname,tcorname
        character*8 tempname,tcname
c
        write(6,'(A)') ' Enter velocity file name (RRSC45.STA) '
        read(5,'(a11)') staname
        write(6,'(A)') ' Enter old temperature file name (T45.PRO) '
        read(5,'(a8)') tempname
        write(6,'(A)') ' Enter corrected temp. file name (RRTC45.COR) '
        read(5,'(a11)') tcorname
        write(6,'(A)') ' Enter corrected temperature file name (T45.COR) '
        read(5,'(a8)') tcname
        write(6,10) staname,tempname,tcorname
    10 format(1x,'The following velocity file: ',a11,/,1x,
      &'and old temperature file: ',a8,' will be opened.',/,
      &1x,'A new corrected temperature file: ',a11,' will be created.',
      &//,1x,'Should we continue? (y/[n])')
        read(5,'(1a1)') in
        if(in .eq. 'y ') go to 1
        if(in .eq. 'Y ') go to 1
        go to 999
c
     1 open(unit=7,file=staname,access='sequential',form='formatted'
      &,status='old')
        open(unit=8,file=tempname,access='sequential',form='formatted'
      &,status='old')
        open(unit=9,file=tcorname,access='sequential',form='formatted'
      &,status='new')
        open(unit=10,file=tcname,access='sequential',form='formatted'
      &,status='new')
        rewind(7)
        rewind(8)
c
c       set constants to known values
c
        dia=0.02/39.37
        emiss=0.25
        sigma=5.67e-8
        tsur_f=90.0
        tsur_k=(tsur_f-32.0)*5.0/9.0+273.15
c
c       read velocity and temperature statistics files
c
        read(7,120) x,r,z,ubar,wbar,up,wp,uw,ruw,dudx
        write(10,110)
```

```fortran
  110 format(1x,'x(mm)',2x,'r(mm)',1x,'vel(m/s)',2x,'T(K)',4x,'ReD',
     &6x,'NuD',2x,'h(W/m2-K)',1x,'Dt(K)',1x,'Tcor(K)')
      do 100 i=1,16
      read(7,120) x,r,z,ubar,wbar,up,wp,uw,ruw,dudx
      read(8,140) x,r,tcel,tkel
c
c     calculate velocity magnitude, Reynolds #, Nusselt #,
c     convection coefficient, temperature correction and
c     radiation loss corrected gas temperature.
c
c                                        calc. magnitude of mean velocity
      vel=(ubar*ubar+wbar*wbar)**0.5
c                                        get thermophysical prop. of air
      call getair(tkel,property)
      vis=property(4)
      thermcon=property(5)
      prandtl=property(7)
c                              calc. Reynolds number based on T.C. bead dia.
      red=vel*dia/vis
c                     Whitaker correlation for heat transfer around sphere
      anu=2.0+(0.4*red**0.5+0.06*red**0.6667)*prandtl**0.4
c                                        convection heat transfer coefficient
      h=anu*thermcon/dia
c                                        calc. correction factor
      deltat=emiss*sigma/h*(tkel**4-tsur_k**4)
      tcorr=deltat+tkel
      write(9,160) x,r,tkel,tcorr,deltat
      write(10,150) x,r,vel,tkel,red,anu,h,deltat,tcorr
c
  100 continue
  120 format(f6.1,f7.2,f8.2,5f8.3,1x,f7.4,e10.4)
  140 format(f7.2,3f8.2)
  150 format(f6.1,f7.2,f8.3,6f8.2)
  160 format(f6.1,f7.2,3f8.2)
c
      close(7)
      close(8)
      close(9)
      close(10)
c
  999 stop
      end
c
      subroutine getair(temper,prop)
c
      dimension temp(35),rho(35),cp(35),dynvis(35),vis(35),thermcon(35)
     &,thdiff(35),prandtl(35),prop(7)
c
c*******************************************************************
c     nomenclature list
c
c     temper   : temperature where air properties are evaluated [Kelvin]
c     prop(1)  : air density [kg/m^3]
c     prop(2)  : air constant pressure specific heat [kJ/kg-K]
```

19-18

```
c          prop(3) : air dynamic viscosity [N-s/m^2] or [kg/m-s]
c          prop(4) : air kinematic viscosity [m^2/s]
c          prop(5) : air thermal conductivity [W/m-K]
c          prop(6) : air thermal diffusivity [m^2/s]
c          prop(7) : air Prandtl number [unitless]
c
c
c     Thermophysical properties for air at atmospheric pressure
c     from Incropera and DeWitt, Fundamentals of Heat and Mass Transfer
c     3rd edition, Appendix A.4, p. A15.
c
c     written by R. D. Gould, 5/16/95
c
c*******************************************************************************
c
c     check that temperature is within range of tabular data
c
      if(temper .lt. 100.0 .or. temper .gt. 3000.0) go to 100
c
      data temp /100.,150.,200.,250.,300.,350.,400.,450.,500.,550.,600.
     &,650.,700.,750.,800.,850.,900.,950.,1000.,1100.,1200.,1300.,1400.
     &,1500.,1600.,1700.,1800.,1900.,2000.,2100.,2200.,2300.,2400.
     &,2500.,3000./
c
      data rho /3.5562,2.3364,1.7458,1.3947,1.1614,.9950,.8711,.7740
     &,.6964,.6329,.5804,.5356,.4975,.4643,.4354,.4097,.3868,.3666,.3482
     &,.3166,.2902,.2679,.2488,.2322,.2177,.2049,.1935,.1833,.1741,.1658
     &,.1582,.1513,.1448,.1389,.1135/
c
      data cp /1.032,1.012,1.007,1.006,1.007,1.009,1.014,1.021,1.030
     &,1.040,1.051,1.063,1.075,1.087,1.099,1.110,1.121,1.131,1.141,1.159
     &,1.175,1.189,1.207,1.230,1.248,1.267,1.286,1.307,1.337,1.372,1.417
     &,1.478,1.558,1.665,2.726/
c
      data dynvis /71.1,103.4,132.5,159.6,184.6,208.2,230.1,250.7,270.1
     &,288.4,305.8,322.5,338.8,354.6,369.8,384.3,398.1,411.3,424.4,449.0
     &,473.0,496.0,530.,557.,584.,611.,637.,663.,689.,715.,740.,766.
     &,792.,818.,955./
c
      data vis /2.00,4.426,7.590,11.44,15.89,20.92,26.41,32.39,38.79
     &,45.57,52.69,60.21,68.10,76.37,84.93,93.80,102.9,112.2,121.9,141.8
     &,162.9,185.1,213.,240.,268.,298.,329.,362.,396.,431.,468.,506.
     &,547.,589.,841./
c
      data thermcon /9.34,13.8,18.1,22.3,26.3,30.0,33.8,37.3,40.7,43.9
     &,46.9,49.7,52.4,54.9,57.3,59.6,62.0,64.3,66.7,71.5,76.3,82.,91.
     &,100.,106.,113.,120.,128.,137.,147.,160.,175.,196.,222.,486./
c
      data thdiff /2.54,5.84,10.3,15.9,22.5,29.9,38.3,47.2,56.7,66.7
     &,76.9,87.3,98.0,109.,120.,131.,143.,155.,168.,195.,224.,238.,303.
     &,350.,390.,435.,482.,534.,589.,646.,714.,783.,869.,960.,1570./
c
      data prandtl /.786,.758,.737,.720,.707,.700,.690,.686,.684,.683
     &,.685,.690,.695,.702,.709,.716,.720,.723,.726,.728,.728,.719,.703
```

```
       &,.685,.688,.685,.683,.677,.672,.667,.655,.647,.630,.613,.536/
c
c      find correct array index in table for specified temperature
c
       num=35
       j=0
       done=0
       do while (done .eq. 0)
       j=j+1
       if((temper .ge. temp(j) .and. temper .le. temp(j+1))
      & .or. (j .eq. num)) done=1
       end do
c
c      linear interpolate for thermophysical data
c
       ratio=(temper-temp(j))/(temp(j+1)-temp(j))
       prop(1)=ratio*(rho(j+1)-rho(j))+rho(j)
       prop(2)=ratio*(cp(j+1)-cp(j))+cp(j)`
       prop(3)=(ratio*(dynvis(j+1)-dynvis(j))+dynvis(j))*1.0e-7
       prop(4)=(ratio*(vis(j+1)-vis(j))+vis(j))*1.0e-6
       prop(5)=(ratio*(thermcon(j+1)-thermcon(j))+thermcon(j))*1.0e-3
       prop(6)=(ratio*(thdiff(j+1)-thdiff(j))+thdiff(j))*1.0e-6
       prop(7)=ratio*(prandtl(j+1)-prandtl(j))+prandtl(j)
       go to 102
c
c      error message - terminate program
c
  100 write(*,101)
  101 format(1x,'Temperature is out of range (100 - 3000 k)!',/)
       stop
c
  102 continue
       return
       end
```

MANIFESTATIONS OF THE STRESS DRIVEN REARRANGEMENT INSTABILITIES IN CREEP, DAMAGING AND FRACTURE

Michael A. Grinfeld
Research Professor of Mechanical and Aerospace Engineering
Department of Mechanical and Aerospace Engineering
Rutgers University
Piscataway, NJ 08844

Final Report for:
Summer Faculty Research Program
Wright-Patterson Laboratory

September, 1995

MANIFESTATIONS OF THE STRESS DRIVEN REARRANGEMENT INSTABILITIES IN CREEP, DAMAGING AND FRACTURE

Michael A. Grinfeld
Research Professor of Mechanical and Aerospace Engineering
Department of Mechanical and Aerospace Engineering
Rutgers University

Abstract

Recent explosive progress of the theory of stress driven rearrangement instability of solids has provided researchers with conceptually new approaches and ideas, and it has allowed to attack successfully many old and modern problems in different branches of materials science. In this study the ideas and mechanisms of the stress driven rearrangement instability of solids are incorporated in the problems of creep, damaging and fracture of solids. These ideas permit to explain simply and naturally the phenomena like nucleation dislocations, initiation of cracking in initially perfect crystalline solids, spatio-temporal localization of damaging; also, without any doubts they allow to present primary, secondary and tertiary creep as a coherent string of inherently connected physical phenomena rather than a manifestation of independent mechanisms of creep. We formulate and investigate conceptually new and relatively simple governing systems of equations allowing to investigate linear and nonlinear stages of the stress driven rearrangement instability and we believe that this study provide researchers with new approaches to the problems of creep, fracture, localization and life-time prediction.

MANIFESTATIONS OF THE STRESS DRIVEN REARRANGEMENT INSTABILITIES IN CREEP, DAMAGING AND FRACTURE

Michael A. Grinfeld

1. Introduction

Macroscopic behavior of substances is predetermined by a wide variety of the processes occurring at meso-, micro- and nano-scale level. All these processes are under intensive theoretical and experimental studies (for about 2 hundred years for macro- level, ~ 50 years for meso- and micro- levels, and ~15 years for nano- level). For a paramount variety of applications in mechanical and aerospace engineering macro-behavior remains to be a major issue of interest. It looked always extremely attractive to develop a purely theoretical derivation of rather complex and versatile macro-properties based on contemporary understanding of several elementary micro- and nano- properties and processes: that approach would be very helpful for further progress in materials understanding at all above mentioned levels. Despite several remarkable successes contemporary state-of-the-art does not allow to achieve such a goal nowadays (presumably, it will not be achieved in visible future if at all). On the other hand, even qualitative understanding of the processes occurring on different sub-levels can be extremely useful for development and further progress in describing constitutive laws and evolution models of macroscopic behavior allowing engineers and researchers to avoid extensive empirism and to get much better organized experimental data which become much more transparent physically: this, in its turn, allows one to generate more reliable predictions of materials behavior based on physical intuition or relatively simple theoretical schemes.

Recently, a remarkable progress in developing of such a compromised robust theory of creep has been achieved by the WPL research team. The authors coined it as a "renewal creep theory" and have unambiguously demonstrated that wide variety of experimental data can be described adequately by means of a simple governing system of ordinary differential equations and few properly chosen material constants [1]-[3]. The renewal theory (RT) is based on a transparent physical picture of the processes occurring on micro-scale level. It assumes that i)there are two (several) populations of defects with different kinetics (depending on overall stresses and temperature), ii)the evolution of the populations obeys a specific stochastic law and can be naturally described with a notion of the "intrinsic" time-scale. In its original formulation the RT was intended to describe primary and secondary creep. Further developments have demonstrated, however, that it is capable to include easily and successfully the well-known concepts of damage theory (like effective cross-section and stress) and, thus, to describe the tertiary creep [4], [5].

Since the extended RT remains to be easily manageable it seems reasonable to incorporate in it some other essential features of creep and fracturing. With this idea in mind we suggest to develop already existing theory in order to take into account that initiation of cracking as well as the fracturing have a robust tendency to be localized in several cross-sections rather than to be uniformly distributed in the specimen. In other words the "intrinsic" time is essentially different in different cross-sections of the specimen. Our goal leads us inevitably to the theory based on partial differential equations though the original and extended RT based on ordinary differential equations. Following the merits of RT we confine ourselves with the demand of maximal mathematical simplicity and physical lucidity of the governing system.

Our central idea is to incorporate in the RT the mechanisms of the stress driven rearrangement instability of a solid with a uniform distribution of mobile defects which immediately leads to appearance of stress localization and of different "intrinsic" time-scales in different domains of the sample. According to the current paradigm creep includes 3 stages: primary, secondary and tertiary creep. A contemporary viewpoint treats the primary creep as the result of migration of vacancies. This phenomenon was explained qualitatively by Nabarro [6] and described theoretically in the framework of a linear approach by Herring [7], Coble [8], Lifshits [9] and others [10], [11] (relevant nonlinear theory of primary creep has been developed recently by Berdichevsky, Hazzledine and Shoykhet [12], [13]). Mechanisms of the secondary and tertiary creep are much more versatile and much less investigated. The approach dominating nowadays treats the secondary creep as intensive proliferation of dislocations. Relevant theory is still in its infancy. The theories of primary and secondary creep have no points of contact (besides, the general understanding that relief of accumulated elastic energy is the motivation of all stages of creep). The ideas of the novel theory of stress driven rearrangement instability [14]-[28] enable us with the opportunity to build "bridges" between different stages of creep. In particular, it explains how the vacancy flux results in intensive nucleation of dislocation: this circumstance makes the secondary creep the natural continuation of the primary creep. The tertiary creep finalizes with fatigue, damage and fracture of solids. All these phenomena have one common bright feature: they clearly demonstrate the localization-like behavior. The stress driven rearrangement instability allows to explain stress localization in a very simple, natural and elegant way and shows that the localization begins from the early stage of deformation.

We believe that incorporating the ideas and different mechanisms of the stress driven rearrangement instability into RT we shall be able to develop a unified, self-consistent and conceptually simple approach and theory of the primary, secondary and tertiary creep and to give the engineers a reliable tool for analyzing creep, fatigue and fracture of polycrystalline solids and composites.

The paper is organized as follows. First, in Section 2 we give the reader intuitive pictures and explanations of the stress driven rearrangement instability by considering two elementary examples. To that end we consider an elementary one-dimensional problem of the rod with movable defects: this problem allows to understand how the stress driven rearrangement instability results in localization of stresses and deformations in the narrow zones of the rod. In order to explain nucleation of dislocations on the basis of the stress driven rearrangement instability we, then, consider in the qualitative manner stress driven corrugation of the free surface of a crystallite.

In the Section 3 we develop an elementary one-dimensional theory of the rod with movable defects. We believe that this theory is helpful because of three following reasons. First of all, it is the simplest theory allowing to describe qualitatively the effects like primary creep, localization of stresses and the finite life time of the rod. Thus, being properly calibrated, this problem might be able to accumulate in the unified self-consistent and physically transparent manner numerous existing experimental data. Secondly, it will enable the researcher with the tool of relatively simple investigation of the life-time evolution of the solid on the base of a relatively simple numerical simulation. Thirdly, some of the problems relating to this simplest model appear to be theoretically non-trivial and challenging: they are of extreme importance in developing relevant new mathematical tools of the investigation of the life-time of loaded solids. One of such problems is the problem of probabilistic prediction of the life-time given some stochastic characteristics of the internal heterogeneity.

We, then, proceed with the study of the role of stress driven rearrangement instability in the secondary creep. To that end we consider two following problems: i)stress driven destabilization of the free boundary due to migration of vacancies and ii)stress driven destabilization of the grain boundary due to interfacial surface diffusion (the results relating to the problem ii) are not included in this report.)

We finish the paper with the summary reviewing the results and discussing the problems of further studies.

2. Intuitive explanation of the stress driven rearrangement instability.

In order to ease comprehension of the relatively new idea of the stress driven rearrangement instability and associated notions, equations and results we begin with qualitative intuitive explanation based on two specific problems.

Example 1. Solid rod with mobile defects.

Let us consider a one-dimensional rod of a fixed nominal cross-section area. We assume that the rod contains a population of mobile defects - vacancies - diminishing effective cross-

section. In the absence of external forces the vacancies appear to exist in neutral equilibrium: their location or migration do not imply any change of accumulated elastic energy. This situation changes dramatically when an external loading is applied to the rod: now changing location of the vacancies we can change elastic energy accumulated by the rod. In accord with general concept of mechanics we assume that migration of vacancies has tendency to diminish this energy. Assume that initial distribution of vacancies deviates slightly from uniform one-dimensional distribution. We ask the following key question: *whether further migration of vacancies* (diminishing elastic energy !) *will result in returning to the uniform distribution or the level of nonuniformity will grow*? It is occurred that the second scenario is energetically favorable, and uniform distribution of vacancies in stressed rod appears to be unstable: it is the simplest example of the stress driven rearrangement instability. To make the intuitive explanation more clear let us "associate" with the nominally uniform rod with vacancies another rod without vacancies. The "associated" rod has nonuniform cross-section area distribution: its area is supposed to be equal to the "effective" area of the original rod (which is equal to the nominal area minus the area of all vacancies locating in the cross-section in question). When the vacancies migrate within the original rod the cross-sectional areas of the associated rod change, respectively. The distribution of the cross-sectional areas of the associated rod can change arbitrarily with the only constraint of conservation of its total volume (this corresponds to the mass conservation of the original rod). Thus we can talk about mass flux in the associated rod (by the way, when using "vacancy"-like language we always imply the flux of atoms!). We can now reformulate our key question in terms of the associated rod area distribution: *is the uniform distribution of cross-sectional areas of the loaded rod is stable with respect to mass flux diminishing accumulated elastic energy*? To address this question let us consider a small disturbance of the uniform distribution of the cross-sectional areas (see Fig.1: the disturbed rod possesses now a small "neck" and "small "bulge"). Because of mechanical equilibrium total force in each cross-section should be the same. Thus, the stress (the force per unit area) in the bulge is smaller than in the uniform part while in the neck it is bigger than in the uniform part. Thus, in order to diminish accumulated elastic energy the material particles will be leaving the neck and accumulating on the bulge. *Hence, the instability of the uniform distribution of mass!* The deeper the depression, the narrower the neck the greater the mass flux. *Hence, the localization!*

Example 2. Stress driven rearrangement instability of traction-free surfaces.

The stress driven rearrangement instability is a purely thermodynamic (energetic) phenomenon. Specific mechanisms of rearrangement of the particles - surface diffusion, vaporization-sublimation, melting-crystallization, migration of defects - play secondary role in destabilization (defining the time-scale of the evolution but not the very fact of the occurrence of the instability). Dwelling now on the stress driven destabilization of a traction-free surface of a

uniaxially prestressed, elastic crystal let us consider the processes of crystallization or sublimation (see, Fig. 2). We explicitly consider two physical effects: namely, elasticity and surface energy. The stresses within the solid can be generated by an applied stress or be internal stresses, such as those associated with heteroepitaxy. For the sake of simplicity, we consider that the solid is only two-dimensional and assume that deposition takes place in the form of elementary square cells of material, as per Fig. 2. We view each cell as a continuum so as not to have to justify the application of elasticity and surface energy at an atomic scale. Uniaxial in-plane deformation changes shape of the elementary cell. In particular, elementary cells of the complete layers become rectangular rather than of a square shape. Thus, the material being deposited has a different lattice parameter than the substrate due to the presence of the uniaxial, lateral stress. When cell A attaches to the uniform ad- layer under it, its bottom stretches to match the lattice parameter of the strained ad-layer. Its top, on the other hand remains at its initial unstrained width and the initially rectangular cell distorts into a trapezoidal shape.

Consider now the possible locations for cell B to attach to the film in the vicinity of cell A. Particle B may attach itself to the ad-layer in, e.g., positions 1, 2, 3, or 4. Since surface energy favors as large a number of nearest neighbors as possible, sites 2 and 4 are preferable to 1 and 3 due to the proximity of cell A. This is why surface energy favors the growth of as smooth of a surface as possible. If cell B attaches to site 1 or 4 it will take on the strained, trapezoidal shape of cell A. If, on the other hand, it attaches to site 2 or 3, the wall B shares with A becomes vertical and therefore both cells A and B become more strained than if cell B was at either site 1 or 4. Therefore, strain energy works against the surface smoothing tendencies of surface energy. Now, consider cell B becoming attached to site 5, on top of A. Since site 5 has the same number of nearest neighbors as site 1 and 4, the surface energy associated with B is the same for attachment to sites 1, 4 or 5. However, while the bottom of cell B would be stretched at sites a 1 or 4, it's bottom is unstretched at site 5 because the top of cell A is unstretched. Therefore, consideration of strain energy favors site 5 over sites 1-4. Depending on the ratio of the surface energy to the strain energy, site 5 may (small ratio) or may not (large ratio) be favored over sites 2 or 3. If the strain and/or the elastic constant are large, the roughness of the surface will increase with continued film growth. This is the stress driven morphological instability.

3. Governing system of evolution of a rod with defects

3.1. Governing system for 1D "effective" rod

Let us consider a rod with the variable cross-sectional area $H(x,t)$ and variable "Lagrangian" coordinates of the endpoints $L_0(t)$, $L_1(t)$. We use the notation $u(x,t)$ of the displacement of the cross-section with coordinate x at a moment t, and suppose that the endpoints have fixed positions in the space:

$$u(L_0(t),t) + L_0(t) = C_0, \quad u(L_1(t),t) + L_1(t) = C_1 \tag{3.1.1}$$

where C_0, C_1 are certain constants or given functions of time.

We derive governing system of quasi-static evolution of the rod assuming that the evolution is motivated by decrease of the total elastic energy E(t):

$$E(t) = \frac{1}{2} \int_{L_0(t)}^{L_1(t)} dx \; H(x,t) G \left(\frac{\partial u(x,t)}{\partial x}\right)^2 \tag{3.1.2}$$

where constant G is the linear elastic modulus.

An evolution of the cross-section area distribution should obey the mass conservation constraint:

$$\int_{L_0(t)}^{L_1(t)} dx \; H(x,t) = const \tag{3.1.3}$$

Denoting Q(x,t) the mass flux through the cross-section x we get the following mass conservation differential equation:

$$\frac{\partial H(x,t)}{\partial t} = \frac{\partial Q(x,t)}{\partial x} \tag{3.1.4}$$

Differentiating (3.1.3) with respect to t, using (3.1.4) and integrating by parts we get

$$\frac{d}{dt} \int_{L_0(t)}^{L_1(t)} dx \; H(x,t) = \int_{L_0(t)}^{L_1(t)} dx \frac{\partial H(x,t)}{\partial t} + H S \Big|_{L_0(t)}^{L_1(t)} = (Q + H S)\Big|_{L_0(t)}^{L_1(t)} = 0 \tag{3.1.5}$$

where $S_0(t) = d\, L_0(t)/dt$ and $S_1(t) = d\, L_1(t)/dt$ are velocities of the end-points. Thus, (3.1.5) leads us to the relationships

$$Q + H S = 0, \quad x = L_0, L_1 \tag{3.1.6}$$

Differentiating the kinematic boundary conditions (3.1.1) we get the following relationships:

$$\frac{\partial u(x,t)}{\partial t}\Big|_{L_0(t)} = - \left[1 + \frac{\partial u(x,t)}{\partial x}\Big|_{L_0(t)}\right] S_0(t) \,, \quad \frac{\partial u(x,t)}{\partial t}\Big|_{L_1(t)} = - \left[1 + \frac{\partial u(x,t)}{\partial x}\Big|_{L_1(t)}\right] S_1(t) \tag{3.1.7}$$

Differentiating the total elastic energy (3.1.2) with respect to time t, making use of (3.1.4), (3.1.6), (3.1.7) and integrating by parts we get

$$\frac{d}{dt} \frac{2}{G} E(t) = \frac{d}{dt} \int_{L_0(t)}^{L_1(t)} dx \; H(x,t) \left(\frac{\partial u(x,t)}{\partial x}\right)^2 = \tag{3.1.8}$$

$$= \int_{L_0(t)}^{L_1(t)} dx \left[2\, H(x,t)\, \frac{\partial u(x,t)}{\partial x}\, \frac{\partial^2 u(x,t)}{\partial x\, \partial t} + \left(\frac{\partial u(x,t)}{\partial x}\right)^2 \frac{\partial H(x,t)}{\partial t} \right] + H \left(\frac{\partial u(x,t)}{\partial x}\right)^2 S(t) \Big|_{L_0(t)}^{L_1(t)} =$$

$$= - \int_{L_0(t)}^{L_1(t)} dx \left[2\, \frac{\partial u(x,t)}{\partial t}\, \frac{\partial}{\partial x}\left(H \frac{\partial u(x,t)}{\partial x} \right) + Q \frac{\partial}{\partial x}\left(\frac{\partial u(x,t)}{\partial x}\right)^2 \right] + \left[H \left(\frac{\partial u(x,t)}{\partial x}\right)^2 S(t) + \right.$$

$$\left. 2\, H \frac{\partial u(x,t)}{\partial x}\, \frac{\partial u(x,t)}{\partial t} + Q \left(\frac{\partial u(x,t)}{\partial x}\right)^2 \right]\Big|_{L_0(t)}^{L_1(t)} = - \int_{L_0(t)}^{L_1(t)} dx \left[2\, \frac{\partial u(x,t)}{\partial t}\, \frac{\partial}{\partial x}\left(H \frac{\partial u(x,t)}{\partial x} \right) + \right.$$

$$\left. Q \frac{\partial}{\partial x}\left(\frac{\partial u(x,t)}{\partial x}\right)^2 \right] - 2\, H \frac{\partial u(x,t)}{\partial x}\left(1 + \frac{\partial u(x,t)}{\partial x} \right) S(t) \Big|_{L_0(t)}^{L_1(t)}$$

The relationship (3.1.8) leads us to the following bulk equations and boundary conditions:

i) mechanical equilibrium within the bulk

$$\frac{\partial}{\partial x}\left(G\, H \frac{\partial u}{\partial x} \right) = 0 \tag{3.1.9}$$

ii) constitutive equation of the mass flux Q within the bulk

$$Q = \chi_b G \frac{\partial}{\partial x}\left(\frac{\partial u}{\partial x}\right)^2 \qquad \chi_b > 0 \tag{3.1.10}$$

iii) velocity of the end-points

$$S = \chi_e\, G \frac{\partial u(x,t)}{\partial x}\left(1 + \frac{\partial u(x,t)}{\partial x} \right),\ x = L_0, L_1\ \ \chi_e > 0 \tag{3.1.11}$$

where χ_b is the bulk diffusion coefficient, whereas χ_e is the boundary diffusion impedance.

In the case of small deformations $\partial u(x,t)/\partial x \ll 1$ we can use the following approximation of (3.1.11)

$$S = \chi_e\, G \frac{\partial u(x,t)}{\partial x},\ x = L_0, L_1 \tag{3.1.12}$$

Combining (3.1.4), (3.1.12), we arrive at the following bulk equation:

$$\frac{\partial H(x,t)}{\partial t} = \chi_b\, G \frac{\partial^2}{\partial x^2}\left(\frac{\partial u}{\partial x}\right)^2 \tag{3.1.13}$$

Excluding Q and S from the mass conservation equation (3.1.6), we get

$$\chi_b \frac{\partial}{\partial x}\left(\frac{\partial u}{\partial x}\right)^2 + \chi_e\, H \frac{\partial u}{\partial x} = 0, \quad x = L_0, L_1 \tag{3.1.14}$$

The bulk equation of mechanical equilibrium (3.1.9) can be easily integrated:

$$H \frac{\partial u}{\partial x} = \frac{p(t)}{G} \tag{3.1.15}$$

where p(t) is the axial force.

Then, we can rewrite (3.1.12), (3.1.13), (3.1.14) in the following forms, respectively:

$$S = \chi_e \frac{p(t)}{H} , \quad x = L_0, L_1 \tag{3.1.16}$$

$$\frac{\partial H(x,t)}{\partial t} = \frac{\chi_b}{G} p^2(t) \frac{\partial^2}{\partial x^2} H^{-2} \tag{3.1.17}$$

$$\chi_b \frac{p(t)}{G} \frac{\partial}{\partial x} H^{-2} + \chi_e = 0, \quad x = L_0, L_1 \tag{3.1.18}$$

The equation (3.1.17) with the boundary conditions (3.1.16), (3.1.18) form the governing system in the case of specified axial force p(t). In the case of specified boundary displacements the function p(t) should be computed with the help of the equations (3.1.1), (3.1.15). Indeed, dividing (3.1.15) by H, integrating over variable interval (L_0, L_1) and using (3.1.1) we arrive at the following formula of p(t):

$$p(t) = G (C_1 - L_1 - C_0 + L_0) \left[\int_{L_0}^{L_1} dx \, H^{-1} \right]^{-1} \tag{3.1.19}$$

Let us now explore an evolution of small perturbations in vicinity of the uniform axially stressed configuration. Linearizing governing equation (3.1.17) we arrive at the following equation of small disturbances of the cross-sectional area distribution $H^*(x,t)$

$$\frac{\partial H^*(x,t)}{\partial t} = \frac{6 \, p_o^2 \chi_b}{G \, H_o^4} \frac{\partial^2}{\partial x^2} H^* \tag{3.1.20}$$

Let us consider the propagating-wave-solution of the equation (3.1.20):

$$H^* (x,t) = Q \exp(\eta t + ikx) \tag{3.1.21}$$

Inserting (3.1.21) in (3.1.20) we arrive at the the following dependence of the growth coefficient η on the wave-number k:

$$\eta = \frac{6 \, p_o^2 \chi_b}{G \, H_o^4} k^2 \tag{3.1.22}$$

Thus, the amplitude of the propagating disturbance is growing exponentially in time and uniform distribution of defects (constant effective thickness) appears to be unstable in complete agreement with the qualitative discussion of Section 2 (see, the Example 1). Theoretical analysis gives us the explicit formula of the growth coefficient η. In order to find a non-uniform equilibrium configuration and nonlinear stage of evolution of the rod we have to return to the nonlinear master system (3.1.9) - (3.1.12).

3.2. Governing system for 1-D rod with mobile defects

Let us consider one-dimensional rod of fixed uniform nominal cross-section. Following the concept of continuum damage mechanics [29], [30] we assume that "effective" cross-area are actually smaller because of the presence of different lattice defects (vacancies, dislocations, cracks, etc...). In the following we assume that there are two sorts of defects: mobile defects with concentration χ_v and immobile defects with concentration χ_c. For brevity, we call the former as vacancies while the latter as cracks. Thus, the effective thickness H_e is the function of both concentrations $H_e = H_e(\chi_v, \chi_c)$. Since the concentrations $\chi_v(x,t)$, $\chi_c(x,t)$ are the functions of the spatial coordinate x and time t the same is true for the effective cross-area.

For the sake of simplicity we assume that total elastic energy is defined by the following "surrogate" formula of linear elasticity:

$$E = \frac{1}{2} \int_{L_0}^{L_1} dx \, H_e(\chi_v, \chi_c) \, G \left(\frac{\partial u(x,t)}{\partial x}\right)^2 \tag{3.2.1}$$

where constant G is the linear elastic module, u(x,t) is a displacement field.

We assume that temporal change of concentration of the mobile defects $\chi_v(x,t)$ is defined by the flux q(x,t):

$$\frac{\partial \chi_v(x,t)}{\partial t} = \frac{\partial q(x,t)}{\partial x} \tag{3.2.2}$$

Using arguments of irreversible thermodynamics we arrive at the following master system of quasi-static evolution in the bulk:

a) equation of mechanical equilibrium within the rod:

$$\frac{\partial}{\partial x} \left(H_e \frac{\partial u(x,t)}{\partial x}\right) = 0 \tag{3.2.3}$$

b) constitutive equation of the flux within specimen

$$q = - \kappa_b \frac{\partial}{\partial x} \left[\frac{\partial H_e}{\partial \chi_v} \frac{G}{2} \left(\frac{\partial u(x,t)}{\partial x}\right)^2\right] \tag{3.2.4}$$

where κ_b is a positive coefficient of diffusion;

c) equation of bulk diffusion

$$\frac{\partial c_v(x,t)}{\partial t} = - K_b \frac{\partial^2}{\partial x^2} \left[\frac{\partial H_e}{\partial \chi_v} \left(\frac{\partial u(x,t)}{\partial x}\right)^2\right] \tag{3.2.5}$$

where $K_b \equiv \kappa_b G/2$.

In order to choose appropriate boundary conditions we notice that mass conservation leads to the following relationship between the "vacancy flux" q and the velocity of the endpoints S(t) = dL(t)/dt:

$$q + \chi_v S = 0, \, x = L_0, L_1 \tag{3.2.6}$$

The accumulated energy decay principle leads to the following "constitutive" equation of S(t):

$$S = \kappa_e \frac{G}{2} \frac{\partial u}{\partial x} \left[\left(H_e + \chi_v \frac{\partial H_e}{\partial \chi_v} \right) \frac{\partial u}{\partial x} + 2H \right], \quad x = L_0, L_1 \tag{3.2.7}$$

where κ_e is a positive constant (the inpedance of the edge).

Combining (3.2.6), (3.2.7), we can eliminate S and q from (3.2.4):

$$\kappa_e \chi_v \frac{\partial u}{\partial x} \left[\left(H_e + \chi_v \frac{\partial H_e}{\partial \chi_v} \right) \frac{\partial u}{\partial x} + 2H \right] - \kappa_b \frac{\partial}{\partial x} \left[\frac{\partial H_e}{\partial \chi_v} \left(\frac{\partial u(x,t)}{\partial x} \right)^2 \right] = 0, \quad x = L_0, L_1 \tag{3.2.8}$$

The governing system (3.2.3), (3.2.5), (3.2.8) should be added with "mechanical" boundary conditions depending on the specific loading and the initial data compatible with (3.2.3), (3.2.5).

4. The stress driven rearrangement instability of interfaces in solids with vacancies

4.1. Nonlinear master system of evolution

Let us consider a solid occupying a variable domain ω_t of the crystal-space (see, [18], [19]) bounded by the surface γ_t. The crystal-space is referred to the coordinates x^i (the Latin indexes run values 1,2,3), the material points of the bounding surface are referred to the Lagrangian coordinates ξ^α (the Greek indexes run values 1,2). Location of the bounding surface in the crystal space is defined by the functions $x^i = x^i(\xi^\alpha, t)$. One part of the surface $\gamma_t - \gamma_t^f$ is supposed to be traction-free, fixed spatial coordinates z^i (ξ^α) are specified on the other part of it - γ_t^z. Using notation $u^i = u^i(x^j, t)$ of the displacement of the point x^j of the crystal space we get the following relationship on γ_t^z:

$$x^i(\xi^\alpha, t) + u^i(x^j(\xi^\alpha, t), t) = z^i(\xi^\alpha) \tag{4.1.1}$$

We use the notation $e(u_{i|j}, \chi)$ of the dependence of the specific energy density per unit volume of the crystal space on the displacement gradients $u_{i|j}$ and concentration of vacancies χ, and found our consideration on the energy E:

$$E = \int_{\omega_t} d\omega \, e(u_{i|j}, \chi) \tag{4.1.2}$$

Conservation of mass of the solid can be expressed in the form:

$$\frac{d}{dt} \int_{\omega_t} d\omega \, (1 - \chi) = 0 \tag{4.1.3}$$

Using notation q^i (x,t) of the vector of vacancy flux we get the following equation of local vacancies conservation:

$$\frac{\partial \chi(x,t)}{\partial t} = \frac{\partial q^i(x,t)}{\partial x^i} \tag{4.1.4}$$

Combining (4.1.3), (4.1.4) and integrating by parts we arrive at the following form of the mass conservation relation:

$$\int_{\gamma_t} d\gamma \, [c(1 - \chi) - q^i n_i] = 0 \tag{4.1.5}$$

where $n_i(\xi,t)$ is the outward unit normal to γ_t whereas $c(\xi,t)$ is the velocity of γ_t the direction of this normal.

Equation (4.1.5) leads us to the following local form of mass conservation:

$$c(1 - \chi) = q^i n_i \tag{4.1.6}$$

Differentiating (4.1.1) with respect to t we arrive at the following constraint on γ_t^z:

$$\frac{\partial u^i(x,t)}{\partial t}\Big|_{\gamma_t^z} + w^j(\xi^\alpha,t)\left(\delta_j^i + u^i_{.ij}\Big|_{\gamma_t^z}\right) = 0 \tag{4.1.7}$$

In (4.1.7) and in the future we use the following vectors $w^j(\xi^\alpha,t)$, $w^\beta(\xi^\alpha,t)$:

$$w^j(\xi^\alpha,t) = \frac{\partial x^j(\xi^\pi,t)}{\partial t}, \quad w^\beta(\xi^\alpha,t) = w^j(\xi^\pi,t)\, x_{ij}(x)\frac{\partial x^i(\xi^\pi,t)}{\partial \xi^\alpha}\, \xi^{\alpha\beta}(\xi^\pi,t) \tag{4.1.8}$$

where $x_{ij}(x)$, $\xi^{\alpha\beta}(\xi^\pi,t)$ are the metric of the crystal space and of the surface γ_t, respectively.

Differentiating (4.1.1), using (4.1.4) and integrating by parts, we arrive at the following formula of the total energy increment:

$$\frac{d}{dt}E = \frac{d}{dt}\int_{\omega_t} d\omega \, e(u_{i|j},\chi) = \int_{\omega_t} d\omega \left[-e^{ij}_{|j}\frac{\partial u_i(x,t)}{\partial t} - q^i e_{\chi|i} \right] + \tag{4.1.9}$$

$$+ \int_{\gamma_t} d\gamma \left(c\, e + e^{ij}\frac{\partial u_i(x,t)}{\partial t} n_j + e_\chi q^i n_i \right)$$

Using the relationship (4.1.9) and the arguments similar to those of Section 3 we arrive at the following bulk equations:

i) mechanical equilibrium

$$e^{ij}_{|j} = 0 \tag{4.1.10}$$

ii) constitutive equation of the vacancy flux q^i:

$$q^i = D^{ij}e_{\chi|j} \tag{4.1.11}$$

where D^{ij} is a positively definite symmetric tensor of diffusion.

Combining (4.1.4), (4.1.11) we arrive at the following bulk equation of diffusion:

$$\frac{\partial \chi(x,t)}{\partial t} = \frac{\partial}{\partial x^i}\left(D^{ij}\frac{\partial}{\partial x^j}e_\chi\right) \tag{4.1.12}$$

The boundary conditions appear to be different on the traction-free part γ_t^f and on the fixed-displacements part γ_t^z.

On the traction-free part γ_t^f we get the standard equation of mechanical equilibrium:

$$e^{ij} n_j = 0 \qquad\qquad (4.1.13)$$

By making use of (4.1.6), (4.1.13), we can rewrite the surface integral in the energy derivative formula (4.1.9) I_γ^f as follows:

$$I_\gamma^f = \int\limits_{\gamma_t} d\gamma \left(c\, e + e^{ij} \frac{\partial u_i(x,t)}{\partial t} n_j + e_\chi\, q^i n_i \right) = \int\limits_{\gamma_\gamma^f} d\gamma\, c \left[e + (1 - \chi)\, e_\chi \right] = \qquad (4.1.14)$$

$$= \int\limits_{\gamma_\gamma^f} d\gamma\, \frac{\partial x^i(\xi,t)}{\partial t} n_i \left[e + (1 - \chi)\, e_\chi \right]$$

The relationship (4.1.14) leads to the following governing differential equation for the function $x^i(\xi,t)$:

$$\frac{\partial x^i(\xi,t)}{\partial t} = - \Delta^{ij} n_j \left[e + (1 - \chi)\, e_\chi \right] \qquad\qquad (4.1.15)$$

where Δ^{ij} is a positively definite symmetric tensor.

On the fixed-displacements part γ_t^z of the boundary the kinematic constraint (4.1.7) allows us to exclude the derivative $\partial u^i(x,t)/\partial t$ and with the help of (4.1.6) to obtain the following formula of the surface integral I_γ^z:

$$I_\gamma^z = \int\limits_{\gamma_t} d\gamma \left(c\, e + e^{ij} \frac{\partial u_i(x,t)}{\partial t} n_j + e_\chi\, q^i n_i \right) = \int\limits_{\gamma_\gamma^z} d\gamma \left[c\, (e + (1 - \chi)\, e_\chi) - e^{kj} (x_{kl} + u_{kl|l})\, n_j \right]$$

$$= \int\limits_{\gamma_\gamma^z} d\gamma\, w^l(\xi,t) \left[(e + (1 - \chi)\, e_\chi)\, n_l - e^{kj} (x_{kl} + u_{kl|l})\, n_j \right] = \qquad (4.1.16)$$

$$= \int\limits_{\gamma_\gamma^z} d\gamma\, w^l(\xi,t) \left[(e + (1 - \chi)\, e_\chi)\, \delta_l^j - P^{jq} X_{ql}(x,t) \sqrt{\frac{X(x,t)}{x(x)}} \right] n_j$$

where P^{jq} - is the Cauchy stress tensor, $X_{ql}(x,t)$ - is the actual metric tensor, $X(x,t) = |X_{ql}(x,t)|$, $x(x) = |x_{ql}(x)|$.

Thus, equation (4.1.6) leads to the following generalization of the equation (4.1.15)

$$\frac{\partial\, x^i(\xi,t)}{\partial t} = - \Delta^{il} \left[(e + (1 - \chi)\, e_\chi)\, \delta_l^j - P^{jq}\, X_{ql}(x,t)\, \sqrt{\frac{X(x,t)}{x(x)}} \right] n_j \qquad (4.1.17)$$

4.2. The stress driven migration of vacancies as the cause of destabilization.

Let us explore some consequences of vacancies migration in vicinity of a traction-free surface of a stressed solid. Since our major concern is the small vicinity of a free surface we can limit ourselves with consideration of the vacancies migration in a uniaxially stressed elastic half-space. For the sake of simplicity we consider a two-dimensional situation and assume that the solid substance is isotropic. We can, then, present the governing equations as follows:

i)within bulk

$$e_{lj}^{ij} = 0 \qquad (4.2.1)$$

$$\frac{\partial\, \chi(x,t)}{\partial t} = \frac{\partial}{\partial x^i} \left(D^{ij} \frac{\partial}{\partial x^j}\, e_\chi \right) \qquad (4.2.2)$$

ii)at the traction-free surface

$$e^{ij}\, n_j = 0 \qquad (4.2.3)$$

$$\frac{\partial\, x^i(\xi,t)}{\partial t} = - \Delta\, n^i \left[e + (1 - \chi)\, e_\chi \right] \qquad (4.2.4)$$

$$\frac{\partial\, x^i(\xi,t)}{\partial t}\, n_i\, (1 - \chi) = D\, e_\chi^{,i}\, n_i \qquad (4.2.5)$$

where D and Δ are the bulk and surface coefficients of diffusion, respectively.

In the following we use the "degree" mark for the parameters of the equilibrium uniaxially stressed configuration and a "prime" for the small disturbances. Linearization of the system (4.2.1) - (4.2.5) gives the following system:

i)within the bulk

$$(e^{oijkl}\, u'_{kll} + e_\chi^{oij}\, \chi')_{lj} = 0 \qquad (4.2.6)$$

$$\frac{\partial\, \chi'(x,t)}{\partial t} = D\, (e_\chi^{oij}\, u'_{ilj} + e_{\chi\chi}^{o}\, \chi')_{l.k}^k \qquad (4.2.7)$$

ii)at the traction free-surface

$$(e^{oijkl}\, u'_{kllt} + e_\chi^{oij}\, \chi'_{lt})n_j^o - e_\chi^{oij}\, x_j^{o.\alpha}\, c'_{l\alpha} = 0; \qquad c' = \frac{\partial\, x'^i(\xi,t)}{\partial t}\, n_i^o \qquad (4.2.8)$$

$$\frac{\partial\, x'^i(\xi,t)}{\partial t} = - \Delta\, n^{oi} \left\{ \left[e^{okl} + (1 - \chi^o)\, e_\chi^{okl} \right] u'_{kll} + (1 - \chi^o) e_{\chi\chi}^{o} \chi' \right\} \qquad (4.2.9)$$

$$D \left[e^{oij} u'_{iljk} + e_{\chi\chi}^{o} \chi'_{lk} \right] n^{ok} + \Delta \left\{ \left[e^{okl} + (1 - \chi^o)\, e_\chi^{okl} \right] u'_{kll} + (1 - \chi^o) e_{\chi\chi}^{o} \chi' \right\} = 0 \qquad (4.2.10)$$

For the Lifshits energy density [8] the system (4.6) - (4.10) can be reduced to the following one:

i)within the bulk

$$e^{oijkl} u'_{kllj} = 0 \qquad (4.2.11)$$

$$\frac{\partial \chi'(x,t)}{\partial t} = \overset{o}{e}_{\chi\chi} \chi'^{k}_{l,k} \qquad (4.2.12)$$

ii)at the traction free-surface

$$e^{oijkl} u'_{kllt} n^o_j + \Delta e^{oij} \left[e^{okl} u'_{kllj} + \overset{o}{e}_{\chi\chi} (1 - \chi^o) \chi'_{lj} \right] = 0 \qquad (4.2.13)$$

$$D \overset{o}{e}_{\chi\chi} \chi'_{lk} n^{ok} + \Delta \left[e^{oij} u'_{ilj} + (1 - \chi^o) \overset{o}{e}_{\chi\chi} \chi' \right] = 0 \qquad (4.2.14)$$

In the case of isotropic linear elastic substance tensor has the following structure:

$$e^{oijkl} = \lambda \, \delta^{ij} \delta^{kl} + \mu \, (\delta^{ik} \delta^{jl} + \delta^{il} \delta^{jk}) \qquad (4.2.15)$$

where λ, μ are the Lame coefficients.

In this case the bulk equations (4.2.11), (4.2.12) have solutions of the following form (in two-dimensional case):

$$\chi' = C_+ \exp(\eta t + ikx + khz), \quad u'_z = \exp(\eta t + ikx)[Q_+ k + R_+ z \exp(kz)], \qquad (4.2.16)$$

$$u'_x = \frac{i}{k} \exp(\eta t + ikx)\{ [Q_+ k + R_+(3 - 4v)]\exp(kz) + R_+ kz \exp(kz) \}, \quad h = \sqrt{1 + \frac{\eta}{k^2 D \overset{o}{e}_{\chi\chi}}}$$

In the case at hand the boundary conditions (4.2.13), (4.2.14) can be written as

$$\frac{\partial}{\partial t}\left(\frac{\partial u'_x}{\partial z} + \frac{\partial u'_z}{\partial x}\right) + \frac{\Delta \tau^2}{m\mu} \frac{\partial}{\partial x}\left[\frac{\partial u'_x}{\partial z} + \frac{\overset{o}{e}_{\chi\chi}}{\tau} (1 - \chi^o)\chi'\right] = 0, \qquad (4.2.17)$$

$$\frac{\partial u'_z}{\partial z} + \frac{v}{1 - v} \frac{\partial u'_x}{\partial x} = 0, \quad \frac{\partial u'_x}{\partial z} + \frac{\Delta \tau}{D \overset{o}{e}_{\chi\chi}} \left[\frac{\partial u'_x}{\partial z} + \frac{\overset{o}{e}_{\chi\chi}}{\tau} (1 - \chi^o)\chi'\right] = 0$$

where m is the mass density per unit volume of the reference crystal-space.

Inserting the solutions (4.2.16) in the boundary conditions (4.2.17) we arrive at the linear homogeneous algebraic system with respect to the coefficients C_+, Q_+ and R_+. Equating its determinant to zero we arrive at the following dispersion equation:

$$[\eta - \frac{\Delta \tau^2}{m\mu}(1 - v)][k\sqrt{1 + \frac{\eta}{k^2 D \overset{o}{e}_{\chi\chi}}} + \frac{\Delta}{D}(1 - \chi^o)] + \frac{\Delta^2 \tau^2}{Dm\mu}(1 - v)(1 - \chi^o) = 0 \quad (4.2.18)$$

The dispersion equation allows to find the dependence of the growth coefficient of the traveling wave η upon its wave-number k and uniaxial (shear) stress τ and materials parameters

of the substance (ν is the Poisson ratio of the substance). In particular, for the short wave-length disturbances - k >> 1 - equation (4.1.18) shows exponential growth with the increment:

$$\eta = \frac{\Delta\tau^2}{m\mu}(1 - \nu) \qquad\qquad (4.2.19)$$

in accordance with the qualitative analysis of Section 3.

5. Conclusions. Some directions of future developments.

The above analysis has demonstrated that different mechanisms of the stress driven rearrangement instability play significant role in all stages of creep - the primary, secondary and tertiary creep - and as a consequence in fracture, damage and fatigue of loaded solids. The ideas of the stress driven rearrangement instability allow to attack, explore and explain the phenomena of nucleation of dislocations and initiation of cracks as well as the effects of spatio-temporal localization of damaging: the phenomena playing a paramount role in creep and fracture.

We have suggested and partially explored theoretically several new problems related to creep, fracture and life-time prediction of loaded solids. The one-dimensional theory of the Section 3 relating to the behavior of a loaded rod with mobile defects is the simplest problem to describe all stages of creep and fracture including spatio-temporal localization and life-time prediction. This theory allows: i)to get a conceptually transparent physical skeleton for presenting already collected experimental data in a coherent string by appropriate choice of several material constants, ii)to explore possible scenarios in the behavior of solids by means of a rather simple numerical simulating, iii)to develop novel theoretical tools, techniques, approaches and methods to the problems of creep, localization, fracture and life-time prediction.

In the Sections 3 and 4 we suggested a theoretical approach for the study of dislocation nucleation and initiation of micro-cracks as a consequence of stress driven migration of vacancies. We have demonstrated that motion of vacancies destabilizes originally smooth traction-free surfaces of stressed solids, leads to development of the concentrators of elastic energy, stresses and deformation. The primary, secondary and tertiary creep can be treated not as a reflection of physically independent phenomena but rather as the "natural" sequence of interrelated events. Also, we have explored the stress driven rearrangement destabilization of grain interfaces in stressed solids, and have established the very fact of such a destabilization which seems to have a variety of manifestations and practical consequences (the results are not presented in this *short* report).

In the interests of further progress of the problems of creep and fracture these studies should be and are supposed to be continued in several directions of which we mention only three:

- So far, our investigations of the role of the stress driven rearrangement instability in creep and fracture were based on the linear analysis of the governing systems of the Sections 3 and 4 although the governing systems themselves are nonlinear and they are sufficient for a complete self-consistent study. The complete nonlinear analysis is of extreme necessity and interest for a deep understanding of nucleation of dislocations and micro-cracks and, thus, of the understanding of the secondary and tertiary creep and of transitional stages between them and the primary creep. The development of theoretical tools and numerical codes and based on them theoretical studies and numerical simulations of the nonlinear effects in different stages of creep should be one of the primary concerns of further studies.

- In addition to its usefulness in the theory of creep the governing system of the Section 3.1 allows to develop new methods of attacking problems of life-time prediction of stressed solids depending on the statistical characteristics of the initial inhomogeneity of loaded solid samples and type of the loading. Despite apparent simplicity of formulation of the master equation of the Section 3.1 it is deeply nonlinear and demands novel powerful tools of stochastic analysis. On the other hand, this problem can be attacked by means of numerical simulation: this simulation itself can give a lot of engineering information and be helpful in establishing the mostly robust stochastic peculiarities and consequences for life-time prediction. Developing mathematical techniques for life-time predictions based on the master systems of the Section 3 in the second major problem for future studies.

- So far, in the studies of the role of the stress driven rearrangement instabilities in creep and fracture we did not include into play different thermodynamic effects, processes on the grain boundaries, environmental agents and did not consider practically representative modes of loading. Though including of the above circumstances is pretty routine and faces no conceptual obstacles their realization is certainly very instructive and useful. We consider these sort of studies as the third major direction of future development.

REFERENCES

1. R.L. Bagley, D.I.G. Jones, A.D. Freed, "Renewal Creep Theory", Metallurgical and Materials Transactions A, v. 26A, 829-843, 1995.
2. R.L. Bagley, A.D. Freed, D.I.G. Jones, "A Renewal Theory of Inelasticity", Mechanics of Materials (in press), 1995.

3. M. French, A.D. Freed, R.L. Bagley, "On the Numerical Implementation of Renewal Inelasticity Theory", Int. Symp. on Recent Advances in Constitutive Laws for Engineering Materials (1995).

4. D.I.G. Jones, M. French, R.L. Bagley, "Modeling Damage in Renewal Inelasticity Theory" (in preparation), 1995.

5. D.I.G. Jones, M. French, R.L. Bagley, "Renewal Inelasticity Theory with a Damage Fuction", Second International Conference on heat Resistant Materials; Gatlinburg, 1995.

6. F.R.N. Nabarro, "Deformation of Crystals by the Motion of Single Ions", Report of a Conference ofn Strength of Solids, The Phys. Soc., 75-90 (1947).

7. C. Herring, "Diffusional Viscosity of a Polycrystalline Solid", J. Appl. Phys., 21, 437-445 (1950)

8. R.J. Coble, "A Model for Boundary-Diffusion Controlled Creep in Polycrystalline Materials", J. Appl. Phys., 34, 1679-1682 (1963).

9. I.M. Lifshitz, "On the Theory of Diffusion-Viscous Flow of Polycrystalline Bodies", Soviet Phys., ZETP, 17, 909-920 (1963).

10. D.Bamman, R.D. Krieg, In: "Unified Constitutive Equations for Creep and Plasticity", Chap. 7 "Summary and Critique", NY, Elsevier, 304-306, 1987.

11. U.F. Kocks, A.S. Argon, M.F. Ashbey, Progress in Materials Science, v. 19, Thermodynamics and Kinetics of Slip, Pergamon Press, Oxford, UK, 1975.

12. V.L. Berdichevsky, P. Hazzledine, B. Shoykhet, "Micromechanics of Diffusional Creep", Preprint (1994).

13. V.L. Berdichevsky, B. Shoykhet, "Homogenization Problem for Bulk Diffusional Creep" (in press), 1995.

14. R.J. Asaro, W.A. Tiller, "Interface Morphology Development During Stress Corrosion Cracking: Part 1. Via Surface Diffusion", Metallurgical Transactions, vol. 3, July, 1789-1796, (1972).

15. M.A. Grinfeld, "The stability of Heterogeneous Equilibrium in Systems Consisting of Solid Elastic Phases". Trans. of the USSR Acad. of Sci.,265, No. 6.(1982).

16. M.A. Grinfeld, "Instability of the Separation Boundary Between a Non-Hydrostatically Stressed Elastic Body and a Melt." Sov. Phys. Doklady : 31, 831-834 (1986).

17. M.A. Grinfeld,. "On the Instability of Equilibrium of the Nonhydrostatically Stressed Body and its Melt." Fluid Dynamics, 22, 169-174, (1987).

18. M.A. Grinfeld M.A. "Continuum Mechanics Methods in Phase Transformations Theory", Moscow, "Nauka", 1990. [in Russian]

19. M.A. Grinfeld, M.A. "Thermodynamic Methods in the Theory of Heterogeneous Systems". Sussex: Longman, (1991).

20. M.A. Grinfeld "On Morphology of the Stress Driven Corrugations of the Phase Boundary Between the Solid and its Melt" J. Phys. (Cond. Matt.) : 4, L. 647-650. (1992).

21. M.A.Grinfeld, "The Stress Driven Instabilities in Crystals: Mathematical Models and Physical Manifestations." J. Nonlinear Sci. 3, 35-80 (1993).

22. M.A. Grinfeld, "The Stress Driven "Rearrangement" Instability in Crystalline Films." J. Intellig. Mater. Syst. Struct. 4, 76-83 (1993).

23. M.A. Grinfeld, "Two-Dimensional Islanding atop Stressed Solid Helium and Epitaxial Films", Phys. Rev., B, 49, 8310-8319 (1994).

24. P.H. Leo, R.F. Sekerka,"The Effect of Surface Stress on Crystal-Melt and Crystal-Crystal Equilibrium","The Effect of Elastic Fields on the Morphological Stability of a Precipitate Grown from Solid Solution", Acta Metall., **37**, 12, 3119-3138, 3139-3148 (1989)

25. P. Noziéres, "Growth and Shape of Crystals." In: Solids Far From Equilibrium, edited by C. Godréche, 1-153. Cambridge: Cambridge Univ. Press (1991).

26. P. Nozières, "Amplitude Expansion for the Grinfeld Instability due to Uniaxial Stress at a Solid Surface." J. Phys. **3**, 681-685 (1993).

27. D.J. Srolovitz, "On the Instability of Surfaces of Stressed Solids." Acta Metall. **37**, 621-629 (1989).

28. R.H. Torii, S. Balibar. "Helium Crystals Under Stress: the Grinfeld Instability." **89**, 391-404 (1992)

29. L.M. Kachanov, "Introduction to Continuum Damage Mechanics", Martinus Nijhoff Publishers, Dortrecht, The Netherlands (1986).

30. J. Lemaitre, "A Course on Damage Mechanics", Springer-Verlag, Berlin (1992).

Figures
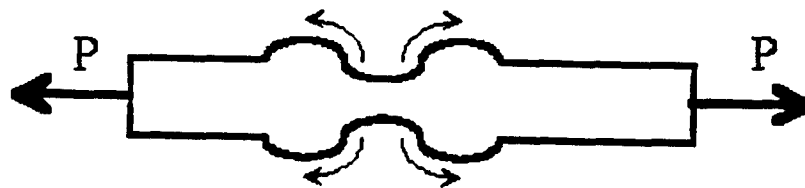
Fig.1. The stress driven mass flux diminishes *total* elastic energy by development corrugations and increase of *local* stress and strain
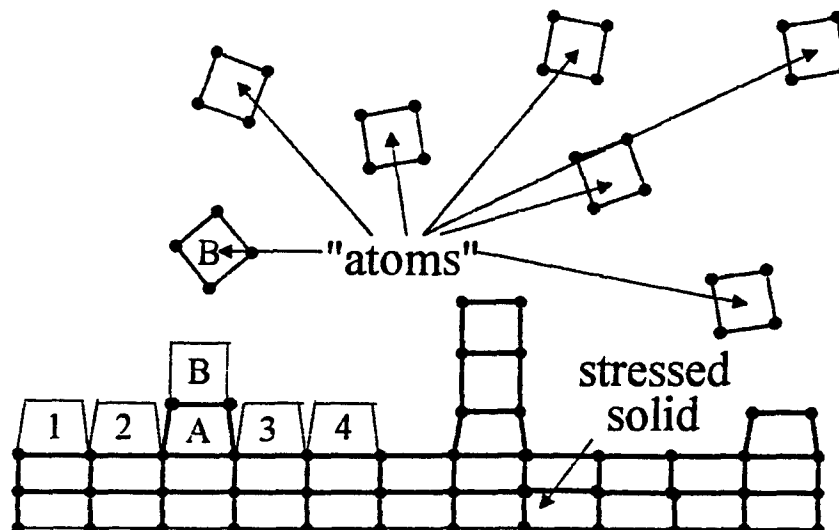
Fig.2. The mechanism of the stress driven rearrangement instability

Modeling and Control of Rotating Stall and Surge for
Compressor Systems in Turbojet Engines

Guoxiang Gu
Associate Professor
Department of Electrical and Computer Engineering

Louisiana State University
Baton Rouge, LA

Final Report for:
Summer Research Program
Wright Laboratory

Modeling and Control of Rotating Stall and Surge for Compressor Systems in Turbojet Engines

Guoxiang Gu

Department of Electrical and Computer Engineering

Louisiana State University, Baton Rouge, LA 70803-5901

September 26, 1995

Abstract

The primary goal of this summer faculty program is the participation of the application research in propulsion related problem. This problem is chosen as the rotating stall and surge in axial flow compressors because of its importance to Air Force mission and to the improvement of the preformance for future aeroengines. Our primary goal has been accomplished successfully at the completion of the summer faculty program. Over 50 research papers have been studied, and four chapters of lecture notes written. Moreover this summer faculty program helped greatly the transition from theoretical oriented research for linear control to application oriented research for nonlinear control that is in the mutual interest of the faculty development and the Air Force Laboratory. This final report summarizes the research work performed at WL/FIGC of the Wright-Patterson Air Force Base by the author during the summer of 1995, sponsored by AFOSR Summer Faculty Research Program. The research objective is to study the rotating stall and surge phenomena in compressor systems that limit the performance of turbojet engines. Roughly speaking, rotating stall is a two-dimensional disturbance localized to the compressor and characterized by regions of reduced or reversed flow that rotate around the annulus of the compressor, while surge is characterized by violent one-dimensional oscillations in the annulus averaged flow throughout the compression system. Both rotating stall and surge are undesirable operating conditions, and can not be tolerated during the compressor operation. In the past two decades, there is a significant development in modeling the rotating stall and surge, and it is only in the past a few years, linear and nonlinear control methods have been employed to actively suppress the rotating stall and surge. The research work performed during this summer faculty program deepened our understanding, and prepared us to undertake research work in the rapidly developing research field of active control for rotating stall and surge in axial flow compressors.

1 Introduction

Compressor rotating stall and surge are primary design constraints which effectively reduce the engine performance, and which consume a major fraction of an engine development program. These are instabilities that arise in the unsteady fluid and structural dynamics. One reason that these unsteady aerodynamic instabilities can lead to large penalties in performance and development costs is that they are difficult to accurately predict during design. Feedback control will have to be employed to suppress the rotating stall and surge in order to extend the stable operating range for compression systems and to improve the engine performance. There are two key developments in this active research field in the past decade. The first is the low order nonlinear model, developed by Moore and Greitzer [28] that captures the nonlinear dynamics of the compressor system through its bifurcation characteristic [25]. The application of classic nonlinear dynamics to rotating stall and surge dynamics motivated second key development: A simplified approach to rotating stall and surge control based on bifurcation theory, developed by Abed annd his coworkers [2, 4], and was shown to be effective for the implementation in industrial turbomachinery by Nett and his group [12, 13]. Another important research work along this direction is the linear control method developed to damp the disturbance through which the stable operating range of the compressor was extended up to close 20% [30, 31].

This final report summarizes the research work for modeling and control of rotating stall and surge in the past decade. It describes most of the major developments in this research field, and speculates the future research direction. The objective is to provide an overall picture for rotating stall and surge control, and to motivate future research along this direction. The topics include linear perturbation model and linear feedback control, Moore-Greitzer nonlinear model, and bifurcation analysis and nonlinear feedback control. This final report is also a summary of the research work performed at WL/FIGC of the Wright-Patterson Air Force Base by the author during the summer of 1995, sponsored by AFOSR Summer Faculty Research Program. The research work on rotating stall and surge was planned before the summer by Dr. Siva Banda, who foresees the important role of active control for improving the performance of future aeroengines. The leadship of Dr. Siva Banda and excellent research environment at WL/FIGC ensures the success of this summer faculty program, through which the author studied over 50 research papers and wrote four chapters of lecture notes. The author would like to thank Dr. Siva Banda for the help he received, and Dr. William Copenhaver for the many discussion he had while working at WL/FIGC. The research work on rotating stall and surge control is in the mutual interest of the faculty development and the Air Force Laboratory. It helped greatly the transition from theory oriented research on linear control to application oriented research on

nonlinear control, and will have enormous impact on author's future research direction.

2 Rotating Stall and Surge in Axial Flow Compressors

Axial flow compressors are subject to two distinct aerodynamic instabilities, rotating stall and surge, which can severely limit the compressor performance. Both these instabilities are disruption of the normal operating condition designed for steady and axisymmetric flow. The transition from normal compressor operation into rotating stall or surge is depicted in Figure 1 where Φ is the circumferential mean of the flow coefficient ϕ, and Ψ is the nondimensionalized pressure rise. As the flow coefficient through the compressor is decreased (i.e., as the downstream throttle closes in an experiment), the pressure rise increases. This trend continues until the system goes into either rotating stall, or surge (deep surge), or both (classic surge).
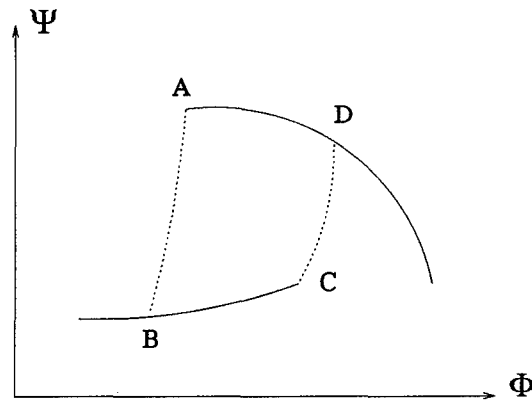

Figure 1 Schematic compressor characteristic, showing rotating stall

For the case of rotating stall, the lowest coefficient at which the compressor can operate with axisymmetric flow is point A, the peak of the characteristic. At lower flows, an abrupt transition occurs into rotating stall (point B). There is a substantial drop in pressure rise and a decrease in flow coefficient (segment A-B). This condition will persist until the flow is increased to point C. Thus there exists a severe 'hysteresis', or range of flow coefficients at which two stable operating conditions exist – steady axisymmetric flow and rotating stall. Once compressor enters fully developed rotating stall, both rotor and stator blades are passing in and out of the stalled flow causing tremendous stress. Any substantial length of time in this mode can result in excessive internal temperatures due to low efficiency associated with the presence of rotating stall. In addition, an even more serious consequence that can occur in an engine is that the low flow rates obtained during rotating stall can lead to substantial overtemperatures in the burner and turbine [16]. At present, the only remedy to get out of the rotating stall is to shut down the engine and

restart it again [28].

Rotating stall is a severely non-axisymmetric distribution of axial flow velocity, though steady in an appropriate (moving) reference frame, around the annulus of the compressor, taking the form of a wave or 'stall cell', that propagates in the circumferential direction at a fraction of the rotor speed. Surge, on the other hand, is an axisymmetric oscillation of the mass flow along the axial length of the compressor. Deep surge is a mostly axisymmetric oscillation with such a large variation of mass flow that during part of the cycle the compressor is operating in reversed flow. The frequency of the surge oscillation is typically an order (or more) of magnitude less than that associated with the passage of rotating stall cells. If surge occurs, the transient consequences, such as large inlet overpressures can also be severe. However the circumstances may well be more favorable for returning to unstalled operation by opening either the throttle or internal bleed valves, since the compressor can operate in an unstalled condition over part of each surge cycle. Often surge and rotating stall are coupled (classic surge) although each can occur without the other. For the case of classic surge, the compressor may pass in and out of rotating stall during a surge cycle, with the rotating stall characteristics appearing to be quite similar to those obtained during steady-state operation. Thus rotating stall and surge, though coupled, is well enough defined that each can be studied alone [30].

The rotating stall and surge are mostly caused by disturbances. Those having largest and most destabilizing effects are: circumferential distortion, planar turbulence, and combustion. All of these types of disturbances present in full-scale aeroengines and are major sources of rotating stall and surge.

- *Circumferential distortion* refers to non-axisymmetric flow patterns which are generated by upstream structures such as bends in inlet duct or boundary layer separation caused by high angle of attack at the engine inlet. The inlet distortion can also be correlated with aircraft angle of attack and yaw angle.

- *Planar turbulence* refers to axisymmetric oscillations in the flow field which are generated, for example, by inlet buzz or ingestion of wakes from nose gear or other aircraft. Planar turbulence is an inherently unsteady flow and has been recognized as an important source of loss in stall margin.

- *Combustion* process introduce large unsteady back-pressure disturbances to the compression system, which cause steady state operating conditions to exhibit fluctuations in pressure and mass flow large enough to cause the system to diverge.

Thus substantial rotating stall and surge margins are required in the design of compressor operating point in order to maintain steady axisymmetric flow condition. Consequently compression systems are force to operate with far less efficient operating point than point A, the peak of the compressor characteristic (Figure 1). Even then, with all the above mentioned disturbances present in the worst case, it does not seem possible for the compressor to escape the rotating stall and surge unless some control action is taken.

3 Linear Perturbation Model and Feedback Control

Rotating stall is characterized by a disturbance wave traveling about the circumference of the machine, surge by a basically one-dimensional fluctuation in mass flow through the machine. These two flow instabilities are distinct in the sense that rotating stall is local to the blade rows and dependent only on the compressor, while surge involves the entire pumping system – compressor, ducting, plenum, and throttle. Yet they are related because both are natural modes of the compression with surge corresponding to the zeroth order mode. Rotating stall and surge generally cannot be tolerated during compressor operation because both reduce the pressure rise in the machine, cause rapid heating of the blades, and can induce severe mechanical distress.

There are basically two approaches to the problem of flow field instabilities. One is characterized by *passive*, and the other by *active*. A passive approach is more traditional. Balanced stage loading and casing treatment are examples of the passive approach that tries to incorporate various features in the aerodynamic design of the compressor to increase the stable operating range. Other examples include surge avoidance and stall avoidance. These techniques have been developed that are based on moving the operating point close to the surge line when surge does not threaten, and then quickly increasing the margin when required, either in an open or closed-loop manner. The open-loop techniques are based on observation, supported by many years of experience, that compressor stability is strongly influenced by inlet distortions and by pressure transients caused by augmented ignition and, in turn, that inlet distortion can be correlated with aircraft angle of attack and yaw angle. Thus, significant gains have been realized by coupling the aircraft flight control and engine fuel control so that the engine operating point is continually adjusted to yield the minimum stall margin required at each instantaneous flight condition [38]. For closed-loop stall avoidance, sensors in the compressor were used to determine the onset of rotating stall by measuring the level of unsteadiness. When stall onset was detected, the control system moved the operating point to higher mass flow, away from the stall line [22]. While showing some effectiveness at low operating speeds, this effort was constrained by limited warning time from

the sensors and limited control authority available to move the compressor operating point.

Active control method is developed more recently. This section will focus on the linear control method develop at MIT for rotating stall only. It was suggested first by Epstein et. al. [11] to actively damp the rotating stall waves when at low amplitude by using linear feedback control. Rotating stall can be viewed as the mature form of the rotating disturbance. Damping of the wave would prevent rotating stall from developing, thus stabilize the flow operating range where A-B segment locates (Figure 1). The philosophy is to measure the wave pattern in a compressor and generate a circumferentially propagating disturbance based on those measurements, so as to damp the growth of the naturally occuring waves. In the particular implementation described in [30, 31], shown schematically in Figure 2 (unwraped compressor), individual vanes in an upstream blade row are "wiggled" to create the traveling wave velocity disturbance. The flow that the upstream sensors (measured with hot wires) and downstream blade rows see is a combination of the naturally occuring instability waves and the imposed control disturbances. As such, the combination of compressor and controller is a different machine from the original compressor — with different dynamic behavior and different operating stability.
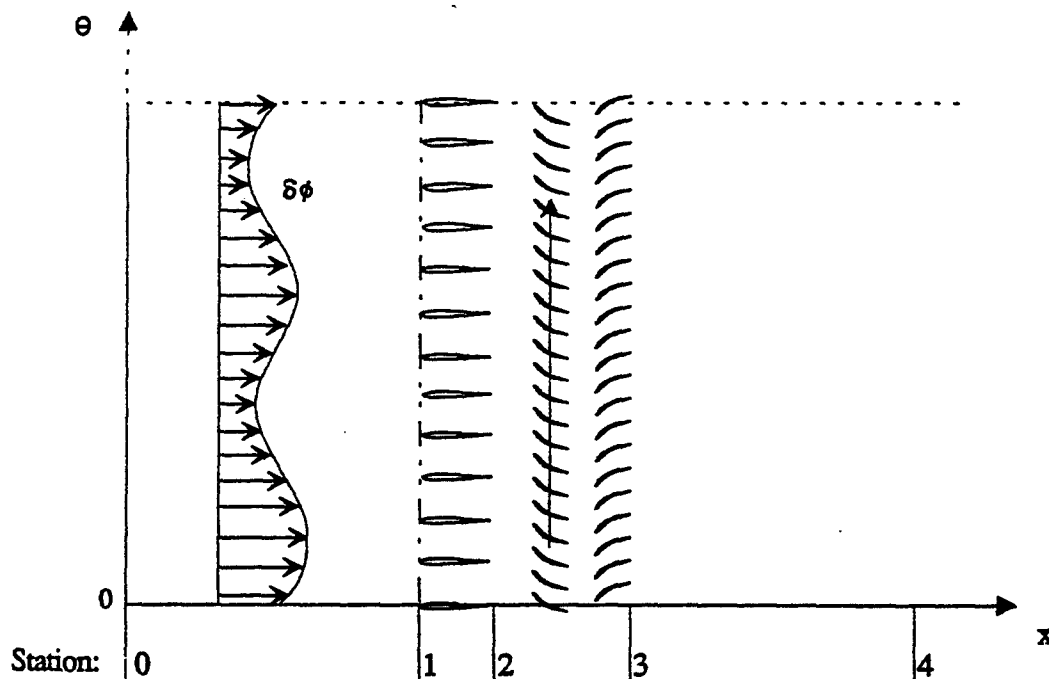
Figure 3.2 Stations in a 2-D axial compression system

We denote ϕ (the ratio of the flow velocity to the rotor speed U) as the local flow coefficient that is a function of both axial length and circumference position, and Ψ (the ratio of the pressure difference between station 2 and 3 in Figure 2 to ρU^2 with ρ flow density) the compressor pressure rise. According to [29], with assumptions of incompressible, invicid flow having no radial variation

and uniform inlet flow, the pressure balance equations (using linear perturbation analysis) for the compression system in Figure 2 are governed by

$$\nabla^2(\delta\tilde{\phi}_1) \;=\; 0, \qquad (1)$$

$$-\frac{\delta p_3}{\rho U^2} - \frac{\delta\tilde{\phi}_1}{\partial\zeta} + \left(\frac{\partial\psi}{\partial\gamma} - \mu_I^2\frac{\Phi}{2}\frac{\partial^2}{\partial\theta\partial\zeta}\right)\delta\gamma - \left[\frac{\partial\psi}{\partial\phi} + \mu_I\frac{\partial}{\partial\zeta} + \mu\frac{\partial}{\partial\zeta} + \lambda\frac{\partial}{\partial\theta}\right]\delta\phi_2 \;=\; 0, \qquad (2)$$

$$-\delta\phi_1 + \delta\phi_2 + \mu_I\Phi\frac{\partial\delta\gamma}{\partial\theta} \;=\; 0, \qquad (3)$$

$$\nabla^2\delta p_4 \;=\; 0, \qquad (4)$$

where the subscripts denote the station number, $\tilde{\phi}$ the disturbance flow potential, ζ the radians of rotor blades travel per unit time, and λ, ν, and μ_I the inertia of rotor, stator, and IGV blades respectively. It should be indicated that all the pressures are static except p_0. The boundary conditions for (1) – (4) are given by

$$\delta\phi_1 \;=\; \frac{\partial\tilde{\phi}_1}{\partial\eta}, \qquad (5)$$

$$\frac{1}{\rho U^2}\frac{\partial\delta p_3}{\partial\eta} \;=\; -\frac{\partial\delta\phi_2}{\partial\zeta}, \qquad (6)$$

where η is the nondimensionalized axial position that is the ratio of the actual axial length to R, the mean radius of the rotor blades. Equations (1) and (4) are of the Laplace. Thus there hold

$$\delta\tilde{\phi} \;=\; \sum_{n\neq 0} A_n(\zeta)e^{n\eta}e^{jn\theta}, \qquad (7)$$

$$\frac{\delta p_4}{\rho U^2} \;=\; \sum_{n\neq 0} \delta\bar{p}_n e^{-n\eta}e^{jn\theta}. \qquad (8)$$

The form of the upstream and downstream solutions can be adopted for all of the variables in the system of equations of (1) – (4):

$$\delta\phi_{\text{upstream}} \;=\; \sum_{n\neq 0} \bar{\phi}_n(\zeta)e^{n(\eta-\eta_{hw})}e^{jn\theta}, \qquad (9)$$

$$\delta\phi_1 \;=\; \sum_{n\neq 0} \bar{\phi}_n(\zeta)e^{-n\eta_{hw}}e^{jn\theta}, \qquad (10)$$

$$\delta\phi_2 \;=\; \sum_{n\neq 0} (\bar{\phi}_2)_n(\zeta)e^{jn\theta}, \qquad (11)$$

$$\delta\gamma \;=\; \sum_{n\neq 0} \bar{\gamma}_n(\zeta)e^{jn\theta}. \qquad (12)$$

Note that $\{\bar{\phi}_n\}$ is defined as the SFC (spatial Fourier coefficient) at the measurement station η_{hw} with "hw" stands for hot wire sensors. Now the PDEs in (1) – (4) are projected into a single ODE

$$\left[\frac{2}{n} + \mu_t\right]\dot{\phi}_n = \left[\frac{\partial\psi}{\partial\phi} + jn\lambda\right]\phi_n - jn\Phi\mu_I\left[\frac{1}{n} + \mu - \frac{\mu_I}{2}\right]\dot{\bar{\gamma}}_n + \left[\left(\frac{\partial\psi}{\partial\gamma} - n^2\Phi\lambda\mu_I\right) + jn\Phi\mu_I\frac{\partial\psi}{\partial\phi}\right]\bar{\gamma}_n,$$

where $j = \sqrt{-1}$, $\mu_t = \mu + \mu_I$, and $\phi_n = e^{-n\eta h w}\bar{\phi}_n$, and $\gamma_n = \bar{\gamma}e^{jn\theta}$. Parametric representation of the above equation gives the following set of complex-coefficient ODEs:

$$\dot{\bar{\phi}}_n = (\sigma_{RS} + j\omega_{RS})\bar{\phi}_n + (b_r + jb_i)\bar{\gamma}_n + jg_i\dot{\bar{\gamma}}, \tag{13}$$

where, if we let $\Pi = (\mu_t + 2/n)$,

$$\sigma_{RS}(n, \Phi) = \frac{\partial\psi}{\partial\phi}/\Pi, \quad \omega_{RS} = n\lambda/\Pi,$$

$$b_r(n, \Phi) = e^{n\eta h w}\left(\frac{\partial\psi}{\partial\gamma} - n^2\Phi\lambda\mu_I\right)/\Pi,$$

$$b_i(n, \Phi) = e^{n\eta h w}n\Phi\mu_I\frac{\partial\psi}{\partial\phi}/\Pi,$$

$$g_i(n, \Phi) = -e^{n\eta h w}n\Phi\mu_I\left(\frac{1}{n} + \mu - \frac{\mu_I}{2}\right)/\Pi.$$

Taking state variables and control inputs as

$$\begin{bmatrix} (x_r)_n \\ (x_i)_n \end{bmatrix} := \begin{bmatrix} \mathrm{Re}(\bar{\phi}_n) \\ \mathrm{Im}(\bar{\phi}_n) \end{bmatrix}, \quad \begin{bmatrix} (u_r)_n \\ (u_i)_n \end{bmatrix} := \begin{bmatrix} \mathrm{Re}(\bar{\gamma}_n) \\ \mathrm{Im}(\bar{\gamma}_n) \end{bmatrix} \tag{14}$$

respectively, it is now straightforward to show that the n-th mode of the SFC for the flow disturbance satisfies the state-space equation

$$\frac{d}{d\zeta}\begin{bmatrix} (x_r)_n \\ (x_i)_n \end{bmatrix} = \begin{bmatrix} \sigma_{RS} & -\omega_{RS} \\ \omega_{RS} & \sigma_{RS} \end{bmatrix}\begin{bmatrix} (x_r)_n \\ (x_i)_n \end{bmatrix} + \begin{bmatrix} b_r & -b_i \\ b_i & b_r \end{bmatrix}\begin{bmatrix} (u_r)_n \\ (u_i)_n \end{bmatrix} + \begin{bmatrix} 0 & -g_i \\ g_i & 0 \end{bmatrix}\begin{bmatrix} (\dot{u}_r)_n \\ (\dot{u}_i)_n \end{bmatrix}.$$

Clearly the stability of uncontrolled system is hinged to the sign of derivative of ψ with respect to ϕ. A nice feature of the linear perturbation model is the decoupling between different modes of the SFC, and thus feedback controller can be synthesize for each mode independently.

System identification methods were employed in [29] to determine parameters $(\sigma_{RS}, \omega_{RS}, b_r, b_i, g_i)$ using open-loop frequency response experiments and least-squares fitting. Once the plant model is available, a proportional feedback control low of the form

$$\delta\bar{\gamma}_n = -k_n\delta\bar{\phi}_n, \quad k_n = \mathrm{Re}(k_n) + j\mathrm{Im}(k_n),$$

is employed to enhance the damping ratio. This is essentially the state feedback control law by the definition of state variables in (14). Through experimental trials, the best values of the magnitude and phase for k were obtained, and implemented that achieve the extension of the stable operating range. For using first mode feedback ($n = 1$), the flow coefficient at stall were reduced by 11%. When the second mode ($n = 2$) was also used for feedback, stall flow coefficient was reduced by 18% [29, 30, 31]. See also [18].

21-9

4   Moore-Greitzer Nonlinear Model

Compression systems are inherently nonlinear, and often a linear model may not be adequate to capture the dynamics feature of the compressor, and may limit the performance improvement using active control. Modeling the nonlinear behavior of the rotating stall and surge in axial compressors has been investigated for about two decades, and Greitzer is clearly a pioneer in this research direction [16, 17]. Although there are many models for rotating stall and surge, the nonlinear model developed by Moore and Greitzer [28] dominates the recent study on active control.

This section gives an overview for the derivation of the Moore-Greitzer model. Similar to the previous section, the flow is assumed to be incompressible and invicid having no radial variation with uniform inlet flow that hold for low speed compressors with high hub-to-tip ratio. With identical blades for both rotors and stators, the momentum equation for the N-stage compressor can be written as

$$\frac{p_3 - p_2}{\rho U^2} = N F(\phi) - \frac{1}{2a}\left(2\frac{\partial \phi}{\partial \zeta} + \frac{\partial \phi}{\partial \theta}\right) \tag{15}$$

where a represents roughly the time lag and $F(\phi)$ the axisymmetric steady performance of a single blade row, recall that p_2 and p_3 are static pressures at station 2 and 3 of Figure 2 respectively. The origin of the nondimensionalized axial distant η is taken to be at station 1, the entrance of the IGVs. The existence of the flow potential $\tilde{\phi}$ implies that

$$\left(\tilde{\phi}_\eta\right)_0 = \phi(\zeta,\eta)|_{\eta=0} = \Phi(\zeta) + g(\zeta,\theta), \quad \left(\tilde{\phi}_\theta\right)_0 = h(\zeta,\theta), \tag{16}$$

where Φ is the circumferential mean of ϕ and thus

$$\int_0^{2\pi} g(\zeta,\theta)\,d\theta = 0, \quad \int_0^{2\pi} h(\zeta,\theta)\,d\theta = 0. \tag{17}$$

For convenience, disturbance potential $\tilde{\varphi}$ is introduced in [28] so that

$$(\tilde{\varphi}_\eta)_0 = g(\zeta,\theta), \quad (\tilde{\varphi}_\theta)_0 = h(\zeta,\theta). \tag{18}$$

By assumption, the circumferential flow takes place at IGVs, and thus, by the Bernoulli equation,

$$\frac{p_2 - p_1}{\rho U^2} = \frac{1}{2}K_G h^2, \quad 0 < K_G \leq 1. \tag{19}$$

For upstream, in the reservoir, $\tilde{\phi}$ is taken to be zero because the flow is at rest. For unsteady flow, with the particular definitions of variables, the result is

$$\frac{p_0 - p_1}{\rho U^2} = \frac{1}{2}\left(\phi^2 + h^2\right) + \left(\tilde{\phi}_\zeta\right)_0. \tag{20}$$

Compared with the linear perturbation model, this equation neglects the dynamical relation between the pressure rise and the flow coefficient. A term $\left(\tilde{\phi}_\zeta\right)_0$ may not be adequate for modeling the unsteady effect at the entrance duct, but simplifies the nonlinear model considerably. The combination of (19) and (20) yields [28]

$$\frac{p_0 - p_2}{\rho U^2} = \frac{1}{2}\phi^2 + l_I\frac{d\Phi}{d\zeta} + (\tilde{\varphi}_\zeta)_0 \,. \tag{21}$$

Define p_S as the static pressure in plenum. The pressure rise at the exit duct is given by [28]

$$\frac{p_S - p_3}{\rho U^2} = (P)_E = -l_E\frac{d\Phi}{d\zeta} - (\lambda - 1)(\tilde{\varphi}_\zeta)_0 \tag{22}$$

where $\lambda = 2$ refers to as a "long enough" exit duct, and $\lambda = 1$ refers to a very short one. Thus the total to static pressure rise is obtained as, by combining (15), (21) and (22) with $K_G = 1$,

$$\Psi := \frac{p_S - p_0}{\rho U^2} = \psi_c(\phi) - \left(l_I + \frac{1}{a} + l_E\right)\frac{d\Phi}{d\zeta} - \lambda(\tilde{\varphi}_\zeta)_0 - \frac{1}{2a}(2\tilde{\varphi}_{\zeta\eta} + \tilde{\varphi}_{\theta\eta})_0 \,, \quad \psi_c(\phi) = NF - \frac{1}{2}\phi^2, \tag{23}$$

that is balanced by pressure difference at the plenum. The isentropic assumption in [28] gives

$$\frac{\dot{m}_c - \dot{m}_T}{V_p} = \frac{d\rho}{dt} = \frac{1}{a_s^2}\frac{d(p_S - p_0)}{dt} \tag{24}$$

where V_p is the volume of the plenum (the gas is compressible inside plenum), a_s is the speed of the sound, and $\dot{m}_c$ is the incoming and $\dot{m}_T$ is outgoing the mass flow rates respectively. It follows that

$$\Phi - \Phi_T = \frac{V_p U}{a_s^2 A_c}\frac{d\Psi}{dt} = 4B^2 l_c\frac{d\Psi}{dt}, \quad B := \frac{U}{2a_s}\sqrt{\frac{V_p}{A_c L_c}} \tag{25}$$

with A_c compressor duct area, and $l_c = l_I + l_E + \frac{1}{a}$. Thus (25) is equivalent to, by parabolic throttle characteristic,

$$l_c\frac{d\Psi}{d\zeta} = \frac{1}{4B^2}(\Phi - \Phi_T(\zeta)) = \frac{1}{4B^2}\left(\Phi - F_T^{-1}(\Psi)\right), \quad \Psi = F_T(\Phi_T) = \frac{1}{\gamma}\Phi_T^2. \tag{26}$$

Since $\tilde{\varphi}$ satisfies Laplace's equation and must vanish at $\eta = -\infty$, the solution of disturbance velocity potential has the form of

$$\tilde{\varphi} = \sum_{n=1}^\infty \frac{1}{n}e^{n\eta}\left(a_n\sin n\theta + b_n\cos n\theta\right), \quad \eta \le 0. \tag{27}$$

If only the first mode is used, there hold, by denoting $Y(\zeta, \theta) := \tilde{\varphi}|_{\eta=0}$,

$$Y_\eta = (\tilde{\varphi}_\eta)_0 = -(\tilde{\varphi}_{\theta\theta})_0 = Y_{\theta\theta} = -g. \tag{28}$$

Substituting the above into (23) and integrate with respect to θ over a period of 2π give

$$\Psi(\zeta) + l_c\frac{d\Phi}{d\zeta} = \frac{1}{2\pi}\int_0^{2\pi}\psi_c(\Phi - Y_{\theta\theta})\,d\theta. \tag{29}$$

If a cubic characteristic is used, then

$$\psi_c(\phi) = \psi_{c0} + H \left[1 + \frac{1}{3}\left(\frac{\phi}{W} - 1\right) - \frac{1}{2}\left(\frac{\phi}{W} - 1\right)^3 \right], \quad \phi = \Phi - Y_{\theta\theta}, \tag{30}$$

where ψ_{c0}, H, and W are parameters [28]. With a single harmonic function,

$$Y = WA(\zeta)\sin(\theta - r(\zeta)), \quad r(\zeta) = f_0\zeta. \tag{31}$$

where $r(\zeta) = f_0\zeta$ provides an unknown phase angle. Simple calculation yields [28], with $J = A^2$ and combining (23), (26) with (31),

$$\frac{d\Psi}{d\zeta} = \frac{W/H}{4B^2}\left[\frac{\Phi}{W} - \frac{1}{W}F_T^{-1}(\Phi)\right]\frac{H}{l_c}, \tag{32}$$

$$\frac{d\Phi}{d\zeta} = \left[-\frac{\Psi - \psi_{c0}}{H} + 1 + \frac{3}{2}\left(\frac{\Phi}{W} - 1\right)\left(1 - \frac{1}{2}J\right) - \frac{1}{2}\left(\frac{\Phi}{W} - 1\right)^3\right]\frac{H}{l_c}, \tag{33}$$

$$\frac{dJ}{d\zeta} = J\left[1 - \left(\frac{\Phi}{W} - 1\right)^2 - \frac{1}{4}J\right]\frac{3aH}{(1 + \lambda a)W}. \tag{34}$$

These are the final equations for instantaneous values of circumferentially averaged flow coefficient Φ, total-to-static pressure rise Ψ, and squared amplitude of angular variation J, all functions of time ζ. Compressor and system parameters which will govern the solutions are diagram steepness H/W, shut-off head ϕ_{c0}/H, compressor duct length l_c and slope m, internal compressor lag a, plenum volume and compressor annulus area B, and the throttle pressure characteristic function $F_T(\Phi)$.

For pure rotating stall, time derivatives in (32) to (34) must vanish (the flow is steady but non-axisymmetric for rotating stall as opposed to surge that is axisymmetric but unsteady), (34) then requires that J either vanish or have the constant "equilibrium" value

$$J_e = 4\left[1 - \left(\frac{\Phi}{W} - 1\right)^2\right]. \tag{35}$$

When J_e from (35) is substituted into the right hand side of (33), which must vanish for rotating stall, one finds the steady performance Ψ:

$$\Psi = \psi_{c0} + H\left[1 - \frac{3}{2}\left(\frac{\Phi}{W} - 1\right) + \frac{5}{2}\left(\frac{\Phi}{W} - 1\right)^3\right] \tag{36}$$

which may be compared with (30) to infer the performance effect of rotating stall. For the case of pure surge, $J = 0$ and (33) becomes simply (37) with cubic ψ_c in (30). In pure rotating stall, amplitude J is constant at an "equilibrium" level defined by J_e, (35). In the case of pure surge, $J = 0$ and (33) becomes simply

$$\Psi = \frac{1}{2\pi}\int_0^{2\pi} \psi_c\left(\Phi_T - \frac{d^2Y}{d\theta^{*2}}\right)d\theta^* \tag{37}$$

21-12

with cubic ψ_c in (30). In pure rotating stall, amplitude J is constant at an "equilibrium" level defined by J_e, (35). Hence the nonlinear Moore-Greitzer model in (32) – (34) permits the existence of pure modes as well as the coupling case. Moreover this model shows that it is impossible for rotating stall to evolve without producing at least some disturbance of Φ or Ψ. In fact if J changes, (33) says that Ψ and Φ must also change. Hence rotating waves should be present at low amplitude prior to stall. This observation is further confirmed in [26, 15] that a prolonged small amplitude disturbance exists prior to fully developed rotating stall. As such, different active control methods are proposed to suppress the stall waves at low amplitude including the linear approach to discussed in the previous section and the nonlinear approach to be discussed in the next section.

5 Bifurcation Analysis and Nonlinear Control

Perhaps one of the most important developments in rotating stall and surge control is the use of classic nonlinear bifurcation analysis and the resulting nonlinear control law [2, 3, 4, 7, 12, 13, 21, 24, 25, 36]. This work was initiated by Abed and his group, and was further studied by McCaughan [24, 25]. To facilitate the analysis, the following changes of variables are used:

$$\tilde{J} = \frac{1}{4}J, \quad \tilde{\Phi} = \frac{\Phi}{W} - 1, \quad \tilde{\Psi} = \frac{\Psi}{H}, \quad \tilde{\zeta} = \frac{H}{Wl_c}\zeta. \tag{38}$$

Denoting $\sigma = 3al_c/(1 + a\lambda)$ and $\beta = 2BH/W$, (32) – (34) are converted into [25]

$$\tilde{\Psi}' = \frac{1}{\beta^2}\left(\tilde{\Phi} - \tilde{\Phi}_T(\tilde{\Psi})\right), \tag{39}$$

$$\tilde{\Phi}' = -\tilde{\Psi} + \tilde{\Psi}_c(\tilde{\Phi}) - 3\tilde{\Phi}\tilde{J}, \tag{40}$$

$$\tilde{J}' = \sigma\tilde{J}\left(1 - \tilde{\Phi}^2 - \tilde{J}\right), \tag{41}$$

where prime denotes derivative with respect to $\tilde{\zeta}$, and $\tilde{\Psi}_c = \tilde{\psi}_{c0} + 1 + \frac{3}{2}\tilde{\phi} - \frac{1}{2}\tilde{\phi}^3$, $\tilde{\psi}_{c0} = \psi_{c0}/H$. Linearizing (39) – (41) about an equilibrium point $(\tilde{\Phi}_e, \tilde{\Psi}_e, \tilde{J}_e)$ gives

$$\begin{bmatrix} \tilde{\Psi}' \\ \tilde{\Phi}' \\ \tilde{J}' \end{bmatrix} = L_e \begin{bmatrix} \tilde{\Psi} \\ \tilde{\Phi} \\ \tilde{J} \end{bmatrix}, \quad L_e = \begin{bmatrix} -\beta^{-2}\tilde{\Phi}_T'(\tilde{\Psi}_e) & \beta^{-2} & 0 \\ -1 & \tilde{\Psi}_c'(\tilde{\Phi}_e) - 3\tilde{J}_e & -3\tilde{\Phi}_e \\ 0 & -2\sigma\tilde{\Phi}_e\tilde{J}_e & \sigma\left(1 - \tilde{\Phi}_e^2 - 2\tilde{J}_e\right) \end{bmatrix}. \tag{42}$$

The study in [25] shows that $\tilde{\psi}_{c0} = 4$ is a critical value. Decreasing the value of γ (that is proportional to the cross-sectional area of the throttle; See (26)) corresponds to reducing the mass flow and causes design flow to loss stability either at transcritical bifurcation point for $\tilde{\psi}_{c0} \neq 4$ or at pitchfork bifurcation point for $\tilde{\psi}_{c0} = 4$. The value of γ at which transcritical

bifurcation or pitchfork bifurcation occurs is denoted by γ_c. For the case of $\tilde{\psi}_{c0} \neq 4$, there is also a saddle node bifurcation at $\gamma = \gamma_s > \gamma_c$ that causes the hysteresis phenomenon depicted in Figure 1. Noted that for stable R_e with $R_e > 0$, it corresponds to steady rotating stall. On the other hand $R_e = 0$ can also be unstable meaning it is unstable in the presence of nonaxisymmetric flow perturbation at either transcritical bifurcation point or pitchfork bifurcation point. For γ close to γ_c, the linear operator L_e has a complex pair of eigenvalues with negative real part and one real eigenvalue [25]. The real eigenvalue becomes positive as γ is decreased causing loss of stability. As γ is decreased further, the real part of the complex pair eigenvalues changes sign at Hopf bifurcation point, and thus the steady axisymmetric flow is completely unstable. Hopf bifurcation exists for both $R_e = 0$ and $R_e \neq 0$ that are dependent on the third parameter β. When $R_e = 0$, the compressor model reduces to 2nd order ODE, and Hopf bifurcation occurs if the slope of the compressor characteristic $\psi_c(\Phi_e)$ has a positive slope. The stability of the periodic orbit was also studied by both Abed group and McCaughan. However we will not go to the details of the bifurcation analysis due to the page limit. The rest of the section will focus on the research work performed by Abed group that demonstrates the importance of nonlinear feedback control when the throttle area γ is used as an actuator.

Abed group has a slightly modified momentum equation from (23) of the Moore-Greitzer model:

$$\Psi = \psi_c(\phi) - \left(l_I + \frac{1}{a} + l_E\right)\frac{d\Phi}{d\zeta} - \lambda\,(\tilde{\varphi}_\zeta)_0 - \frac{1}{2a}\left(2\tilde{\varphi}_{\zeta\eta} + \tilde{\varphi}_{\theta\eta} - \mu\tilde{\varphi}_{\theta\theta\eta}\right)_0, \qquad (43)$$

where $\mu > 0$ is the gas viscosity, neglected in [28]. The viscosity introduced tends to damp out spatial perturbations. With $\mu > 0$, (34) can be written as

$$\frac{dA}{d\zeta} = \frac{\sigma}{2}\left(1 - \tilde{\Phi}^2 - \frac{\mu W}{3aH}\right)A - 8\sigma A^3, \quad A = A_1 = \sqrt{a_1^2 + b_1^2}, \qquad (44)$$

with a_1 and b_1 as in (27), recall $J = A^2$. Thus linearized model about $\tilde{\Psi} = \tilde{\Psi}_e$, $\tilde{\Phi} = \tilde{\Phi}_e$, and $A = A_e = 0$ has the form

$$\begin{bmatrix} \tilde{\Psi}' \\ \tilde{\Phi}' \\ \tilde{A}' \end{bmatrix} = Le \begin{bmatrix} \tilde{\Psi} \\ \tilde{\Phi} \\ \tilde{A} \end{bmatrix}, \quad L_e = \begin{bmatrix} -\beta^{-2}\tilde{\Phi}'_T(\tilde{\Psi}_e) & \beta^{-2} & 0 \\ -1 & \tilde{\Psi}'_c(\tilde{\Phi}_e) & 0 \\ 0 & 0 & \sigma\left(1 - \tilde{\Phi}_e^2 - \frac{\mu W}{3aH}\right) \end{bmatrix}. \qquad (45)$$

It follows that the linearized model has one zero eigenvalue if $\Phi_e = W(1 + \sqrt{1 - \mu W/(3aH)})$. This implies that a stationary bifurcation may occur from the equilibrium point for some value of γ_0. That is the loss of stability of the nominal equilibrium point coincides with an eigenvalue passing through 0. Another way for an equilibrium point to lose stability is through Hopf bifurcation which involves a complex pair of eigenvalues crossing the imaginary axis, giving rise to small-amplitude periodic solution near the nominal equilibrium.

The results in [36] show that the uniform flow equilibrium point becomes unstable after the parameter γ crosses the critical value γ_0, the stall bifurcation point. The local bifurcation solutions, near the stall point, may not be stable. If such a condition occurs, the compression system will exhibit a jump from the stable nominal equilibrium when the parameter crosses the critical value γ_0. This results in a hysteresis loop of the stable equilibrium. An interesting observation in [21, 36] is the lack of controllability for linearized model about $A_e = 0$ if $\gamma = \gamma_0 + \Delta\gamma$ is used as an actuator where γ_0 is the nominal value and $\Delta\gamma$ is the control variable $u = \Delta\gamma$. Because in the linearized model only the term $\tilde{\Phi}'_T(\tilde{\Psi}_e)$ involves control input, the state variable A is not linearly controllable. This implies that we can not extend the stable region of the parameter γ crossing γ_0 for the unstalled equilibrium point by using linear state feedback. Nonlinear control has to be used. A quadratic feedback control law

$$u = KA^2 = KA_1^2 = K(a_1^2 + b_1^2) \tag{46}$$

was proposed in [21, 36] to stabilize the local bifurcation solutions. Under the condition that $\psi_c(\Phi_e) \neq 0$ and $\Phi_e \neq W$, it is shown in [36] that the quadratic control law can guarantee the stationary bifurcation of the modified nonlinear Moore-Greitzer model at the equilibrium point $(\Psi_e, \Phi_e, A_e = 0)$ with $\gamma = \gamma_0$ to be a supercritical pitchfork bifurcation instead of subcritical pitchfork bifurcation in absence of the nonlinear feedback control. This control law was successfully implemented by Nett group [7, 12, 13] using the same measurement on the flow coefficient as the linear feedback control in section 3.

According to [7] the nonlinear control discussed in this section has several advantages over the linear one. First the nonlinear control attenuates the effects of persistent disturbance by reducing the amount that these disturbances throttle the equilibrium point. Thus a reduction in the required amount of stable axisymmetric flow range extension is achieved. Second the nonlinear feedback control uses 2D sensing, but only 1D actuation is used that is contrast to the linear feedback control where 2D actuation is required. Third the actuator bandwidth requirements are relatively low, since the controller does not require or act upon rotating stall phase information. Finally the nonlinear feedback control enlarges the domain of attraction and thus increase the effective stable flow range of the complex without increasing the theoretical stable flow range.

6 Further Developments on Modeling and Control

In the past several years there have been significant new developments in modeling and control for rotating stall and surge in axial compressors. The Moore-Greitzer model has been used in [23] to derive a set of $2N + 2$ nonlinear ODEs where N is the number of spatial Fourier coefficients to

be modeled. Moreover the time lag between the velocity perturbation across the compressor and the development of perturbation pressure rise has been taken account in [23]. This new model has been used to develop a Lyapunov stability analysis of rotating stall and surge [23] as well as preliminary nonlinear control design [35].

Control oriented high-frequency turbomachinery modeling led by Nett is an important piece of work in this research direction. The models developed in [5, 6] are both inherently high-frequency, exhibiting expected compressor surge and rotating stall phenomena, and well suited for control design due to their relative low complexity and accompanying uncertainty characterization. Notable research work on compressor modeling also include 2D models for both linearized and nonlinear compressible flow. In [19], the model assumes 2D linearized compressible flow in all of the inter-blade passages and ducts, and 1D linearized compressible flow in the blade passages. Using this model, additional modes of compressor aerodynamic oscillation were identified in [34]. This model was augmented with sensors and actuators in [14] and is now suitable for controller synthesis and analysis. Compressible 2D nonlinear models are currently under development at MIT and UTRC, including 3D nonlinear model. The removable of the incompressible flow assumption is important because axial compressors used in aeroengines typically have high hub-to-tip ratio with high rotor speeds and large pressure ratios.

For rotating stall and surge control, many different sensor-actuator schemes are available [33, 20]. Recently there is an increased interest in using air injectors as actuators and pressure transducers as sensors because of the initial work in [20, 9]. In [10] a set of three air injectors are equally placed on the sensor ring in front of the rotor. The basic strategy of the control algorithm was to sense the location and magnitude of a stall cell with three equally spaced dynamic pressure transducers and apply pulses of air to locations of decreased pressure. In [8, 14], the use of jet actuators is more sophisticated where a circumferential array of 12 jet actuators is paced 63 mm upstream of the compressor face with down stream static pressure as measured output. The linearized compressible flow model developed in [19] was modified in [14] to develop a rational transfer matrix relating the actuator input and sensor output determined by system identification methods, and the LQG control methodology is then used to synthesize the feedback controller for active suppression of rotating stall. Regarding the use of sensors, flow rate measurements with hot wires are less reliable than static pressure measurements with pressure transducer. Moreover hot wires are very delicate and difficult to survive the hostile environment such as high speed axial compressors.

Up to present, three different types of actuators have been implemented and tested experimentally: inlet guide vanes [30, 31], air injection [9, 14, 10], and bleed valves [7]. Because inlet guide

vanes involve 2D actuation and requires large torque motors, this actuation scheme is not likely to be used in aeroengines due to the limit of weight and power supply. On the other hand bleed valves involve only 1D actuation and thus admit considerable advantages over inlet guide vanes. Moreover the research work in using bleed valves as actuators has been advanced significantly for the last several years that results in bifurcation based nonlinear feedback control. Hence the research work along this line is quite mature. A less developed control scheme is the use of air injector as actuators where only logic type or linear control has been studied so far. For the use of sensors, Static pressure measurements have a more promising future. More and more research work tend to employ pressure transducers [14, 10, 1] because they are less expensive and more reliable. Thus it is believed that the future research will focus on nonlinear feedback control with jet actuators and pressure sensors.

7 Conclusion

This final report has summarized the research work in the research field of active control for rotating stall and surge in axial compressors. It is also a summary of the author's work in 1995 summer faculty program performed at WPAFB under the direction of Dr. Siva Banda. With the research opportunity provided by summer faculty program, the author has acquired substantial knowledge on aerodynamics and nonlinear bifurcation analysis and active control of rotating stall and surge that will help greatly for his future research in this important and rapidly developing research field.

References

[1] J.F. Anderton, P.I. King and W.W. Copenhaver, "Stall analysis of high-frequency data for three swept-blade compressor rotors," in *SPIE Conference on Sensing, Actuation and Control in Aeropropulsion*, 1995.

[2] R.A. Adomaitis and E.H. Abed, "Bifurcation analysis of nonuniform flow patterns in axial-flow gas compressors," in *1st World Congress of Nonlinear Analysis*," Aug. 1992.

[3] R.A. Adomaitis and E.H. Abed, "Local nonlinear control of stall inception in axial flow compressors," in *19th Joint Propulsion Conference*, June 1993. AIAA Paper #93-2230.

[4] E.H. Abed, P.K. Houpt, and W.M. Hosny, "Bifurcation analysis of surge and rotating stall in axial flow compressors," *J. Turbomachinery*, vol 115, 817-824, Oct. 1993.

[5] O.O. Badmus, E.M. Eveker, and C.N. Nett, "Control-oriented high-frequency turbomachinery modeling: Theoretical foundations," in *1992 AIAA Joint Propulsion Conference*, July 1992, AIAA Paper No. 92-3314.

[6] O.O. Badmus, S. Chowdhury, E.M. Eveker, and C.N. Nett, "Control-oriented high-frequency turbomachinery modeling: Single-stage compression system 1D model," in *ASME Int'l. Gas Turbine and Aeroengine Congress and Exposition*, 1993. ASME 93-GT-18.

[7] O.O. Badmus, S. Chowdhury, E.M. Eveker, C.N. Nett, and C.J. Rivera, "A simplified approach for control of rotating stall – Part 1/2," in *29th Joint Propulsion Conference and Exhibit*, June 1993. AIAA Paper #93-2229/2334.

[8] R.G. Berndt, H.J. Weigl, J.D. Paduano and A.H. Epstein, "Experimental techniques for actuation, sensing and measurement of rotating stall dynamics in high speed compressors," in *SPIE Conference on Sensing, Actuation and Control in Aeropropulsion*, 1995.

[9] I.J. Day, "Active suppression of of rotating stall and surge in axial compressors," *J. of Turbomachinery*, vol. 115, 40-47, 1993.

[10] R. D'Andrea, R.L. Behnken and R.M. Murray, "Active control of rotating stall using pulsed air injection: experimental results on a low-speed, axial flow compressor," in *SPIE Conference on Sensing, Actuation and Control in Aeropropulsion*, 1995.

[11] A.H. Epstein, J.E. Ffowcs Williams, and E.M. Greitzer, "Active suppression of aerodynamic instabilities in turbomachinery," *J. Propulsion*, vol. 5, 204-211, 1989.

[12] K.M. Eveker, D.L. Gysling, C.N. Nett and O.P. Sharma, "Integrated control of rotating stall and surge in aeroengines," in *SPIE Conference on Sensing, Actuation and Control in Aeropropulsion*, 1995.

[13] K.M. Eveker, D.L. Gysling, C.N. Nett and H.O. Wang, "Rotating stall and surge control," US Patent Application, US Serial Number 08355763, 1994.

[14] M.R. Feulner, G.J. Hendricks, and J.D. Paduano, "Modeling for control of rotating stall in high speed multi-stage axial compressors, in *ASME Gas Turbine Conference*, June 1994.

[15] V.H. Garnier, A.H. Epstein and E.M. Greitzer, "Rotating waves at a stall inception indication in axial compressors," *ASME J. of Turbomachinery*, vol. 113, 290-302, 1991.

[16] E.M. Greitzer, "Surge and rotating stall in axial flow compressors – Part I/II," *J. Engineering for Power*, 199-217, April 1976.

[17] E.M. Greitzer, "The stability of pumping systems – The 1980 Freeman Scholar Lecture," *J. of Fluids Engineering*, vol. 103, 193-237, 1981.

[18] J.M. Haynes, G.J. Hendricks, and A.H. Epstein, "Active stabilization of rotating stall in a three-stage axial compressor," in *ASME Int'l Gas Turbine and Aeroengine Congress and Exposition*, 1993. ASME 93-GT-346.

[19] G.J. Hendricks, L.P. Bonnaure, J.P. Longley, E.M. Greitzer, and A.E. Epstein, "Analysis of rotating stall onset in high-speed axial flow compressions," in AIAA Paper 93-2233, June 1993.

[20] G.J. Hendricks and D.L. Gysling, "Theoretical study of sensor-actuator schemes for rotating stall control," *J. Propulsion and Power*, vol. 10, 101-109, 1994.

[21] D.-C. Liaw and E.H. Abed, "Active control of compressor stall inception: A bifurcation-theoretical approach," Technical Report, Institute for Systems Research, University of Maryland, 1992.

[22] G.R. Ludwig and J.P. Nenni, "Tests of an improved rotating stall control system on a J-85 turbojet engine," *ASME J. of Engineering for Power*, vol. 102, 903-911, 1980.

[23] C.A. Mansoux, J.D. Setiawan, D.L. Gysling, and J.D. Paduano, "Distributed nonlinear modeling and stability analysis of axial compressor stall and surge," in *American Control Conference*, 1994.

[24] F.E. McCaughan, "Application of bifurcation theory to axial flow compressor instability," *J. Turbomachinery*, vol. 111, 426-433, 1989.

[25] F.E. McCaughan, "Bifurcation analysis of axial flow compressor stability," *SIAM J. Applied Mathematics*, vol. 20, 1232-1253, 1990.

[26] N.M. McDougall N.A. Cumpsty and T.P. Hynes, "Stall inception in axial compressors," *ASME J. of Turbomachinery*, vol. 112, 116-125, 1990.

[27] F.K. Moore, "A theory of rotating stall of multistage axial compressors: Part I, II, III," *J. of Turbomachinery*, 313-336, vol. 106, 1996.

[28] F.K. Moore and E.M. Greitzer, "A theory of post-stall transients in axial compressors: Part I – development of the equations," *ASME J. of Engr. for Gas Turbines and Power*, vol. 108, pp. 68-76, 1986.

[29] J.D. Paduano, *Active Control of Rotating Stall in Axial Compressors*, Ph.D Thesis, MIT, 1992.

[30] J.D. Paduano, A.H. Epstein, L. Valavani, J.P. Longley, E.M. Greitzer, and G.R. Guenette, "Active control of rotating stall in a low-speed axial compressor," *J. Turbomachinery*, vol. 115, 48-56.

[31] J.D. Paduano, L. Valavani, A.H. Epstein, E.M. Greitzer, and G.R. Guenette, "Modeling for control of rotating stall," *Automatica*, vol. 30, 1357-1373, 1994.

[32] J.E. Pinsley, G.R. Guenette, A.H. Epstein, and E.M. Greitzer, "Active stabilization of centrifugal compressor surge," *J. Turbomachinery*, vol. 113, 723-732, 1991.

[33] J.S. Simon, L. Valavani, A.H. Epstein, and E.M. Greitzer, "Evaluation of approaches to active compressor surge stabilization," *J. Turbomachinery*, vol. 115, 57-67, 1993.

[34] M. Tryfonidis, O. Etchevers, J.D. Paduano, and A.H. Epstein, "Pre-stall behavior of several high-speed compressors," in *ASME Gas Turbine Conference*, June 1994.

[35] H.J. Weigl, "Nonlinear control of axial compressor instability," 2.152 final project report, MIT, May 1994.

[36] H.O. Wang, R.A. Adomatis and E.H. Abed, "Nonlinear analysis and control of rotating stall in axial flow compressors," in *American Control Conference*, 2317-2321, 1994.

[37] H. Ziegler, "Effect of active compressor stabilization on inlet sizing and aircraft performance," Internal Report, Northrop Corporation, Aerosciences Systems Integration/Advanced Projects B2 Division, 1992.

[38] W.A. Yonke, R.J. Landy, and J.F. Stewart, "HIDEC adaptive engine control system flight evaluation results," ASME Paper # 87-GT-257.

PART I: FINAL DEVELOPMENT OF SURFACE-OBSTACLE INSTRUMENT FOR
SKIN-FRICTION AND FLOW DIRECTION MEASUREMENT

PART II: EXPLORATORY STUDY OF A NEW CONCEPT FOR FLOW SIMULATION
AT HIGH MACH NUMBERS

by

Raimo J. Hakkinen
Professor and Director, Fluid Mechanics Laboratory
Department of Mechanical Engineering

Washington University
One Brookings Drive
Saint Louis, Missouri 63130

September 1995

PART I: FINAL DEVELOPMENT OF SURFACE-OBSTACLE INSTRUMENT FOR SKIN-FRICTION AND FLOW DIRECTION MEASUREMENT

PART II: EXPLORATORY STUDY OF A NEW CONCEPT FOR FLOW SIMULATION AT HIGH MACH NUMBERS

Raimo J. Hakkinen
Professor and Director, Fluid Mechanics Laboratory
Department of Mechanical Engineering
Washington University

Abstract

PART I: The technical background of surface-obstacle skin friction meters were thoroughly reviewed during the 1993 Summer Program, and the emphasis of the 1994 Summer Program was to complete the detailed design of a specific instrument, to initiate its fabrication, and to define test programs for facilities available at Wright Laboratory (WL) and Washington University (WU). These objectives were completed, and fabrication of the instrument was approved at Wright Laboratory. However, during the 1995 summer program, the fabrication and the calibration tests tentatively planned for the WL M3 and M6 supersonic wind tunnels could not be scheduled. Using a simple proof-of-concept prototype instrument manufactured under private funding, a series of incompressible-flow calibration data was acquired in the Washington University Low-Speed Wind Tunnel in April, 1995. Summaries of all previous work and the new incompressible calibration data were presented in a USAF-sponsored international symposium in July, 1995. The 1995 Summer Program effort reported in Part I consisted primarily of a detailed analysis of the 1995 Washington University data. The resulting correlations of incompressible calibration data obtained in a flat-plate boundary layer at one laminar and two turbulent conditions essentially verify the calibration characteristic of the new instrument postulated in earlier work.

PART II: The second part of the 1995 Summer Program Final Report describes a preliminary feasibility study of a new hypersonic test facility concept. For further information on this item, please contact Norman E. Scaggs, WL/FIMO.

PART I: FINAL DEVELOPMENT OF SURFACE-OBSTACLE INSTRUMENT FOR SKIN-FRICTION AND FLOW DIRECTION MEASUREMENT

Raimo J. Hakkinen

Introduction

Accurate determination of skin friction drag is of primary importance in efficient aerodynamic design; it may constitute as much as fifty percent of the drag of a cruising aircraft, and knowledge of the shear stress distribution is an essential part of understanding the flow field of any complex flight vehicle in any speed range. Acquisition of precise experimental data has also become essential for validating the emerging computational techniques for the prediction of local skin friction distributions on general, three-dimensional vehicle configurations. While a great variety of experimental techniques exists for the measurement of local skin friction, there is at present no universally applicable method, and a choice must be made according to particular wind tunnel or flight test conditions.

As discussed in detail in [1] and [2], limitations of the available techniques are especially severe if measurements are desired for general conditions that may include non-planar surfaces, unknown flow direction, and significant pressure gradients. The objective of the present project, initiated at Wright Laboratory (WL) under the 1993 Air Force Office of Scientific Research Summer Research Program, is to develop and demonstrate an instrument that would overcome some of these limitations and thus become a useful addition to the repertoire of practical skin friction measurement techniques.

The instrument under development is based on the surface-obstacle principle, where the sensed physical quantity is the difference between the pressure on the face of a small obstacle placed on the surface and the local undisturbed static pressure; this pressure differential is calibrated against the shear stress exerted by the boundary layer on the flow in front of the obstacle. The calibration is expressible in terms of dimensionless variables that depend on the physical flow parameters at the wall and the size of the probe. Examples of devices operating on this principle are the surface blocks, sublayer fences, Stanton tubes and Preston tubes, as discussed in the surveys referenced above.

The novel features of the proposed surface-obstacle instrument are twofold: (a) adjustable operation using the principle of minimum protrusion required to sense the pressure differential with satisfactory accuracy and (b) capability of sensing the direction of the flow adjacent to the surface through the angular location of the face pressure pattern given by orifices evenly spaced around the axisymmetric obstacle.

22-3

The principle of minimum protrusion was adopted (a) to avoid disturbing the flow in the boundary layer more than absolutely necessary, especially in measurements related to laminar flow control or characterization of turbulent flow structures; (b) to minimize shear-stress measurement errors caused by surface static pressure gradients, (c) to minimize effects of exposure to hostile environments, with the option of withdrawing the probe before and after the measurement; and (d) to provide a realistic indication of the limiting flow direction at the surface.

The technical background and calibration of surface-obstacle skin friction meters were thoroughly reviewed in the 1993 Summer Program Final Report [1], and a summary was presented in [2]. The emphasis of the 1994 Summer Program was to complete the detailed design of the specific instrument proposed in [1], to initiate its fabrication, and to define test programs for the Wright Laboratory (WL) supersonic M3 and M6 tunnels and the Washington University (WU) Low-Speed Wind Tunnel, as reported in the 1994 Summer Program Final Report [3]. These objectives were completed, and fabrication of the instrument was approved at Wright Laboratory. Because of scheduling considerations, the fabrication and the calibration tests tentatively planned for the WL M3 and M6 supersonic wind tunnels could not be completed during the 1995 summer program. However, the operation of a simple proof-of-concept prototype instrument had been explored under private funding in the Washington University Low-Speed Wind Tunnel in April, 1994, and a series of incompressible-flow calibration data were acquired in April, 1995. Summaries of all previous work and the new incompressible calibration data were presented in [4]. The 1995 Summer Program results consist primarily of detailed analysis of the 1995 Washington University data. The correlation of incompressible calibration data obtained in a flat-plate boundary layer at one laminar and two turbulent conditions essentially verifies the hypothetical characteristic of the new instrument postulated in [1] and [2].

Technical Background

As demonstrated in [1], practical calibration relationships of surface-obstacle devices can be expressed in terms of dimensionless variables containing fluid properties at the wall: density ρ, dynamic viscosity μ, kinematic viscosity v, and static pressure p_e; the surface shear stress τ; the protrusion height of the obstacle h; and the difference Δp between the pressure on the face of the obstacle and p_e. The surface static pressure p_e is normally assumed equal to the local static pressure outside the boundary layer.

The general calibration relationship can then be expressed as

$$\tilde{p} = f(\tilde{\tau}, \tilde{p}_e)$$

(2)

where

$$\widetilde{p} = \Delta p\, h^2 / \rho\, v^2, \quad \widetilde{p}_e = p_e\, h^2 / \rho\, v^2, \text{ and } \quad \widetilde{\tau} = \tau\, h^2 / \rho\, v^2.$$

The conversion of available calibrations to the form of Eq. (2) was reviewed and the resulting general expressions presented in [1]. It was expected that the surface-obstacle design developed in this project would be characterized by a similar calibration pattern; indeed, as discussed later in this report, the preliminary results obtained in proof-of-concept prototype tests in the WU Low-Speed Wind Tunnel in laminar and turbulent boundary layers fully supported this premise.

For the purpose of expressing the measured pressure rise, Δp, and the skin friction stress, τ, in dimensionless forms independent of the protrusion height, h, the general calibration relationship, Eq. (2), was written as:

$$\frac{\Delta p}{p_e} = \frac{\widetilde{p}}{\widetilde{p}_e} = \frac{1}{\widetilde{p}_e} F\left(\frac{\tau}{p_e}\widetilde{p}_e, \widetilde{p}_e\right) = \overline{F}\left(\frac{\tau}{p_e}, \widetilde{p}_e\right) \tag{3}$$

where h appears in only one parameter, $\widetilde{p}_e$[1]. The dimensionless parameter $\widetilde{p}_e$, which is independent of the shear stress τ, is introduced to the calibration relationships in the form of Eq. (2) by compressibility effects, and disappears from most equations in their absence. However, in the form of Eq. (3), $\widetilde{p}_e$ is always present because of the normalization of τ and Δp by pe.

As shown in [1] for Preston-tube calibrations, compressibility effects were in most cases included by introducing the concept of probe Mach number, M_p, which is defined by the isentropic face pressure differential-to-static pressure ratio

$$\frac{\Delta p}{p_e} = \frac{\widetilde{p}}{\widetilde{p}_e} = \left(1 + \frac{\gamma - 1}{2} M_p^2\right)^{\frac{\gamma}{\gamma - 1}} - 1 \tag{4}$$

or, at supersonic values of Mp, by the normal shock loss combined with isentropic expansion

$$\frac{\Delta p}{p_e} = \frac{\widetilde{p}}{\widetilde{p}_e} = \frac{\left(\frac{\gamma + 1}{2} M_p^2\right)^{\frac{\gamma}{\gamma - 1}}}{\left[\left(\frac{\gamma - 1}{\gamma + 1}\right)\left(\frac{2\gamma}{\gamma - 1} M_p^2 - 1\right)\right]^{\frac{1}{\gamma - 1}}} - 1 \tag{5}$$

Definition of a *probe dynamic pressure*

$$\tilde{q}_p = \frac{\gamma}{2} \tilde{p}_e M_e^{2}$$

(6)

allowed the expression of the compressible calibration laws by replacement of $\tilde{p}$ by $\tilde{q}_p$, and a common calibration chart could then be prepared covering both compressible and incompressible regimes (Fig. 1 of [1]). As $M_p \to 0$, $\tilde{q}_p \to \tilde{p}$, and in most cases the parameter $\tilde{p}_e$ disappeared from the equation.

Very few data were available to determine the presence of compressibility effects in the Stanton-range. As a working hypothesis, the use of the probe dynamic pressure, $\tilde{q}_p$, in place of $\tilde{p}$ appeared reasonable in this regime for compressible boundary layers. It was also anticipated that differences in calibration would probably occur between laminar and turbulent boundary layers.

Characterization of Surface Obstacle Calibration

Using the data collected and analyzed in [1] as the working hypothesis, the following expressions were proposed for general characterization of surface-obstacle calibration:

$12{,}600 < \tilde{\tau} < 100{,}000$:

$$\tilde{q}_p = 35.55\, \tilde{\tau}^{1.13}$$

(7a)

$200 < \tilde{\tau} < 12{,}600$:

$$\log_{10} \tilde{\tau} = 2.7741 - 1.1106 \log_{10} \tilde{q}_p + 0.3234 \left[\log_{10} \tilde{q}_p \right]^{2} - 0.0177 \left[\log_{10} \tilde{q}_p \right]^{3}$$

(7b)

$10 < \tilde{\tau} < 200$:

$$\tilde{q}_p = 1.117\, \tilde{\tau}^{5/3}$$

(7c)

$\tilde{\tau} < 10$:

$$\tilde{p} \approx 1.2 \tilde{\tau}$$

(7d)

The calibration correlations in the two upper ranges have been established for turbulent boundary layers; in the two lower ranges of $\tilde{\tau}$, both laminar and turbulent boundary layers may be found, and care must be exercised in using calibration relations not established for the particular experimental conditions.

As discussed in [1], the integration of the Preston tube calibration laws with the lower range was based on certain assumptions and extensions of the available data base. In the specific case of round tubes, the 5/3-power relationship has not been directly demonstrated over most of its expected range. For Stanton tubes and sublayer fences, the 5/3-power law rests on firmer ground; however, in neither case is the question of compressibility effects entirely clear.

There exists a vast array of calibration data for various types of surface devices where specific power laws have been identified, the 4/3-power relationship being a common choice. Generally, such experiments can be placed in the transitional regime between the 5/3-power and the 1.13-power regions. This particular question was part of the motivation for an exploratory series of low-speed measurements with a simplified proof-of-concept prototype instrument under private funding at Washington University in April, 1994, and April, 1995 [4].

Low-Speed Exploratory Measurements at Washington University.

The proof-of-concept prototype instrument designed and fabricated at Washington University was mounted on the existing flat plate installed in the 2 ft-by-2 ft Low-Speed Wind Tunnel in the Fluid Mechanics Laboratory. The probe assembly was mounted into the existing 0.5 in-thick, polished Plexiglas test plate, at a distance of 42 inches from a contoured semi-elliptic leading edge with a continuous-curvature spline faired into the flat portion leading edge. Laminar flow can be obtained up to a Reynolds number of one million at the test location.

The configuration of the prototype instrument was similar to the final instrument described in [3], the main differences being the use of only one groove in the sliding, 10 mm-diameter flat-ended, obstacle plug, and the location of the pressure orifice in the groove approximately 2 mm from the top surface. The probe was fitted tightly into a sleeve, which was installed flush with the plate surface. The 0.5 mm square groove extended approximately 5 mm down the side from the end face. The pressure differential between the pressure orifice located in the groove and the flat plate static pressure orifice at the same streamwise location on the plate was measured on a calibrated Validyne 3-in(water) full-range transducer with electronic readout.

In the initial, exploratory experiments in April, 1994, the existing boundary-layer pitot probe positioning mechanism was used for adjusting the protrusion of the probe and reading it by means of the calibrated Linear Variable Differential Transformer system connected to the laboratory computer. The value of the reference skin friction was determined from pitot-probe velocity-profile data, which were matched by the laboratory computer to the Blasius solution in the laminar case and to the Clauser-chart version of the logarithmic law-region in the turbulent case. The experiment yielded preliminary

calibration curves at fixed values of shear stress in a laminar boundary layer at an approximate running Reynolds number of 750,000, and in a turbulent boundary layer at a Reynols number of 1,750,000. The observed functional dependence of the results was completely consistent with the general calibration relationships postulated in [1] and [2]. The sensitivity of the instrument to flow direction was also explored in a qualitative sense.

To obtain more accurate calibration data, the experiment in the Washington University Low-Speed Wind Tunnel was repeated in April, 1995, at a laminar Reynolds number of 743,000, and at turbulent Reynolds numbers of 1,264,000 and 2,616,000. The mounting of the test plate had been reinforced to eliminate velocity-dependent deflection errors, and a precision micrometer with an accuracy of 0.0002 inches was used to read the protrusion height of the probe..

The boundary layer velocity profiles were again measured by means of the existing adjustable, flattened pitot probe, mounted at the same location as the surface obstacle instrument. The pressure signal from the probe, relative to that from an adjacent static orifice on the plate, was measured with a Validyne differential pressure transducer of a range of +/- 3 in(water). The measured profiles were graphically compared with the Blasius solution in the laminar case, and with the logarithmic law in the Clauser-chart form in the turbulent case. In both situations, the shear stress was determined with an estimated total uncertainty of +/- 5 per cent.

The probe vs. static differential pressures recorded from the digital transducer readout fluctuated within +/-5 per cent about a mean value in the main part of the laminar range, and within up to +/- 2 per cent in the turbulent case. Considerably larger fluctuations seen at very small protrusions. The mean values were estimated from the observed maximum and minimum readings and used in calculating the shear stress- vs. pressure differential parameter relationships presented in Fig. 1. These data were included in the publication of the results of the 1993 and 1994 Summer Programs in [4].

In spite of the significant uncertainties and fluctuation levels of the data, the turbulent measurements shown in Figure 1 agree remarkably well over a range of several logarithmic cycles. The general nature of the observed relationship is again that postulated in analogy with the Preston- and Stanton-probe characteristics [1], although the numerical coefficients are, as expected, different from the postulated in Eqs. (7a) through (7d).

The laminar calibration shows the expected 5/3-power relationship in essential agreement with the Stanton-tube based postulated calibration, while the turbulent calibration shows the same relationship but with a considerably lower coefficient. As discussed in [3], this difference has been observed in previous experiments with small surface obstacles, and its origin has been speculated to lie in possible non-linear rectification of the fluctuating probe- and static pressure-signals in the leads between the

measuring orifices and the transducer. Some effort was spent during the 1994 Summer Program to collect and analyze available data on the turbulent flow environment around the probe in an attempt to isolate a specific physical mechanism responsible for the observed difference; especially in view of the fact that the surface shear stress in turbulent flow fluctuates over a very wide ranges of magnitude and direction. In the 1995 experiments, simple attempts to modify the internal resistance of the manometer leads did not produce significant variations in the level of the pressure signals, although this observation cannot be considered conclusive. It is believed, however, that the direct effect of the violent velocity gradient fluctuations, both streamwise and lateral, inherent in any turbulent boundary layer should be investigated in more detail.

During the 1995 Summer Program, the calibration characteristics measured in April, 1995, at Washington University were analyzed in more detail. In addition to the general data in Fig. 4, the probe pressures measured at each constant shear stress were plotted as a function of the protrusion height, and compared against the predictions of the general relationship postulated in [1]. In the 5/3-power and intermediate ranges, as shown in Figures 1 and 2,. the laminar calibration curve yields a pressure differential essentially at the postulated value, while the turbulent comparisons in Figures 3 and 4 yield pressure differentials of approximately 40 per cent of the postulate in this range. When the probe protrusion in the turbulent cases enters the parametric Preston-tube range, the functional relationship is approximately 70 per cent of the well-established Preston-tube calibration. In view of the different geometric shapes of the Preston tube and the present obstacle probe, this result is entirely reasonable.

In all calibration characteristics shown in Figures 1, 2, 3 and 4, a departure above the calibration laws is noticeable at the higher values of the parametric range. These measurements were deliberately taken beyond the expected validity of the calibration laws, to demonstrate the effect of approaching the edge of the boundary layer. In fact, if protruding beyond the edge, in incompressible flow the probe will read the free-stream dynamic pressure, which implies the relationship

$$\tilde{p} = (1/c_f)\tilde{\tau} \tag{8}$$

The deviation above the calibration law is the beginning of the asymptotic approach to Eq. (8), which has been verified by additional extended measurements. The asymptotes given by Eq. (8) are shown in Fig. 1 as dotted lines for each test condition.

It is of interest to note that in the curves shown in Figs. 3 and 4, the most efficient region, i.e. the maximum increase of pressure differential vs. probe extension, is in the lower parametric ranges, and penetration into the Preston-type range appears considerably less beneficial. In contrast, Preston-tubes have been strictly limited to the higher parametric range and many published calibrations include

22-9

warnings about using Preston-tubes of small diameters. Therefore, it appears that these new results would provide a sound basis for the development of the present instrument into a simple, effective diagnostic tool with minimal flow disturbance. A programmed protrusion sequence, preceded and followed by complete retraction, would yield considerable information about the boundary layer, such as its laminar or turbulent state, and the magnitude and direction of the skin friction vector.

Design of instrument for Wright Laboratory

The specifications determined in [1] for the instrument to be used in the M3 and M6 tunnels included the following requirements: (a) mounting into the existing wall and flat-plate model locations; (b) adjustable-protrusion (maximum 5 mm), circular (10 mm diameter) obstacle to provide adequate face-pressure-differential and directional sensitivity with minimum disturbance to the boundary layer; (c) precision fit of the obstacle cylinder to prevent air leakage but provide for accurate, smooth extension and retraction of the device by direct manual or remote control; (d) evenly spaced pressure orifices (twelve) of minimum practical size located along edge of obstacle opening to provide both maximum face pressure for determination of shear stress and circumferential pattern for determination of flow direction; (e) provision for measurement of static pressure and surface temperature for direct calculation of dimensionless calibration parameters; (f) use of commercially available pressure transducers, and (g) an accurate internal or external means for measurement of the protrusion height of the obstacle. A sketch of the proposed instrument was presented in [1]. and [4].

During the 1994 Summer Program, a detailed design satisfying these requirements was prepared and documented in a series of computerized (AUTOCAD-12) drawings. Representative sketches of these drawings were included in the 1994 Summer Program Final Report [3].

The BM4CC motor-driven micrometer/actuator with 4 mm total motion, manufactured by the Newport/Klinger Corporation, was selected for accurate positioning of the movable sensor element. The readout resolution is better than 0.05 μm with an axial load capacity of 73 N. The actuator is controlled by a Newport/Klinger Motionmaster 2000 single-axis PC-based control and readout system. These parts were acquired by WL in 1994, and a preliminary checkout and calibration of the actuator system was performed by the author at WL during a privately funded visit in November, 1994.

The design is compatible with existing mounting provisions for both the M3 and M6 wind tunnels, and is basically interchangeable with the existing WL/FIMO floating-element skin friction meter. A modification of the existing flow shield is being designed for the M6 installation to accommodate the actuator unit. During the 1995 Summer Project, the remaining design details were finalized in cooperation with WL personnel, who are expected to complete the design and initiate manufacturing of

the instrument during the remainder of 1995. The objectives and the plan for the calibration test series at WL were presented also in [3].

Future work

Completion of construction of the instrument and the test series are dependent on further support for WL personnel. It is recommended that provisions for further participation by the Principal Investigator would include verification and extension of the calibration tests in the WU Low-Speed Wind Tunnel using the actual WL instrument with its precision actuator and directional capability.

The ultimate development objective is a remotely adjustable instrument capable of skin friction and surface flow direction measurements in general conditions, including curved surfaces and the presence of arbitrary pressure gradients. The simple design of the instrument combined with operation at minimal protrusion and complete retraction after measurement should facilitate measurements at elevated surface temperatures and in other demanding environmental conditions.

References

1. Hakkinen, Raimo J., Skin Friction and Flow Direction Measurement by Surface-Obstacle Instruments, AFOSR Summer Program Report, August 1993.
2. Hakkinen, R. J., Calibration of Surface-Obstacle Skin Friction Meters, American Physical Society Fluid Dynamics Division Meeting, Albuquerque, NM, November 1993.
3. Hakkinen, Raimo J., Further Development of Surface-Obstacle Instrument for Skin Friction and Flow Direction Measurement, AFOSR Summer Program Report, September 1994.
4. Hakkinen, Raimo J., Design and Calibration of a New Surface-Obstacle Skin-Friction and Flow Direction Meter, 16th International Congress on Instrumentation in Aerospace Simulation Facilities, Dayton, Ohio, July 18-21, 1995.
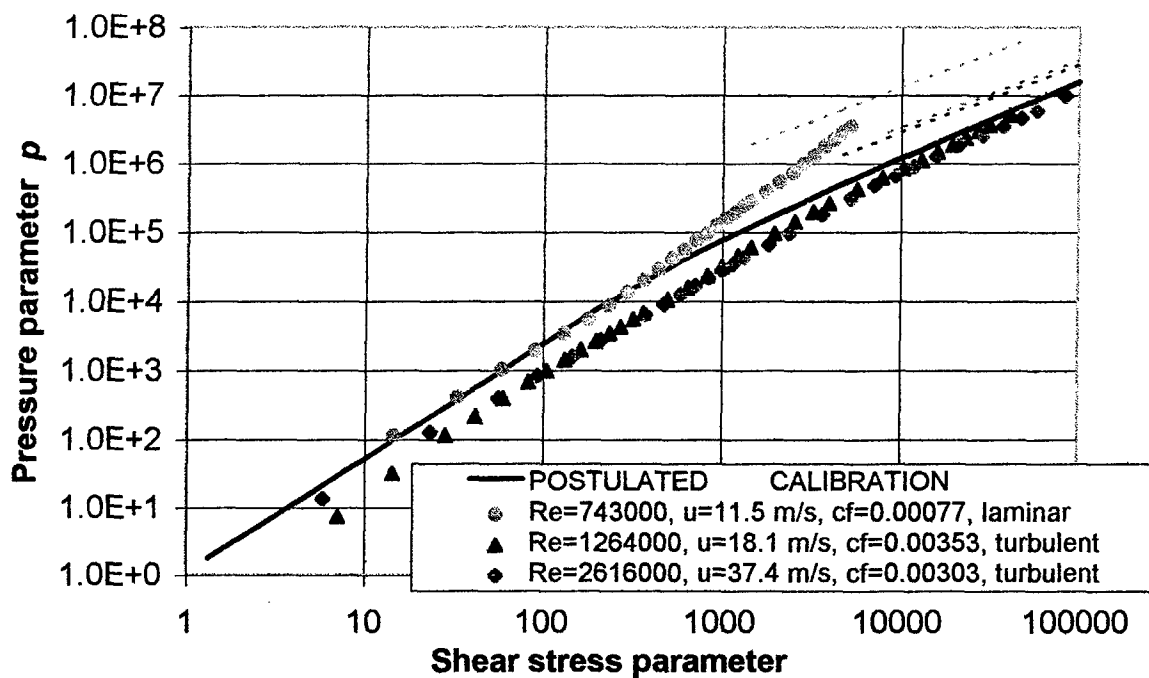
Fig. 1. Experimental results with prototype probe compared with postulated calibration.
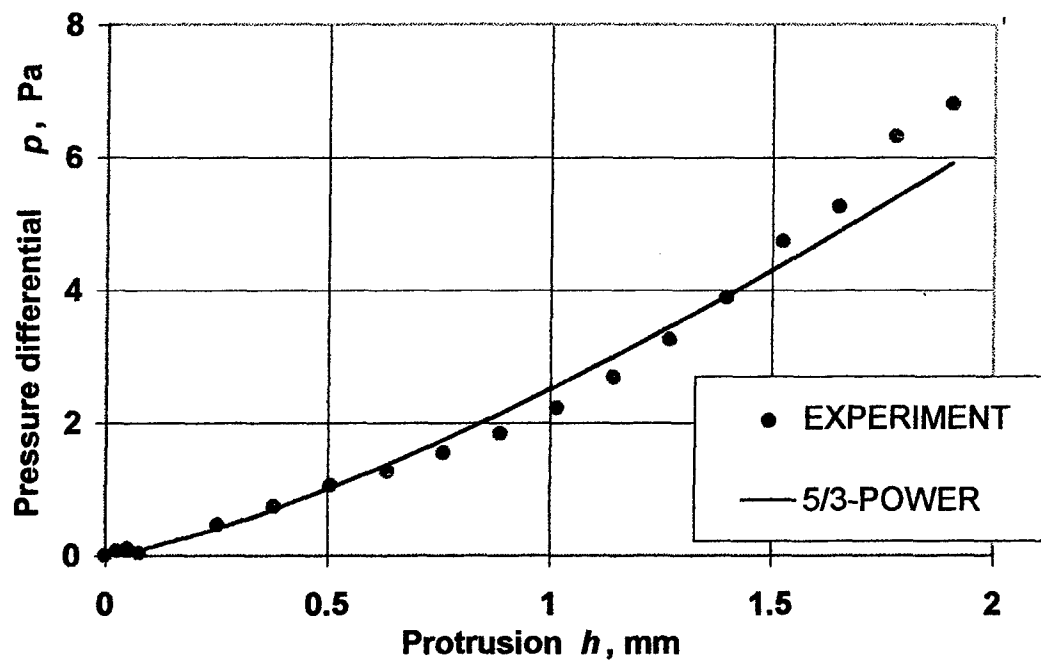Dotted lines represent free-stream dynamic pressure (Eq. 8).

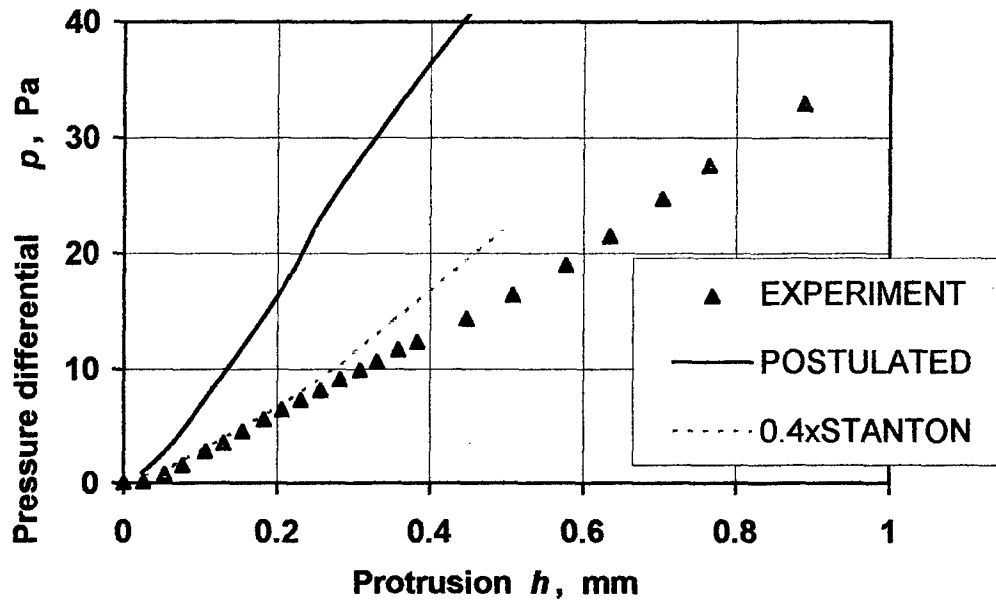Fig. 2. Experiment in laminar flow at Re = 743,000 compared with Stanton-tube calibration law.

Fig. 3. Experiment in turbulent flow at Re = 1,264,000; small-protrusion (Stanton) region compared with 5/3-power calibration law.
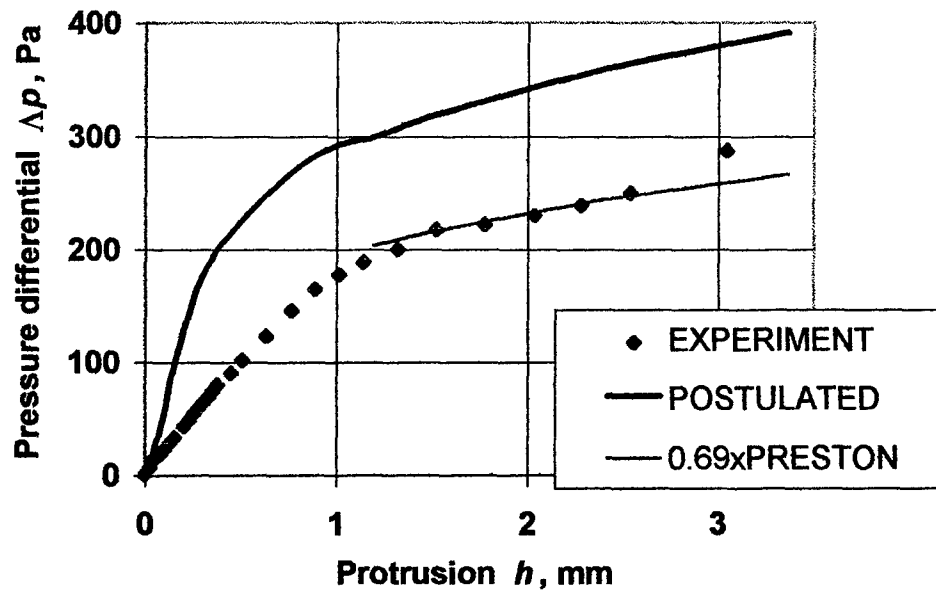

Fig. 4. Experiment in turbulent flow at Re = 2,616,000; large-protrusion region compared with round Preston-tube calibration law.

PART II: EXPLORATORY STUDY OF A NEW CONCEPT FOR FLOW SIMULATION AT HIGH MACH NUMBERS

Raimo J. Hakkinen

(For further information on this item, please contact Norman E. Scaggs, WL/FIMO).

EFFECT OF HUMIDITY ON WEAR OF
M-50 STEEL WITH A DEMNUM LUBRICANT

Larry S. Helmick
Professor of Chemistry
Department of Science and Mathematics

Cedarville College
Box 601
Cedarville, OH 45314

EFFECT OF HUMIDITY ON WEAR OF
M-50 STEEL WITH A DEMNUM LUBRICANT

Larry S. Helmick
Professor of Chemistry
Department of Science and Mathematics
Cedarville College

Abstract

Using a Cameron-Plint tribometer under controlled environmental conditions, wear of M-50 steel with a Demnum (a linear perfluoropolyalkyl ether) lubricant was studied under boundary lubrication conditions at 50 and 150 C with relative humidity ranging from 1% to 95%. In general, both wear and friction decrease sharply as humidity is increased from 1 to 5%, then are constant as humidity increases to 95%. Thus, wear is highly dependent on humidity when relative humidity is less than 5%. Wear at low humidities for this lubricant, which does not contain difluoroacetal groups, is compared to wear previously reported for Fomblin Z, a linear perfluoropolyalkyl ether containing difluoroacetal groups.

EFFECT OF HUMIDITY ON WEAR OF
M-50 STEEL WITH A DEMNUM LUBRICANT

Larry S. Helmick

Introduction

Perfluoropolyalkyl ethers (PFPAE) are presently being investigated as liquid lubricants for aerospace applications (1,2). PFPAE fluids have been tested with the four-ball tribometer (3,4) and the newer Cameron-Plint reciprocating tribometer under sliding boundary lubrication conditions with the test cell exposed to the environmental atmosphere. When testing linear PFPAE fluids containing difluoroacetal groups (OCF_2) with steel specimens with either instrument, erratic results are sometimes obtained. A recent investigation revealed that environmental relative humidity has a major effect on friction and wear for a linear PFPAE fluid containing difluoroacetal groups (5), and therefore may be a major cause of these erratic results. However, this study did not include linear PFPAE fluids which do not possess difluoroacetal groups. Therefore, the current study was initiated to broaden the investigation and determine whether humidity also affects friction and wear for a linear PFPAE fluid that does not contain difluoroacetal groups. If humidity affects friction and wear for this fluid also, then it may be necessary to measure and control humidity when evaluating potential antiwear additives (6-8) under sliding

boundary lubrication conditions on steel specimens with other PFPAE fluids as well.

Experimental Procedure

The commercially available fluid used in this study was Demnum S-65, a linear PFPAE with a C/O ratio of 3/1, which does not contain difluoroacetal groups. Data obtained with this fluid are compared to data previously obtained under similar conditions (5) using Fomblin Z-04, a linear PFPAE with a C/O ratio of 1.4/1, which does contain difluoroacetal groups.

Demnum was tested in air under sliding boundary lubrication conditions using a modified Cameron-Plint Tribometer with a controlled environmental chamber and automatic data acquisition system. A schematic diagram and a full description of this instrument are given in references 5 and 9.

The detailed test procedure is described in reference 5, but a brief review here may be helpful. An M-50 steel cylinder was loaded and slid with a reciprocating motion against an M-50 flat specimen. Friction was monitored throughout the 5 hour runs and recorded at 30 second intervals. An average coefficient of friction was calculated for each run by dividing the average friction by the 250 N load.

Data were obtained with specimen temperatures of 50 and 150 C +/-

2 C and ambient atmospheric temperatures (29 +/- 3 C). Specimen temperatures and electrical resistance between the cylinder and disk were also recorded at 30 second intervals throughout the runs. Formation of films on the surface of the wear scar were indicated by an increase in contact point electrical resistance and confirmed by Fourier transform infrared spectroscopy, as described in reference (10).

Relative humidity (RH) was measured (+/- 0.1%) at ambient temperature and recorded at 30 second intervals as well. Humidities below ambient (approximately 50%) were obtained by controlling the flow rate of dry air into the environment chamber, and were constant to +/- 0.3% or less. Humidities above ambient were obtained by controlling the flow rate of air through a Tatung TUH-500H Ultrasonic Humidifier, and were constant to +/- 1.5% or less.

Areas of wear scars were determined by measuring (+/- 1 X 10^{-3}mm) the length and width of the wear scar on the cylinder at the end of the 5 hr runs.

All temperature, humidity, friction, and wear data for Demnum are recorded in Table 1 and plotted in Figures 1-4, along with data previously reported for Fomblin (5), for easy comparison.

Results

Figures 1 and 2 show the effect of humidity on wear scar area for both fluids at 50 and 150 C, respectively. At 50 C (Figure 1), there is a sharp decrease in wear scar area as humidity increases from 1 to 5% for Demnum. No additional decrease is obvious as humidity increases from 5 to 95%. A similar sharp decrease in wear scar area occurs for Fomblin as humidity increases from 5 to 20%, and then is constant as humidity increases to 100%. At 150 C (Figure 2), the sharp decrease in wear scar areas for both fluids is even more pronounced, with the decrease for Fomblin again occurring at a slightly higher humidity than for Demnum. Again, no further decrease in wear is observed for either fluid as the humidity increases to 100%.

Figures 3 and 4 show the average coefficient of friction plotted vs relative humidity for both fluids at the two test temperatures. The plot at 50 C (Figure 3) shows that the coefficient of friction tends to decrease as humidity increases from 1 to 100% for both fluids. The lower values at high humidities may be due to the adsorption of moisture on the metal surface since the temperature is well below the boiling point of water. At 150 C (Figure 4), a sharp decrease in friction is observed as humidity increases from 1 to 5% for Demnum, and from 5 to 15% for Fomblin, but no additional decrease occurs for either fluid as humidity increases to 100%. The sharp decrease in friction at low humidities also appears to occur for both

fluids at 50 C, but is not nearly as pronounced.

Electrical resistance at the contact point varied with time as well as with relative humidity. The resistance is generally high initially due to poor metal-metal contact, but then drops rapidly when the 250 N load is applied and metal-metal contact improves. For low humidity runs, it then stays relatively low, demonstrating good metal-metal contact throughout the 5 hour run. For high humidity runs, however, it rapidly increases again, indicating that an electrically insulating film is being formed on the wear scar surface as the run continues. The formation of this film at high humidities has now been observed by FTIR spectroscopy for Demnum just as it was previously for Fomblin (10).

Discussion

The dependence of both friction and wear on humidity was previously observed for Fomblin and assumed to be related to the presence of difluoroacetal groups (5). Therefore, it is interesting that a similar dependence should now be observed for Demnum, which does not possess difluoroacetal groups. Thus it is now clear that this dependence is not due solely to the presence of difluoroacetal groups in Fomblin. If it were, friction and wear for Demnum would be independent of humidity.

The cause of the high wear at low humidity is not yet clear. It

may be corrosive wear, in which case it would be directly related to the rate of decomposition of the PFPAE fluid to form corrosive products. Or it may be abrasive wear, in which case it would be inversely related to the rate of formation and thickness of the film which is produced at higher humidities, which in turn may also be related to the decomposition of the PFPAE fluid.

It is also not yet clear whether the lower wear observed for Demnum compared with Fomblin at low humidities is significant. The difference may simply be due to the difference in viscosities of the two fluids, or it may be due to different decomposition reaction mechanisms or products which are a result of the different chemical structures of the two fluids. In any event, the reaction mechanisms for decomposition of PFPAE fluids under tribological conditions, and the chemistry of film formation are being investigated (9-14).

Conclusions

Under boundary lubrication conditions, wear of M-50 steel with linear perfluoropolyalkylether lubricants with and without difluoroacetal groups depends strongly on relative humidity for humidities below 20%, but is nearly independent of humidity above 20%. Therefore, this dependence cannot be attributed solely to the presence of difluoroacetal groups in the PFPAE lubricant. Furthermore, for tests performed below 20% relative humidity, humidity should be monitored and carefully controlled. Tests

under low humidity conditions are extremely useful in screening boundary lubrication additives, since the difference in performance of the base oil and the formulated oil (base oil plus additive) may be more readily observed.

Disclaimer

The U. S. Air Force does not endorse for other purposes or criticize the materials used in this study.

References

1. Fusaro, R.L., and Khonsari, M.M., "Liquid Lubrication for Space Applications," NASA TM-105198, 1992.

2. Fusaro, R.L., "Tribology Needs for Future Space and Aeronautical Systems", NASA TM-104525, 1991.

3. Masuko, M., Jones, W.R., Jr., and Helmick, L.S., "Tribological Characteristics of Perfluoropolyether Liquid Lubricants Under Sliding Conditions in High Vacuum," NASA TM-106257, 1993.

4. Masuko, M., Jones, W.R., Jr., Jansen, R., Ebihara, B., Pepper, S.V., and Helmick, L.S., "A Vacuum Four-Ball Tribometer to Evaluate Liquid Lubricants for Space Applications," NASA TM-106264, 1994.

5. Helmick, L.S., and Sharma, S.K., "Effect of Humidity on Friction and Wear for a Linear Perfluoropolyalkyl Ether Fluid Under Boundary Lubrication Conditions," accepted for publication, Lubrication Engineering, (1995).

6. Gschwender, L.J., Snyder, C.E. Jr., and Fultz, G.W., "Soluble Additives for Perfluoropolyalkylether Liquid Lubricants," Lubr. Eng., 49, 9, 702-708 (1993).

7. Srinivasan, P., Corti, C., Montagna, L. and Savelli, P., "Soluble Additives for Perfluorinated Lubricants," JSL, 10, 2, 143-164 (1993).

8. Sharma, S.K., Gschwender, L.J., and Snyder, C.E., Jr., "Development of a Soluble Lubricity Additive for Perfluoropolyalkylether Fluids," JSL, 7, 1, 15-23 (1990).

9. Cavdar, B., Sharma, S.K., and Gschwender, L.J., "Wear-Reducing Surface Films Formed by a Fluorinated Sulfonamide Additive in a Chlorotrifluoroethylene-based Fluid," Lubrication Engineering, 150, 11, 895-902 (1994).

10. Liang, J., and Helmick, L.S., "Tribochemistry of a PFPAE Fluid on M-50 Surfaces by FTIR Spectroscopy," accepted for publication, Lubrication Engineering, (1995).

11. Karis, T.E., Novotny, V.J., and Johnson, R.D., "Mechanical Scission of Perfluoropolyethers", J. Appl. Polym. Sci., 50, 1357-1368 (1993).

12. Zehe, M.J., and Fout, O.D., "Acidic attack of Perfluorinated Alkyl Ether Lubricant Molecules by Metal Oxide Surfaces", Trib. Trans., 33, 634-640 (1990).

13. Kasai, P.H. "Perfluoropolyethers: Intramolecular Disproportionation," Macromolecules, 25, 6791-6799 (199).

14. Vurens, G., Zehringer, R., and Saperstein, D., "The Decomposition Mechanism of Perfluoropolyether Lubricants during Wear," Chapter 10 in <u>Surface Science Investigations in Tribology,</u> Chung, Y.W., Homola, A.M., Sheet, G.B., eds., ACS Symposium Series, American Chemical Society, 1992.

TABLE 1
Temperature, Humidity, Friction, and Wear Data

Run Number	Temperature (C)	Rel. Humid. (%)	Avg. Coef. of Friction	Wear Area (mm²)
1	50	1	0.132	1.943
2	50	1	0.124	1.843
3	50	3	0.119	1.472
4	50	5	0.104	0.539
5	50	5	0.105	0.555
6	50	10	0.109	0.667
7	50	15	0.105	0.557
8	50	30	0.102	0.717
9	50	65	0.089	0.811
10	50	95	0.067	1.088
11	150	1	0.140	3.761
12	150	1	0.150	4.464
13	150	3	0.138	3.729
14	150	5	0.123	3.258
15	150	5	0.100	0.651
16	150	7	0.112	0.607
17	150	10	0.111	1.014
18	150	15	0.116	0.718
19	150	30	0.119	0.879
20	150	60	0.112	0.987
21	150	95	0.120	1.070

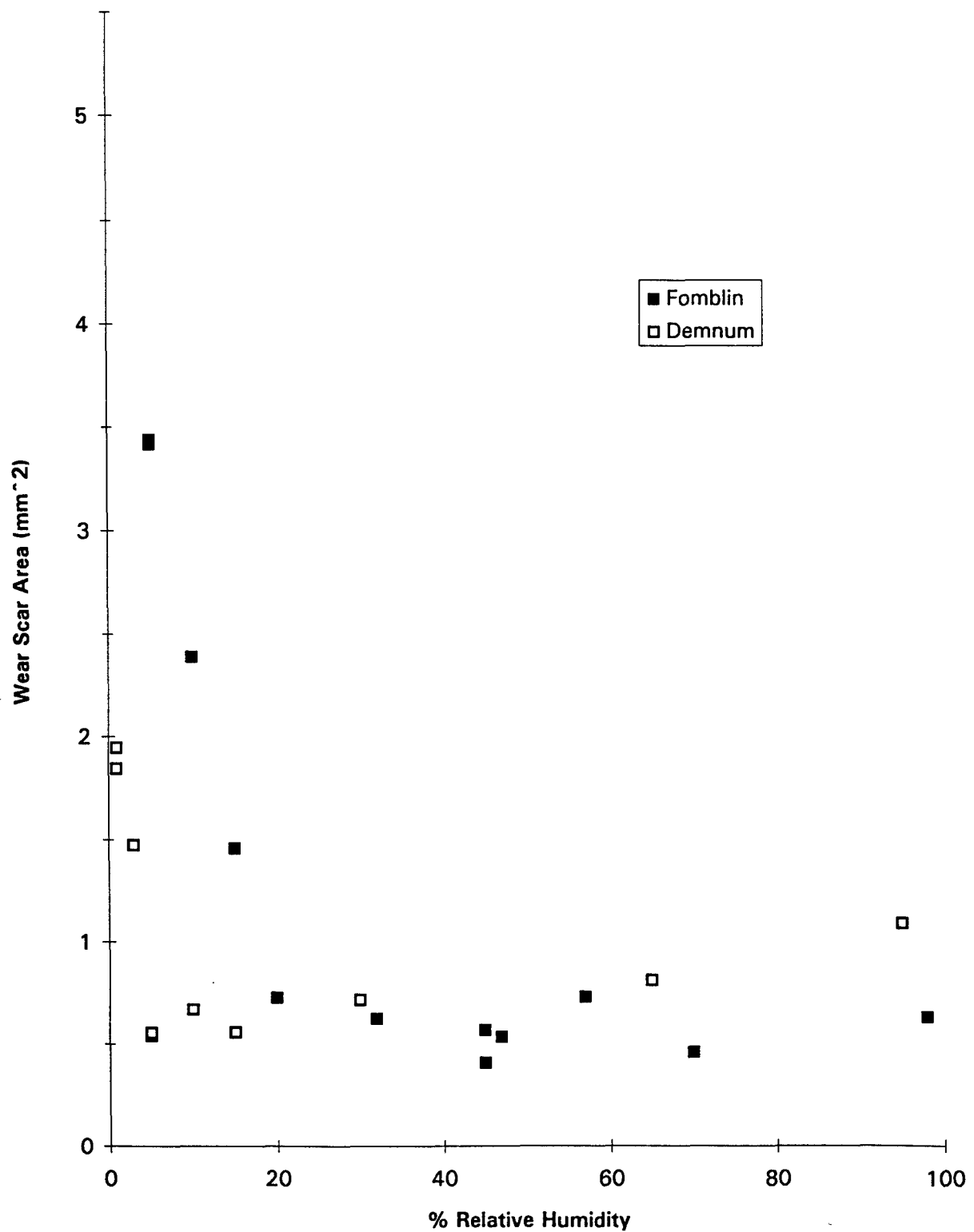Figure 1

Wear Scar Area vs Relative Humidity at 50 C

Figure 2

Wear Scar Area vs Relative Humidity at 150 C
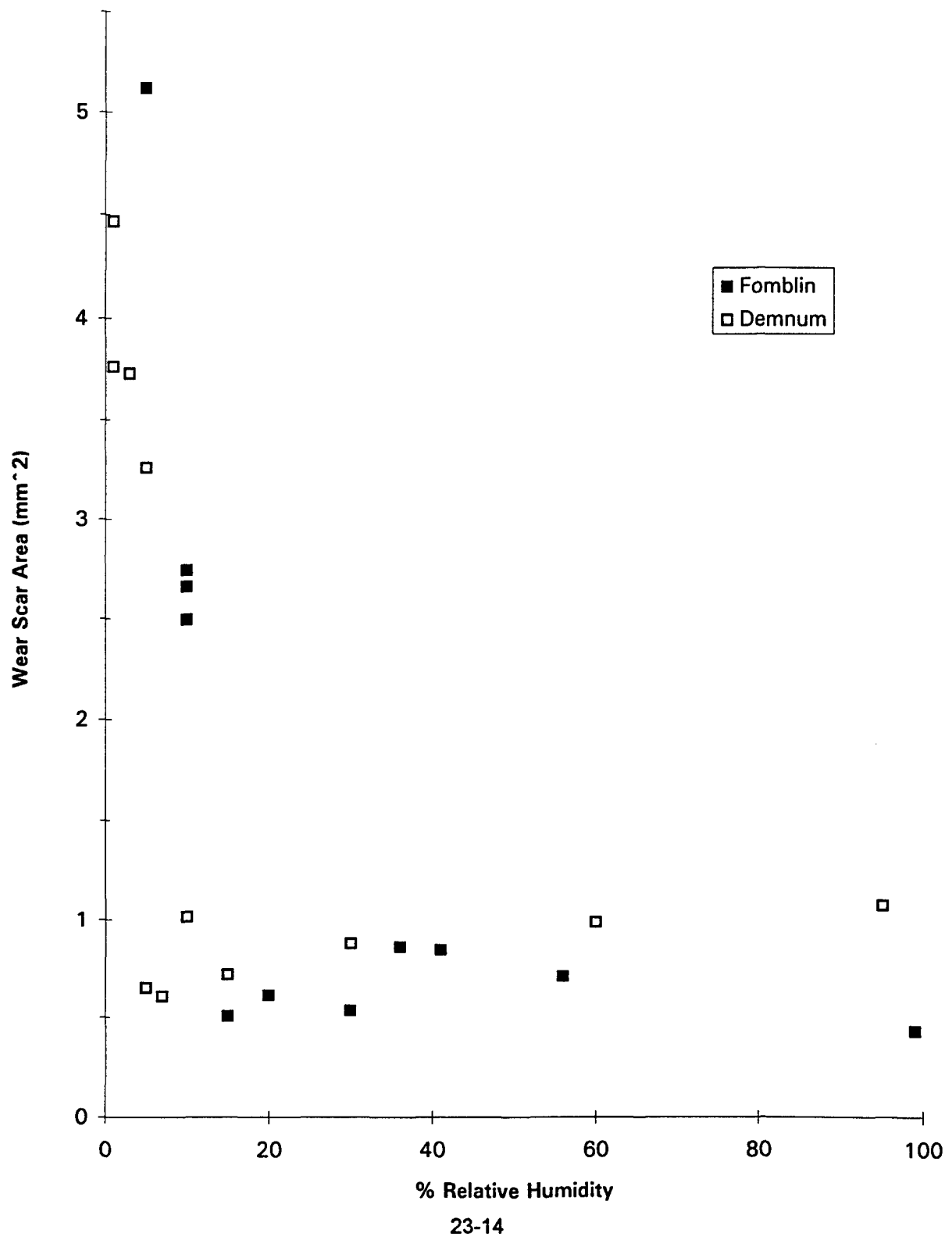
23-14

Figure 3

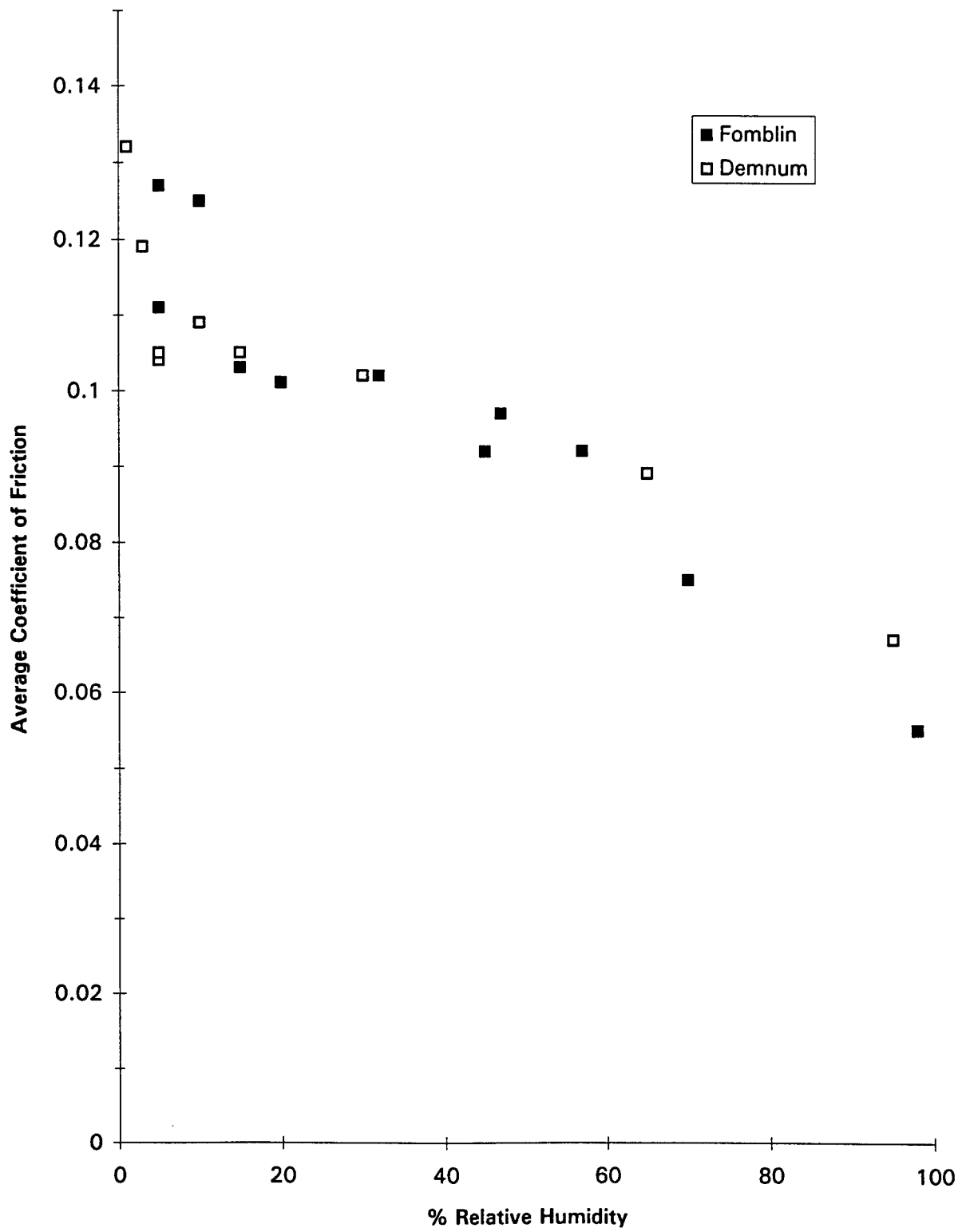## Average Coefficient of Friction vs Relative Humidity at 50 C

Figure 4

Average Coefficient of Friction vs Relative Humidity at 150 C